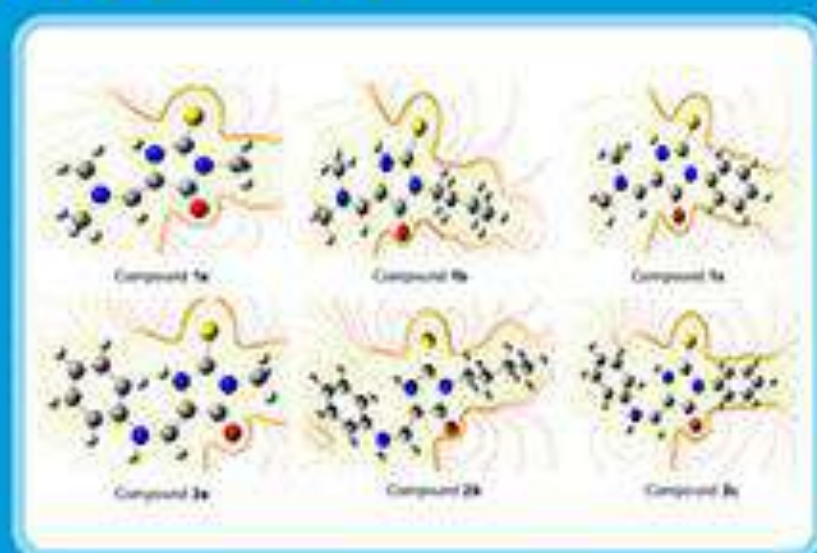


ISSN: 1411-9420 (print); 2460-1578 (online)

Indonesian Journal of Chemistry

Vol. 23, No. 6, December 2023



Approved by PDI TEA 1999
No. 65/M/KPT/2020

Indones. J. Chem.

Vol. 23

No. 6

PP. 1470-1757

Yogyakarta
December 2023

http://www.ijc.umsida.ac.id

Improving the Electrical Conductivity of the Composite Comprising Bismuth Oxide, Activated Carbon, and Graphite for Use as a Battery Anode

Yayuk Astuti*, Faradina Azahra Zaqia, Aulia Zahra Ekaningsih,
Gunawan Gunawan, and Adi Darmawan

Department of Chemistry, Faculty of Science and Mathematics, Diponegoro University,
Jl. Prof. Soedharto SH, Tembalang, Semarang 50275, Indonesia

* Corresponding author:

email: yayuk.astuti@live.undip.ac.id

Received: April 17, 2022

Accepted: June 13, 2023

DOI: 10.22146/ijc.74155

Abstract: This research is concerned with the synthesis and characterization of a composite material that may be used as a battery electrode. Bismuth oxide (Bi_2O_3) was synthesized from $\text{Bi}(\text{NO}_3)_3 \cdot 5\text{H}_2\text{O}$, Na_2SO_4 , and NaOH mixed with commercial activated carbon and graphite. The composite formation process was carried out using the hydrothermal method at 110°C for 5 h. The characterization data indicated the composites produced contained Bi_2O_3 with a monoclinic crystal system, and Bi_2O_3 particles were evenly distributed in the composite. The composites were characterized to be mesoporous, with the electrical conductivity reaching 10^{-1} S m^{-1} . The development of this composite material has potential applications in the field of energy storage, particularly in the development of battery anode.

Keywords: bismuth oxide; commercial activated carbon; graphite doping; battery anode

■ INTRODUCTION

Batteries are widely regarded as the most efficient and convenient power source for electronic devices, thanks to their adaptable structure and extended operational duration. They operate by transforming chemical energy from their active components into electrical energy through electrochemical reactions [1]. A good indicator of a working battery is the electrochemical cycle performance, which depends on the materials comprising the anode. Materials that are used as anodes must have good charge or ionic conductivity characteristics ($> 10^3 \text{ S cm}^{-1}$), large energy capacity, high coulomb output (A h g^{-1}), high effectiveness as a reducing agent, excellent stability, straightforward manufacturing, and affordability [1].

Bismuth oxide (Bi_2O_3) is a promising candidate for utilization as a battery anode due to its favorable electrochemical stability, strong redox reversibility, and substantial capacity, as demonstrated in recent research [2-4]. Notably, Bi_2O_3 boasts a volumetric capacity of $3765 \text{ mA h cm}^{-3}$, a potential difference of 2.8 V, and it offers the additional advantages of being non-toxic and

cost-effective [5]. However, in using Bi_2O_3 as an anode, an issue of low electrical conductivity value [6-7] that inhibits the conductivity of electrons in the battery needs to be overcome. This can be done through the addition of other materials, namely commercial activated carbon and graphite, which can increase electrical conductivity.

Utilizing commercially produced activated carbon sourced from coconut shells results in the creation of carbon materials characterized by minimal internal resistance and excellent electrical conductivity, as evidenced in reference [8]. These carbons offer substantial volumetric capacity and a significant potential difference, as indicated in reference [9]. In contrast, graphite exhibits remarkable electrical conductivity, a high energy density (implying a high specific capacity), and an exceptionally long cycle life [10]. Some researchers reported the electrical conductivity of graphite depends on the humidity [11] and grain composition [12]. Said characteristics of activated carbon and graphite are expected to be able to promote Bi_2O_3 ability as a battery anode.

Astuti et al. [13] conducted research on the synthesis and characterization of Bi_2O_3 /activated carbon

composite for battery anode. They employed the hydrothermal method with varying weight ratios of activated carbon to bismuth nitrate pentahydrate, specifically 2:1, 1:1, and 1:2. In their findings, the electrical conductivities were measured at 0.59×10^{-5} , 1.24×10^{-5} , and $0.51 \times 10^{-5} \text{ Sm}^{-1}$ for the respective ratios. These conductivity values are relatively low. It is plausible that the composite had not yet achieved optimal Bi_2O_3 formation, and carbon distribution appeared to be more dominant than Bi_2O_3 within the material.

Hence, there is a need to refine the synthesis process to create an improved Bi_2O_3 /activated carbon composite with a more precise composition. To date, no prior research has explored the synthesis of a composite consisting of Bi_2O_3 , activated carbon, and graphite. This current study aims to fill this research gap and hopes to offer valuable insights into the potential applications of metal oxide and carbon-based composites in electrode technology.

■ EXPERIMENTAL SECTION

Materials

The substances employed in this investigation encompassed $\text{Bi}(\text{NO}_3)_3 \cdot 5\text{H}_2\text{O}$ from Sigma Aldrich, distilled water, 60% H_3PO_4 (v/v), Na_2SO_4 powder, NaOH crystal sourced from Merck, as well as commercially available activated carbon (AC) and graphite.

Instrumentation

The instrumentations used in this research were Fourier transform infrared (Shimadzu IRAffinity-1), X-ray diffraction (XRD, Shimadzu 7000), scanning electron microscope (SEM, Jeol JED 6510LA model), thermogravimetric analysis (TGA, Mettler Toledo TGA/DSC 3+), gas sorption analysis (GSA, Tristar II 3020) and LCR meter (HIOKI 3532-50).

Procedure

Synthesis of Bi_2O_3 /AC/graphite composite

A total of 8 mmol of $\text{Bi}(\text{NO}_3)_3 \cdot 5\text{H}_2\text{O}$ was combined with 12 mmol of Na_2SO_4 , which were then dissolved in 40 mL of distilled water and stirred using a magnetic stirrer (IKA RH Basic KT/C) at 1500 rpm for 45 min. The solution was agitated using a magnetic stirrer (IKA RH

Basic KT/C) at 1500 rpm for 45 min. Subsequently, 40 mL of a 72 mmol NaOH solution [14] was added to the mixture. To this blend, 0.5 g of commercially available AC and 0.1 g of graphite were introduced. The resulting mixture was then introduced into a hydrothermal reactor and subjected to a temperature of 110 °C for a duration of 5 h. During this process, the reactants within the sealed container were heated by rapidly increasing temperature and pressure generated by water [6,15]. The temperature and pressure exerted by the water played a crucial role in facilitating the formation of the composite. Following the hydrothermal treatment, the mixture was cooled and subsequently filtered. The precipitate obtained from the filtration was dried in an oven (Fisher Scientific) at 110 °C for 60 min and subsequently sieved to a 100-mesh size. The same procedure was replicated for the synthesis of composites with varying amounts of $\text{Bi}(\text{NO}_3)_3 \cdot 5\text{H}_2\text{O}$, specifically 24 and 32 mmol. Accordingly, the composites synthesized with 8, 24, and 32 mmol of Bi_2O_3 in conjunction with commercial AC and graphite were designated as BCG1, BCG2, and BCG3, respectively.

Characterization of the Bi_2O_3 /AC/graphite composite material

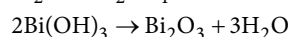
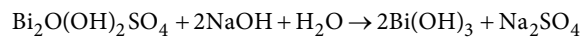
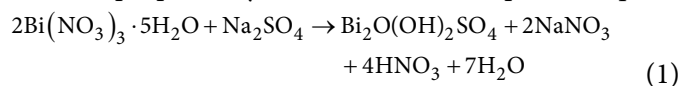
The resultant composite materials of Bi_2O_3 , AC, and graphite underwent a series of characterization processes. FTIR analysis was conducted to elucidate the functional groups present in the composites. FTIR measurements were carried out in the spectral range of 4000 to 400 cm^{-1} , with a scanning rate of 0.25 cm^{-1} , all at room temperature. Furthermore, the composites underwent XRD analysis to identify their crystalline structures. This analysis was performed by measuring 2θ angles with Cu-K α radiation ($\lambda = 0.15406 \text{ nm}$). The surface morphology and the spatial distribution of Bi_2O_3 and AC within the composite were assessed using a SEM. This analysis was conducted at magnifications of 100 \times and 5000 \times and was complemented by mapping and energy dispersive X-ray (EDX) analysis. Thermal decomposition and stability of the composite materials were investigated through TGA and differential thermogravimetric analysis (DTG). The samples were subjected to a temperature range of 40–800 °C at a

heating rate of 4 °C/min under a nitrogen (N₂) atmosphere. To assess the size and distribution of pores within the composites, GSA was conducted. This analysis involved the use of N₂ gas. Lastly, the conductivity of the composites was determined through LCR characterization. The samples were prepared in pellet form, with a diameter of 1.5 cm and a thickness ranging from 2 to 5 mm.

RESULTS AND DISCUSSION

Preparation of Graphite Doped Bi₂O₃/AC Composite

The synthesis of the composite consisting of Bi₂O₃, commercial AC, and graphite, with varying mole ratios of bismuth nitrate pentahydrate, was initiated by carrying out a reaction involving the precursor compounds Bi(NO₃)₃·5H₂O, Na₂SO₄, and NaOH. This procedure closely followed the protocol outlined by Wu et al. [14]. Subsequently, commercial AC and graphite were introduced into the solution, followed by thorough homogenization, before subjecting the mixture to hydrothermal heating. The formation mechanism of Bi₂O₃, as proposed by Wu et al. [14] underpinned Eq. (1).



The BCG1 composite product had grayish-black powder form, while the BCG2 and BCG3 composites showed gray color. The BCG3 had an agglomerated appearance, as shown in Fig. 1. The resulting coloration of the material exhibited a gray hue, which emerged as a result of the combination of the pale-yellow tint contributed by Bi₂O₃ [16] and the black color imparted by the presence of AC and graphite.

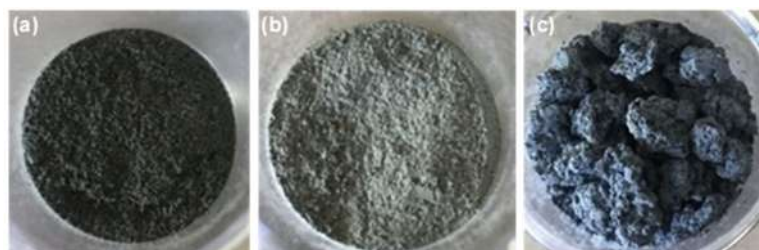


Fig 1. Composite products (a) BCG1, (b) BCG2, and (c) BCG3

Material Characterization

Functional group structure

FTIR characterization was conducted to determine the functional groups present in the composite sample. The FTIR spectra of the composite samples, along with pure Bi₂O₃, commercial AC, and graphite, are shown in Fig. 2. Fig. 2 presents the FTIR spectra of commercial AC, having absorption at wavenumbers of 1600–1475 cm⁻¹, denoting the C=C group [18] and 1320–1000 cm⁻¹, denoting C–O group [19]. In the absorption spectra for graphite, the presence of a C=C group is indicated at wavenumber 1633 cm⁻¹ [20]. Similar absorptions were also shown by each composite sample, with the C=C group in the absorption area of about 1626 and 1642 cm⁻¹ and the C–O group in the absorption area of about 1103 cm⁻¹.

The above data present that the three composite samples have almost the same pattern of absorptions with the presence of a fairly sharp absorption in the area

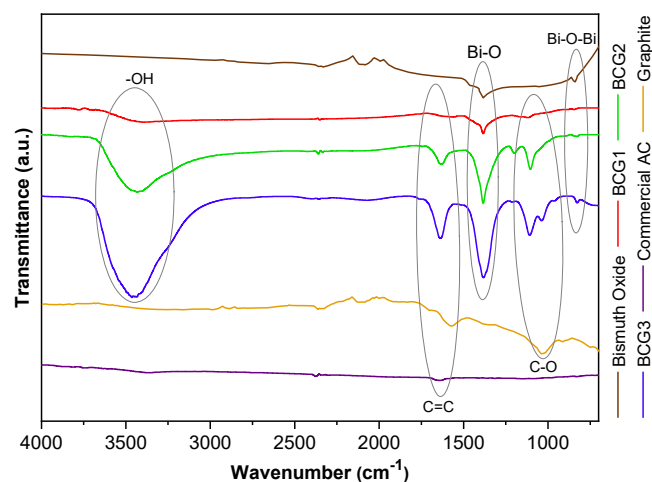


Fig 2. FTIR spectra of composite products, pure bismuth oxide [17], commercial AC [15], and graphite [15]

around 820–842 cm^{-1} , indicating the Bi–O–Bi group and the absorption in the area around 1383 cm^{-1} , which indicates the Bi–O group. The same absorption was also shown by the pure Bi_2O_3 samples [13], i.e., the absorption of Bi–O–Bi groups in the 829 cm^{-1} area [21], and at the wavenumber of about 1380 cm^{-1} , showing the presence of a Bi–O group [13,22]. This implies that Bi_2O_3 was formed in each composite sample. Additionally, the three composite samples contain O–H groups observed at the wavenumber of about 3400 cm^{-1} [23]. It is expected due to the by-product and imperfect reaction as presented in Eq. (1). The three composite samples had the same group absorption, however, with different intensities. The comprehensive data pertaining to the functional groups present in the three composite products, namely pure

Bi_2O_3 , commercial AC, and graphite, as determined through FTIR testing, are detailed in Table 1.

Crystal structure

Characterization of composite samples using XRD was carried out to determine the success of the formation of Bi_2O_3 in the composite and to determine the crystal structure of Bi_2O_3 in the composite. The results of the XRD diffractograms of all the composites made and the comprising components can be seen in Fig. 3. The XRD characterization results (Fig. 3) show that the diffractogram of the BCG1 composite has a notable match with the α - Bi_2O_3 diffractogram. The BCG1 composite has high peak 2θ values at 27.386°, 33.248°, and 46.309°. The 2θ values are almost similar to the 2θ values of α - Bi_2O_3 peaks at 27.377°, 33.039°, and 46.305° (JCPDS no. 41-1449).

Table 1. Functional groups identification from the FTIR analysis

Functional group	Wavenumber (cm^{-1})					
	Sample			Bismuth oxide	Commercial activated carbon	Graphite
	BCG1	BCG2	BCG3			
Bi–O	1383.54	1383.61	1383.07	1400–1300	-	-
Bi–O–Bi	842.50	841.60	820.60	900–700	-	-
C–O	1103.39	1104.09	1108.28	-	1032.86	-
C=C	1626.10	1637.36	1630.14	-	1570.01	1642.90
–OH	3399.10	3433.74	3464.66	-	-	-

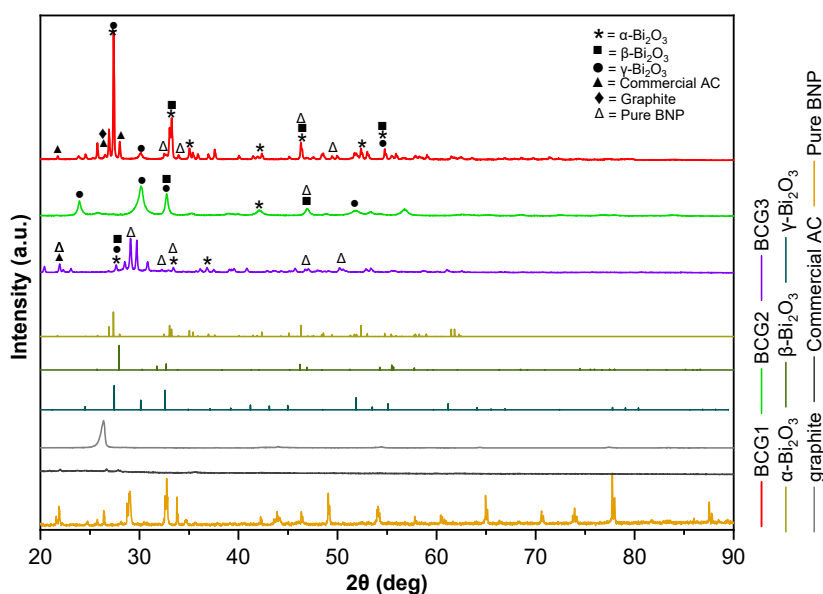


Fig 3. Diffractograms of composite products, Bi_2O_3 (JCPDS), bismuth nitrate pentahydrate [6], commercial AC [15], and graphite [15]

The BCG2 composite diffractogram shows that there are sharp peaks that are almost similar to the cubic crystal system (γ - Bi_2O_3), though at low intensity, namely at 2θ values of 30.159° , 32.746° , and 51.788° (JCPDS no. 27-0052). The sharp but low-intensity peaks indicate that Bi_2O_3 with a cubic crystal system (γ - Bi_2O_3) may have been formed but to a small degree. Wu et al. [14] on the XRD diffractogram of the by-product (Eq. (1)) in the form of $\text{Bi}_2(\text{OH})_2\text{SO}_4$ presented sharp peaks at the value of 2θ around 30.159° to 32.746° , similar to the composite. The diffractogram results indicate that the BCG2 composite still has residual reaction by-products in the form of $\text{Bi}_2(\text{OH})_2\text{SO}_4$, meaning that less Bi_2O_3 was produced.

The BCG3 composite diffractogram shows the presence of sharp peaks with considerable intensity at the 2θ values of 21.941° , 29.099° , 32.904° , and 33.425° , which matched the bismuth nitrate pentahydrate diffractogram peaks. These peaks are also thought to be the peaks of the by-product $\text{Bi}_2(\text{OH})_2\text{SO}_4 + \text{Bi}(\text{OH})_3$ [14] formed during the reaction (Eq. (1)). The BCG3 composite diffractogram also displays small peaks at 27.651° , 33.425° , and 36.824° having a good match with the α - Bi_2O_3 diffractogram (JCPDS no. 41-1449), indicating that the BCG3 composite contained more $\text{Bi}(\text{NO}_3)_3 \cdot 5\text{H}_2\text{O}$ (BNP) precursor and reaction by-products compared to Bi_2O_3 .

Morphology and particle distribution

In Fig. 4, it can be observed that the BCG1 composite exhibited a morphology characterized by rod-shaped particles, with lengths ranging from 6.6 to 11.2 μm and widths spanning 1.4 to 2.4 μm . This rod-like particle structure is indicative of the presence of Bi_2O_3 within the composite, consistent with findings reported by Wu et al. [14]. Meanwhile, the BCG2 composite showed irregular particle shapes, with few that were shaped like rods with a length ranging from 14–35 μm and a width between 4–9 μm . Alternatively, the BCG3 composite showed particles having irregular shapes and agglomeration, with a length between 2–5.4 μm and a width of about 1–4 μm . Furthermore, Fig. 5 presents the SEM mapping images of the three composite samples.

In Fig. 5, the distribution of elements, including bismuth (Bi), carbon (C), oxygen (O), and silicon (Si), within the BCG1, BCG2, and BCG3 composites is depicted. These elements are denoted by the colors red, green, yellowish green, and blue, respectively. It is evident that in the BCG1 composite, the distribution of Bi and C appears relatively balanced and evenly spread across the material's surface. In the case of BCG2, the surface is noticeably dominated by the presence of the Bi element.

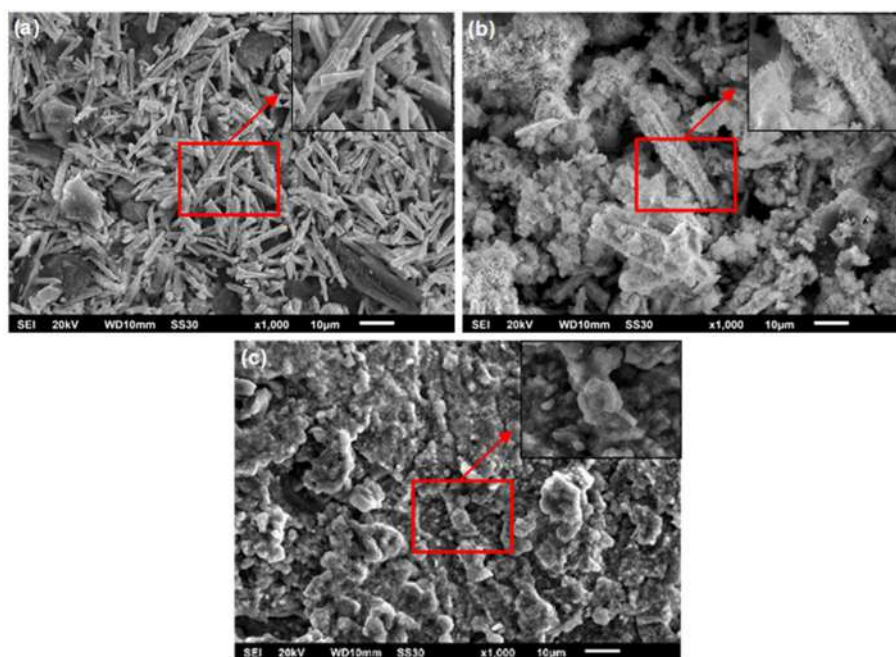


Fig 4. SEM images of composites (a) BCG1, (b) BCG2, and (c) BCG3

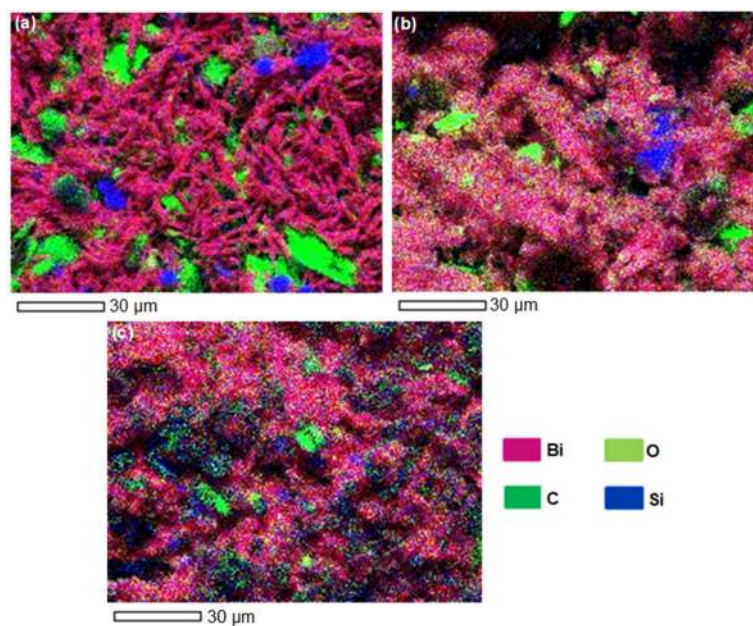


Fig 5. Mapping images of composites (a) BCG1, (b) BCG2, and (c) BCG3

Conversely, in BCG3, both Bi and O elements are prevalent on the sample surface, making the presence of C less conspicuous. The EDX data presented in Fig. 6 corroborates the distribution patterns of these elements.

Based on the EDX results shown in Fig. 6, the three composite samples contained elements such as C, Bi, O, and a small amount of Na and Si. The C element indicated the presence of carbon in the composite. The Bi and O elements in BCG1 originated from Bi_2O_3 formed, as suggested by the XRD results (Fig. 3). The presence of a small amount of Na is thought to have come from the remaining precursor (NaOH), whereas the Si element is assumed to have come from the activated carbon. The elements in the BCG2 composite are thought to have originated from the precursor materials and reaction by-products, as per the XRD data where the Bi_2O_3 formed in BCG2 was very small. Furthermore, in the EDX results of the BCG3 composite, in addition to the C, Bi, O, Na, and Si elements, the elements of N, P, and S were also present. Elements such as Bi, O, N, Na, and S are thought to have come from Eq. (1) by-product or the left-over precursors as indicated by the XRD results (Fig. 3). Overall, the C element decreased in amount with increasing mole variation of BNP, causing the distribution of the C element to be increasingly invisible on the surface of the material in the mapping results shown in Fig. 5.

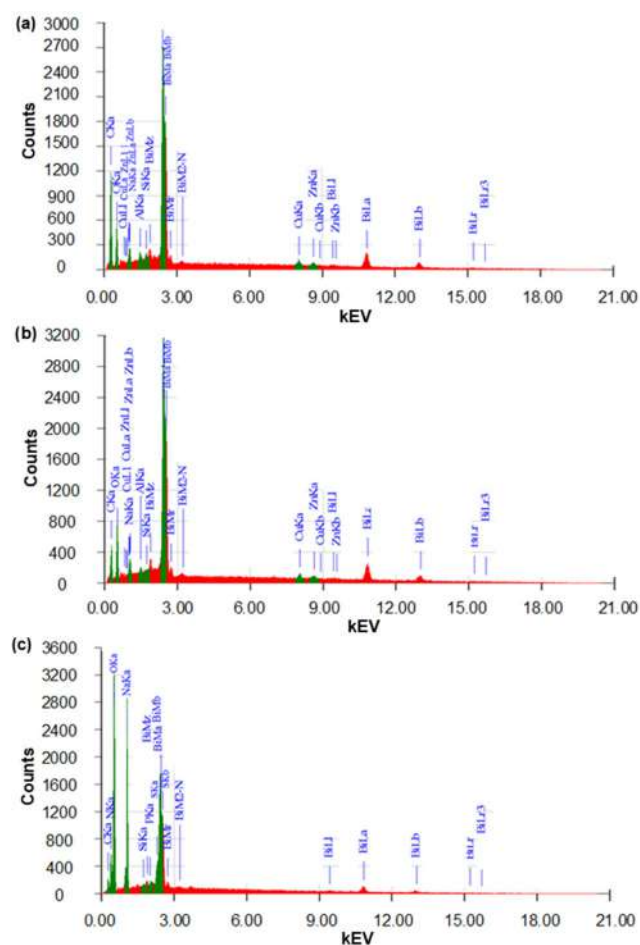


Fig 6. EDX spectra of composites (a) BCG1, (b) BCG2, and (c) BCG3

TGA-DTG composite characterization

TGA-DSC analysis was employed to assess the decomposition mechanism and thermal stability of the composite materials. The TGA-DTG results for these composites are presented in Fig. 7. Based on the results, the composite BCG1 and BCG2 underwent five stages of the decomposition process, while the BCG3 composite experienced four stages of decomposition. Stage I of the three composites occurred at a temperature of 200–310 °C, denoting the removal process of several functional groups such as $-\text{COO}-$, $-\text{CO}-$, and $-\text{OH}-$ from graphite [24] as well as materials other than carbon such as cellulose and hemicellulose from AC [25].

In the second stage, which occurred within the temperature range of 250 to 380 °C, it is presumed that the process involved the removal of amorphous residues

[26], including substances such as NaNO_3 , NaOH , and SO_4^{2-} . Notably, in BCG3, there was a more substantial weight loss during this stage in comparison to BCG1 and BCG2. This suggests that the BCG3 composite experienced a greater decomposition of amorphous residues, possibly due to the presence of reaction by-products such as $\text{Bi}_2\text{O}(\text{OH})_2\text{SO}_4$ and the BNP precursor, as indicated by the XRD results (Fig. 3).

Stage III occurred at a temperature range of 300–400 °C, denoting the mass transformation process of the precursors to form Bi_2O_3 [27]. In stage IV, composites undergo a transformation from a monoclinic structure ($\alpha\text{-Bi}_2\text{O}_3$) into a body-centered cubic structure ($\gamma\text{-Bi}_2\text{O}_3$) at a temperature of about 500 °C. Stage V indicates the retransformation of the body-centered cubic ($\gamma\text{-Bi}_2\text{O}_3$) structure into the monoclinic structure ($\alpha\text{-Bi}_2\text{O}_3$) [28] at

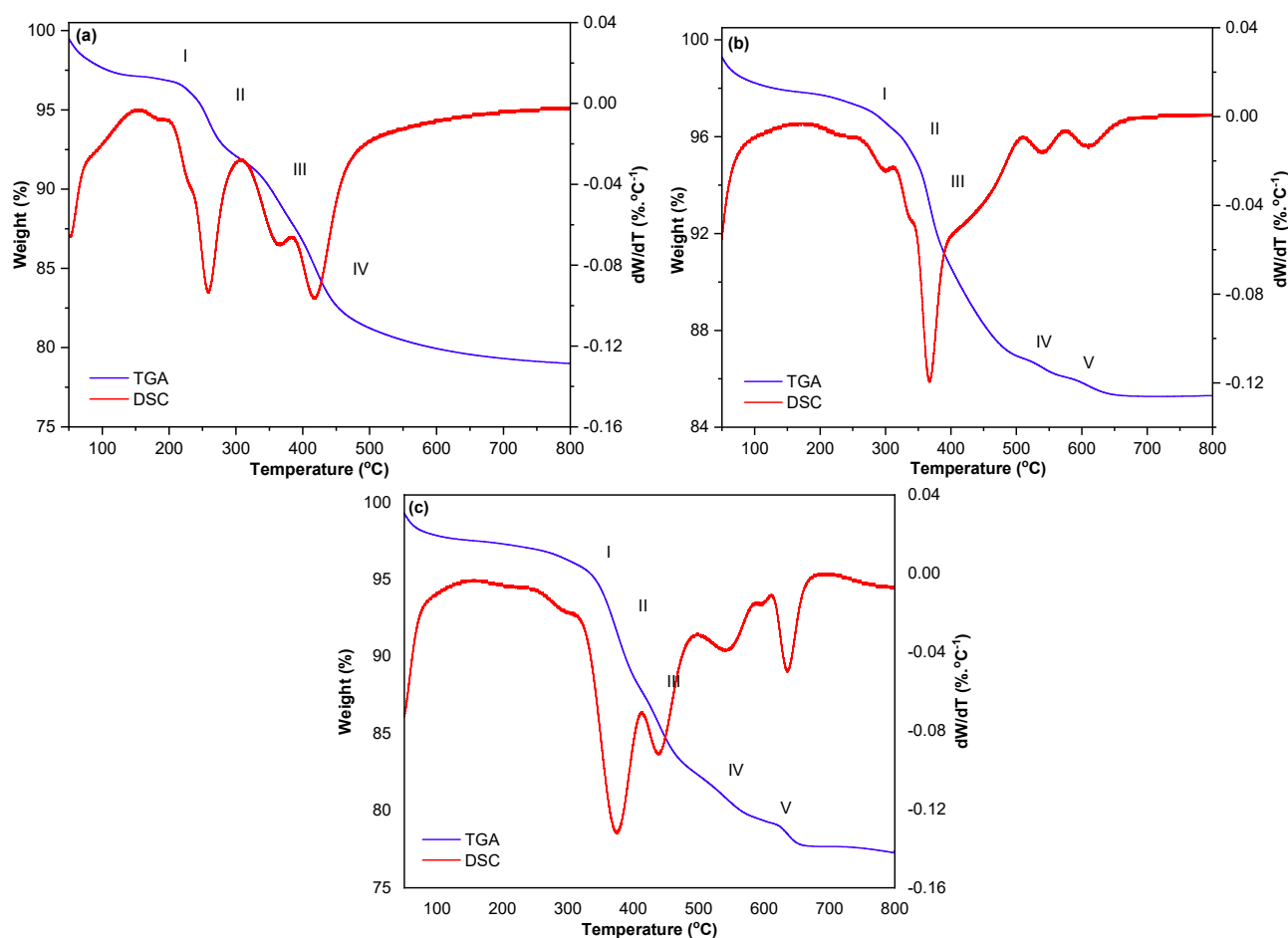


Fig 7. TGA-DTG results of composites (a) BCG1, (b) BCG2, and (c) BCG3

a temperature of about 600 °C. The TG-DTG curves of the three composite samples show that thermal stability was obtained at ≥ 700 °C.

Surface area and pore size

Fig. 8 presented the evidence that the three composite samples exhibit similar isotherm patterns, specifically of type IV, which is characterized by the presence of a hysteresis loop. The presence of this hysteresis pattern signifies that the samples possess a porous nature. The results obtained from GSA analysis for the BCG1, BCG2, and BCG3 composites are summarized in Table 2.

Table 2 reveals that all three composite samples have mesoporous structures, featuring pore radii ranging from 3 to 50 nm [29]. As reported in a study by Agrawal et al. [30] on the production and characterization of nitrogen-

doped hard carbon as a battery anode material, porosity plays a significant role in influencing a sample's conductivity. Samples with high porosity, meaning they contain numerous small-sized pores, tend to exhibit lower conductivity due to increased resistance caused by the abundance of small pores. This correlation is supported by the GSA and LCR characterization results for the BCG3 composite, which possesses the largest pore size at 15.168 nm. Interestingly, despite having a small pore volume and surface area (0.011 cm³/g and 2.792 m²/g,

Table 2. Surface area and pore size

Sample	S_{BET} (m ² /g)	V_{pore} (cm ³ /g)	Pore size (nm)
BCG1	2.311	0.007	12.822
BCG2	5.594	0.016	11.664
BCG3	2.792	0.011	15.168

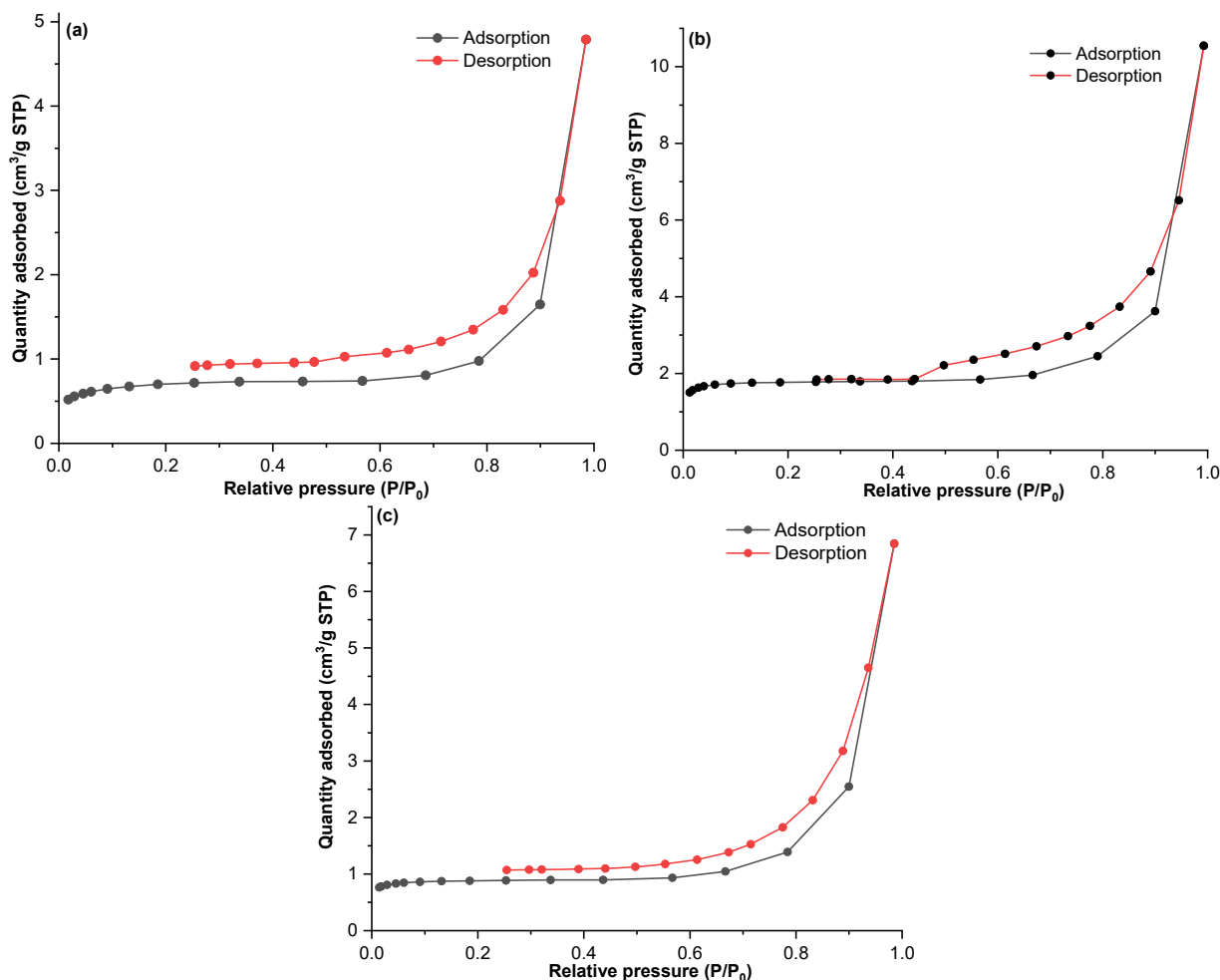


Fig 8. N₂ adsorption/desorption isotherm graphs of composites (a) BCG1, (b) BCG2, (c) BCG3

Table 3. LCR Meter conductivity measurement

Sample	Conductivity value ($S\ m^{-1}$)
BCG1	0.02×10^{-1}
BCG2	0.01×10^{-1}
BCG3	1.02×10^{-1}
Commercial AC	7.41×10^{-6}
Bi_2O_3 [7]	1.55×10^{-7}
Graphite	4.03×10^1

respectively), the BCG3 composite exhibits low measured resistance and high sample conductivity. These findings suggest that the BCG3 composite has a relatively low porosity or a small number of pores, resulting in enhanced conductivity.

Electrical conductivity

The conductivity values of the BCG1, BCG2, and BCG3 composites, Bi_2O_3 , commercial AC and graphite are shown in Table 3. As presented in Table 3, the conductivity values of commercial AC and graphite are higher than the conductivity values of pure Bi_2O_3 . Correspondingly, the conductivity values of the synthesized products were higher compared to pure Bi_2O_3 , implying that the addition of AC and graphite can increase conductivity.

The composite conductivity values from the highest to the lowest were BCG3, BCG1, and BCG2. The conductivity value obtained can be related to the crystallinity of the composite produced based on the XRD results (Fig. 3). High level of composite crystallinity causes the resulting conductivity value to also be higher [31-32]. BCG2 composite has the lowest conductivity value because the crystal content of Bi_2O_3 contained in the composite was very small (see Fig. 3). The low crystallinity level of the composite caused the arrangement of the lattice between the atoms to be irregular, and the mobility of the electrons is, therefore, inhibited and the value of the electrical conductivity is low.

The BCG1 composite has a higher conductivity value than BCG2, although not too significant. This is attributed to the balanced composition of precursor materials for Bi_2O_3 formation and the addition of AC in the BCG1 composite. Consequently, Bi_2O_3 formation (as observed in Fig. 2 and 3) is uniformly distributed across the material's surface (as depicted in Fig. 5). This uniform

distribution of Bi_2O_3 enhances electron mobility within the material, resulting in an increased conductivity value. Conversely, the BCG3 composite exhibits notably high conductivity because of the impurities present in the composite, according to the XRD results shown in Fig. 3.

CONCLUSION

Bi_2O_3 /AC/graphite composites have been successfully synthesized by the hydrothermal method. The composition of the precursors used affects the formation of composites and, thus, their characteristics which can be seen from the presence of functional groups, crystal structure, morphology, surface area, pore size, and particle distribution. Additionally, identification of the thermal stability of the products formed presented different stages of thermal decomposition, although, in the end, the electrical conductivity values of the three samples do not differ significantly.

ACKNOWLEDGMENTS

The authors would like to thank Diponegoro University for the research funding provided through the World Class Research Universitas Diponegoro (WCRU) 2023 scheme with grant No. 118-12/UN7.6.1/PP/2021 in the fiscal year 2023.

AUTHOR CONTRIBUTIONS

Yayuk Astuti did the conceptualization, methodology, investigation, resources, data curation, writing, supervision, review and editing. Faradina Azahra Zaqia did the experiment, data curation, and writing draft preparation. Aulia Zahra Ekaningsih did the data curation, validation, review and editing. Gunawan did the validation, review and editing. Adi Darmawan did the validation, review and editing. All authors have read and agreed to the published version of the manuscript.

REFERENCES

- [1] Linden, D., and Reddy, T.B., 2002, *Linden's Handbook of Batteries*, 4th Ed., McGraw-Hill Education, New York, US.
- [2] Li, Y., Song, J., Ji, Y., Lu, X., Tian, Q., Chen, J., and Sui, Z., 2022, Bismuth/bismuth trioxide with a dual-

- carbon support for high and long life lithium storage, *J. Phys. Chem. Solids*, 163, 110562.
- [3] Ud Din, M.A., Li, C., Zhang, L., Han, C., and Li, B., 2021, Recent progress and challenges on the bismuth-based anode for sodium-ion batteries and potassium-ion batteries, *Mater. Today Phys.*, 21, 100486.
- [4] Fu, H., Shi, C., Nie, J., Wang, J., and Yao, S., 2022, Bi₂O₃ nanospheres coated in electrospun carbon spheres derived Bi@C used as anode materials for lithium-ion batteries, *J. Alloys Compd.*, 918, 165666.
- [5] Li, Y., Trujillo, M.A., Fu, E., Patterson, B., Fei, L., Xu, Y., Deng, S., Smirnov, S., and Luo, H., 2013, Bismuth oxide: A new lithium-ion battery anode, *J. Mater. Chem. A*, 1 (39), 12123–12127.
- [6] Astuti, Y., Mei, R., Darmawan, A., Arnelli, A., and Widiyandari, H., 2022, Enhancement of electrical conductivity of bismuth oxide/activated carbon composite, *Sci. Iran.*, 29 (6), 3119–3131.
- [7] Astuti, Y., Musthafa, F., Arnelli, A., and Nurhasanah, I., 2022, French fries-like bismuth oxide: Physicochemical properties, electrical conductivity and photocatalytic activity, *Bull. Chem. React. Eng. Catal.*, 17 (1), 146–156.
- [8] Taer, E., Taslim, R., Putri, A.W., Apriwandi, A., and Agustino, A., 2018, Activated carbon electrode made from coconut husk waste for supercapacitor application, *Int. J. Electrochem. Sci.*, 13 (12), 12072–12084.
- [9] Kim, T., Jo, C., Lim, W.G., Lee, J., Lee, J., and Lee, K.H., 2016, Facile conversion of activated carbon to battery anode material using microwave graphitization, *Carbon*, 104, 106–111.
- [10] Zhang, H., Yang, Y., Ren, D., Wang, L., and He, X., 2021, Graphite as anode materials: Fundamental mechanism, recent progress and advances, *Energy Storage Mater.*, 36, 147–170.
- [11] Mahtab, S., Joshi, P., Arya, B., Zaidi, M.G.H., and Siddiqui, T.I., 2020, Effect of humidity on electrical conductivity of graphite nanocomposite based electrodes: A review, *Mater. Sci. Res. India*, 17 (1), 8–15.
- [12] Budko, O., Butenko, O., Chernysh, O., Khomenko, V., Tverdokhlib, V., and Barsukov, V., 2022, Effect of grain composition of natural graphites on electrical conductivity of graphite-based composite materials, *Mater. Today: Proc.*, 50, 535–538.
- [13] Astuti, Y., Aprialdi, F., Arnelli, A., and Haryanto, I., 2019, Synthesis of activated carbon/bismuth oxide composite and its characterization for battery electrode, *IOP Conf. Ser.: Mater. Sci. Eng.*, 509 (1), 012153
- [14] Wu, C., Shen, L., Huang, Q., and Zhang, Y.C., 2011, Hydrothermal synthesis and characterization of Bi₂O₃ nanowires, *Mater. Lett.*, 65 (7), 1134–1136.
- [15] Astuti, Y., Farihah, D.N., Ekaningsih, A.Z., and Darmawan, A., 2023, Electrochemical performance of one-pot hydrothermal-derived bismuth oxide/commercial activated carbon/graphite composite, *Mater. Sci. Technol.*, 39 (14), 1802–1815.
- [16] Astuti, Y., Fauziyah, A., Nurhayati, S., Wulansari, A.D., Andianingrum, R., Hakim, A.R., and Bhaduri, G., 2016, Synthesis of α -bismuth oxide using solution combustion method and its photocatalytic properties, *IOP Conf. Ser.: Mater. Sci. Eng.*, 107 (1), 012006.
- [17] Astuti, Y., Elesta, P.P., Widodo, D.S., Widiyandari, H., and Balgis, R., 2020, Hydrazine and urea fueled-solution combustion method for Bi₂O₃ synthesis: Characterization of physicochemical properties and photocatalytic activity, *Bull. Chem. React. Eng. Catal.*, 15 (1), 104–111.
- [18] Das, D., Samal, D.P., and Meikap, B.C., 2015, Preparation of activated carbon from green coconut shell and its characterization, *J. Chem. Eng. Process Technol.*, 6 (5), 1–7.
- [19] Sastrohamidjojo, H., 2018, *Dasar-dasar Spektroskopi*, Gajah Mada University Press, Yogyakarta, Indonesia.
- [20] Das, T.R., Patra, S., Madhuri, R., and Sharma, P.K., 2018, Bismuth oxide decorated graphene oxide nanocomposites synthesized via sonochemical assisted hydrothermal method for adsorption of cationic organic dyes, *J. Colloid Interface Sci.*, 509, 82–93.

- [21] Gondal, M.A., Saleh, T.A., and Drmosh, Q., 2012, Optical properties of bismuth oxide nanoparticles synthesized by pulsed laser ablation in liquids, *Sci. Adv. Mater.*, 4 (3-4), 507–510.
- [22] Bandyopadhyay, S., and Dutta, A., 2017, Thermal, optical and dielectric properties of phase stabilized δ - Dy-Bi₂O₃ ionic conductors, *J. Phys. Chem. Solids*, 102, 12–20.
- [23] Ikemoto, Y., Harada, Y., Tanaka, M., Nishimura, S., Murakami, D., Kurahashi, N., Moriwaki, T., Yamazoe, K., Washizu, H., Ishii, Y., and Torii, H., 2022, Infrared spectra and hydrogen-bond configurations of water molecules at the interface of water-insoluble polymers under humidified conditions, *J. Phys. Chem. B*, 126 (22), 4143–4151.
- [24] Deng, Z., Liu, T., Chen, T., Jiang, J., Yang, W., Guo, J., Zhao, J., Wang, H., and Gao, L., 2017, Enhanced electrochemical performances of Bi₂O₃/rGO nanocomposite via chemical bonding as anode materials for lithium ion batteries, *ACS Appl. Mater. Interfaces*, 9 (14), 12469–12477.
- [25] Nurdiansyah, H., and Susanti, D., 2013, Pengaruh variasi temperatur karbonisasi dan temperatur aktivasi fisika dari elektroda karbon aktif tempurung kelapa dan tempurung kluwak terhadap nilai kapasitansi electric double layer capacitor (EDLC), *J. Tek. ITS*, 2 (1), 13–18.
- [26] Zhang, J., and Delichatsios, M., 2011, TGA maximum heat release rate and mass loss rate and comparison with the cone calorimeter, *Fire Saf. Sci., Proc. Int. Symp.*, 10, 1333–1346.
- [27] Ma, M.G., Zhu, J.F., Sun, R.C., and Zhu, Y.J., 2010, Microwave-assisted synthesis of hierarchical Bi₂O₃ spheres assembled from nanosheets with pore structure, *Mater. Lett.*, 64 (13), 1524–1527.
- [28] Klinkova, L.A., Nikolaichik, V.I., Barkovskii, N.V., and Fedotov, V.K., 2007, Thermal stability of Bi₂O₃, *Russ. J. Inorg. Chem.*, 52 (12), 1822–1829.
- [29] Thommes, M., Kaneko, K., Neimark, A.V., Olivier, J.P., Rodriguez-Reinoso, F., Rouquerol, J., and Sing, K.S., 2015, Physisorption of gases, with special reference to the evaluation of surface area and pore size distribution (IUPAC Technical Report), *Pure Appl. Chem.*, 87 (9-10), 1051–1069.
- [30] Agrawal, A., Janakiraman, S., Biswas, K., Venimadhav, A., Srivastava, S.K., and Ghosh, S., 2019, Understanding the improved electrochemical performance of nitrogen-doped hard carbons as an anode for sodium ion battery, *Electrochim. Acta*, 317, 164–172.
- [31] Alves, A.M., Cavalcanti, S.N., da Silva, M.P., Freitas, D.M., Agrawal, P., and de Mélo, T.J.A., 2021, Electrical, rheological, and mechanical properties copolymer/carbon black composites, *J. Vinyl Addit. Technol.*, 27 (2), 445–458.
- [32] Kim, M., Lee, C., and Jang, J., 2014, Fabrication of highly flexible, scalable, and high-performance supercapacitors using polyaniline/reduced graphene oxide film with enhanced electrical conductivity and crystallinity, *Adv. Funct. Mater.*, 24 (17), 2489–2499.

Involvement of Fenton Reaction on Biodecolorization and Biodegradation of Methylene Blue Dye by Brown Rot Fungi *Daedalea dickinsii*

Adi Setyo Purnomo*, Alya Awinatul Rohmah, Weni Sri Ekowati,
Hamdan Dwi Rizqi, and Asranudin Asranudin

Department of Chemistry, Faculty of Science and Data Analytics, Institut Teknologi Sepuluh Nopember (ITS),
Kampus ITS Sukolilo, Surabaya 60111, Indonesia

* Corresponding author:

email: adi_setyo@chem.its.ac.id

Received: September 12, 2022

Accepted: July 3, 2023

DOI: 10.22146/ijc.77689

Abstract: The disposal of dye wastewater has become a major global concern. Meanwhile, microorganisms have shown high potential in the treatment of wastewater pollutants. In this study, the involvement of the Fenton reaction in the biodecolorization and biodegradation of methylene blue (MB) by the brown rot fungus *Daedalea dickinsii* was investigated. Subsequently, *D. dickinsii* is a fungus capable of producing hydroxyl radicals ($\bullet\text{OH}$). This experiment was conducted with an initial MB concentration of 75 mg/L, and different incubation times of 0, 7, 14, 21, and 28 d respectively. The result showed that the Fenton reaction played an important role, and this was demonstrated by the addition of FeSO_4 as a Fe^{2+} source. The removal of MB by *D. dickinsii* with the addition of Fe^{2+} reached 91.454% at 28 d in a mineral salt medium. It was higher compared to *D. dickinsii* culture treatment without Fe^{2+} addition, 86.427%. Furthermore, the metabolic degradation product was analyzed using LC-TOF/MS and identified as 2-amino-3-hydroxy-5-(methylamino) benzenesulfonic acid and N-(3,4-dihydroxy phenyl)-N-methyl formamide.

Keywords: decolorization; degradation; *Daedalea dickinsii*; methylene blue; Fenton reaction

■ INTRODUCTION

Synthetic dyes are widely used in various industrial sectors, such as textiles, paper, cosmetics, and leather, due to their long-term stability, low cost, and ability to produce derivative colors [1]. However, it is undeniable that these industries also generate dye wastewater, which can cause severe environmental problems. This dye wastewater is toxic and harmful to aquatic life when it is not properly treated, as it reduces light penetration and hinders the photosynthesis process in water bodies [2]. Moreover, the accumulation of toxic synthetic dyes in animals and human bodies can pose health risks [3], particularly as many dyes contain heavy metals and are carcinogenic [4].

Methylene blue (MB) is a synthetic dye with a stable molecular structure commonly used for coloring textiles such as wool and silk, as well as microorganisms [4]. To prevent its discharge into the environment, it is important

to carry out pre-treatment for removing MB. Various physical and chemical methods can be used to eliminate dye effluents from the environment through adsorption, flocculation, filtration, and irradiation [5]. However, they have some drawbacks, such as high cost, limited efficiency, and potentially produced hazardous by-products [5]. Meanwhile, the biological method using microorganisms or enzymes is categorized as an eco-friendly and costs less method [6].

Brown rot fungi (BRF) are functional microorganisms that contribute to biomass recycling and soil fertility by breaking down wooden structures such as hemicellulose and cellulose. However, BRF cannot degrade lignin as they do not produce ligninolytic enzymes [7]. BRF produces hydrogen peroxide (H_2O_2) and utilizes Fe^{2+} from the media and substrate to carry out the Fenton reaction, leading to hydroxyl radical ($\bullet\text{OH}$) production. These fungi were

reported using hydroxyl radicals produced through the Fenton reaction ($\text{Fe}^{2+} + \text{H}_2\text{O}_2$) to degrade xenobiotic compounds [8]. Previous studies have shown that BRF species such as *Gloeophyllum trabeum*, *Fomitopsis pinicola*, and *Daedalea dickinsii* can degrade 1,1,1-trichloro-2,2-bis(4-chlorophenyl) ethane (DDT) by the involvement of Fenton reaction [9]. Moreover, *G. trabeum* also could improve lignocellulose degradation efficiency [10]. BRF isolated from sludge of textile industry effluent can also eliminate azo dyes acid red and orange II [11].

BRF *D. dickinsii* was also successfully decolorized and degraded MB [12]. However, the involvement of the Fenton reaction was not analyzed yet. Therefore, in this study, a further experiment involving MB removal by the Fenton reaction produced by *D. dickinsii* was observed. This was induced by adding Fe^{2+} to the treatment media (MSM), and there may be confirmation that the Fenton reaction plays a role in MB degradation. It was also supported by LC-TOF/MS for knowledge of its degradation product. Moreover, the degradation pathway was also proposed in this study.

■ EXPERIMENTAL SECTION

Materials

In this experiment, MB and Potato dextrose agar (PDA) media were purchased from Merck. Potato dextrose broth (PDB) media was purchased from Himedia. Furthermore, all of the Merck chemicals including magnesium sulfate (MgSO_4), calcium chloride dihydrate ($\text{CaCl}_2 \cdot 2\text{H}_2\text{O}$), boric acid (H_3BO_3), cobalt sulfate ($\text{CoSO}_4 \cdot 7\text{H}_2\text{O}$), copper sulfate pentahydrate ($\text{CuSO}_4 \cdot 5\text{H}_2\text{O}$), ammonium molybdate tetrahydrate ($(\text{NH}_4)_6\text{Mo}_7\text{O}_{24} \cdot 4\text{H}_2\text{O}$), manganese sulfate monohydrate ($\text{MnSO}_4 \cdot \text{H}_2\text{O}$), zinc sulfate (ZnSO_4), and ferrous sulfate heptahydrate ($\text{FeSO}_4 \cdot 7\text{H}_2\text{O}$) were in analytical grade.

Instrumentation

Petri dish, inoculation loop, Erlenmeyer 100 mL, measuring glass, beaker glass, micropipette, UV-vis spectrophotometer (GENESYS 10S, Thermo scientific), time-of-flight liquid chromatography-mass spectrometry (LC-TOF/MS) spectroscopy (Model, manufacturer), and

Fourier transform infra-red (FTIR) spectroscopy (Model, manufacturer) were used in this work.

Procedure

Microorganism and culture condition

D. dickinsii NBRC 31163 (NITE Biological Resource Center, Japan) was obtained from the Microorganism Chemistry Laboratory, Department of Chemistry, ITS, Indonesia. *D. dickinsii* was cultivated on PDA media for 7 d and incubated at 30 °C [12]. Then, the mycelium was homogenized in 50 mL of sterile demineralized water by using the sterilized blender. Furthermore, 1 mL fungal culture (9.2×10^4 CFU/mL) was inoculated into 9 mL PDB for 7 d within static incubation at 30 °C. Then the culture media was removed from *D. dickinsii* after its pre-incubation, and the mycelium was washed three times with sterile demineralized water [12].

Decolorization and degradation of MB using *D. dickinsii*

Biodecolorization and biodegradation of MB were performed on MSM, prepared according to modified Kirk's medium [8], by dissolving 0.8 mM MgSO_4 , 0.2 mM $\text{CaCl}_2 \cdot 2\text{H}_2\text{O}$, 12 μM H_3BO_3 , 0.4 μM $\text{CoSO}_4 \cdot 7\text{H}_2\text{O}$, 0.2 μM $\text{CuSO}_4 \cdot 5\text{H}_2\text{O}$, 0.04 μM $(\text{NH}_4)_6\text{Mo}_7\text{O}_{24} \cdot 4\text{H}_2\text{O}$, 2 μM $\text{MnSO}_4 \cdot \text{H}_2\text{O}$, and 0.4 μM ZnSO_4 in 1 L of demineralized water. Then it was sterilized at 121 °C for 20 min. For Fe^{2+} source involvement, MSM was added to 100 μM $\text{FeSO}_4 \cdot 7\text{H}_2\text{O}$ [8].

The mycelium culture of *D. dickinsii* was inoculated to MSM and supplemented with MB at its final concentration of 75 mg/L. It was incubated under the static condition at 30 °C for various times 7, 14, 21, and 28 d respectively. The involvement of the Fenton reaction on MB degradation was evaluated by comparing treatment within Fe^{2+} and without Fe^{2+} addition. The supernatant was obtained by centrifugation at 3000 rpm for 10 min. The decolorization percentage was calculated by using Eq. (1);

$$\text{Decolorization}(\%) = \frac{A_0 - A_1}{A_0} \times 100\% \quad (1)$$

where A_0 and A_1 are the initial absorbances and the absorbance of the treatment culture, respectively.

Statistical analysis was conducted by the average measurement from triple analysis results. Significant differences between the discoloration and degradation process groups were determined using a t-test within a confidence level of 5% ($P < 0.05$).

Identification of metabolite products

Degradation metabolites of MB were detected by analysis of the supernatants by LC-TOF/MS. At a mass range of 50–350, the ionization source used the electrospray ionization (ESI) technique. A flow rate of 0.2 mL/min was used for the first 3 min of the gradient elution procedure, followed by 0.4 mL/min for the next 7 min. The mobile phase used was methanol and water in a volume ratio of 99:1 for the first 3 min and 61:39 for the next 7 min. Furthermore, an Acclaim TM RSC 120 C18 type column (2.1×100 mm, 33°C) was used [12]. Degradation analysis of MD using FTIR spectroscopy was also conducted to know its functional groups.

RESULTS AND DISCUSSION

Decolorization and Degradation of *D. dickinsii*

Biodecolorization and biodegradation of MB by *D. dickinsii* were carried out throughout the incubation phase. The various incubation times for degrading MB were 0, 7, 14, and 28 d, respectively. Furthermore, the supernatant was examined using a UV-vis spectrophotometer at 200–800 nm after centrifugation at 3000 rpm for 10 min. Fig. 1(a) shows MB decolorization by *D. dickinsii* without Fe^{2+} addition, while Fig. 1(b) shows MB decolorization with Fe^{2+} addition. Both absorbance

profiles decreased since the increment of incubation time. The lowest absorbance at MB maximum wavelength 665 nm was obtained after 28 d of culture incubation [13]. Fe^{2+} was added to induce the involvement of the Fenton reaction in MB removal. Therefore, this can be a validation that MB decolorization was also supported by the Fenton reaction.

Fig. 2 shows the percentage results of MB decolorization by *D. dickinsii* without Fe^{2+} addition and with Fe^{2+} addition. The ability of *D. dickinsii* to decolorize MB was increased throughout its incubation time. The highest results were 86.420% and 90.084% for 28 d of incubation, respectively. The culture of *D. dickinsii* with Fe^{2+} addition showed the highest percentage of decolorization compared to treatment without Fe^{2+} addition, and the gap was approximately 3.657%. The result indicates that Fe^{2+} addition supported *D. dickinsii* to enhance MB decolorization and degradation. On the first day of treatment (0 d), according to Tables 1 and 2, *D. dickinsii* decolorized MB by 5.041% and 20.062% for without and within the addition of Fe^{2+} , respectively. Subsequently, *D. dickinsii* within Fe^{2+} addition showed the highest result from the beginning. Fungi have a special ability that can adsorb pollutants, including dye, through their cell interaction [14]. Therefore, biosorption was processed by the interaction between active and inactive cell surface microorganisms within the functional group of pollutants (e.g. electrostatic interaction and ion exchange) [15].

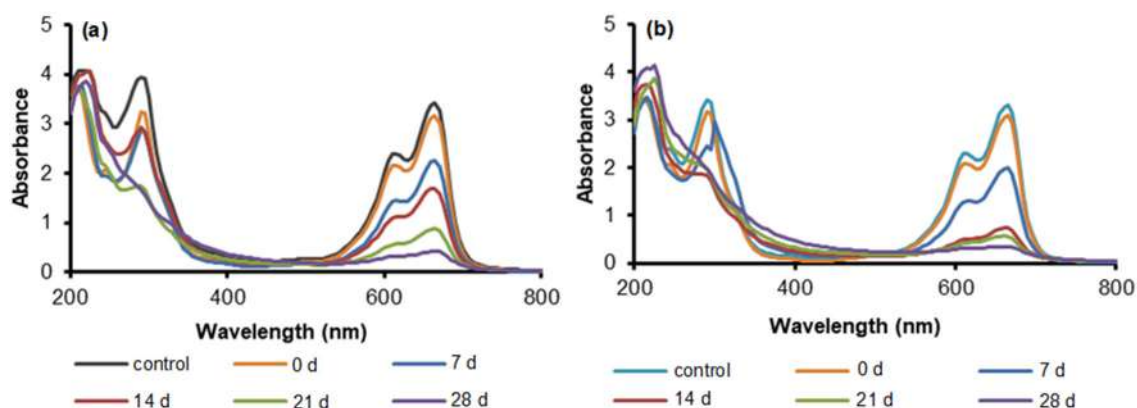


Fig 1. MB biodecolorization by *D. dickinsii*, (a) without Fe^{2+} addition and (b) within Fe^{2+} addition absorbance profiles

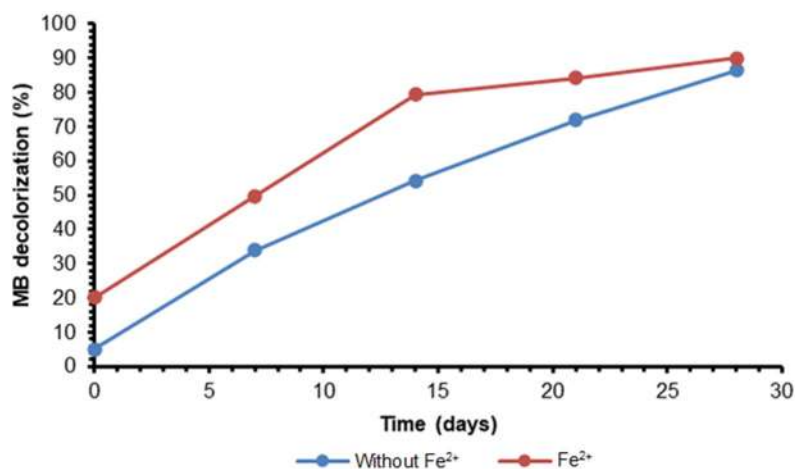


Fig 2. Percent removal (%) of MB biodecolorization by *D. dickinsii*

Table 1. Percentage of MB bio decolorization by *D. dickinsii* without Fe²⁺ addition

Incubation time (days)	Control concentration (ppm)	Treatment concentration (ppm)	Decolorization (%)
0	55.782	52.970	5.041
7	55.782	36.801	33.962
14	55.782	25.554	54.146
21	55.782	15.596	72.014
28	55.782	7.564	86.427

Table 2. Percentage of MB bio decolorization by *D. dickinsii* with Fe²⁺ addition

Incubation time (days)	Control concentration (ppm)	Treatment concentration (ppm)	Decolorization (%)
0	62.636	50.070	20.062
7	62.636	31.441	49.803
14	62.636	12.907	79.394
21	62.636	9.866	84.249
28	62.636	6.211	90.084

A study found that *D. dickinsii* can produce extracellular hydroxyl radicals ($\bullet\text{OH}$) caused by the Fenton reaction during the incubation process [16]. The Fenton reaction also influenced the biodegradation of DDT by the BRF *D. dickinsii* and *Fomitopsis pinicola*, which only produced very low levels of $\bullet\text{OH}$ (5.1 and 1.2 M, respectively) [9]. In addition to the Fenton reaction, Singh discovered that some fungi could generate degradative enzymes such as laccase and peroxidase [17].

Based on the experiment carried out by Rizqi and Purnomo [12], it was reported that *D. dickinsii* decolorized MB on PDB media by approximately 53.55% after 14 d of incubation. However, this study was significantly

different, which obtained about 79.394% by Fe²⁺ addition in MSM. These experiments proved that the Fenton reaction was involved in this MB decolorization. In addition, it can also happen because $\bullet\text{OH}$ was highly produced. Purnomo et al. [9] found that the addition of Fe²⁺ to the medium boosted $\bullet\text{OH}$ production.

Identification of Metabolite Products

LC-TOF/MS identified the MB biodegradation metabolite products. MB was found in a relative mass of 284 g/mol with a retention time of 16.09 min (Fig. 3(a)), this is shown in the chromatogram Fig. 4(a). The intensity of the MB treatment peak was lower than the

control peak, indicating that it was degraded. Furthermore, at retention times of 7.80 and 8.67 min, two metabolites were found in the chromatogram treatment (Fig. 4(b) and 4(c)), respectively. Table 3 shows the proposed metabolites products of MB degradation. At a retention time of 7.80 min, the peak had $m/z = 218$ (Fig. 3(b)), which was identified as 2-amino-3-hydroxy-5-(methylamino)benzenesulfonic acid. Moreover, the peak with $m/z = 167$ (Fig. 3(c)) at a retention time of 8.67 min was identified as *N*-(3,4-dihydroxy phenyl)-*N*-methylformamide. These metabolite results were reported previously by Houas et al. [18], who revealed the photocatalytic degradation pathway on MB in the water.

The MB degradation product was also analyzed for its functional group by using FTIR spectroscopy analysis (Fig. 5). Compared with MB dye analysis, the result shows that broad peak spectra at around 3000 nm^{-1} were observed as $-\text{OH}$ stretching vibration overlapping within the amine group ($-\text{NH}$). At the same time, peaks at 2935 nm^{-1} were analyzed from the $\text{C}-\text{H}$ symmetrical stretching band. However, there was a new peak on degraded MB result at 1725 nm^{-1} that was different within MB spectra, referring to the $\text{C}=\text{O}$ group [19]. This result was consistent with the purpose of MB metabolite

degradation above. Meanwhile, $\text{C}=\text{C}$ from aromatic rings were identified at a wavenumber of 1600 nm^{-1} [20].

Based on the identification of metabolite products, the MB biodegradation pathway was proposed in Scheme 1. MB was transformed into two pathways, both

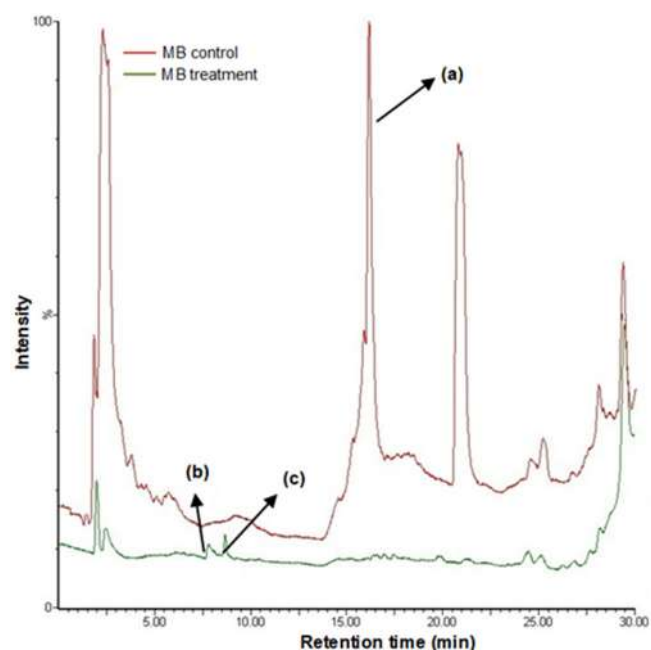


Fig 4. Chromatogram profile of MB degradation by *D. dickinsii* with Fe^{2+} addition

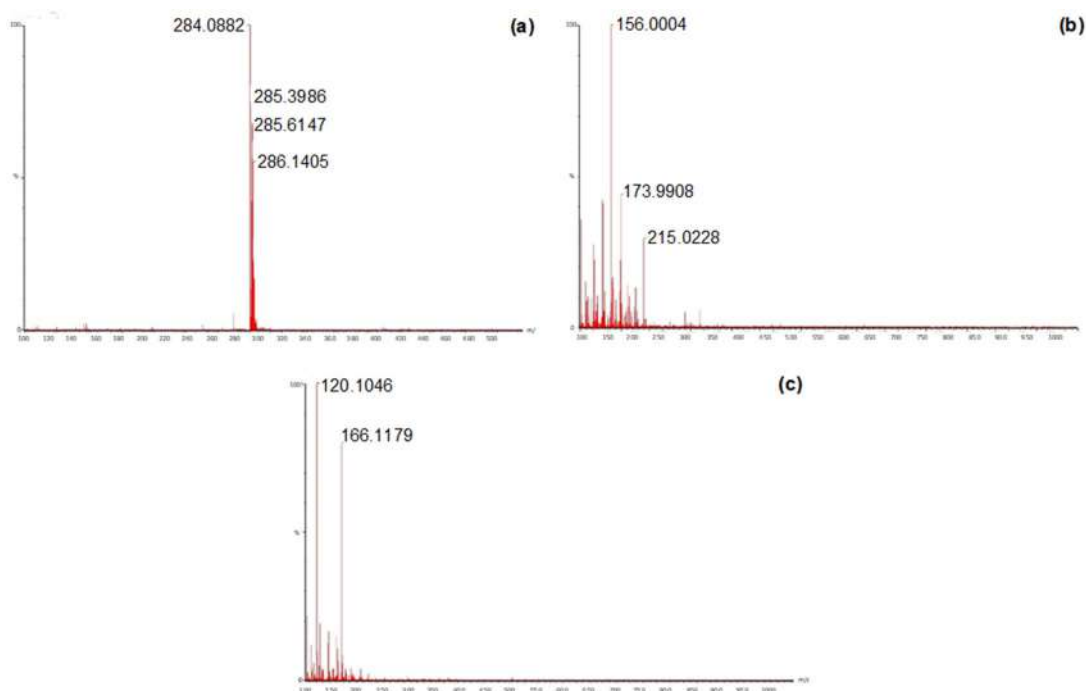
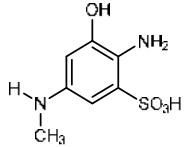
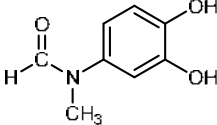
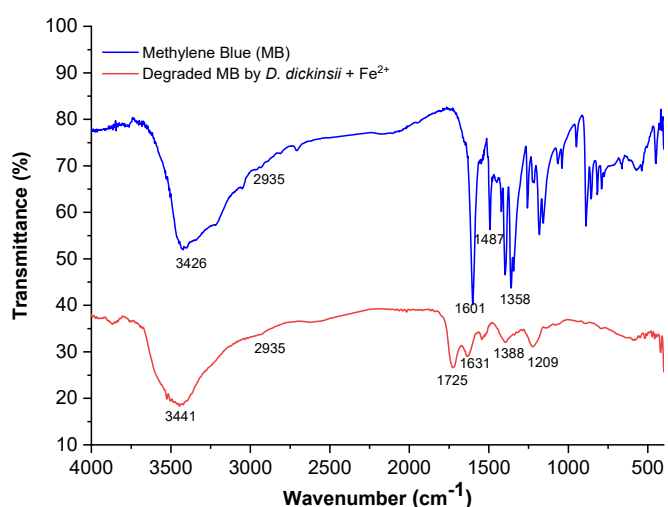


Fig 3. Images of mass spectra of (a) control MB, (b) peak at 7.80 min, and (c) peak at 8.67 min

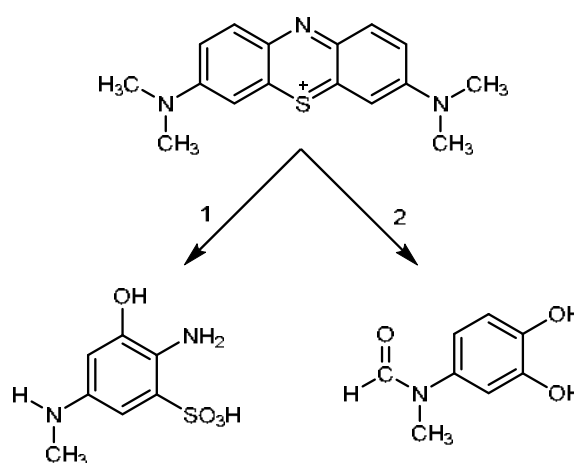
Table 3. Metabolites of MB degradation by *D. dickinsii* with Fe²⁺ addition

Retention time(min)	Relative mass	Chemical formula	Molecular structure
7.80	218	C ₇ H ₁₀ N ₂ O ₄ S	
8.67	167	C ₈ H ₉ NO ₃	

**Fig 5.** FTIR analysis result of MB degradation

paths have only one benzenic ring affected by •OH attack. In the first pathway, MB was oxidized by the formation of a sulfide group, followed by cleavage of the chromophore bond in NH₂ because of •OH generated by the Fenton reaction. The amine group was demethylated, and one site on the benzenic ring was hydroxylated by continuous •OH attack from the Fenton reaction. The second pathway, amine (chromophore) and sulfide bonds MB were hydroxylated, dissociating another ring. Then the •OH attacked the methyl group, and the amine group became the amide (aldehyde) group.

Wood rot fungus can be classified into three types based on the type of decay and their breakdown. There are BRF, white rot fungi (WRF), and soft rot fungi (SRF) [21]. Subsequently, WRF can degrade lignin and other compounds in particular when it ingests food [22]. The reason is WRF has a special ligninolytic enzyme system mechanism, including laccase, lignin peroxidase (LiP),

**Scheme 1.** A proposed route pathway of MB degradation by *D. dickinsii* with Fe²⁺ addition

mangan peroxidase (MnP), and other extracellular enzymes, which are capable of synergistically degrading lignin even on mild media conditions [23]. According to a previous study reported by Zeng et al. [24], semi-solid-state fermentation of agricultural waste rice straw mixed with *Phanerochaete chrysosporium* fungus can be degraded and decolorize MB by 84.8% at an initial concentration of 0.4 g/L. Furthermore, white rot fungi *Pleurotus ostreatus* also can degrade MB, proved by the increasing decolorization percentage at 25–700 mg/L concentration [25]. SRF typically attack higher moisture and degrade lower lignin cell wood. Although, there are still no studies that mention the enzymatic degradation system [26].

BRF are capable of breaking down wood substrate both enzymatically and non-enzymatically [7], resulting in a brownish discoloration of the cell wall. Naturally, BRF preferentially targets polysaccharides such as

cellulose and hemicellulose for nutritional purposes rather than lignin and possesses a cellulolytic enzyme system that can partially oxidize lignin without the need for ligninolytic enzymes [7]. However, the enzymes produced by BRF are unable to penetrate the cell wall's pores, which are larger than the enzymes themselves. Hence, BRF needs a low-molecular-weight-biochemical agent, which can penetrate cell-wall pores and degrade/depolymerize cellulose [27]. This mechanism is caused by extracellular oxidants (free radicals), which are small, diffusible, and could react on distance from hyphae [16].

BRF possess a unique non-enzymatic system that allows them to produce $\bullet\text{OH}$ through the Fenton reaction (Scheme 2), enabling them to decay wooden cells [27]. BRF can produce more H_2O_2 from glucose than WRF does. The Fenton reaction has been proven to be an effective technology, which uses a catalytic oxidation process by mixing H_2O_2 and Fe^{2+} to produce $\bullet\text{OH}$. These $\bullet\text{OH}$ radicals could be used as the strongest oxidant currently available in biological systems to degrade a wide range of xenobiotic and organic contaminants [28].

According to Su et al. [29], Fenton-like catalysis using iron-containing minerals could be an alternative optimum method for eliminating refractory organic pollutants. The $\bullet\text{OH}$ radicals are non-selective robust species in water which could oxidize organic substrates, with an estimated oxidation potential of 2.8 and 1.9 V at pH 0 and 14, respectively [29]. The removal of one hydrogen atom from hydrocarbons and other organic substrates can be affected by $\bullet\text{OH}$. This is possible because the hydrogen bond has a lower energy than the O-H bond, which has an energy of 109 kcal/mol [29].

Studies have suggested that $\bullet\text{OH}$ is particularly effective at breaking down wood components compared to other related oxygen species [30]. Due to its strong oxidizing agent capabilities, it can degrade raw material feedstock (complex organic chemical component). The $\bullet\text{OH}$ can react with complex organic compounds containing an aromatic ring in two ways: 1) by introducing an electrophile to the aromatic ring or 2) by abstracting a proton (H^+) from aliphatic [21]. Under low pH conditions, $\bullet\text{OH}$ not only abstracts the H^+ but also can

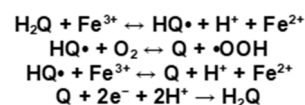
eliminate H_2O and produce an aryl cation. This is followed by carbon-carbon linkages cleavage and other degradation [21].

The Fenton chemical reaction requires Fe^{2+} and H_2O_2 as the main components to produce $\bullet\text{OH}$. Naturally, BRF reduces Fe^{3+} to Fe^{2+} and produces H_2O_2 through the extracellular hydroquinone-quinone redox cycle, as shown below [31] where Q is quinone, H_2Q is hydroquinone, $\text{HQ}\bullet$ is semiquinone, and $\bullet\text{OOH}$ is perhydroxyl radical (Scheme 3). It further suggested that cellobiose dehydrogenase or iron-binding catechols reducing Fe^{3+} outside the BRF mycelium can initiate and generate Fenton chemistry [32]. The hypothesis that the Fenton reaction plays a role in the BRF mechanism can be supported by the addition of FeSO_4 , which can ionize Fe^{2+} as additional Fe^{2+} to aid the Fenton reaction in the decolorization of MB by *D. dickinsii*. Fe^{2+} oxidizes and then becomes Fe^{3+} [8]. Moreover, the concentration of H_2O_2 produced by *D. dickinsii* could be analyzed by using the ferrous ion oxidation-xylenol orange (FOX) method. Purnomo et al. [9] showed that by the FOX method, *D. dickinsii* could produce 21 mM H_2O_2 during 14 d of incubation time.

Another previous study reported by Purnomo et al. [33] showed that three species of BRF *Gloeophyllum trabeum*, *Fomitopsis pinicola*, and *D. dickinsii* could degrade synthetic dye methyl orange. The proposed metabolite degradation pathway consists of three-step processes: (1) demethylation, (2) desulfonylation, and (3) hydroxylation. Furthermore, Alkas et al. [34] reported that *D. dickinsii* immobilized into sodium alginate-polyvinyl alcohol supported by UiO-66 could adsorb and degrade MB within its maximum capacity of 0.329 mg/g. The metabolite products $\text{C}_{16}\text{H}_{20}\text{N}_3\text{S}$ ($m/z = 286$), $\text{C}_{22}\text{H}_{32}\text{N}_3\text{O}_5\text{S}$ ($m/z = 450$), and $\text{C}_{12}\text{H}_{13}\text{N}_3\text{O}_7$ ($m/z = 311$)



Scheme 2. Fenton reaction



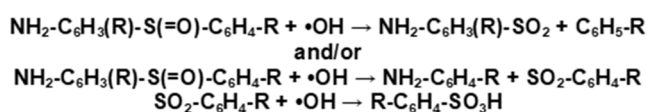
Scheme 3. Scheme of regulation Fe^{2+} reaction on Fenton reaction

were also identified. Furthermore, another BRF species that can degrade Violet S3RL, Yellow Brown S2RFL, Red W4BS, Yellow SRLP and Red S3B was successfully analyzed [35].

To identify metabolite products in this recent study, LC-TOF/MS was used for the analysis. The MB peak is found at 16.09 min retention time with m/z 284 g/mol, as shown in the chromatogram (Fig. 4). The MB treatment was degraded because the peak intensity was generally lower than the MB's control peak. The metabolites products were detected on two new peaks at retention times of 7.80 (m/z = 218) and 8.67 min (m/z = 167), which are proposed as 2-amino-3-hydroxy-5-(methylamino) benzenesulfonic acid and *N*-(3,4-dihydroxyphenyl)-*N*-methyl formamide, respectively. These metabolites were discovered during a research project on the photocatalytic degradation of MB in water [18].

Rizqi and Purnomo [12] reported that *D. dickinsii* can degrade MB into three metabolites, namely 3-(dimethyl amino)-7-(methylamino)phenothiazine ($C_{15}H_{16}N_3S^+$, m/z = 280), 3,7-bis(dimethylamino)-4*H*-phenothiazine-5-one ($C_{16}H_{19}N_3OS$, m/z = 300), and 4-(dimethylamino)-2-[*m*-(dimethylamino)phenylsulfinyl]benzene-amine ($C_{16}H_{21}N_3OS$, m/z = 303). Meanwhile, Houas et al. [18] experiment also showed that MB can be degraded into $C_{16}H_{21}N_3OS$ with m/z = 303, by the attack of $\bullet OH$. It also explained that MB was attacked by $\bullet OH$ on C-S⁺=C functional group, and to open the center ring, double bond conjugation conservation was required. The sulfoxide group of $C_{16}H_{21}N_3OS$ was attacked again by $\bullet OH$ and dissociated the two aromatic rings (not detected/reaction Scheme 4) [18].

Furthermore, the sulfone can be attacked by a third $\bullet OH$, resulting in the formation of a sulfonic acid found in metabolites with m/z of 218 and 158. According to Houas et al. [18], sulfur has attained its maximum oxidation degree (+6) in reaction 8. Furthermore, SO_4^{2-} ions could be attacked again by $\bullet OH$ until they become phenolic.



Scheme 4. Two kinds of aromatic ring were dissociated by hydroxyl radical

CONCLUSION

This study showed that BRF *D. dickinsii* with the addition of Fe^{2+} has a greater capability to decolorize and degrade MB in MSM compared to *D. dickinsii* culture without Fe^{2+} addition. The highest results of decolorization were achieved at 90.084 and 86.427%, respectively, at 30 °C for 28 d of incubation, and a decolorization gap of 3.657%. These results suggest that the Fenton reaction is involved in MB removal by $\bullet OH$ production. The MB degradation metabolites by *D. dickinsii* were analyzed by LC-TOF/MS and FTIR spectroscopy and identified as 2-amino-3-hydroxy-5-(methylamino) benzenesulfonic acid and *N*-(3,4-dihydroxyphenyl)-*N*-dimethylformamide.

ACKNOWLEDGMENTS

The authors gratefully acknowledge financial support from the Institut Teknologi Sepuluh Nopember for this work, under project scheme of the Publication Writing and IPR Incentive Program (PPHKI) 2023.

REFERENCES

- Purnaningtyas, M.A.K., Sudiono, S., and Siswanta, D., 2020, Synthesis of activated carbon/chitosan/alginate beads powder as an adsorbent for methylene blue and methyl violet 2b dyes, *Indones. J. Chem.*, 20 (5), 1119–1130.
- Vezentsev, A.I., Thuy, D.M., Goldovskaya-Peristaya, L.F., and Glukhareva, N.A., 2018, Adsorption of methylene blue on the composite sorbent based on bentonite-like clay and hydroxyapatite, *Indones. J. Chem.*, 18 (4), 733–741.
- Rizzi, V., Longo, A., Fini, P., Semeraro, P., Cosma, P., Franco, E., García, R., Ferrándiz, M., Núñez, E., Gabaldón, J.A., Fortea, I., Pérez, E., and Ferrándiz, M., 2014, Applicative study (Part I): The excellent conditions to remove in batch direct textile dyes (direct red, direct blue and direct yellow) from aqueous solutions by adsorption processes on low-cost chitosan films under different conditions, *Adv. Chem. Eng. Sci.*, 4 (4), 454–469.
- Shalini, S., and Setty, Y.P., 2019, Multistage fluidized bed bioreactor for dye decolorization

- using immobilized polyurethane foam: A novel approach, *Biochem. Eng. J.*, 152, 107368.
- [5] Boumediene, M., Benaïssa, H., George, B., Molina, S., and Merlin, A., 2018, Effects of pH and ionic strength on methylene blue removal from synthetic aqueous solutions by sorption onto orange peel and desorption study, *J. Mater. Environ. Sci.*, 9 (6), 1700–1711.
- [6] Sarioglu, O.F., Keskin, N.O.S., Celebioglu, A., Tekinay, T., and Uyar, T., 2017, Bacteria encapsulated electrospun nanofibrous webs for remediation of methylene blue dye in water, *Colloids Surf., B*, 152, 245–251.
- [7] Negi, R., and Suthar, S., 2018, Degradation of paper mill wastewater sludge and cow dung by brown-rot fungi *Oligoporus placenta* and earthworm (*Eisenia fetida*) during vermicomposting, *J. Cleaner Prod.*, 201, 842–852.
- [8] Purnomo, A.S., Asranudin, A., Rachmawati, N., Rizqi, H.D., Nawfa, R., and Putra, S.R., 2022, Role of Fe²⁺-dependent reaction in biodecolorization of methyl orange by brown-rot fungus *Fomitopsis pinicola*, *HAYATI J. Biosci.*, 29 (2), 146–154.
- [9] Purnomo, A.S., Mori, T., and Kondo, R., 2010, Involvement of Fenton reaction in DDT degradation by brown-rot fungi, *Int. Biodeterior. Biodegrad.*, 64 (7), 560–565.
- [10] Zhu, N., Zhu, Y., Li, B., Jin, H., and Dong, Y., 2021, Increased enzyme activities and fungal degraders by *Gloeophyllum trabeum* inoculation improve lignocellulose degradation efficiency during manure-straw composting, *Bioresour. Technol.*, 337, 125427.
- [11] Ali, N., Hameed, A., and Ahmed, S., 2010, Role of brown-rot fungi in the bioremoval of azo dyes under different conditions, *Braz. J. Microbiol.*, 41 (4), 907–915.
- [12] Rizqi, H.D., and Purnomo, A.S., 2017, The ability of brown-rot fungus *Daedalea dickinsii* to decolorize and transform methylene blue dye, *World J. Microbiol. Biotechnol.*, 33 (5), 92.
- [13] Hasan, R., Ying, W.J., Cheng, C.C., Jaafar, N.F., Jusoh, R., Abdul Jalil, A., and Setiabudi, H.D., 2020, Methylene blue adsorption onto cockle shells-treated banana pith: Optimization, isotherm, kinetic, and thermodynamic studies, *Indones. J. Chem.*, 20 (2), 368–378.
- [14] Divya, L., and Sadasivan, C., 2016, *Trichoderma viride* laccase plays a crucial role in defense mechanism against antagonistic organisms, *Front. Microbiol.*, 7, 741.
- [15] Zuurro, A., Maffei, G., and Lavecchia, R., 2017, Kinetic modeling of azo dye adsorption on non-living cells of *Nannochloropsis oceanica*, *J. Environ. Chem. Eng.*, 5 (4), 4121–4127.
- [16] Nabilah, B., Purnomo, A.S., Rizqi, H.D., Putro, H.S., and Nawfa, R., 2022, The effect of *Ralstonia pickettii* bacterium addition on methylene blue dye biodecolorization by brown-rot fungus *Daedalea dickinsii*, *Heliyon*, 8 (2), e08963.
- [17] Singh, R.L., Singh, P.K., and Singh, R.P., 2015, Enzymatic decolorization and degradation of azo dyes - A review, *Int. Biodeterior. Biodegrad.*, 104, 21–31.
- [18] Houas, A., Lachheb, H., Ksibi, M., Elaloui, E., Guillard, C., and Herrmann, J.M., 2001, Photocatalytic degradation pathway of methylene blue in water, *Appl. Catal., B*, 31 (2), 145–157.
- [19] Masruroh, M., Santjojo, D.J.D.H., Abdurrouf, A., Abdillah, M.A., Padaga, M.C., and Sakti, S.P., 2019, Effect of electron density and temperature in oxygen plasma treatment of polystyrene surface, *IOP Conf. Ser.: Mater. Sci. Eng.*, 515 (1), 012061.
- [20] Xia, Y., Yao, Q., Zhang, W., Zhang, Y., and Zhao, M., 2019, Comparative adsorption of methylene blue by magnetic baker's yeast and EDTA-modified magnetic baker's yeast: Equilibrium and kinetic study, *Arabian J. Chem.*, 12 (8), 2448–2456.
- [21] Singh, S.K., 2021, Biological treatment of plant biomass and factors affecting bioactivity, *J. Cleaner Prod.*, 279, 123546.
- [22] Purnomo, A.S., Maulianawati, D., and Kamei, I., 2019, *Ralstonia pickettii* enhance the DDT biodegradation by *Pleurotus eryngii*, *J. Microbiol. Biotechnol.*, 29 (9), 1424–1433.
- [23] Rouches, E., Herpöel-Gimbert, I., Steyer, J.P., and Carrere, H., 2016, Improvement of anaerobic degradation by white-rot fungi pretreatment of

- lignocellulosic biomass: A review, *Renewable Sustainable Energy Rev.*, 59, 179–198.
- [24] Zeng, G., Cheng, M., Huang, D., Lai, C., Xu, P., Wei, Z., Li, N., Zhang, C., He, X., and He, Y., 2015, Study of the degradation of methylene blue by semi-solid-state fermentation of agricultural residues with *Phanerochaete chrysosporium* and reutilization of fermented residues, *Waste Manage.*, 38, 424–430.
- [25] Abo-State, M.A.M., Reyad, B., Ali, M., Gomaa, O., and Youssif, E.A., 2011, Comparing decolorization of dye by white rot fungi, free enzyme and immobilized enzyme, *World Appl. Sci. J.*, 14 (10), 1469–1486.
- [26] Karunasekera, H., Terziev, N., and Daniel, G., 2017, Does copper tolerance provide a competitive advantage for degrading copper treated wood by soft rot fungi?, *Int. Biodeterior. Biodegrad.*, 117, 105–114.
- [27] Zelinka, S.L., Jakes, J.E., Kirker, G.T., Bishell, A.B., Boardman, C.R., Lai, B., Sterbinsky, G.E., Jellison, J., and Goodell, B., 2021, Oxidation states of iron and manganese in lignocellulose altered by the brown rot fungus *Gloeophyllum trabeum* measured in-situ using X-ray absorption near edge spectroscopy (XANES), *Int. Biodeterior. Biodegrad.*, 158, 105162.
- [28] Zhu, G.C., Shou, J.X., Qian, J.W., Xin, H.Z., and Qiu, M.Q., 2015, Degradation of methylene blue by Fenton-like reaction, *Adv. Mater. Res.*, 1065-1069, 3127–3130.
- [29] Su, S., Liu, Y., Liu, X., Jin, W., and Zhao, Y., 2019, Transformation pathway and degradation mechanism of methylene blue through β -FeOOH@GO catalyzed photo-Fenton-like system, *Chemosphere*, 218, 83–92.
- [30] Jung, Y.H., Kim, H.K., Park, H.M., Park, Y.C., Park, K., Seo, J.H., and Kim, K.H., 2015, Mimicking the Fenton reaction-induced wood decay by fungi for pretreatment of lignocellulose, *Bioresour. Technol.*, 179, 467–472.
- [31] Ahmed, M.B., Zhou, J.L., Ngo, H.H., Guo, W., Thomaidis, N.S., and Xu, J., 2017, Progress in the biological and chemical treatment technologies for emerging contaminant removal from wastewater: A critical review, *J. Hazard. Mater.*, 323, 274–298.
- [32] Hyde, S.M., and Wood, P.M., 1997, A mechanism for production of hydroxyl radicals by the brown-rot fungus *Coniophora puteana*: Fe(III) reduction by cellobiose dehydrogenase and Fe(II) oxidation at a distance from the hyphae, *Microbiology*, 143 (1), 259–266.
- [33] Purnomo, A.S., Mauliddawati, V.T., Khoirudin, M., Yonda, A.F., Nawfa, R., and Putra, S.R., 2019, Biodecolorization and novel bio-transformation of methyl orange by brown-rot fungi, *Int. J. Environ. Sci. Technol.*, 16 (11), 7555–7564.
- [34] Alkas, T.R., Purnomo, A.S., Pratiwi, A.N., Nurwijayanti, Y., Ediati, R., Ersam, T., and Kusumawati, Y., 2023, Immobilization of UiO-66/Brown-rot fungi (BRF) in PVA-SA matrix and its performance for methylene blue decolorization, *Mater. Today Chem.*, 29, 101411.
- [35] Mahmood, R.T., Asad, M.J., Asgher, M., Gulfranz, M., and Mukhtar, T., 2017, Analysis of lingo-lytic enzymes and decolorization of disperse violet S3RL, yellow brown S2RFL, red W4BS, yellow SRLP and red S3B by brown rot fungi, *Pak. J. Agric. Sci.*, 54 (2), 407–413.

Supplementary Data

This supplementary data is a part of a paper entitled “Green Synthesis of New Heterocyclic Surfactant Compounds by Multicomponent Reactions and Their Antibacterial and Corrosion Inhibitor Study on Carbon Steel Alloy in Acid Media 2 M HCl”.

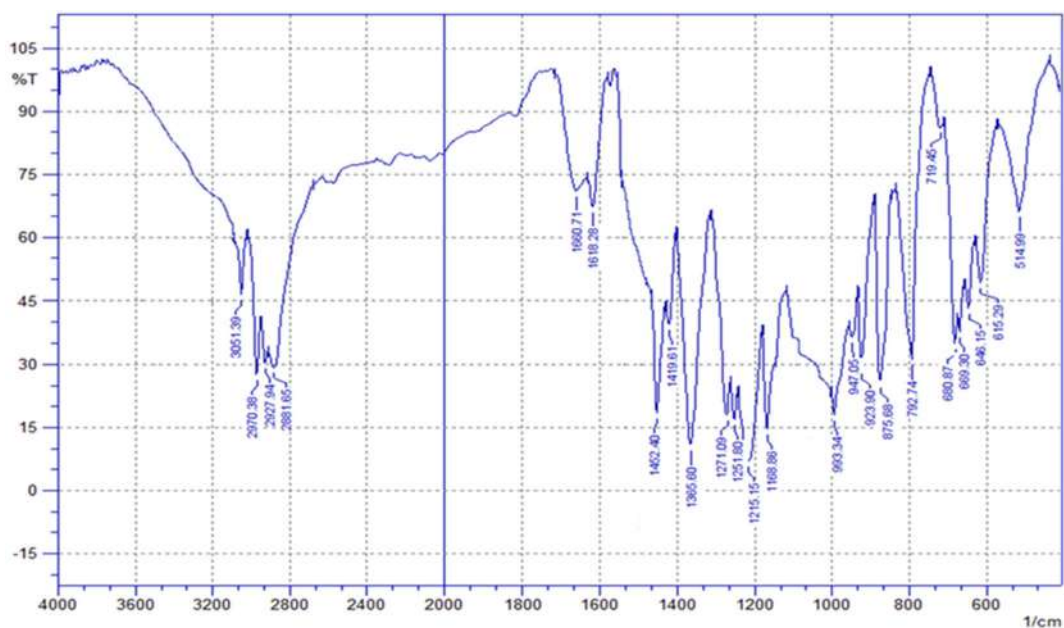


Fig S1. FTIR spectrum of the synthesized heterocyclic compound D

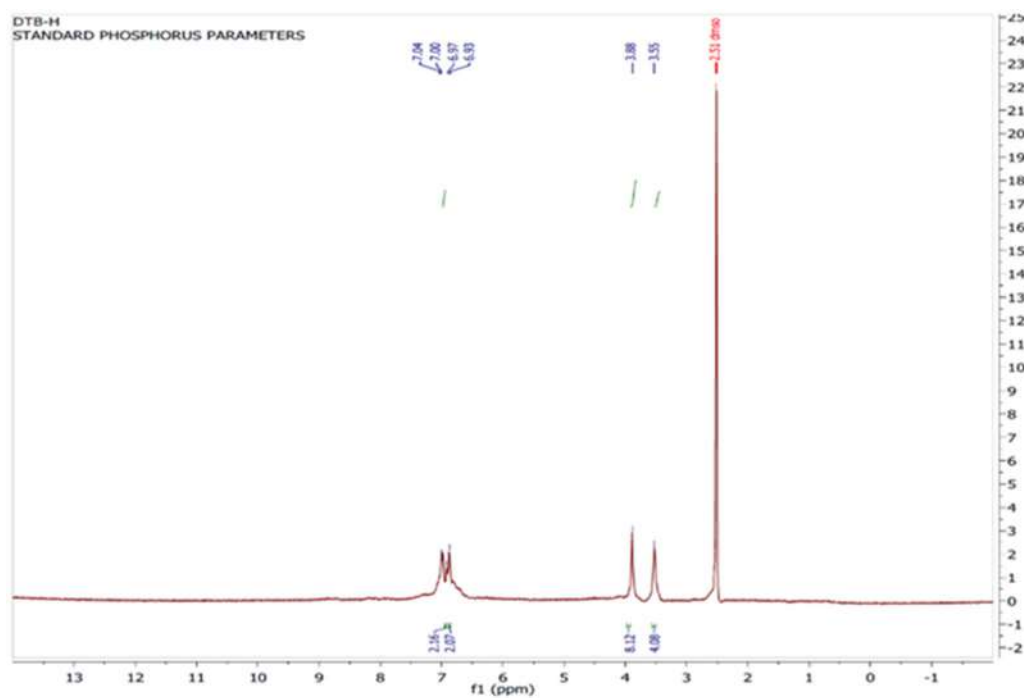


Fig S2. ¹H-NMR spectrum of the synthesized heterocyclic compound D

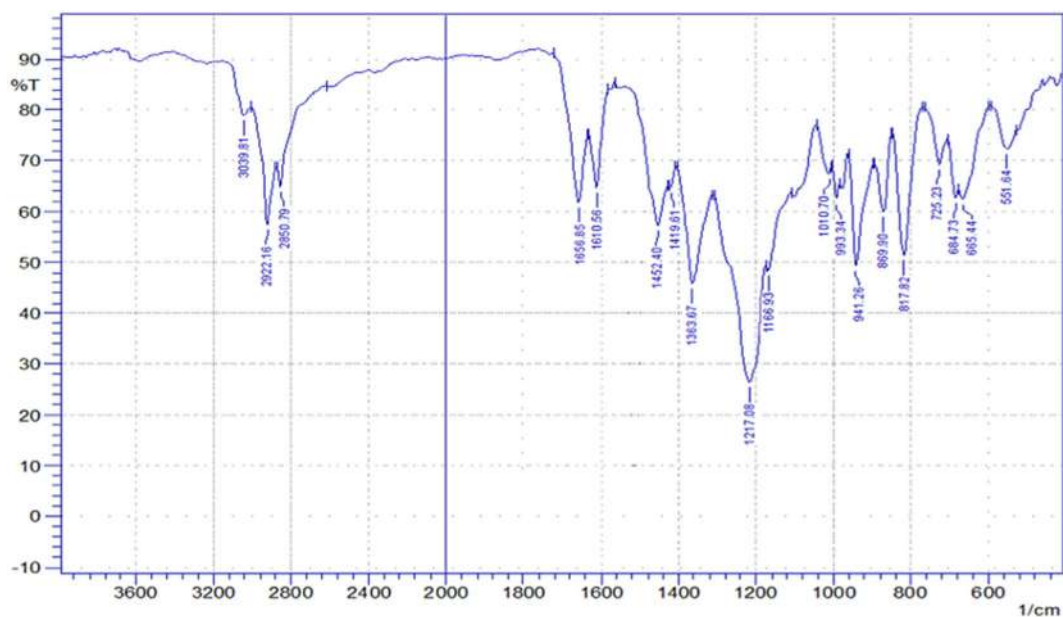


Fig S3. FTIR spectrum of the synthesized heterocyclic-Gemini surfactant E

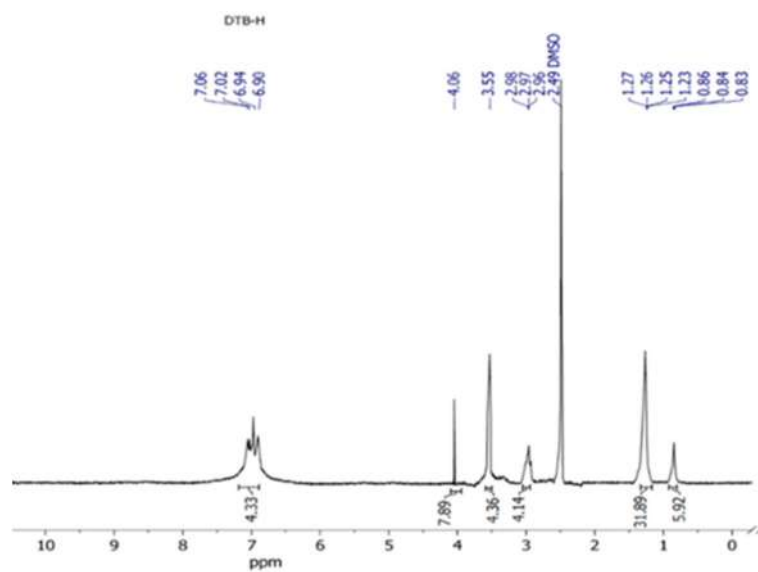


Fig S4. ^1H -NMR spectrum of the synthesized heterocyclic-Gemini surfactant E

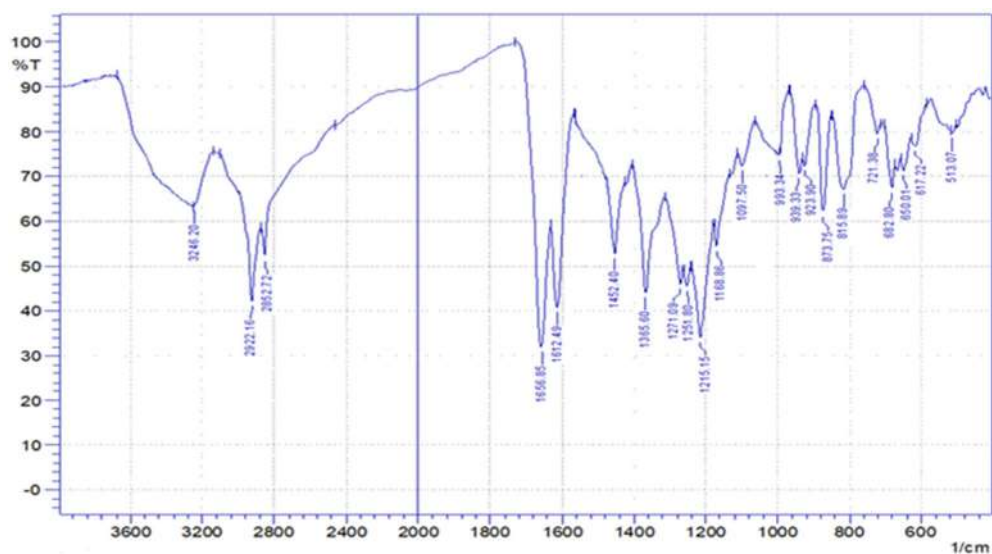


Fig S5. FTIR spectrum of the synthesized heterocyclic-Gemini surfactant F

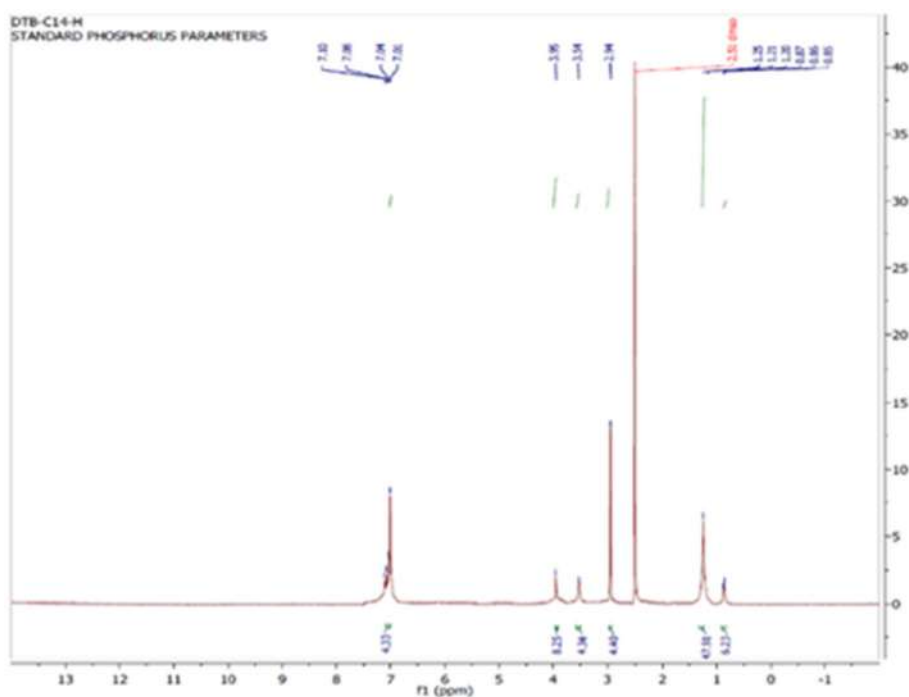


Fig S6. ¹H-NMR spectrum of the synthesized heterocyclic-Gemini surfactant F

Green Synthesis of New Heterocyclic Surfactant Compounds by Multicomponent Reactions and Their Antibacterial and Corrosion Inhibitor Study on Carbon Steel Alloy in Acid Media 2 M HCl

Raneen Salim Al-Hilfi¹, Najlaa Zaki Al-Ameri^{2*}, and Mouhanad Jwad Al-Asadi¹

¹Department of Chemistry, College of Pure Science Education, University of Basrah, Basra 00964, Iraq

²Department of Second Party, Basra Oil Company (BOC) Iraqi Oil Ministry, Basra 00964, Iraq

* **Corresponding author:**

email: najlaa078@yahoo.com

Received: December 18, 2022

Accepted: February 19, 2023

DOI: 10.22146/ijc.80347

Abstract: Heterocyclic 1,4-di(1,3,5-dithiazinan-5-yl)benzene (D) and two heterocyclic-cationic Gemini surfactant 5,5'-(1,4-phenylene)bis(5-decyl-1,3,5-dithiazinan-5-ium)bromide (E) and 5,5'-(1,4-phenylene)bis(5-tetradecyl-1,3,5-dithiazinan-5-ium)bromide (F) were prepared and identified by FTIR, ¹H-NMR spectroscopies, and GC-MS. Then, they were tested as corrosion inhibitors against carbon steel corrosion in 2.0 M aggressive HCl medium at 25 and 50 °C. They have different carbon chain tails, i.e., E (10 carbons), and F (14 carbons). These new heterocyclic and surfactant categories as corrosion inhibitors. The corrosion process has been studied electrochemically (Tafel Plot). The inhibition efficiency clarified that the decrease in IE(%) is in the order of F > E > D. The biological activity of compounds D and F was investigated using the aforementioned drilling procedure with a cork drill. At a dosage of 3000 mcg/mL, the biological action of compound D demonstrated effective resistance against the two types of negative bacteria. The cation has a diameter of 20 mm against E. coli and 19 mm against S. epidermis bacteria. At the same concentration, the chemical F is solely effective against E. coli with an inhibition diameter of 14 mm.

Keywords: antibacterial; carbon steel alloy; cationic Gemini; cyclothiomethylation; Tafel plot

■ INTRODUCTION

The "green synthesis" approach of useful chemicals with minimal material, power, effort, and time costs has attracted much attention in recent years. One of these techniques is multicomponent reactions (MCRs), which allow for one-pot multistep synthesis without the requirement for intermediate separation and purification, hence decreasing chemical waste. Thiomethylation (reagent atom efficiency of 100% by the C, N, and S atoms) is the most efficient reaction in a sequence of "green" MCRs, yielding water as the only side product in addition to the target products [1-2]. Because of their chemical composition, organic corrosion inhibitors performed particularly well against steel corrosion. Some functional groups, such as oxygen, nitrogen, sulfur, phosphorous, and double bonds, may act as electronic-

rich active sites for adsorption on the surface of corroded materials, thereby increasing steel protection [3-4].

The electronic-rich group can interact with the vacant *d*-orbital to form a protective layer, shielding the surface from the aggressive medium [5]. Surfactants have been shown to be promising corrosion inhibitors due to their unusual structure, which includes two opposing polarities: hydrophobic and hydrophilic portions at the same time. The hydrophilic heads, in particular, are electrically rich groups with a strong attraction to steel surfaces, whereas the hydrophobic surfactant tail acts as a protective coating [6-7]. Surfactants are used in various applications, including corrosion inhibitors, emulsifiers, drug technology, pharmaceutical formulation, nanotechnology, wetting agents, detergents, and catalyst technologies [8].

Gemini surfactants are identified by two identical parts separated by a spacer, each with the hydrophilic and lipophilic moieties. Compared to standard monomeric surfactants, this unusual structure governs their surface performance in solution. Gemini is a more effective surfactant with a lower critical micelle concentration (CMC) [4,7,9]. As a result, there has been a greater emphasis on developing innovative Gemini surfactants. Some of the novel Gemini surfactants have been created including heterocyclic cationic Gemini surfactants [4,9]. Because the former Gemini species has two hydrophilic heads with various charges, it can be classified as cationic-nonionic, anionic-nonionic, or anionic-cationic depending on its hydrophilic charges. Because of the changed charged ionic moiety, which lessens the repulsive force and allows for a closer distance, these unique categories result in a stronger adsorption tendency and a different aggregation structure than classic Gemini ones [10-11].

In this study, we prepared three inhibitors, named heterocyclic compounds and cationic heterocyclic Gemini surfactants with various carbon tails (D, E, and F). Electrochemical investigations were used to evaluate their corrosion resistance to steel corrosion. To our knowledge, these new heterocyclics and cationic heterocyclic Gemini surfactants were examined as corrosion inhibitors and antifungicidal agents for the first time. These new surfactants feature both positive and negative adsorption centers and several other electronic-rich function groups that may boost their adsorption capabilities. Electrochemical methods (Tafel plots) were used to study the steel surface, demonstrating the formation of a surfactant protective layer on the steel surface.

■ EXPERIMENTAL SECTION

Materials

All chemicals for the synthesis were commercially available with a purity of at least 97%: diaminobenzene

(C₆H₈N₂, Sigma Aldrich), acetone ((CH₃)₂CO, Scharlau), 37% hydrochloric acid (HCl, B.D.H), 37% aqueous formaldehyde solution (CH₂O, Merck), 1-bromotetradecane (C₁₄H₂₉Br, Scharlau), 1-bromodecane (C₁₀H₂₁Br, Scharlau), ethanol (C₂H₅OH, B.D.H), sodium sulfide (Na₂S, Scharlau), dichloromethane (CH₂Cl₂, B.D.H), potassium hydroxide (KOH, B.D.H), and diethyl ether (C₄H₁₀O, Scharlau).

Instrumentation

The reaction products were identified using ¹H NMR spectra acquired on spectrometers (Bruker Avance 400 MHz), using internal standard TMS and DMSO-*d*₆ as the solvent. IR spectra were recorded on a Shimadzu, 84005 FTIR spectrometer, 400–4000 cm⁻¹, using KBr pellets. The melting point was determined by Thermo Scientific. GC-MS spectra were recorded on 5977 A MSD, Agilent 7890B GC device 70 eV, carrier gas helium, temperature program: rise from 40 to 300 °C at a rate of 10°/min. Individuality and purity of synthesized compounds were controlled using TLC on Silufol UV-254 plates; I₂ was used as a developer. Electrochemical measurements by Tafel polarization were carried out using Bank Elektronik-Intelligent Controls Type MLab 200.

Procedure

Steel composition and aggressive solution

The aggressive media was chosen to be 2 M HCl. It's made by diluting a concentrated HCl solution with doubly distilled water. The composition of the investigated steel specimen is shown in Table 1.

The examined steel was utilized in the electrochemical tests, with dimensions of 5 × 2 × 0.3 cm for length, width, and thickness, respectively. The SiC (grade 140, 320) was used to polish the carbon steel, which was then cleaned with distilled water, acetone, and completely dried in a desiccator [12].

Table 1. Components of the carbon steel alloy (C-95)

Element	Fe	C	Mn	P	S	Si	Cr	Ni	Cu	Mo	V
Percentage (%)	97.784	0.330	1.400	0.003	0.002	0.190	0.240	0.019	0.021	0.007	0.004

Potentiodynamic polarization experiments

This testing was performed using a three-electrode setup and an Auto lab. The polarization experiment was carried out by changing the inhibitor concentration (1×10^{-4} , 5×10^{-4} , 1×10^{-3} , 5×10^{-3}) at 25 and 50 °C.

Synthesis of 1,4-di(1,3,5-dithiazinan-5-yl)benzene (D)

The synthesis is carried out in two steps: First, formaldehyde (4.9 mL, 0.06 mol) and ethanol (50 mL) were added to a three-neck flask, followed by hydrogen sulfide (0.04 mol) bubbled with stirring for 30 min at room temperature [13-14]. The second step was dissolving diaminobenzene (1.08 g, 0.01 mol) in ethanol (50 mL) and dropwise addition to a water solution of formaldehyde (37%), saturating with H₂S with the diaminobenzene:H₂S:CH₂O ratio of 1:4:6. The mixture was refluxed for 48 h at 75 °C. The precipitate was then filtered and recrystallized with hot dichloromethane to get the target product D: Yield (70.0%) as a yellow crystal, m.p. (215–220 °C), as shown in Scheme 1 [13-16].

Synthesis of 5,5'-(1,4-phenylene)bis(5-decyl-1,3,5-dithiazinan-5-ium)bromide (E)

Compound D (1.6 g, 0.005 mol) was dissolved in the beaker with dichloromethane (20 mL), and then followed by the addition of 1-bromodecane (2.14 mL, 0.01 mol). For 24 h, the mixture was agitated on a magnetic stirrer at room temperature. The precipitate was then filtered, washed twice with diethyl ether, and air-dried to get the

target product E: Yield (80.0%) as a yellow crystal, m.p. (200–205 °C), as shown in Scheme 1 [13,17].

Synthesis of 5,5'-(1,4-phenylene)bis(5-tetradecyl-1,3,5-dithiazinan-5-ium) bromide (F)

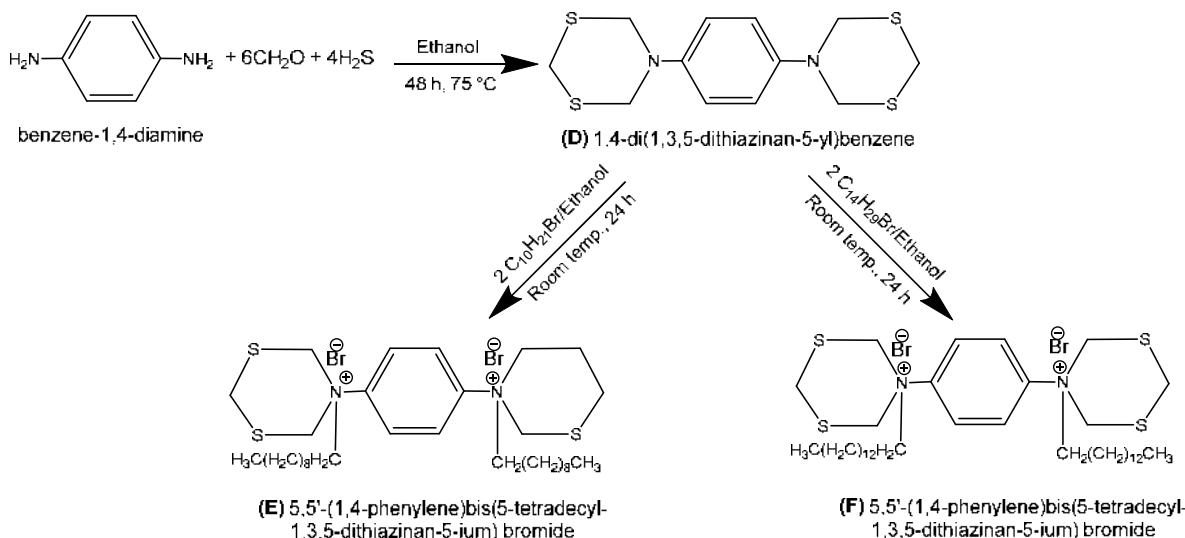
Compound D (1.6 g, 0.005 mol) was dissolved in the beaker with dichloromethane (20 mL), and 1-bromotetradecane (2.9 mL, 0.01 mol) was added to it. For 24 h, the mixture was stirred at room temperature. The precipitate was then filtered, washed twice with diethyl ether, and air-dried to get the target product E: Yield (87.5%) as a yellow crystal, m.p. (220–225 °C), as shown in Scheme 1 [13,17].

RESULTS AND DISCUSSION

Characterization of the Synthesized Compounds

Infrared spectrum of the compound D

We notice in Fig. S1 and Table 2 of the compound D the appearance of a band at 3051.39 cm⁻¹ when it returns to the C–H vibration of the stretching of the aromatic bond of the benzene ring, and the appearance of two strong bands at 2970.38 and 2881.65 cm⁻¹ and absorption bands with limits at 1419.16 and 1356.60 cm⁻¹ due to shear vibration of the C–H aliphatic bond. The appearance of a weak bundle at 514.99 cm⁻¹ to the C–S bond, a bundle at 1215.15 cm⁻¹ return to the vibration of the stretching of the C–N wrist, and a bundle at 1660.71 cm⁻¹ returns to stretching the C=C bond in the benzene ring.



Scheme 1. Synthesis of heterocyclic and Gemini quaternary surfactants

Table 2. The most important bands in the infrared spectrum of the prepared compounds

Compd.	C-H Stretching aromatic (cm ⁻¹)	C-H Stretching aliphatic (cm ⁻¹)	C-H bending (cm ⁻¹)	C-S (cm ⁻¹)	C-N (cm ⁻¹)	C=C (cm ⁻¹)	N-H bending (cm ⁻¹)
D	3051.39	2970.38 & 2881.65	1419.16 & 1356.60	514.99 (w.b)	1215.15 (m)	1660.71 (m)	-
E	3039.81	2922.60 & 2850.79	1452.40 & 1363.67	551.64 (w.b)	1217.08 (m)	1656.85 (m)	-
F	3246.20	2922.16 & 2852.72	1452.40 & 1365.60	513.07 (w.b)	1215.15 (m)	1656.85 (m)	-

Infrared spectrum of the compound E

We observe in Fig. S3 and Table 2 of the compound E the appearance of a band at 3039.81 cm⁻¹ for C-H vibration of the stretching of the aromatic bond of the benzene ring. The appearance of two strong bands at 2922.6 and 2850.79 cm⁻¹ and absorption bands with limits at 1452.40 and 1363.67 cm⁻¹ due to shear vibration of the aliphatic C-H bond. The appearance of a weak bundle at 551.64 cm⁻¹ return to the C-S bond, a bundle at 1217.08 cm⁻¹ for the vibration of the C-N stretching of the wrist, and a bundle at 1656.85 cm⁻¹ for the stretching of C=C bond in the benzene ring.

Infrared spectrum of the compound F

We found in Fig. S5 and Table 2 of the compound F the appearance of a band at 3246.20 cm⁻¹ for the C-H vibration of the stretching of the aromatic bond of the benzene ring. The appearance of two strong bands at 2922.16 and 2852.72 cm⁻¹ and absorption bands at 1452.40 and 1356.60 cm⁻¹ due to shear vibration of the

aliphatic C-H bond. The appearance of a weak bundle at 513.07 cm⁻¹ for the C-S bond, a bundle at 1215.15 cm⁻¹ for the vibration of the C-N stretching of the wrist, and a signal at 1656.85 cm⁻¹ returns to stretching the C=C bond in the benzene ring.

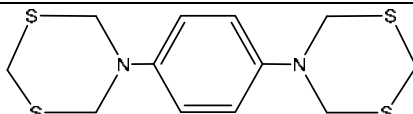
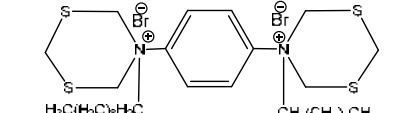
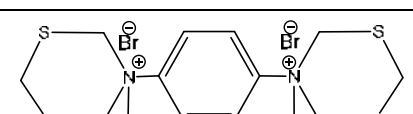
NMR spectrum of the compound D

The ¹H-NMR spectrum (Table 3 and Fig. S2) showed the appearance of a singlet signal at 3.55 ppm belonging to the protons of the carbon atom represented by the CH₂ group attached to two sulfur atoms and the number of 4 protons, and a single signal at 3.88 ppm represented by the CH₂ group attached to the sulfur and nitrogen atoms and the number of 8 protons, and a multiplet signal at 6.93–7.04 ppm refers to the protons of the aromatic ring and the number of 4 protons.

NMR spectrum of the compound E

The ¹H-NMR spectrum (Table 3 and Fig. S4) showed the appearance of a triplet signal at 0.83–0.86 ppm belonging to the protons of the carbon CH₃

Table 3. The most important signals appearing in the NMR spectrum of compounds D, E, and F

Signals	Chemical shift (ppm)	Chemical structures	Compound
(s, 4H, S- <u>CH₂</u> -S);	3.55		D
(s, 8H, N- <u>CH₂</u> -S);	3.88		
(m, 4H, Ph- <u>H</u>)	6.93–7.04		
(t, 6H, (CH ₂) ₈ <u>CH₃</u>);	0.83–0.86		E
(m, 32H, (<u>CH₂</u>) ₈ CH ₃);	1.23–1.27		
(t, 4H, N- <u>CH₂</u>);	2.96–2.98		
(s, 4H, S- <u>CH₂</u> -S);	3.55		
(s, 8H, N- <u>CH₂</u> -S);	4.06		
(m, 4H, Ph- <u>H</u>)	6.90–7.06		
(t, 6H, (CH ₂) ₁₂ <u>CH₃</u>);	0.85–0.87		F
(m, 48H, (<u>CH₂</u>) ₁₂ CH ₃);	1.19–1.29		
(t, 4H, N- <u>CH₂</u>);	2.93–2.96		
(s, 4H, S- <u>CH₂</u> -S);	3.54		
(s, 8H, N- <u>CH₂</u> -S);	3.95		
(m, 4H, Ph- <u>H</u>)	7.01–7.10		

represented by a group linked to the long chain $(\text{CH}_2)_8$ and the number of 6 protons. A multiplet signal at 1.23–1.27 ppm belonging to the protons of the carbon atom represented by the $(\text{CH}_2)_8$ group associated with the CH_3 group and the number of 32 protons. A triplet signal at 2.96–2.98 ppm referring to the protons of the carbon atom represented by the CH_2 group associated with the nitrogen atom and the number of 4 protons. A singlet signal at 3.55 ppm refers to the carbon atom represented by the CH_2 group attached to two sulfur atoms and the number of 4 protons and a singlet signal at 4.06 ppm represented by the CH_2 group attached to the sulfur and nitrogen atoms and the number of 8 protons. A multiplet signal at 6.90–7.06 ppm refers to the protons of the aromatic ring and the number of 4 protons.

NMR spectrum of the compound F

The $^1\text{H-NMR}$ spectrum (Table 3 and Fig. S6) was characterized by the appearance of a triplet signal at 0.85–0.87 ppm belonging to the protons of the CH_3 carbon represented by a group linked to the long chain $(\text{CH}_3)_{12}$ and the number of 6 protons, and a multiplet signal at 1.19–1.29 ppm belonging to the protons of the carbon atom represented by the $(\text{CH}_2)_{12}$ group associated with the CH_3 group and the number of 48 protons. A triplet signal at 2.93–2.96 ppm referring to the protons of the carbon atom represented by the CH_2 group associated with the nitrogen atom and the number of 4 protons. A singlet signal at 3.54 ppm refers to the carbon atom represented by the CH_2 group attached to two sulfur atoms and the number of 4 protons. A singlet signal at 3.95 ppm represented by the CH_2 group attached to the sulfur and nitrogen atoms and the number of 8 protons. A multiplet signal at 7.01–7.10 ppm refers to the protons of the aromatic ring and the number of 4 protons.

Mass spectrum of the prepared compounds

During our current study, the mass spectrum of the prepared compounds D, E, and F was recorded in order to prove their molecular formula (Tables 4–6 and Fig. 1–3) the aforementioned spectra showed a group of peaks of different molecular weights, with variation in their relative abundance as it gave a peak of fragmentation at $m/z = 781.1$, 758.6, and 316.1 with their relative abundance ranged (13.5,

9.32, and 2.26%) which is due to the parent molecular ion of the compounds D, E, and F, respectively.

Potentiodynamic Polarization Studies

Tables 7 and 8 illustrate the polarization of carbon steel alloy corrosion in the absence and presence of various dosages (1×10^{-4} , 5×10^{-4} , 1×10^{-3} , 5×10^{-3}) M of D, E, and F inhibitors at 25 and 50 °C. Fig. 4–8 illustrate the polarization curves. According to the data, the uninhibited sample had the maximum corrosion current density. However, when the inhibitor concentration rises, so does the corrosion current density, I_{corr} ($\mu\text{A cm}^{-2}$). Corrosion rate CR (mpy) values exhibit the same tendency as current density, with values decreasing as inhibitor concentration increases. The

Table 4. The important fragments and relative abundance of the compound D

Fragments	m/z	% Relative abundance
$[\text{M}]^+$	316.1	13.5
$[\text{C}_{11}\text{H}_{11}\text{N}_2\text{S}_3]^+$	267.2	2.7
$[\text{C}_{10}\text{H}_{12}\text{N}_2\text{S}_2]^+$	224.1	6.5
$[\text{C}_8\text{H}_4\text{NS}_2]^+$	178.1	3.5
$[\text{C}_8\text{H}_4\text{NS}]^+$	146.1	9.2
$[\text{C}_8\text{H}_8\text{N}_2]^+$	132.1	14.1
$[\text{C}_8\text{H}_8\text{N}]^+$	118.1	7.7

Table 5. The important fragments and relative abundance of the compound E

Fragments	m/z	% Relative abundance
$[\text{M}]^+$	758.6	9.3
$[\text{C}_{32}\text{H}_{58}\text{N}_2\text{S}_4\text{Br}]^+$	679.0	13.9
$[\text{C}_{11}\text{H}_{13}\text{N}_2\text{S}_4]^+$	301.2	1.3
$[\text{C}_{10}\text{H}_{17}\text{N}_2\text{S}_2]^+$	229.0	20.8
$[\text{C}_8\text{H}_3\text{NS}_2]^+$	177.1	13.9

Table 6. The important fragments and relative abundance of the compound F

Fragments	m/z	% Relative abundance
$[\text{M}]^+$	871.1	2.6
$[\text{C}_{40}\text{H}_{78}\text{N}_2\text{S}_4]^+$	711.1	5.3
$[\text{C}_{26}\text{H}_{67}\text{N}_2\text{S}_4]^+$	535.5	1.7
$[\text{C}_{22}\text{H}_{79}\text{N}_2\text{S}_4]^+$	341.2	8.9
$[\text{C}_{10}\text{H}_{23}\text{N}_2\text{S}_3]^+$	267.2	10.9
$[\text{C}_7\text{H}_{25}\text{NS}_2]^+$	137.1	14.3

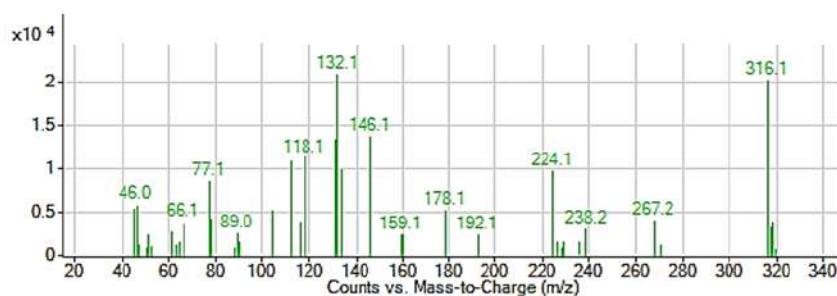


Fig 1. Mass spectrum of the synthesized heterocyclic compound D

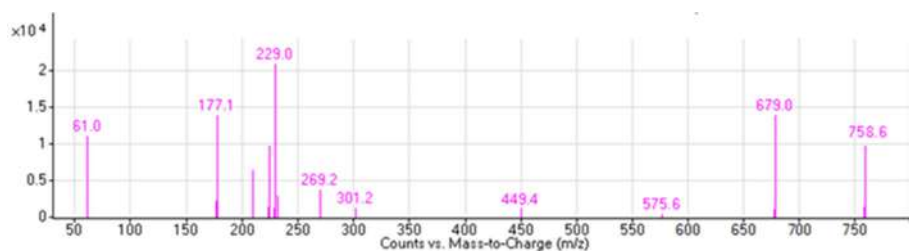


Fig 2. Mass spectrum of the synthesized heterocyclic - Gemini surfactant E

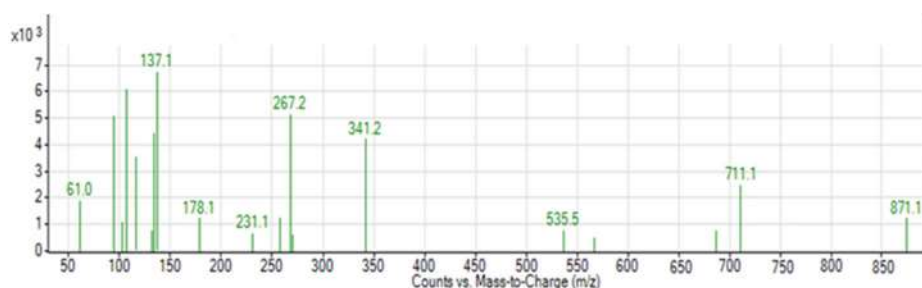


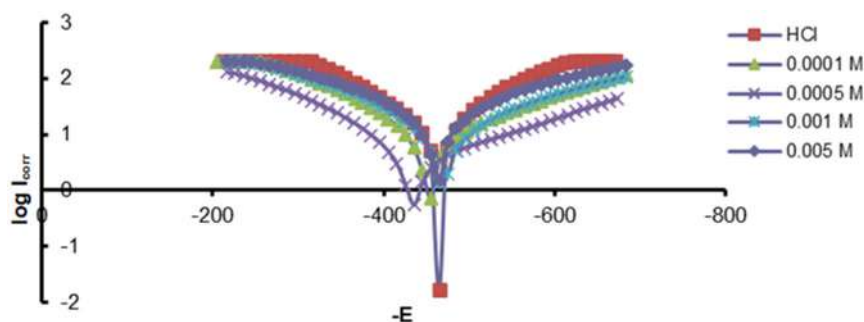
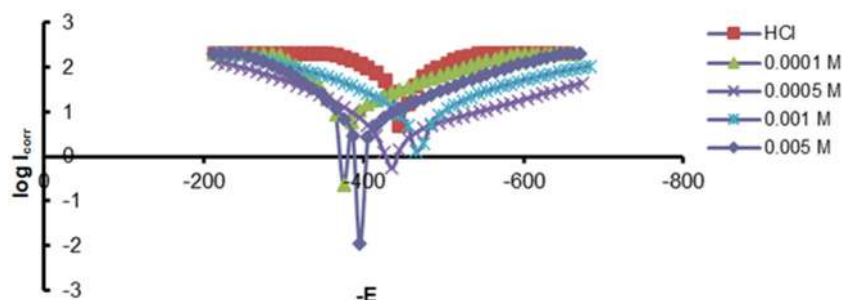
Fig 3. Mass spectrum of the synthesized heterocyclic-Gemini surfactant F

Table 7. Tafel polarization parameters in the absence and presence of various concentrations of inhibitors for carbon steel C95 in 2 M HCl at 298 K

Inhibitor	Conc. of inhibitor (M)	$-E_{corr}$ (mV)	CR (mpy)	I_{corr} ($\mu\text{A cm}^{-2}$)	β_c (mV dec^{-1})	β_a (mV dec^{-1})	IE%	Θ
D	0	462.80	14.81	32.56	-198.20	193.00	-	-
	1×10^{-4}	470.50	5.99	13.18	-223.60	197.20	59.50	0.59
	5×10^{-4}	415.40	4.51	9.90	-187.30	206.40	69.50	0.69
	1×10^{-3}	468.60	3.89	8.55	-196.60	150.20	73.70	0.73
	5×10^{-3}	377.50	1.42	3.13	-145.70	78.10	90.30	0.90
E	0	462.80	14.81	32.56	-198.20	193.00	-	-
	1×10^{-4}	446.10	5.99	13.17	-141.90	192.00	59.50	0.59
	5×10^{-4}	460.80	4.82	9.41	-222.10	158.20	71.20	0.71
	1×10^{-3}	375.30	2.97	6.53	-197.40	204.60	79.90	0.79
	5×10^{-3}	529.90	1.32	2.90	-203.90	293.10	91.00	0.91
F	0	462.80	14.81	32.56	-198.20	193.00	-	-
	1×10^{-4}	441.20	5.93	13.05	-208.60	163.20	59.90	0.59
	5×10^{-4}	390.30	2.93	6.45	-201.90	121.60	80.10	0.80
	1×10^{-3}	370.60	1.04	5.55	-142.40	68.60	83.00	0.83
	5×10^{-3}	433.70	1.03	2.28	-162.00	119.80	92.90	0.92

Table 8. Tafel polarization parameters in the absence and presence of various concentrations of inhibitors for carbon steel C95 in 2 M HCl at 323 K

Inhibitor	Conc. of inhibitor (M)	$-E_{\text{corr}}$ (mV)	CR (mpy)	I_{corr} ($\mu\text{A cm}^{-2}$)	β_c (mV dec $^{-1}$)	β_a (mV dec $^{-1}$)	IE%	Θ
D	0	445.80	25.68	56.44	-171.70	148.30	-	-
	1×10^{-4}	519.20	14.56	32.00	-227.50	338.70	43.30	0.43
	5×10^{-4}	452.30	9.85	21.67	-200.50	163.50	61.60	0.61
	1×10^{-3}	468.50	8.24	18.12	-160.60	144.20	67.80	0.67
	5×10^{-3}	476.10	6.38	14.04	-288.20	240.80	75.10	0.75
E	0	445.80	25.68	56.44	-171.70	148.30	-	-
	1×10^{-4}	377.80	10.90	24.08	-210.30	250.90	57.30	0.57
	5×10^{-4}	501.40	9.41	20.70	-238.30	197.50	63.30	0.63
	1×10^{-3}	372.00	7.80	17.15	-251.80	195.80	69.60	0.69
	5×10^{-3}	354.40	2.04	9.49	-159.80	158.00	83.10	0.83
F	0	445.80	25.68	56.44	-171.70	148.30	-	-
	1×10^{-4}	373.80	10.72	23.58	-199.30	123.40	58.20	0.58
	5×10^{-4}	404.30	5.14	11.31	-225.00	137.10	79.90	0.79
	1×10^{-3}	376.30	2.68	9.91	-228.80	124.10	82.40	0.82
	5×10^{-3}	424.80	1.92	8.28	-177.60	114.80	84.30	0.84

**Fig 4.** The potentiodynamic polarization curve for C95 alloy in (2 M HCl solution + various concentrations of compound D) at 298 K**Fig 5.** The potentiodynamic polarization curve for C95 alloy in (2 M HCl solution + various concentrations of compound D) at 323 K

obtained inhibitor efficiency followed a similar trend, as previously stated. All of this suggests that as the concentration of the inhibitor increases, so does its efficacy [17-23]. Adsorption of sulfur atoms in inhibitors

(D, E, and F) on the steel surface, and surfactants that represent the CR, is referred to as dropping the CR (E and F). The adsorption process improves as the inhibitor concentrations rise [24].

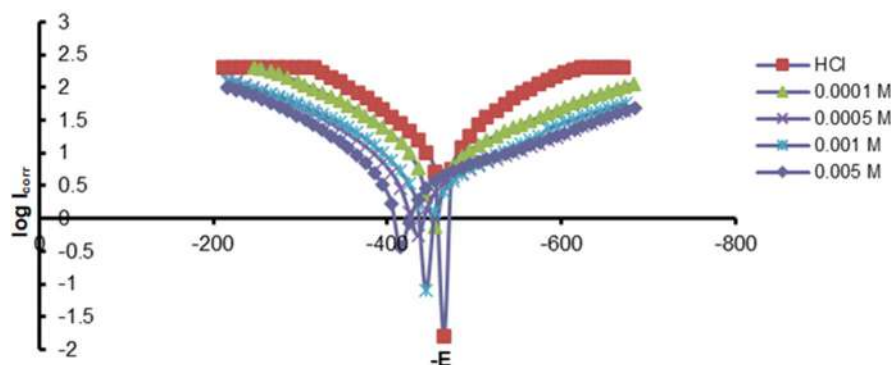


Fig 6. The potentiodynamic polarization curve for C95 alloy in (2 M HCl solution + various concentrations of compound E) at 298 K

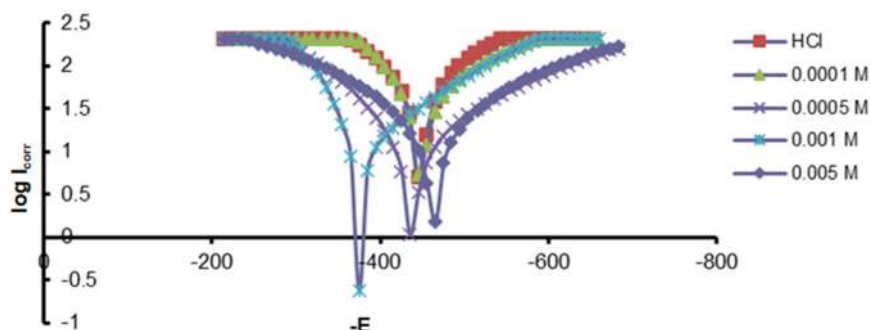


Fig 7. The potentiodynamic polarization curve for C 95 alloy in (2 M HCl solution + various concentrations of compound E) at 323 K

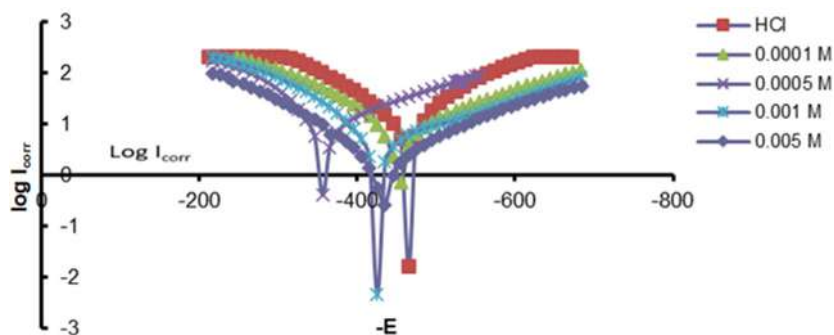


Fig 8. The potentiodynamic polarization curve for C 95 alloy in (2 M HCl solution + various concentrations of compound F) at 298 K

The adsorption of D, E, and F on the steel surface creates a protective barrier that keeps the steel surface from being corroded. Steel protection is improved by increasing the concentration of surfactant-inhibitors [17,24]. The findings also show that the inhibitory passivity gradually increased, caused by the inhibitor's passive film clinging to the electrode surface. Because there is variance in both cathodic (β_c), and anodic (β_a) responses when compared to blank, both cathodic and

anodic reactions are inhibited with the administration of inhibitors [25-27]. When the displacement of corrosion potential (E_{corr}) from the corrosion potential of the blank exceeds 85 mV, the inhibitor is either cathodic or anodic. If the displacement in (E_{corr}) is less than 85 mV, the corrosion inhibitor is of the mixed type [28-29]. The displacements in (E_{corr}) in the current study are 85.3, 67.1, and 29.1 mV for D, E, and F, respectively, as calculated by Eq. (1).

$$\%IE = \frac{I_{\text{corr}}^{\circ} - I_{\text{corr}}}{I_{\text{corr}}^{\circ}} \times 100 \quad (1)$$

where: I_{corr}° and I_{corr} is corrosion current density in the absence and presence of inhibitors, respectively. As a result, the inhibitors tested (E and F) are mixer kinds, with (D) being somewhat more cathodic or anodic as shown in Fig. 4–8 [23,27].

The following Eq. (2) and (3) [17,27,29] can be used to assess inhibitory efficiency.

$$\%IE = \left(\frac{I_{\text{corr}}^{\circ} - I_{\text{corr}}}{I_{\text{corr}}^{\circ}} \right) \quad (2)$$

$$\theta = \frac{I_{\text{corr}}^{\circ} - I_{\text{corr}}}{I_{\text{corr}}^{\circ}} \quad (3)$$

The corrosion rate (CR mpy) of a carbon steel alloy (C95) in an acidic solution in the absence and presence of varied concentrations of heterocyclic organic compounds as inhibitors and within the temperatures (298, 323 K) was estimated using the following Eq. (4) [17,27,29].

$$CR = K \times \frac{I_{\text{corr}}}{\rho} \times EW \quad (4)$$

The surfactant-inhibitor results (Tables 7 and 8, Fig. 6-9) show how inhibition effectiveness affects the hydrophobic structure. Increasing the hydrophobic nature of the surfactant tail elongation increases the steel inhibition efficacy. Surfactant F is more effective than surfactant E because it has a tail with 14 carbon atoms, whereas E has just a tail with 10 carbon atoms [30-31]. For example, at a concentration of 5×10^{-3} M, the IE% of inhibitors E and F at 25 °C is 66.6 and 68.1%, respectively (Table 7). As previously noted, increasing the carbon tail length increases surface adsorption affinity [31-32]. As a result, the surfactant tail modulates surfactant inhibitor adsorption on the surface, increasing surface coverage and

inhibition effectiveness [33-35].

The temperature has a major impact on the performance of the inhibitors investigated. Temperature increases of the corrosive solution containing the synthesized D, E, and F inhibitors enhanced the steel's corresponding CR, as indicated in Tables 7 and 8. The findings demonstrate a constant increase in CR as the temperature of the solution rises, confirming the presence of the investigated D, E, and F inhibitors [32,35]. The growing CR with temperature trend reflects the affinity of the generated inhibitors for chemical adsorption on the steel surface. The chemical structure of the E and F Gemini surfactant-inhibitors changed as the solution temperature increased, resulting in larger electronic densities of the active centers and, as a result, higher adsorption on the corroded surface [36-37]. The negatively charged center of the inhibitors generated interacts electrostatically with the negatively charged center formed on the surface of steel after it has been dipped in a vigorous acidic solution [12,38].

Inhibition Mechanism

The adsorption of these compounds to the metal solution interface could explain why D, E, and F have an inhibitory effect on the corrosion of carbon steel in 2 M HCl solution. The nature of the metal, the chemical structure of the inhibitors, the inhibitor concentration, the inhibitor active sites, the electronic cloud, the composition of the electrolyte, and the temperature influence the amount of inhibitor adsorption [39]. Adsorption on the metal surface was proposed to occur via the active center present on inhibitor molecules and to be charge density dependent, as shown in Schemes 2–4 [4,40].

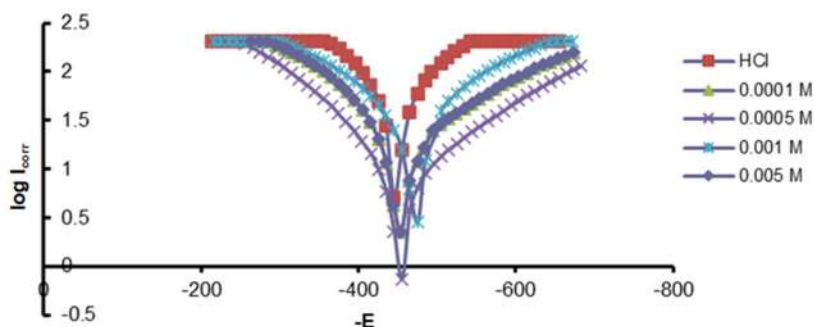


Fig 9. The potentiodynamic polarization curve for C 95 alloy in (2 M HCl solution + various concentrations of compound F) at 323 K

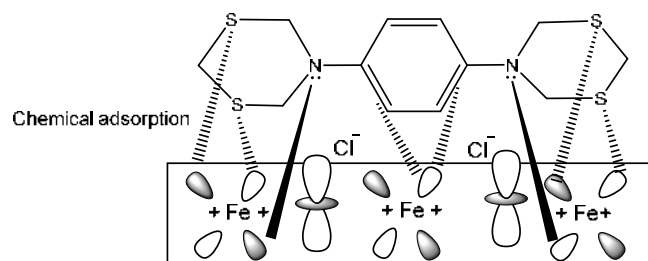
According to the inhibition efficiency, the decline in %IE occurs in the following order: $F > E > D$. Compound F (designed as 14-pH-14) has a stronger adsorption propensity on interfaces than the shorter chain surfactant E (designed as 10-pH-10) and thus has a slightly better inhibitory impact on corrosion than compound E [30,39]. The surfactant tail essentially increases adsorption at interfaces, promoting their activity as corrosion inhibitors. As a result, the surfactant tail increases the adsorption proclivity on the steel surface, delaying the attack of the corrosive solution. The positively charged quaternary ammonium nitrogen interacts electrostatically with the bridging negatively charged (Cl^-) ions on the positively charged metal surface to form a protective layer that isolates the surface from contact with an aggressive medium, thereby slowing steel corrosion, as shown in Schemes 2–4 [17,40].

Furthermore, our synthesized aromatic heterocyclic inhibitors had several electronic rich functional groups such as N, S, C–N, and C=C that might interact with the iron's unoccupied d -orbital and improve their adsorption effectiveness on the tested carbon steel [13,41]. In this scenario, the inhibitory effect is caused by the interaction of the π -electron and the existence of an electron donor for four sulfur atoms, which forms a connection with the metal atom's unoccupied d -orbital at the interface.

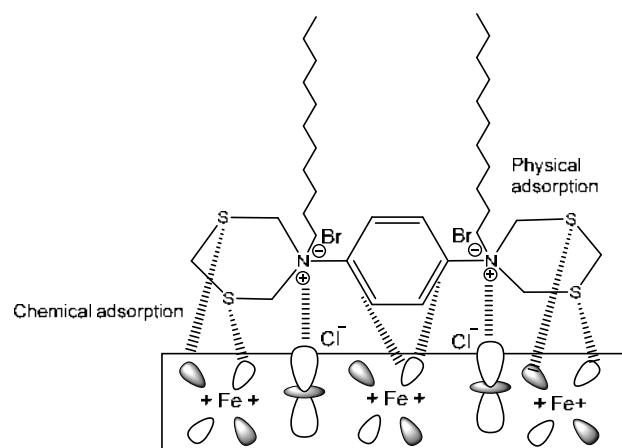
In general, two adsorption mechanisms on the metal surface in acid media are examined [13]. In the first model, neutral molecules may be adsorbed on the surface of carbon steel via the chemisorption mechanism, which involves the displacement of water molecules from the surface of carbon steel and the sharing of electrons between heteroatoms and iron [39,42]. Based on donor-acceptor interactions between their π -electrons and unoccupied d -orbitals of surface iron, inhibitor molecules may likewise be adsorbed on the carbon steel surface [13].

In the second model, it is well known that electrostatic repulsion makes it difficult for protonated molecules to approach the positively charged carbon steel surface. Because Cl^- has a lower degree of hydration, it may bring excess negative charges near the interface, allowing for more adsorption of positively charged inhibitor molecules. Protonated inhibitors adsorb via

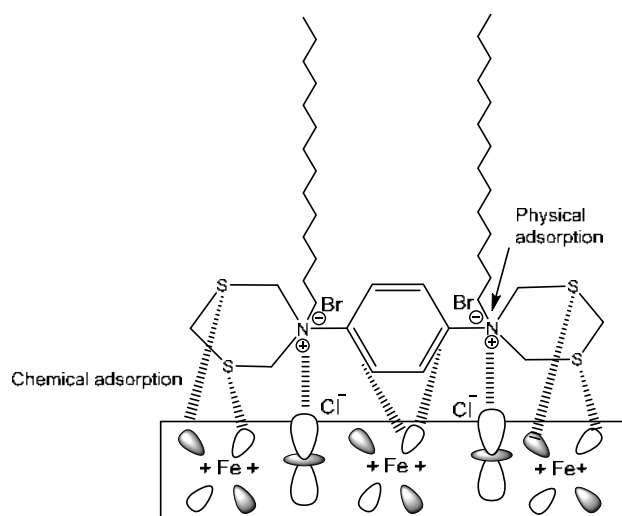
electrostatic interactions between positively charged molecules and the negatively charged metal surface. As a result, adsorbed Cl^- ions and protonated inhibitors work together [4,43].



Scheme 2. Adsorption of the synthesized inhibitor D on the steel surface is predicted



Scheme 3. Adsorption of the synthesized inhibitor E on the steel surface is predicted



Scheme 4. Adsorption of the synthesized inhibitor F on the steel surface is predicted

Biological Assay

The tendency of their remedies to disintegrate the outer cell wall, resulting in the exudation of cell fluids and the death of pathogenic bacteria, makes heterocyclic compounds physiologically efficient in suppressing many different types of pathogenic bacteria [44]. The existence of unique active groups within the composition of cyclic compounds, such as groups C-S, C-N, and NH₂ may result in the formation of complexes with elements in the cell body, such as copper, iron, and divalent cobalt ions, which leads to cell death owing to their loss, these are the items [44].

Because of the existence of a form of corrosion induced by bacteria in the ground (in reservoir water and oil) that convert some sulfur-containing oil molecules to H₂S, SO₂, and SO₃, which degrades metals by converting them to sulfurous acid in the presence of water, which is one of the reasons. Because heterocyclic compounds include nitrogen and sulfur atoms that differentiate them for associating with various elements, much and ongoing research have been undertaken in the field of suppressing various forms of bacteria, i.e., negative for cream dye (*S. epidermis*) and positive for cream dye (*E. coli*) [44-45].

The aforementioned drilling procedure was used in conjunction with a cork drill, and the damping diameters were measured in millimeters using a ruler. The results demonstrated the biological action of solutions of various chemicals generated from it with the bacteria under research at a concentration of 1000 ppm. The compound D demonstrated effective resistance to both types of negative bacteria. At a concentration of 3000 mcg mL⁻¹, the cation has a diameter of 20 mm against *E. coli* bacteria and 19 mm against *S. epidermis* bacteria. At the same concentration, the compound F is solely effective against gram-negative bacteria (*E. coli*), with an inhibition diameter of 14 mm, as shown in Fig. 10 and 11 [46].

It was discovered that the complexes had a stronger inhibitory efficiency than the ligands based on the results provided in Table 9 arising from the action of the produced compounds against the specified species of bacteria. The effects of metal on normal biological processes [46].



Fig 10. Effect of the prepared compound on growth *S. epidermis*



Fig 11. Effect of the prepared compound on growth *S. epidermis*

Table 9. The inhibition zones resulting from the biological activity of compounds D and F

No	Compounds	Concentration (mg mL ⁻¹)	Inhibition zone (mm)	
			<i>S. epidermis</i>	<i>E. coli</i>
1	D	3000	19	20
2	F	3000	0	14

CONCLUSION

In summary, the test medium used is a very strong acid of 2 M HCl and thus corrosive to the carbon steel alloy. The heterocyclic and heterocyclic cationic Gemini surfactants inhibitors were found effective by providing a protective film barrier, emanating from the heteroatom's adsorption and the positive quaternary ammonium nitrogen molecules adsorption on the metal surface thus preventing the metal surface test solution interactive corrosion reactions. At all of the concentrations used, the inhibitors D, E, and F gave relatively good and effective protection against corrosion HCl, which was confirmed by electrochemical results. However, the highest concentration of the inhibitor gave the best corrosion inhibition performance at 25 °C. The inhibition efficiency revealed that the decline in %IE occurs in the

following order: F > E > D. The results indicated the biological impact of several chemical solutions made from it with the bacteria under study at 1000 ppm. Compound D was efficient against both types of negative bacteria with a diameter of 20 mm against *E. coli* bacteria and 19 mm *S. epidermis* bacteria at a dosage of 3000 mcg mL⁻¹. With an inhibition diameter of 14 mm, compound F is only effective against *E. coli* at the same dose.

■ ACKNOWLEDGMENTS

The Laboratory Department in Basra Oil Company (BOC) appreciates the support offered in carrying out this research work.

■ REFERENCES

- [1] Khabibullina, G.R., Fedotova, E.S., Anpilogova, G.R., Akhmetova, V.R., and Ibragimov, A.G., 2016, Multicomponent cyclothiomethylation of phenylenediamines and 4,4'-diaminodiphenyls with formaldehyde and 1,2-ethanedithiol, *Russ. J. Gen. Chem.*, 86, 1608–1612.
- [2] Akhmetova, V.R., Khairullina, R.R., Tyumkina, T.V., Nelyubina, Y.V., Smol'yakov, A.F., Bushmarinov, I.S., Starikova, Z.A., Abdullin, M.F., and Kunakova, R.V., 2010, Cyclothiomethylation of carboxylic acid hydrazides with aldehydes and H₂S, *Russ. Chem. Bull.*, 59 (2), 425–433.
- [3] Liu, Y., Zhang, H., Liu, Y., Li, J., and Li, W., 2019, Inhibitive effect of quaternary ammonium-type surfactants on the self-corrosion of the anode in alkaline aluminium-air battery, *J. Power Sources*, 434, 226723.
- [4] Pakiet, M., Kowalczyk, I., Leiva Garcia, R., Akid, R., and Brycki, B., 2020, Cationic cleavable surfactants as highly efficient corrosion inhibitors of stainless steel AISI 304: Electrochemical study, *J. Mol. Liq.*, 315, 113675.
- [5] Kamal, M.S., Hussein, I., Mahmoud, M., Sultan, A.S., and Saad, M.A.S., 2018, Oilfield scale formation and chemical removal: A review, *J. Pet. Sci. Eng.*, 171, 127–139.
- [6] Liu, D., Quan, X., Zhu, H., Huang, Q., and Zhou, L., 2020, Evaluation of modified waste concrete powder used as a novel phosphorus remover, *J. Cleaner Prod.*, 257, 120646.
- [7] Tung, N.T., Tran, C.S., Nguyen, T.L., Pham, T.M.H., Chi, S.C., Nguyen, H.A., Bui, Q.D., Bui, D.N., and Tran, T.Q., 2021, Effect of surfactant on the *in vitro* dissolution and the oral bioavailability of a weakly basic drug from an amorphous solid dispersion, *Eur. J. Pharm. Sci.*, 162, 105836.
- [8] Dandigunta, B., Karthick, A., Chattopadhyay, P., and Dhoble, A.S., 2019, Impact of temperature and surfactant addition on milk foams, *J. Food Eng.*, 299, 110509.
- [9] Saad, M.A., Abdurahman, N.H., and Mohd Yunus, R., 2021, Synthesis, characterization, and demulsification of water in crude oil emulsion via a corn oil-based demulsifier, *Mater. Today: Proc.*, 42, 251–258.
- [10] Lei, Z., Gao H., Chang, X., Zhang, L., Wen, X., and Wang, Y., 2020, An application of green surfactant synergistically metal supported cordierite catalyst in denitration of selective catalytic oxidation, *J. Cleaner Prod.*, 249, 119307.
- [11] Vimal Kumar, K., and Appa Rao, B.V., 2019, Phosphorylated xanthan gum, an environment-friendly, efficient inhibitor for mild steel corrosion in aqueous 200 ppm NaCl, *Mater. Today: Proc.*, 15, 155–165.
- [12] Azzam, E.M., Abd El-Salam, H.M., Mohamed, R.A., Shaban, S.M., and Shokry, A., 2018, Control the corrosion of mild steel using synthesized polymers based on polyacrylamide, *Egypt. J. Pet.*, 27 (4), 897–910.
- [13] Fouda, A.E.A.S., Abd el-Maksoud, S.A., El-Sayed, E.H., Elbaz, H.A., and Abousalem, A.S., 2021, Effectiveness of some novel heterocyclic compounds as corrosion inhibitors for carbon steel in 1 M HCl using practical and theoretical methods, *RSC Adv.*, 11 (31), 19294–19309.
- [14] Akhmetova, V.R., Niatshina, Z.T., Starikova, Z.A., Korzhova, L.F., and Ibragimov, A.G., 2011, Thiomethylation of heteroaromatic amines, *Russ. J. Org. Chem.*, 47 (6), 920–927.

- [15] Akhmetova, V.R., and Rakhimova, E.B., 2014, One-pot cyclothiomethylation of amines as efficient method for the synthesis of saturated five-, six-, seven-, and eight-membered *S,N*-heterocycles, *Russ. J. Org. Chem.*, 50, 1711–1731.
- [16] Akhmetova, V.R., Nadyrgulova, G.R., Niatshina, Z.T., and Dzhemilev, U.M., 2009, Cyclothiomethylation of primary amines with formaldehyde and hydrogen sulfide to nitrogen- and sulfur-containing heterocycles (Review), *Chem. Heterocycl. Compd.*, 45, 1155–1176.
- [17] Shaban, S.M., and Elsharif, A.M., Elged, A.H., Eluskkary, M.M., Aiad, I., and Soliman, E.A., 2021, Some new phospho-zwitterionic Gemini surfactants as corrosion inhibitors for carbon steel in 1.0 M HCl solution, *Environ. Technol. Innovation*, 24, 102051.
- [18] Khafizova, S.R., Akhmetova, V.R., Kunakova, R.V., and Dzhemilev, U.M., 2003, Thiomethylation of aromatic amines: Efficient method for the synthesis of heterocyclic compounds, *Russ. Chem. Bull.*, 52 (8), 817–1821.
- [19] Akhmetova, V.R., Akhmadiev, N.S., and Ibragimov, A.G., 2016, Catalytic multimolecular reactions of 1,3-dicarbonyl CH acids with CH_2O and *S*- and *N*-nucleophiles, *Russ. Chem. Bull.*, 65 (7), 1653–1666.
- [20] Akhmetova, V.R., Khabibullina, G.R., Galimzyanova, N.F., and Ibragimov, A.G., 2014, One-pot synthesis and fungicidal activity of 2-(1,5,3-dithiazepan-3-yl)ethanol and *N,N'*-bis(2-hydroxyethyl)tetrathiadiazacycloalkanes, *Russ. J. Appl. Chem.*, 87 (3) 294–298.
- [21] Akhmetova, V.R., Khairullina, R.R., Nadyrgulova, G.R., Kunakova, R.V., and Dzhemilev, U.M., 2008, Multicomponent heterocyclization of carboxamides with H_2S and CH_2O , *Russ. J. Org. Chem.*, 44 (2), 190–196.
- [22] Wang, D., Li, Y., Chen, B., and Zhang, L., 2020, Novel surfactants as green corrosion inhibitors for mild steel in 15% HCl: Experimental and theoretical studies, *Chem. Eng. J.*, 402, 126219.
- [23] Loto, C.A., Fayomi, O.S.I., Loto, R.T., and Popoola, A.P.I., 2019, Potentiodynamic polarization and gravimetric evaluation of corrosion of copper in 2 M H_2SO_4 and its inhibition with ammonium dichromate, *Procedia Manuf.*, 35, 413–418.
- [24] Akhmetova, V.R., Akhmadiev, N.S., Zainullin, R.A., Khayrullina, V.R., Mescheryakova, E.S., and Glushkova, N.A., 2020, Synthesis, *in vitro* and *in silico* studies of inhibitory activity towards α -amylase of *bis*-azole scaffolds linked by an alkylsulfanyl chain, *Can. J. Chem.*, 98 (11), 725–735.
- [25] Flitt, H.J., and Schweinsberg, D.P., 2005, Evaluation of corrosion rate from polarisation curves not exhibiting a Tafel region, *Corros. Sci.*, 47 (12), 3034–3052.
- [26] Markhali, B.P., Naderi, R., Mahdavian, M., Sayebani, M., and Arman, S.Y., 2013, Electrochemical impedance spectroscopy and electrochemical noise measurements as tools to evaluate corrosion inhibition of azole compounds on stainless steel in acidic media, *Corros. Sci.*, 75, 269–279.
- [27] Solomon, M.M., and Umoren, S.A., 2015, Electrochemical and gravimetric measurements of inhibition of aluminum corrosion by poly (methacrylic acid) in H_2SO_4 solution and synergistic effect of iodide ions, *Measurement*, 76, 104–116.
- [28] Liu, Y., Liu, Z., Xu, A., and Liu, X., 2022, Understanding pitting corrosion behavior of AZ91 alloy and its MAO coating in 3.5% NaCl solution by cyclic potentiodynamic polarization, *J. Magnesium Alloys*, 10 (5), 1368–1380.
- [29] El Hajjaji, F., Belghiti, M.E., Drissi, M., Fahim, M., Salim, R., Hammouti, B., Taleb, M., and Nahlé, A., 2019, Electrochemical, quantum calculations and Monte Carlo simulation studies of *N1,N2*-bis(1-phenylethylidene)ethane-1,2-diamine as a corrosion inhibitor for carbon steel in a 1.0 M hydrochloric acid solution, *Port. Electrochim. Acta*, 37 (1), 23–42.
- [30] El Basiony, N.M., Badr, E.E., Baker, S.A., and El-Tabei, A.S., 2021, Experimental and theoretical (DFT & MC) studies for the adsorption of the synthesized Gemini cationic surfactant based on hydrazide moiety as X-65 steel acid corrosion inhibitor, *Appl. Surf. Sci.*, 539, 148246.
- [31] Elged, A.H., Shabana, S.M., Eluskkary, M.M., Aiad, I., Soliman, E.A., Elsharif, A.M., and Kim, D.H.,

- 2021, Impact of hydrophobic tails of new phospho-zwitterionic surfactants on the structure, catalytic, and biological activities of AgNPs, *J. Ind. Eng. Chem.*, 94, 435–447.
- [32] Fouda, A.S., Elmorsi, M.A., Shaban, S.M., Fayed, T., and Azazy, O., 2018, Evaluation of *N*-(3-(dimethyl hexadecyl ammonio)propyl) palmitamide bromide as cationic surfactant corrosion inhibitor for API N80 steel in acidic environment, *Egypt. J. Pet.*, 27 (4), 683–694.
- [33] Abd-Elaal, A.A., Elbasiony, N.M., Shaban, S.M., and Zaki, E.G., 2018, Studying the corrosion inhibition of some prepared nonionic surfactants based on 3-(4-hydroxyphenyl) propanoic acid and estimating the influence of silver nanoparticles on the surface parameters, *J. Mol. Liq.*, 249, 304–317.
- [34] Mobin, M., and Aslam, R., 2018, Experimental and theoretical study on corrosion inhibition performance of environmentally benign non-ionic surfactants for mild steel in 3.5% NaCl solution, *Process Saf. Environ. Prot.*, 114, 279–295.
- [35] Aiad, I., Shaban, S.M., Elged, A.H., and Aljoboury, O.H., 2018, Cationic surfactant based on alginate as green corrosion inhibitors for the mild steel in 1.0 M HCl, *Egypt. J. Pet.*, 27, 877–885.
- [36] Deyab, M.A., 2019, Enhancement of corrosion resistance in MSF desalination plants during acid cleaning operation by cationic surfactant, *Desalination*, 456, 32–37.
- [37] Zhou, T., Yuan, J., Zhang, Z., Xin, X., and Xu, G., 2019, The comparison of imidazolium Gemini surfactant [C₁₄-4-C₁₄im]Br₂ and its corresponding monomer as corrosion inhibitors for A3 carbon steel in hydrochloric acid solutions: Experimental and quantum chemical studies, *Colloids Surf., A*, 575, 57–65.
- [38] Shaban, S.M., Abd Elsamad, S., Tawfik, S.M., Abdel-Rahman, A.A.H., and Aiad, I., 2020, Studying surface and thermodynamic behavior of a new multi-hydroxyl Gemini cationic surfactant and investigating their performance as corrosion inhibitor and biocide, *J. Mol. Liq.*, 316, 113881.
- [39] Chafiq, M., Chaouiki, A., Damej, M., Lgaz, H., Salghi, R., Ali, I.H., Benmessaoud, M., Masroor, S., and Chung, I.M., 2020, Bolaamphiphile-class surfactants as corrosion inhibitor model compounds against acid corrosion of mild steel, *J. Mol. Liq.*, 309, 113070.
- [40] Wang, J., Liu, D., Cao, S., Pan, S., Luo, H., Wang, T., Ding, H., Mamba, B.B., and Gui, J., 2020, Inhibition effect of monomeric/polymerized imidazole zwitterions as corrosion inhibitors for carbon steel in acid medium, *J. Mol. Liq.*, 312, 113436.
- [41] Srivastava, V., Haque, J., Verma, C., Singh, P., Lgaz, H., Salghi, R., and Quraishi, M.A., 2017, Amino acid-based imidazolium zwitterions as novel and green corrosion inhibitors for mild steel: Experimental, DFT and MD studies, *J. Mol. Liq.*, 244, 340–352.
- [42] Arabahmadi, R., 2019, Cobalt(II) complexes derived from azo-azomethine ligands: Synthesis, characterization, solvatochromic, fluorescence, thermal, electrochemical and antimicrobial properties, *ChemistrySelect*, 4 (17), 4883–4891.
- [43] Azam, M., Al-Resayes, S.I., Wabaidur, S.M., Altaf, M., Chaurasia, B., Alam, M., Shukla, S.N., Gaur, P., Albaqami, N.T.M., Islam, M.S., and Park, S., 2018, Synthesis, structural characterization and antimicrobial activity of Cu(II) and Fe(III) complexes incorporating azo-azomethine ligand, *Molecules*, 23 (4), 813.
- [44] Fontana, M.G., and Staehle, R.W., 1980, “Biological Corrosion” in *Advances in Corrosion Science and Technology*, 1st Ed., Springer, New York, 1–42.
- [45] Jone Kirubavathy, S., and Chitra, S., 2017, Structural, theoretical investigations and biological evaluation of Cu(II), Ni(II) and Co(II) complexes of mercapto-pyrimidine Schiff bases, *J. Mol. Struct.*, 1147, 797–809.
- [46] Zorofchian Moghadamtousi, S., Abdul Kadir, H., Hassandarvish, P., Tajik, H., Abubakar, S., and Zandi, K., 2014, A review on antibacterial, antiviral, and antifungal activity of curcumin, *BioMed Res. Int.*, 2014, 186864.

Synergistic Ti-Fe Oxides on Fishbone-Derived Carbon Sulfonate: Enhanced Styrene Oxidation Catalysis

Mukhamad Nurhadi^{1*}, Ratna Kusumawardani¹, Teguh Wirawan², Sin Yuan Lai^{3,4,5}, and Hadi Nur^{6,7}

¹Department of Chemical Education, Universitas Mulawarman, Kampus Gunung Kelua, Samarinda 75119, Indonesia

²Department of Chemistry, Faculty of Mathematics and Natural Sciences, Universitas Mulawarman, Samarinda 75119, Indonesia

³School of Energy and Chemical Engineering, Xiamen University Malaysia, Selangor Darul Ehsan 43900, Malaysia

⁴Kelip-kelip! Center of Excellence for Light Enabling Technologies, Xiamen University Malaysia, Bandar Sunsuria, Sepang 43900, Malaysia

⁵College of Chemistry and Chemical Engineering, Xiamen University, Xiamen 361005, China

⁶Department of Chemistry, Faculty of Mathematics and Natural Sciences, Universitas Negeri Malang, Jl. Semarang No. 5, Malang 65145, Indonesia

⁷Center of Advanced Materials for Renewable Energy (CAMRY), Universitas Negeri Malang, Jl. Semarang No. 5, Malang 65145, Indonesia

* **Corresponding author:**

email: nurhadi1969@yahoo.co.id

Received: December 27, 2022

Accepted: September 26, 2023

DOI: 10.22146/ijc.80667

Abstract: Fishbone-derived carbon sulfonate, modified through incipient wetness impregnation with titanium tetraisopropoxide and iron nitrate salts, displays catalytic activity in the oxidation of styrene with hydrogen peroxide (H₂O₂) as an oxidant. This was done to develop a cost-effective, non-toxic, and environmentally friendly bimetallic oxide catalyst, incorporating titanium and iron oxides on mesoporous-derived carbon fishbone to enhance styrene conversion and benzaldehyde selectivity in styrene oxidation using aqueous H₂O₂. The catalyst, featuring a combination of titanium and iron oxides on the surface of the fishbone-derived carbon sulfonate, demonstrates higher catalytic activity than single oxide catalysts, such as titanium or iron oxides alone. Factors influencing the catalyst's performance are investigated by using FTIR, XRD, XRF, SEM, and BET surface area. The results reveal that the presence of both titanium and iron oxides on the surface of the fishbone-derived carbon sulfonate and the catalyst's surface area creates a synergistic effect, the primary factors affecting its catalytic activity in styrene oxidation using H₂O₂ as an oxidant.

Keywords: iron; oxidation; styrene; synergistic effect; titanium

■ INTRODUCTION

The styrene oxidation on various transition metal-substituted catalysts remains a topic of significant interest in both academic and commercial fields. The process is crucial for synthesizing three vital products, namely styrene oxide, phenylacetaldehyde, and benzaldehyde, using hydrogen peroxide (H₂O₂) [1-3]. Benzaldehyde, the primary product of styrene oxidation, is an industrially important and versatile organic compound. It is extensively used as a key intermediate in synthesizing

perfume materials, anthelmintics, epoxy resins, plasticizers, drugs, sweeteners, chiral pharmaceuticals, pesticides, and epoxy paints [4-6]. Currently, two processes are employed for industrial production: (1) toluene reacts with oxygen to give benzoic acid in the catalytic oxidation, and (2) the hydrolysis of benzyl chloride [7-8]. It is significant to note that both catalytic oxidation and hydrolysis reactions demonstrate some crucial drawbacks, including high energy consumption, extended reaction duration, and the generation of

chloride waste. These issues have resulted in inferior conversion performance, low benzaldehyde yield (up to 20%) and selectivity. Contrarily, styrene selective oxidation could be a more appealing alternative compared to those complex approaches, drastic conditions, and toxic waste disposal of existing procedures. In an effort to elevate styrene catalytic oxidation, benzaldehyde yield, and selectivity, the utilization of heterogeneous catalysts is generally deemed more promising, particularly those containing transition metals as active sites.

Developing a bimetallic oxide heterogeneous oxidation catalyst, which combines titanium and iron oxides as active sites, while the catalyst support consists of carbon mesoporous-derived fishbone, offering an approach to enhance the catalytic activity. This catalyst system offers advantages, such as being cost-effective, innocuous, and eco-friendly. To further validate the advantages bestowed by this catalytic system design, the bimetallic composite was compared with monometallic transition metals (Ti or Fe), which both were supported onto carbon-derived fish bones. The catalytic activity of these two systems was investigated in a model reaction, namely an oxidation reaction containing styrene with aqueous H_2O_2 .

The styrene oxidation using H_2O_2 has been studied using monometallic oxide transition metals supported on different materials as catalysts. This is one of the reactions that can be employed as it is interesting from both industrial and scientific perspectives. Examples of monometallic transition metals introduced onto material support in styrene oxidation reactions include MCM-48 [9], Cu [10], Pd [11], La [6], Ti [7,12-14], Mn [15-16], Fe [13], V [17], and Cr [18]. However, styrene conversion and benzaldehyde selectivity remain low when monometallic transition metals are used on diverse material supports as catalysts.

Recently, numerous researchers have become increasingly interested in examining bimetallic oxides supported on various materials as catalysts. Bimetallic catalysts, composed of two different metals, exhibit unique characteristics. The synergistic effects of bimetallic oxide catalysts often result in novel physicochemical properties that render the catalyst

superior to either monometallic oxide component [19]. Bimetallic oxide catalysts have been extensively applied in the oxidation reactions. Several bimetallic catalysts have been explored to augment styrene conversion and benzaldehyde selectivity in styrene oxidation, such as MOF-74(Cu/Co) [3], Mn, Co-MCM-41 [20], La-Zn bimetallic oxide [21], CoNiPW [22], Cu_x-Co_y-MOF [23], and Co-Vanadium oxide supported on reduced graphene [24].

It reveals that despite the advances in bimetallic catalysts, there is still room for improvement in styrene conversion and benzaldehyde selectivity. The proposed novel bimetallic oxide catalyst system, consisting of titanium and iron oxides supported on carbon mesoporous-derived fishbone, has the potential to address these challenges. This innovative approach aims to enhance the catalytic performance while offering the benefits of being cost-effective, non-toxic, and environmentally friendly.

This study systematically investigated the catalytic activity and selectivity of the titanium and iron bimetallic oxide catalyst supported on carbon mesoporous-derived fishbone in the styrene oxidation reaction using aqueous H_2O_2 as an oxidant. We compared the performance of this bimetallic catalyst with those of monometallic transition metal (Ti or Fe) catalysts supported on carbon-derived fish bones. Additionally, we will explore the effect of varying the metal ratio, catalyst loading, and reaction conditions (e.g., temperature, pressure, and reaction time) on the catalytic performance.

By addressing the existing gap in the research, our study aims to develop a more efficient and environmentally friendly catalyst system for styrene oxidation. This would not only contribute to the advancement of knowledge in the field of heterogeneous catalysis but also provide potential industrial applications, particularly in the synthesis of valuable chemicals such as benzaldehyde and its derivatives. Ultimately, the successful development and implementation of this bimetallic oxide catalyst system could significantly improve the efficiency, selectivity, and sustainability of styrene oxidation processes.

■ EXPERIMENTAL SECTION

Materials

Sulfuric acid (H_2SO_4 , 97%) was received from JT Beker, Germany. Titanium(IV) isopropoxide ($\text{Ti}\{\text{OCH}(\text{CH}_3)_2\}_4$, 97%) was obtained from Sigma Aldrich, USA. Iron(III) nitrate ($\text{Fe}(\text{NO}_3)_3$) was ordered from Merck, Germany. Acetone ($\text{C}_3\text{H}_6\text{O}$, 99.75%) used as solvent was obtained from Mallinckrodt. Ethanol ($\text{C}_2\text{H}_6\text{O}$, 96%) used as solvent was received from Merck, Germany. Styrene ($\text{C}_6\text{H}_5\text{CH}=\text{CH}_2$, 99%) used as the reductant was bought from Sigma Aldrich, USA. Acetonitrile (CH_3CN , 100%) used as solvent was received from Merck, USA. H_2O_2 (30%) used as oxidant was obtained from Merck, USA. Fishbone waste was collected from many companies in Samarinda, Indonesia.

Instrumentation

The equipment and instruments used in this study included a furnace (Thermo Scientific) used for the carbonization process, oven (Mettler), FTIR spectrometer (IR-Prestige-21 Shimadzu), XRD instrument (Phillips PANalytical X'Pert PRO), X-ray fluorescence (WDXRF PANalytical, Minipal 4), SEM (FEI Inspect S50), the nitrogen adsorption-desorption isotherms (Quantachrome NovaWin instrument version 11.0), GC-2010 Shimadzu-gas chromatography equipped with an SH-Rxi-5ms column (30 m \times 0.25 mm ID \times 0.25 μm df) (serial 1652111), a flame ionization detector (FID) and nitrogen as the carrier gas.

Procedure

Carbonization process

Carbon was prepared from the fishbone waste from

many food companies around Samarinda, East Kalimantan, Indonesia. The fishbone was cleaned from impurities and dried. The fishbone was crushed to powdered form and then carbonized in a furnace at 500 °C for 2 h to form carbon. The fishbone-derived carbon was labeled as FBC.

Sulfonation process

Every 1 g of FBC was soaked in 10 mL of H_2SO_4 (1 M, JT Beker) and stirred at room temperature for 24 h. The mixer was filtered and washed with distillate water to remove any loosely bound acid, and it was dried at 110 °C overnight to obtain sulfonated fishbone-derived carbon (SFBC).

Ti and Fe impregnation

The process of impregnation follows the previous research [12]. Every 1 g of SFBC was impregnated with titanium tetraisopropoxide (500 μmol) and iron(III) nitrate (500 μmol) that was soaked in 10 mL acetone and stirred until all of the acetone solvents completely evaporated. The residual acetone was removed from the SFBC sample with ethanol (Merck) and dried at 110 °C overnight. The amount of Ti and Fe impregnated in the catalysts varied, such as 1:1, 2:1, and 1:2, respectively. Furthermore, the catalysts were calcined at 350 °C for 2 h. The catalysts were denoted as Ti-Fe(x:y)/SFBC, whereas x = concentration of Ti and y = concentration of Fe. For example, Ti-Fe(1:1)/SFBC was generated from SFBC that was prepared by carbonization process at 500 °C for 2 h, and the resultant was impregnated by titanium tetraisopropoxide (500 μmol) and iron(III) nitrate (500 μmol) and calcined at 350 °C for 2 h. The codes of all catalysts are listed in Table 1.

Table 1. Types of samples and treatments

Samples	Type of treatment	Concentration of Ti (μmol)	Concentration of Fe (μmol)
FBC	-	-	-
SFBC	Sulfonation	-	-
Ti/ SFBC	Sulfonation	500	-
Fe/ SFBC	Sulfonation	-	500
Ti-Fe(1:1)/SFBC	Sulfonation	500	500
Ti-Fe(2:1)/SFBC	Sulfonation	1000	500
Ti-Fe(1:2)/SFBC	Sulfonation	500	1000

Catalysts characterization

The characterization of catalysts was performed by using FTIR, XRD, XRF, SEM, and BET surface area. FTIR spectrometer with a spectral resolution of 2 cm^{-1} , scans 10 s, temperature at $20\text{ }^{\circ}\text{C}$ and wavenumber from 400 to 4000 cm^{-1} , was used to identify the functional groups in the catalyst. The crystallinity and phase content of the catalyst were analyzed using the XRD with the Cu K α ($\lambda = 1.5406\text{ \AA}$) radiation as the diffracted monochromatic beam at 40 kV and 40 mA. The pattern was scanned in the 2θ ranges between 7° and 60° at a step of 0.03° and step time of 1 s. The catalysts' chemical composition and physical properties were investigated using 1 kW wavelength dispersive XRF. The SEM with an accelerating voltage of 15 kV was used to determine the surface morphology and element containing the catalyst. The nitrogen adsorption-desorption isotherms were measured at a bath temperature of 77.3 K and an outgassed temperature of $300\text{ }^{\circ}\text{C}$ using a Quantachrome NovaWin instrument version 11.0.

Catalytic test

The performance of catalysts was evaluated by an oxidation of styrene with H_2O_2 as an oxidant. The procedure of reactions was conducted according to the previous research [25-27]. All reactions were performed by mixing styrene (5 mmol), H_2O_2 (30%, 5 mmol), acetonitrile (4.5 mL), and catalyst (0.1 g) with stirring for 24 h at room temperature. The products were then analyzed by GC and nitrogen as the carrier gas. The temperatures of the injector and detector were programmed at 250 and $260\text{ }^{\circ}\text{C}$, respectively. The column

oven temperature was programmed to increase from 80 to $140\text{ }^{\circ}\text{C}$, at a rate of $10\text{ }^{\circ}\text{C}/\text{min}$.

RESULTS AND DISCUSSION

The results of WDXRF analysis revealed that calcium (Ca) and phosphorus (P) were the major elements in the FBC. After undergoing the processes of sulfonation, impregnation with titanium (Ti) and iron (Fe), and calcination, the samples were found to be dominated by calcium (Ca), sulfur (S), titanium (Ti), and iron (Fe). These aforementioned elements indicate the success of the sulfonation and metal impregnation processes. A comprehensive list of all the elements detected is provided in Table 2.

Fig. 1 displays the FTIR spectra of Ti-Fe (1:1)/SFBC, Ti-Fe (2:1)/SFBC, and Ti-Fe (1:2)/SFBC, which are compared to Fe_2O_3 , TiO_2 , and hydroxyapatite (HA). The spectra of all three Ti-Fe/SFBC samples (1:1, 2:1, and 1:2) are quite similar, indicating they share similar characteristics. Specifically, the absorption bands at $2500\text{--}3600$ and 1626 cm^{-1} correspond to the stretching mode of the hydroxyl (O-H) group of organic compounds. The presence of HA in the sample is indicated by the carbonate ion (CO_3^{2-}) and phosphate ion (PO_4^{3-}) groups, which were detected through absorption bands at $2100\text{--}2450\text{ cm}^{-1}$ and wavenumbers ranging from 1150 to 460 cm^{-1} , respectively [28-33]. The P-O stretching asymmetric was identified by the absorption bands around $1150\text{--}1000\text{ cm}^{-1}$. The bending vibration of PO_4^{3-} was observed through bands at $510\text{--}620\text{ cm}^{-1}$, while the band at 874 cm^{-1} was assigned to the acidic phosphate group (HPO_4^{2-}) [34]. The presence of

Table 2. Elements analysis of Ti-Fe(1:1)/SFBC, Ti-Fe(1:2)/SFBC and Ti-Fe(2:1)/SFBC obtained using WDXRF

Elements	FBC	Ti-Fe (1:1)/SFBC	Ti-Fe (1:2)/SFBC	Ti-Fe (2:1)/SFBC
P	16.300	-	-	-
S	-	29.200	29.200	27.600
Ca	81.200	58.500	58.100	55.600
Ti	-	4.600	2.720	9.000
Fe	0.063	7.200	8.360	7.060
V	-	0.130	0.076	0.210
Cu	0.041	0.038	0.042	0.044
Sr	0.580	0.350	0.350	0.310

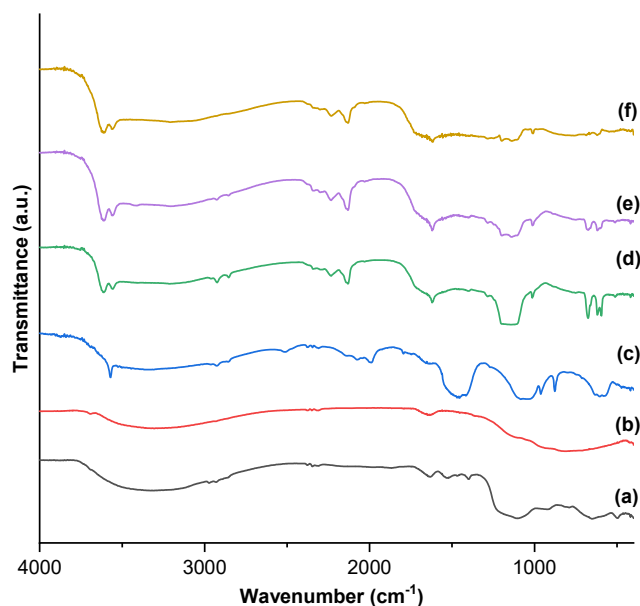


Fig 1. FTIR spectra of (a) Fe_2O_3 , (b) TiO_2 , (c) HA, (d) Ti-Fe(1:1)/SFBC, (e) Ti-Fe(2:1)/SFBC, and (f) Ti-Fe(1:2)/SFBC

iron was identified through absorptions around 540 and 442 cm^{-1} , which have been associated with Fe–O vibrations of Fe_2O_3 [31]. Framework titanium was characterized by an adsorption band in the $900\text{--}975\text{ cm}^{-1}$ range, which was attributed to symmetric O–Ti–O stretching that caused the vibration of the Ti–O bond. In Fig. 1(d) and (f), the absorption around $900\text{--}975\text{ cm}^{-1}$ is not detected due to the small amount of titanium, but it appears after the titanium was doubled, as seen in Fig. 1(e).

The XRD pattern in Fig. 2 was used to determine the crystallinity of Ti-Fe(1:1)/SFBC, Ti-Fe(2:1)/SFBC, and Ti-Fe(1:2)/SFBC, as well as control samples of Fe_2O_3 , TiO_2 , and HA. The HA crystallinity (JCPDS-PDF 74-0565) was identified in Fig. 2(a) by the diffraction peaks at $2\theta = 25.8, 32.0, 39.7, 46.8, 49.4,$ and 53.0 . The Fe_2O_3 crystallinity was determined in Fig. 2(b) by the diffraction peaks at $2\theta = 25.2, 36.9, 37.7, 38.5, 47.9, 53.8,$ and 54.9 . The crystallinity of Ti-Fe(1:1)/SFBC, Ti-Fe(2:1)/SFBC, and Ti-Fe(1:2)/SFBC was found to be almost the same at 52.2, 46.1, and 50.1%, respectively. In all three Ti-Fe/SFBC samples, the presence of titanium, iron, and HA crystals was detected through diffraction peaks at $2\theta = 25.2$ and 38.5 for titanium; $2\theta = 40.8, 43.5,$ and 49.4 for iron; and $2\theta = 22.8, 31.6, 32.8,$ and 57.1 for HA.

Fig. 3 displays the SEM images of FBC, Ti-Fe(1:1)/SFBC, Ti-Fe(1:2)/SFBC, and Ti-Fe(2:1)/SFBC. All samples exhibited rough and irregular surface morphology [35]. The surface area and pore structure of all samples were determined through Nitrogen adsorption-desorption isotherm analysis. Fig. 4 shows the isotherms for Ti-Fe(1:1)/SFBC, Ti-Fe(1:2)/SFBC, and

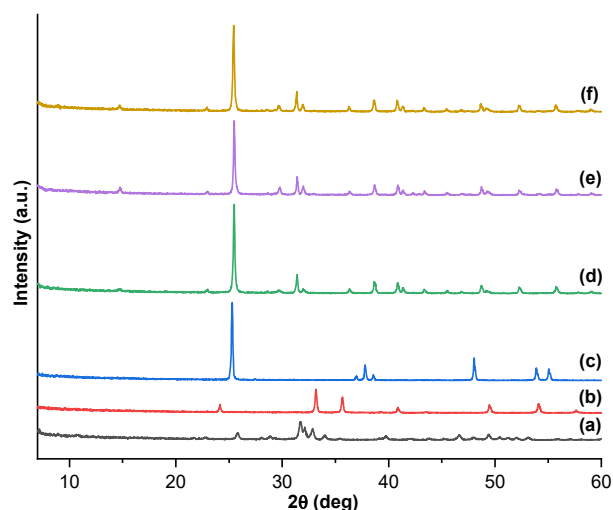


Fig 2. XRD pattern of (a) HA, (b) Fe_2O_3 , (c) TiO_2 , (d) Ti-Fe(1:1)/FBC, (e) Ti-Fe(1:1)/SFBC, (f) Ti-Fe(2:1)/SFBC, and (g) Ti-Fe(1:2)/SFBC

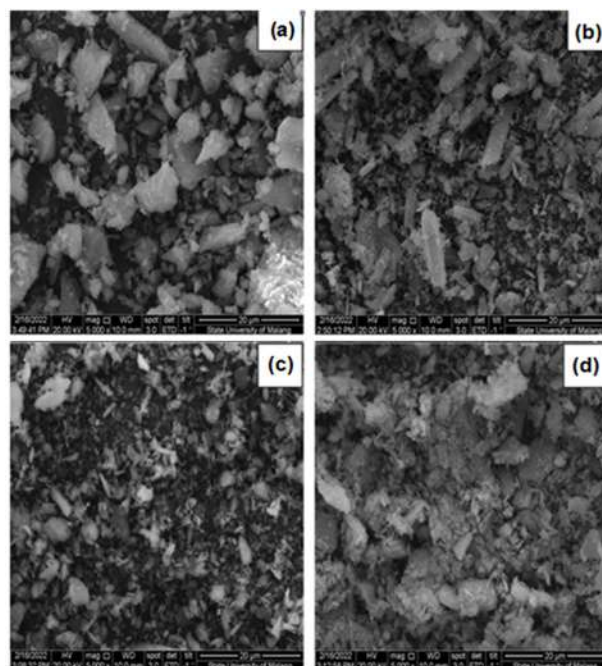


Fig 3. SEM Image of (a) CFB, (b) Ti-Fe(1:1)/FBC, (c) Ti-Fe(1:2)/FBC, and (d) Ti-Fe(2:1)/FBC

Ti-Fe(2:1)/SFBC, which were all classified as Type IV according to IUPAC, typical for mesoporous materials. The isotherms exhibited narrow hysteresis loops in the relative pressure range of ~ 0.6 – 1.0 (Ti-Fe(1:1)/SFBC), ~ 0.5 – 1.0 (Ti-Fe(1:2)/SFBC), and ~ 0.55 – 1.0 (Ti-Fe(2:1)/SFBC).

Table 3 presents the surface area, pore volume, and mean pore size for all samples. The presence of uniform mesopores was indicated by mean pore sizes greater than 2 nm. Metal impregnation (Ti and Fe) was found to increase the surface area, with Ti impregnation resulting in a higher increase than Fe impregnation.

Catalytic Performance

The yields of styrene oxidation products catalyzed by SFBC-loaded titanium-iron oxides are presented in Table 4. The primary products obtained using H_2O_2 as an oxidant were benzaldehyde, phenylacetaldehyde, and styrene oxide, with benzaldehyde being the dominant product. The mechanism starts from the adsorption of H_2O_2 on bimetallic oxides/SFBC, followed by the formation of hydroperoxyl species, then transfer of oxygen from bimetallic oxides to styrene, finally cleavage of the metalloepoxy intermediate, and also cleavage of the C=C bond (Fig. 5).

To compare, FBC, SFBC, Ti/SFBC, and Fe/SFBC were also used as catalysts for styrene oxidation. The performance of each catalyst was evaluated based on styrene conversion and benzaldehyde selectivity. FBC exhibited a styrene conversion of 0.7% and benzaldehyde selectivity of 35% at room temperature for 24 h. SFBC, however, showed increased performance with a styrene conversion of 2.6% and benzaldehyde selectivity of 93%. The presence of $-SO_3H$ groups resulting from the

sulfonation process of FBC influenced the catalytic performance of SFBC.

To evaluate the influence of titanium and iron, Ti/SFBC and Fe/SFBC were compared with the Ti-Fe/SFBC catalyst. Ti/SFBC showed higher catalytic activity than Fe/SFBC, with a styrene conversion of 23% and benzaldehyde selectivity of 90, 12, and 73%, respectively. The styrene conversion and benzaldehyde

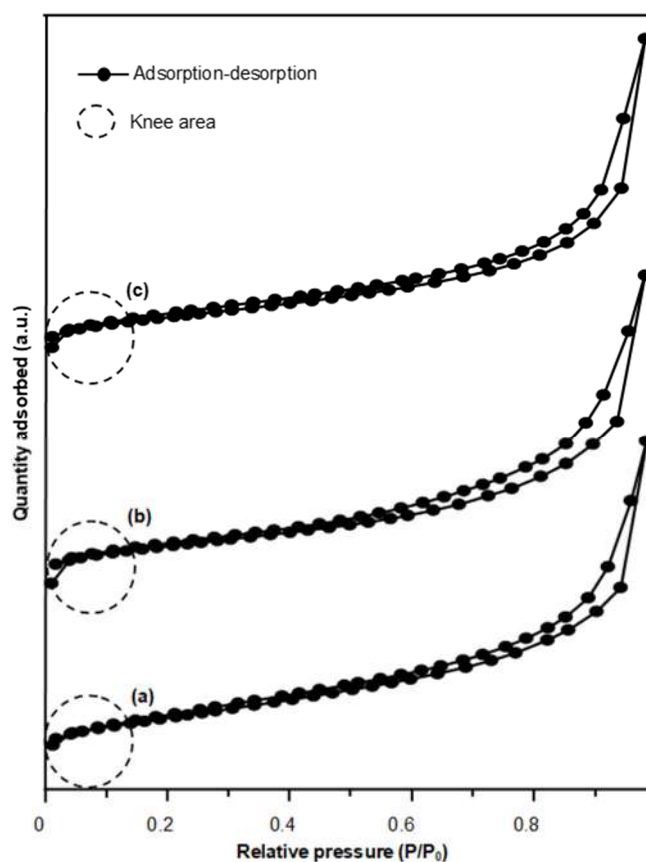


Fig 4. The physisorption isotherms of (a) Ti-Fe(1:1)/FBC, (b) Ti-Fe(1:2)/FBC, and (c) Ti-Fe(2:1)/FBC

Table 3. Physical properties of the catalysts

Samples	BET surface area (m^2/g)	Pore volume (cm^3/g)	Mean pore size (nm)
SCFB	6.8	0.0147	4.3
Ti/SCFB	13.9	0.0350	5.0
Fe/SCFB	7.6	0.0386	10.2
Ti-Fe(1:1)/SCFB	35.1	0.1172	6.7
Ti-Fe(2:1)/SCFB	34.8	0.1122	6.4
Ti-Fe(1:2)/SCFB	16.9	0.0616	7.3

Table 4. Catalytic performance of the catalysts in the oxidation of styrene

Catalyst	Conversion (%) ^a	Selectivity (%)			
		BzA ^b	PhA ^c	SO ^d	Other
FBC	0.7	34.6	13.1	17.1	35.2
SFBC	2.6	93.4	0.0	3.5	3.1
Ti/SFBC	23.0	90.0	3.0	3.0	4.0
Fe/SFBC	11.6	73.0	0.4	7.0	19.6
Ti-Fe(1:1)/SFBC	41.2	90.8	0.7	0.5	8.0
Ti-Fe(2:1)/SFBC	44.2	88.8	0.5	4.1	6.6
Ti-Fe(1:2)/SFBC	29.3	92.9	1.2	1.5	4.4

^a Reaction conditions: The reactions were carried out at room temperature for 24 h with styrene (5 mmol), 30% H₂O₂ (5 mmol), and catalyst (100 mg). BzA^b = benzaldehyde, PhA^c = phenylacetaldehyde, and SO^d = styrene oxide

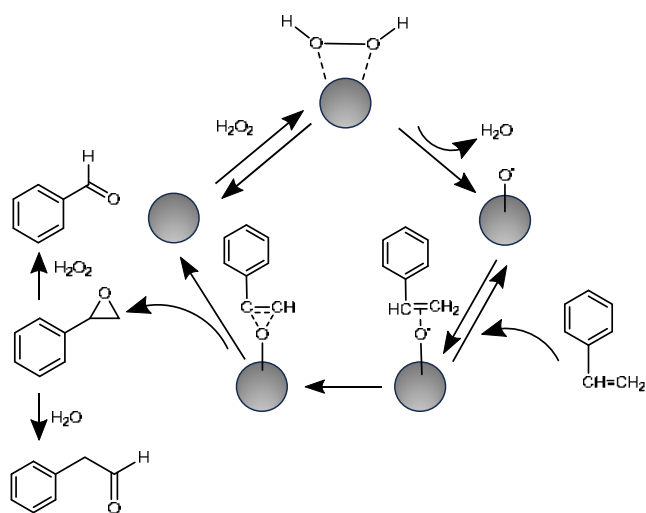


Fig 5. The mechanistic pathway of styrene oxidation using bimetallic oxides loaded sulfonated carbon-derived fishbone catalyst

selectivity were further increased to 41 and 88% for Ti-Fe(1:1)/SFBC, 44 and 88% for Ti-Fe(2:1)/SFBC, and 29 and 93% for Ti-Fe(1:2)/SFBC, respectively. The higher catalytic performance of Ti-Fe(1:1)/SFBC can be attributed to its higher total surface area compared to Ti/SFBC and Fe/SFBC. Doubling the number of titanium active sites did not affect the styrene oxidation conversion because it was not accompanied by an increase in the catalyst's surface area. However, doubling the number of iron active sites led to a decrease in styrene oxidation conversion due to a decrease in the surface area of the catalyst. These results are consistent with previous studies, which found that adding Ti and Fe active sites

does not necessarily increase styrene conversion, and Fe impregnation leads to lower styrene conversion compared to Ti impregnation [13]. The above results reveal that the presence of both titanium and iron oxides on the surface of SFBC and the catalyst's surface area creates a synergistic effect, which are the primary factors affecting its catalytic activity in styrene oxidation using H₂O₂ as an oxidant. This synergistic effect can be attributed to several scientific reasons [36-39].

Firstly, incorporating titanium and iron oxides provides multiple active sites on the catalyst surface. These active sites are crucial for enhancing the catalytic activity because they facilitate the adsorption and activation of the reactants, as well as the desorption of the products. Consequently, the presence of both metals can enhance the catalytic performance by promoting the interaction between the reactants and the catalyst surface. Secondly, the combination of titanium and iron oxides may result in the formation of mixed metal oxide phases. These mixed phases can exhibit unique electronic and structural properties enhancing the catalytic activity. For instance, the formation of mixed phases can lead to improved electron transfer between the metals, which can, in turn, facilitate the activation of the reactants and the subsequent oxidation reactions.

Moreover, the presence of both titanium and iron oxides can also lead to the formation of a more porous catalyst structure, which can increase the surface area available for catalytic reactions. As demonstrated in Table 2, the bimetallic catalyst, Ti-Fe (1:1)/SFBC, has a

higher total surface area compared to the monometallic catalysts, Ti/SFBC and Fe/SFBC. A higher surface area is crucial for catalytic activity, as it increases the number of active sites available for the reactants to interact with, thus promoting the oxidation reaction.

However, it is essential to note that simply increasing the number of active sites for one of the metals does not necessarily lead to a higher conversion of styrene. For instance, when the number of titanium active sites was doubled (Ti-Fe(2:1)/SFBC), it did not result in an increase in styrene oxidation conversion due to the absence of a corresponding increase in the catalyst's surface area. Furthermore, when the number of iron active sites was doubled (Ti-Fe(1:2)/SFBC), the styrene oxidation conversion decreased, as the addition of iron active sites led to a reduction in the catalyst's surface area.

The synergistic effect observed in the Ti-Fe/SFBC catalyst for styrene oxidation can be attributed to the presence of both titanium and iron oxides, which provide multiple active sites, promote the formation of mixed metal oxide phases, and contribute to a higher surface area. However, it is crucial to maintain a proper balance between the active sites and the catalyst's surface area to optimize the catalytic performance.

The study has several limitations that should be considered. First, it is focused solely on the Ti-Fe/SFBC catalyst for styrene oxidation, which means that the findings may not apply to other types of catalysts or reaction systems. Second, the investigation of the

relationship between catalyst structure and catalytic properties is limited by the techniques and methods used in this study, which may not capture all aspects of the catalyst's behavior. Lastly, the study does not address the long-term stability and reusability of the Ti-Fe/SFBC catalyst, which are important factors for practical applications.

To gain a deeper understanding of the synergistic effect and the relationship between catalyst structure and catalytic properties, further studies should explore several aspects. Investigate the Ti-Fe/SFBC catalyst's performance in other oxidation reactions to assess the generality of the observed synergistic effect. Employ advanced characterization techniques to gain a more detailed understanding of the catalyst's structure, including the nature of the active sites and the interaction between titanium and iron oxides. Examine the effect of varying the ratio of titanium and iron oxides in the catalyst to identify the optimal balance between active sites and surface area for enhanced catalytic performance. Lastly, evaluate the long-term stability and reusability of the Ti-Fe/SFBC catalyst under various reaction conditions to determine its practical applicability. By addressing these aspects, future studies can contribute to developing more efficient and versatile catalysts for styrene oxidation and other related reactions.

To check the reusability and stability of the Ti-Fe(1:1)/SFBC, Ti-Fe(2:1)/SFBC, and Ti-Fe(1:2)/SFBC, all catalysts were recovered and recycled for further reaction.

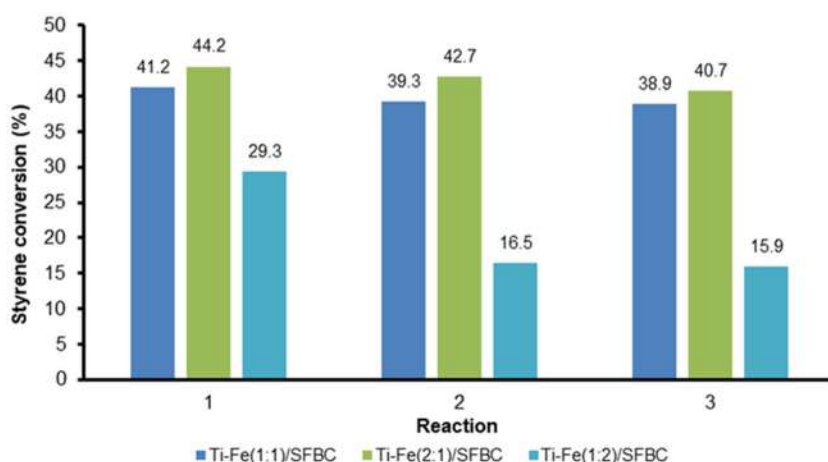


Fig 6. The reuse of catalysts in the oxidation of styrene (5 mmol), 30% H₂O₂ (5 mmol) and catalyst (100 mg) at room temperature for 24 h

After each use, both catalysts were recycled by washing with ethanol and centrifugation thrice and drying at 110 °C in a vacuum oven overnight. The conversion of styrene oxidation was used to compare all catalysts. As shown in Fig. 6, Ti-Fe(1:1)/SFBC and Ti-Fe(2:1)/SFBC catalysts were higher and more stable after three reaction cycles than Ti-Fe(1:2)/SFBC catalyst. The decrease in the styrene conversion from the first reaction cycle to the second and third reaction cycles were 44.2, 42.7, and 40.7% for Ti-Fe(2:1)/SFBC; 41.2, 39.3, and 38.9% for Ti-Fe(1:1)/SFBC. Different from the Ti-Fe(1:2)/SFBC catalyst, the decrease in the yield of styrene conversion was very drastic at 29.3, 16.5, and 15.9%. Based on catalytic performance for styrene oxidation with H₂O₂ as oxidant, after three cycles of reaction and wash, we predicted that around 94% of the Ti-Fe(1:1)/SFBC, 92% of Ti-Fe(2:1)/SFBC, and 54% catalytic sites of fresh catalysts should remain on the catalyst under the reaction conditions used in this study. The explanation might be used as the physical loss of some catalyst powder during the recycling step. During the washing step, titanium and iron active sites directly interact with ethanol as the solvent; hence, the leaching cannot be avoided.

■ CONCLUSION

The utilization of bimetallic titanium-iron oxide loaded SFBC as a catalyst has been investigated in the oxidation of styrene using aqueous H₂O₂. The study found that the catalytic performance of SFBC was superior to that of FBC, and Ti/SFBC was greater than Fe/SFBC. A synergistic effect was observed due to the coexistence of titanium (Ti) and iron (Fe) oxides, which enhanced the catalytic performance. The presence of titanium and iron oxides influenced the surface area and the catalytic activity of the catalysts in the oxidation of styrene, employing aqueous H₂O₂ as an oxidant. Upon examining reusability and stability, it was concluded that a specific ratio of Ti-Fe/SFBC demonstrated better stability compared to other Ti-Fe/SFBC ratios.

■ ACKNOWLEDGMENTS

The authors gratefully acknowledge the research grant from the Ministry of Education, Culture, Research

and Technology of the Republic of Indonesia by contract number: 297/UN17.L1/HK/2022.

■ AUTHOR CONTRIBUTIONS

Mukhamad Nurhadi: conceptualization, methodology, supervision, investigation, resources, data curation, writing, review, and editing; Ratna Kusumawardani: conceptualization, methodology, formal analysis, data curation, writing draft preparation, and project administration; Teguh Wirawan: conceptualization, methodology, investigation, resources, data curation, and writing draft preparation; Sin Yuan Lai: proofreading, writing, review, and editing; Hadi Nur: proofreading, writing, review, and editing. All authors have read and agreed to the published version of the manuscript.

■ REFERENCES

- [1] Ito, S., Kon, Y., Nakashima, T., Hong, D., Konno, H., Ino, D., and Sato, K., 2019, Titania-catalyzed H₂O₂ thermal oxidation of styrenes to aldehydes, *Molecules*, 24 (14), 2520.
- [2] Batra, M.S., Dwivedi, R., and Prasad, R., 2019, Recent developments in heterogeneous catalyzed epoxidation of styrene to styrene oxide, *ChemistrySelect*, 4 (40), 11636–11673.
- [3] Andrade, M.A., and Martins, L.M.D.R.S., 2021, Selective styrene oxidation to benzaldehyde over recently developed heterogeneous catalysts, *Molecules*, 26 (6), 1680.
- [4] Aberkouks, A., Mekkaoui, A.A., Boualy, B., El Houssame, S., Ait Ali, M., and El Firdoussi, L., 2018, Selective oxidation of styrene to benzaldehyde by Co-Ag codoped ZnO catalyst and H₂O₂ as oxidant, *Adv. Mater. Sci. Eng.*, 2018, 2716435.
- [5] Xie, L., Wang, H., Lu, B., Zhao, J., and Cai, Q., 2018, Highly selective oxidation of styrene to benzaldehyde over Fe₃O₄ using H₂O₂ aqueous solution as oxidant, *React. Kinet., Mech. Catal.*, 125 (2), 743–756.
- [6] Sakthivel, B., Josephine, D.S.R., Sethuraman, K., and Dhakshinamoorthy, A., 2018, Oxidation of styrene using TiO₂-graphene oxide composite as

- solid heterogeneous catalyst with hydroperoxide as oxidant, *Catal. Commun.*, 108, 41–45.
- [7] Hulea, V., and Dumitriu, E., 2004, tyrene oxidation with H₂O₂ over Ti-containing molecular sieves with MFI, BEA and MCM-41 topologies, *Appl. Catal., A*, 277 (1-2), 99–106.
- [8] Jafarpour, M., Ghahramaninezhad, M., and Rezaeifard, A., 2014, Catalytic activity and selectivity of reusable α -MoO₃ nanobelts toward oxidation of olefins and sulfides using economical peroxides, *RSC Adv.*, 4 (4), 1601–1608.
- [9] Wang, H., Qian, W., Chen, J., Wu, Y., Xu, X., Wang, J., and Kong, Y., 2014, Spherical V-MCM-48: The synthesis, characterization and catalytic performance in styrene oxidation, *RSC Adv.*, 4 (92), 50832–50839.
- [10] Cancino, P., Paredes-García, V., Aguirre, P., and Spodine, E., 2014, A reusable Cu^{II} based metal-organic framework as a catalyst for the oxidation of olefins, *Catal. Sci. Technol.*, 4 (8), 2599–2607.
- [11] Zhang, Y., Wei, N., Xing, Z., and Han, Z.B., 2020, Functional hexanuclear Y(III) cluster-based MOFs supported Pd(II) single site catalysts for aerobic selective oxidation of styrene, *Appl. Catal., A*, 602, 117668.
- [12] Nurhadi, M., Kusumawardani, R., Wirawan, T., Sumari, S., Lai, S.Y., and Nur, H., 2021, Catalytic performance of TiO₂-carbon mesoporous-derived from fish bones in styrene oxidation with aqueous hydrogen peroxide as an oxidant, *Bull. Chem. React. Eng. Catal.*, 16 (1), 88–96.
- [13] Tanglumlert, W., Imae, T., White, T.J., and Wongkasemjit, S., 2009, Styrene oxidation with H₂O₂ over Fe- and Ti-SBA-1 mesoporous silica, *Catal. Commun.*, 10 (7), 1070–1073.
- [14] Kusumawardani, R., Nurhadi, M., Wirawan, T., Prasetyo, A., Agusti, N.N., Lai, S.Y., and Nur, H., 2022, Kinetic study of styrene oxidation over titania catalyst supported on sulfonated fish bone-derived carbon, *Bull. Chem. React. Eng. Catal.*, 17 (1), 194–204.
- [15] Ha, Y., Mu, M., Liu, Q., Ji, N., Song, C., and Ma, D., 2017, Mn-MIL-100 heterogeneous catalyst for the selective oxidative cleavage of alkenes to aldehydes, *Catal. Commun.*, 103, 51–55.
- [16] Ghosh, R., Son, Y.C., Makwana, V.D., and Suib, S.L., 2004, Liquid-phase epoxidation of olefins by manganese oxide octahedral molecular sieves, *J. Catal.*, 224 (2), 288–296.
- [17] Zou, H., Xiao, G., Chen, K., and Peng, X., 2018, Noble metal free V₂O₅/g-C₃N₄ composite for selective oxidation of olefins using hydrogen peroxide as oxidant, *Dalton Trans.*, 47 (38), 13565–13572.
- [18] Saux, C., and Pierella, L.B., 2011, Studies on styrene selective oxidation to benzaldehyde catalyzed by Cr-ZSM-5: Reaction parameters effects and kinetics, *Appl. Catal., A*, 400 (1-2), 117–121.
- [19] Fiorenza, R., 2020, Bimetallic catalysts for volatile organic compound oxidation, *Catalysts*, 10 (6), 661.
- [20] Vetrivel, S., and Pandurangan, A., 2005, Supported metal oxide catalysts: Their activity to vapor phase oxidation of ethylbenzene, *Ind. Eng. Chem. Res.*, 44 (4), 692–701.
- [21] Das, S., Gupta, A., Singh, D., and Mahajani, S., 2019, La/Zn bimetallic oxide catalyst for epoxidation of styrene by cumene hydroperoxide: Kinetics and reaction engineering aspects, *Ind. Eng. Chem. Res.*, 58, 7448–7460.
- [22] Zhang, Y., Wang, H., Li, S., Lu, B., Zhao, J., and Cai, Q., 2021, Catalytic oxidation of styrene and its reaction mechanism consideration over bimetal modified phosphotungstates, *Mol. Catal.*, 515, 111940.
- [23] Huang, K., Yu, S., Li, X., and Cai, Z., 2020, One-pot synthesis of bimetal MOFs as highly efficient catalysts for selective oxidation of styrene, *J. Chem. Sci.*, 132 (1), 139.
- [24] Zou, H., Hu, C., Chen, K., Xiao, G., and Peng, X., 2018, Cobalt vanadium oxide supported on reduced graphene oxide for the oxidation of styrene derivatives to aldehydes with hydrogen peroxide as oxidant, *Synlett*, 29 (16), 2181–2184.
- [25] Nurhadi, M., 2017, Modification of coal char-loaded TiO₂ by sulfonation and alkylsilylation to enhance catalytic activity in styrene oxidation with hydrogen peroxide as oxidant, *Bull. Chem. React. Eng. Catal.*, 12 (1), 55–61.
- [26] Nurhadi, M., Efendi, J., Lee, S.L., Indra Mahlia, T.M.,

- Chandren, S., Ho, C.S., and Nur, H., 2015, Utilization of low rank coal as oxidation catalyst by controllable removal of its carbonaceous component, *J. Taiwan Inst. Chem. Eng.*, 46, 183–190.
- [27] Nurhadi, M., Chandren, S., Yuan, L.S., Ho, C.S., Indra Mahlia, T.M., and Nur, H., 2017, Titania-loaded coal char as catalyst in oxidation of styrene with aqueous hydrogen peroxide, *Int. J. Chem. React. Eng.*, 15 (1), 20160088.
- [28] Chakraborty, R., and Chowdhury, D.R., 2013, Fish bone derived natural hydroxyapatite-supported copper acid catalyst: Taguchi optimization of semibatch oleic acid esterification, *Chem. Eng. J.*, 215-216, 491–499.
- [29] Patel, S., Han, J., Qiu, W., and Gao, W., 2015, Synthesis and characterisation of mesoporous bone char obtained by pyrolysis of animal bones, for environmental application, *J. Environ. Chem. Eng.*, 3 (4, Part A), 2368–2377.
- [30] Yin, T., Park, J.W., and Xiong, S., 2015, Physicochemical properties of nano fish bone prepared by wet media milling, *LWT - Food Sci. Technol.*, 64 (1), 367–373.
- [31] Zayed, E.M., Sokker, H.H., Albishri, H.M., and Farag, A.M., 2013, Potential use of novel modified fishbone for anchoring hazardous metal ions from their solutions, *Ecol. Eng.*, 61, 390–393.
- [32] Lestari, S., Nurhadi, M., Kusumawardani, R., Saputro, E., Pujisupiaty, R., Muskita, N.S., Fortuna, N., Purwandari, A.S., Aryani, F., Lai, S.Y., and Nur, H., 2022, Comparative adsorption performance of carbon-containing hydroxyapatite derived tenggiri (*Scomberomorini*) and belida (*Chitala*) fish bone for methylene blue, *Bull. Chem. React. Eng. Catal.*, 17 (3), 565–576.
- [33] Nurhadi, M., Kusumawardani, R., Nurhadi, M., Wirhanuddin, W., Gunawan, R., and Nur, H., 2019, Carbon-containing hydroxyapatite obtained from fish bone as low-cost mesoporous material for methylene blue adsorption, *Bull. Chem. React. Eng. Catal.*, 14 (3), 660–671.
- [34] Jaber, H.L., Hammood, A.S., and Parvin, N., 2018, Synthesis and characterization of hydroxyapatite powder from natural *Camelus* bone, *J. Aust. Ceram. Soc.*, 54 (1), 1–10.
- [35] Abdullah, N.H., Mohamed Noor, A., Mat Rasat, M.S., Mamat, S., Mohamed, M., Mohd Shohaimi, N.A., Ab Halim, A.Z., Mohd Shukri, N., Azhar Abdul Razab, M.K., and Mohd Amin, M.F., 2020, Preparation and characterization of calcium hydroxyphosphate (hydroxyapatite) from tilapia fish bones and scales via calcination method, *Mater. Sci. Forum*, 1010, 596–601.
- [36] Goulas, K.A., Sreekumar, S., Song, Y., Kharidehal, P., Gunbas, G., Dietrich, P.J., Johnson, G.R., Wang, Y.C., Grippo, A.M., Grabow, L.C., Gokhale, A.A., and Toste, F.D., 2016, Synergistic effects in bimetallic palladium–copper catalysts improve selectivity in oxygenate coupling reactions, *J. Am. Chem. Soc.*, 138 (21), 6805–6812.
- [37] He, L., Gong, X., Ye, L., Duan, X., and Yuan, Y., 2016, Synergistic effects of bimetallic Cu-Fe/SiO₂ nanocatalysts in selective hydrogenation of diethyl malonate to 1,3-propanediol, *J. Energy Chem.*, 25 (6), 1038–1044.
- [38] Stucchi, M., Capelli, S., Cardaci, S., Cattaneo, S., Jouve, A., Beck, A., Sáfrán, G., Evangelisti, C., Villa, A., and Prati, L., 2020, Synergistic effect in Au-Cu bimetallic catalysts for the valorization of lignin-derived compounds, *Catalysts*, 10 (3), 332.
- [39] Ehsan, M.A., Hakeem, A.S., and Rehman, A., 2020, Synergistic effects in bimetallic Pd–CoO electrocatalytic thin films for oxygen evolution reaction, *Sci. Rep.*, 10 (1), 14469.

The Green Approach of Cerium Oxide Nanoparticle and Its Application for Photo-degradation of Phenol Dye

Gusliani Eka Putri^{1*}, Syukri Arief², Ahmad Hafizullah Ritonga³, Wiya Elsa Fitri⁴, Eliza Arman¹, Arniat Christiani Telaumbanua¹, and Rahmi Novita Yusuf¹

¹Department of Medical Laboratory Technology, Sekolah Tinggi Ilmu Kesehatan Syedza Saintika, Jl. Prof. Dr. Hamka No. 228, Padang 25132, Indonesia

²Department of Chemistry, Faculty of Mathematics and Natural Sciences, Andalas University, Limau Manis Campus, Padang 25163, Indonesia

³Institut Kesehatan Medistra Lubuk Pakam, Jl. Sudirman No. 38, Deli Serdang 20512, Indonesia

⁴Department of Public Health, Sekolah Tinggi Ilmu Kesehatan Syedza Saintika, Jl. Prof. Dr. Hamka No. 228, Padang 25132, Indonesia

* **Corresponding author:**

email: guslianiekaputri@gmail.com

Received: January 25, 2023

Accepted: September 28, 2023

DOI: 10.22146/ijc.81657

Abstract: The approach to the synthesis of cerium oxide nanoparticles (CeO₂NPs) using plants as capping agents has been widely researched because of its eco-friendly, low-cost, simple, effective, and reusability. In this research, we used Moringa oleifera leaf extract-mediated CeO₂NPs. CeO₂NPs were characterized by XRD, FTIR, SEM, TEM, and DRS UV-vis. The photocatalytic activity of CeO₂NPs was tested using a phenol dye concentration of 7 mg/L with variations in photocatalyst weight of 10, 20, 30, 40, 50, 60, 70, 80, 90, and 100 mg under UV irradiation, respectively, with time variations of 15, 30, 45, 60, 75, 90, 105, 120, 135, and 150 min. SEM and TEM morphology results showed that the CeO₂NPs were spherical and agglomerated. The crystal structure is cubic, with a crystal size of 18 nm with a band gap of 2.87 eV. CeO₂NPs showed high photo-degradation phenol dye of 94.45% under visible light in 120 min irradiation time. The results show that M. oleifera leaf extract could be as inexpensive and safe for synthesizing other metal oxide nanoparticles, potentially having applications in the biomedical and environmental fields.

Keywords: cerium oxide nanoparticles; approach synthesis; phenol; Moringa oleifera; photocatalytic

■ INTRODUCTION

Medical waste contains many chemical compounds that harm humans and the environment [1-2]. Phenol dye is one of the hazardous chemicals in medical waste [3-5]. Based on the Decree of the Environment Ministry of Indonesia Republic No. 51, concentrations of phenol according to quality standards shall be in a range of 0.5–1.0 mg/L. Phenol concentration above the quality standard can cause effects on humans, including liver and kidney damage, decreased blood pressure, weakened heart rate, and even death [6-7].

Central General Hospital Dr. M. Djamil Padang is the largest type A hospital in West Sumatra. Based on this condition, many patients' treatment will increase the amount of liquid waste produced, including phenolic compounds. Conventional methods that have been applied to decompose phenol wastes are steam distillation [8], liquid-liquid extraction [9], solid-phase extraction [10], and biodegradation [11]. In the last decade, many studies have proven that photocatalyst technology is better at degrading organic compounds; thus, it is more economical in energy use and can reduce the use of chemicals [12].

Photocatalyst processes usually use metals and metal oxides such as TiO_2 [13-14], ZnO [15], and Ag [16]. However, the use of this metal in the degradation of phenol waste still gets a percentage of phenol waste under 50%, and optimal conversion data for phenolic waste has yet to be obtained. So, in recent years, many researchers have been interested in using cerium oxide (CeO_2) as a photocatalyst. CeO_2 is a semiconductor with a 3.0–3.9 eV band gap in bulk, chemical stability, thermal stability, and high conductivity that can absorb UV light and has catalytic and optical properties [17-18]. Various fields of application, such as UV absorbers [19], biosensors [20], sunscreens cosmetics [21], biomedical applications [22], and photo-catalysts [23], have been reported. CeO_2 nanoparticles (CeO_2NPs) act as heterogeneous catalysts [24], so they easily separate from the waste after the photocatalyst process is completed so as not to harm the environment [25].

The synthesis of the CeO_2NPs had previously been used utilizing chemical substances such as acids (acetic acid) or bases (ammonium hydroxide) [26]. Various leaf extracts from plants have been used in the green synthesis of CeO_2NPs , including *Gloriosa superba* leaf extract [27], *Olei europaea* leaf extract [28], *Prosopis juliflora* leaf extract [29], and *Calotropis procera* flower extract [30]. In this study, *Moringa oleifera* leaf extract was used to perform green synthesis of CeO_2NPs . A literature search revealed that no prior work has used this extract to create CeO_2NPs . Phytochemical testing of *M. oleifera* leaf extract contains flavonoids, triterpenoids, steroids, saponins, and tannins. They act as capping agents in the process of synthesis of nanoparticles. The usage of this technique is more environmentally beneficial because it does not use harmful chemicals in nanoparticle synthesis [17,31].

The increased phenol content in wastewater has forced dye manufacturers to address their environmental impact. Conventional chemical methods do not effectively decompose phenol into innocuous byproducts, according to prior studies. This situation became the main reason for the scientific community to develop new effective processes for the decomposition of phenol dye. Due to its affordability, environmental friendliness, and simplicity in process control, photocatalytic techniques

have attracted the attention of numerous phenol degradation researchers [32].

For the development of CeO_2NPs in the degradation of phenol under visible light irradiation, *M. oleifera* potential reduction agents and stabilizing activity may be utilized as a suitable green synthesis method. Based on research gaps, the present research showed the potential activity reduction and stabilization agent of *M. oleifera* extract for the photosynthesis of CeO_2NPs . According to related literature, there have not been any investigations into the photocatalytic activity of CeO_2NPs mediating *M. oleifera* for phenol degradation.

■ EXPERIMENTAL SECTION

Materials

The materials used in this study were *M. oleifera* leaves from *Balai Benih Induk Tanaman* (Center for Mother Plant Seed) at Lubuk Minturun, Koto Tangah, Padang, West Sumatra, Indonesia. Sigma-Aldrich offered phenol with a 99% purity and cerium nitrate hexahydrate ($\text{Ce}(\text{NO}_3)_3 \cdot 6\text{H}_2\text{O}$) with a 99.99% purity.

Instrumentation

The powder X-ray diffractogram (XRD) of synthesized and calcined samples was recorded on a Rigaku Miniflex diffractometer with $\text{Cu-K}\alpha$ radiation between 20 and 90° (2θ) with a scanning rate of 1°/min. TEM micrographs of the samples were obtained with a JEOL 100CX microscope with 100 kV of acceleration voltage. SEM using the JEOL-JSM 6360 LA.

Procedure

Synthesis of CeO_2NPs

M. oleifera were collected from the Balai Benih Induk Tanaman (Center for Mother Plant Seed) and taxonomic identification was carried out in Herbarium Universitas Andalas (ANDA), Andalas University, Padang, Indonesia. Secondary metabolites were identified at the Laboratory of Natural Products, Chemistry Department, Andalas University. The leaves were shade-dried at room temperature for about 5 d, and the dried leaves were then mashed up to obtain a fine powder. As much as 10 g of *M. oleifera* leaf powder was dissolved in 50 mL double distilled water for 30 min at 65 °C. The

obtained extract was filtered with Whatman No.1 filter paper and stored in a sealed bottle at 4 °C for further use.

Ce(NO₃)₃·6H₂O (0.1 mol) was added to 200 mL of *M. oleifera* leaf extract and stirred at a speed of 500 rpm at a temperature of 80 °C for 2 h. The solution was filtered, washed with distilled water, and dried in an oven at 80 °C for 4 h. CeO₂ was synthesized in a furnace at 600 °C for 2 h [2].

Degradation of phenol dye

Photocatalytic degradation was carried out at room temperature using a batch photo-reactor setup. The photocatalytic activity of CeO₂NPs is used to decompose phenol with known concentrations. The six beaker glasses were wrapped in black plastic, each with 250 mL of phenol, and added with the CeO₂ photocatalyst (0, 10, 20, 30, 40, 50, 60, 70, 80, 90, and 100 mg). The beaker glasses were put into a radiation box and wrapped with the new black plastic. Next, the beaker glasses were irradiated with a visible 300 W Xenon lamp (Cermax® Xenon, Excelitas, USA) with a wavelength (λ) > 400 nm with time variations for 15, 30, 45, 60, 75, 90, 105, and 120 min. After the radiation process, the suspension from each beaker glass was centrifuged. The absorbance of the supernatant was measured with a UV-vis spectrophotometer at the maximum length of phenol.

RESULTS AND DISCUSSION

The concentration phenol of medical waste from Central General Hospital (RSUP) Dr. M. Djamil Padang was analyzed in the Chemistry Laboratory, Medical Laboratory Technology Department, STIKES Syedza Saintika. The analyzed parameters were the concentration of phenol and pH measurement using a spectrophotometer and pH meter. It can be shown in Table 1 according to the standard based on Minister of Environment Regulation of the Republic of Indonesia No. 5 of 2014 on "Wastewater Quality Standards".

The phenolic concentration in a liquid waste sample in the initial reservoir before processing is 6.65 mg/L with pH 8, then used to make an artificial phenol solution become 7 mg/L. This research used CeO₂ as a photocatalyst with variations in the weight and degradation time.

Nanoparticle Characterization

The aim of XRD characterization is to know the crystal structure. The specific peaks of CeO₂ at 2θ 28.83, 32.82, 47.34, 56.71, 69.96, and 76.66, respectively, represent for hkl (111), (200), (220), (311), (400), and (420), as shown in Fig. 1(a). The CeO₂NPs have a cubic structure according to ICPDS Card No. 34-0394. This spectrum showed no impurity peaks, which confirmed that single-phase CeO₂ crystals were successively formed. The strong crystallinity of CeO₂NPs and spectrum diffraction peak was narrow with a crystal size calculated using the Debye-Scherrer equation (Eq. (1)).

$$D = \frac{\lambda}{\beta \cos \theta} \quad (1)$$

Here, the full width at half maximum (FWHM) value is β, the diffraction angle is θ, the size of the crystallite is D, the numerical factor corresponding to the crystallite shape factor is K, and the wavelength of X-ray is λ [30].

Table 1. The chemical parameters in the hospital waste

Parameters	Unit	Sample	The wastewater quality standard*
Phenol	mg/L	6.65	0.50–1.00
pH	mg/L	8.0	6.0–9.0

*based on Minister of Environment Regulation of the Republic of Indonesia No. 5 of 2014

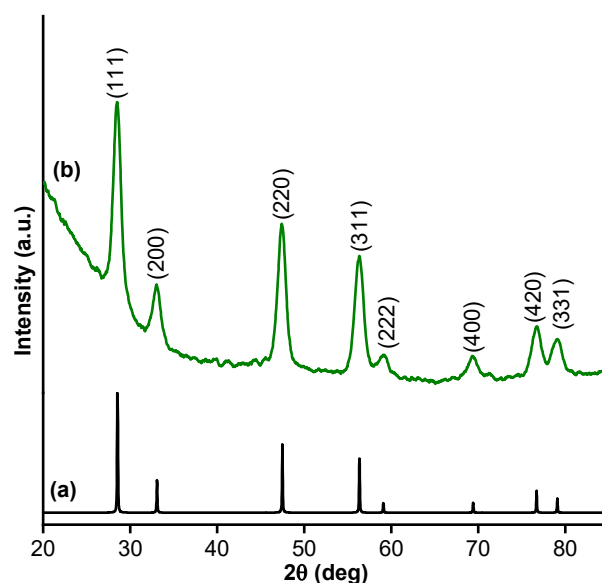


Fig 1. XRD profile of (a) standard of CeO₂ (ICSD-34-0394) (b) as-synthesized CeO₂NPs

It became known that the average crystallite size of CeO_2 NPs produced using *M. oleifera* leaf extract was 28 nm.

Fig. 2 shows the CeO_2 NPs FTIR spectrum. The KBr pellet method was applied to conduct the FTIR study, which was scanned in the $400\text{--}4000\text{ cm}^{-1}$ wavelength range. The absorption bands at 1300, around 1600, and 3300 cm^{-1} are referred to as N-O stretching, H-O-H bond, and OH stretching in the FTIR spectra of $\text{CeNO}_3\cdot 6\text{H}_2\text{O}$ respectively (Fig. 2(a)). The FTIR absorption spectrum of CeO_2 NPs after calcination in Fig. 2(b) shows the intensity of 453 and 685 cm^{-1} , which are referred to Ce-O stretching and O-Ce-O bonding, respectively. It was observed that the OH peak of the water appears to be reduced in CeO_2 form. The results of this study are in line with Arumugam et al. [27], who also found the peak of Ce-O stretching to be 451 cm^{-1} .

The morphology of the nanoparticles was shown from the SEM, TEM, and HRTEM analysis. Fig. 3(a)

morphology analysis that can show the TEM image. It can SEM data show the CeO_2 NPs morphology where the

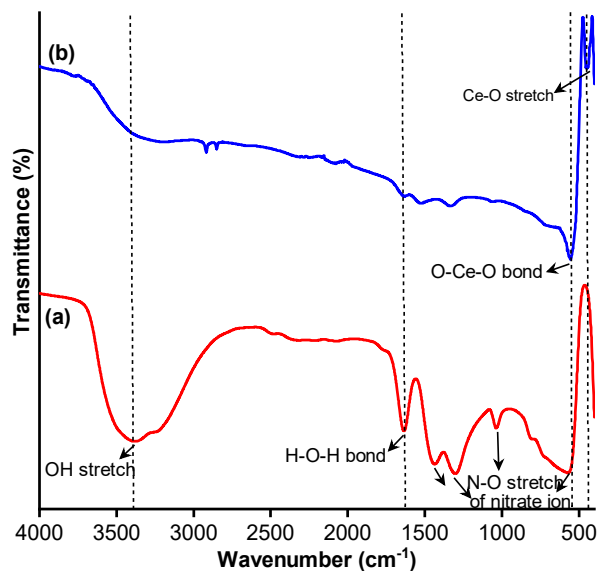


Fig 2. FTIR spectra of (a) $\text{CeNO}_3\cdot 6\text{H}_2\text{O}$ precursor (b) as-synthesized CeO_2 NPs

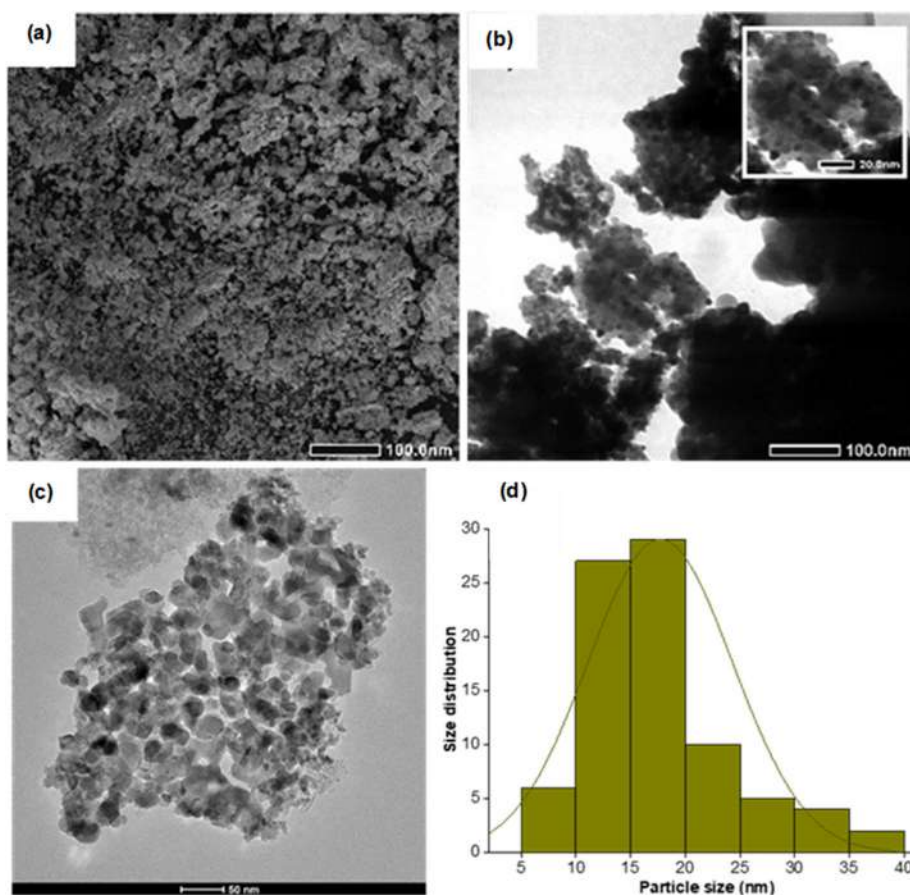


Fig 3. (a) SEM, (b) TEM, (c) HR TEM, and (d) size distribution diagram of as-synthesized CeO_2 NPs

particles are agglomerated. Fig. 3(b) is a microstructural be shown that the particles are spherical and agglomerated. The clear microstructural morphology analysis can be shown in HRTEM data in Fig. 3(c). Particle size was calculated using the Image J application from HRTEM image data and obtained a particle size of 5–40 nm, with a mean particle size of 18 nm described in the histogram in Fig. 3(d).

The Kubelka-Munk equation (Eq. (2)), which has the following formula, was used to compute the amount of absorption whereas $F(R)$ is known as the Kubelka-Munk function, K is the molar absorbance coefficient, S is the scattering factor, R is the material's reflectance value.

$$F(R) = \frac{K}{S} = \frac{(1-R)^2}{2R} \quad (2)$$

Band gap energy obtained from the graph of the relationship between $h\nu$ (eV) vs $(F(R)h\nu)^{1/2}$ determined by Eq. (3);

$$E_g = h\nu = \frac{hc}{\lambda} \quad (3)$$

where h is Planck's constant (6.624×10^{-34} J s), c is the speed of light in the air (2.998×10^8 m/s), λ is the wavelength (nm), and E_g represents the band gap energy (eV). The value of the $h\nu$ at $(F(R)h\nu)^{1/2} = 0$, which is determined by the linear regression equation of the curve [33] (Fig. 4). The band gap of CeO_2 in its bulk form is relatively large, with values ranging from 3.0 to 3.9 eV.

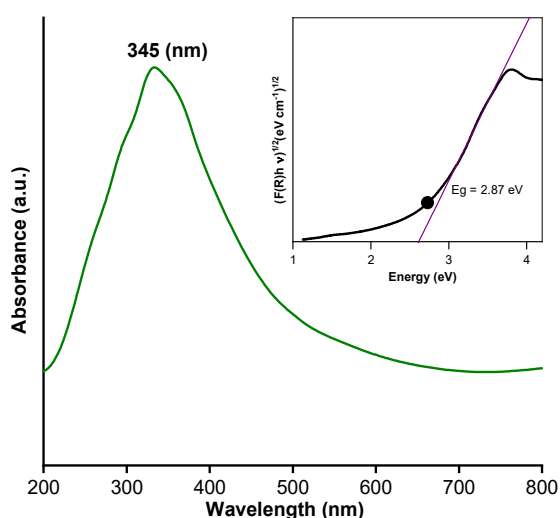


Fig 4. DRS UV-vis spectrum of CeO_2NPs inserts band gap value of CeO_2NPs by Kubelka Munk equation

According to preliminary research, a few investigations have reported on reducing the band gap of CeO_2 without the use of dopants. However, it is frequently applied using harsh techniques at relatively high temperatures. Scott et al. [34] synthesized CeO_2 NPs with a minimum band gap of 2.73 eV but using a thermal treatment at 600 °C for 4 h to remove the CeOHCO_3 phase formed during the synthesis process. This research e gab value was 2.87 eV at 600 °C for 2 h. The narrowing of the band gap is achieved thanks to the high structural disorder of the nanoparticles synthesized. The smaller the nanoparticles, the smaller the band gap value. The literature shows the opposite behavior for nanoparticles due to the quantum confinement effect [35]. Additionally, because it causes a change in the strength of attachment of the atoms in the crystalline structure, the structural disorder assists in decreasing the band gap. This information matches XRD results that suggest a crystallite size of 28 nm. The visible region can use a photocatalyst because the energy gap value was 2.87 eV (Fig. 4). The photocatalyst will absorb light with a lower energy level when the gap energy is reduced, but there is a higher chance of electron recombination is greater.

The Photocatalysis Application

The weight of CeO_2NPs was varied at 10, 20, 30, 40, 50, 60, 70, 80, 90, and 100 mg. The degradation time variation of phenol dye using CeO_2 NPs photocatalyst was 0, 30, 45, 60, 75, 90, 105, and 120 min. The artificial solution volume is 250 mL, and the used time is 100 min with a pH of 8. The result can be seen in Fig. 5 and 6 whereas visible light data refer to the absence of CeO_2 NPs while blank data refer to the absence of both CeO_2 NPs and visible light.

Based on Fig. 5 and 6, when the photocatalyst weight is 100 mg, it can decompose 92.45% of the phenol dye, and the removal concentration becomes 0.4 mg/L.

In this study, the phenol dye degradation time variation using CeO_2NPs photocatalyst was 0, 30, 45, 60, 75, 90, 105, and 120 min. The volume of the artificial solution is 250 mL, and the mass of the photocatalyst used is 100 mg, with a pH of 8. Respectively, CeO_2NPs showed high phenol degradation up to 94.45% at 120 min

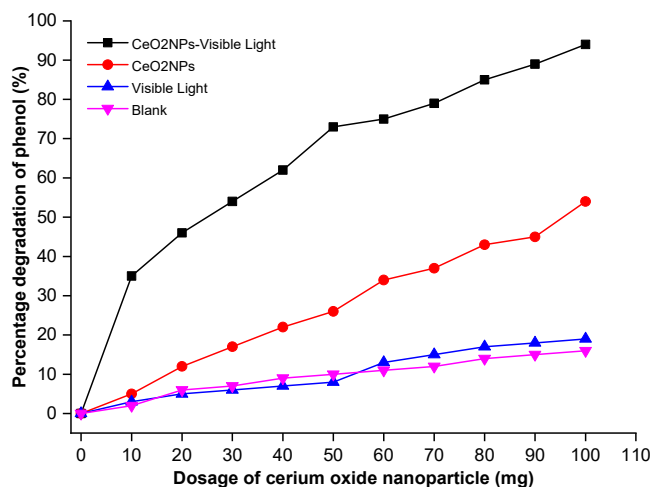


Fig 5. The percentage degradation of phenol versus dosage of CeO₂ using visible light irradiation

of irradiation time, as shown in Fig. 7 and 8. CeO₂NPs show a high degree of photocatalytic activity as a result of photogenerated electron-hole pairs on the photocatalyst surface. It was also comparable to other metal oxide photocatalysts described in the literature and shown in Table 2 when phenol was photocatalytically degraded on the surface of CeO₂NPs catalysts for photosynthesis in the presence of a visible light source.

The comparison of other metal oxide photocatalysts is shown in Table 2. The activity photo-degradation of CeO₂NPs synthesized was compared with other literature using metal oxide for phenol degradation.

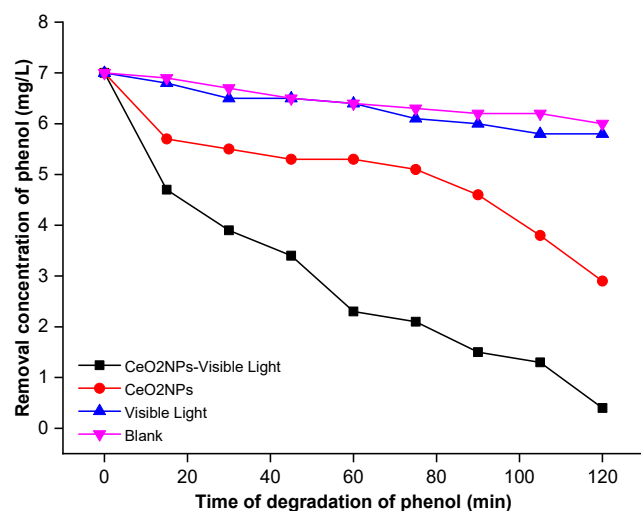


Fig 7. The removal concentration of phenol versus irradiation time using visible light irradiation

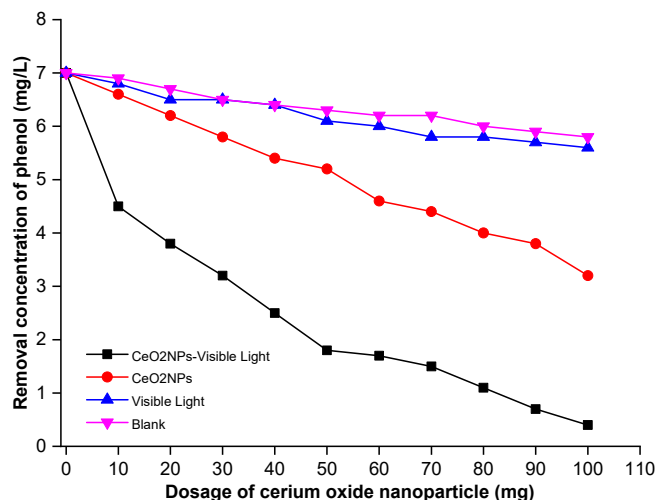


Fig 6. The removal concentration of phenol versus dosage of CeO₂ using visible light irradiation

It can be concluded that metal oxides cause different photo-degradation activities. The photo-degradation activity of CeO₂NPs in this study was reported in the range of 70–89%. It shows that the CeO₂NPs photocatalyst synthesized by the green synthesis method can also degrade phenol waste with visible light source irradiation.

The illustration of the phenol degradation mechanism compounds in the presence of visible light on the surface of CeO₂NPs is shown in Fig. 9. When the CeO₂NPs photocatalyst absorbs photon light irradiation, phenol degradation occurs on the surface of

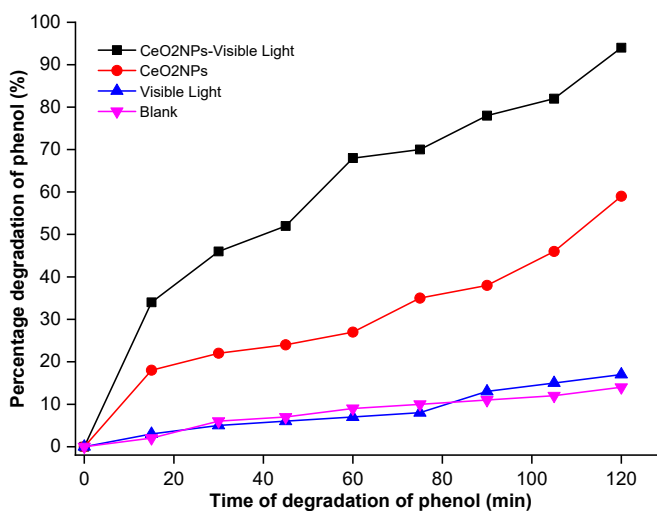
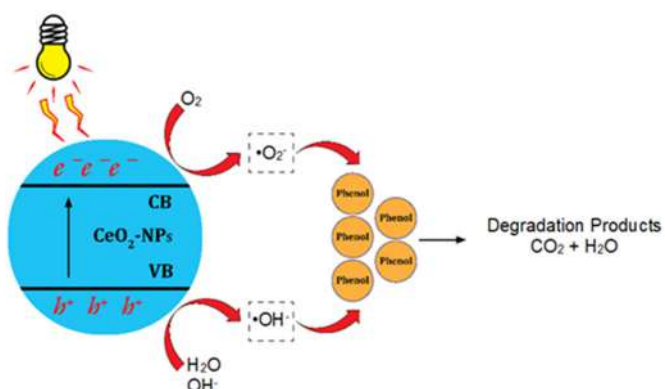


Fig 8. The percentage degradation of phenol versus irradiation time using visible light irradiation

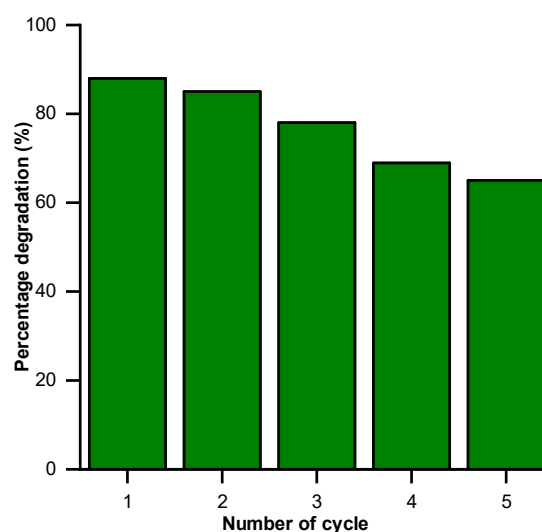
Table 2. The comparison of degradation percentages on phenol degradation by metal oxide nanoparticles

Catalyst	Dosage (mg/L)	Time (min)	Percentage degradation rate (%)	Ref.
TiO ₂ nanoparticle	150	105	82.00	[36]
Ni nanoparticle	200	120	78.00	[37]
Zirconia nanoparticle	100	150	79.00	[38]
Zinc oxide nanorod	100	180	45.00	[39]
Ag nanoparticle	200	100	89.00	[40]
CeO ₂ NPs	100	120	94.45	This work

**Fig 9.** The phenol degradation mechanism

the CeO₂NPs photocatalyst through superoxide (O_2^-) radicals and the hydroxyl (OH) radical. According to the degradation mechanism, when the CeO₂NPs photocatalyst absorbs photon light, electrons jump from the valence band (VB) to the conduction band (CB). Then, holes (h^+) were formed in VB and electrons (e^-) in CB. The electron-hole pairs photogenerated onto the surface of the and generated free OH radicals on the CeO₂NPs surface [41]. It indicates that CeO₂NPs have a good ability to generate OH radicals in the phenol waste solution. The photogenerated electrons in the CB can generate superoxide radicals. The superoxide radical anion has a significantly more ability to remove pollutants than of OH [2]. Thus, more hole pairs will reach the CeO₂NPs surface, increasing the phenol degradation.

During photocatalyst reusability under UV light exposure with five recycle uses, the photocatalytic activity of CeO₂NPs was additionally examined. In the first cycle, the photodegradation efficiency for the phenol dye using CeO₂NPs was 94.45%. After the first cycle concluded, the CeO₂NPs were separated by centrifugation, then washed with aquadest and dried for 2 h at 100 °C in an oven. For the subsequent cycle of photodegradation of phenol dye

**Fig 10.** Reusability of CeO₂NPs for five cycles

under the same conditions, the dried photocatalyst was utilized. Fig. 10 illustrates the CeO₂NPs' five-cycle recyclability. The recycling study over five cycles, which showed a higher turnover rate and photocatalyst stability, did not substantially impact the photodegradation efficiency of CeO₂NPs. The photocatalytic activity of CeO₂NPs showed a dramatically decreased of phenol degradation percentage, probably caused by the material loss during the recovery procedure [38]. In addition, the reduction in surface area during treatment eventually caused the photocatalytic effectiveness to decrease. Because no substantial leaching occurred after seven additional trials, the CeO₂NPs catalyst was very stable and active, demonstrating that it is appropriate for use in photodegradation reactions.

■ CONCLUSION

Synthesis of CeO₂NPs from *Moringa oleifera* leaf extract can be used for the photo-degradation of phenol. The morphology of nanoparticles is spherical, with a

particle size of 18 nm. CeO₂NPs showed high photo-degradation by percentage degradation of phenol dye is 94.45% in 120 min irradiation time under visible light. Reusability shows stable results in degrading phenol waste so that it has the potential to be used to remove phenol dye.

■ ACKNOWLEDGMENTS

We would like to thank the Center Research and Community Service Sekolah Tinggi Ilmu Kesehatan Syedza Saintika for funding this research with grant number 02/STIKES-SS/PENEL/VIII-2021.

■ AUTHOR CONTRIBUTIONS

Gusliani Eka Putri, Syukri Arief, and Ahmad Hafizullah Ritonga conducted the experiment, Gusliani Eka Putri and Ahmad Hafizullah Ritonga conducted the analysis of XRD, Eliza Arman, Arniat, Rahmi Yovita Yusuf, and Wiya Elsa Fitri, wrote and revised the manuscript. All authors agreed to the final version of this manuscript.

■ REFERENCES

- [1] Adusei, J.K., Agorku, E.S., Voegborlo, R.B., Ampong, F.K., Danu, B.Y., and Amarh, F.A., 2022, Removal of methyl red in aqueous systems using synthesized NaAlg-g-CHIT/nZVI adsorbent, *Sci. Afr.*, 17, e01273.
- [2] Shu, Z., Zhang, Y., Ouyang, J., and Yang, H., 2017, Characterization and synergetic antibacterial properties of ZnO and CeO₂ supported by halloysite, *Appl. Surf. Sci.*, 420, 833–838.
- [3] Mohamed, A., Abuarab, M.E., Mehawed, H.S., and Kasem, M.A., 2021, Water footprint as a tool of water resources management - Review, *Egypt. J. Chem.*, 64 (12), 7231–7237.
- [4] Prince, J., Tzompantzi, F., Mendoza-Damián, G., Hernández-Beltrán, F., and Valente, J.S., 2015, Photocatalytic degradation of phenol by semiconducting mixed oxides derived from Zn(Ga)Al layered double hydroxides, *Appl. Catal., B*, 163, 352–360.
- [5] Ahmad, T., Iqbal, J., Bustam, M.A., Zulfiqar, M., Muhammad, N., Al Hajeri, B.M., Irfan, M., Anwaar Asghar, H.M., and Ullah, S., 2020, Phytosynthesis of cerium oxide nanoparticles and investigation of their photocatalytic potential for degradation of phenol under visible light, *J. Mol. Struct.*, 1217, 128292.
- [6] Shukla, S.S., Dorris, K.L., and Chikkaveeraiah, B.V., 2009, Photocatalytic degradation of 2,4-dinitrophenol, *J. Hazard. Mater.*, 164 (1), 310–314.
- [7] Ibrahim, M.A., Helmy, E.M., Nazawi, A.M.A., Sadek, M.W., and Abdelatif, M.S., 2021, Biodegradation of nonylphenol ethoxylate in wastewater by *Penicillium chrysogenum*, *Egypt. J. Chem.*, 64 (12), 7251–7262.
- [8] de Elguea-Culebras, G.O., Bravo, E.M., and Sánchez-Vioque, R., 2022, Potential sources and methodologies for the recovery of phenolic compounds from distillation residues of Mediterranean aromatic plants. An approach to the valuation of by-products of the essential oil market – A review, *Ind. Crops Prod.*, 175, 114261.
- [9] Afshar Mogaddam, M.R., Farajzadeh, M.A., Tuzen, M., Jouyban, A., and Khandaghi, J., 2021, Organic solvent-free elevated temperature liquid–liquid extraction combined with a new switchable deep eutectic solvent-based dispersive liquid–liquid microextraction of three phenolic antioxidants from oil samples, *Microchem. J.*, 168, 106433.
- [10] Gamonchuang, J., and Burakham, R., 2021, Amino-based magneto-polymeric-modified mixed iron hydroxides for magnetic solid phase extraction of phenol residues in environmental samples, *J. Chromatogr. A*, 1643, 462071.
- [11] Gong, Y., Ding, P., Xu, M.J., Zhang, C.M., Xing, K., and Qin, S., 2021, Biodegradation of phenol by a halotolerant versatile yeast *Candida tropicalis* SDP-1 in wastewater and soil under high salinity conditions, *J. Environ. Manage.*, 289, 112525.
- [12] Parisi, F., Lazzara, G., Merli, M., Milioto, S., Princivalle, F., and Sciascia, L., 2019, Simultaneous removal and recovery of metal ions and dyes from wastewater through montmorillonite clay mineral, *Nanomaterials*, 9 (12), 1699.
- [13] Ciobanu, C.S., Popa, C.L., and Predoi, D., 2016, Cerium-doped hydroxyapatite nanoparticles synthesized by the co-precipitation method, *J. Serb. Chem. Soc.*, 81 (4), 433–446.

- [14] Sánchez-Rodríguez, D., Méndez Medrano, M.G., Remita, H., and Escobar-Barrios, V., 2018, Photocatalytic properties of BiOCl-TiO₂ composites for phenol photodegradation, *J. Environ. Chem. Eng.*, 6 (2), 1601–1612.
- [15] Handani, S., Emriadi, Dahlan, D., and Arief, S., 2020, Enhanced structural, optical and morphological properties of ZnO thin film using green chemical approach, *Vacuum*, 179, 109513.
- [16] Feng, C., Chen, Z., Jing, J., and Hou, J., 2020, The photocatalytic phenol degradation mechanism of Ag-modified ZnO nanorods, *J. Mater. Chem. C*, 8 (9), 3000–3009.
- [17] Putri, G.E., Rilda, Y., Syukri, S., Labanni, A., and Arief, S., 2021, Highly antimicrobial activity of cerium oxide nanoparticles synthesized using *Moringa oleifera* leaf extract by a rapid green precipitation method, *J. Mater. Res. Technol.*, 15, 2355–2364.
- [18] Putri, G.E., Rilda, Y., Syukri, S., Labanni, A., and Arief, S., 2022, Enhancing morphological and optical properties of montmorillonite/chitosan-modified cerium oxide nanoparticles for antimicrobial applications, *Surf. Interfaces*, 32, 102166.
- [19] Putri, G.E., Arief, S., Jamarun, N., Gusti, F.R., and Fisli, A., 2019, High performance of photocatalytic activity of cerium doped silica mesoporous operating under visible light irradiation, *KnE Eng.*, 4 (2), 128–140.
- [20] Kumar, S., Tripathy, S., Singh, O.K., and Singh, S.G., 2021, Cerium oxide nanofiber based electroanalytical sensor for TNF- α detection: Improved interfacial stability with Nafion, *Bioelectrochemistry*, 138, 107725.
- [21] Onoda, H., and Tanaka, R., 2019, Synthesis of cerium phosphate white pigments from cerium carbonate for cosmetics, *J. Mater. Res. Technol.*, 8 (6), 5524–5528.
- [22] Caputo, F., Mameli, M., Sienkiewicz, A., Licoccia, S., Stellacci, F., Ghibelli, L., and Traversa, E., 2017, A novel synthetic approach of cerium oxide nanoparticles with improved biomedical activity, *Sci. Rep.*, 7 (1), 4636.
- [23] Bui, H.T., Weon, S., Bae, J.W., Kim, E.J., Kim, B., Ahn, Y.Y., Kim, K., Lee, H., and Kim, W., 2021, Oxygen vacancy engineering of cerium oxide for the selective photocatalytic oxidation of aromatic pollutants, *J. Hazard. Mater.*, 404, 123976.
- [24] Radić, N., Grbić, B., Petrović, S., Stojadinović, S., Tadić, N., and Stefanov, P., 2020, Effect of cerium oxide doping on the photocatalytic properties of rutile TiO₂ films prepared by spray pyrolysis, *Phys. B*, 599, 412544.
- [25] Putri, G.E., Gusti, F.R., Sary, A.N., Arief, S., Jamarun, N., and Amar B, S., 2019, Synthesis and antimicrobial activity of cerium oxide/AG dopes silica mesoporous modification as nanofillers for food packaging applications, *Malays. Appl. Biol.*, 48 (4), 25–32.
- [26] Feng, N., Liu, Y., Dai, X., Wang, Y., Guo, Q., and Li, Q., 2022, Advanced applications of cerium oxide based nanozymes in cancer, *RSC Adv.*, 12 (3), 1486–1493.
- [27] Arumugam, A., Karthikeyan, C., Haja Hameed, A.S., Gopinath, K., Gowri, S., and Karthika, V., 2015, Synthesis of cerium oxide nanoparticles using *Gloriosa superba* L. leaf extract and their structural, optical and antibacterial properties, *Mater. Sci. Eng., C*, 49, 408–415.
- [28] Singh, K.R.B., Nayak, V., Sarkar, T., and Singh, R.P., 2020, Cerium oxide nanoparticles: Properties, biosynthesis and biomedical application, *RSC Adv.*, 10 (45), 27194–27214.
- [29] Arunachalam, T., Karpagasundaram, U., and Rajarathinam, N., 2017, Ultrasound assisted green synthesis of cerium oxide nanoparticles using *Prosopis juliflora* leaf extract and their structural, optical and antibacterial properties, *Mater. Sci.-Pol.*, 35 (4), 791–798.
- [30] Muthuvel, A., Jothibas, M., Mohana, V., and Manoharan, C., 2020, Green synthesis of cerium oxide nanoparticles using *Calotropis procera* flower extract and their photocatalytic degradation and antibacterial activity, *Inorg. Chem. Commun.*, 119, 108086.

- [31] Fan, Y., Li, P., Hu, B., Liu, T., Huang, Z., Shan, C., Cao, J., Cheng, B., Liu, W., and Tang, Y., 2019, A smart photosensitizer-cerium oxide nanoprobe for highly selective and efficient photodynamic therapy, *Inorg. Chem.*, 58 (11), 7295–7302.
- [32] Zamri, M.S.F.A., and Sapawe, N., 2019, Kinetic study on photocatalytic degradation of phenol using green electrosynthesized TiO₂ nanoparticles, *Mater. Today: Proc.*, 19, 1261–1266.
- [33] Pathak, T.K., Coetsee-Hugo, E., Swart, H.C., Swart, C.W., and Kroon, R.E., 2020, Preparation and characterization of Ce doped ZnO nanomaterial for photocatalytic and biological applications, *Mater. Sci. Eng., B*, 261, 114780.
- [34] Scott, T., Zhao, H., Deng, W., Feng, X., and Li, Y., 2019, Photocatalytic degradation of phenol in water under simulated sunlight by an ultrathin MgO coated Ag/TiO₂ nanocomposite, *Chemosphere*, 216, 1–8.
- [35] Fujishima, A., Zhang, X., and Tryk, D.A., 2008, TiO₂ photocatalysis and related surface phenomena, *Surf. Sci. Rep.*, 63 (12), 515–582.
- [36] Liu, J., Wang, H., Chang, M.J., Sun, M., Zhang, C.M., Yang, L.Q., Du, H.L., and Luo, Z.M., 2022, Facile synthesis of BiOCl with extremely superior visible light photocatalytic activity synergistically enhanced by Co doping and oxygen vacancies, *Sep. Purif. Technol.*, 301, 121953.
- [37] Thulasinathan, B., Jayabalan, T., Arumugam, N., Rasu Kulanthaisamy, M., Kim, W., Kumar, P., Govarthan, M., and Alagarsamy, A., 2022, Wastewater substrates in microbial fuel cell systems for carbon-neutral bioelectricity generation: An overview, *Fuel*, 317, 123369.
- [38] AlSalhi, M.S., Devanesan, S., Asemi, N., and Ahamed, A., 2023, Concurrent fabrication of ZnO–ZnFe₂O₄ hybrid nanocomposite for enhancing photocatalytic degradation of organic pollutants and its bacterial inactivation, *Chemosphere*, 318, 137928.
- [39] Karimi-Maleh, H., Kumar, B.G., Rajendran, S., Qin, J., Vadivel, S., Durgalakshmi, D., Gracia, F., Soto-Moscoso, M., Orooji, Y., and Karimi, F., 2020, Tuning of metal oxides photocatalytic performance using Ag nanoparticles integration, *J. Mol. Liq.*, 314, 113588.
- [40] Guan, X., Zhang, R., Jia, B., Liu, G., Yan, B., Lu, P., and Peng, G.D., 2022, Influence of ring structures on luminescence properties of trivalent cerium in Ge-doped silica optical fiber, *J. Non-Cryst. Solids*, 576, 121251.
- [41] Orooji, Y., Tanhaei, B., Ayati, A., Tabrizi, S.H., Alizadeh, M., Bamoharram, F.F., Karimi, F., Salmanpour, S., Rouhi, J., Afshar, S., Sillanpää, M., Darabi, R., and Karimi-Maleh, H., 2021, Heterogeneous UV-switchable Au nanoparticles decorated tungstophosphoric acid/TiO₂ for efficient photocatalytic degradation process, *Chemosphere*, 281, 130795.

Supplementary Data

This supplementary data is a part of a paper entitled "Synthesis and Estimation of the Insecticide and Antibacterial Activities for Some New Amide Derivatives".

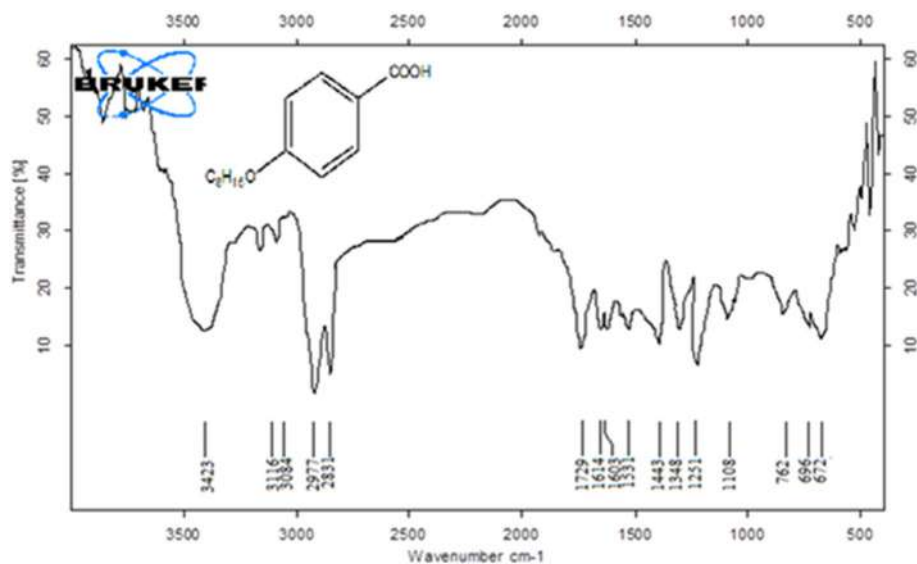


Fig S1. FTIR spectrum of A2

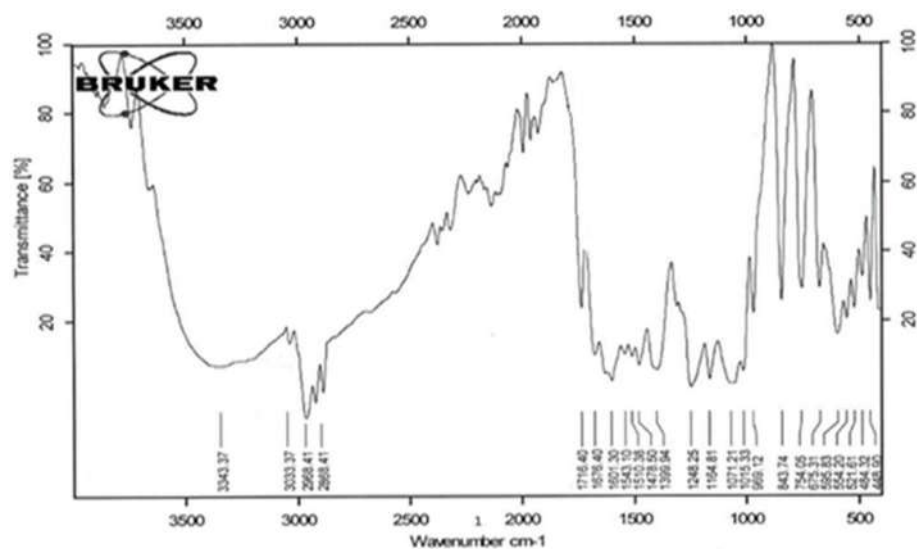
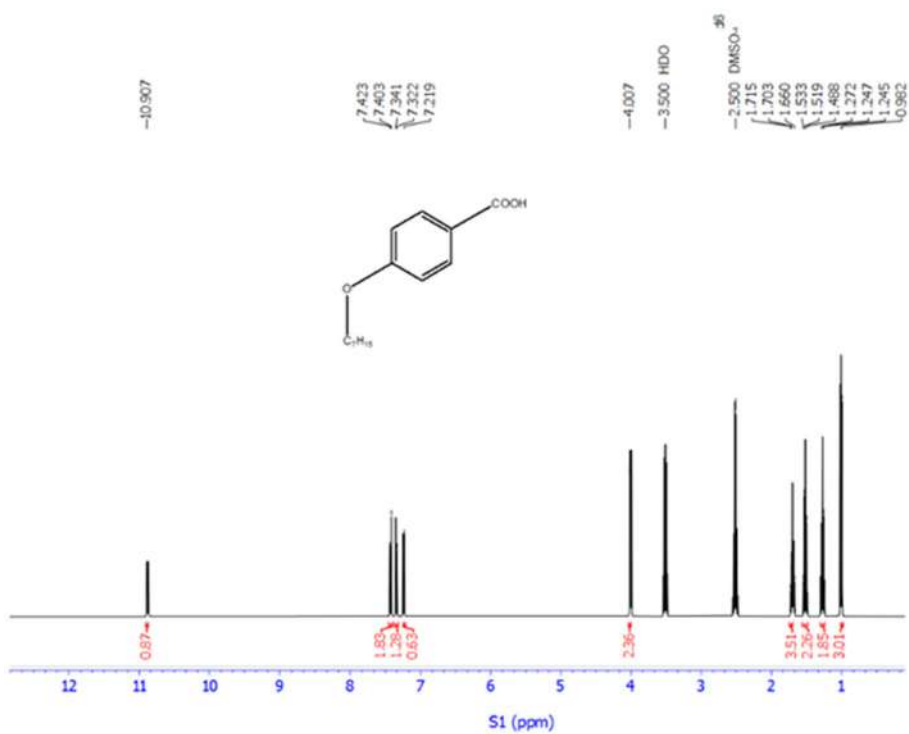
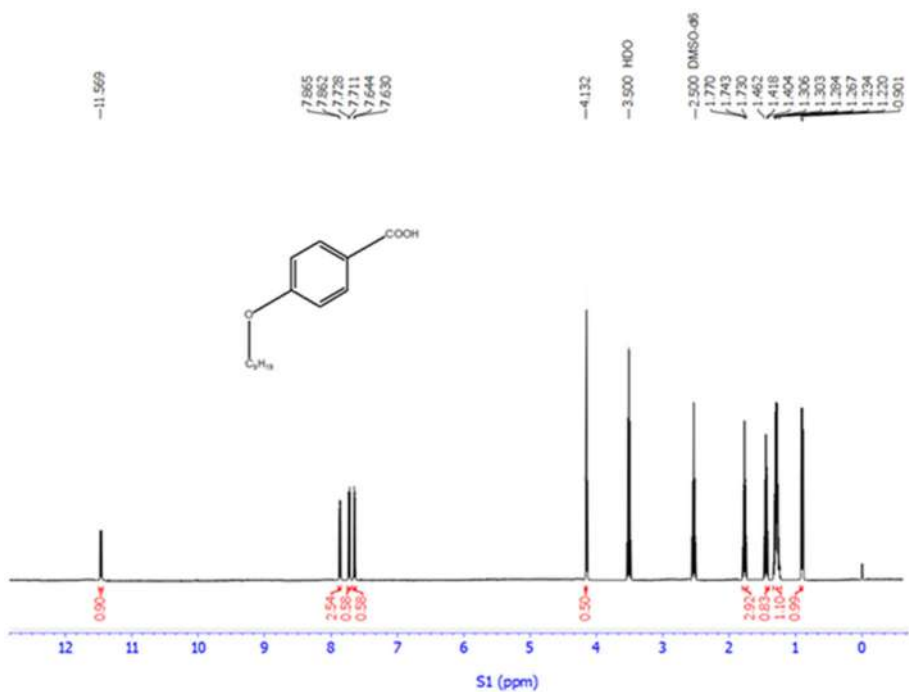


Fig S2. FTIR spectrum of A3

Fig S3. ¹H-NMR spectrum of A1Fig S4. ¹H-NMR spectrum of A3

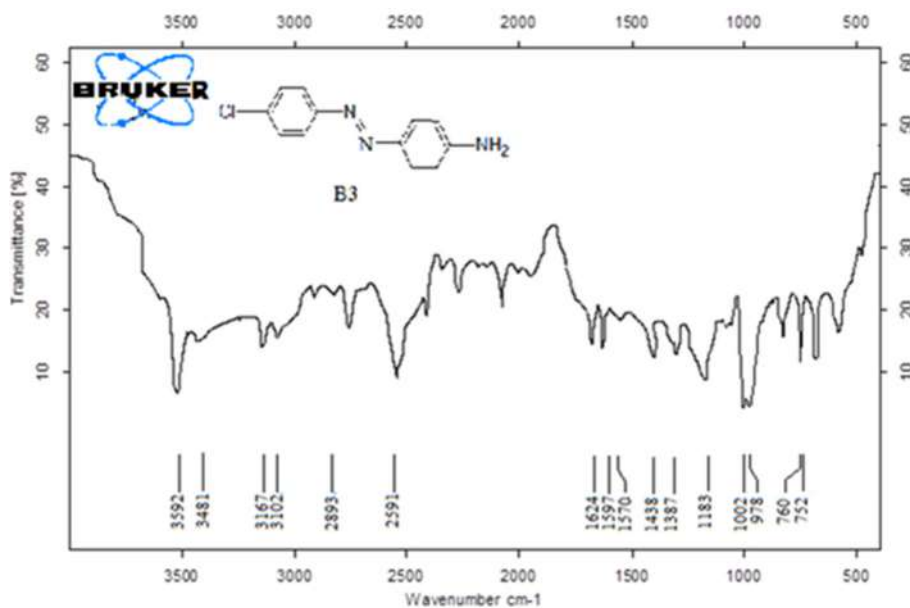


Fig S5. FTIR spectrum of B3

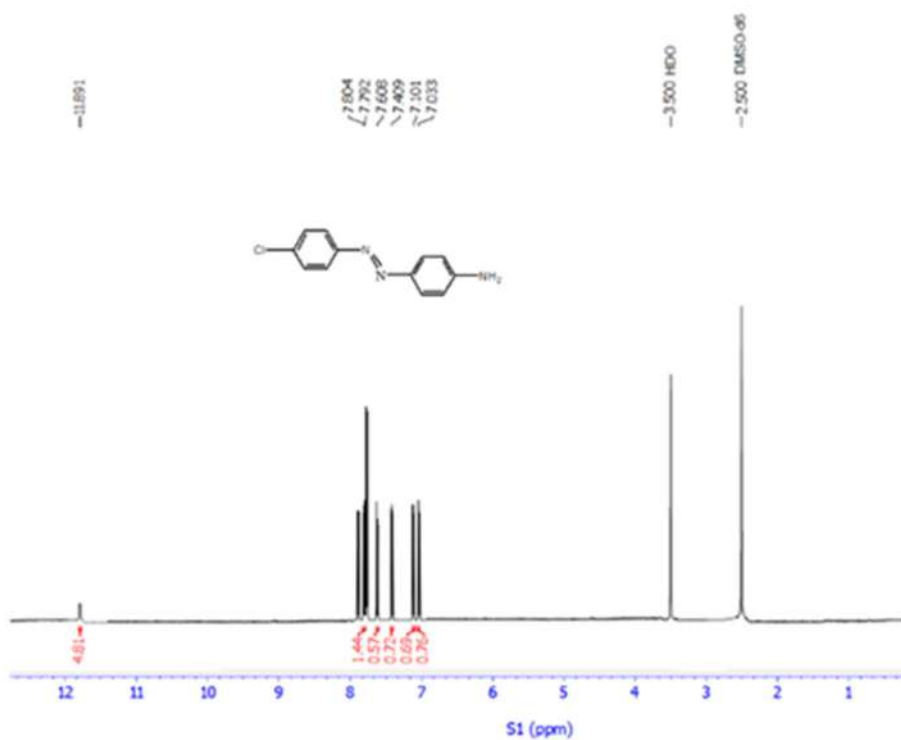


Fig S6. ¹H-NMR spectrum of B3

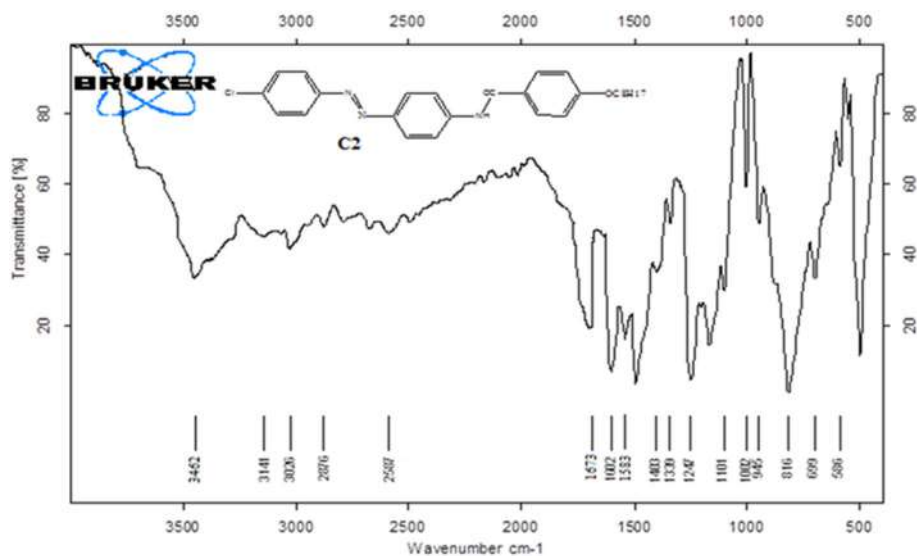


Fig S7. FTIR spectrum of C2

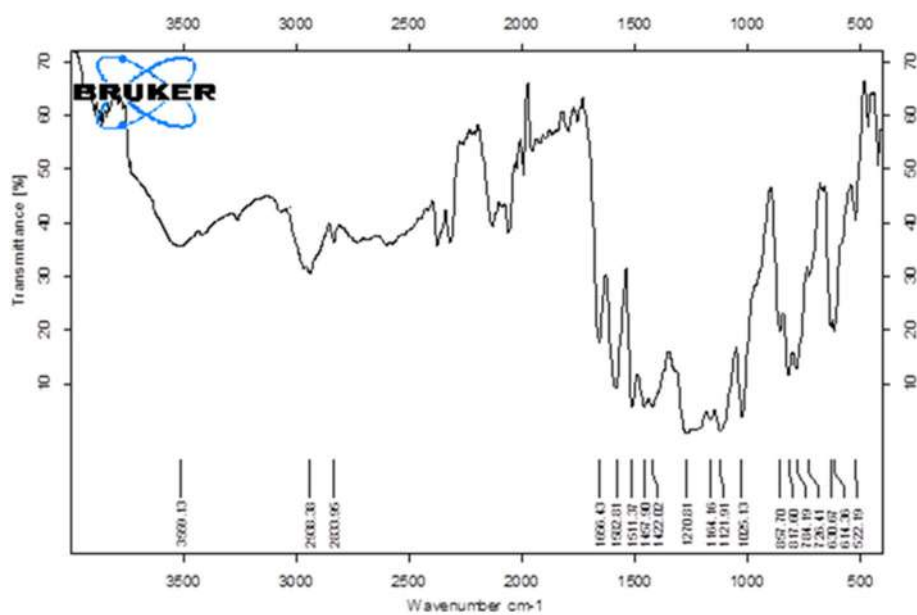


Fig S8. FTIR spectrum of C3

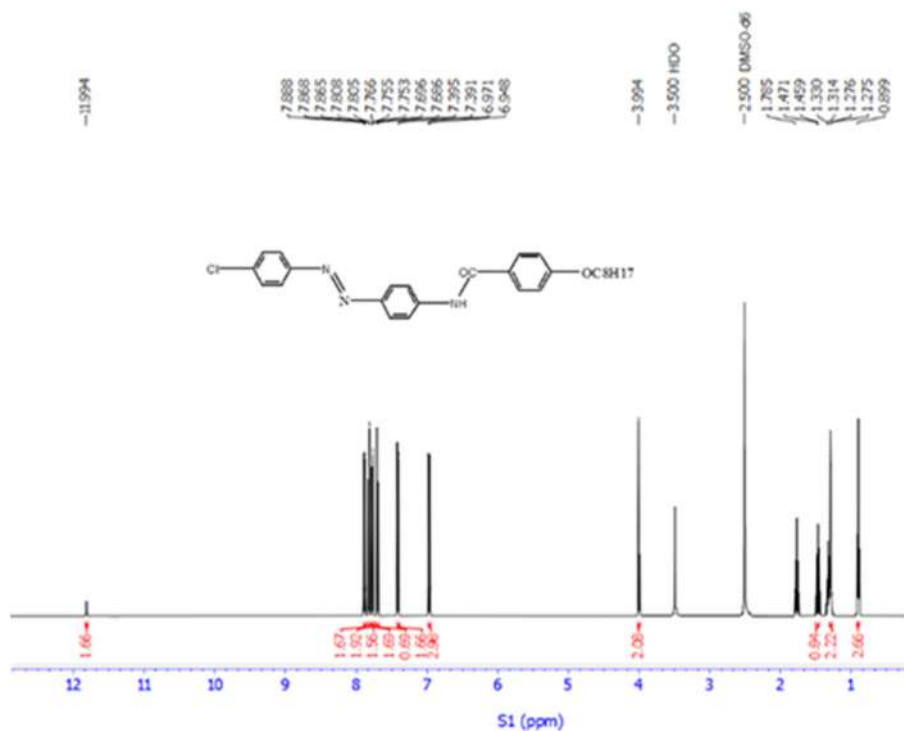


Fig S9. ¹H-NMR spectrum of C1

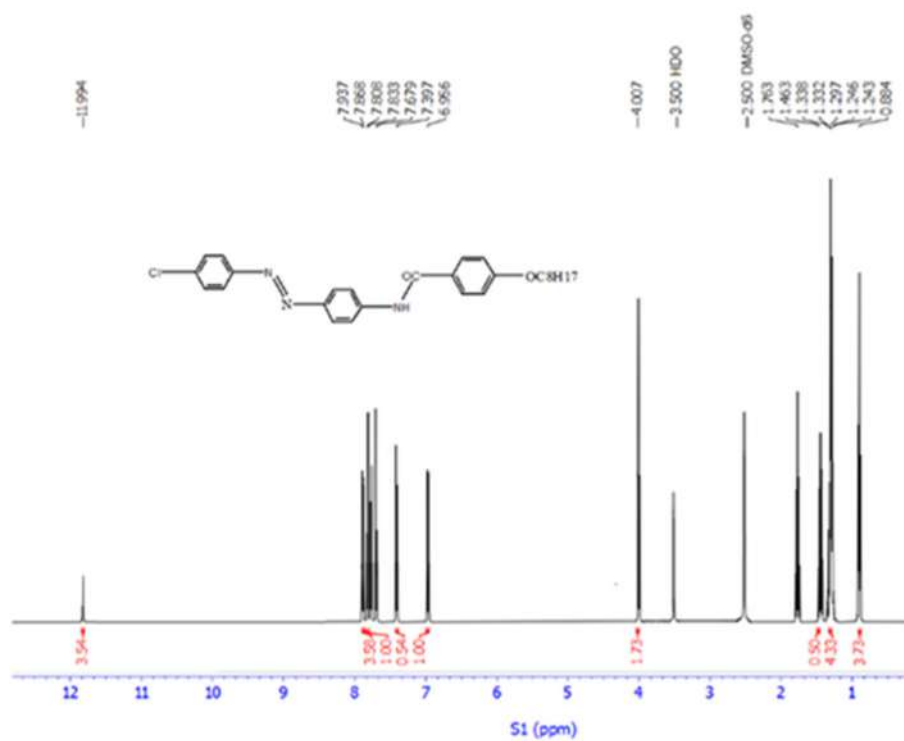


Fig S10. ¹H-NMR spectrum of C2

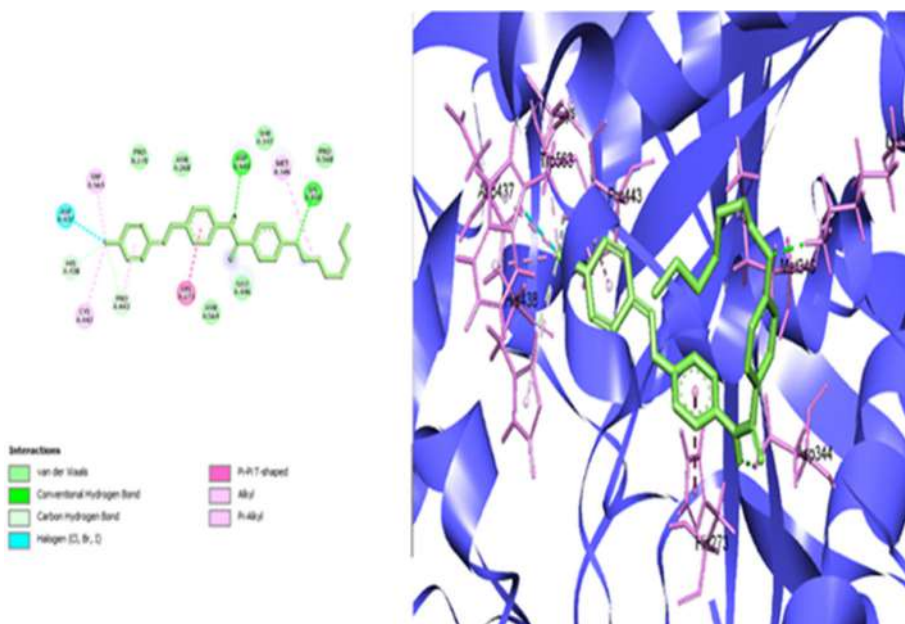


Fig S11. Docking profile of heptyl derivative with AChE receptor

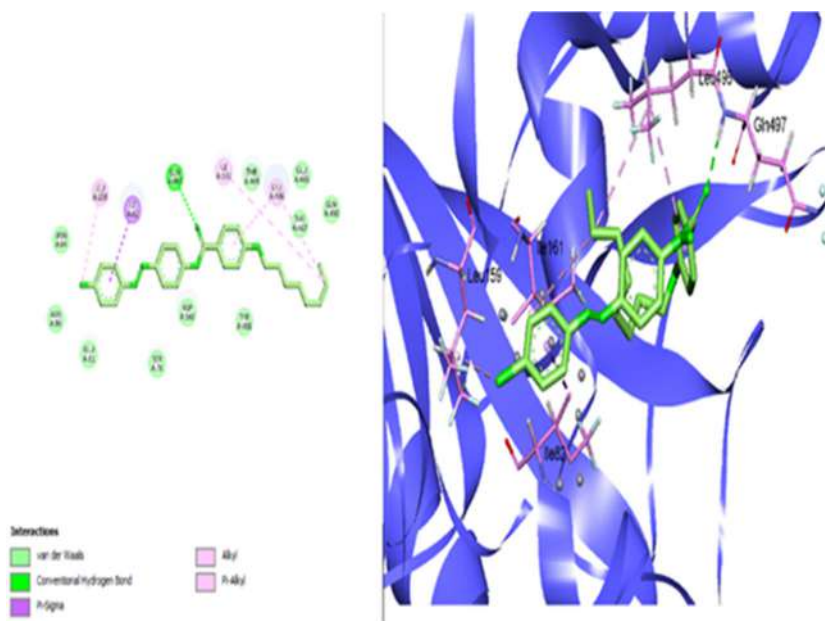


Fig S12. Docking profile of octyl derivative with AChE receptor

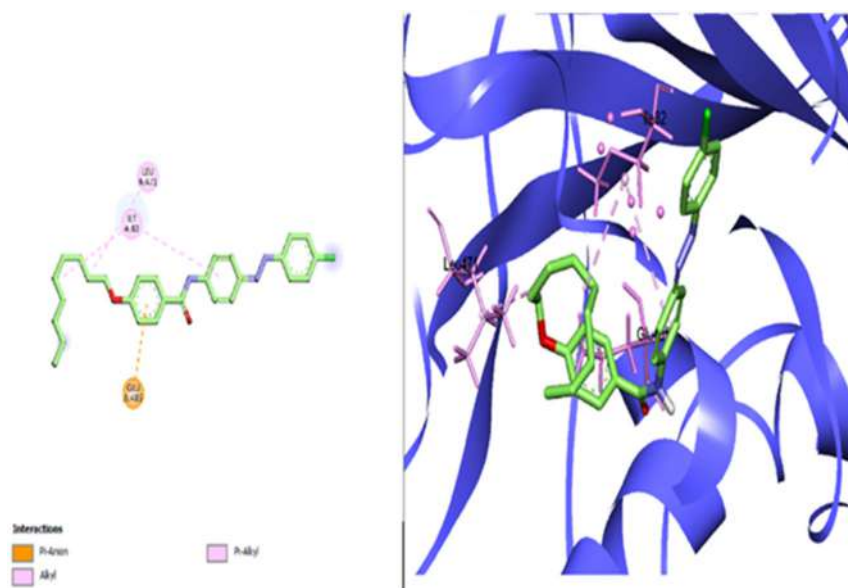


Fig S13. Docking profile of nonyl derivative with AChE receptor

Synthesis and Estimation of the Insecticide and Antibacterial Activities for Some New Amide Derivatives

Zinah Hussein Ali¹, Dina Saleem^{1*}, Abbas Khudhair Abbas², Baneen Salam Rasool³, and Mustafa Sabri Cheyad⁴

¹Department of Pharmaceutical Chemistry, College of Pharmacy, Al-Mustansiriyah University, Baghdad 10052, Iraq

²Muthanna Agriculture Directorate, Ministry of Agriculture, Al-Muthanna 66001, Iraq

³College of Science, Al-Nahrain University, Baghdad 10072, Iraq

⁴Oil Products Distribution Company (OPDC), Ministry of Oil, Baghdad 10022, Iraq

* **Corresponding author:**

email:

dina.saleem@uomustansiriyah.edu.iq

Received: February 2, 2023

Accepted: May 30, 2023

DOI: 10.22146/ijc.81972

Abstract: In this work, new compounds of amide derivatives (C1-C3) were synthesized through the conversion reaction of p-chloroaniline to diazonium salt (B1), which reacts with aniline to form a new azo-compound (B3). Synthesized of p-alkoxybenzoic acid (A1-A3) and reacts with SOCl₂ to form A4-A6 compounds that react with B3 compound to form amide compounds (C1-C3). The synthesized derivatives were tested by docking analysis and characterized via FTIR, ¹H-NMR spectra. In the docking study, the interaction diagram also displays many van der Waals interactions, which are used to estimate the synthetic compounds' activity as insecticides like anti-termites. Heptyl came in first on the binding score, followed by octyl and then nonyl. Due to the compounds' modified conformation in interacting with the enzyme's binding pocket, the length of the alkyl residue of the derivative adversely impacted their binding inhibition. The synthesized compounds (C1 and C3) give a good result as anti-E. coli and anti-Staphylococcus strains.

Keywords: amide; azo; insecticide; bacterial

■ INTRODUCTION

The amide's function is unarguable and of primary importance, being the constituent of natural and synthetic polymers and found in a wide variety of bioactive small molecules prepared both by nature and in the laboratory. In addition, amides have been employed as reaction partners in diverse transformations, representing the source for both the carbonyl and amine groups [1].

The amide functional group is one of the most important in organic synthesis, with a wide range of applications in different fields. For example, therapeutic peptides have demonstrated their effectiveness in pharmaceutical chemistry [2], and approximately 25% of marketed drugs and two-thirds of drug candidates contain at least one amide function. Furthermore, the use of amides in material and polymer chemistry is of great importance, such as for OLED applications, dentistry, or

nanocomposites. In organic synthesis, amides are also significant, owing to their outstanding reactivity as nucleophiles [3]. A peptide bond exists between the nitrogen and carbon of the carbonyl group [4-5].

Amides are a kind of substance that has been used in a variety of industries, including pharmaceuticals, agrochemistry, and materials research. Amides have had a significant impact on the pharmaceutical industry, as evidenced by the significant number of medications having an amide component and the high fraction of amide-linking processes performed by medicinal chemists [6]. Various chemical processes use amides as catalysts, ligands, reagents, solvents, and substrates. Because of their usefulness, new amide synthesis techniques are continually being developed [7-8].

The reaction of acid chlorides with amines is the most effective and widely used procedure for the manufacture of amides. Azo dyes are chemical

compounds that include the N=N functional group. They are a commercially important class of azo compounds [9]. Azo dyes now provide a more significant part of the dye chemical industry, and their relevance is likely to grow in the coming years. They are essential in the management of the dye and printing markets. These dyes are made using a simple diazotization and coupling method. A variety of techniques and adjustments are used to achieve the appropriate color characteristics, yield, and particle size of the dye for better dispersibility. The most widely used dyes, accounting for around 60% of all dye manufacturing, are azo dyes [10]. Azo dyes account for more than 70% of all dyes used in the industry [11]. The most widely used synthetic colorants are azo dyes, which are used in textiles, printing, and paper.

Escherichia coli (*E. coli*) is one of the most common Gram-negative foodborne pathogens, which usually is used as an indicator bacterium in tests for fecal contamination of food [12]. Staphylococcal infections, commonly called staph infections, are caused by a genus of bacteria called *Staphylococcus*. The most common human pathogen is *S. aureus*. A pathogen is an organism that causes disease [13]. Insecticides are chemicals that are used to keep insects under control by killing them or stopping them from acting in undesired or damaging ways. Their structure and mode of action are used to classify them. Many pesticides work by blocking the enzyme cholinesterase in the insect's brain. Other pesticides work as growth regulators or endotoxins [14].

■ EXPERIMENTAL SECTION

Materials

The materials used in this study were *p*-chloroaniline (C₆H₆ClN), ethanol (C₂H₆O), aniline (C₆H₇N), thionyl chloride (SOCl₂), 4-hydroxybenzoic acid (C₇H₆O₃, 99% purity, Sigma Aldrich, USA), potassium carbonate (K₂CO₃), 1-heptylbromide (CH₃(CH₂)₆Br), 1-octylbromide (CH₃(CH₂)₇Br), nonylbromide (CH₃(CH₂)₈Br, 97% purity Merck, Germany), high-quality absolute ethanol and dimethylformamide (DMF, 99% purity Merck, Germany).

Instrumentation

The instrumentations used in this study were Fourier-

transform infrared (FTIR) spectroscopy (ALPHA II, Bruker, Germany), and ¹H-NMR hydrogen nuclear magnetic resonance (NMR 400 MHz, ACF 400, Bruker, Germany).

Procedure

General procedure for the synthesis of azo compound (B3) [15]

In an ice water bath, add 6 mL of 10% HCl solution to *p*-chloroaniline (0.01 mol) with 3 drops of HCl in a test tube. The test tube contained 0.02 mol (1.38 g) of NaNO₂ in 7 mL of distilled water. In the ice bath (5 °C), the first solution was added to another solution in the test tube. A 0.01 mol of aniline solution in 10 mL of 10% NaOH was added in test tube No.3. Then, in test tube No.3, add the solution mixture. Finally, the final product was filtered, and the precipitate was collected, which led to the necessary products being made. The melting point of B3 was 204–209 °C and has yellow color.

General procedure for the synthesis of *p*-alkoxybenzoic acid compounds (A1-A3) [16]

Dissolved 15 mL of ethanol with 0.01 mol (1.38 g) 4-hydroxybenzoic acid and alkyl bromide (R: heptyl, octyl, and nonyl) and refluxed for 24 h. The solution was added to 0.02 mol (1.2 g) of K₂CO₃, diluted in a small quantity of water (around 5 mL), and heated for 1–3 h. The solvent was evaporated, and an equivalent volume of water was added, followed by heating the solution until it became pure. Acidification with HCl resulted in the formation of a solid precipitate.

Synthesis of 4-alkoxybenzoyl chloride (A4-A6) [17]

For 3–4 h, a mixture of each 0.01 mol of 4-alkoxybenzoic acid (A1–A3) and 15 mL of SOCl₂ was refluxed with a few drops of DMF as solvent. After evaporating the excess SOCl₂, the result is a dark brown precipitate of 4-alkoxybenzoyl chloride. Finally, the acid chloride residue was utilized straight for the further reaction without purification.

Synthesis of N-(4-(4-Chloro-phenylazo)-phenyl)-4-alkoxy-benzamide compounds (C1-C3) [18]

The compound (A4-A6) 0.001 mol was dissolved in 15 mL of pyridine and added by 0.001 mol of B3. The solution was stirred at 25 °C for 24 h. Following that, the

mixtures were put into ice cubes, filtered, and rinsed with distilled water.

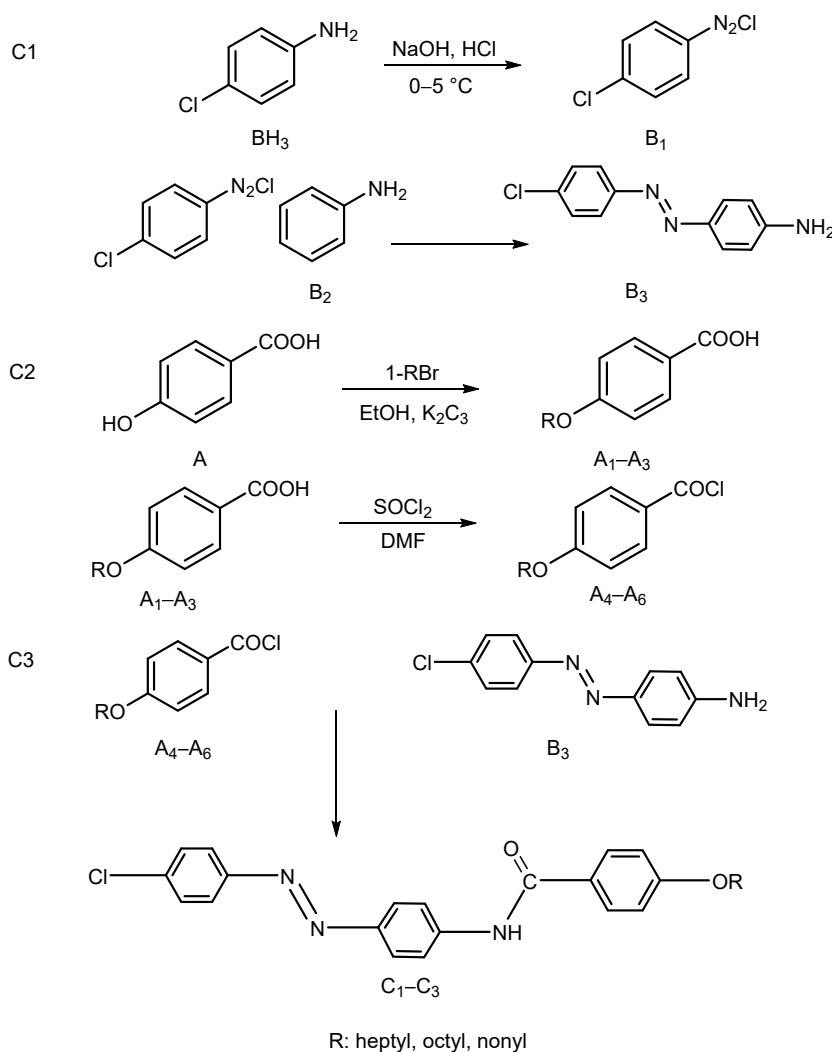
Docking analysis

Acetylcholinesterase (AChEcrystallographic)'s 3D structure was obtained from the protein data bank (PDB code: 6xyu). Using Swiss Protein Viewer, the enzyme structure was subjected to energy reduction (version 4.1). Following a series of preparation procedures, the co-crystallized ligands and water molecules were taken out, the structure was adjusted, and polar hydrogens were added. ChemDraw extreme (version 18.0) was used to draw out the synthesized compounds, and the sdf files were then saved and transformed using Open Babel software to PDB files. Using Autodock Tools (version 1.5.6) [19] and a pdbqt file format, the docking operation

was carried out after energy reduction for both the enzyme and the receptor was complete. Autodock Vina was used to perform molecular docking along with Auto Grid software with a grid box of size (30 × 30 × 30) and a grid center (39.787 * 53.325 * 5.243), which represent the x, y, and z dimensions, respectively. The docking parameters were set to default values, and ten conformations were generated. Discovery Studio [20] is used for generating visualization images.

RESULTS AND DISCUSSION

4-Alkoxybenzoic acid (A1-A3) was synthesized via the reaction of 4-hydroxybenzoic acid with alkyl bromide (1-bromoheptane, 1-bromooctane, and 1-bromononane). From Scheme 1, an azo dye can only be



Scheme 1. Routs for the synthesized compounds C1-C3

manufactured using two organic molecules, a coupling component and a diazonium salt. The diazonium salt interacts as an electrophile with an electron-rich coupling element, such as aniline, through an electrophilic aromatic substitution process. The amine group is positioned at para to the aryl diazonium ion. The described compounds were synthesized through the condensation reaction between previously produced compounds (B3) and 4-alkoxybenzoyl chloride (A4-A6). The physicochemical properties of the synthesized compounds are listed in Table 1.

Insecticide activity and the efficacy of compounds C1, C2, and C3 as pesticides against *Aphidoidea* insects were studied in the Department of Plant Protection (Al-Muthanna Agriculture Directorate) in Al Muthanna Governorate. The concentrations of 3000, 4000, and 5000 ppm of the prepared compounds C1, C2, and C3, which have been dissolved with paraffin. The synthesized compounds were used as pesticides by spraying the

solution on the insect using the spray method. The synthesized compounds that were used as pesticides in the application gave positive results by killing the insects at the different concentrations used. The efficacy of compounds C1, C2, and C3 as pesticides against *Aphidoidea* insects. The synthesized compounds used as pesticides in the application gave positive results by killing the insects at different concentrations at different times, as shown in Table 2.

The compounds synthesized were evaluation evaluated against various types of Gram-positive and Gram-negative bacteria. All compounds give good results by inhibiting the zone growth of each bacteria used, as shown in Table 3.

Fig. S1 explained FTIR for compound A2, the broadband at 3423 cm^{-1} for OH group, 3116 and 3084 cm^{-1} for C-H aromatic, 2977 and 2831 cm^{-1} for C-H aliphatic, 1729 cm^{-1} detected for C=O and 1614 cm^{-1}

Table 1. Physicochemical properties of synthesized compounds B3, C1–C3

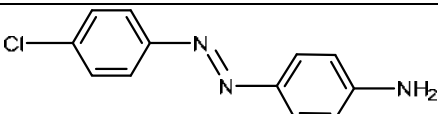
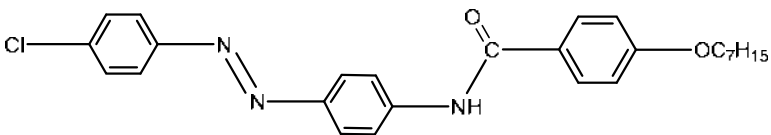
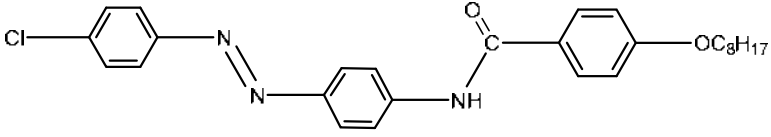
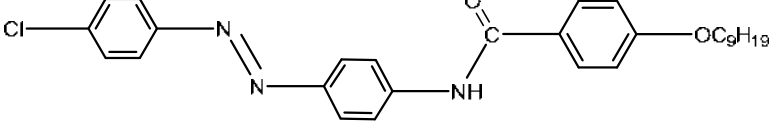
Compound No.	Structure	Yield %	M.p °C	Color
B3		76	204–209	Yellow
C1		72	183–188	Brown
C2		74	171–175	Dark Brown
C3		78	158–162	Orange

Table 2. Anti-insect activities of the compounds C1–C3

Compound No.	Time (min) to kill <i>Aphidoidea</i> insects		
	3000	4000	5000
C1	3.00	2.00	1.75
C2	4.00	3.00	2.75
C3	4.00	3.50	2.25

Table 3. Antibacterial activities of the compounds C1–C3

Bacteria name	Zone of inhibition (mm)	
	C1	C3
<i>Staphylococcus</i>	+	++
<i>Escherichia coli</i>	++	+

Note: (+) less than 13 mm, and (++) more or equal to 13

for C=C aromatic [21]. Fig. S2 explained FTIR for compound A3, the broadband at 3443 cm^{-1} for the OH group, 3033 cm^{-1} for C-H aromatic, 2968 and 2866 cm^{-1} for C-H aliphatic, 1716 cm^{-1} detected for the C=O and 1601 cm^{-1} for C=C aromatic [21]. The FTIR spectrum of compound B3 in Fig. S5 showed the two bands 3543 and 3406 cm^{-1} (NH_2), 3077 cm^{-1} (C-H aromatic stretching), 1614 cm^{-1} (C=C), 1578 cm^{-1} (N=N), 1112 cm^{-1} (C-N bending), 716 cm^{-1} (C-Cl). The FTIR spectrum of compound C2 in Fig. S7 showed 1251 cm^{-1} (C-O), 3084 and 3116 cm^{-1} detected for C-H of stretching aromatic rings, the peaks at 2977 cm^{-1} returned to C-H aliphatic stretching, 1711 cm^{-1} detected for carbonyl of amide, the wide band 3421 cm^{-1} for N-H group, 1413 – 1530 cm^{-1} (C=C aromatic stretching) [21]. The FTIR spectrum of compound C3 in Fig. S8 showed the bands 3569 cm^{-1} (N-H), 2983 cm^{-1} (C-H aliphatic stretching), 1666 cm^{-1} (C=O), 1582 cm^{-1} (N=N), 1270 cm^{-1} (C-O), 1121 cm^{-1} (C-N), 630 cm^{-1} (C-Cl).

$^1\text{H-NMR}$ ($\text{DMSO-}d_6$ 500 MHz) spectra of the compounds A1 and A3 are shown in Fig. S3 and S4, δ 10.9 (s, 1H) and 11.5 (s, 1H) ppm detected for the proton of acid group (OH), δ 7.8–7.2 (m, 2H) ppm for aromatic protons, δ 4.1 ppm for OCH_2 protons, δ 1.7–1.2 (m, 6H) ppm for CH_2 protons, and δ 0.90 and 0.92 (m, 2H) ppm for methyl protons [22]. The $^1\text{H-NMR}$ spectrum of compound B3 is shown in Fig. S6 ($\text{DMSO-}d_6$ 500 MHz): δ 7.8–7.0 (m, 4H) ppm for aromatic protons and δ 11.8 (s, 1H) ppm for amino protons. The $^1\text{H-NMR}$ spectrum of compound C1 is shown in Fig. S9, δ 7.8–6.9 (m, 7H) ppm detected for aromatic protons, δ 3.9 (m, 1H) ppm for OCH_2 protons, δ 3.2–1.2 (m, 7H) ppm for $(\text{CH}_2)_5$ protons, δ 0.8 (m, 2H) ppm for methyl protons, and the peak at δ 11.1 (s, 1H) detected for NH. The $^1\text{H-NMR}$ spectrum of compound C2 is shown in Fig. S10, δ 7.9–6.9 (m, 7H) ppm detected for aromatic protons, δ 4.0 (m, 1H) ppm for OCH_2 protons, δ 1.20–1.27 (m, 9H) for $(\text{CH}_2)_6$ protons, δ 0.8 (m, 2H) ppm for methyl protons, and the peak at δ 11.1 (s, 1H) ppm detected for NH [22].

In docking analysis, the docking simulations were done to explore the possible mechanistic inhibition of AChE. The binding scores of the synthesized compounds are ranked according to their binding affinities. The

results show that heptyl derivatives have the best binding scores compared to others. Fig. S11 demonstrates the interactions between the target enzyme and an octyl derivative. The most noticeable interaction was a formed halogen bonding between ASP437 and the chloro of the compound. At the same time, the straight alkyl residue of a heptyl derivative forms an alkyl interaction. The interaction diagram also shows multiple van der Waals interactions. The ranking order of the binding score was heptyl > octyl > nonyl. The length of the alkyl residue of the derivative negatively affected their binding inhibition, which could be attributed to changing the conformation of the compounds to interact with the binding pocket of the enzyme. Fig. S12 and S13 show the binding modes for octyl and nonyl, respectively [23].

■ CONCLUSION

In conclusion, three new amide derivatives, C1–C3, have been synthesized. Furthermore, the newly synthesized amide compounds, C1 and C3, act as bacterial inhibitors, including *S. aureus*, and *E. coli* bacteria. Finally, the first quarter was critical as an antidote to earthworms. The heptyl group was ranked first, followed by octyl, and the nonyl group in the structures of final synthesized compounds because the length of the derivative's alkyl residue had a detrimental impact on their binding inhibition by an effect on the AChE enzyme. The synthesized compounds give an excellent result as anti-bacteria.

■ ACKNOWLEDGMENTS

The authors thank the College of Pharmacy, Al-Mustansiriyah University, Al-Nahrain University, and Muthanna Agriculture Directorate for their support and equipment for this research.

■ SUPPORTING INFORMATION

Amide compounds as organic molecules that are synthesized and characterized by using FTIR and $^1\text{H-NMR}$ in addition to using docking analysis.

■ AUTHOR CONTRIBUTIONS

Dina Saleem and Zinah Hussein Ali conducted the experiment, Mustafa Sabri Cheyad and Baneen Salam

Rasool conducted the FTIR and ¹H-NMR spectroscopy and molecular docking analysis, and Abbas Khudhair Abbas wrote and revised the manuscript. All authors agreed to the final version of this manuscript.

■ REFERENCES

- [1] Massolo, E., Pirola, M., and Benaglia, M., 2020, Amide bond formation strategies: Latest advances on a dateless transformation, *Eur. J. Org. Chem.*, 2020 (30), 4641–4651.
- [2] Adler, P., Gras, M., and Smietana, M., 2023, Catalytic and sustainable amide bond formation using a DABCO/Dichlorotriazine system, *ChemCatChem*, 15 (20), e202300264.
- [3] Haas, B., Goetz, A., Bahamonde, A., McWilliams, J.C., and Sigman, M.S., 2022, Predicting relative efficiency of amide bond formation using multivariate linear regression, *Proc. Natl. Acad. Sci. U. S. A.*, 119 (16), e2118451119.
- [4] Weiser, L.J., and Santiso, E.E., 2019, A CGenFF-based force field for simulations of peptoids with both cis and trans peptide bonds, *J. Comput. Chem.*, 40 (22), 1946–1956.
- [5] Conic, D., Pierloot, K., Parac-Vogt, T.N., and Harvey, J.N., 2020, Mechanism of the highly effective peptide bond hydrolysis by MOF-808 catalyst under biologically relevant conditions, *Phys. Chem. Chem. Phys.*, 22 (43), 25136–25145.
- [6] Henninot, A., Collins, J.C., and Nuss, J.M., 2018, The current state of peptide drug discovery: Back to the future, *J. Med. Chem.*, 61 (4), 1382–1414.
- [7] Bousfield, T.W., Pearce, K.P.R., Nyamini, S.B., Angelis-Dimakis, A., and Camp, J.E., 2019, Synthesis of amides from acid chlorides and amines in the bio-based solvent Cyrene™, *Green Chem.*, 21 (13), 3675–3681.
- [8] Sanz Sharley, D.D., and Williams, J.M.J., 2017, Acetic acid is a catalyst for the N-acylation of amines using esters as the acyl source, *Chem. Commun.*, 53 (12), 2020–2023.
- [9] Shankarling, G.S., Deshmukh, P.P., and Joglekar, A.R., 2017, Process intensification in azo dyes, *J. Environ. Chem. Eng.*, 5 (4), 3302–3308.
- [10] Gürses, A., Açıkyıldız, M., Güneş, K., and Gürses, M., 2016, “Classification of Dye and Pigments” in *Dyes and Pigments*, Springer International Publishing, Cham, Switzerland, 31–45.
- [11] Shah, M., 2014, Effective treatment systems for azo dye degradation: A joint venture between Physico-chemical & microbiological process, *Int. J. Environ. Biorem. Biodegrad.*, 2 (5), 231–242.
- [12] Zhu, Y., and Zhang, S., 2020, Antibacterial activity and mechanism of lacidophilin from *Lactobacillus pentosus* against *Staphylococcus aureus* and *Escherichia coli*, *Front. Microbiol.*, 11, 582349.
- [13] Cheung, G.Y.C., Bae, J.S., and Otto, M., 2021, Pathogenicity and virulence of *Staphylococcus aureus*, *Virulence*, 12 (1), 547–569.
- [14] Sharma, K., 2019, Cholinesterase inhibitors as Alzheimer's therapeutics (Review), *Mol. Med. Rep.*, 20 (2), 1479–1487.
- [15] Al-Jamali, N.M., 2013, Synthesis and identification of oxazipen, diazipene compounds via peri cyclic reactions, *J. Chem. Chem. Sci.*, 3 (2), 64–69.
- [16] Sivasri, J., Pardhasaradhi, P., Madhav, B.T.P., Tejaswi, M., and Manepalli, R.K.N.R., 2020, Birefringence studies on alkoxy benzoic acids with dispersed Fe₃O₄ nanoparticles, *Liq. Cryst.*, 47 (32), 330–344.
- [17] Gaffer, H.E., 2019, Antimicrobial sulphonamide azo dyes, *Color. Technol.*, 135 (6), 484–500.
- [18] Hadi, D.M., and Jber, N.R., 2017, Synthesis and spectroscopic characterization of bis-swallow tailed mesogen, *Int. J. Sci. Res.*, 6 (1), 1909–1915.
- [19] Eberhardt, J., Santos-Martins, D., Tillack, A.F., and Forli, S., 2021, AutoDock Vina 1.2.0: New docking methods, expanded force field, and Python bindings, *J. Chem. Inf. Model.*, 61 (8), 3891–3898.
- [20] Trott, O., and Olson, A.J., 2010, AutoDock Vina: Improving the speed and accuracy of docking with a new scoring function, efficient optimization, and multithreading, *J. Comput. Chem.*, 31 (2), 455–461.
- [21] Ozaki, Y., Huck, C., Tsuchikawa, S., and Engelsen, S.B., 2021, *Near-Infrared Spectroscopy: Theory, Spectral Analysis, Instrumentation, and Applications*, Springer, Singapore.

- [22] Sharma, S.K., Verma, D.S., Khan, L.U., Kumar, S., and Khan, S.B., 2018, *Handbook of Materials Characterization*, Springer, Cham, Switzerland.
- [23] Singh, K.D., Labala, R.K., Devi, T.B., Singh, N.I., Chanu, H.D., Sougrakpam, S., Nameirakpam, B.S., Sahoo, D., and Rajashekar, Y., 2017, Biochemical efficacy, molecular docking and inhibitory effect of 2,3-dimethylmaleic anhydride on insect acetylcholinesterase, *Sci. Rep.*, 7 (22), 12483.

Glutaraldehyde Crosslinked Alginate-Chitosan Nanoparticles as Paracetamol Adsorbent

Nurmala Nurmala, Adhitasari Suratman*, and Suherman Suherman

Department of Chemistry, Faculty of Mathematics and Natural Sciences, Universitas Gadjah Mada, Sekip Utara, Yogyakarta 55281, Indonesia

* **Corresponding author:**

email: adhitasari@ugm.ac.id

Received: February 19, 2023

Accepted: September 11, 2023

DOI: 10.22146/ijc.82431

Abstract: Paracetamol contained in wastewater can cause adverse effects on animal ecosystems, such as fish living in waters and cause harmful effects on humans. Adsorption techniques are used to remove these pharmaceutical compounds. Alginate-chitosan nanoparticles are non-toxic and effectively used as adsorbents to remove pharmaceutical compounds in wastewater. Research on glutaraldehyde crosslinked alginate-chitosan nanoparticles as paracetamol adsorbent has been carried out. This research used the ionic gelation method. Nanoparticles were characterized using transmission electron microscopy (TEM), scanning electron microscope (SEM-EDX) and Fourier transform infra-red spectrophotometer (FTIR). Furthermore, the nanoparticles were used for paracetamol adsorption. The results showed that the form nanoparticles are coarse solid powder and brownish yellow. The TEM image shows an average nanoparticle size of 8.22 nm. Glutaraldehyde crosslinked alginate-chitosan nanoparticles adsorbed paracetamol with adsorption kinetics followed a pseudo-second-order or Ho-McKay model, the adsorption rate constant of $0.0324 \text{ g mg}^{-1} \text{ min}^{-1}$. The isotherm study of paracetamol adsorption by glutaraldehyde cross-linked alginate-chitosan nanoparticles followed the isotherm Dubinin-Radushkevich isotherm model with a free energy value of $707.1068 \text{ kJ mol}^{-1}$, and this value indicates the adsorption process by chemically or chemisorption.

Keywords: adsorption; alginate; chitosan; glutaraldehyde; paracetamol

■ INTRODUCTION

Pharmaceutical waste has increased in recent years due to the COVID-19 pandemic, and the drugs used increased more than 2.5 times [1]. The main contaminants found in wastewater are pharmaceutical compounds including antibiotic, analgesic, and antipyretic [2]. Paracetamol is one of the analgesic and antipyretic pharmaceutical compounds often used for medical practice and consumed for human health [3]. Based on reports, paracetamol will be excreted from the body by 58–68% after consumption and then will be released into the wastewater system [4]. High concentrations of paracetamol were detected in Indonesian coastal waters, specifically in Jakarta Bay, namely Angke (610 ng/L) and Ancol (420 ng/L) [5]. High concentrations of paracetamol in wastewater can cause

dangerous diseases in humans, such as liver failure, gastrointestinal, and hepatotoxicity [6]. Paracetamol is non-biodegradable and easily accumulates in the aquatic environment, which can have adverse effects on human health and other living things [7]. Therefore, there must be an effort to overcome the problem of wastewater from pharmaceutical compounds such as paracetamol.

The advantages of separating pharmaceutical compounds using adsorption techniques are easy processing, low cost, high efficiency, and can be regenerated [8]. Nanoparticles can be used as an efficient adsorbent for the removal of pharmaceutical compounds in wastewater; nanoparticles have a small size, large surface area and many active binding sites, which can increase the adsorption capacity [2]. Polysaccharide-based materials can be used to

synthesize nanoparticles and as adsorbents, including chitosan and sodium alginate. Chitosan provides an advantage in the adsorption process because it has amino and hydroxyl groups as active groups and is able to interact with pharmaceutical compounds, phenols, metals, pesticides, and other compounds contained in wastewater [9]. Modifications are required for the synthesis of nanoparticles from chitosan because chitosan is very sensitive to pH and has low thermal stability [10].

Chitosan can be modified by combining certain polymers and crosslinkers to improve the stability and adsorption capacity of chitosan [11]. Alginate is an anionic polymer, that has non-toxic, biodegradable, biocompatible properties, and the anionic properties of alginate can interact with the cationic properties of chitosan to form more stable nanoparticles [11]. Ferrah et al. [12] reported chitosan combined with alginate and polyethyleneimine methylene phosphonic acid to be able to be a promising and efficient adsorbent for removing the pharmaceutical compounds sodium diclofenac and ibuprofen from wastewater.

Chitosan also requires certain crosslinkers for the synthesis of chitosan-based nanoparticles to improve adsorption capacity [4]. Glutaraldehyde is a chitosan crosslinker that can improve the chemical stability of chitosan in acidic solutions and adsorption performance [13]. Kyzas et al. [14] reported chitosan was modified and cross-linked with glutaraldehyde and combined with sulfonate group or *N*-(2-carboxybenzyl) was able to remove pramipexole dihydrochloride, a pharmaceutical compound used to treat symptoms of Parkinson's disease and as a pharmaceutical compound in wastewater. Based on the background, it is necessary to conduct research using polysaccharide-based nanoparticles, such as chitosan and alginate, to remove pharmaceutical compounds such as paracetamol in wastewater.

■ EXPERIMENTAL SECTION

Materials

The materials used in this study came from Merck and Sigma Aldrich with pro analytical quality. These materials include chitosan (Deacetylation Degree $\geq 85\%$), sodium alginate, glutaraldehyde, CaCl_2 , aquabidest, 10%

(v/v) methanol solution, 1% (v/v) acetic acid solution, sodium hydroxide (NaOH), hydrochloric acid (HCl), and paracetamol from pharma grade.

Instrumentation

The instruments used in this study include laboratory glassware, analytical balance, pH meter, magnetic stirrer, hot plate, centrifugation (Sorvall Biofuge Primo), Fourier transform infra-red spectrophotometer (FTIR, Shimadzu Prestige-21) was observed in the absorption range of $400\text{--}4000\text{ cm}^{-1}$. Samples were prepared in a powder state, molded with KBr, and then pressed to form pellets. Nanoparticle size was characterized using transmission electron microscopy (TEM, JEM-1400 JEOL/EO) on a scale of 20–500 nm. Samples were prepared and then characterized. The morphology of the nanoparticles was characterized using a scanning electron microscope (SEM-EDX, JSM-6510 JEOL/EO). The sample was glued to the specimen holder, and then the sample was characterized with the specifications of voltage = 15 kV and magnification of 500–10,000 times. The concentration of paracetamol solution before and after adsorption was determined at 200–400 nm absorption using a UV-vis spectrophotometer (GENESYS 50 Thermo Scientific).

Procedure

Synthesis of glutaraldehyde cross-linked alginate-chitosan nanoparticles

Sodium alginate (3 mg/mL) and CaCl_2 (3.35 mg/mL) solutions were prepared by dissolving in aquabidest. Chitosan was prepared at 3 mg/mL concentration, dissolved in 1% (v/v) acetic acid. 0.1 M HCl solution and 0.1 M NaOH solution were used to adjust the pH of alginate and chitosan solutions to pH 5. Synthesis of glutaraldehyde crosslinked alginate-chitosan nanoparticles was prepared according to Rajaonarivony method with modifications [15]. Calcium alginate (Ca-Alg) in the pre-gel phase was initially prepared by adding 2 mL of CaCl_2 to 10 mL of sodium alginate solution with continuous stirring for 30 min. After that, 10 mL of chitosan solution was added, and then 5 mL of glutaraldehyde was added to the solution while still stirring at constant speed at room

temperature. Stirring process was carried out for 2 h, then centrifuged at 5,000 rpm for 30 min. Nanoparticles were filtered using filter paper and then dried.

Characterization of glutaraldehyde crosslinked alginate-chitosan nanoparticles

Glutaraldehyde crosslinked alginate-chitosan nanoparticles were characterized using a FTIR. The sample was prepared in a powder state, then formed with KBr and pressed to form pellets. FTIR spectra were determined at a wavenumber between 400–4000 cm^{-1} . The size of glutaraldehyde crosslinked alginate-chitosan nanoparticles was characterized using TEM on a scale of 20–500 nm. The samples were dispersed and placed in the grid. The samples in the grid were waited until dry, and the samples were ready for characterization. The morphology of glutaraldehyde crosslinked alginate-chitosan nanoparticles was characterized by SEM. The samples were attached to the specimen holder, and then the samples were ready for characterization with a voltage specification of 15 kV and magnification of 500–10,000 times.

Effect of pH on paracetamol adsorption

Paracetamol solution 10 mg/L, volume of 50 mL was adjusted to pH 2, 3, 4, 5, 6, 7, and 8 with the addition of HCl or NaOH solutions. Glutaraldehyde crosslinked alginate-chitosan nanoparticles adsorbent (20 mg) was added to each paracetamol solution for adsorption. The stirring process was carried out for 60 min, and then the filtrate was filtered. The concentration of paracetamol was analyzed with a UV-vis spectrophotometer at the maximum wavelength (λ_{max}).

Effect of adsorbent mass on paracetamol adsorption

Paracetamol solution 10 mg/L, volume of 50 mL in 9 different containers adjusted to the optimum pH by adding HCl or NaOH solution. Glutaraldehyde crosslinked alginate-chitosan nanoparticles were added to paracetamol solution for the adsorption process with mass variations of 5, 10, 15, 20, 25, 30, 35, and 40 mg and stirred for 60 min then the filtrate was filtered. The concentration of paracetamol was analyzed with a UV-vis spectrophotometer at λ_{max} .

Effect of contact time on paracetamol adsorption

Paracetamol solution 10 mg/L, volume of 50 mL in 7 different containers adjusted to the optimum pH by adding HCl or NaOH solution. Glutaraldehyde crosslinked alginate-chitosan nanoparticles were added to paracetamol solution for the adsorption process at the optimum mass and stirred at various times of 15, 30, 45, 60, 90, and 120 min, then the filtrate was filtered. The concentration of paracetamol was analyzed with a UV-vis spectrophotometer at λ_{max} . The adsorption capacity can be used to determine the adsorption kinetics model.

Effect of initial concentration of paracetamol

Paracetamol solutions are prepared with various concentrations of 10, 12, 14, 16, and 18 mg/L. Paracetamol solution 50 mL in 10 different containers was adjusted to the optimum pH by adding HCl or NaOH solutions. Paracetamol solutions of varying concentrations were prepared for control (without adsorbent) and adsorption (with adsorbent). Glutaraldehyde crosslinked alginate-chitosan nanoparticles were added to the paracetamol solution at optimum mass. The stirring process was carried out according to the optimum contact time, and then the filtrate was filtered. The concentration of paracetamol was analyzed by UV-vis spectrophotometer at λ_{max} .

RESULTS AND DISCUSSION

FTIR Characterization

The identification of functional groups in the base material and the synthesized nanoparticles was carried out using an FTIR spectrophotometer. The results of the FTIR spectra of alginate, chitosan, glutaraldehyde, and glutaraldehyde crosslinked alginate-chitosan nanoparticles can be seen in Fig. 1. Fig. 1(a) shows characteristic peaks at 3448, 1410, 1620 and 1026 cm^{-1} which shows stretching vibration –OH, symmetric and asymmetric stretching vibration C=O and stretching vibration C–O–C of alginate [16-18]. Fig. 1(b) shows characteristic peaks at 3450, 1647, 1419 and 1028 cm^{-1} , which shows the stretching of the –NH and –OH groups, the primary amine (–NH₂) bending vibration, –CH₂ and C–O–C stretching vibrations of chitosan [19-21].

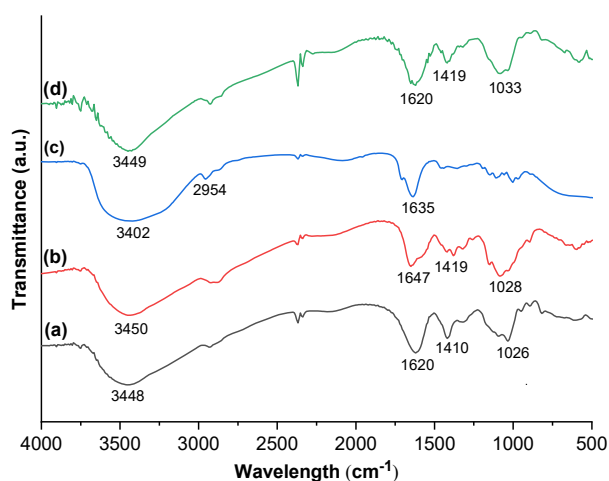


Fig 1. FTIR spectra of (a) alginate, (b) chitosan, (c) glutaraldehyde, and (d) glutaraldehyde crosslinked alginate-chitosan nanoparticles

Fig. 1(c) shows characteristic peaks at 3402, 2954, and 1635 cm^{-1} , which shows $-\text{OH}$ stretching vibrations, symmetric $\text{C}-\text{H}$ vibrations, and $\text{C}=\text{O}$ stretching vibrations of glutaraldehyde [22]. Fig. 1(d) shows the alginate peak at 3448 cm^{-1} , indicating the presence of $-\text{OH}$ stretching vibrations, and chitosan peaks at 3450 cm^{-1} , indicating the stretching vibrations of $-\text{OH}$ and $-\text{NH}$, shifted the wavenumber to 3449 cm^{-1} . This shift occurs due to electrostatic interactions between the

carboxylic groups from alginate and the amine groups from chitosan to form a polyelectrolyte complex [23]. The chitosan peak at 1647 cm^{-1} wavelength, the alginate peak at 1620 cm^{-1} and the glutaraldehyde peak at 1635 cm^{-1} shifted to 1620 cm^{-1} wavelength, indicating the presence of $-\text{NH}$ bending vibrations from chitosan and $\text{C}=\text{O}$ asymmetric stretching vibrations from alginate and indicating the $\text{C}=\text{O}$ group in glutaraldehyde interacts with the amine groups in chitosan to form $\text{C}=\text{N}$ bonds (imines) [24]. Furthermore, there was a shift in 1419 cm^{-1} wavelength from the alginate peak at 1410 cm^{-1} and chitosan at 1405 cm^{-1} , indicating the presence of $-\text{CH}_2$ bending vibrations from chitosan and $\text{C}=\text{O}$ symmetrical stretching vibrations from alginate. Then, 1028 cm^{-1} of chitosan and 1026 cm^{-1} of alginate shifts to 1033 cm^{-1} wavelength indicating the presence of $\text{C}-\text{O}-\text{C}$ stretching vibrations.

SEM-EDX Characterization

The surface morphology and elemental composition of glutaraldehyde cross-linked alginate-chitosan nanoparticles are determined by using SEM-EDX before and after adsorption. SEM images taken at 5000 times magnification of the nanoparticles before and after adsorption can be seen in Fig. 2. Fig. 2(a) shows

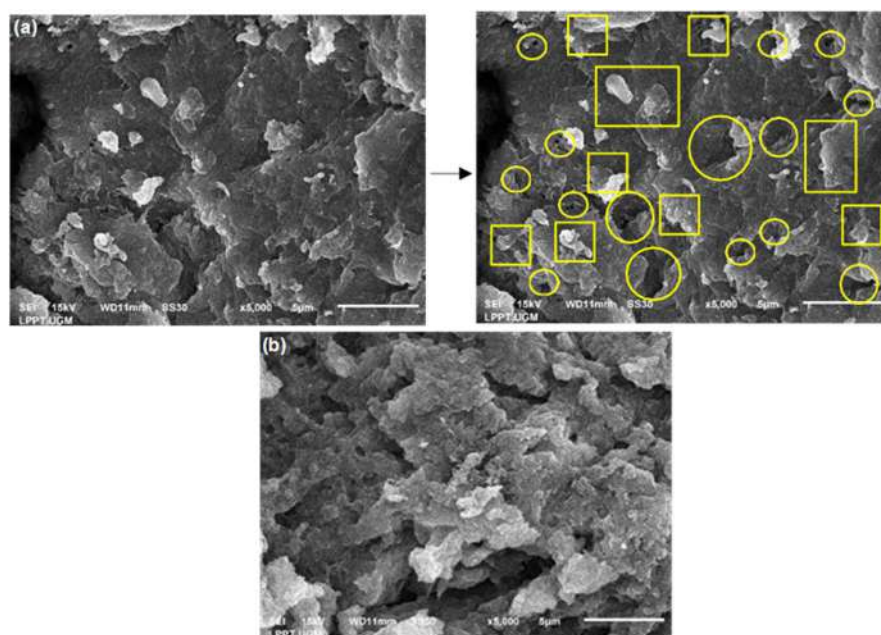


Fig 2. SEM image (a) glutaraldehyde crosslinked alginate-chitosan nanoparticles before adsorption and (b) glutaraldehyde crosslinked alginate-chitosan nanoparticles after adsorption

the nanoparticles before adsorption have a rough, irregular, slightly porous surface, and there are parts that form aggregates. There is a difference between the nanoparticles after and before adsorption in Fig. 2(b); the loss of the porous structure in the SEM image of the nanoparticles after adsorption is possible because the surface of the adsorbent has been covered by paracetamol. The elemental composition data of alginate-chitosan nanoparticles crosslinked with glutaraldehyde before adsorption and after adsorption can be seen in Table 1.

The adsorption process on glutaraldehyde crosslinked alginate-chitosan nanoparticles can be seen from changes in the elemental composition of nanoparticles before and after adsorption. The composition of C and O elements in nanoparticles has increased, as can be seen in Table 1. The C element has a weight and atomic percentage of 37.41 and 43.98%; after adsorption, the percentage of weight and atomic increases to 38.79 and 45.01%. Then, the weight and atomic percentage of O elements were 43.85 and 38.70%, after adsorption increased to 45.92 and 40.00%. Increasing the composition of C and O elements, which are the elemental composition of paracetamol indicates paracetamol was adsorbed on glutaraldehyde crosslinked alginate-chitosan nanoparticles.

TEM Characterization

Nanoparticle characterization using TEM was carried out to determine the inner morphology and average size of the nanoparticles. The results of the characterization of glutaraldehyde crosslinked alginate-chitosan nanoparticles by TEM at a magnification scale of

50 nm are shown in Fig. 3. Based on Fig. 3(a), the TEM image of the nanoparticles has a shape like black spheres but relatively irregular. The graph of the particle size distribution of nanoparticles can be seen in Fig. 3(b). The glutaraldehyde crosslinked alginate-chitosan nanoparticles sample has an average particle size of 8.22 nm. This indicates the ionic gelation method is able to produce smaller particle sizes.

Effect of pH

Based on Fig. 4(a), the adsorption capacity in adsorbing paracetamol has the highest value at pH 4, which is 18.64 mg/g. As the pH of the solution increases, the adsorption capacity value decreases. Fig. 4(b) is a pH point of zero charges (pH_{pzc}) glutaraldehyde crosslinked alginate-chitosan nanoparticle adsorbent. The pH_{pzc} curve shows the intersection at pH 4.773; at that pH, the nanoparticles adsorbent has an uncharged structure. The nanoparticle adsorbent has a positively charged structure when the pH solution is below pH_{pzc} ($pH < 4.773$), while the pH solution is above pH_{pzc} ($pH > 4.773$). Glutaraldehyde crosslinked alginate-chitosan nanoparticles adsorbent has a negatively charged structure.

Based on Fig. 4(a), increasing adsorption capacity occurs at pH 2–4 because the positively charged nanoparticles adsorbent resulted in an electrostatic attraction force with a negative charge on paracetamol. While, decreasing adsorption capacity occurs at pH 5–8 because the nanoparticles adsorbent is negatively charged, and as the pH increases, paracetamol becomes ionized and negatively charged, resulting in a repulsive force between the adsorbent and the adsorbent [25-26].

Table 1. Elemental composition data of glutaraldehyde crosslinked alginate-chitosan nanoparticles before and after adsorption

Element	Weight %		Atom %	
	Before adsorption	After adsorption	Before adsorption	After adsorption
C	37.41	38.79	43.98	45.01
N	15.67	14.92	15.80	14.85
O	43.85	45.92	38.70	40.00
Na	1.58	0.05	0.97	0.03
Cl	0.61	0.10	0.24	0.04
Ca	0.89	0.22	0.31	0.08

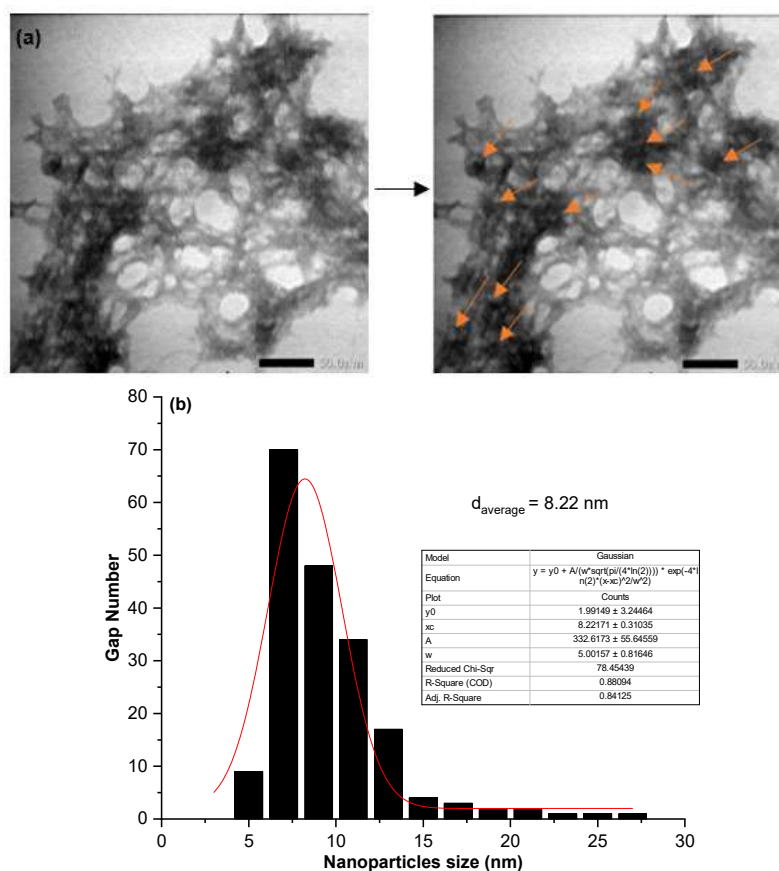


Fig 3. (a) TEM image of glutaraldehyde crosslinked alginate-chitosan nanoparticles, (b) Particle size distribution of glutaraldehyde crosslinked alginate-chitosan nanoparticles

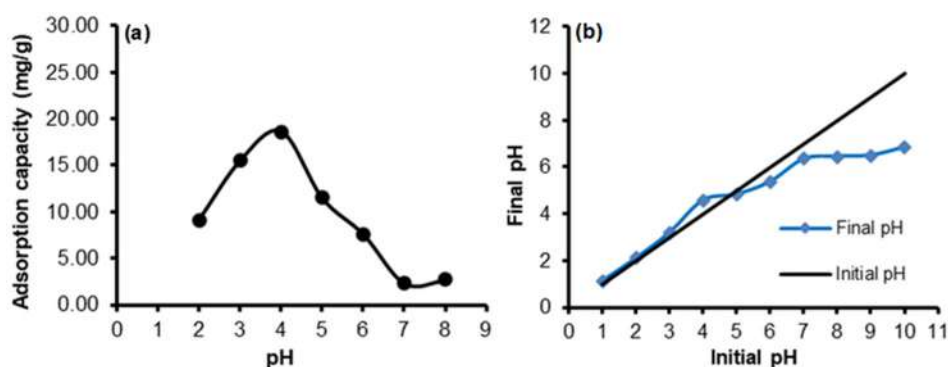


Fig 4. (a) Effect of pH on paracetamol adsorption by glutaraldehyde crosslinked alginate-chitosan nanoparticles adsorbent and (b) pH curve point of zero charge (pH_{pzc}) glutaraldehyde crosslinked alginate-chitosan nanoparticles adsorbent

Effect of Adsorbent Mass

Fig. 5 shows the effect of adsorbent mass on the mass of paracetamol adsorbed by glutaraldehyde crosslinked alginate-chitosan nanoparticles, the optimum point at 30 mg adsorbent mass. The mass of paracetamol obtained

was 0.3501 mg at the optimum mass point of the adsorption process. The mass of paracetamol adsorbed by the nanoparticles will also increase as the adsorbent mass increases. This increase was related to the number of active sites and the surface area of the adsorbent. The

greater the mass of the adsorbent, the greater the surface area, causing more opportunities for contact or interaction between the adsorbent and adsorbate. Based on Fig. 5, decreasing the mass of paracetamol adsorbed by nanoparticles occurs when the adsorbent mass is greater than 30 mg. The equilibrium of the adsorption process occurs when the adsorbed paracetamol has reached the optimum point, so the addition of the amount of adsorbent will disturb the equilibrium [27].

Effect of Contact Time

Fig. 6 shows the equilibrium adsorption of paracetamol by nanoparticles with the largest adsorption capacity of 10.06 mg/g obtained at 45 min. Then, the adsorption capacity of paracetamol decreased after the optimum contact time. This is because after reaching an equilibrium state, the adsorbent becomes saturated so that the active site is no longer able to interact with the adsorbate. In this research, the study of adsorption on the effect of contact time was used to determine the kinetic model of paracetamol adsorption by glutaraldehyde crosslinked alginate-chitosan nanoparticles. The adsorption kinetics models used are pseudo-first-order kinetic models and pseudo-second-order kinetic models. The pseudo-first-order kinetic model is expressed by Eq. (1);

$$\ln(q_e - q_t) = \ln q_e - k_1 t \quad (1)$$

where q_e (mg g^{-1}) is the adsorption capacity at equilibrium, q_t (mg g^{-1}) is the adsorption capacity at time t (min), k_1 (min^{-1}) is the pseudo-first-order rate constant.

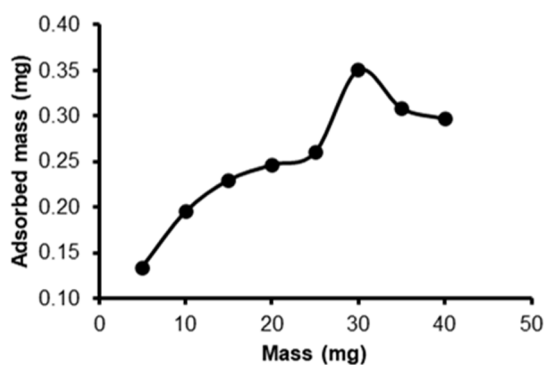


Fig 5. Effect of adsorbent mass on the mass of paracetamol adsorbed by glutaraldehyde crosslinked alginate-chitosan nanoparticles

The graph of the sum of $\ln(q_e - q_t)$ against time can determine the value of q_e from the intercept and k_1 from the slope [27]. The pseudo-second-order kinetic model is expressed by Eq. (2).

$$\frac{t}{q_t} = \left(\frac{1}{k_2 q_e^2} \right) + \frac{1}{q_e} t \quad (2)$$

In Eq. (2), q_e (mg g^{-1}) is the adsorption capacity at equilibrium, q_t (mg g^{-1}) is the adsorption capacity at a certain t (min), k_2 ($\text{g mg}^{-1} \text{min}^{-1}$) is the pseudo-second-order adsorption rate constant. A linear graph of $\frac{t}{q_t}$ against time can determine the value of q_e from the slope and k_2 from the intercept [28].

The linear graphs of the two adsorption kinetics models used are shown in Fig. 7, and the adsorption kinetics parameter values of the two adsorption kinetics models are presented in Table 2. The kinetic model has a linearity value (R^2) close to 1, is the pseudo-second-order kinetics model or the Ho-McKay model, which is equal to 0.9993 and the line equation obtained is $y = 0.097x + 0.2908$ in Fig. 7. The linearity value indicates the adsorption of paracetamol by nanoparticles following the pseudo-second-order kinetic model. In Table 2, the pseudo-second-order kinetic model obtained the value of the adsorption rate constant (k) of $0.0324 \text{ g mg}^{-1} \text{min}^{-1}$ and adsorption capacity value (q_e) of $10.3093 \text{ mg g}^{-1}$. The pseudo-second-order kinetic model assumes the chemisorption process occurs at the determination of the adsorption rate [29]. The adsorption rate is not influenced by the adsorbate

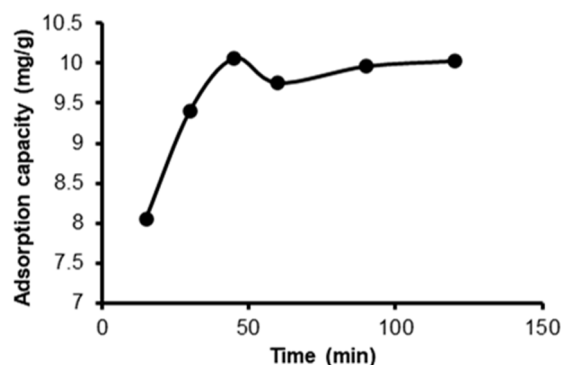


Fig 6. Effect of contact time on paracetamol adsorption by glutaraldehyde crosslinked alginate-chitosan nanoparticle

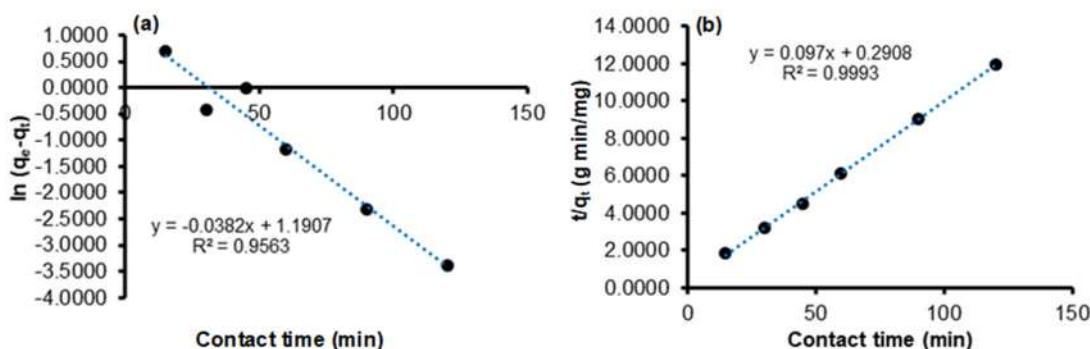


Fig 7. Plot of adsorption kinetics model (a) pseudo-first-order and (b) pseudo-second-order models on the adsorption process of paracetamol by glutaraldehyde crosslinked alginate-chitosan nanoparticles

Table 2. The parameter calculation result of pseudo-first-order and pseudo-second-order models

Model	Parameter	Score
Pseudo-first-order or Lagergren model	R^2	0.9563
	k (min^{-1})	0.0382
	q_e (mg/g)	3.2894
Pseudo-second-order or Ho-McKay model	R^2	0.9993
	k ($\text{g mg}^{-1} \text{min}^{-1}$)	0.0324
	q_e (mg/g)	10.3093

concentration but is influenced by the adsorption capacity at these conditions [30].

Effect of Initial Concentration

Fig. 8 shows the equilibrium condition for paracetamol adsorption by glutaraldehyde crosslinked alginate-chitosan nanoparticles was reached at an initial paracetamol concentration of 16 ppm, and the largest adsorption capacity was 14.3396 mg/g. The adsorption capacity of paracetamol decreased after the optimum condition was reached. The number of adsorbate active sites in the solution is greater due to the greater initial concentration of paracetamol. Meanwhile, the constant mass of the adsorbent causes the number of active sites available on the adsorbent to also remain constant, so when passing through the optimum conditions with a larger initial paracetamol concentration, the amount of adsorbate in solution with the number of particles and the available active sites of the adsorbent becomes unbalanced.

The adsorption capacity obtained will decrease because saturation conditions have been reached [31]. The study of the effect of the initial concentration of

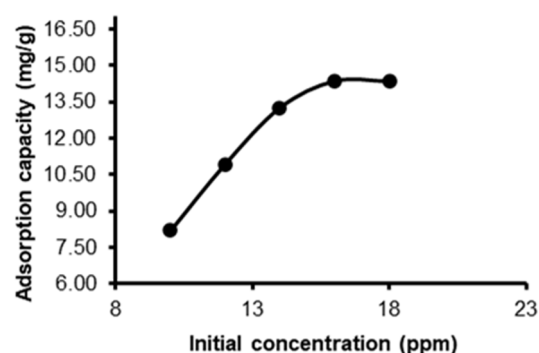


Fig 8. Effect of initial concentration on paracetamol adsorption by glutaraldehyde crosslinked alginate-chitosan nanoparticles

paracetamol will be able to also determine the adsorption isotherm of paracetamol by nanoparticles. The adsorption isotherm in this study was studied using four adsorption isotherm models: Langmuir, Freundlich, Temkin, and Dubinin-Radushkevich isotherm models. The Langmuir isotherm model can be expressed in Eq. (3);

$$\frac{C_e}{q_e} = \frac{1}{k_L q_m} + \frac{C_e}{q_m} \quad (3)$$

where q_m (mg g^{-1}) is the maximum monolayer adsorption capacity, k_L (L mol^{-1}) is the maximum monolayer adsorption capacity, q_e (mg g^{-1}) is the adsorption capacity at equilibrium, and C_e (mol L^{-1}) is the adsorbate concentration at equilibrium. A linear graph between $\frac{C_e}{q_e}$ against C_e can determine the value of q_m from the slope and the value of k_L from the intercept [32]. The Freundlich isotherm model can be expressed in Eq. (4);

$$\log q_e = \log k_F + \frac{1}{n} \log C_e \quad (4)$$

where k_F ($L \text{ mol}^{-1}$) is the Freundlich constant, $\frac{1}{n}$ is the adsorption intensity, q_e (mg g^{-1}) is the adsorption capacity at equilibrium, and C_e (mol L^{-1}) is the adsorbate concentration at equilibrium. $\frac{1}{n}$ value of the slope and k_F value of the intercept can be determined by making a linear graph of $\log q_e$ against $\log C_e$. The Temkin isotherm model can be expressed in Eq. (5);

$$q_e = \frac{RT}{b} \ln(k_T) + \frac{RT}{b} \ln(C_e) \quad (5)$$

where k_T ($L \text{ mol}^{-1}$) is the equilibrium binding constant, b is the heat of adsorption, R is the gas constant ($8.314 \text{ J K}^{-1} \text{ mol}^{-1}$), T (K) is the temperature, q_e (mg g^{-1}) is the adsorption capacity at equilibrium, and C_e (mol L^{-1}) is the adsorbate concentration at equilibrium. A linear graph between q_e and $\ln(C_e)$ will give a straight line with $\frac{RT}{b}$ as the slope and $\frac{RT \ln(k_T)}{b}$ as the intercept [32]. The Dubinin Radushkevich (D-R) isotherm model can be expressed in Eq. (6);

$$\ln q_e = \ln q_m - \beta \varepsilon^2 \quad (6)$$

where q_e (mg g^{-1}) is the adsorption capacity at equilibrium, q_m (mg g^{-1}) is the theoretical isotherm saturation capacity, β ($\text{mol}^2 \text{ J}^{-2}$) is the adsorption energy constant, and ε (J mol^{-1}) is the Polanyi potential. Polanyi potential can be calculated in Eq. (7);

$$\varepsilon = RT \ln \left(1 + \frac{1}{C_e} \right) \quad (7)$$

where T (K) is the temperature, R is the gas constant ($8.314 \text{ J K}^{-1} \text{ mol}^{-1}$), and C_e (mg L^{-1}) is the concentration of adsorbate solution in the adsorbent at equilibrium. A linear graph between $\ln q_e$ and ε^2 can determine the β value from the slope and the q_e value from the intercept. The β value will give the average adsorption free energy (E , kJ mol^{-1}) per adsorbate molecule at the time of its transfer to the surface of the solid from the solution, following Eq. (8) [32].

$$E = \frac{1}{(2\beta)^{1/2}} \quad (8)$$

The linear graph of the adsorption isotherm model is shown in Fig. 9, and Table 3 is a summary of the parameter calculation results for each paracetamol adsorption isotherm model by nanoparticles. Fig. 9 shows the plot of the adsorption isotherm model. Fig. 9(d) is the

Dubinin-Radushkevich isotherm model having a linearity value (R^2) closest to 1, equal to 0.9819 and the equation of the line is $y = -1 \times 10^{-6}x + 2.8629$. Based on this, the adsorption of paracetamol by nanoparticles follows the Dubinin-Radushkevich isotherm model. In Table 3, the Dubinin-Radushkevich isotherm model has a value of q_e of $17.5122 \text{ mg g}^{-1}$. The value of adsorption energy (E) is $707.1068 \text{ kJ mol}^{-1}$.

Based on the adsorption energy (E) value obtained of $707.1068 \text{ kJ mol}^{-1}$, it shows the adsorption of paracetamol by glutaraldehyde crosslinked alginate-chitosan nanoparticles occurs through a chemical adsorption process. This is because the E value obtained has a value greater than 16 kJ mol^{-1} . This is in accordance with the statement on the Dubinin-Radushkevich isotherm model that the type of adsorption on the experimental results is chemical adsorption if the E value has a value greater than 16 kJ mol^{-1} [33].

Possible interactions between paracetamol and glutaraldehyde crosslinked alginate-chitosan nanoparticles include hydrogen bonds between N atoms on the adsorbent and H atoms on paracetamol, H atoms on the adsorbent and O atoms on paracetamol, and $n-\pi$ bonds between the adsorbent and adsorbate (Fig. 10).

Table 3. Parameter calculation results for paracetamol adsorption isotherm models by glutaraldehyde crosslinked alginate-chitosan nanoparticles

Model and parameter	Score
Langmuir isotherm	
R^2	0.7954
k_L ($L \text{ mol}^{-1}$)	0.1680
q_m (mg g^{-1})	31.1526
Freundlich isotherm	
R^2	0.9047
k_F ($L \text{ mol}^{-1}$)	4.9477
N	1.5038
Temkin isotherm	
R^2	0.9229
k_T ($L \text{ mol}^{-1}$)	4.5563
B	19964.3191
Dubinin-Radushkevich (D-R) isotherm	
R^2	0.9819
q_e (mg g^{-1})	17.5122
E (kJ mol^{-1})	707.1068

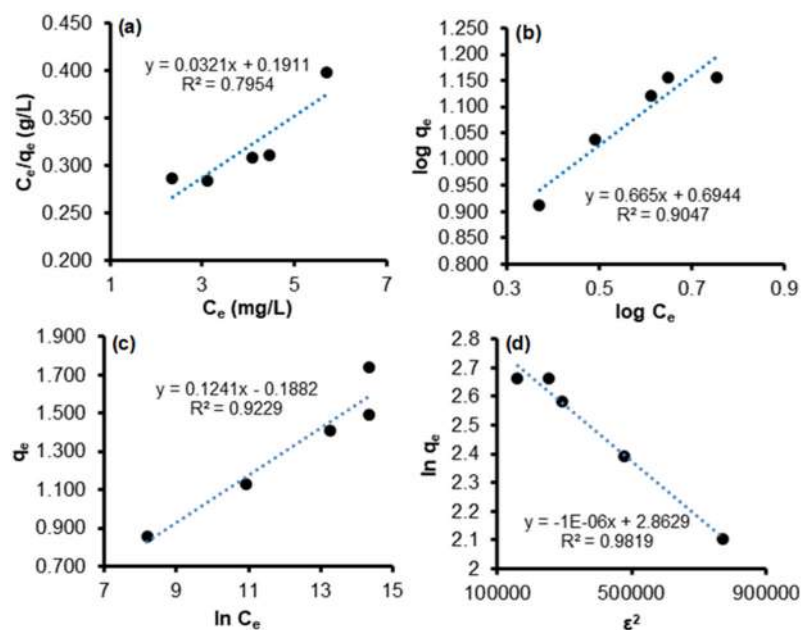


Fig 9. Plot of adsorption isotherm models: (a) Langmuir isotherm, (b) Freundlich isotherm, (c) Temkin isotherm, and (d) Dubinin-Radushkevich isotherm on paracetamol adsorption process by glutaraldehyde crosslinked alginate-chitosan nanoparticles

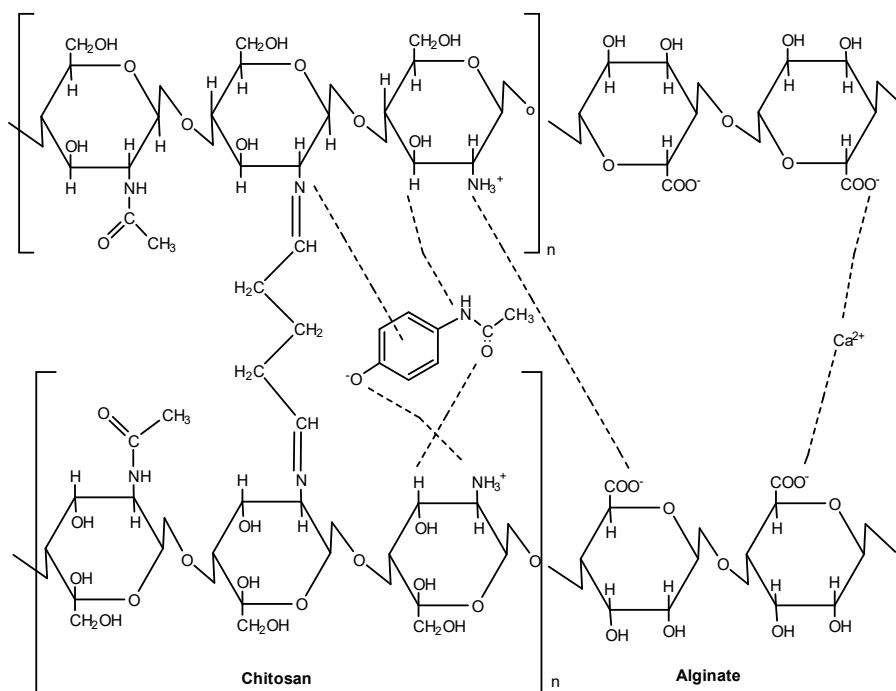


Fig 10. Possible interactions between paracetamol and glutaraldehyde crosslinked alginate-chitosan nanoparticles

■ CONCLUSION

Glutaraldehyde crosslinked alginate-chitosan nanoparticles were successfully synthesized using the ionic gelation method. The nanoparticles have an average

particle size of 8.22 nm. Optimum conditions for paracetamol adsorption by nanoparticles were obtained at pH 4, adsorbent mass of 0.030 g, adsorption contact time of 45 min and initial concentration of paracetamol

at 16 ppm with optimum adsorption capacity of 14.3396 mg/g. The adsorption kinetics model used for paracetamol adsorption by nanoparticles follows the pseudo-second-order kinetic model or the Ho-McKay model, with an adsorption rate constant value of $0.0324 \text{ g mg}^{-1} \text{ min}^{-1}$, and the adsorption process occurs follows the Dubinin-Radushkevich isotherm model with an adsorption free energy value of $707.1068 \text{ kJ mol}^{-1}$, this value indicates the adsorption process occurs chemically or chemisorption.

■ AUTHOR CONTRIBUTIONS

Nurmala served as researcher, data collector, writer, conducting revisions. Adhitasari Suratman as correspondent writer, research supervisor, checks revision results, provides suggestions for improvements, final assessment of the data and written reports and Suherman served as research supervisor, checks revision results, and provides suggestions for improvements to data and written reports.

■ REFERENCES

- [1] Vinayagam, V., Murugan, S., Kumaresan, R., Narayanan, M., Sillanpää, M., Viet N Vo, D., Kushwaha, O.S., Jenis, P., Potdar, P., and Gadiya, S., 2022, Sustainable adsorbents for the removal of pharmaceuticals from wastewater: A review, *Chemosphere*, 300, 134597.
- [2] Dhiman, N., and Sharma, N., 2019, Removal of pharmaceutical drugs from binary mixtures by use of ZnO nanoparticles: (Competitive adsorption of drugs), *Environ. Technol. Innovation*, 15, 100392.
- [3] Bernal, V., Giraldo, L., and Moreno-Piraján, J.C., 2021, Understanding the solid- liquid equilibria between paracetamol and activated carbon: Thermodynamic approach of the interactions adsorbent-adsorbate using equilibrium, kinetic and calorimetry data, *J. Hazard. Mater.*, 419, 126432.
- [4] Amouzgar, P., Vakili, M., Chan, E.S., and Salamatinia, B., 2017, Effects of beading parameters for development of chitosan-nano-activated carbon biocomposite for acetaminophen elimination from aqueous sources, *Environ. Eng. Sci.*, 34 (11), 805–815.
- [5] Koagouw, W., Arifin, Z., Olivier, G.W.J., and Ciocan, C., 2021, High concentrations of paracetamol in effluent dominated waters of Jakarta Bay, Indonesia, *Mar. Pollut. Bull.*, 169, 112558.
- [6] Mashayekh-Salehi, A., and Moussavi, G., 2015, Removal of acetaminophen from the contaminated water using adsorption onto carbon activated with NH_4Cl , *Desalin. Water Treat.*, 57 (27), 12861–12873.
- [7] Igwegbe, C.A., Aniagor, C.O., Oba, S.N., Yap, P.S., Iwuchukwu, F.U., Liu, T., de Souza, E.C., and Ighalo, J.O., 2021, Environmental protection by the adsorptive elimination of acetaminophen from water: A comprehensive review, *J. Ind. Eng. Chem.*, 104, 117–135.
- [8] Shokry, A., El Tahan, A., Ibrahim, H., Soliman, M., and Ebrahim, S., 2019, Polyaniline/akaganéite superparamagnetic nanocomposite for cadmium uptake from polluted water, *Desalin. Water Treat.*, 171, 205–215.
- [9] Liakos, E.V., Lazaridou, M., Michailidou, G., Koumentakou, I., Lambropoulou, D.A., Bikiaris, D.N., and Kyzas, G.Z., 2021, Chitosan adsorbent derivatives for pharmaceuticals removal from effluents: A review, *Macromol*, 1 (2), 130–154.
- [10] Zekić, E., Vuković, Ž., and Halkijević, I., 2018, Application of nanotechnology in wastewater treatment, *Grđevinar*, 70 (4), 315–323.
- [11] Niculescu, A.G., and Grumezescu, A.M., 2022, Applications of chitosan-alginate-based nanoparticles—An up-to-date review, *Nanomaterials*, 12 (2), 186.
- [12] Ferrah, N., Merghache, D., Meftah, S., and Benbellil, S., 2022, A new alternative of a green polymeric matrix chitosan/alginate-polyethylenimine-thylene phosphonic acid for pharmaceutical residues adsorption, *Environ. Sci. Pollut. Res.*, 29 (9), 13675–13687.
- [13] Zhou, Z., Lin, S., Yue, T., and Lee, T.C., 2014, Adsorption of food dyes from aqueous solution by glutaraldehyde cross-linked magnetic chitosan nanoparticles, *J. Food Eng.*, 126, 133–141.
- [14] Kyzas, G.Z., Kostoglou, M., Lazaridis, N.K.,

- Lambropoulou, D.A., and Bikiaris, D.N., 2013, Environmental friendly technology for the removal of pharmaceutical contaminants from wastewaters using modified chitosan adsorbents, *Chem. Eng. J.*, 222, 248–258.
- [15] Al-Ogaidi, I., 2018, Evaluation of the antioxidant and anticancer effects of biodegradable/biocompatible chitosan–alginate nanoparticles loaded with vitamin C, *Int. J. Pharm. Res. Allied Sci.*, 7 (3), 189–197.
- [16] Karthikeyan, P., Banu, H.A.T., and Meenakshi, S., 2019, Synthesis and characterization of metal loaded chitosan–alginate biopolymeric hybrid beads for the efficient removal of phosphate and nitrate ions from aqueous solution, *Int. J. Biol. Macromol.*, 130, 407–418.
- [17] Kulig, D., Zimoch-Korzycka, A., Jarmoluk, A., and Marycz, K., 2016, Study on alginate–chitosan complex formed with different polymers ratio, *Polymers*, 8 (5), 167.
- [18] Kunjumon, R., Viswanathan, G., and Baby, S., 2021, Biocompatible madecassoside encapsulated alginate chitosan nanoparticles, their anti- proliferative activity on C6 glioma cells, *Carbohydr. Polym. Technol. Appl.*, 2, 100106.
- [19] Shaheen, T.I., Montaser, A.S., and Li, S., 2019, Effect of cellulose nanocrystals on scaffolds comprising chitosan, alginate and hydroxyapatite for bone tissue engineering, *Int. J. Biol. Macromol.*, 121, 814–821.
- [20] Othayoth, R., Mathi, P., Bheemanapally, K., Kakarla, L., and Botlagunta, M., 2015, Characterization of vitamin–cisplatin-loaded chitosan nanoparticles for chemoprevention and cancer fatigue, *J. Microencapsulation*, 32 (6), 578–588.
- [21] Shamszadeh, S., Akrami, M., and Asgary, S., 2022, Size-dependent bioactivity of electrosprayed core–shell chitosan–alginate particles for protein delivery, *Sci. Rep.*, 12 (1), 20097.
- [22] Galan, J., Trilleras, J., Zapata, P.A., Arana, V.A., and Grande-Tovar, C.D., 2021, Optimization of chitosan glutaraldehyde-crosslinked beads for reactive blue 4 anionic dye removal using a surface response methodology, *Life*, 11 (2), 85.
- [23] Ramli, R.H., Soon, C.F., and Mohd Rus, A.Z., 2016, Synthesis of chitosan/alginate/silver nanoparticles hydrogel scaffold, *MATEC Web Conf.*, 78, 01031.
- [24] Islam, N., Wang, H., Maqbool, F., and Ferro, V., 2019, *In vitro* enzymatic digestibility of glutaraldehyde-crosslinked chitosan nanoparticles in lysozyme solution and their applicability in pulmonary drug delivery, *Molecules*, 24 (7), 1271.
- [25] Liakos, E.V., Lazaridou, M., Michailidou, G., Koumentakou, I., Lambropoulou, D.A., Bikiaris, D.N., and Kyzas, G.Z., 2021, Chitosan adsorbent derivatives for pharmaceuticals removal from effluents: A review, *Macromol*, 1 (2), 130–154.
- [26] Spaltro, A., Pila, M.N., Colasurdo, D.D., Nosedo Grau, E., Román, G., Simonetti, S., and Ruiz, D.L., 2021, Removal of paracetamol from aqueous solution by activated carbon and silica. experimental and computational study, *J. Contam. Hydrol.*, 236, 103739.
- [27] Rahdar, S., Taghavi, M., Khaksefidi, R., and Ahmadi, S., 2019, Adsorption of arsenic(V) from aqueous solution using modified saxaul ash: isotherm and thermodynamic study, *Appl. Water Sci.*, 9 (4), 87.
- [28] Rezaei, H., Haghshenasfard, M., and Moheb, A., 2017, Optimization of dye adsorption using Fe₃O₄ nanoparticles encapsulated with alginate beads by Taguchi method, *Adsorpt. Sci. Technol.*, 35 (1-2), 55–71.
- [29] Chakraborty, R., Asthana, A., Singh, A.K., Jain, B., and Susan, A.B.H., 2022, Adsorption of heavy metal ions by various low-cost adsorbents: A review, *Int. J. Environ. Anal. Chem.*, 102 (2), 342–379.
- [30] Sahoo, T.R., and Prelot, B., 2020, “Adsorption processes for the removal of contaminants from wastewater: The perspective role of nanomaterials and nanotechnology” in *Nanomaterials for the Detection and Removal of Wastewater Pollutants*, Eds. Bonelli, B., Freyria, F.S., Rossetti, I., and Sethi, R., Elsevier, Amsterdam, Netherlands, 161–222.
- [31] Sun, Z., Qu, K., Cheng, Y., You, Y., Huang, Z., Umar, A., Ibrahim, Y.S., Algadi, H., Castañeda, L.,

- Colorado, H.A., and Guo, Z., 2021, Corncob-derived activated carbon for efficient adsorption dye in sewage, *ES Food Agrofor.*, 4, 61–73.
- [32] Piccin, J.S., Dotto, G.L., and Pinto, L.A.A., 2011, Adsorption isotherms and thermochemical data of FD&C red N 40 binding by chitosan, *Braz. J. Chem. Eng.*, 28 (2), 295–304.
- [33] Iryani, A., Ilmi, M.M., and Hartanto, D., 2017, Adsorption study of Congo red dye with ZSM-5 directly synthesized from Bangka kaolin without organic template, *Malays. J. Fundam. Appl. Sci.*, 13 (4), 832–839.

Synthesis and Characterization of a Novel Azo-Dye Schiff Base and Its Metal Ion Complexes Based on 1,2,4-Triazole Derivatives

Nada Ahmed Rasheed Al-qasii¹, Ali Talib Bader^{2*}, and Zaiied Mosaa²

¹Department of Chemistry, College of Science, University of Baghdad, Baghdad 11001, Iraq

²Department of Chemistry, College of Sciences for Woman, University of Babylon, Hilla 51001, Iraq

* **Corresponding author:**

email: wsc.ali.taleb@uobabylon.edu.iq

Received: March 30, 2023

Accepted: May 17, 2023

DOI: 10.22146/ijc.83509

Abstract: The study focused on producing and examining the properties of the 2-(((3-mercapto-5-(4-nitrophenyl)-4H-1,2,4-triazol-4-yl)imino)methyl)-4-(((4-mercaptophenyl) diazenyl)phenol) ligand (L) and its complexes with three transition metal ions, namely Ni(II), Co(II), and Cu(II). The ligand was formed through diazotization and coupling reactions between 4-aminobenzenethiol and a coupling Schiff base derived from 1,2,4-triazole. The characterization of the ligand and its metal ion complexes was carried out using analytical techniques such as FTIR, ¹H- and ¹³C-NMR, UV-visible spectroscopy, and thermal analysis (TGA and DTG). Various physical methods were employed to synthesize and analyze the properties of the three mononuclear Co(II), Ni(II), and Cu(II) complexes with the azo-dye Schiff's base ligand. Based on the microanalysis and spectroscopic results, it was determined that the coordination between the azo Schiff base ligand and the central metal ion occurred through the NOS-donating atoms of the ligand. The analysis of the electronic spectra revealed that the synthesized Co(II) and Ni(II) complexes exhibited an octahedral geometry, while the Cu(II) complex had a distorted octahedral geometry. The implications of the finding regarding the octahedral and distorted-octahedral geometries include expanding the structural diversity in coordination chemistry, providing insights into ligand-metal interactions, and understanding the influence of geometry on properties.

Keywords: azo-dye; Schiff base; metal ion complex; triazol

■ INTRODUCTION

The field of coordination chemistry has captivated the interest of chemists and researchers due to its potential for the development of pharmaco-therapeutic fields [1]. Azo-Schiff bases could be created by combining azo-dyes and Schiff-bases with the azo-methine-C=N linkage [2]. The incorporation of two complex chromophores in one compound has been shown to enhance the biological and physicochemical properties of this versatile family of ligands and related metal complexes. There are many novel synthetic azo dyes, including 1,2,4-triazoles, which are particularly interesting for several reasons. The chemistry of 1,2,4-triazoles is complex and well-known, and they are stable substances [3]. The isolation of a variety of different macro-acyclic ligands has been made easier by the addition of 1,2,4-triazole compounds of

transition metals with intriguing magnetic and electrochemical characteristics [4]. Azo compounds have been widely used for dyeing textile fibers, coloring various materials, and in biological-medical research, among other applications, making them the most commonly used class of dyes for many years [5].

In addition, Schiff bases are one of the most flexible and multidimensional classes of ligands [6]. Heterocyclic azo-dyes have been used as histological stains for anatomical research and as indicators in conventional analytical processes [3]. A -OH group increases the reactivity of Schiff bases substantially, especially when it is in the -ortho position. Bi-, tri-, and tetradentate metal complexes with a number of transition and inner-transition metals. In biological systems, Schiff bases with transport donor atoms of nitrogen, oxygen, or sulfur are

important [7]. Due to their outstanding coordination potential and wide range of pharmacological effects, including antibacterial, antifungal, and anticancer activities, transition metal complexes with a 1,2,4-triazole substituted moiety have attracted a lot of attention [8-9]. We reported herein the syntheses and structural characterization of novel azo containing Schiff bases derivative ligand (2-(((3-mercapto-5-(4-nitrophenyl)-4*H*-1,2,4-triazol-4-yl)imino)methyl)-4-((4-mercaptophenyl)diazanyl)-6-methoxyphenol) (*L*) and its complexes with Co(II), Ni(II), and Cu(II) ions. The synthesized compounds have been characterized by Fourier-transform infrared spectroscopy (FTIR), proton- ($^1\text{H-NMR}$) and carbon-nuclear magnetic resonance ($^{13}\text{C-NMR}$), UV-vis spectroscopy, thermogravimetric analysis (TGA), and differential thermal analysis (DTA).

■ EXPERIMENTAL SECTION

Materials

Chemicals used in the research included *p*-nitrobenzoic acid (Fluka, Germany), sulfuric acid (H_2SO_4), absolute ethanol ($\text{C}_2\text{H}_6\text{O}$), methanol (CH_3OH), and dichloromethane (CH_2Cl_2) from Merck. Sodium bicarbonate (NaHCO_3 , Fluka), anhydrous magnesium sulphate (MgSO_4 , BDH), hydrazine hydrate (N_2H_4 , 80%), and carbon disulphide (CS_2) were obtained from CDH. Potassium hydroxide (KOH), hydrochloric acid (HCl, 35%), and 2-hydroxy benzaldehyde were obtained from Merck. Sodium nitrate (NaNO_3 , Fluka), *p*-aminothiophenol (Merck), cobalt acetate tetrahydrate ($(\text{CH}_3\text{COO})_2\text{Co}\cdot 4\text{H}_2\text{O}$), nickel acetate tetrahydrate ($(\text{Ni}(\text{OCOCH}_3)_2\cdot 4\text{H}_2\text{O})$), and copper acetate dihydrate ($\text{C}_4\text{H}_{10}\text{CuO}_6$) were obtained from BDH.

Instrumentation

The FTIR measurements of the prepared compounds were performed at $4000\text{--}400\text{ cm}^{-1}$ using a KBr disc with an 8400 FTIR Shimadzu spectrophotometer. The UV-vis spectra were measured on a UV-1700 Shimadzu spectrophotometer in the range of 300–800 nm. The thermal analysis of the ligand and complex was conducted by using TGA on DTG-60. The melting point was conducted using Stuart SMP30 (UK). The produced

compounds were measured by NMR at 400 MHz (Germany) at Isfahan University of Technology (IUT, Iran).

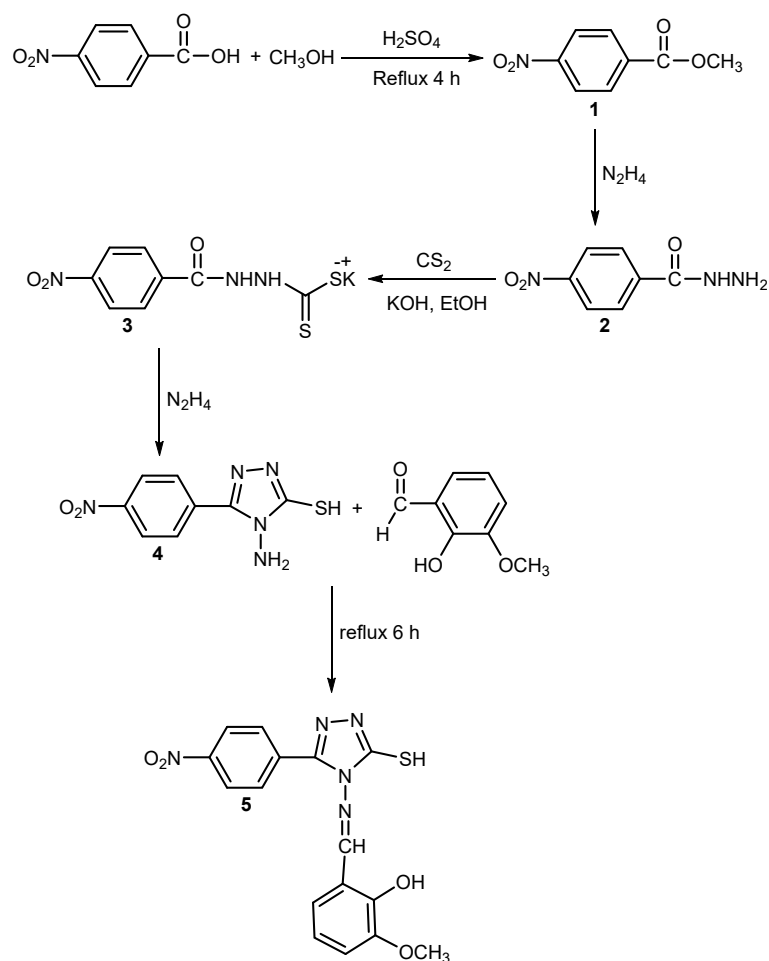
Procedure

Synthesis of methyl 4-nitrobenzoate compound (1)

In a 250 mL round bottom flask, 10 g (0.059 mol) of 4-nitrobenzoic acid was dissolved in 50 mL of methanol and added with 4 mL of concentrated sulfuric acid (Scheme 1). The reaction mixture was heated under a reflux for 6 h. After the reaction was finished, the extra alcohol was evaporated using a rotary evaporator. A separating funnel held 250 mL of water, and the residue was emptied. The separating funnel was filled with dichloromethane (20 mL), and the mixture was agitated briskly. The methyl 4-nitrobenzoate in the dichloromethane separated when the solution was let to stand and collected at the bottom of the separating funnel. The upper aqueous layer was excluded after the lower layer had been thoroughly removed. To eliminate all of the free acid, the methyl 4-nitrobenzoate was put back into the funnel and agitated with a strong sodium bicarbonate solution. In a little dry conical flask with 2 g of anhydrous magnesium sulphate, methyl 4-nitrobenzoate was dried after being rinsed with water once. Five minutes of shaking was followed by 1 h of standing. A small piece of fluted filter paper was used to funnel the methyl 4-nitrobenzoate solution into a distillation flask. The flask was equipped with a condenser, a 360-degree thermometer, and a receiving flask. The methyl 4-nitrobenzoate was extracted from the flask following the distillation of dichloromethane at $40\text{ }^\circ\text{C}$. For the recrystallization of the ester, ethanol was used as a solvent [10].

Synthesis of *p*-nitrobenzohydrazide compound (2)

The synthesized *p*-nitrobenzohydrazide as shown in Scheme 1 was prepared by dissolving methyl 4-nitrobenzoate (6 g, 0.023 mol) in 50 mL of ethanol and then hydrazine hydrate (80%, 22 mL) was added to the solution. The mixture was then heated through reflux for 10 h. Finally, after letting the mixture cool, a solid was extracted and then filtered, washed with ice water, dried, and then re-crystallized with ethanol [11].



Scheme 1. The synthesized scheme for Schiff base 5 in this work

Synthesis of potassium salt of hydrazide compound (3)

Absolute ethanol was used to dissolve KOH (4 g, 0.021 mol) and compound 2 (4 g, 0.021 mol) in 100 mL and the mixture was placed in an ice bath. Carbon disulfide (20 mL) was added dropwise and the reaction mixture was continually stirred for 6 h. Then, anhydrous ether was used to dilute it. After precipitation, the resulting potassium dithiocarbamate was isolated by filtration. The precipitate was washed with 100 mL of anhydrous ether and subsequently vacuum-dried. The obtained potassium salt was in quantitative yield and was not subjected to further purification as it was utilized in the subsequent step [12].

Synthesized of 3-mercapto-4-amino-5-(4'-nitrophenyl)-1,2,4-triazole (4)

A solution containing 3 g (0.01 mol) of compound 3

and excess hydrazine hydrate was refluxed for 30 min in 25 mL of water. As the reaction proceeded, hydrogen sulfide gas evolved, and the mixture turned green. A homogeneous reaction mixture was obtained throughout the process. After diluting the reaction mixture with 150 mL of water, it was cooled to room temperature. Upon acidification with hydrochloric acid, the necessary triazole precipitated out and was washed with cold water, then recrystallized from ethanol [13].

Synthesized of Schiff base of [1,2,4]-triazole-3-thiol derivative (5)

In 50 mL of absolute ethanol, 1.9 g (0.012 mmol) of 2-hydroxy-3-methoxybenzaldehyde was dissolved, and 3 g of (0.012 mol) compound 4 was added. The reaction mixture was refluxed for 6 h. The resulting solid was filtered, washed with cold ethanol, and recrystallized by ethanol [14].

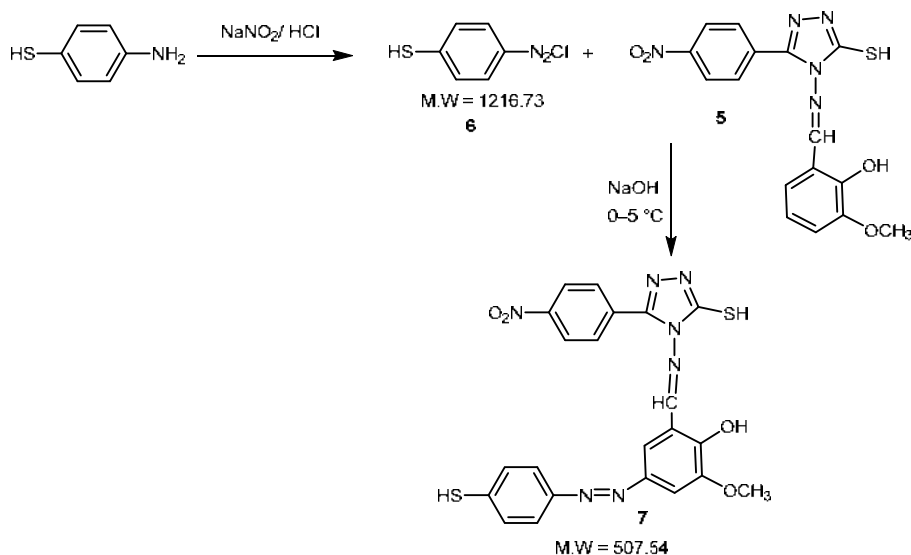
Synthesized azo-dye Schiff base ligand (6)

To a solution of *p*-aminothiophenol (1 g, 0.008 mol) in 10 mL water, concentrated hydrochloric acid (10 mL) was gradually added with stirring (Scheme 2). The clear solution was added to an ice water mixture that had been diazotized for 20 min at 0 to 5 °C with sodium nitrite (0.6 g, 0.008 mol) and 5 mL of water. During 30 min period at a temperature between 0–5 °C, the cold diazo solution was gradually added to a solution of the Schiff base compound (3 g, 0.008 mol) in water (50 mL) containing sodium hydroxide (1 g) and sodium carbonate (10 g). The reaction mixture was shaken for 1 h in an ice

bath, the filtration was collected and recrystallized from ethanol with water [1,15].

Synthesized metal ion complexes (Co₍₁₎ to Co₍₃₎)

Metal ion complexes were synthesized by adding hot ethanolic metal ion solutions M(CH₃COO)₂·nH₂O to a hot ethanolic ligand solution (0.50 g, 0.01 mol/L) at a 1:1 molar ratio of metal:ligand (Scheme 3). After refluxing for 3 h, colored precipitates formed, which were filtered and recrystallized using ethanol. Table 1 shows the metal salt quantities in the resulting complexes [16].



Scheme 2. The synthesized scheme for Schiff base 6

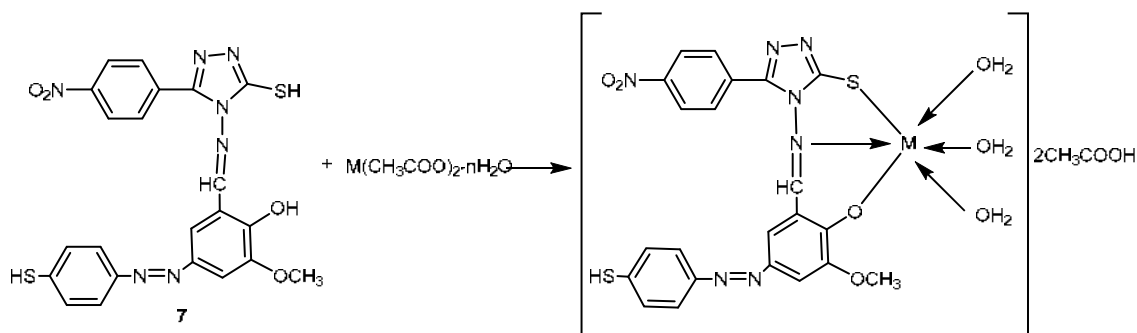


Table 1. Amount of metal salt quantities in the resulting complexes

Symbol compound	Suggested formula	Metal ion salts	Mass (g)
Co ₍₁₎	[Co(L)(H ₂ O) ₃] ₂ CH ₃ COOH	Co(OAc) ₂ ·4H ₂ O	0.245
Co ₍₂₎	[Ni(L)(H ₂ O) ₃] ₂ CH ₃ COOH	Ni(OAc) ₂ ·4H ₂ O	0.245
Co ₍₃₎	[Cu(L)(H ₂ O) ₂] ₂ CH ₃ COOH	Cu(OAc) ₂ ·2H ₂ O	0.196

■ RESULTS AND DISCUSSION

¹H-NMR for Azo-Dye Schiff Base (Ligand 6)

Fig. 1 displays the ¹H-NMR peaks of ligand (azo-dye Schiff base) in DMSO while Table 2 lists the peak assignments. Methyl protons were detected as a singlet peak at δ 3.8 ppm [17]. DMSO peak was found at 2.5 ppm. At 6.69–7.51 ppm, broad multiplets were found and identified as aromatic protons. Signals at 9.10, 10.28, and 3.70 ppm represented the CH=N proton, OH, S–H thiophenol and S–H tetrazole, respectively [18].

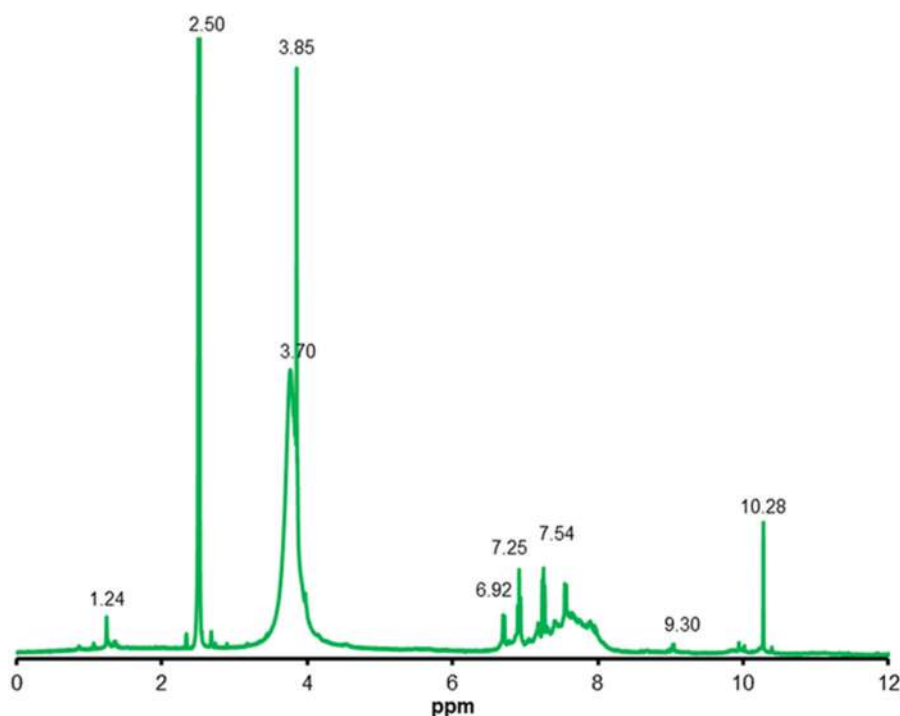


Fig 1. ¹H-NMR spectrum for ligand L

Table 2. ¹H-NMR data for ligand

Compound	Assignment ligand	Chemical shift
Ligand		δ DMSO (2.50 ppm)
		δ -OCH ₃ (3.80 ppm)
		δ aromatic rings (6.69–7.51 ppm)
		δ CH=N (9.10 ppm)
		δ O-H (10.20 ppm)
		δ S-H (3.70 ppm)

¹³C-NMR Data for Ligand 6

The ¹³C-NMR spectrum of azo dye-Schiff base is shown in Fig. 2. The spectral measurements from ¹³C-NMR provided additional support for the synthesized ligand. In accordance with the findings from the chemical shift's spectrum, the L molecular structure can be seen in Table 3 [19].

FTIR Spectra of Ligand

To identify the active group of complexes, the KBr disc was used to compare the IR spectra of ligands with

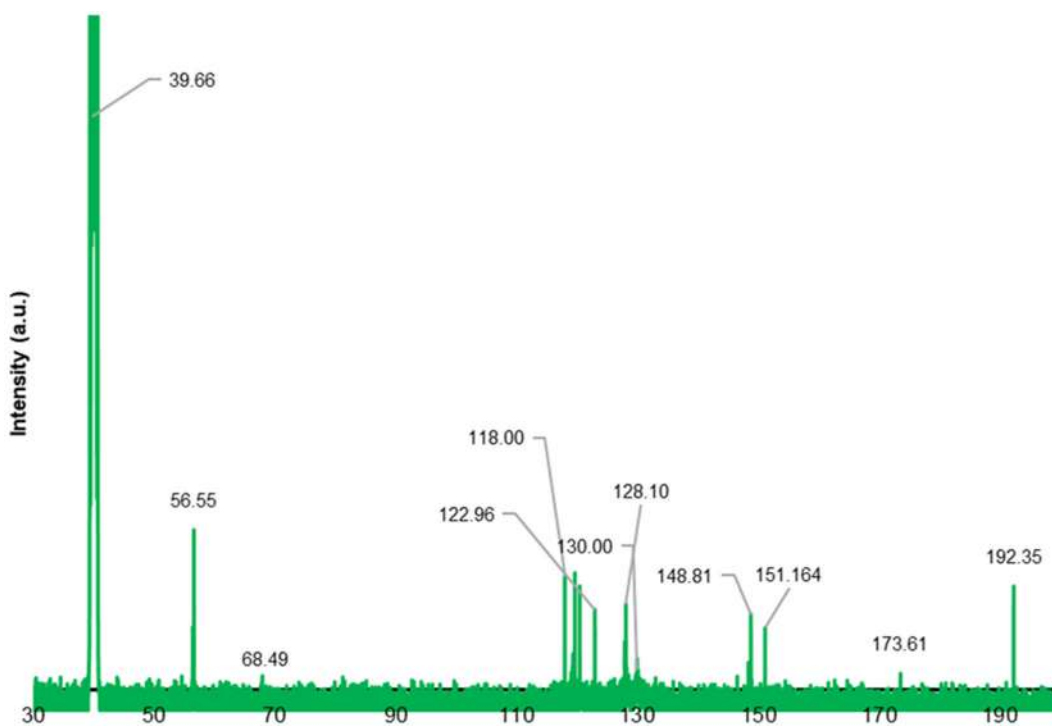


Fig 2. ^{13}C -NMR spectrum for ligand L

Table 3. ^{13}C -NMR data for ligand

Chemical shifts (ppm)	Assignments
118.12	C-aromatic
148.00	C=N=N
151.16	C=N tetrazole
130.00	C-SH thiophenol
173.00	C=N Schiff base
162.00	SH-tetrazole

their complex IR spectra in the range of 4000 to 400 cm^{-1} . This method was also used to identify the inorganic active site of the two ligands that bound to the metal ions at wave numbers between 4000 and 400 cm^{-1} . The FTIR spectra of the essential components used in synthesis must be mentioned before diving into the spectrum of the ligand L.

FTIR of 3-mercapto-4-amino-5-(4'-nitrophenyl)-1,2,4-triazole

The FTIR spectra of this compound are illustrated in Fig. 3 with two bands at 3275 and 3360 cm^{-1} , respectively, corresponding to the two weak bands of stretch asymmetric and symmetric NH_2 group. At 1090

and 2550 cm^{-1} , respectively, two medium-intensity bands are attributed to C=S and S-H vibrations [20].

FTIR spectra of Schiff base 5

Fig. 3 shows the FTIR spectrum of Schiff base compound, the band at 1640 cm^{-1} due to $\nu(\text{C}=\text{N})$, the broad band corresponding to $\nu(\text{O}-\text{H})$ and $\nu(\text{CH}_2)$ appearance at 2940 cm^{-1} [21].

FTIR spectra of azo-dye Schiff base (ligand 6)

The FTIR spectra for the ligand compound are listed in Table 4. Table 4 shows new bands observed and changes in intensity. The new band at 1480 cm^{-1} due to $\nu(\text{N}=\text{N})$, 1643 cm^{-1} corresponding to $\nu(\text{C}=\text{N})$ and $\nu(\text{S}-\text{H})$ at 2550 cm^{-1} . Comparing the spectra of the free ligand L sites involved in chelation with their complexes makes it easy to determine the structure of the complexes. The imine group of the ligand in each complex shifted to a lower wavenumber due to the coordinated interaction between the ligand L imine group (C=N) and the metal via the nitrogen atom. The spectra of the complexes indicated the formation of stable five-membered chelate rings by coordinating

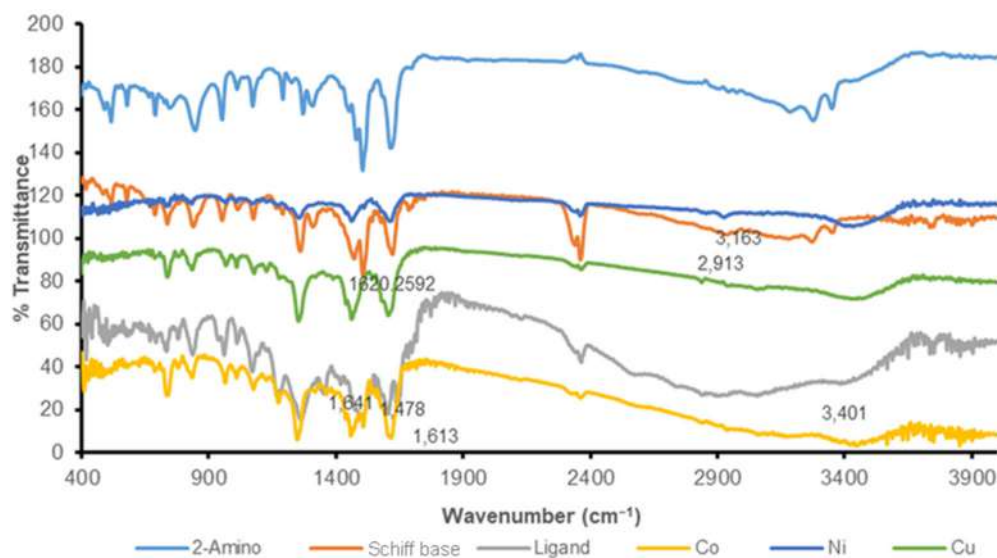


Fig 3. FTIR spectra for ligand and their metal ion complexes

Table 4. List the primary FTIR spectra of the ligand L and their complex

Compound	$\nu(\text{NH}_2)$ (cm^{-1})	$\nu(\text{C}=\text{N})$ cyclic $\nu(\text{C}=\text{N})$ (cm^{-1})	$\nu(\text{OH})$ (cm^{-1})	$\nu(\text{CH}_2)$ (cm^{-1})	$\nu(\text{SH})$ (cm^{-1})
1,2,4-triazole derivative	3275, 3260	1624			2550
Schiff base		1621 1640	3190	2940	2550
Azo-dye Schiff base (L)		1622 1643	3390	2950	2550
[Co(L)] complex		1620	3200		2545
[Ni(L)] complex		1612	3200		2540
[Cu(L)] complex		1612	3250		2543

metal ions with nitrogen atoms from imine groups, oxygen atoms from hydroxy groups, and sulfur atoms from thiol groups. However, they also displayed changes such as the transition to higher frequencies or the appearance of multiple bands with varying shapes and reduced intensities [22].

Electronic Spectra of Ligand and Their Metal Complexes

Two bands at 280 nm ($35,714 \text{ cm}^{-1}$) and 320 nm ($31,250 \text{ cm}^{-1}$) were identified in the UV-vis absorption spectrum of the ligand L in ethanol and were attributed to the $n \rightarrow \pi^*$ and $\pi \rightarrow \pi^*$ transitions shown in Fig. 4 and summarized in Table 5. Two spin-allowed bands in the visible range of the electronic spectrum of L1Co, show that peaks at 420 ($15,337 \text{ cm}^{-1}$) and 595 nm ($23,810 \text{ cm}^{-1}$)

in Fig. 4 may correspond to the transitions ${}^4\text{T}_{1g} \rightarrow {}^4\text{A}_{2g(\text{F})}$ (ν_3) and ${}^4\text{T}_{1g} \rightarrow {}^4\text{T}_{1g(\text{P})}$ (ν_2), respectively. The bands' positions are consistent with those reported for an octahedral geometry. In Fig. 4, three bands at 15337, 21231, and 30769 cm^{-1} , corresponding to the ${}^3\text{A}_{2g} \rightarrow {}^3\text{T}_{2g}$, ${}^3\text{A}_{2g} \rightarrow {}^3\text{T}_{1g(\text{F})}$, and ${}^3\text{A}_{2g} \rightarrow {}^3\text{T}_{1g(\text{P})}$ transitions, are visible in the electronic spectra of the Ni(II) complex. These bands suggest an octahedral geometry surrounding the Ni(II) ion, and the absence of the frequency at 20000 cm^{-1} indicates that the complex was excluded from the square planer. Additionally, a weak band that was observed at 9803 cm^{-1} may also suggest the presence of octahedral geometry in the complex. The spectra should be viewed similarly to how the spectra of the d4 ion and the 2D term of the free ion are predicted to divide in a crystal field. The LCu complex spectrum in DMF exhibits a

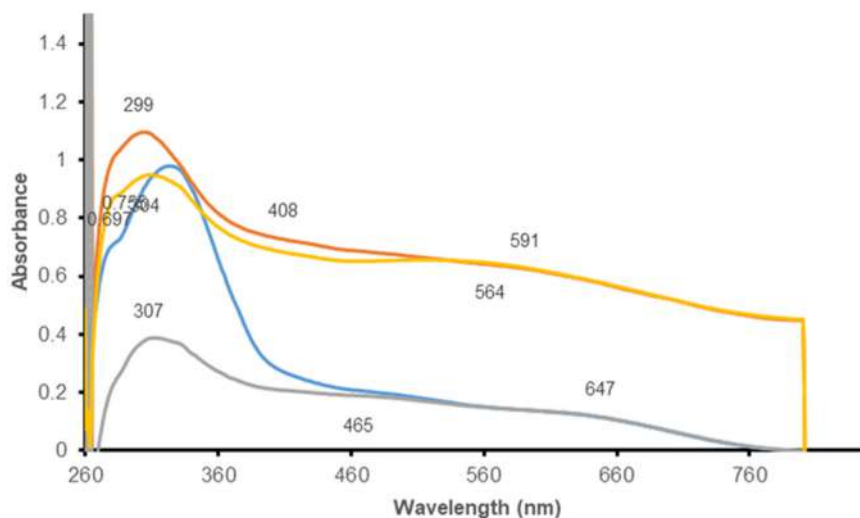


Fig 4. UV-vis spectra for ligand and their metal complex

Table 5. Electronic spectral data for ligand and their metal ion complexes

Compounds	Maximum absorption ν_{\max} (cm^{-1})	Band assignment	Suggested geometry
Ligand	35,714	$n \rightarrow \pi^*$	-
	31,250	$\pi \rightarrow \pi^*$	-
Co(L) complex	15,337	${}^4T_{1g} \rightarrow {}^4A_{2g(F)}$	Octahedral geometry
	23,810	${}^4T_{1g} \rightarrow {}^4T_{1g(P)}$	
Ni(L) complex	15,337	${}^3A_{2g} \rightarrow {}^3T_{2g}$,	Octahedral geometry
	21,231	${}^3A_{2g} \rightarrow {}^3T_{1g(F)}$,	
	30,769	${}^3A_{2g} \rightarrow {}^3T_{1g(P)}$	
Cu(L) complex	18,518	${}^2B_{1g} \rightarrow {}^2A_{1g}$	Distorted octahedral geometry
	30,303	${}^2B_{1g} \rightarrow {}^2B_{2g} + {}^2E_g$	

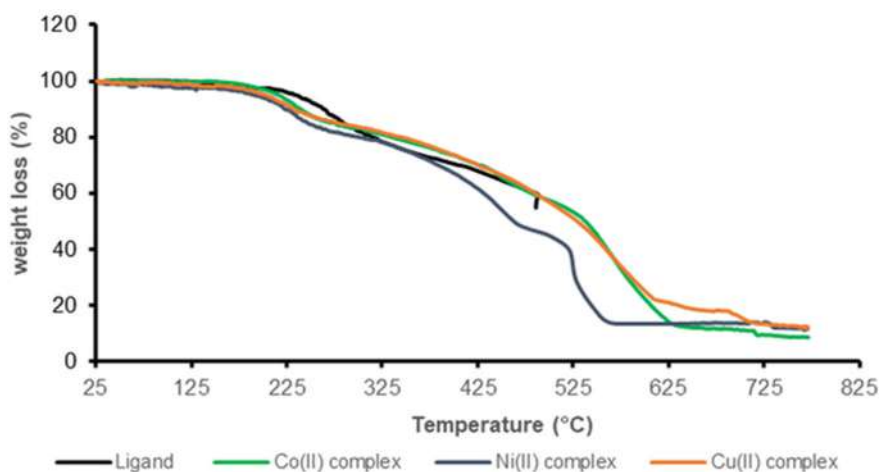


Fig 5. TG curves of the ligand and its metal ion complexes

broad band at (540 nm, $18,518 \text{ cm}^{-1}$), which corresponds to the ${}^2B_{1g} \rightarrow {}^2A_{1g}$ (ν_1) transition and a shoulder band at (330 nm, $30,303 \text{ cm}^{-1}$) that corresponds to the ${}^2B_{1g} \rightarrow {}^2B_{2g}$

+ 2E_g (ν_2) transitions. The position of these bands is consistent with highly distorted octahedral geometry [23-25].

Thermal Analysis

Fig. 5 and 6 show the thermal degradation process, TGA was conducted on both azo-linked Schiff base ligands and their metal complexes over a temperature range of 30–800 °C. Table 6 contains the thermal stability data. The findings from the TG study made it abundantly evident that the complexes decompose in four steps for the complexes of Co(II) and Ni(II), or three steps for the complex of Cu(II). Between 50 and 300 °C, water molecules were lost, and at temperatures above 600 °C,

complexes of the elements Co(II), Ni(II), and Cu(II) formed metal oxides. Meanwhile, 600 °C was the temperature at which all compounds completely decomposed [26-27].

CONCLUSION

The study involved synthesizing a novel azo dye-Schiff base ligand and forming complexes with Co(II), Ni(II), and Cu(II) metals. The structures of these complexes were confirmed through various spectroscopic

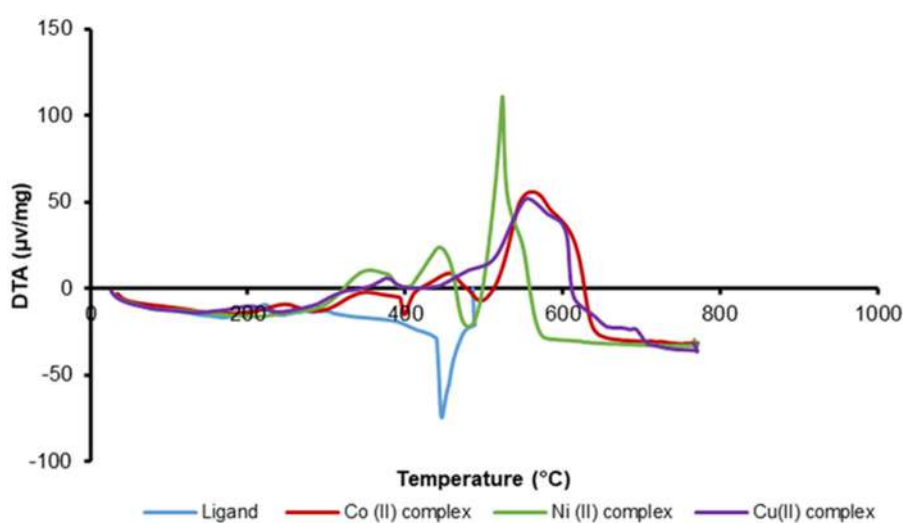


Fig 6. DTA curves of the ligand and its metal ion complexes

Table 6. Thermal decomposition TGA data for azo-dye (ligand) and their metal ion

Compound	Molecular formula	Molecular weight	Step	Temperature range of the decomposition (°C)	Mass (%)
Ligand (L)	$C_{22}H_{17}N_7O_4S_2$	507.54	1	33–409	30.705
			2	409–488	10.069
			3	488–498	5.166
				>500 (Residue)	
[Co(L)]	$[Co(C_{22}H_{17}N_7O_4S_2)(H_2O)_3]_2CH_3COOH$	740.57	1	33–320	17.990
			2	320–506	24.341
			3	506–630	45.000
			4	>630 (Residue)	
[Ni(L)]	$[Ni(C_{22}H_{17}N_7O_4S_2)(H_2O)_3]_2CH_3COOH$	740.57	1	38–306	27.081
			2	306–490	33.616
			3	490–568	32.029
			4	>570 (Residue)	
[Cu(L)]	$[Cu(C_{22}H_{17}N_7O_4S_2)(H_2O)_2]_2CH_3COOH$	727.04	1	33–305	15.875
			2	305–606	61.610
			3	606–766	10.051
			4	>770 (Residue)	

techniques such as FTIR, UV-vis, $^1\text{H-NMR}$, $^{13}\text{C-NMR}$, and TG-DTA. The metal ions in the complexes were bonded to the ligand via the azomethine nitrogen and thiol sulfur groups, forming five-membered chelate rings. The results indicated that the suggested structures of the complexes had an octahedral geometry. Furthermore, the thermal degradation profiles of metal complexes were examined using TG/DTA in an inert atmosphere. The major components of the $\text{Co}_{(1)}$ and $\text{Co}_{(2)}$ complexes were degraded in two phases, while those of the $\text{Co}_{(3)}$ complex were degraded in a single step. These results could be helpful in predicting organisms' biological activities and behavior. The findings provide a promising avenue for the discovery of new compounds with diverse and potentially valuable properties.

■ ACKNOWLEDGMENTS

We sincerely thank the University of Babylon, the College of Science for Women, and the University of Baghdad, Iraq for providing the necessary infrastructural facilities. All of the authors are thankful to their respective institutions for their support.

■ AUTHOR CONTRIBUTIONS

Conceptualization: Nada Ahmed Rasheed Al-qasii, Ali Talib Bader, and Zaid Mosaa. Synthesis and data curation: Nada Ahmed Rasheed Al-qasii and Ali Talib Bader; measurements and assignment data analysis: Zaid Mosaa. The manuscript and the supporting information were written and reviewed with Nada Ahmed Rasheed Al-qasii and Ali Talib Bader. All authors have read and agreed to the published version of the manuscript.

■ REFERENCES

- [1] Íspir, E., 2009, The synthesis, characterization, electrochemical character, catalytic and antimicrobial activity of novel, azo-containing Schiff bases and their metal complexes, *Dyes Pigm.*, 82 (1), 13–19.
- [2] Alghool, S., Abd El-Halim, H.F., and Dahshan, A., 2010, Synthesis, spectroscopic thermal and biological activity studies on azo-containing Schiff base dye and its cobalt(II), chromium(III) and strontium(II) complexes, *J. Mol. Struct.*, 983 (1-3), 32–38.
- [3] Sancak, K., Er, M., Ünver, Y., Yildirim, M., Degirmencioglu, I., and Serbest, K., 2007, Cu(II), Ni(II) and Fe(II) complexes with a new substituted [1,2,4] triazole Schiff base derived from 4-amino-5-(thien-2-yl ethyl)-2,4-dihydro-3H-1,2,4-triazol-3-one and 2-hydroxy-1-naphthaldehyde: Synthesis, characterization and a comparison of theoretical and experimental results by *Ab initio* calculation, *Transition Met. Chem.*, 32 (1), 16–22.
- [4] Klingele, M.H., Noble, A., Boyd, P.D.W., and Brooker, S., 2007, Synthesis and X-ray crystal structures of some mononuclear and dinuclear complexes of 4-isobutyl-3,5-di(2-pyridyl)-4H-1,2,4-triazole, *Polyhedron*, 26 (2), 479–485.
- [5] Gouda, M.A., Eldien, H.F., Girges, M.M., and Berghot, M.A., 2016, Synthesis and antitumor evaluation of thiophene based azo dyes incorporating pyrazolone moiety, *J. Saudi Chem. Soc.*, 20 (2), 151–157.
- [6] Yaman, M., İpek Dirin, E., Kaplan, G., Seferoğlu, N., and Seferoğlu, Z., 2022, The synthesis, photophysical properties, DFT study and textile applications of fluorescent azo dyes bearing coumarin-thiazole, *J. Mol. Liq.*, 368, 120718.
- [7] Kumari, S., Maddipoti, K., Das, B., and Ray, S., 2019, Palladium-Schiff base complexes encapsulated in zeolite-Y host: Functionality controlled by the structure of a guest complex, *Inorg. Chem.*, 58 (2), 1527–1540.
- [8] Diaz-Ortiz, A., Prieto, P., Carrillo, J.R., Martin, R., and Torres, I., 2015, Applications of metal-free 1,2,4-triazole derivatives in materials science, *Curr. Org. Chem.*, 19 (7), 568–584.
- [9] Bazhina, E.S., Bovkunova, A.A., Shmelev, M.A., Korlyukov, A.A., Pavlov, A.A., Hochvaldová, L., Kvítek, L., Panáček, A., Kopel, P., Eremenko, I., and Kiskin, M.A., 2023, Zinc(II) and copper(II) complexes with *N*-substituted imines derived from 4-amino-1,2,4-triazole: Synthesis, crystal structure, and biological activity, *Inorg. Chim. Acta*, 547, 121359.
- [10] Bader, A.T., Al-qasii, N.A.R., Shntaif, A.H., El Marouani, M., Majidi, M.I.H.A., Trif, L., and

- Boulhaoua, M., 2022, Synthesis, structural analysis and thermal behavior of new 1,2,4-triazole derivative and its transition metal complexes, *Indones. J. Chem.*, 22 (1), 223–232.
- [11] Nonkuntod, P., Senawong, T., Soikum, C., Chaveerach, P., Watwiangkham, A., Suthirakun, S., and Chaveerach, U., 2022, Copper(II) compounds of 4-nitrobenzohydrazide with different anions (ClO_4^- , NO_3^- and Br^-): Synthesis, characterization, DFT calculations, DNA interactions and cytotoxic properties, *Chem. Biodiversity*, 19 (3), e202100708.
- [12] Bader, A.T., Rasheed, N.A., Aljeboree, M., and Alkaiml, A.F., 2020, Synthesis, characterization of new 5-(4-nitrophenyl)-4-((4-phenoxybenzylidene)amino)-4H-1,2,4-triazole-3-thiol metal complexes and study of the antibacterial activity, *J. Phys.: Conf. Ser.*, 1664, 012100.
- [13] Beyzaei, H., Ghanbari Kudeyani, M., Samareh Delarami, H., and Aryan, R., 2020, Synthesis, antimicrobial and antioxidant evaluation, and molecular docking study of 4,5-disubstituted 1,2,4-triazole-3-thiones, *J. Mol. Struct.*, 1215, 128273.
- [14] Oderinlo, O.O., Jordaan, A., Seldon, R., Isaacs, M., Hoppe, H.C., Warner, D.F., Tukulula, M., and Khanye, S.D., 2023, Hydrazone-tethered 5-(pyridin-4-yl)-4H-1,2,4-triazole-3-thiol hybrids: Synthesis, characterisation, *in silico* ADME studies, and *in vitro* antimycobacterial evaluation and cytotoxicity, *ChemMedChem*, 18 (6), e202200572.
- [15] Almáši, M., Vilková, M., and Bednarčík, J., 2021, Synthesis, characterization and spectral properties of novel azo-azomethine-tetracarboxylic Schiff base ligand and its Co(II), Ni(II), Cu(II) and Pd(II) complexes, *Inorg. Chim. Acta*, 515, 120064.
- [16] Alothman, A.A., Albaqami, M.D., and Alshgari, R.A., 2021, Synthesis, spectral characterization, quantum chemical calculations, thermal studies and biological screening of nitrogen and oxygen donor atoms containing Azo-dye Cu(II), Ni(II) and Co(II) complexes, *J. Mol. Struct.*, 1223, 128984.
- [17] Piegat, A., Goszczyńska, A., Idzik, T., and Niemczyk, A., 2019, The importance of reaction conditions on the chemical structure of *N,O*-acylated chitosan derivatives, *Molecules*, 24 (17), 3047.
- [18] Hari, S., Swaroop, T.R., Preetham, H.D., Mohan, C.D., Muddegowda, U., Basappa, S., Sethi, G., and Rangappa, K.S., 2020, Synthesis, cytotoxic and heparanase inhibition studies of 5-oxo-1-arylpyrrolidine-3-carboxamides of hydrazides and 4-amino-5-aryl-4H-1,2,4-triazole-3-thiol, *Curr. Org. Synth.*, 17 (3), 243–250.
- [19] Aggarwal, R., Hooda, M., Kumar, P., and Sumran, G., 2022, Vision on synthetic and medicinal facets of 1,2,4-triazolo[3,4-b][1,3,4]thiadiazine scaffold, *Top. Curr. Chem.*, 380 (2), 10.
- [20] Panda, K.C., Ravi Kumar, B.V.V., and Sahoo, B.M., 2022, Microwave induced synthesis of 1,2,4-triazole derivatives and study of their anthelmintic and antimicrobial activities, *Res. J. Pharm. Technol.*, 15 (12), 5746–5750.
- [21] Xie, W., Zhang, H., He, J., Zhang, J., Yu, Q., Luo, C., and Li, S., 2017, Synthesis and biological evaluation of novel hydroxybenzaldehyde-based kojic acid analogues as inhibitors of mushroom tyrosinase, *Bioorg. Med. Chem. Lett.*, 27 (3), 530–532.
- [22] Pavia, D.L., Lampman, G.M., Kriz, G.S., and Vyvyan, J.A., 2014, Introduction to Spectroscopy, 5th Ed., Cengage Learning, Stamford, CT, US.
- [23] de Araújo, E.L., Barbosa, H.F.G., Dockal, E.R., and Cavalheiro, É.T.G., 2017, Synthesis, characterization and biological activity of Cu(II), Ni(II) and Zn(II) complexes of biopolymeric Schiff bases of salicylaldehydes and chitosan, *Int. J. Biol. Macromol.*, 95, 168–176.
- [24] Abdel-Rahman, L.H., Abu-Dief, A.M., Moustafa, H., and Hamdan, S.K., 2017, Ni(II) and Cu(II) complexes with ONNO asymmetric tetradentate Schiff base ligand: Synthesis, spectroscopic characterization, theoretical calculations, DNA interaction and antimicrobial studies, *Appl. Organomet. Chem.*, 31 (2), e3555.
- [25] Retnam, C.T.G., Rose, S.V., and Kumari, B.S., 2023, Synthesis, characterization, biological activity and molecular docking study of transition metal

- complexes from heterocyclic ligand system, *J. Mol. Struct.*, 1282, 135162.
- [26] Al Zoubi, W., Al-Hamdani, A.A.S., and Ko, Y.G., 2017, Schiff bases and their complexes: Recent progress in thermal analysis, *Sep. Sci. Technol.*, 52 (6), 1052–1069.
- [27] Kavitha, N., and Anantha Lakshmi, P.V., 2017, Synthesis, characterization and thermogravimetric analysis of Co(II), Ni(II), Cu(II) and Zn(II) complexes supported by ONNO tetradentate Schiff base ligand derived from hydrazino benzoxazine, *J. Saudi Chem. Soc.*, 21, S457–S466.

Organic Geochemical Characteristics of Ngrayong Formation Polaman Sediment Rock, Northeast Java Basin-Indonesia

Yulfi Zetra^{1*}, Rafwan Year Perry Burhan¹, Sulistiyono Sulistiyono², Arizal Firmansyah³, and Darin Salsabila¹

¹Department of Chemistry, Faculty of Science and Data Analytics, Institut Teknologi Sepuluh Nopember Surabaya, Kampus ITS Keputih, Surabaya 60111, Indonesia

²Polytechnic of Energy and Mineral Akamigas, Jl. Gajah Mada No. 38, Cepu 58315, Indonesia

³Department of Chemistry Education, Faculty of Science and Technology, Universitas Islam Negeri Walisongo Semarang, Kampus 3, Ngaliyan, Semarang 50185, Indonesia

* **Corresponding author:**

email: yzetra@chem.its.ac.id

Received: March 31, 2023

Accepted: October 11, 2023

DOI: 10.22146/ijc.83534

Abstract: A study of the sedimentary rocks of the Ngrayong formation has been carried out on five samples from the Polaman outcrop point to determine the potential of coal as a source rock for producing oil and gas through GC-MS analysis. Biomarker analysis shows the presence of n-alkanes (C₁₆-C₃₆) with a bimodal distribution, indicating that the source of organic material in sedimentary rocks comes from bacteria, algae, and vascular plants, which is supported by several parameters such as CPI, OEP, LHCPI, wax index, ACL and AlkTerr values. This dominant source of terrigenous organic matter is also proven by the TAR value, C₃₁/C₁₉, C₂₉/C₁₇ ratio, and several aromatic compounds and their derivatives. Bacterial input as an organic source of allouctonic sedimentary rocks is also proven by the presence of hopanoid, de-A-lupane biomarkers, and C₁₇/C₃₁ ratio. The oxic deposition environment is indicated by the Pr/Ph ratio. CPI and OEP parameters, C₂₉ bb/ab ratio > 0.15 and C₃₁ 22S/(22S+22R) < 1 indicate low maturity of the sediment sample. Several parameters and the presence of biomarkers stated above conclude that Ngrayong coal as a source rock has the potential to produce oil and gas.

Keywords: aliphatic hydrocarbons; aromatic hydrocarbons; biomarkers; Ngrayong formation; Polaman sediments

■ INTRODUCTION

Oil and gas exploration is inseparable from the petroleum system. This concept is an integration of the source rock, reservoir, migration, trapping model, and the presence of overburden. The research area is centered on the northern part of the East Java Basin. Several types of source rock commonly exist in this basin, including lacustrine (Ngimbang formation), shale (Kujung formation), and coal (Ngrayong formation), which is considered as the secondary source of hydrocarbons. The Middle Miocene-aged Ngrayong formation that was deposited in a tidal area has transgressed into the middle to outer exposure environment. The dominance of lithology was in the form of clean sand, generating a main

reservoir in the Rembang zone, especially the Cepu district. The Ngrayong formation can be represented as an outcrop on the Braholo river and the Polaman outcrop in the previous quartz sandstone mine. The Polaman outcrop occurred in the Middle Miocene, with the clay stone composed at the bottom. This outcrop enables it to turn upwards, becoming an interlude between sandstone and shale. The PLM 1, PLM 2, PLM 3, PLM 4, and PLM 5 samples were taken at five different points from the Polaman outcrop. The shale rock exhibited a dark color and contained organic material. These two lithologies are promising candidates for source rock based on petroleum systems [1-2]. Several researchers have reported organic geochemical characteristics through biomarker analysis to determine

the source of organic compounds, thermal maturity, and depositional environment of a geological sediment sample [3]. The dominance of long-chain *n*-alkanes homologues over short-chain *n*-alkanes confirmed vascular plants as the source of organic compounds. The presence of hopanoid compounds such as 17 α (*H*),21 β (*H*)-hopane, 17 β (*H*),21 α (*H*)-hopane, and 17 α (*H*),21 β (*H*)-30-homohopane with 22*S* and 22*R* configurations assigned the contribution of bacteria during the process of organic compounds formation. Hopanoid compounds were also an indicator of the thermal maturity of a sediment. The dominance of 17 α (*H*),21 β (*H*)-homohopane (22*R*) against 17 α (*H*),21 β (*H*)-homohopane (22*S*) was a sign of low maturity [4-8]. Environmental conditions of sediment deposition can be investigated through the distribution of pristane and phytane compounds [6,9].

The biomarker analysis provided information on the organic geochemical allowing the hydrocarbon potential hydrocarbons in the Polaman sediments of the Ngrayong formation, Northeast Java Basin. This analysis was adopted due to its feasibility and accuracy since the biomarker inferred the characteristics of oil and gas in the

reservoir. In addition, this analysis was mostly applied in the oil and gas exploration field. Biomarkers were extracted using the Soxhlet method and fractionated over TLC SiO₂ GF₂₅₄. Extraction and fractionation results were further identified by gas chromatography-mass spectrometry (GC-MS).

■ EXPERIMENTAL SECTION

Materials

Sediment samples were obtained from five different coordinate points with characteristics as mentioned in Table 1. The five sedimentary rock objects are outcrop pattern sediment samples. The organic solvents used in this study were *n*-hexane and dichloromethane (grade pro analysis, Sigma-Aldrich). Other materials were copper powder and silica gel GF₂₅₄ TLC plate (Sigma-Aldrich).

Instrumentation

Identification of biomarkers in this work used the Agilent D5975C GC-MS with column type of HP-5MS (60 μ m \times 250 μ m \times 0.33 μ m).

Table 1. Characteristics of PLM sediment samples PLM 1-PLM 5

Sample number	Coordinate		Rock description
	Latitude	Longitude	
PLM 1	6°54'11.02"S	111°26'30.17"E	Type: Shale stone Color: Brownish gray Grain size: Very fine sand Evolved sedimentary structure: Flake General composition: Silica cement Presence of mature organic/fossil: Few fossils form
PLM 2	6°54'11.11"S	111°26'30.14"E	Type: Shale stone Color: Light gray Grain size: Very fine sand Developed sedimentary structure: Slightly laminated General composition: Silica cement Organic/fossil maturity state: Organic maturity present
PLM 3	6°54'11.20"S	111°26'30.13"E	Type: Clay Color: Light gray Granule Size: Clay Evolved sedimentary structure: Conchoidal General composition: Silica cement Organic/fossil maturity state: Slightly organic maturity

Sample number	Coordinate		Rock description
	Latitude	Longitude	
PLM 4	6°54'11.28"S	111°26'30.11"E	Type: Shale Color: Gray Grain size: Very fine sand Evolved sedimentary structure: Laminate General composition: Silica cement Organic/fossil maturity state: Carbon strike
PLM 5	6°54'11.36"S	111°26'30.09"E	Type: Shale Color: Blackish gray Grain size: Very fine sand Evolved sedimentary structure: Flake General composition: Silica cement Organic/fossil maturity state: Carbon strike

Procedure

About 100 mg of Polaman sediment was extracted in dichloromethane to obtain a total organic extract. The organic extract was fractionated by the thin layer chromatography (TLC) method with *n*-hexane as eluent to separate aliphatic, aromatic, and polar hydrocarbon fractions. The aromatic hydrocarbon fraction was then desulfurized using copper (Cu) powder. The aliphatic and aromatic fractions were further analyzed using GC-MS. Each Polaman sediment sample was dissolved in *n*-hexane and injected into GC-MS afterward [8].

Helium as carrier gas, flowed at the rate of 1 mL/min. The oven temperature was programmed with an initial temperature at 70 °C held for 3 min, ramped at 10 °C/min to 160 °C, and a final ramp of 3 °C/min to 320 °C maintained for 27.5 min. The sample was injected with a split ratio of 50:1, and analysis was conducted with a solvent delay of 4 min. The mass spectrometer is operated with an electron energy of 70 eV. The data obtained were further analyzed with Enhanced Chemstation software. The compounds were identified based on the specific *m/z* fragmentogram, retention time pattern, and mass spectrum fragmentation. The identification results were compared to previous studies [4,10-13].

RESULTS AND DISCUSSION

Aliphatic Hydrocarbon Fraction

The result of biomarker aliphatic hydrocarbon fraction identification of sediment samples using GC-MS

is depicted in Fig. 1. It was observed that all samples contained *n*-alkanes, isoprenoids, and triterpenoids. The *n*-alkanes were found in PLM 1-5, while isoprenoids only existed in samples PLM 2 and PLM 3.

n-Alkanes and isoprenoids

The *n*-alkanes and op were identified based on the specific fragmentogram *m/z* 57 that showed the presence of short-chain (*n*-C₁₆-*n*-C₂₀), medium (*n*-C₂₁-*n*-C₂₅), and long-chain (*n*-C₂₆-*n*-C₃₇) of alkanes over bimodal distribution (Fig. 2). The length of the alkane chain assigned the organic matter source, where the short chain represented bacteria (i.e. cyanobacteria) and algae. The medium chain confirmed the contribution of bacteria, algae, and machropyte, including the submerged and floating ones. In addition, the vascular plant as the source of organic matter was affirmed by the long-chain alkane [14-20].

All samples exhibited a wide range of alkanes, with the highest and the lowest abundance being *n*-C₂₇ and *n*-C₁₆, respectively. This result concludes that the organic matter source originated from bacteria, algae, and vascular plants, as found in sediments in Teluk Bunai, eastern Malaysia [20]. In terms of isoprenoid, pristane was observed in PLM 2, and phytane was found in PLM 2 as well as PLM 3. The abundance of alkane and isoprenoid is illustrated in Table 2. This table explains several parameters, i.e., carbon preference index (CPI), odd/even predominance (OEP), low-to-high chain carbon preference index (LHCPI), Pr/Ph, Pr/*n*-C₁₇, Ph/*n*-C₁₈,

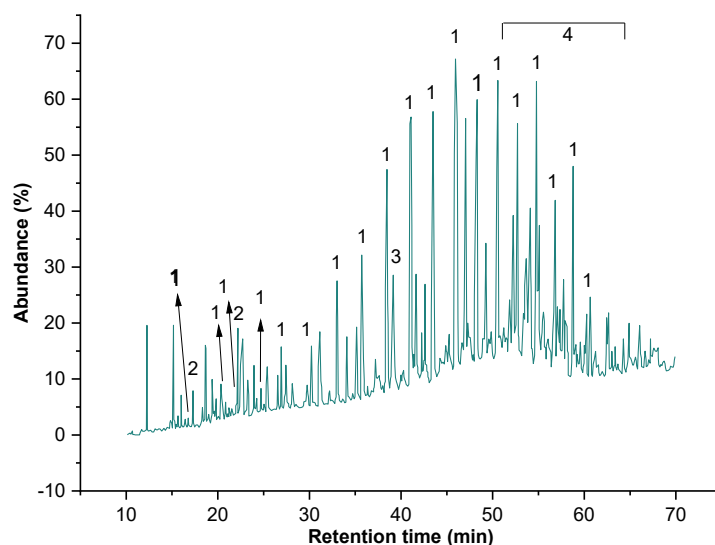


Fig 1. Total ion chromatogram of aliphatic hydrocarbon fraction of PLM sediment samples 1-5. (1) *n*-alkane, (2) isoprenoids, (3) sesterterpenoids, and (4) pentacyclic triterpenoids

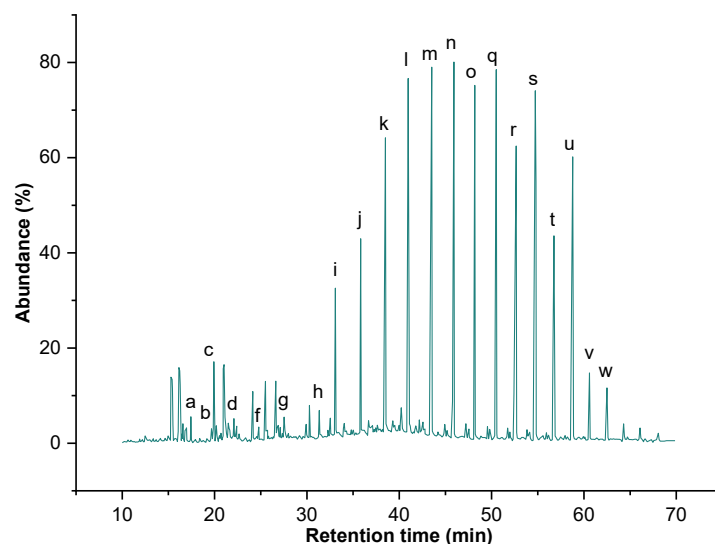


Fig 2. Fragmentogram of *n*-alkane and isoprenoid compounds on m/z 57 sediment samples PLM 1-5

Table 2. The abundance of aliphatic hydrocarbon fractions in PLM sediment samples 1-5

Peak	Compound	Molecular formula	Base peak (m/z)	M^+ (m/z)	Composition (%)				
					PLM-1	PLM-2	PLM-3	PLM-4	PLM-5
<i>n</i> -alkanes, and isoprenoids									
a	<i>n</i> -C ₁₆	C ₁₆ H ₃₄	57	226	0.21	0.10	-	-	-
b	<i>n</i> -C ₁₇	C ₁₇ H ₃₆	57	240	0.30	0.29	0.41	-	-
c	pristane	C ₁₉ H ₄₀	57	268	-	0.21	0.58	-	-
d	<i>n</i> -C ₁₈	C ₁₈ H ₃₈	57	254	0.42	0.46	0.54	-	-
e	phytane	C ₂₀ H ₄₂	57	282	-	0.17	-	-	-
f	<i>n</i> -C ₁₉	C ₁₉ H ₄₀	57	268	0.27	0.51	0.46	0.14	0.20
g	<i>n</i> -C ₂₀	C ₂₀ H ₄₂	57	282	0.59	1.20	0.87	0.30	0.34

Peak	Compound	Molecular formula	Base peak (m/z)	M ⁺ (m/z)	Composition (%)				
					PLM-1	PLM-2	PLM-3	PLM-4	PLM-5
h	<i>n</i> -C ₂₁	C ₂₁ H ₄₄	57	296	0.62	1.44	0.93	0.59	0.66
i	<i>n</i> -C ₂₂	C ₂₂ H ₄₆	57	310	3.34	3.54	3.73	2.42	2.56
j	<i>n</i> -C ₂₃	C ₂₃ H ₄₈	57	324	4.77	4.72	4.17	3.59	3.39
k	<i>n</i> -C ₂₄	C ₂₄ H ₅₀	57	338	7.93	7.79	7.54	6.57	6.58
l	<i>n</i> -C ₂₅	C ₂₅ H ₅₂	57	352	9.31	10.65	9.72	10.30	9.00
m	<i>n</i> -C ₂₆	C ₂₆ H ₅₄	57	366	9.91	10.90	10.53	9.43	10.86
n	<i>n</i> -C ₂₇	C ₂₇ H ₅₆	57	380	10.14	12.31	10.86	11.44	11.71
o	<i>n</i> -C ₂₈	C ₂₈ H ₅₈	57	394	8.95	9.98	9.37	9.57	10.35
p	<i>n</i> -C ₂₉	C ₂₉ H ₆₀	57	408	9.80	9.18	9.42	10.15	10.93
q	<i>n</i> -C ₃₀	C ₃₀ H ₆₂	57	422	7.52	7.36	6.92	8.17	8.27
r	<i>n</i> -C ₃₁	C ₃₁ H ₆₄	57	436	9.94	7.87	9.87	10.68	10.41
s	<i>n</i> -C ₃₂	C ₃₂ H ₆₆	57	450	5.04	4.26	4.82	5.52	4.92
t	<i>n</i> -C ₃₃	C ₃₃ H ₆₈	57	464	7.41	5.25	4.84	7.16	6.17
u	<i>n</i> -C ₃₄	C ₃₄ H ₇₀	57	478	1.72	1.83	2.14	2.06	1.75
v	<i>n</i> -C ₃₅	C ₃₅ H ₇₂	57	492	1.35	-	1.65	1.31	1.28
w	<i>n</i> -C ₃₆	C ₃₆ H ₇₄	57	506	0.47	-	0.63	0.19	0.61
x	<i>n</i> -C ₃₇	C ₃₇ H ₇₆	57	520	-	-	-	0.40	-
Sesterterpenoids									
a	de-A-lupane	C ₂₄ H ₄₂	123	330	37.82	17.68	24.21	13.16	28.09
Pentacyclic Triterpenoids									
b	17 α (<i>H</i>)-22,29,30-trisnorhopane (Tm)	C ₂₇ H ₄₆	191	370	2.36	-	-	-	3.25
c	17 β (<i>H</i>)-22,29,30-trisnorhopane	C ₂₇ H ₄₆	191	370	15.40	8.64	8.80	18.59	14.83
d	olean-12-ene	C ₃₀ H ₅₀	218	410	5.44	43.27	23.70	-	3.18
e	17 α (<i>H</i>),21 β (<i>H</i>)-30-norhopane	C ₂₉ H ₅₀	191	398	-	-	-	10.19	-
f	17 β (<i>H</i>),21 β (<i>H</i>)-30-norhopane	C ₂₉ H ₅₀	177	398	8.07	9.18	6.11	22.78	8.78
g	17 β (<i>H</i>), 21 β (<i>H</i>)-hopane	C ₃₀ H ₅₂	191	412	3.78	-	2.89	8.85	5.44
h	17 β (<i>H</i>),21 α (<i>H</i>)-30-normorethane	C ₂₉ H ₅₀	177	398	11.33	-	10.98	10.38	12.49
i	17 α (<i>H</i>),21 β (<i>H</i>)-30-homohopane (22 <i>S</i>)	C ₃₁ H ₅₄	191	426	2.77	4.09	5.29	5.68	4.42
j	17 α (<i>H</i>),21 β (<i>H</i>)-30-homohopane (22 <i>R</i>)	C ₃₁ H ₅₄	191	426	10.13	7.40	11.93	10.37	10.41
k	gamaserane	C ₃₀ H ₅₂	191	412	-	6.90	-	-	-
l	17 β (<i>H</i>),21 β (<i>H</i>)-30-homohopane	C ₃₁ H ₅₄	205	426	2.91	2.85	6.09	-	9.11

wax index, average chain length (ACL), Paq, terrigenous/aquatic ratio (TAR), low molecular weight to high molecular weight (LMW/HMW), alkane terrigenous (AlkTerr), *n*-C₂₉/*n*-C₁₇, and *n*-C₃₁/*n*-C₁₉ [19,21].

The maturity, organic matter source, and sediment were represented by the parameters mentioned in Table 3. CPI assigned the organic compound source. When the CPI value was lower than one indicated bacteria and algae,

while the higher value affirmed the vascular plants. All samples possessed CPI values higher than 1, confirming the vascular plant as the major source. The highest CPI value of 1.35 belonged to PLM 4, and the lowest value of 1.00 was exhibited by PLM 2. The same result was also found in the investigation of the Yellow River in China [17,22]. The CPI index also indicated the maturity of sediment samples; higher CPI pointed to a higher

maturity [23]. All samples possessed CPI values lower than 1, confirming the low maturity of coal [6,24-25].

The OEP value of sediments was found to be lower than 1 and dominated by odd carbon, which confirms aquatic creatures as the main source of organic compounds [11,23,26]. All samples showed a narrow range of OEP values from 1.14–1.20, confirming vascular plants as the major organic source origin, as observed in the Posidonia and Hils Syncline sediment samples in Germany, and eastern Junggar, China [9,11,23,26].

The LHCPI also confirmed the organic compound source through the presence of alkane in sediment. The vascular plant's role in the formation of organic sources was confirmed by LHCP value of below one. Beyond that, the short chain was claimed by the high LHCPI value that points to the role of bacteria. The LHCPI also provided information on the maturity of Polaman sediments. It was confirmed that the major organic compound source was vascular plants, as affirmed by all samples possessing LHCPI lower than one, mentioned on Teluk Brunei sediment, Malaysia [20]. Another parameter was the wax index as an affirmation of the organic source. The dominance of short-chain *n*-alkanes over long chains was inferred by a wax value of higher than 1, confirming the

bacteria and algae as the main contributors [8]. All samples have a wax index lower than one, with the highest wax index of 0.15 and the lowest of 0.26. This value informed that the source of organic compounds was dominated by vascular plants [8].

Average chain length enabled the prediction of organic sources through the abundance of odd-chain alkanes (C_{25} - C_{33}) [22,27]. The benchmark ACL value was 28; the value below this point represented the wax layer. Inversely, the ACL value above 28 pointed to the role of vascular plants. Specifically, *n*- C_{31} and *n*- C_{33} confirmed that grass and herbs are the origin of organic compounds. Generally, all samples provided generated ACL values in the span of 28.32 to 28.83, confirming the wax and vascular plant as the source of the organic compound. This result was also observed in the study of Guanabara sediment [22,28].

The Paq parameter value represents the origin of the coal. The Paq values of PLM 1, PLM 2, PLM 3, PLM 4, and PLM 5 are 0.42, 0.47, 0.42, 0.40, and 0.37, respectively (Fig. 2). Paq values < 0.1 were for vascular plants, 0.1–0.4 for emergent macrophytes, and 0.4–1.0 for submerged/floating macrophytes [11,16,18-19]. Coal samples from PLM 1-4 were indicated to originate from

Table 3. Parameter values of *n*-alkane, isoprenoid, and triterpenoid compounds in PLM sediments 1-5

Parameter	Sample				
	PLM-1	PLM-2	PLM-3	PLM-4	PLM-5
CPI	1.30	1.22	1.23	1.35	1.26
OEP	1.19	-	1.14	1.20	1.14
LHCPI	0.03	0.03	0.05	-	-
Pr/Ph	-	1.26	-	-	-
Pr/ <i>n</i> - C_{17}	-	0.73	-	-	-
Ph/ <i>n</i> - C_{18}	-	0.36	-	-	-
Wax index	0.21	0.26	0.25	0.15	0.15
ACL	28.83	28.32	28.52	28.72	28.71
Paq	0.42	0.47	0.42	0.40	0.37
TAR	-	36.92	-	-	-
LMW/HMW	-	0.02	-	-	-
AlkTerr	0.39	0.34	-	-	-
<i>n</i> - C_{29} / <i>n</i> - C_{17}	32.67	32.11	22.71	-	-
<i>n</i> - C_{31} / <i>n</i> - C_{19}	36.81	15.46	21.66	75.35	51.35
<i>n</i> - C_{17} / <i>n</i> - C_{31}	0.03	0.03	0.04	-	-
C_{29} $\beta\beta/\alpha\beta$				2.24	
C_{31} 22S/(22S + 22R)	0.22	0.33	0.31	0.35	0.30

submerged/floating macrophytes, similar to the sediments of the Cochin mangrove forest on the west coast of India, while PLM 5 came from emergent macrophytes [29].

The relationship of organic matter sources with aquatic and terrestrial environments was evaluated through the TAR parameter, which was obtained from the ratio of the total *n*-alkanes C₂₇, C₂₉, and C₃₁ to the total *n*-alkanes C₁₅, C₁₇, and C₁₉. The TAR value of PLM 2 was 36.92, indicating a higher contribution of vascular plants in the terrestrial environment [11,19]. Parameter LMW/HMW was calculated by comparing the abundance of *n*-alkane \leq C₂₁ with *n*-alkane \geq C₂₁ as well as coastal sediments of St. Lawrence Estuary and Gulf, Quebec, Canada [30]. The PLM 2 sample has an LMW/HMW value of 0.02 (< 1) (Table 3), confirming that the organic matter comes from vascular plants.

The main role of vascular plants as the source of organic matter for PLM samples is confirmed by the AlkTERR value, as found in the Brunei Bay sediments, East Malaysia [20]. The AlkTERR value of PLM 1 samples was 0.39, and PLM 2 was 0.34 (or > 0.3), confirming the main role of vascular plants as the origin of organic matter and indicating the dominance of terrestrial higher plants. The contribution of terrestrial or marine organisms is confirmed by the C₃₁/C₁₉ ratio. The value of the C₃₁/C₁₉ ratio of each PLM 1 to PLM 5 is 36.81, 15.46, 21.66, 75.35, and 51.35, respectively, which shows that terrestrial organisms are more dominant than marine organisms as a source of organic matter, such as sediments in surface sediments of the Bohai Sea, Yellow Sea, and East China Sea [31].

The C₂₉/C₁₇ ratio can also conclude that the source of organic matter comes from the terrestrial or aquatic environment. The C₂₉/C₁₇ ratio of PLM 1, PLM 2, and PLM 3 were 32.67, 32.11, and 22.71, respectively, confirming that the source of organic matter is a contribution from the terrestrial environment, such as sediments in surface sediments of the Bohai Sea, Yellow Sea, and East China Sea [29,31]. The C₁₇/C₃₁ ratio determined the presence of autochthonous or allochthonous organic matter sources, and the C₁₇/C₃₁ ratio of samples PLM 1, PLM 2, and PLM 3 are 0.03, 0.03, and 0.04 respectively, representing allochthonous

sources, such as on the sediments of the East Yellow Sea, Northwest Pacific Ocean, China [22,32].

The ratio of Pr/Ph compounds describes the depositional environment of geological sediments. If the Pr/Ph ratio is more than > 1, it indicates an oxic depositional environment, while a ratio less than < 1 indicates an anoxic depositional environment. A Pr/Ph ratio higher than 1 as an indicator of oxic deposition was reported in the Brunei Bay sediments in Malaysia [20]. Table 2 shows the presence of pristane in PLM 2 and PLM 3, while phytane was only identified in PLM 2 [10,33-34]. The Pr/Ph ratio of the PLM 2 sample yielded a value of 1.26, indicating an oxic depositional environment (Table 3). Based on Pr/*n*-C₁₇ ratio (0.73) and Ph/*n*-C₁₈ ratio (0.36) indicate that PLM 3 is in the oxic region [20]. This ratio has been applied in the Liaodong Bay subbasin, Bohai Bay Basin, China [35].

Triterpenoid

The identification of triterpenoids in the sediment samples based upon the specific fragmentogram *m/z* 191 confirmed the presence of de-A-lupane compounds and pentacyclic triterpenoids, as observed in Fig. 3 and Table 2.

Table 2 describes the presence of de-A-lupane, 17 β (*H*)-22,29,30-trisnorhopane, 17 β (*H*),21 β (*H*)-30-norhopane, and 17 α (*H*),21 β (*H*)-30-homohopane with 22*S* and 22*R* configurations in all samples. The 17 α (*H*)-22,29,30-trisnorhopane (Tm) was only observed in PLM 1 and PLM 5 sediments; olean-12-ene and 17 β (*H*),21 β (*H*)-30-homohopane existed in all sample but PLM-4. The 17 α (*H*),21 β (*H*)-30-norhopane was only identified in PLM 4 while the 17 β (*H*), 21 β (*H*)-hopane and 17 β (*H*),21 α (*H*)-30-normorethane were only absent in PLM 4. In addition, the gamaserane was only identified in PLM 2.

The presence of triterpenoid compounds was beneficial in determining the source of organic matter from Polaman sediments. De-A-lupane, a non-hopanoid triterpenoid group, was formed due to bacterial activity, resulting in the degradation of the lupane compound during the deposition period. Diagenesis, the compound of lupane, was derived from lupeol as a precursor of vascular plants Angiosperms [36-38]. Therefore, the

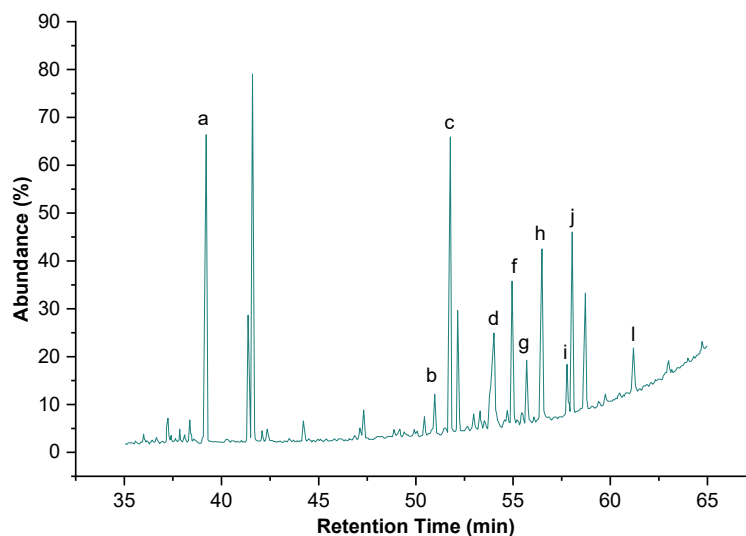


Fig 3. Fragmentogram of pentacyclic sesterterpenoids and triterpenoids on m/z 191

presence of de-A-lupane in Polaman sediments affirmed the organic origin from higher terrestrial plants Angiosperms and the presence of bacterial input during sediment deposition [37,39]. This result was also supported by the presence of similar biomarkers in the Bikaner, Nagaur, Jalore, Jaisalmer, and Barmer districts of Rajasthan, western India, and Papua Basin, Papua New Guinea, as indicators of sources of terrestrial higher plant organic matter [40-41]. The origin of organic compounds from Angiosperms was also affirmed by the presence of olean-12-ene compounds in PLM 1, 2, 3, and 5 which derived from β -amirin as a precursor. A similar result was reported in the study of coastal sediments and soils around the city of Tromso [41-42]. The hopanoid triterpenoid compounds in Polaman sediments depicted the presence of C_{27} - C_{30} hopane homologues such as Tm, $17\beta(H)$ -22,29,30-trisnorhopane, $17\alpha(H)$, $21\beta(H)$ -30-norhopane, $17\beta(H)$, $21\beta(H)$ -30-norhopane, $17\beta(H)$, $21\beta(H)$ -hopane, and $17\beta(H)$, $21\alpha(H)$ -30-normorethane. These compounds were derived from the hopanoids diploptene and diplopterol. In addition, there were C_{31} hopane compounds, entitled $17\alpha(H)$, $21\beta(H)$ -30-homohopane with 22S and 22R configurations, and $17\beta(H)$, $21\beta(H)$ -30-homohopane originated from bacteriohopanetetrol in the membranes of prokaryotic bacteria [43]. Subsequently, the presence of hopanoid compounds indicated the contribution of bacteria to the source of organic compounds in Polaman sediments. The

contribution from this bacterium was also inferred by the presence of the compound gamacerane, since this compound was associated with dehydrated and hydrogenated tetrahymanol precursors on the protozoan membrane [44-45]. Thus, the identification of gamacerane compounds justified the role of bacteria in the PLM 2 sediment. Hopanoid and gamacerane compounds were also observed in Upper Cretaceous petroleum source rocks from the Gippsland Basin, Australia [8].

The hopanoid compounds in all samples were also employed as an indicator of sample maturity based on the ratio of C_{29} $\beta\beta/\alpha\beta$ and C_{31} $22S/(22S + 22R)$, as written in Table 3. The C_{29} $\beta\beta/\alpha\beta$ parameter was calculated based on the ratio of $17\alpha(H)$, $21\beta(H)$ -30-norhopane to $17\beta(H)$, $21\beta(H)$ -30-norhopane in PLM 4. C_{29} $\beta\beta/\alpha\beta$ ratio value > 0.15 confirmed low maturity, while the value < 0.15 inferred high maturity [23,46]. Based on Table 3, PLM 4 exhibited low maturity with the C_{29} $\beta\beta/\alpha\beta$ ratio value of 2.24.

Meanwhile, the parameter C_{31} $22S/(22S + 22R)$ was generated from the ratio of the 22S configuration to the sum of the S + R configurations of $17\alpha(H)$, $21\beta(H)$ -homohopane. The 22S configuration of the $17\alpha(H)$, $21\beta(H)$ -homohopane structure is more stable compared to the 22R configuration. The low abundance of $17\alpha(H)$, $21\beta(H)$ -homohopane (22S) compared to 22R indicates a low maturity level. A value of C_{31} $22S/(22S + 22R)$ lower than 1 indicated low maturity, while a value

higher than one affirmed high maturity [5-6,24]. The ratio value of $C_{31} 22S/(22 S+ 22R)$ values for PLM 1 to PLM 5 sediments were 0.22, 0.33, 0.31, 0.35, and 0.30, respectively. All these values demonstrated low maturity. Similar results were also found for Wondama coal, Indonesia, with a ratio value of 0.27 as an indicator of low maturity [6]. The low thermal maturity of the Polaman sediments was also rationalized by the presence of bacterial activity during the sedimentary deposition process. This bacterial activity had been continuing in the early stages of diagenesis, so the presence of bacterial input in the formation of sediment organic matter indicates low maturity of sediment [3,47]. Hopanoid biomarkers are also adopted as indicators of Polaman sediment maturity. The low maturity of sediment was assigned by the presence of $17\beta(H)$ -22,29,30-trisnorhopane compounds with relatively low structural stability [8,48]. Notably, PLM 4 exhibited high maturity by the presence of $17\alpha(H)$, $21\beta(H)$ -30-norhopane with stable structural over $17\beta(H)$, $21\beta(H)$ -30-trisnorhopane.

Apart from the indicator of thermal maturity, triterpenoid compounds were capable of determining the depositional environment of Polaman sediments. The formation of De-A-triterpenoids through the degradation of pentacyclic triterpenoids also affirmed the presence of an oxic depositional environment [33-34]. This environment was also pointed by De-A-triterpenoid compounds with the lupane, ursane, and oleanane

structure as the result of photochemical or microbial degradation of pentacyclic triterpenoids. The process was characterized by the release of ring A in the oxidative environment [37]. Therefore, the finding of this compound in Polaman sediments indicates an oxic depositional environment. Gamaserane compounds as indicators of reductive and hypersaline depositional environments were also identified in very low abundance in PLM 2 samples.

Aromatic Hydrocarbon Fraction

The results of the identification of aromatic hydrocarbon fraction biomarkers using GC-MS spectrometer were presented as total ion chromatogram (TIC) in Fig. 4 and their abundance in Table 4. Fig. 3 and Table 4 exhibited alkyl benzene groups, naphthalene derivatives, phenanthrene derivatives, and pentacyclic aromatic triterpenoids as biomarkers. However, alkyl benzene was only observed in PLM 1 and PLM 4 samples.

Alkyl benzene and naphthalene derivatives

Identification of the m/z 91 fragmentogram in PLM 4 inferred the presence of eight alkyl benzene compounds such as (4,5-dimethyl)nonylbenzene, (2,7-dimethyl)nonylbenzene, (4,6-dimethyl)decylbenzene, (3,6-dimethyl)decylbenzene, (2,8-dimethyl)decylbenzene, (5,6-dimethyl)undecylbenzene, (2,3,6-trimethyl)decyl benzene, and (3,8-dimethyl)undecylbenzene. The m/z 105

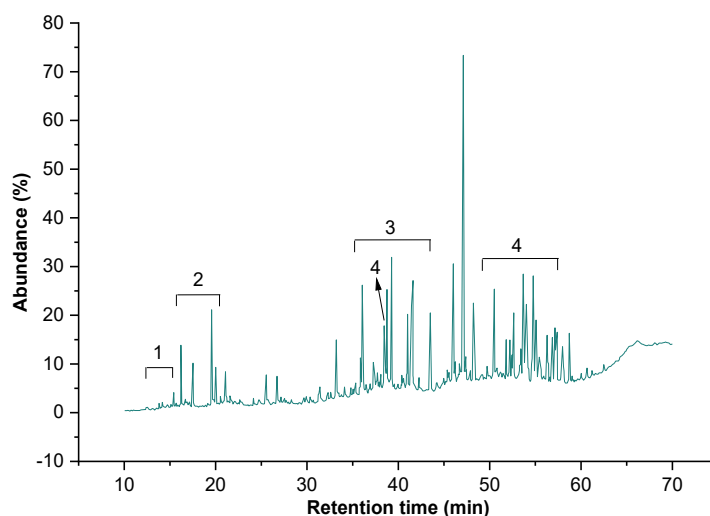


Fig 4. TIC of aromatic hydrocarbon fraction of PLM sediment sample PLM 1-PLM 5. (1) Alkylbenzene, (2) naphthalene derivatives, (3) phenanthrene derivatives, and (4) aromatic pentacyclic triterpenoids

Table 4. The abundance of aromatic hydrocarbon fraction in PLM sediment samples 1-5

Compound name	Molecular formula	Base peak	M ⁺	Composition (%)				
				PLM 1	PLM 2	PLM 3	PLM 4	PLM 5
Naphthalene derivatives								
cadalene	C ₁₅ H ₁₈	183	198	93.31	100.00	96.58	-	100.00
isocadalene	C ₁₅ H ₁₈	183	198	6.69	-	3.42	-	-
norcadalene	C ₁₄ H ₁₆	169	184	100.00	-	-	-	-
calamene	C ₁₄ H ₁₆	159	202	83.19	100.00	84.05	100.00	-
5,6,7,8-tetrahydrocadalene	C ₁₅ H ₂₂	187	202	16.81	-	15.95	-	-
Phenanthrene derivatives								
phenanthrene	C ₁₄ H ₁₀	178	178	100.00	100.00	100.00	-	100.00
chrysene	C ₁₈ H ₁₂	228	228	-	100.00	-	-	-
3,4,7-trimethyl-1,2,3,4-tetrahydrochrycene	C ₂₁ H ₂₂	259	274	59.36	-	100.00	-	-
3,3,7-trimethyl-1,2,3,4-tetrahydrochrycene	C ₂₁ H ₂₂	218	274	40.64	-	-	-	-
Aromatic pentacyclic triterpenoids								
dinoroleane-1,3,5(10),12-tetraene	C ₂₈ H ₄₀	145	376	44.65	31.06	51.70	-	50.07
dinoursa-1,3,5(10),12-tetraene	C ₂₈ H ₄₀	145	376	20.17	-	15.81	-	12.24
dinoroleane-1,3,5(10)-triene	C ₂₈ H ₄₀	145	378	35.18	41.30	32.49	-	37.69
dinorlupa-1,3,5(10)-triene	C ₂₈ H ₄₀	145	378	-	27.64	-	-	-
1,2,4 <i>a</i> ,9-tetramethyl-1,2,3,4,4 <i>a</i> ,5,6,14 <i>b</i> -octahdropicene	C ₂₆ H ₃₀	342	342	75.53	-	64.77	-	82.15
2,2,4 <i>a</i> ,9-tetramethyl-1,2,3,4,4 <i>a</i> ,5,6,14 <i>b</i> -octahdropicene	C ₂₆ H ₃₀	257	342	24.47	-	35.23	-	17.85
8,14-triaromatic secolupane	C ₂₇ H ₃₂	169	356	65.64	-	63.88	-	65.28
8,14-triaromatic secooleanane	C ₂₇ H ₃₂	169	356	34.36	-	36.12	-	34.72
1,2-dimethyl-1,2,3,4-tetrahydropicene	C ₂₄ H ₂₂	295	310	100.00	-	-	-	-
1,2,9-trimethyl-1,2,3,4-tetrahydropicene	C ₂₅ H ₂₄	324	324	-	-	42.25	-	-
2,2,9-trimethyl-1,2,3,4-tetrahydropicene	C ₂₅ H ₂₄	324	324	-	-	57.75	-	-
Alkyl benzene								
(4,5-dimethyl)nonylbenzene	C ₁₇ H ₂₈	91	232	-	-	-	9.20	-
(2,7-dimethyl)nonylbenzene	C ₁₇ H ₂₈	91	232	-	-	-	6.44	-
(4,6-dimethyl)decylbenzene	C ₁₈ H ₃₀	91	246	-	-	-	19.05	-
(3,6-dimethyl)decylbenzene	C ₁₈ H ₃₀	91	246	-	-	-	10.86	-
(2,8-dimethyl)decylbenzene	C ₁₈ H ₃₀	91	246	-	-	-	9.19	-
(5,6-dimethyl)undecylbenzene	C ₁₉ H ₃₂	91	260	-	-	-	19.89	-
(2,3,6-dimethyl)decylbenzene	C ₁₉ H ₃₂	91	260	-	-	-	15.53	-
(3,8-dimethyl)undecylbenzene	C ₁₉ H ₃₂	91	260	-	-	-	9.83	-
methyldecylbenzene	C ₁₅ H ₂₄	105	204	44.09	-	-	-	-
heptyldimethylbenzene	C ₁₅ H ₂₄	119	204	55.91	-	-	-	-
methyldecylbenzene	C ₁₇ H ₂₈	105	232	-	-	-	39.32	-
methylundecylbenzene	C ₁₈ H ₃₀	105	246	-	-	-	16.21	-
methylundecylbenzene	C ₁₉ H ₃₂	105	260	-	-	-	44.46	-

fragmentogram confirmed the methyl octyl benzene in PLM 1 and PLM 4 possessed methyldecylbenzene, methylundecylbenzene, and methylundecylbenzene. The

m/z 119 fragmentogram showed the heptyl dimethylbenzene compounds, an indicator of organic matter derived from carotenoids as precursors produced

by higher terrestrial plants, algae, and cyanobacteria during the diagenesis process. In addition, alkylbenzene compounds also indicated the presence of bacterial activity in the formation of sediment [49-52].

Naphthalene derivatives such as cadalene and isocadalene were identified based on the fragmentogram m/z 183, calamene at m/z 159, norcadalene at m/z 169, and 5,6,7,8,9-tetrahydrocadalene at m/z 187. Cadalene compounds were observed in all PLM samples. Isocadalene and 5,6,7,8-tetrahydrocadalene compounds were only identified in PLM 1, PLM 2, and PLM 3. Norcadalene compounds were only found in PLM 1 and 2 while calamene in PLM 1-4. The presence of naphthalene derivatives conveyed the source of organic matter. The abundance of cadalene, isocadalene, and norcadalene compounds in Polaman sediments confirmed the contribution of vascular plants Angiosperms from the Dipterocarpaceae family [4]. Presumably, cadalene was produced by polymerization of polycadinene resins in Dipterocarpaceae plants during the catagenesis stage [53-56]. In addition, the presence of cadalene and isocadalene also justifies the thermal maturity [4]. Isocadalene formed at high temperatures was a more stable isomer than cadalene [57]. Therefore, the high intensity of cadalene compared to isocadalene indicates the low maturity of the Polaman sample [58-59]. A high abundance of the compound cadalene was also found in the coal of the Kutai Basin, Indonesia [53].

The presence of calamene biomarkers and 5,6,7,8-tetrahydrocadalene as derivatives of sesquiterpenoids supported the contribution from Angiosperms plants (Dipterocarpaceae family) and Gymnosperms plants (Cupressaceae family) [57,60-61]. These compounds were also present in rocks Upper Cretaceous petroleum resource, Gipssland Basin, Australia [12].

Phenanthrene derivatives

The phenanthrene group was identified based on the m/z 178, 228, 259, and 218 fragmentograms. The presence of phenanthrene compounds in the sediments of PLM 1, PLM 2, PLM 3, and PLM 5 was identified based on the m/z 178, conveying Angiosperms and Gymnosperms as the source of organic matter. This compound existed in geological samples of the Middle Miocene [53,62]. The

m/z 228 confirmed the chrysene in PLM 2, the m/z 259 assigned 3,4,7-trimethyl-1,2,3,4-tetrahydrochrysene compounds in PLM 1 as well as PLM 3, and the m/z 218 for the compound 3,3,7-trimethyl-1,2,3,4-tetrahydrochrysene. These compounds are isomers yet originated from different structural origins. The compound 3,4,7-trimethyl-1,2,3,4-tetrahydrochrysene is derived from ursane, while 3,3,7-trimethyl-1,2,3,4-tetrahydrochrysene is derived from oleanane [39,63-64]. The presence of these compounds confirmed the contribution of Angiosperm plants, which originated from the degradation of β -amyrin in the early stages of diagenesis [61,63,65]. Hence, these two compounds were promising indicators of Angiosperm contribution in Polaman sediment. The existence of these compounds was also found in the Upper Cretaceous petroleum source rocks of the Latrobe Group, Gippsland Basin, Australia [12].

Pentacyclic aromatic triterpenoids

The pentacyclic triterpenoid aromatic compounds in Polaman sediments were identified based on the fragmentograms m/z 145, 257, 295, 324, and 356 [10,12,38,40]. The dinoroleane-1,3,5(10),12-tetraene, and dinoroleane-1,3,5(10)-triene in PLM 1, PLM 2, PLM 3, and PLM 5 were studied according to the specific fragmentogram m/z 145. Dinorursa-1,3,5(10),12-tetraene biomarkers were identified in PLM 1, PLM 3, and PLM 5, while dinorlupa-1,3,5(10)-triene was only identified in PLM 2 sediments. Dinoroleane-1,3,5(10),12-tetraene, dinorursa-1,3,5(10),12-tetraene, dinoroleane-1,3,5(10)-triene, and dinorlupa-1,3,5(10)-triene are a group of pentacyclic triterpenoid monoaromatic compounds with oleanane, ursane and lupane frame. These compounds were derived from β -amyrin and α -amyrin as precursors of higher terrestrial plants, especially Angiosperms. It is worth noted only a small number of Gymnosperm plants can produce these compounds [10,66]. Therefore, the presence of these three compounds in Polaman sediments indicates the dominance of organic matter from higher vascular plants, especially Angiosperms. These three compounds were also identified in siliclastic deposits of the Orava-Nowy Targ Basin [66].

Based on the m/z 257 fragmentogram, the 1,2,4*a*,9-tetramethyl-1,2,3,4,4*a*,5,6,14*b*-octahydropsene and 2,2,4*a*,9-tetramethyl-1,2,3,4,4*a*,5,6,14*b*-octahydropsene were observed in PLM 1, PLM 2, and PLM 3. These two compounds indicated that organic matter originated from β -amyrin and α -amyrin as precursors in higher plants Angiosperms [10,40]. The presence of these compounds 1,2,9-trimethyl-1,2,3,4-tetrahydropicene and 2,2,9-trimethyl-1,2,3,4-tetrahydropycene in the analyzed Polaman samples proved of the vascular plant as the source of organic matter [10,53,60]. This pentacyclic tetraaromatic compound was also found in the Eagle Ford Group drilling Central Texas [48]. In addition, PLM 1, PLM 2, PLM 3 consist of 8,14-triaromaticsecolupane and 8,14-triaromaticsecoleanane compounds based on the m/z 356 fragmentogram, providing evidence of higher plants Angiosperms as the origin of organic compounds [10,47]. These two compounds were also found in sediments from Mulga Rock, Australia [38]. These two biomarkers were synthesized from the alteration and aromatization of triterpenoids present in Angiosperms during the diagenesis stage. This aromatization process took place as the temperature increased, forming simpler compounds [10,38]. Therefore, the presence of these two biomarkers in the sediment indicated immature samples [10,38,47].

Based on the m/z 324 fragmentogram, the biomarkers of 1,2,9-trimethyl-1,2,3,4-tetrahydropycene and 2,2,9-trimethyl-1,2,3,4-tetrahydropycene were identified in PLM 3. Biomarkers formed due to bacterial contribution in the early stages of diagenesis were diagenetic products of β -amyrin, namely pentacyclic triterpenoid with oleanane framework [10,48,53,60]. The same compound was also found in Sangata coal, East Borneo, Kutai Basin coal, and Eagle Ford Group source rock, Texas [10,48,53].

■ CONCLUSION

Organic geochemical analysis of Polaman sediment samples, the Ngrayong formation as source rock was carried out to determine its potential as an oil and gas producer. Geochemical characteristics are related to the source of organic material, sediment maturity, and

ancient depositional environment. The *n*-alkane biomarker with a bimodal distribution in all samples indicated that the organic material came from various sources. Several parameters such as $CPI > 1.00$, C_{31}/C_{19} ratio > 0.40 , Paq 0.37–0.47, and the presence of naphthalene, phenanthrene, and pentacyclic monoaromatic triterpenoid derivatives indicate that the source of organic matter comes from higher plants, algae, and bacteria. This dominant source of terrigenous organic matter is also proven by a TAR value > 1 , a C_{29}/C_{17} ratio > 1 , and the presence of aromatic hydrocarbon compounds derived from naphthalene, phenanthrene, pentacyclic triterpenoids, and alkyl benzene. Apart from that, the inclusion of bacteria in the formation of organic matter is also proven by the presence of hopanoid compounds. This varied source of organic material is also proven by the C_{17}/C_{31} ratio < 1 as an indicator of allochthonous organic material. The presence of pentacyclic monoaromatic triterpenoids and hopanoids with β isomers indicates low thermal maturity. The oxic deposition environment in the coal formation process is indicated by a Pr/Ph ratio > 1 , a high abundance of de-A-lupane. The existence of several biomarkers with the above parameters indicates that coal is a source rock that has the potential to produce oil and gas.

■ ACKNOWLEDGMENTS

The authors gratefully acknowledged financial support from the Institut Teknologi Sepuluh Nopember for this work under the project scheme of the Publication Writing and IPR Incentive Program (PPHKI) 2023. The authors also thank Lulah, Elsy, Putri, and Ferry for providing data support in this study. Thanks also to Muhammad Salman Al Kahfi, who has improved all the figures.

■ AUTHOR CONTRIBUTIONS

Yulfi Zetra conceptualized research, wrote, and reviewed draft articles. Rafwan Year Perry Burhan conceptualized this work, designed the research methodology, supervised the research, and reviewed the manuscript. Sulistiyono validated the data and reviewed the manuscript. Arizal Firmansyah edited and evaluated

the manuscript. Darin Salsabila collected data, carried out the research methodologies, and wrote the manuscript.

■ REFERENCES

- [1] Husein, S., Titisari, A.D., Freski, Y.R., and Utama, P.P., 2016, *Buku Panduan Ekskursi Geologi Regional, Jawa Timur Bagian Barat, Indonesia*, Department of Geological Engineering, Faculty of Engineering, UGM, Yogyakarta.
- [2] Dhamayanti, E., Raharjanti, N.A., and Hartati, I.A., 2016, Dinamika Sedimentasi Singkapan Formasi Ngrayong dengan Analogi Lingkungan Pengendapan Modern, Studi Kasus Singkapan Polaman dan Braholo dengan Analogi Pesisir Pantai Utara Jawa, *The 9th Seminar Nasional Kebumihan*, Grha Sabha Pramana, Yogyakarta, Indonesia, 6-7 October 2016, 725–735.
- [3] Killops, S., and Killops, V., 2005, *Introduction to Organic Geochemistry*, 2nd Ed., Blackwell Publishers, Oxford, UK.
- [4] Ajuaba, S., Sachsenhofer, R.F., Meier, V., Gross, D., Schnyder, J., Omodeo-Salé, S., Moscariello, A., and Misch, D., 2023, Coaly and lacustrine hydrocarbon source rocks in Permo-Carboniferous graben deposits (Weiach well, Northern Switzerland), *Mar. Petrol. Geol.*, 150, 106147.
- [5] Cieřlik, E., and Fabiańska, M.J., 2021, Preservation of geochemical markers during co-combustion of hard coal and various domestic waste materials, *Sci. Total Environ.*, 768, 144638.
- [6] Zetra, Y., Burhan, R.Y.P., Pratama, A.D., and Wahyudi, A., 2020, Origin and maturity of biomarker aliphatic hydrocarbon in Wondama coal Indonesia, *J. Idn. Chem. Soc.*, 3 (2), 107–116.
- [7] Kumar, S., Dutta, S., and Bhui, U.K., 2021, Provenance of organic matter in an intracratonic rift basin: Insights from biomarker distribution in Palaeogene crude oils of Cambay Basin, western India, *Org. Geochem.*, 162, 104329.
- [8] Jiang, L. and George, S.C., 2018, Biomarker signatures of Upper Cretaceous Latrobe Group hydrocarbon source rocks, Gippsland Basin, Australia: Distribution and palaeoenvironment significance of aliphatic hydrocarbons, *Int. J. Coal Geol.*, 196, 29–42.
- [9] Zhu, Z., Li, M., Li, J., Qi, L., Liu, X., Xiao, H., and Leng, J., 2022, Identification, distribution and geochemical significance of dinaphthofurans in coals. *Org. Geochem*, 166, 104399.
- [10] Nádudvari, Á., Misz-Kennan, M., Fabiańska, M., Ciesielczuk, J., Krzykowski, T., Simoneit, B.R.T., and Marynowski, L., 2023, Preservation of labile organic compounds in sapropelic coals from the Upper Silesian Coal Basin, Poland, *Int. J. Coal Geol.*, 267, 104186.
- [11] Fang, R., Littke, R., Zieger, L., Baniasad, A., Li, M., and Schwarzbauer, J., 2019, Changes of composition and content of tricyclic terpane, hopane, sterane, and aromatic biomarkers throughout the oil window: A detailed study on maturity parameters of Lower Toarcian Posidonia Shale of the Hils Syncline, NW Germany, *Org. Geochem.*, 138, 103928.
- [12] Jiang, L., and George, S.C., 2019, Biomarker signatures of Upper Cretaceous Latrobe Group petroleum source rocks, Gippsland Basin, Australia: Distribution and geological significance of aromatic hydrocarbons, *Org. Geochem.*, 138, 103905.
- [13] Simoneit, B.R.T., Oros, D.R., Karwowski, Ł., Szendera, Ł., Smolarek-Lach, J., Goryl, M., Bucha, M., Rybicki, M., and Marynowski, L., 2020, Terpenoid biomarkers of ambers from Miocene tropical paleoenvironments in Borneo and of their potential extant plant sources, *Int. J. Coal Geol.*, 221, 103430.
- [14] Nádudvari, Á., Forzese, M., Maniscalco, R., Di Stefano, A., Misz-Kennan, M., Marynowski, L., Krzykowski, T., and Simoneit, B.R.T., 2022, The transition toward the Messinian evaporites identified by biomarker records in the organic-rich shales of the Tripoli Formation (Sicily, Italy), *Int. J. Coal Geol.*, 260, 104053.
- [15] Körmös, S., Sachsenhofer, R.F., Bechtel, A., Radovics, B.G., Milota, K., and Schubert, F., 2021, Source rock potential, crude oil characteristics and oil-to-source rock correlation in a Central Paratethys sub-basin, the Hungarian Palaeogene

- Basin (Pannonian basin), *Mar. Pet. Geol.*, 127, 104955.
- [16] El-Sabagh, S.M., El-Naggar, A.Y., El Nady, M.M., Ebiad, M.A., Rashad, A.M., and Abdullah, E.S., 2018, Distribution of triterpanes and steranes biomarkers as indication of organic matters input and depositional environments of crude oils of oilfields in Gulf of Suez, Egypt, *Egypt. J. Pet.*, 27 (4), 969–977.
- [17] Lee, D.H., Kim, S.H., Choi, J., Kang, N.K., Hwang, I.G., and Shin, K.H., 2022, Geochemical signatures of organic matter associated with gas generation in the Pohang Basin, South Korea, *Geosci. J.*, 26 (5), 555–567.
- [18] Chen, Q., Guo, Z., Yu, M., Sachs, J.P., Hou, P., Li, L., Jin, G., Liu, Y., and Zhao, M., 2021, Lipid biomarker estimates of seasonal variations of aerosol organic carbon sources in coastal Qingdao, China, *Org. Geochem.*, 151, 104148.
- [19] Zetra, Y., Burhan, R.Y.P., Firdaus, A.W., Nugrahaeni, Z.V., and Gunawan, T., 2021, Characteristics of Cepu block oil, Wonocolo formation, East Java Indonesia: Study of aliphatic biomarkers, *AIP Conf. Proc.*, 2349 (1), 020040.
- [20] Pang, S.Y., Suratmman, S., Tay, J.H., and Mohd Tahir, N., 2021, Investigation of aliphatic and polycyclic aromatic hydrocarbons in surface sediments of Brunei Bay, East Malaysia, *Asian J. Chem.*, 33 (2), 439–446.
- [21] de Sousa, A.A.C., Sousa, E.S., Rocha, M.S., Sousa Junior, G.R., de Souza, I.V.A.F., Brito, A.S., Souza, S.S., Lopes, J.A.D., Nogueira, A.C.R., and de Lima, S.G., 2020, Aliphatic and aromatic biomarkers of the Devonian source rocks from the Western Parnaíba Basin Brazil: Pimenteiras formation, *J. South Am. Earth Sci.*, 99, 102493.
- [22] Jin, J., Guo, H., Gao, Z., Mao, R., and Lu, H., 2022, Biodegradation of dissolved organic matter and sedimentary organic matter in high arsenic groundwater system: Evidence from lipid biomarkers and compound-specific carbon isotopes, *Chem. Geol.*, 612, 121140.
- [23] Kang, S., Shao, L., Qin, L., Li, S., Liu, J., Shen, W., Chen, X., Eriksson, K.A., and Zhou, Q., 2020, Hydrocarbon generation potential and depositional setting of Eocene oil-prone coaly source rocks in the Xihu Sag, East China Sea Shelf Basin, *ACS Omega*, 5 (50), 32267–32285.
- [24] Patra, S., Dirghangi, S.S., Rudra, A., Dutta, S., Ghosh, S., Varma, A.K., Shome, D., and Kalpana, M.S., 2018, Effects of thermal maturity on biomarker distributions in Gondwana coals from the Satpura and Damodar Valley Basins, India, *Int. J. Coal Geol.*, 196, 63–81.
- [25] Herrera-Herrera, A.V., Leierer, L., Jambrina-Enríquez, M., Connolly, R., and Mallol, C., 2020, Evaluating different methods for calculating the Carbon Preference Index (CPI): Implications for palaeoecological and archaeological research, *Org. Geochem.*, 146, 104056.
- [26] Yu, X., Lü, X., Meyers, P.A., and Huang, X., 2021, Comparison of molecular distributions and carbon and hydrogen isotope compositions of *n*-alkanes from aquatic plants in shallow freshwater lakes along the middle and lower reaches of the Yangtze River, China, *Org. Geochem.*, 158, 104270.
- [27] Bliedtner, M., Schäfer, M.I.K., Zech, R., and von Suchodoletz, H., 2018, Leaf wax *n*-alkanes in modern plants and topsoils from eastern Georgia (Caucasus) – Implications for reconstructing regional paleovegetation, *Biogeosciences*, 15 (12), 3927–3936.
- [28] Ceccopieri, M., Scofield, A.L., Almeida, L., and Wagener, A.L.R., 2018, Compound-specific $\delta^{13}\text{C}$ of *n*-alkanes: Clean-up methods appraisal and application to recent sediments of a highly contaminated bay, *J. Braz. Chem. Soc.*, 29 (11), 2363–2377.
- [29] Ratheesh Kumar, C.S., Renjith, K.R., Joseph, M.M., Salas, P.M., Resmi, P., and Chandramohanakumar, N., 2019, Inventory of aliphatic hydrocarbons in a tropical mangrove estuary: A biomarker approach, *Environ. Forensics*, 20 (4), 370–384.
- [30] Imfeld, A., Ouellet, A., Douglas, P.M.J., Kos, G., and Gélinais, Y., 2022, Molecular and stable isotope analysis ($\delta^{13}\text{C}$, $\delta^2\text{H}$) of sedimentary *n*-alkanes in the St. Lawrence Estuary and Gulf, Quebec, Canada: Importance of even numbered *n*-alkanes in coastal

- systems, *Org. Geochem.*, 164, 104367.
- [31] Zou, Y., Wang, C., Liu, X., and Wang, H., 2022, Spatial distribution, compositional pattern and source apportionment of *n*-alkanes in surface sediments of the Bohai Sea, Yellow Sea, and East China Sea and implications of carbon sink, *Mar. Pollut. Bull.*, 178, 113639.
- [32] Özdemir, A., Palabiyik, Y., Karataş, A., and Şahinoğlu, A., 2022, Mature petroleum hydrocarbons contamination in surface and subsurface waters of Kızılırmak Graben (Central Anatolia, Turkey): Geochemical evidence for a working petroleum system associated with a possible salt diapir, *Turk. J. Eng.*, 6 (1), 1–15.
- [33] Zhu, Z., Li, M., Li, J., Qi, L., Liu, X., Xiao, H., and Leng, J., 2022, Identification, distribution and geochemical significance of dinaphthofurans in coals, *Org. Geochem.*, 166, 104399.
- [34] Al-Areeq, N.M., Al-Badani, M.A., Salman, A.H., and Albaroot, M.A., 2018, Petroleum source rocks characterization and hydrocarbon generation of the Upper Jurassic succession in Jabal Ayban field, Sabatayn Basin, Yemen, *Egypt. J. Pet.*, 27 (4), 835, 835–851.
- [35] Wang, N., Xu, Y., Li, W., Wang, F., Chen, G., Liu, Y., Cheng, R., and Liu, H., 2022, The compositions of biomarkers and macerals in the first member of the Shahejie Formation in the Liaodong Bay subbasin, Bohai Bay Basin: Implications for biological sources and seawater incursions, *J. Pet. Sci. Eng.*, 218, 110947.
- [36] Schaeffer, P., Bailly, L., Motsch, E., and Adam, P., 2019, The effects of diagenetic aromatization on the carbon and hydrogen isotopic composition of higher plant di- and triterpenoids: Evidence from buried wood, *Org. Geochem.*, 136, 103889.
- [37] Lopes, A.A., Pereira, V.B., Amora-Nogueira, L., Marotta, H., Moreira, L.S., Cordeiro, R.C., Vanini, G., and Azevedo, D.A., 2021, Hydrocarbon sedimentary organic matter composition from different water-type floodplain lakes in the Brazilian Amazon, *Org. Geochem.*, 159, 104287.
- [38] Greenwood, P.F., Shan, C., Holman, A.I., and Grice, K., 2018, The composition and radiolysis impact on aromatic hydrocarbons in sedimentary organic matter from the Mulga Rock (Australia) uranium deposit, *Org. Geochem.*, 123, 103–112.
- [39] Wang, N., Xu, Y.H., Wang, F.L., Liu, Y., Huang, Q., and Huang, X., 2022, Identification and geochemical significance of unusual C₂₄ tetracyclic terpanes in Shahejie Formation source rocks in the Bozhong subbasin, Bohai Bay Basin, *Pet. Sci.*, 19 (5), 1993–2003.
- [40] Xu, M., Hou, D., Lin, X., Liu, J., Ding, W., and Xie, R., 2022, Organic geochemical signatures of source rocks and oil-source correlation in the Papuan Basin, Papua New Guinea, *J. Pet. Sci. Eng.*, 210, 109972.
- [41] Kumar, D., Ghosh, S., Tiwari, B., Varma, A.K., Mathews, R.P., and Chetia, R., 2021, Palaeocene-Eocene organic sedimentary archives of Bikaner-Nagaur Basin, Rajasthan, India: An integrated revelation from biogeochemical and elemental proxies, *Int. J. Coal Geol.*, 247, 103848.
- [42] Morgunova, I., Kursheva, A., Petrova, V., Litvinenko, I., Batova, G., and Renaud, P., 2019, Hydrocarbon Monitoring in Coastal Sediments and Soils Around the City of Tromsø: Complex Molecular Geochemical Approach, *The 29th International Meeting on Organic Geochemistry (IMOG)*, European Association of Organic Geochemist, Gothenburg, Sweden, 1-6 September 2019, 1–2.
- [43] Synnott, D.P., Schwark, L., Dewing, K., Percy, E.L., and Pedersen, P.K., 2021, The diagenetic continuum of hopanoid hydrocarbon transformation from early diagenesis into the oil window, *Geochim. Cosmochim. Acta*, 308, 136–156.
- [44] Liu, B., Vrabec, M., Markič, M., and Püttmann, W., 2019, Reconstruction of paleobotanical and paleoenvironmental changes in the Pliocene Velenje Basin, Slovenia, by molecular and stable isotope analysis of lignites, *Int. J. Coal Geol.*, 206, 31–45.
- [45] Cordova-Gonzalez, A., Birgel, D., Kappler, A., and Peckmann, J., 2020, Carbon stable isotope patterns of cyclic terpenoids: A comparison of cultured alkaliphilic aerobic methanotrophic bacteria and methane-seep environments, *Org. Geochem.*, 139, 103940.

- [46] Samad, S.K., Mishra, D.K., Mathews, R.P., Ghosh, S., Mendhe, V.A., and Varma, A.K., 2020, Geochemical attributes for source rock and palaeoclimatic reconstruction of the Auranga Basin, India, *J. Pet. Sci. Eng.*, 185, 106665.
- [47] Nakamura, H., 2019, Plant-derived triterpenoid biomarkers and their applications in paleoenvironmental reconstructions: Chemotaxonomy, geological alteration, and vegetation reconstruction, *Org. Geochem.*, 35 (2), 11–35.
- [48] French, K.L., Birdwell, J.E., and Whidden, K.J., 2019, Geochemistry of a thermally immature Eagle Ford Group drill core in central Texas, *Org. Geochem.*, 131, 19–33.
- [49] Plet, C., Grice, K., Scarlett, A.G., Ruebsam, W., Holman, A.I., and Schwark, L., 2020, Aromatic hydrocarbons provide new insight into carbonate concretion formation and the impact of eogenesis on organic matter, *Org. Geochem.*, 143, 103961.
- [50] French, K.L., Birdwell, J.E., and Vanden Berg, M.D., 2020, Biomarker similarities between the saline lacustrine Eocene Green River and the Paleoproterozoic Barney Creek Formations, *Geochim. Cosmochim. Acta*, 274, 228–245.
- [51] Xiao, H., Li, M., Wang, T., You, B., Lu, X., and Wang, X., 2022, Organic molecular evidence in the ~1.40 Ga Xiamaling Formation black shales in North China Craton for biological diversity and paleoenvironment of mid-Proterozoic ocean, *Precambrian Res.*, 381, 106848.
- [52] Ghosh, S., Dutta, S., Bhattacharyya, S., Konar, R., and Priya, T., 2022, Paradigms of biomarker and PAH distributions in lower Gondwana bituminous coal lithotypes, *Int. J. Coal Geol.*, 260, 104067.
- [53] Jiang, L., Ding, W., and George, S.C., 2020, Late Cretaceous–Paleogene palaeoclimate reconstruction of the Gippsland Basin, SE Australia, *Palaeogeogr., Palaeoclimatol., Palaeoecol.*, 556, 109885.
- [54] Kumar, S., and Dutta, S., 2021, Utility of comprehensive GC×GC-TOFMS in elucidation of aromatic hydrocarbon biomarkers, *Fuel*, 283, 118890.
- [55] Burhan, R.Y.P., Zetra, Y., and Amini, Y.A., 2020, Paleoenvironmental and maturity indicator of Cepu Block Oil, Wonocolo Formation, East Java Indonesia, *Jurnal Teknologi*, 82 (5), 173–182.
- [56] Murillo, W.A., Horsfield, B., and Vieth-Hillebrand, A., 2019, Unraveling petroleum mixtures from the South Viking Graben, North Sea: A study based on $\delta^{13}\text{C}$ of individual hydrocarbons and molecular data, *Org. Geochem.*, 137, 103900.
- [57] Lopes Martins, L., Schulz, H.M., Portugal Severiano Ribeiro, H.J., Adolphsson do Nascimento, C., Soares de Souza, E., and Feitosa da Cruz, G., 2020, Cadalenes and norcadalenes in organic-rich shales of the Permian Irati Formation (Paraná Basin, Brazil): Tracers for terrestrial input or also indicators of temperature-controlled organic-inorganic interactions, *Org. Geochem.*, 140, 103962.
- [58] Petersen, H.I., Fyhn, M.B.W., Nytoft, H.P., Dybkjær, K., and Nielsen, L.H., 2022, Miocene coals in the Hanoi trough, onshore northern Vietnam: Depositional environment, vegetation, maturity, and source rock quality, *Int. J. Coal Geol.*, 253, 103953.
- [59] Li, Z., Huang, H., and George, S.C., 2022, Organic Geochemistry Unusual occurrence of alkyl-naphthalene isomers in upper Eocene to Oligocene sediments from the western margin of Tasmania, Australia, *Org. Geochem.*, 168, 104418.
- [60] Ding, W., Hou, D., Gan, J., Zhang, Z., and George, S.C., 2022, Aromatic hydrocarbon signatures of the late Miocene-early Pliocene in the Yinggehai Basin, South China Sea: Implications for climate variations, *Mar. Petrol. Geol.*, 142, 105733.
- [61] Simoneit, B.R.T., Otto, A., Menor-Sálvan, C., Oros, D.R., Wilde, V., and Riegel, W., 2021, Composition of resinates from the Eocene Geiseltal brown coal basin, Saxony-Anhalt, Germany and comparison to their possible botanical analogues, *Org. Geochem.*, 152, 104138.
- [62] Lu, Z., Li, Q., Ju, Y., Gu, S., Xia, P., Gao, W., Yan, Z., and Gong, C., 2022, Biodegradation of coal organic matter associated with the generation of secondary biogenic gas in the Huaibei Coalfield, *Fuel*, 323,

- 124281.
- [63] Walters, C.C., Wang, F.C., Higgins, M.B., and Madincea, M.E., 2018, Universal biomarker analysis: Aromatic hydrocarbon, *Org. Geochem.*, 124, 205–214.
- [64] Wakeham, S.G., and Canuel, E.A., 2016, Biogenic polycyclic aromatic hydrocarbons in sediments of the San Joaquin River in California (USA), and current paradigms on their formation, *Environ. Sci. Pollut. Res.*, 23 (11), 10426–10442.
- [65] El Diasty, W.S., Peters, K.E., Moldowan, J.M., Essa, G.I., and Hammad, M.M., 2020, Organic geochemistry of condensates and natural gases in the northwest Nile Delta offshore Egypt, *J. Pet. Sci. Eng.*, 187, 106819.
- [66] Jaroszewicz, E., Bojanowski, M., Marynowski, Łoziński, M.L., and Wysocka, A., 2018, Paleoenvironmental conditions, source and maturation of Neogene organic matter from the siliciclastic deposits of the Orava-Nowy Targ Basin, *Int. J. Coal Geol.*, 196, 288–301.

Integration of Copperas and *Moringa oleifera* Seeds as Hybrid Coagulant for Turbidity and Ammonia Removal from Aquaculture Wastewater

Sofiah Hamzah¹, Nazaitulshila Rasit^{1*}, Nurul Aqilah Mohamad¹, Mohammad Hakim Che Harun¹, Alyza Azzura Abd Rahman Azmi^{1,2}, Nur Hanis Hayati Hairom³, Ahmad Ariff Fahmi Mustofa⁴, Mohd Salleh Amri Zahid⁴, Norhafiza Ilyana Yatim⁵, and Nor Azman Kasan⁵

¹Environmental Sustainable Material Research Interest Group, Faculty of Ocean Engineering, Technology, and Informatics, Universiti Malaysia Terengganu, Kuala Nerus 21030, Malaysia

²Faculty of Science and Marine Environment, Universiti Malaysia Terengganu, Kuala Nerus 21030, Malaysia

³Faculty of Engineering Technology, Universiti Tun Hussein Onn Malaysia, Hab Pendidikan Tinggi Pagoh, Km 1, Jalan Panchor, Muar 84600, Malaysia

⁴Venator Asia Sdn. Bhd., Teluk Kalung, Kemaman 24007, Malaysia

⁵Higher Institution Centre of Excellence (HiCoE), Institute of Tropical Aquaculture and Fisheries, Universiti Malaysia Terengganu, Kuala Nerus 21030, Malaysia

* Corresponding author:

email: nazaitulshila@umt.edu.my

Received: April 4, 2023

Accepted: September 12, 2023

DOI: 10.22146/ijc.83634

Abstract: The rapid development of the aquaculture industry has contributed to the high amount of nutrients in wastewater that subsequently led to eutrophication and deterioration of water quality. Aquaculture wastewater consists of uneaten fish feed, fecal and other excretion or residue of chemicals used. Thus, this study aimed to evaluate the performance of hybrid coagulants of *Moringa oleifera* (MO) and copperas for aquaculture wastewater treatment. In this present study, different formulations of MO and copperas were explored in the coagulation treatment of aquaculture wastewater using a jar test experiment. The FTIR and SEM analysis are used to determine the morphology and surface of MO. This study focuses on the effect of coagulant aids formulation, coagulant dosage, the effect of initial pH and coagulation time on turbidity and ammonia removal in the coagulation of aquaculture wastewater. The finding shows that the highest removal of turbidity and ammonia was obtained with the use of 80% MO and 20% copperas at the condition of initial pH of 6 at 20 min of coagulation time, with the highest percentage removal of 66% and 91%, respectively. The coagulation isotherm of hybrid coagulant 80:20 is well described with the Freundlich isotherm model which describes the surface heterogeneity.

Keywords: aquaculture wastewater; coagulation-flocculation; copperas; *Moringa oleifera*

■ INTRODUCTION

The aquaculture industry is one of the fastest-growing industries all around the world. However, the long-term sustainability of the aquatic environment has raised worries over the environmental impact of this imperative sector because of its negative impact on aquatic ecology and systems. This is due to aquaculture intensification requiring the use of highly nutritious feeds

and other compounds that produce waste that is hard to curb and is harmful to aquatic life in most cases [1]. Most aquaculture systems produce great amounts of wastewater containing compounds such as suspended solids, nitrogen, and phosphorus [2]. Any discharge of wastewater into aquatic ecosystems in the form of effluents may lead to changes in the receiving environment. High organic load in wastewater from aquaculture will contribute to the eutrophication of

receiving water bodies, which causes a lot of havoc in aquatic ecosystems on biodiversity. The aquaculture sector contains a complex mixture of pollutants.

The most common toxic pollutants are ammonia, nitrogen, phosphorus, pathogens, and ammoniacal nitrogen. Ammonia is a colorless gas with a strong scent which contains compounds of nitrogen and hydrogen [3]. Ammonia in water is converted to nitrite and nitrate through the nitrification process by two bacteria, *Nitrosomonas* and *Nitrobacter* [4]. When the levels of nitrogenous compounds (ammonia, nitrite, and nitrate) exceed the prescribed limits can affect aquatic life. One of the main reasons for unexplained losses in hatcheries is the toxicity of ammonia. Although the ammonia molecule is an essential nutrient, excessive amounts of ammonia may accumulate and alter the organism's metabolism or raise the pH level in the body.

Because hazardous contaminants and other factors affecting water quality have a direct impact on the effectiveness of feed and growth rates for fish health and survival. Due to the evident cause of environmental climate change, these characteristics have not remained constant for a while now. There is a need for improvement in the development and transfer of technology in catfish breeding and hatchery to stabilize the supply of fish.

Treatment of wastewater for pollutant removal is very crucial since it can cause a threat to potable drinking water sources, fisheries, and recreational water bodies. Membrane technology [5-6], liquid membrane [7], and adsorption [8-11] are a few of the treatment techniques and technologies utilized to treat wastewater. However, certain technologies already in use still struggle to comply with the standard of discharge, the restrictions that have been set up, difficulty in scaling up, and come at a high cost. Several studies have been conducted for efficient systems for wastewater treatment, including constructed wetland technology [12], the use of fish meal in removing heavy metals [13], microalgae [14], and others [15]. It is believed that wetland was one of the most cost-effective and well-known treatment methods that have been established [16].

Another method for treating aquaculture wastewater is coagulation-flocculation which helps to

remove suspended solids, turbidity, and other inorganic compounds that can disturb the water quality and water ecosystem. Coagulation-flocculation is considered an excellent pre-treatment method for wastewater since there is low energy required, the cost is reasonable, and it is easy to operate. The removal mechanism is primarily caused by cationic hydrolysis products' ability to charge-neutralize negatively charged colloids, which facilitates the formation of microflocs by encouraging early colloidal particle aggregation [17]. Two types of coagulants used for the removal of pollutants are either natural coagulants or chemical coagulants. Using chemical coagulants such as aluminum sulphate (alum) is a very common treatment method that is used mainly in the water treatment process. Inorganic coagulants such as alum, ferrous sulphate, and ferric chloride has been used to recover pollutant removal through coagulation-flocculation and was demonstrated successfully efficient in achieving the aims. However, excessive use of chemical coagulants may be unacceptable for aquaculture purposes as they have negative effects on aquatic life.

It has been demonstrated that a natural coagulant like *Moringa oleifera* (MO) can be utilized to treat effluent from aquaculture mainly to remove ammoniacal nitrogen, phosphorus, and turbidity [18-20]. Treatment sequence of wastewater using MO seeds by coagulation-flocculation to sedimentation-filtration showed maximum turbidity and elimination of suspended materials. Powdered seeds produce less volume of sludge and promote the removal of chemical oxygen demand (COD) [21]. The seeds have successful properties of coagulation that were verified in laboratory studies. The seeds do not hurt humans or animals. It is also very effective in reducing the presence of microorganisms in raw water. The physicochemical treatment shows encouraging pollutant mitigation efficiency. These may be due to relatively active flocs produced at the relatively high dosage of seeds. The extreme flocs are more likely to resist the hydraulic shear forces encountered during filtration.

Water handled with MO seeds is therefore better compared to alum. The seeds did not affect the water's

pH value significantly, but they served as a pH corrector. For comparison, when treated with alum, the pH value decreased to 4.2. It has shown that MO seeds will be more economical and environmentally important for wastewater treatment than aluminum or other chemicals. A by-product of the titanium industry, copperas is chemically known as ferrous sulfate. By lowering the electrostatic surface charge in an acidic or alkaline pH range, the presence of this hydrolyzed metal species can encourage the agglomeration of particles in wastewater. Copperas and MO seeds have lately gained interest in water and wastewater treatment technologies due to their exceptional efficacy and cost-effectiveness. Hybrid components are novel materials with a high potential to treat wastewater when compared to inorganic coagulants and organic flocculants, respectively [22]. There have recently been many previous works of coagulation/flocculation techniques for treating water and wastewater. However, the hybrid materials chosen in this study have not been extensively compared and discussed.

The ultimate objective of this present study is to determine the efficiency of hybrid coagulants (copperas and MO seed) for aquaculture wastewater treatment. Copperas and MO were characterized in terms of morphology and chemical composition, using scanning electron microscopy (SEM), Fourier transform infrared (FTIR), and X-ray diffraction (XRD). The removal of turbidity and ammonia with this hybrid coagulant is being studied at various formulations, dosages, and initial pH levels. The Freundlich and Langmuir isotherm models were utilized in a coagulation equilibrium investigation, and ANOVA was used to statistically validate the data.

■ EXPERIMENTAL SECTION

Materials

The aquaculture wastewater used in this study was obtained from the discharged point of a catfish pond in UMT Hatchery. Aquaculture effluent that was discharged was collected in 40 L plastic containers in an acceptable amount. Before being taken to the lab, the containers were labelled and sealed appropriately. Prior to use, this wastewater was maintained below 4 °C to prevent sample degradation brought on by microbial activity.

Venator Asia Sdn. Bhd., Teluk Kalung, Terengganu, Malaysia, provided the copperas while the analytical grade of calcium hydroxide ($\text{Ca}(\text{OH})_2$), sodium hydroxide (NaOH), and hydrochloric acid (HCl) were acquired from Sigma-Aldrich in the United States.

Instrumentation

A JEOL JSM-6360 LA model SEM was used to analyze the surface morphology of copperas. The sample was transferred to the microscope and viewed at 2,000× magnification after sputtering with gold. FTIR analysis was used to identify the functional groups found in copperas (Shimadzu/IRTracer-100 model). In a sample holder, an FTIR scan was carried out at frequencies ranging from 4,000 to 400 cm^{-1} with a spectral resolution of 4 cm^{-1} .

Procedure

Preparation of hybrid coagulant solution copperas/Moringa oleifera

MO was rinsed with distilled water slowly and dried at 35 °C in an oven, then grounded to obtain a fine powder. The MO powder was dissolved in distilled water to a final concentration of 1000 mg/L and mixed for 30 min using a stirrer to get a uniform solution and the extract was then passed through a muslin cloth. This solution was prepared freshly to avoid the reduction in its coagulation efficiency, and it was kept in a cool place at around 20 °C to avoid viscosity and pH changes. The prepared MO solution was integrated with 1000 ppm copperas solution based on different ratios (100% MO, 100% copperas, 50:50, 80:20 and 20:80 MO:copperas) to form hybrid coagulant.

Coagulation-flocculation process (jar test experiments)

To coagulate aquaculture effluent, flocculation tests were performed using a standard jar-test apparatus with six paddle rotors. For each test run, a 1 L beaker containing 500 mL of wastewater was used. The ambient temperature for all tests was between 24 and 28 °C. Using either an acid (1.0 M HCl) or a base (1.0 M NaOH), the pH value was changed to the desired value. Different coagulant dosages (40–200 mg/L) and the

sample's initial pH (3–8) were used in the jar test. The aquaculture wastewater sample was subjected to 150 rpm of rapid mixing for 10 min, then 20 min of slow mixing at 25 rpm. After coagulation, samples of the treated wastewater were taken for analysis from a depth of 2 cm. Eq. (1) was used to calculate the turbidity and ammonia removal efficiency;

$$\text{Removal (\%)} = \frac{C_i - C_f}{C_i} \times 100\% \quad (1)$$

where C_i and C_f are the initial and final readings, respectively, of turbidity and ammonia.

Determination of aquaculture wastewater characteristics

The characterization of aquaculture wastewater involves two methods: field measurement and laboratory experiments. The tests involved were pH, turbidity, and ammoniacal nitrogen (HACH Method 10031). The pH and turbidity were tested using pH and turbidity meters (Orion AQ3010), respectively, while ammoniacal nitrogen was tested using DR900. All testing was performed in triplicates and the results were presented as the average of three values.

Coagulation equilibrium

The isotherm model, which can also explain the interaction between the coagulant and the sample of aquaculture effluent, can describe coagulation equilibrium. In order to assess the efficacy of two isotherm models, the Freundlich and Langmuir models were used to determine whether coagulation results from multilayer or monolayer development of the coagulant particles. By setting the coagulant and its dosage for wastewater samples at the optimum condition for turbidity reduction, the adsorption experiments were carried out.

Surface heterogeneity of the adsorbates is introduced by the Freundlich isotherm model with a variable energy level distribution of adsorption [23–24]. This model shows whether the coagulant particles have adsorbed the adsorbent in a multilayer formation [23,25]. According to Eq. (2), this isotherm model is an empirical representation of the Langmuir isotherm model.

$$q_e = K_f (C_e)^{1/n} \quad (2)$$

The linear form of the Freundlich isotherm is presented in Eq. (3):

$$\log \log q_e = \log K_f + \frac{1}{n} \log C_e \quad (3)$$

where q_e is the coagulation adsorption capacity (mg/mg), K_f is the Freundlich affinity coefficient (L/mg), C_e is the equilibrium concentrations of turbidity in aquaculture wastewater, and n is the exponential constant of the Freundlich model. Hussain et al. [25] stated that the adsorption intensity, q_e , usually decreases as the values of $1/n$ increase and decreases as K_f decreases. Lin et al. [24] mentioned that favorable adsorption would occur if the value of $1/n$ is less than 1.

The surface homogeneity of the adsorbent serves as the foundation for the Langmuir isotherm model [23]. This model explains how a monolayer form on the adsorbate's adsorbent surface [24–26]. According to Nhut et al. [18], this model also demonstrates that once the adsorbent is linked to the particular adsorbent site, no further adsorbent molecule can occupy the adsorbent site. Once a sorbate molecule resides at a location, no more adsorptions will take place there. The Langmuir isotherm model suggests that the adsorbed molecules do not interact with one another in order to explain adsorption in an aqueous solution [22]. The Langmuir isotherm model was determined as Eq. 4.

$$q_e = \frac{(abC)_e}{(1+aC)_e} \quad (4)$$

The linear form of the Langmuir isotherm is presented in Eq. (5):

$$\frac{1}{q_e} = \frac{1}{(abC)_e} + \frac{1}{b} \quad (5)$$

where a is the Langmuir constant and b is the maximum coagulation value

Statistical analysis

An important step in carrying out various statistical procedures is statistical data analysis. ANOVA is a statistical technique for testing a hypothesis about the model's input parameters by breaking down the total variation in a set of data into components linked to certain sources of variation. ANOVA's null hypothesis states that there are no significant differences between

the groups that were chosen, but the alternative hypothesis holds that there are at least one or more significant differences between the groups that were chosen [22].

■ RESULTS AND DISCUSSION

Characteristics and Properties of Hybrid Coagulant

Fig. 1 shows the surface morphology of MO and copperas viewed under SEM. The morphology of MO (Fig. 1(a)) shows a heterogeneous and relatively porous matrix. This structure facilitates ion adsorption processes due to the interstices and, more importantly, the presence of the seed protein component. The coagulant surface tends to be irregular and rough at some points and at

others smooth. Small pores were found around the edges, indicating the possibility of sorption at a smaller magnitude. Thus, based on these characteristics, it can be concluded that this material has an adequate morphological profile for retaining metal ions.

Copperas morphology shows that this compound has much asperity and is more coarsely grained, creating a large contact area [22]. The depicted image also shows a compact gel network structure which is more favorable for coagulating colloidal particles and forming bridge aggregation between flocs than a branched structure [27].

Using FTIR analysis, it was possible to determine the chemical composition and functional group of copperas and MO, as shown in Fig. 2. Generally, all spectra

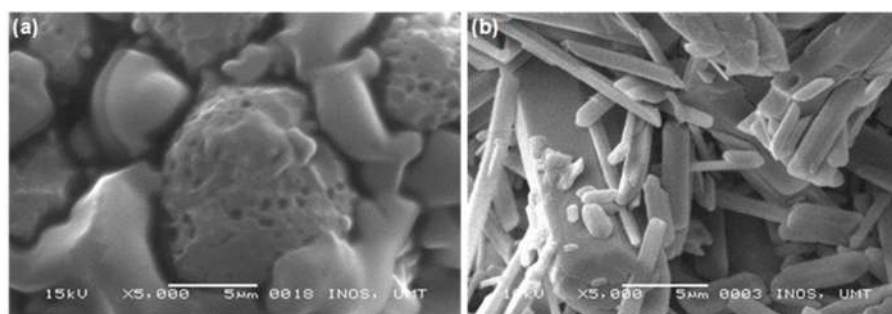


Fig 1. Morphology of (a) MO and (b) copperas

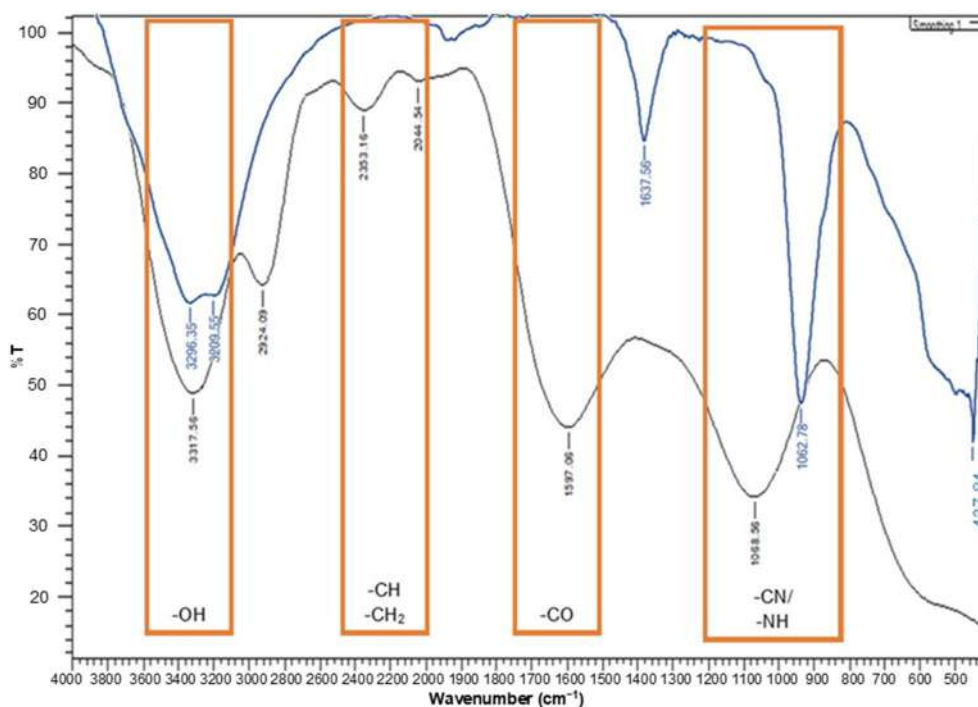


Fig 2. FTIR analysis of MO (black line) and copperas (blue line) [22]

display the same profile, which is a broad band attributed to O–H stretching with a center at $3,317\text{ cm}^{-1}$. This functional group is mostly found in the fatty acid and protein structures of MO seeds. The N–H stretching of amide groups also contributes to this region because of the high protein content in seeds. The C–H of the CH_2 group found in fatty acids is stretched symmetrically and asymmetrically, resulting in peaks at $2,353$ and $2,044\text{ cm}^{-1}$, respectively. Three strong bands with the C–O bond stretching are located between $1,597$ and $1,400\text{ cm}^{-1}$. The fatty acid and protein structures contained the carbonyl group. It is possible to attribute the presence of a peak at $1,068\text{ cm}^{-1}$ to C–N stretching or N–H deformation. The existence of this band demonstrates the MO seeds' protein structure. In the treatment of contaminated water, the high protein content of MO is functional as an electrical cationic.

Physical and Chemical Characteristics of Aquaculture Wastewater

The initial parameters of aquaculture effluent that came from a catfish pond are shown in Table 1. According to high levels of turbidity and ammonia, the aquaculture effluent needed additional treatment before being discharged to a neighboring watercourse. However, research on the technology used to remove ammonia from aquaculture wastewater is relatively limited. Since the coagulant and coagulant aids employed in this study

have strong removal capacities for this type of pollutant, ammonia removal is one of the parameters that has been focused on in the present study.

Coagulation of Aquaculture Wastewater Using Hybrid Coagulant of MO and Copperas

Coagulation of aquaculture wastewater was initially done using different formulations of hybrid coagulant MO/copperas at different dosages varied from 40 to 200 mg/L with 40 mg/L intervals. Other parameters were kept constant, with rapid mixing at 150 rpm for 10 min, slow mixing at 25 rpm for 20 min, and settling down for 30 min.

Effect of Hybrid Coagulant Formula and Coagulant Dosage

The coagulants used were native MO, native copperas and the integrated MO and copperas at different formulations (50:50, 80:20, 20:80). Fig. 3(a) and (b) display the results for this stage of the coagulation study.

Table 1. Physico-chemical characteristics for examined aquaculture wastewater

Parameter	Value
Turbidity	77.0 NTU
Ammonia	2.3 mg/L
pH	6.0

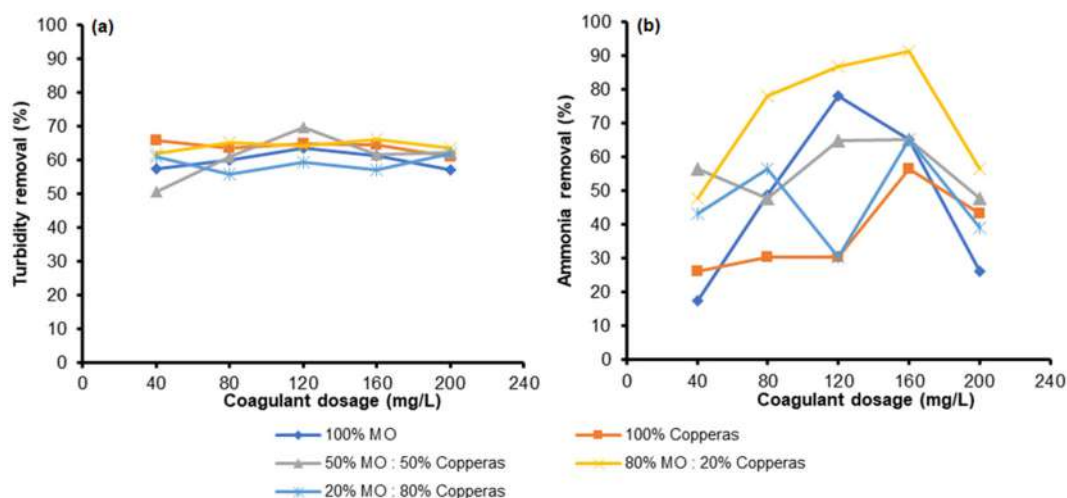


Fig 3. Effects of coagulant formulation and dosage on turbidity removal in aquaculture wastewater treatment (Experimental condition: pH 6, ambient temperature)

From observation, the best removal was obtained by coagulant formulation of 80% MO and 20% copperas at 160 mg/L coagulant dosage. At this condition, optimum turbidity and ammonia removal reached 66% and 91%, respectively. The use of 80% MO as a coagulant provides high cationic polyelectrolytes of protein, which destabilizes the particle charge in wastewater and eventually forms a bridge between the particles. These bridging particles then formed a large aggregate and precipitated during the sedimentation process [28]. The addition of 20% copperas during coagulation results in the formation of corresponding gel such as hydroxides and some positively charged mononuclear and polynuclear species. The positively charged Fe^{2+} interacts with negatively charged colloidal particles present in the wastewater by charge neutralization mechanism and when these hydroxides and complexed hydroxides are settled under gravity, they sweep away and precipitate remaining uncharged or charged colloidal particles from the wastewater. However, at higher dosage of coagulant (more than 160 mg/L) the coagulation activity decreased due to the repulsion between the same charge from the coagulant protein of MO and Fe^{2+} species. The excessive cationic polyelectrolytes were also cause destabilization of aggregates and deflocculation [29].

Effect of Initial pH Wastewater

In this experiment, the pH of aquaculture wastewater was adjusted from pH 3 to 8 at fixed coagulant dosages 160 mg/L of 80:20 MO:copperas. The initial solution of pH was adjusted by H_2SO_4 and NaOH . The pH is one of the most important parameters affecting any wastewater treatment process. According to the result, pH 6 is identified as the optimum pH due to the highest removal efficiency of turbidity and ammonia. As seen from Fig. 4, the percentage removal efficiency of turbidity and ammonia had reached the highest removal of pollutants which was 66 and 91%, respectively. This dependence is closely related to the acid-base properties of various functional groups on the adsorbent surfaces [30]. The literature shows that an aqueous heterogeneous mixture of MO seeds presents various functional groups, mainly amino and acid groups. These groups are capable of interacting with metal ions, which is dependent on the pH. An increase in metal adsorption with increasing pH values can be explained by rivalry between the proton and metal ions for the same functional groups and a decrease in the positive surface charge resulting in a higher electrostatic attraction between the surface and the metal. The pH value of the point of zero charge for the proposed

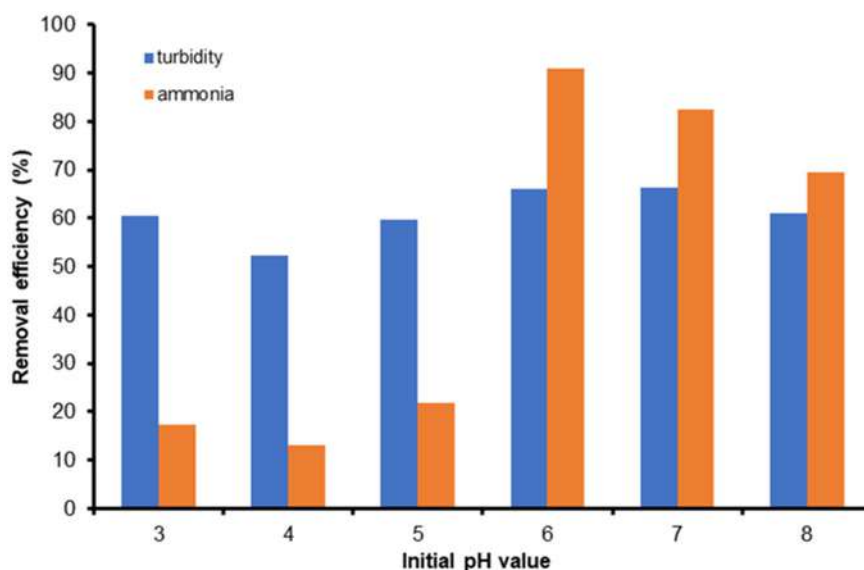


Fig 4. Effects of initial pH on turbidity and ammonia removal in aquaculture wastewater treatment (Experimental conditions: 160 mg/L of 80:20 MO:copperas at ambient temperature)

adsorbent was within the range of 6 to 7. Thus, above this pH range, the surface of the sorbent will be negatively charged and will adsorb positively charged species.

Effect of Coagulation Time

Coagulation time is one of the crucial parameters in the coagulation/flocculation process to ensure that the coagulant is mixed properly in order to treat the sample at the optimal time [31]. This hybrid coagulant showed a good performance as the coagulation time was up to 45 min with the turbidity removal about 80%. For ammonia removal, 80% MO with 20% copperas gave a good performance at a lower coagulation time with 91% removal as represented in Fig. 5. Increasing the

coagulation time resulted in poor removal of ammonia since the pollutant and the coagulant used had a low collision between them hence lowering down the formation of floc during sedimentation [32].

ANOVA

ANOVA is a one-way test used in this study to validate the experimental data for the effect of coagulant dosage, initial pH and coagulation time for the best coagulant which was 80% MO with 20% copperas as tabulated in Tables 1-3. The analysis was accomplished by employing the final value of turbidity and ammonia. The findings showed that there was a significant difference (p -value < 0.05) in all parameters studied, indicating that

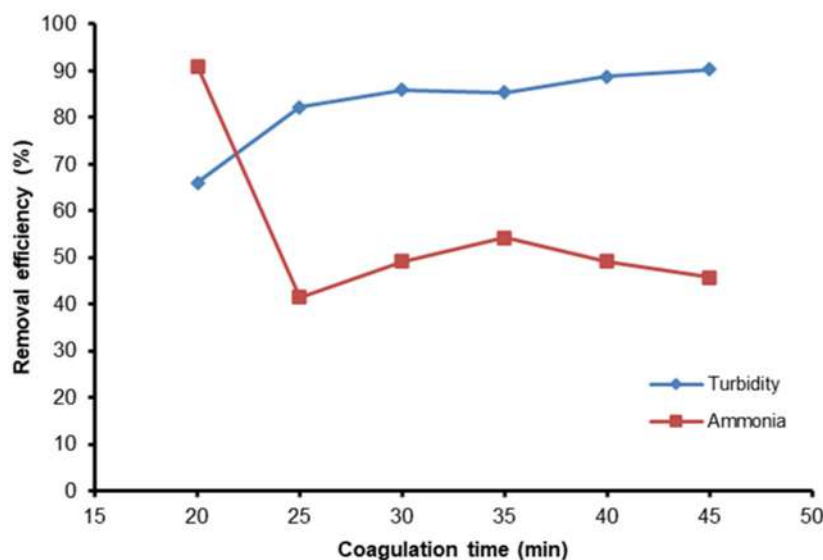


Fig 5. Effects of coagulation time on turbidity and ammonia removal in aquaculture wastewater treatment (Experimental conditions: 160 mg/L of 80:20 MO:copperas at ambient temperature and pH 6)

Table 1. ANOVA test of 80% of MO and 20% of copperas at different coagulant dosage for both turbidity and ammonia removal

Source of variation	Sum of square (SS)	Degree of freedom (DF)	Mean square (MS)	F-test	p-value
Turbidity removal					
Treatment	21372.130	1	21372.130	10.682	0.011385
Error	16006.090	8	2000.762		
Sum	37378.220	9			
Ammonia removal					
Treatment	35617.020	1	35617.020	17.808	0.002916
Error	16000.770	8	2000.097		
Sum	51617.800	9			

Table 2. ANOVA test of 80% of MO and 20% of copperas at different initial pH value for both turbidity and ammonia removal

Source of variation	Sum of square (SS)	Degree of freedom (DF)	Mean square (MS)	F-test	p-value
Turbidity removal					
Treatment	1948.2010	1	1948.201	253.0514	1.99E-08
Error	76.9883	10	7.698833		
Sum	2025.1890	11			
Ammonia removal					
Treatment	51.6675	1	51.6675	26.1541	0.000455
Error	19.7550	10	1.9755		
Sum	71.4225	11			

Table 3. ANOVA test of 80% of MO and 20% of copperas at different coagulation time for both turbidity and ammonia removal

Source of Variation	Sum of square (SS)	Degree of freedom (DF)	Mean square (MS)	F-test	p-value
Turbidity removal					
Treatment	1176.1200	1	1176.1200	17.5159	0.001872
Error	671.4600	10	67.1460		
Sum	1847.5800	11			
Ammonia removal					
Treatment	709.9408	1	709.9408	9.0269	0.013242
Error	786.4683	10	78.6468		
Sum	1496.4090	11			

Table 4. Isotherm model for aquaculture wastewater treated with 80:20 MO:copperas

Isotherm model	Unit	80:20 (MO:copperas)
Langmuir	a	18.93706
	b	0.033385
	R ²	0.499216
Freundlich	n	0.933595
	K _f	0.717376
	R ²	0.992175

the null hypothesis should be rejected which assumes the dosage and initial pH (treatment) were equal for all the parameter removals. This means that the data have a significant difference between the means of groups.

Coagulation Equilibrium

Coagulation equilibrium studies were to evaluate their performance and determine whether coagulation occurs due to multilayer or monolayer formation of the

coagulant particles in describing the interaction between the used coagulant and the aquaculture wastewater sample. The adsorption experiments were conducted by fixing the coagulant and its dosage for wastewater samples at the optimum condition for ammonia removal.

Table 4 shows the coagulation equilibrium studies performed by using both Langmuir and Freundlich isotherm models. As tabulated in Table 4, the Langmuir isotherm model shows the a and b values are positive and stipulated that the 80:20 MO:copperas based on monolayer adsorption supported by Hussain et al. [25]. Fig. 6 represents the linear form of both isotherm models, Langmuir and Freundlich. The coagulation-adsorption analysis revealed that 80:20 MO:copperas showed monolayer formation of the coagulant, which is well-described in the Freundlich Isotherm model, which describes surface heterogeneity.

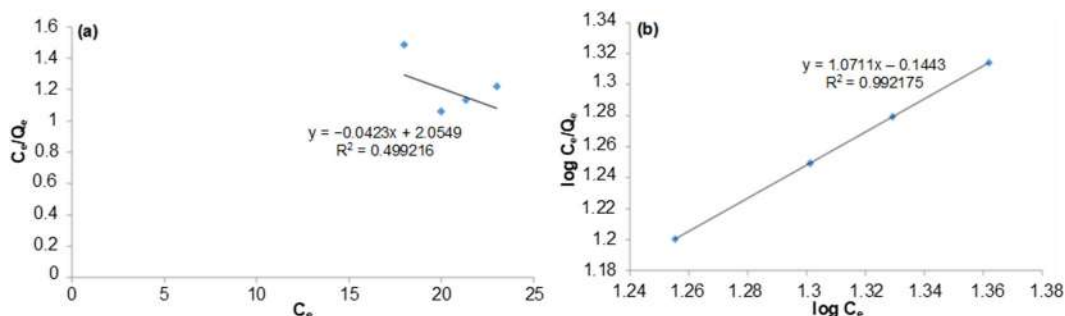


Fig 6. (a) Langmuir and (b) Freundlich Isotherm model for 80:2 MO:copperas in treating aquaculture wastewater

CONCLUSION

Overall results showed that for the aquaculture wastewater sample employing 80:20 MO:copperas as a hybrid coagulant with the optimal conditions for pollutant removal in aquaculture wastewater were 160 mg/L of coagulant dose, pH 6, and 20 min of coagulation time. This ratio of MO:copperas shows monolayer development of the coagulant, which is well-described in the Freundlich isotherm model, according to the coagulation-adsorption analysis. These results could be a baseline research for creating a pilot plant for effective hatchery wastewater treatment as well as important information for the aquaculture sector in implementing efficient chemical treatment.

ACKNOWLEDGMENTS

The authors would like to thank Universiti Malaysia Terengganu for the funding of TAPE-RG (VOT 55325) and Venator Asia Sdn. Bhd. for the contribution and support of this project.

AUTHOR CONTRIBUTIONS

Sofiah Hamzah, Nurul Aqilah Mohamad, and Mohammad Hakim Che Harun conducted the experiment. Alyza Azzura Abd Rahman Azmi, Nur Hanis Hayati Hairom, Ahmad Ariff Fahmi Mustoffa, and Mohd Salleh Amri Zahid conducted the calculations. Norhafiza Ilyana Yatim revised the literature review and analysis section. Nor Azman contributed to the analysis section and proofread the manuscript. Sofiah Hamzah and Nazaitulshila Rasit wrote and revised the overall manuscript prior to publication. All authors agreed to the final version of this manuscript.

REFERENCES

- [1] Omitoyin, B.O., Ajani, E.K., Okeleye, O.I., Akpoilih, B.U., and Ogunjobi, A.A., 2017, Biological treatments of fish farm effluent and its reuse in the culture of Nile tilapia (*Oreochromis niloticus*), *J. Aquacult. Res. Dev.*, 8 (2), 1000469.
- [2] Turcios, A.E., and Papenbrock, J., 2014, Sustainable treatment of aquaculture effluents—What can we learn from the past for the future?, *Sustainability*, 6 (2), 836–856.
- [3] Li, Z., Wang, C., Qiu, J., Ma, Y., Wang, C., Sun, X., Li, K., Ning, P., and Wang, F., 2023, Advances in selective catalytic oxidation of ammonia (NH₃-SCO): A review of catalyst structure-activity relationship and design principles, *Chin. Chem. Lett.*, 35 (1), 108432.
- [4] Romano, A., Ortiz, I., and Urtiaga, A.M., 2021, Comprehensive kinetics of electrochemically assisted ammonia removal in marine aquaculture recirculating systems, *J. Electroanal. Chem.*, 897, 115619.
- [5] Ali, A., Awang, M., Mat, R., Johari, A., Kamaruddin, M.J., and Wan Sulaiman, W.R., 2014, Influence of hydrophilic polymer on pure water permeation, permeability coefficient, and porosity of polysulfone blend membranes, *Adv. Mater. Res.*, 931-932, 168–172.
- [6] Rakcho, Y., Mouiya, M., Bouazizi, A., Abouliatim, Y., Sehaqui, H., Mansouri, S., Benhammou, A., Hannache, H., Alami, J., and Abourriche, A., 2023, Treatment of seawater and wastewater using a novel low-cost ceramic membrane fabricated with red clay and tea waste, *Arabian J. Chem.*, 16 (11), 105277.

- [7] Othman, N., Chui Heng, L., Mohamed Noah, N.F., Zing Yi, O., Jusoh, N., Nasruddin, N.A., Ali, N., and Hamzah, S., 2015, Removal of phenol from wastewater by supported liquid membrane process, *Jurnal Teknologi*, 74 (7), 117–121.
- [8] Mohd Azmi, L.H., Williams, D.R., and Ladewig, B.P., 2021, Polymer-assisted modification of metal-organic framework MIL-96 (Al): Influence of HPAM concentration on particle size, crystal morphology and removal of harmful environmental pollutant PFOA, *Chemosphere*, 262, 128072.
- [9] Mustapha, S., Shuaib, D.T., Ndamitso, M.M., Etsuyankpa, M.B., Sumaila, A., Mohammed, U.M., and Nasirudeen, M.B., 2019, Adsorption isotherm, kinetic and thermodynamic studies for the removal of Pb(II), Cd(II), Zn(II) and Cu(II) ions from aqueous solutions using *Albizia lebbbeck* pods, *Appl. Water Sci.*, 9 (6), 142.
- [10] Hamzah, S., Yatim, N.I., Alias, M., and Ali, A., 2019, Extraction of hydroxyapatite from fish scales and its integration with rice husk for ammonia removal in aquaculture wastewater, *Indones. J. Chem.*, 19 (4), 1019–1030.
- [11] Ali, A., Ing, A.W.C., Abdullah, W.R.W., Hamzah, S., and Azaman, F., 2020, Preparation of high-performance adsorbent from low-cost agricultural waste (peanut husk) using full factorial design: Application to dye removal, *Biointerface Res. Appl. Chem.*, 10 (6), 6619–6628.
- [12] Wu, H., Fan, J., Zhang, J., Ngo, H.H., Guo, W., Liang, S., Hu, Z., and Liu, H., 2015, Strategies and techniques to enhance constructed wetland performance for sustainable wastewater treatment, *Environ. Sci. Pollut. Res.*, 22 (19), 14637–14650.
- [13] Zhang, S., Ding, J., Razanajatovo, R.M., Jiang, H., Zou, H., and Zhu, W., 2019, Interactive effects of polystyrene microplastics and roxithromycin on bioaccumulation and biochemical status in the freshwater fish red tilapia (*Oreochromis niloticus*), *Sci. Total Environ.*, 648, 1431–1439.
- [14] Han, P., Lu, Q., Fan, L., and Zhou, W., 2019, A Review on the use of microalgae for sustainable aquaculture, *Appl. Sci.*, 9 (11), 2377.
- [15] Chatla, D., Padmavathi, P., and Srinu, G., 2020, “Wastewater Treatment Techniques for Sustainable Aquaculture” in *Waste Management as Economic Industry Towards Circular Economy*, Eds. Ghosh, S.K., Springer Singapore, Singapore, 159–166.
- [16] Waly, M.M., Ahmed, T., Abunada, Z., Mickovski, S.B., and Thomson, C., 2022, Constructed wetland for sustainable and low-cost wastewater treatment: Review article, *Land*, 11 (9), 1388.
- [17] Gibson, T.F., Watanabe, W.O., Losordo, T.M., Whitehead, R.F., and Carroll, P.M., 2020, Evaluation of chemical polymers as coagulation aids to remove suspended solids from marine finfish recirculating aquaculture system discharge using a geotextile bag, *Aquacult. Eng.*, 90, 102065.
- [18] Nhut, H.T., Hung, N.T.Q., Lap, B.Q., Han, L.T.N., Tri, T.Q., Bang, N.H.K., Hiep, N.T., and Ky, N.M., 2021, Use of *Moringa oleifera* seeds powder as bio-coagulants for the surface water treatment, *Int. J. Environ. Sci. Technol.*, 18 (8), 2173–2180.
- [19] Karnena, M.K., Konni, M., and Dwarapureddi, B.K., 2022, Blend of natural coagulants as a sustainable solution for challenges of pollution from aquaculture wastewater, *Appl. Water Sci.*, 12 (3), 47.
- [20] Aziz Zaid, A.Q., and Ghazali, S., 2019, Preliminary investigation of water treatment using *Moringa oleifera* seeds powder as natural coagulant: A case study of Belat River, Malaysia, *Int. J. Eng. Sci.*, 8 (2), 79–85.
- [21] Bhuptawat, H., Folkard, G.K., and Chaudhari, S., 2007, Innovative physico-chemical treatment of wastewater incorporating *Moringa oleifera* seed coagulant, *J. Hazard. Mater.*, 142 (1-2), 477–482.
- [22] Mohamad, N.A., Hamzah, S., Che Harun, M.H., Ali, A., Rasit, N., Awang, M., Wan Abd. Rahman, W.R., Azmi, A.A.A.R., Abu Habib, A.A., Amri Zahid, M.S., Fahmi Mustofa, A.A., Latfi, S.A., Mohd Aripin, S., and Saad, R., 2021, Integration of copperas and calcium hydroxide as a chemical coagulant and coagulant aid for efficient treatment of palm oil mill effluent, *Chemosphere*, 281, 130873.
- [23] Hossain, M.S., Omar, F., Asis, A.J., Bachmann, R.T.,

- Islam Sarker, M.Z., and Ab Kadir, M.O., 2019, Effective treatment of palm oil mill effluent using $\text{FeSO}_4 \cdot 7\text{H}_2\text{O}$ waste from titanium oxide industry: Coagulation adsorption isotherm and kinetics studies, *J. Cleaner Prod.*, 219, 86–98.
- [24] Lin, J., Zhan, Y., and Zhu, Z., 2011, Adsorption characteristics of copper(II) ions from aqueous solution onto humic acid-immobilized surfactant-modified zeolite, *Colloids Surf., A*, 384 (1-3), 9–16.
- [25] Hussain, S., van Leeuwen, J., Chow, C., Beecham, S., Kamruzzaman, M., Wang, D., Drikas, M., and Aryal, R., 2013, Removal of organic contaminants from river and reservoir waters by three different aluminum-based metal salts: Coagulation adsorption and kinetics studies, *Chem. Eng. J.*, 225, 394–405.
- [26] Gök, Ö., Özcan, A., Erdem, B., and Özcan, A.S., 2008, Prediction of the kinetics, equilibrium and thermodynamic parameters of adsorption of copper (II) ions onto 8-hydroxy quinoline immobilized bentonite, *Colloids Surf., A*, 317 (1-3), 174–185.
- [27] Zhu, G., Zheng, H., Zhang, Z., Tshukudu, T., Zhang, P., and Xiang, X., 2011, Characterization and coagulation–flocculation behavior of polymeric aluminum ferric sulfate (PAFS), *Chem. Eng. J.*, 178, 50–59.
- [28] Lee, C.S., Robinson, J., and Chong, M.F., 2014, A review on application of flocculants in wastewater treatment, *Process Saf. Environ. Prot.*, 92 (6), 489–508.
- [29] Ostolska, I., and Wiśniewska, M., 2014, Application of the zeta potential measurements to explanation of colloidal Cr_2O_3 stability mechanism in the presence of the ionic polyamino acids, *Colloid. Polym. Sci.*, 292 (10), 2453–2464.
- [30] Wang, L.L., Wang, L.F., Ren, X.M., Ye, X.D., Li, W.W., Yuan, S.J., Sun, M., Sheng, G.P., Yu, H.Q., and Wang, X.K., 2012, pH Dependence of structure and surface properties of microbial EPS, *Environ. Sci. Technol.*, 46 (2), 737–744.
- [31] Mohamad, N.A., Hamzah, S., Che Harun, M.H., Ali, A., Rasit, N., Awang, M., Wan Abdul Rahman, W.R., Abd. Rahman Azmi, A.A., Zahid, M.S.A., Mustofa, A.A.F., Ahmed Latfi, S., Mohd Aripin, S., and Saad, R., 2021, Copperas as iron-based coagulant for water and wastewater treatment: A review, *Biointerface Res. Appl. Chem.*, 12 (3), 4155–4176.
- [32] Ngteni, R., Hossain, M.S., Ab Kadir, M.O., Asis, A.J., and Tajudin, Z., 2020, Kinetics and isotherm modeling for the treatment of rubber processing effluent using iron(II) sulphate waste as a coagulant, *Water*, 12 (6), 1747.

The Comparative of α - and β -Cyclodextrin as Stabilizing Agents on AuNPs and Application as Colorimetric Sensors for Fe^{3+} in Tap Water

Adhi Maulana Yusuf^{1,2}, Satrio Kuntolaksono², and Agustina Sus Andreani^{1*}

¹Research Centre for Chemistry, National Research and Innovation Agency (BRIN), Kawasan Puspiptek, Building 452, Serpong, Banten 15314, Indonesia

²Department of Chemical Engineering, Institut Teknologi Indonesia, Jl. Raya Puspiptek, Serpong, Banten 15314, Indonesia

* Corresponding author:

email: agus147@brin.go.id

Received: April 10, 2023

Accepted: July 17, 2023

DOI: 10.22146/ijc.83796

Abstract: In this study, AuNPs were reduced using ortho-hydroxybenzoic acid (o-HBA) and various stabilizing agents (α -CDs and β -CDs). The stability, shape, size, and sensitivity of the Fe^{3+} detection of AuNPs α -CDs and AuNP β -CDs are compared. Both nanomaterials were characterized using ultraviolet-visible (UV-vis) spectroscopy, Fourier transform infrared (FTIR) spectroscopy, and transmission electron microscopes (TEM). After the addition of Fe^{3+} , the absorption rate of surface plasma resonance (SPR) increased to 524 nm, and the color of AuNPs α -CDs and AuNPs β -CDs was changed from pink to red and purple, respectively. AuNPs α -CDs are more uniform in shape and size than AuNPs β -CDs with a size of 23.34 nm. Further, AuNPs α -CDs are more stable, and the absorption rate at 524 nm wavelength decreases by 17.76%. AuNPs α -CDs have a good linear relationship with a linear regression coefficient of 0.996. The sensitivity of AuNPs α -CDs was good with LoD and LoQ both with 1.21 and 4.02 ppm, respectively. These results show that the sensor is superior in determining Fe^{3+} . In addition, AuNPs α -CDs were used to detect Fe^{3+} in the tap water in South Tangerang, Banten, Indonesia.

Keywords: AuNPs α -CDs; AuNPs β -CDs; colorimetric detection; Fe^{3+} ; tap water

■ INTRODUCTION

Heavy metals have become the most dangerous chemical for water bodies, soil, and air due to the growth of contemporary industry [1]. Heavy metals are non-biodegradable and cannot be digested, therefore, they will be accumulated in living organisms after entering their food chain [2] which has become an issue due to their significant impact on environmental and health problems [3]. An example of a toxic heavy metal is elemental iron (Fe). Fe element is the most important element and is also important in the natural environment [4]. Ion Fe^{3+} plays critical roles in many pathological and physiological processes, including cell metabolism, enzyme catalysis, nucleic acid synthesis, and electron transport [5]. Neither excess accumulation nor lack of Fe^{3+} leads to several diseases, such as cancer, Parkinson's syndrome, Alzheimer's disease, and anemia [6-7]. Therefore, it must

be controlled at a significant level to avoid disease. This condition has been driving researchers and academicians to focus on constructive methods for the qualitative and quantitative detection of Fe^{3+} ions [8]. On the other hand, several methods have been developed for the determination of Fe^{3+} , including inductively coupled plasma mass spectroscopy (ICP-MS) [9], high-performance liquid chromatography (HPLC) [10], atomic absorption spectroscopy (AAS) [11], fluorescence spectroscopic analysis [12], electrochemical methods [13], and UV-visible spectrophotometer [14]. However, these methods require advanced equipment, technical expertise, and need time for sample preparation steps. Therefore, it is thought that these techniques are not economical and user-friendly. In order to overcome these disadvantages, the colorimetric method has been developed for the detection of metal ions in aqueous solutions [15]. Nowadays, metallic nanoparticle sensors

have been widely used for colorimetric detection of Fe^{3+} ions due to their strong surface plasmon resonance (SPR), stable dispersion, biocompatibility, and controllable physical/chemical properties [16]. Due to this reason, colorimetric sensors are the best way to detect Fe^{3+} ions.

In recent years, gold nanoparticles (AuNPs) have attracted a lot of attention as research materials recently and have been widely used in a wide range of applications, such as sensing, electronics, surface-enhanced Raman spectroscopy, drug delivery, bioimaging, catalysis, colorimetric sensors, gene therapy, and so on [17]. The AuNPs exhibit specific optical characteristics in the 380–750 nm wavelength region (visible region). The SPR phenomenon is the result of surface plasmon confinement near a nanoparticle in which the size of the nanoparticle is smaller than the wavelength of incident light; this is known as the optical characteristics of the metallic nanoparticles. This phenomenon stems from the coherent oscillation of the surface conduction electrons excited by electromagnetic radiation. This phenomenon can be found in materials with a negative real and small positive imaginary dielectric constant [18]. The mechanism of SPR sensors is based on the sensitivity of the frequency of the oscillating electron to the environment of the plasmonic nanoparticles [19]. The dependency of frequency and intensity of the surface plasmon resonance adsorption bands on the type, shape, size, and size distribution of the nanoparticles provide a wide variety of sensing applications [20]. Additionally, AuNPs can be used to provide a method for detecting iron concentration in tap water samples.

Cyclodextrins (CDs) are cyclic oligosaccharides consisting of (α -1,4)-linked D-glucopyranose units. The most common natural CDs and the only ones used in pharmaceutical products are α -CDs and β -CDs consisting of 6 and 7 D-glucopyranose units. The α -CDs and β -CDs are doughnut-shaped molecules with a hydrophilic outer surface and a slightly lipophilic central cavity. The outside of the CDs toroid is hydrophilic due to the hydroxyl groups, giving the molecules with good water solubility, whereas the inside is relatively hydrophobic because of the glycosidic oxygen bridges [21]. CDs are non-toxic, biodegradable and biocompatible, along with the

collective effects of inclusion, size specificity, controlled release capability, and transport properties, making them suitable as host molecules [22].

Both α - and β -CDs can be used as the stabilizing agent to synthesize AuNPs. For instance, the work of Gopalan [23] using β -CDs to stabilize metal nanoparticles (AuNPs and AgNPs), concluding gold and silver nanoparticles are relatively stable and make it possible to control the size and distribution of the nanoparticles using β -CDs as a stabilizer. Also, Liu et al. [24] report control of the size and distribution of AuNPs were synthesized by the reduction of hydrogen tetrachloroaurate(III) trihydrate by sodium citrate and different CDs (α -, β - and γ -) used as the stabilizer, concluding the main reason for why cyclodextrins stabilize gold colloids is considered to be hydrophobic-hydrophobic interactions between CDs and AuNPs. The work of Lakkakula et al. [25] synthesized gold nanoclusters using β -CDs to stabilize for bioimaging and selective label-free intracellular sensing of Co^{2+} ions, concluding highly selective, rapid detection method using gold nanoclusters stabilized by CD and highly biocompatible with did not affect cell growth phases. Furthermore, Co^{2+} can be detected fast (within 5 min) with high sensitivity and selectivity.

In this study, we described the fabrication of AuNPs using *ortho*-hydroxybenzoic acid (*o*-HBA) with α -CDs and β -CDs, namely AuNPs α -CDs and AuNPs β -CDs. The *o*-HBA contains hydroxyl phenolic and carboxylate functional groups that would be suitable to act as reducing. Furthermore, we also compare the synthesis of AuNPs with a combination of α -CDs and β -CDs to act as stabilizers to obtain stability, sensitivity, selectivity, LoD (limit of detection), and LoQ (limit of quantitation). In the last, AuNPs combination with α -CDs was utilized to determine Fe^{3+} in tap waters.

■ EXPERIMENTAL SECTION

Materials

The materials used in this study were *o*-hydroxybenzoic acid from Central Drug House, New Delhi, India. α -CDs, β -CDs, sodium hydroxide, HAuCl_4 , and ethylenediaminetetraacetic acid (EDTA) were

purchased from Sigma-Aldrich. The standard solutions like Fe^{3+} , Ni^{2+} , Cd^{2+} , Pb^{2+} , Cu^{2+} , Sn^{2+} , Co^{2+} , and Mg^{2+} were obtained from Merck KGaA, Darmstadt, Germany. HCl and HNO_3 were purchased from Mallinckrodt. All these chemical agents were used as received.

Instrumentation

The instrumentations used in this study were ultraviolet-visible (UV-vis) spectra using Agilent Cary 60 UV-vis spectroscopy between 200–800 nm range. The size distribution and morphology of nanoparticles were analyzed by transmission electron microscope (TEM) Tecnai G2 20S-Twin Function. Fourier transform infrared spectroscopy (FTIR) spectra were measured using Shimadzu IR Prestige 21 in the 400–4000 cm^{-1} range. The Fe^{3+} content of the tap water samples was determined using an Agilent 280FS AA.

Procedure

Synthesis of AuNPs-CDs

The synthesis of AuNPs α -CDs and AuNPs β -CDs was carried out by mixing 100 ppm HAuCl_4 , 0.01 M *o*-HBA at pH 12, and a concentration of 0.02 M CDs (α or β) with the volume ratio of 1:1:1 in a water bath at 98 °C for 20 min.

Stability of AuNPs-CDs

The stability of AuNPs α -CDs and AuNPs β -CDs was carried out by storing the synthesized AuNPs for 3 months in the refrigerator at 4 °C, then examining them with UV-vis spectrometry to compare with the SPR spectra results of the AuNPs-CDs when they were synthesized.

Colorimetric response of AuNPs-CDs towards metals

The synthesized AuNPs α -CDs and AuNPs β -CDs were evaluated for their colorimetric response to Fe^{3+} , Mg^{2+} , Ni^{2+} , Cd^{2+} , Pb^{2+} , Cu^{2+} , Sn^{2+} , and Co^{2+} . One mL of 10 ppm heavy metal solution at room temperature was combined with 1 mL of AuNPs α -CDs and β -CDs synthesized under optimum conditions (100 ppm HAuCl_4 , 0.01 M *o*-HBA at pH 12, and 0.02 M α or β CDs with a 1:1:1 volume ratio). The combination was then shaken to homogenization and analyzed using UV-vis spectrometry.

Other metal ion interference in the reaction of AuNPs-CDs with Fe^{3+}

The interference is evaluated by including additional heavy metal ions in the AuNPs α -CDs + Fe^{3+} and AuNPs β -CDs + Fe^{3+} . One mL of Fe^{3+} (10 ppm) and 1 mL of each of the additional (10 ppm) heavy metal ions: Mg^{2+} , Ni^{2+} , Cd^{2+} , Pb^{2+} , Cu^{2+} , Sn^{2+} , and Co^{2+} were added to the mixture with a 2:1:1 volume ratio, which was then shaken to homogenization and subjected to UV-vis spectrometric analysis.

Analytical performance

For the calibration plot, the absorbance values at 524 nm versus the concentration of Fe^{3+} were applied. The LoD and LoQ were determined from three times the standard deviation of the blank signal and ten times the standard deviation of the blank signal, respectively [26]. The LoD and LoQ of the developed colorimetric sensor were calculated using Eq. (1) and (2):

$$\text{LoD} = 3 \times \frac{S_y}{a} \quad (1)$$

$$\text{LoQ} = 10 \times \frac{S_y}{a} \quad (2)$$

where S_y is the standard deviation, and a is the slope of the calibration curve, were used to estimate the LoD and LoQ with variation in concentration of Fe^{3+} (2, 6, 10, 14, 18 ppm). Three times of the detection Fe^{3+} standard solution analysis using AuNPs α -CDs and AuNPs β -CDs under ideal conditions were tested for repeatability and reproducibility. The spiking method was used to determine the accuracy parameters. In tap water, the measurement of the Fe^{3+} standard solution's recovery value was analyzed.

Reusability of AuNPs-CDs as Fe^{3+} colorimetric sensor

The reusability test was performed by introducing 1 mL of Fe^{3+} 10 ppm and 1 mL of EDTA 25 ppm to 1 mL of AuNPs α -CDs and adding 1 mL of EDTA 40 ppm to AuNPs β -CDs with a 1:1 volume ratio. The resulting mixture was then homogenized by shaking and analyzed using UV-vis spectrometry.

Application test to tap water

Three water samples collected from different tap water areas in South Tangerang, Banten, Indonesia, were filtered with 0.45 μm filter paper and preserved with

HNO₃ to pH < 2. Samples were analyzed by AAS to compare the results. The application test was performed by 1 mL samples added with 1 mL of AuNPs α -CDs analyzed by UV-vis spectrometry.

RESULTS AND DISCUSSION

Synthesis of AuNPs-CDs

o-HBA was chosen as the reducing agent of AuNPs due to its ability to convert Au³⁺ to Au⁰ with an optimization peak which is found in *o*-HBA at pH 12 [27]. α - and β -CDs were selected as a stabilizer because CDs are hollow compounds that have steric hindrance, so they can stabilize the nanoparticles. After the production of AuNPs α -CDs and β -CDs, the maximum wavelength for the SPR is detected at 524 nm which is included in the specific optical SPR of AuNPs in the wavelength region of 350–750 nm (visible region) [18] with an absorbance of 0.49 for AuNPs α -CDs and 0.51 for AuNPs β -CDs with the color of the resulting solution is bright pink (Fig. 1). The size of AuNPs α -CDs and β -CDs was relatively small because the SPR peak was sharp [28]. The size of AuNPs α -CDs and β -CDs was confirmed by the TEM.

The stability of AuNPs after 3 months of incubation of AuNPs α -CDs and AuNPs β -CDs in the refrigerator at 4 °C did not change the color solution. There is a decrease in absorbance at the same wavelength at 524 nm from 0.49 to 0.40 (17.76%) for AuNPs α -CDs and from 0.51 to 0.39 (22.95%) for AuNPs β -CDs. Thus, AuNPs α -CDs are

more stable than AuNPs β -CDs (Fig. 2).

After testing using TEM, the average results of nanoparticle size for AuNPs α -CDs and AuNPs β -CDs were 23.34 and 40.74 nm, respectively. The shape of the AuNPs α -CDs is spherical, and the shape of the AuNPs β -CDs is various (triangle, hexagon, and square). Thus, AuNPs α -CDs nanoparticles are more uniform in shape than AuNPs β -CDs (Fig. 3).

Colorimetric Response of AuNPs-CDs toward Metals

The comparison of AuNPs using different stabilizers of α -CDs and β -CDs with the presence of heavy

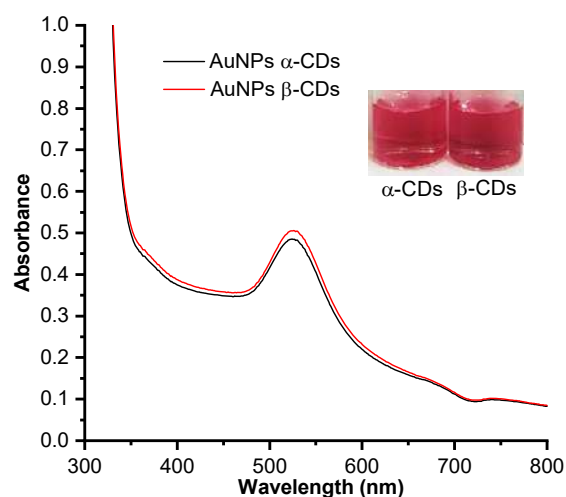


Fig 1. The UV-vis spectra of AuNPs α -CDs and AuNPs β -CDs with their color solution as inset

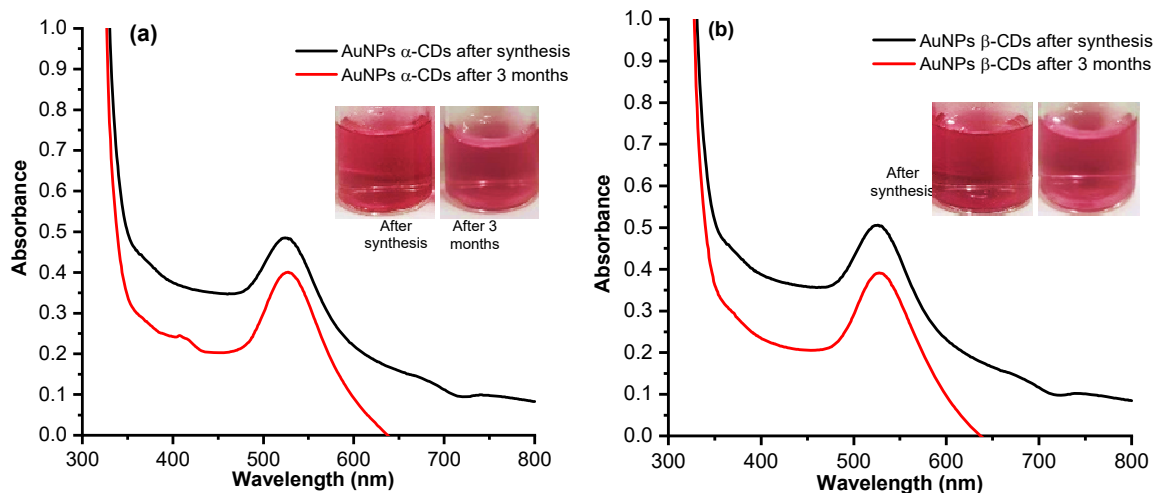


Fig 2. SPR spectra of the stability of AuNPs after 3 months incubation (a) AuNPs α -CDs and (b) AuNPs β -CDs with their color solution as inset

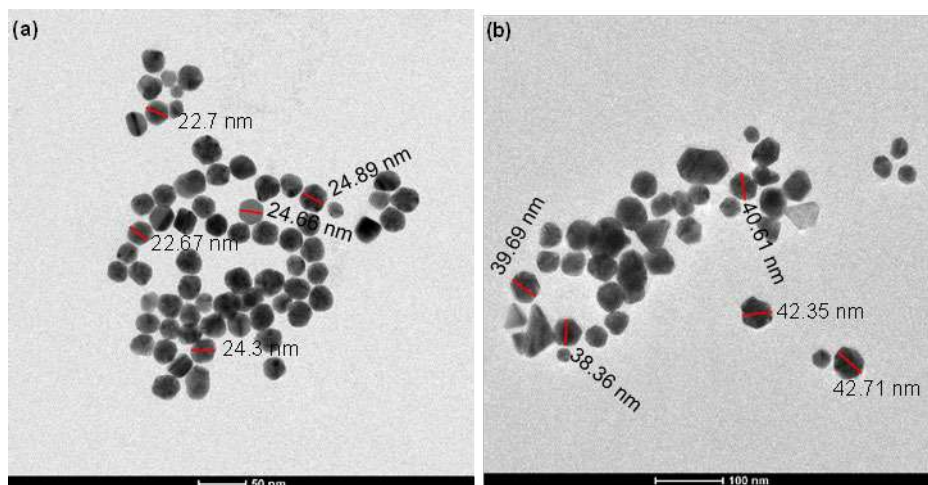


Fig 3. TEM images of (a) AuNPs α -CDs and (b) AuNPs β -CDs

metal ions. Several heavy metal ions such as Fe^{3+} , Mg^{2+} , Ni^{2+} , Cd^{2+} , Pb^{2+} , Cu^{2+} , Sn^{2+} , and Co^{2+} with a concentration of 10 ppm were added with AuNPs-CDs in a 1:1 ratio volume. The SPR of AuNPs α -CDs and AuNPs β -CDs before being added with metal ions are 524 nm. The only metal ions that changed the color and absorbance of AuNPs-CDs at 524 nm were Fe^{3+} [29-30]. The color of AuNPs α -CDs and AuNPs β -CDs were changed from bright pink to red and purple, respectively. The response time of color change by the addition of Fe^{3+} is about 2 s because there was a rapid color change when Fe^{3+} drops

into AuNPs (less than 1 min, rapid detection). Moreover, the change in color is visible to the naked eye (Fig. 4). On the other hand, the selectivity of AuNPs α -CDs and AuNPs β -CDs with the addition of several heavy metal ions. Some heavy metal ions did not change the absorbance of AuNPs α -CDs and AuNPs β -CDs at 524 nm. However, only Fe^{3+} increases the absorbance of the AuNPs α -CDs and AuNPs β -CDs at 524 nm from 0.18 to 0.37 and 0.23 to 0.39, respectively. This indicates that AuNPs α -CDs and AuNPs β -CDs are selective for detecting ion Fe^{3+} (Fig. 5).

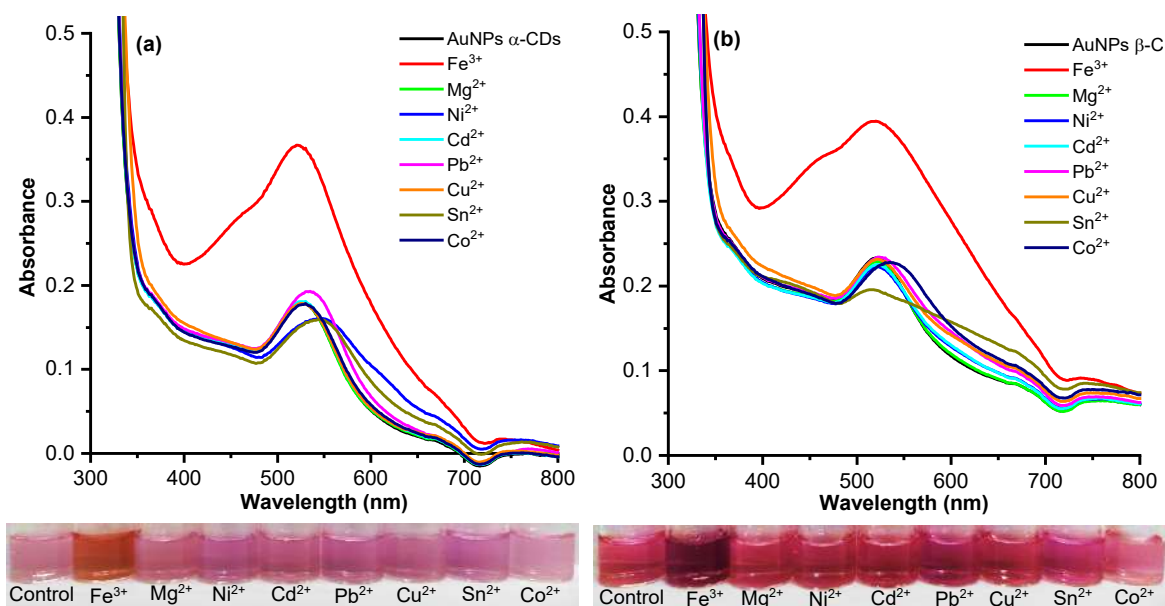


Fig 4. The UV-vis spectra of AuNPs using different stabilizer agents, (a) α -CDs and (b) β -CDs in the presence of various metal ions (10 ppm)

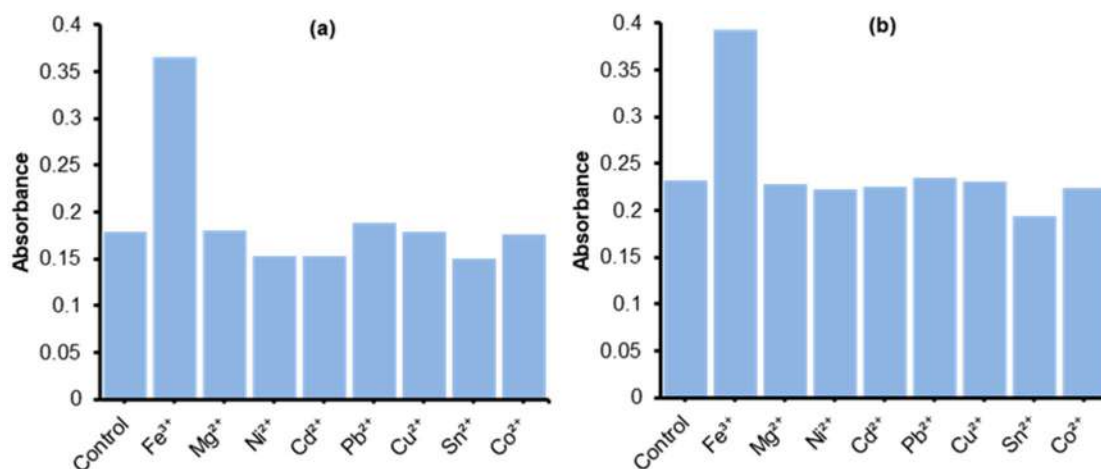


Fig 5. The selectivity of AuNPs in the presence of different stabilizers, (a) α -CDs and (b) β -CDs and metal ions concentration of 10 ppm from the absorbance data at 524 nm

Other Metal Ions Interference in the Reaction of AuNPs-CDs with Fe³⁺

The other metal ions were added, and their effects on the selectivity of AuNPs α -CDs or AuNPs β -CDs towards Fe³⁺ were investigated using a UV-vis spectrophotometer three times. It was shown that the absorbance of AuNPs α -CDs or AuNPs β -CDs with Fe³⁺ was not significantly affected by the addition of the other metal ions (Fig. 6). Thus, under the optimum conditions of Fe³⁺ sensing using AuNPs α -CDs or AuNPs β -CDs, the addition of other metal ions does not cause interference which proves good selectivity of AuNPs α -CDs or AuNPs β -CDs for colorimetric sensors of Fe³⁺.

Analytical Performance

The dynamic linear range of the calibration curve is one crucial factor to consider when assessing the effectiveness of AuNPs α -CDs and AuNPs β -CDs as colorimetric sensors of Fe³⁺. Changes in the absorbance (Δ Abs) of AuNPs α -CDs and AuNPs β -CDs at 524 nm towards the changes in Fe³⁺ concentration were monitored with UV-vis spectrometry. As the Fe³⁺ concentration increased, the color changed AuNPs α -CDs and AuNPs β -CDs to red and purple, respectively, and the absorbance at 524 nm increased. The Δ absorbance of AuNPs α -CDs and AuNPs β -CDs versus concentration of Fe³⁺ was plotted as a linear calibration

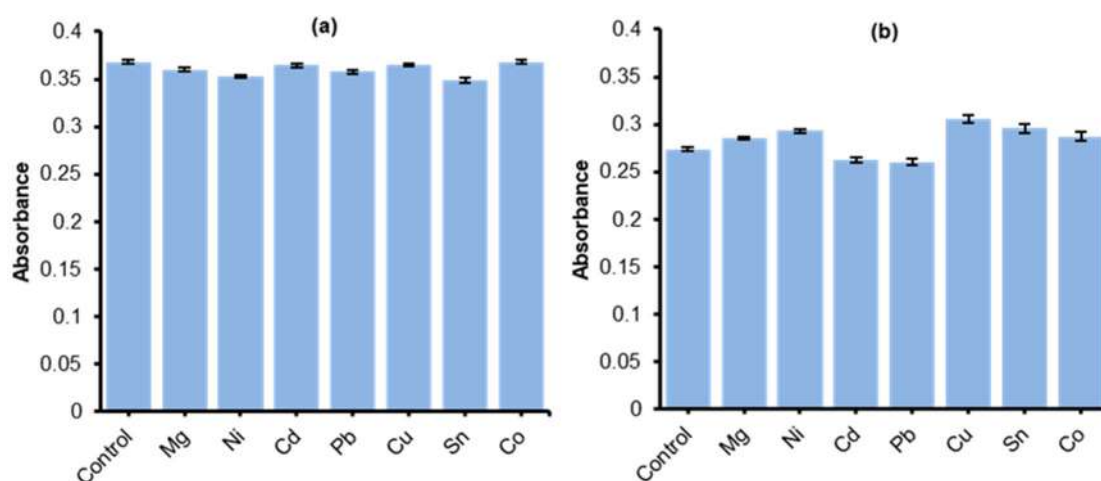


Fig 6. The interference of AuNPs in the presence of different stabilizers, (a) α -CDs and (b) β -CDs and metal ions concentration of 10 ppm from the absorbance data at 524 nm

plot in the range of 2–18 ppm. The rise in absorbance following the addition of Fe^{3+} is compared to the original absorbance before the addition of Fe^{3+} to determine Δ absorbance.

The calibration curve at 524 nm as a function of Fe^{3+} concentration is given in (Fig. 7). When the relationship between the absorbance of AuNPs and the concentration of Fe^{3+} is linear, this plot can be used to determine the level of Fe in the sample. The value of R^2 obtained was 0.996 for AuNPs α -CDs and 0.902 for AuNPs β -CDs with LoD 1.21 ppm, LoQ 4.02 ppm for AuNPs α -CDs and LoD 6.21 ppm, LoQ 20.72 ppm for AuNPs β -CDs, respectively. In the same concentration range, AuNPs α -CDs are more sensitive than AuNPs β -CDs evidenced by the LoD value of AuNPs α -CDs smaller than AuNPs β -CDs. Based on the same correlation coefficient (R^2) value obtained, it can be categorized into a good linear regression equation ($R^2 \geq 0.99$) for AuNPs α -CDs, so it is used for the detection of Fe^{3+} in tap water.

Table 1 shows the list time of analysis and the LoD for some colorimetric Fe^{3+} sensors developed based on SPR sensitivity as others [31-32]; it was more sensitive than other works [33-34]. The sensor developed here had the advantage of a short analysis time (less than 1 min). It proved that this research developed a Fe^{3+} colorimetric sensor that provided better sensitivity and rapid detection.

Precision and Recovery

The repeatability and reproducibility for colorimetric of AuNPs α -CDs and AuNPs β -CDs are given in Table 2. The repeatability of the sensor reflected the quality of sensor response and was investigated by measuring its absorbance at 524 nm in optimum conditions for 3.0 determination ($n = 3$) on the same day resulting in an acceptable relative standard deviation (RSD) lower than that determined by AOAC (7.3%) and Horwitz (11.3%) [35] confirms good repeatability. The

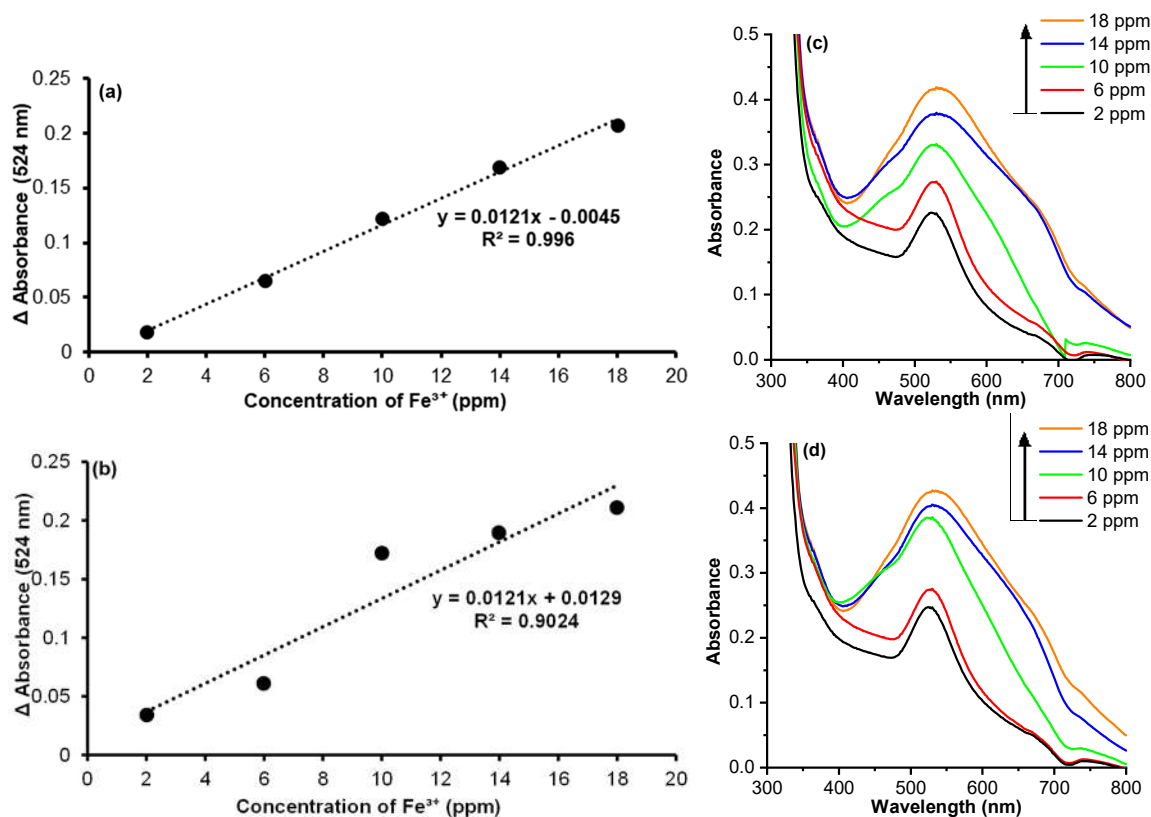


Fig 7. The linear relationship between the concentration of Fe^{3+} and Δ Absorbance of (a) AuNPs α -CDs and (b) AuNPs β -CDs at 524 nm. UV-vis Spectra of (c) AuNPs α -CDs and (d) AuNPs β -CDs with various concentrations of Fe^{3+} from 2 to 18 ppm

Table 1. Comparison of AuNPs α -CDs based UV-vis spectrometric method with the reported methods for detection of Fe^{3+}

Capping Reagents	Samples	Time of analysis	LoD	Ref.
pyrophosphate	Lake water samples	30 min	312 ng/mL	[31]
oxamic acid, <i>p</i> -aminobenzoic acid	Water, urine, and plasma samples	15 min	330 ng/mL	[32]
acidic thiourea mixture	-	15 min	50 ppm	[33]
ascorbic acid, some proteins and flavonoids from <i>Hibiscus cannabinus</i>	-	2 min	8.1 ppm	[34]
<i>o</i> -hydroxybenzoic acid and α - cyclodextrin	Tap water	< 1 min	1.2 ppm	This work

Table 2. Repeatability and reproducibility of (a) AuNPs α -CDs and (b) AuNPs β -CDs at 524 nm

(a)	Repeatability		Reproducibility	
	RSD (%)		RSD (%)	
Concentration Fe^{3+} (ppm)	AOAC	Horwitz	AOAC	Horwitz
2	0.02	1.80	6.63	1.80
6	0.32	1.53	4.30	1.53
10	0.18	1.41	1.29	1.41
14	0.45	1.34	2.40	1.34
18	0.06	1.29	3.32	1.29
(b)	Repeatability		Reproducibility	
	RSD (%)		RSD (%)	
Concentration Fe^{3+} (ppm)	AOAC	Horwitz	AOAC	Horwitz
2	0.03	1.80	4.12	1.80
6	0.10	1.53	4.15	1.53
10	0.06	1.41	0.86	1.41
14	0.02	1.34	1.46	1.34
18	0.05	1.29	0.93	1.29

reproducibility was examined at an absorbance of 524 nm in optimal conditions on different days so that the obtained RSD was lower than that determined by the AOAC (7.3%) and Horwitz (11.3%) [35] confirming good reproducibility.

AuNPs α -CDs are used in recovery because of their average size, shape uniformity, stability and sensitivity better than AuNPs β -CDs. Recovery tests with real samples were carried out using tap water taken at 3 different places in South Tangerang, Banten, Indonesia. Tap water samples were spiked with standard ion Fe^{3+} solutions (10 ppm) and then analyzed. The results summarized in (Table 3) demonstrated the recovery

range of 86.4 to 109.9% when compared with acceptable recovery percentages according to the concentration level of analyte in 10 ppm (80–110%) [35]. The results obtained are within that range so that the recovery results are acceptable and clearly confirm the applicability of the developed colorimetric sensor for the accurate determination of Fe^{3+} ions in tap water.

Reusability

The reusability of AuNPs α -CDs and β -CDs was carried out by adding EDTA which is commonly used as a binding agent or ligand for several metal ions or elements, especially Fe^{3+} . The use of EDTA is expected to bind Fe^{3+} ions so that AuNPs-CDs can be used again. In order to recover the initial absorbance from AuNPs α -CDs and β -CDs, the concentration EDTA for AuNPs α -CDs and β -CDs is 25 and 40 ppm, respectively. Further, the color change AuNPs α -CDs and AuNPs β -CDs after the addition of Fe^{3+} is red and purple, respectively.

Table 3. Recovery of AuNPs α -CDs for the analysis of Fe^{3+} in the samples

Samples	Spiked (ppm)	Detected by AAS (ppm)	Recovery (%)
Sample I	6.68	0.51	86.4
	8.05	0.51	92.4
Sample II	5.75	ND	97.8
	6.30	ND	93.7
Sample III	9.66	0.59	109.9
	10.52	0.59	105.1

ND: Not Detected is the content of Fe^{3+} is below the limit of detection (LoD) of AAS

The color change after the addition of EDTA in AuNPs α -CDs + Fe^{3+} and AuNPs β -CDs + Fe^{3+} was from red and purple to bright purple, respectively. The change in color and widening of the absorbance peaks indicate (Fig. 8) that the shape and size of the AuNPs α -CDs and β -CDs cannot return to their original shape and size. Thus, AuNPs α -CDs and β -CDs can be reused only twice (Fig. 9).

Application Test to Tap Water

The average size, shape uniformity, stability and sensitivity of AuNPs α -CDs are better than AuNPs β -CDs, so AuNPs α -CDs are chosen for application test to tap water. The analytical results of Fe^{3+} using the AuNPs α -CDs which were obtained by the proposed method, were not significantly different from those obtained by AAS, as shown in Table 4. That's because the correlations between the as-developed method and the AAS obtained t-test

values of 0.04; 0.52; and 0.04, respectively (the t-test value is 4.30 at a 95% confidence level); it is possible that the two methods did not reveal significantly different results. The outcomes of this application, therefore, demonstrated the applicability of the AuNPs α -CDs sensor method to the samples.

Characterization of AuNPs-CDs

TEM analysis

AuNPs α -CDs are used for test applications to tap water, so for characterization using TEM, only AuNPs

Table 4. Results of Fe^{3+} detection in samples of tap water

Samples	Developed method (ppm)	AAS (ppm)
Sample I	0.55	0.51
Sample II	0.52	ND
Sample III	0.55	0.59

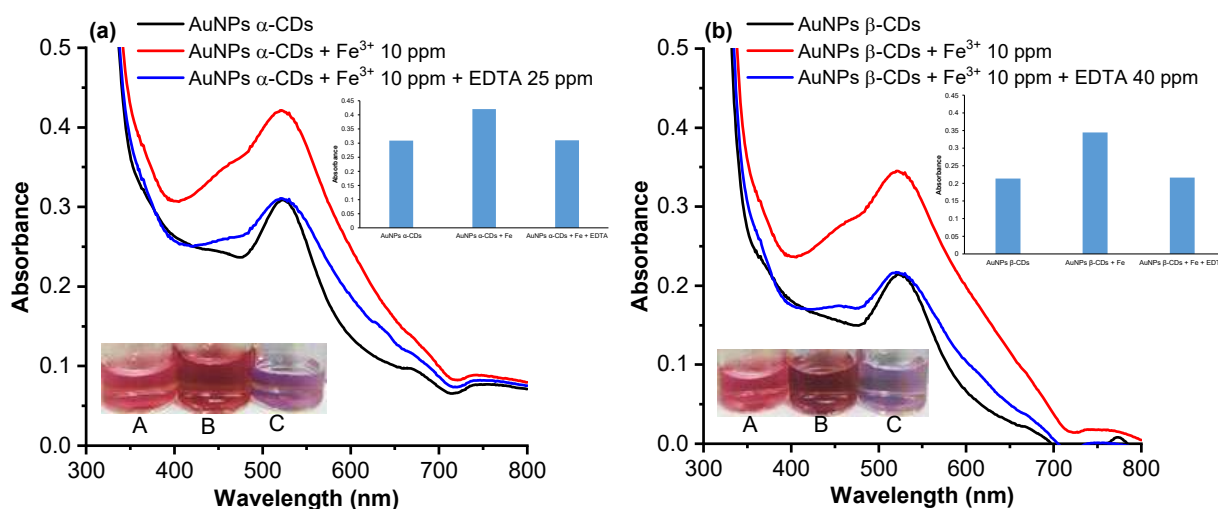


Fig 8. Reversibility of Fe^{3+} in the presence of various EDTA by using different stabilize agents, (a) α -CDs and (b) β -CDs. The color of AuNPs α -CDs and β -CDs (A) with change color after the addition of Fe^{3+} (B) and after the addition of EDTA (C). Bar diagram exhibiting magnitude of absorbance for reversibility as inset

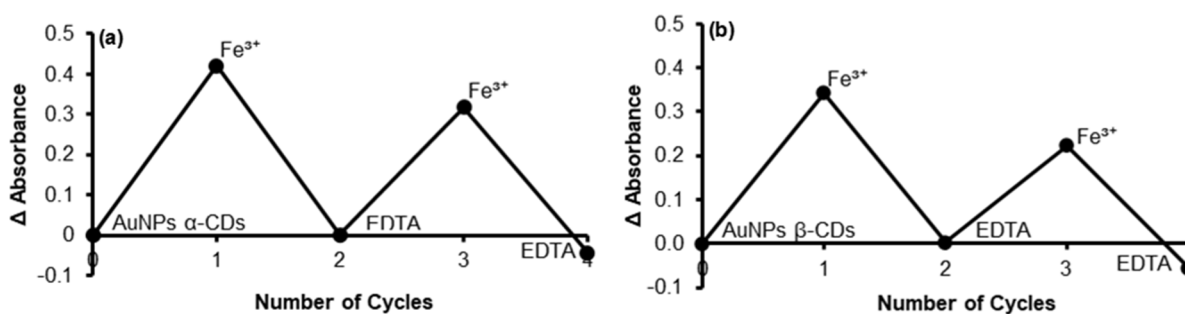


Fig 9. Reversible cycles of AuNPs α -CDs (a) and AuNPs β -CDs (b) addition with Fe^{3+} system with EDTA

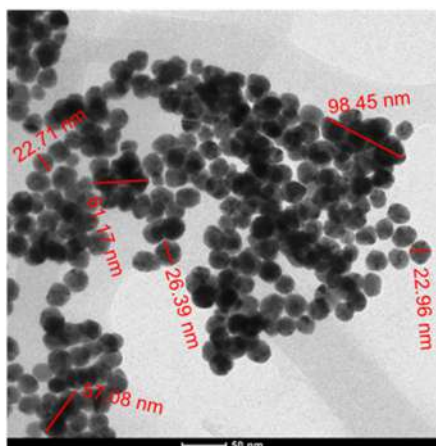


Fig 10. TEM images of the AuNPs α -CDs + Fe^{3+}

α -CDs + Fe^{3+} are used. The average results of nanoparticle size for AuNPs α -CDs + Fe^{3+} were 24.02 to 72.23 nm. The TEM images (Fig. 10) show that the presence of Fe^{3+} reduces the distance between the AuNPs α -CDs, but the AuNPs α -CDs retain their original shape, and aggregation occurs.

FTIR analysis

The IR spectra of AuNPs α -CDs and AuNPs α -CDs + Fe^{3+} (Fig. 11(a)) and AuNPs β -CDs and AuNPs β -CDs + Fe^{3+} (Fig. 11(b)) state an absorption peak which corresponded a C–H stretching + C–H (CH_2) stretching and C–H stretching at 2920 and 2860 cm^{-1} probably owned by cyclodextrin (α -CDs and β -CDs) [36]. Absorption peak which corresponded to a ketone C=O

stretching ortho for AuNPs α -CDs and AuNPs α -CDs + Fe^{3+} (Fig. 11(a)) at 1732 cm^{-1} , for AuNPs β -CDs at 1732 cm^{-1} and AuNPs β -CDs + Fe^{3+} at 1730 cm^{-1} , proved that *o*-HBA acts as a reducing agent and cyclodextrin acts as a stabilizer [37]. Stretching vibration of C=O carbonyl for AuNPs α -CDs and AuNPs β -CDs emerge at 1642 and 1643 cm^{-1} due to the presence of an electrostatic bond C=O with Au metal (Table 5). After the addition of Fe^{3+} (AuNPs α -CDs + Fe^{3+} and AuNPs β -CDs + Fe^{3+}), the wavenumber at the C=O stretching vibration carbonyl was shifted to 1647 and 1695 cm^{-1} . The shift of wavenumber was caused by the C=O carbonyl groups that were believed to bind with Fe^{3+} [37]. Other than that, O–H bending carbonyl and C=C stretching aromatic of AuNPs α -CDs and AuNPs β -CDs appeared at 1602 and 1452 cm^{-1} . After the addition of Fe^{3+} (AuNPs α -CDs + Fe^{3+}), the wavenumber at the O–H bending carbonyl and C=C stretching aromatic were shifted to 1608 and 1455 cm^{-1} , respectively. The shift of wavenumber was caused by the O–H bending carbonyl and C=C stretching aromatic to form bridges between AuNPs, causing a decrease in the distance among AuNPs α -CDs and AuNPs β -CDs. Therefore, the schematic between AuNPs α -CDs, AuNPs β -CDs, and Fe^{3+} based on FTIR results may be interpreted as shown in Scheme 1.

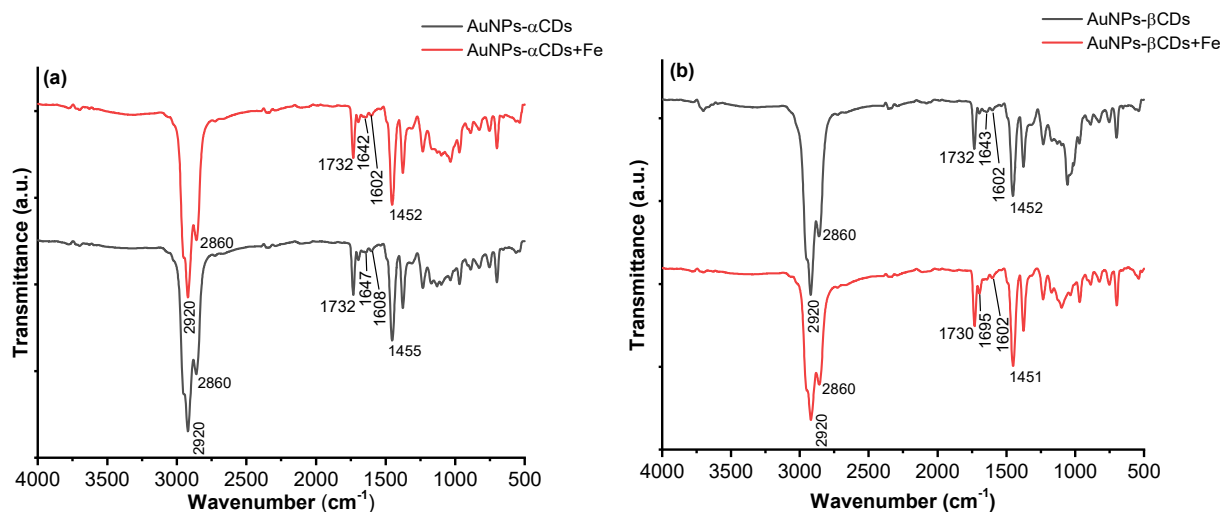
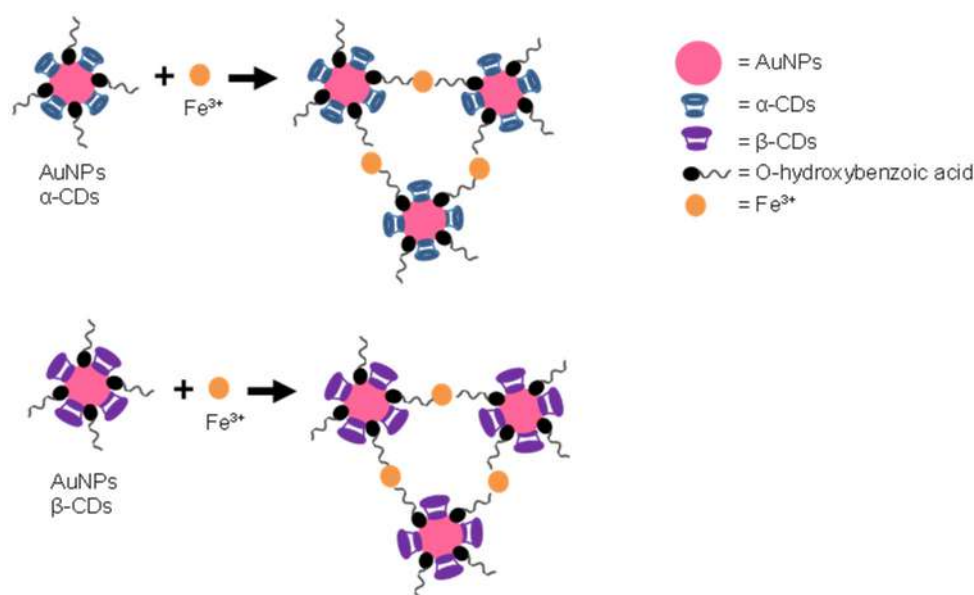


Fig 11. FTIR spectra of (a) AuNPs α -CDs and AuNPs α -CDs + Fe^{3+} and (b) AuNPs β -CDs and AuNPs β -CDs + Fe^{3+}

Table 5. Wavenumbers (cm^{-1}) of AuNPs CDs and AuNPs CDs- Fe^{3+} complexes

AuNPs α -CDs	AuNPs α -CDs + Fe^{3+}	AuNPs β -CDs	AuNPs β -CDs + Fe^{3+}	
2920	2920	2920	2920	C-H stretching + C-H (CH_2) stretching
2860	2860	2860	2860	C-H stretching
1732	1732	1732	1730	Ketone C=O stretching <i>ortho</i>
1642	1647	1643	1695	C=O stretching vibration carbonyl
1602	1608	1602	1602	O-H bending carbonyl
1452	1455	1452	1451	C=C stretching aromatic

**Scheme 1.** Scheme illustration of AuNPs AuNPs α -CDs and AuNPs β -CDs

CONCLUSION

This study's results indicated that AuNPs α -CDs were more stable than AuNPs β -CDs, with an absorbance drop of 17.76% at a 524 nm wavelength. With the average size of 23.34 nm, AuNPs α -CDs have a more consistent nanoparticle size and shape. The linear calibration curve at 524 nm's R^2 value of 0.996 with a LoD of 1.21 ppm and a LoQ of 4.02 ppm confirms the AuNPs α -CDs are more sensitive than AuNPs β -CDs. From this comparison, AuNPs α -CDs can be utilized to detect Fe^{3+} in tap water because it exhibits good precision, accuracy, and recovery.

ACKNOWLEDGMENTS

This research would like to acknowledge funding from the *RIIM Gelombang 3 (2023) 12/II.7/HK/2023* and the facilities, scientific and technical supports from Advanced Characterization Laboratories Serpong, National

Research and Innovation Agency (BRIN) through *E-Layanan Sains, Badan Riset dan Inovasi Nasional*.

AUTHOR CONTRIBUTIONS

Adhi Maulana Yusuf: data curation, investigation, formal analysis, writing-original draft; Satrio Kuntolaksono: investigation, methodology, validation, supervision, and writing-review; Agustina Sus Andreani: conceptualization, formal analysis, funding acquisition, investigation, methodology, supervision, validation, writing-review & editing.

REFERENCES

- [1] Liang, W., Wang, G., Peng, C., Tan, J., Wan, J., Sun, P., Li, Q., Ji, X., Zhang, Q., Wu, Y., and Zhang, W., 2022, Recent advances of carbon-based nano zero valent iron for heavy metals remediation in soil and

- water: A critical review, *J. Hazard Mater.*, 426, 127993.
- [2] Amirjani, A., Kamani, P., Hosseini, H.R.M., and Sadrnezhaad, S.K., 2022, SPR-based assay kit for rapid determination of Pb^{2+} , *Anal. Chim. Acta*, 1220, 340030.
- [3] Li, H.Y., Zhao, S.N., Zang, S.Q., and Li, J., 2020, Functional metal-organic frameworks as effective sensors of gases and volatile compounds, *Chem. Soc. Rev.*, 49 (17), 6364–6401.
- [4] Zuo, Z., Song, X., Guo, D., Guo, Z., and Niu, Q., 2019, A dual responsive colorimetric/fluorescent turn-on sensor for highly selective, sensitive and fast detection of Fe^{3+} ions and its applications, *J. Photochem. Photobiol., A*, 382, 111876.
- [5] Tammina, S.K., Yang, D., Li, X., Koppala, S., and Yang, Y., 2019, High photoluminescent nitrogen and zinc doped carbon dots for sensing Fe^{3+} ions and temperature, *Spectrochim. Acta, Part A*, 222, 117141.
- [6] Amirjani, A., and Haghshenas, D.F., 2018, Ag nanostructures as the surface plasmon resonance (SPR)-based sensors: A mechanistic study with an emphasis on heavy metallic ions detection, *Sens. Actuators, B*, 273, 1768–1779.
- [7] Wu, Y., Pang, H., Liu, Y., Wang, X., Yu, S., Fu, D., Chen, J., and Wang, X., 2019, Environmental remediation of heavy metal ions by novel-nanomaterials: A review, *Environ. Pollut.*, 246, 608–620.
- [8] Liu, X., Li, N., Xu, M.M., Wang, J., Jiang, C., Song, G., and Wang, Y., 2018, Specific colorimetric detection of Fe^{3+} ions in aqueous solution by squaraine-based chemosensor, *RSC Adv.*, 8 (61), 34860–34866.
- [9] Wang, R., Jiao, L., Zhou, X., Guo, Z., Bian, H., and Dai, H., 2021, Highly fluorescent graphene quantum dots from biorefinery waste for tri-channel sensitive detection of Fe^{3+} ions, *J. Hazard. Mater.*, 412, 105962.
- [10] Xiong, X., Zhang, J., Wang, Z., Liu, C., Xiao, W., Han, J., and Shi, Q., 2020, Simultaneous multiplexed detection of protein and metal ions by a colorimetric microfluidic paper-based analytical device, *Biochip J.*, 14 (4), 429–437.
- [11] Soares, B.M., Santos, R.F., Bolzan, R.C., Muller, E.I., Primel, E.G., and Duarte, F.A., 2016, Simultaneous determination of iron and nickel in fluoropolymers by solid sampling high-resolution continuum source graphite furnace atomic absorption spectrometry, *Talanta*, 160, 454–460.
- [12] Lv, X., Man, H., Dong, L., Huang, J., and Wang, X., 2020, Preparation of highly crystalline nitrogen-doped carbon dots and their application in sequential fluorescent detection of Fe^{3+} and ascorbic acid, *Food Chem.*, 326, 126935.
- [13] Pang, L.Y., Wang, P., Gao, J.J., Wen, Y., and Liu, H., 2019, An active metal-organic anion framework with highly exposed SO_4^{2-} on {001} facets for the enhanced electrochemical detection of trace Fe^{3+} , *J. Electroanal. Chem.*, 836, 85–93.
- [14] Karami, C., Alizadeh, A., Taher, M.A., Hamidi, Z., and Bahrami, B., 2016, UV-visible spectroscopy detection of iron(III) ion on modified gold nanoparticles with a hydroxamic acid, *J. Appl. Spectrosc.*, 83 (4), 687–693.
- [15] Uzunoglu, D., Ergut, M., Kodaman, C.G., and Ozer, A., 2020, Biosynthesized silver nanoparticles for colorimetric detection of Fe^{3+} ions, *Arabian J. Sci. Eng.*, s13369-020-04760-8.
- [16] Chen, X., Zhao, Q., Zou, W., Qu, Q., and Wang, F., 2017, A colorimetric Fe^{3+} sensor based on an anionic poly(3,4-propylenedioxythiophene) derivative, *Sens. Actuators, B*, 244, 891–896.
- [17] Kumar, A., Zhang, X., and Liang, X.J., 2013, Gold nanoparticles: Emerging paradigm for targeted drug delivery system, *Biotechnol. Adv.*, 31 (5), 593–606.
- [18] Amirjani, A., and Fatmehsari, D.H., 2018, Colorimetric detection of ammonia using smartphones based on localized surface plasmon resonance of silver nanoparticles, *Talanta*, 176, 242–246.
- [19] Amirjani, A., Salehi, K., and Sadrnezhaad, S.K., 2022, Simple SPR-based colorimetric sensor to differentiate Mg^{2+} and Ca^{2+} in aqueous solutions, *Spectrochim. Acta, Part A*, 268, 120692.

- [20] Amirjani, A., Bagheri, M., Heydari, M., and Hesarak, S., 2016, Label-free surface plasmon resonance detection of hydrogen peroxide; A bio-inspired approach, *Sens. Actuators, B*, 227, 373–382.
- [21] Jansook, P., Ogawa, N., and Loftsson, T., 2018, Cyclodextrins: Structure, physicochemical properties and pharmaceutical applications, *Int. J. Pharm.*, 535 (1-2), 272–284.
- [22] Roy, N., Bomzan, P., and Nath Roy, M., 2020, Probing host-guest inclusion complexes of ambroxol hydrochloride with α - & β -cyclodextrins by physicochemical contrivance subsequently optimized by molecular modeling simulations, *Chem. Phys. Lett.*, 748, 137372.
- [23] Gopalan, P.R., 2010, Cyclodextrin-stabilized metal nanoparticles: Synthesis and characterization, *Int. J. Nanosci.*, 9 (5), 487–494.
- [24] Liu, Y., Male, K.B., Bouvrette, P., and Luong, J.H.T., 2003, Control of the size and distribution of gold nanoparticles by unmodified cyclodextrins, *Chem. Mater.*, 15 (22), 4172–4180.
- [25] Lakkakula, J.R., Divakaran, D., Thakur, M., Kumawat, M.K., and Srivastava, R., 2018, Cyclodextrin-stabilized gold nanoclusters for bioimaging and selective label-free intracellular sensing of Co^{2+} ions, *Sens. Actuators, B*, 262, 270–281.
- [26] Soomro, R.A., Nafady, A., Sirajuddin, S., Memon, N., Sherazi, T.H., and Kalwar, N.H., 2014, L-cysteine protected copper nanoparticles as colorimetric sensor for mercuric ions, *Talanta*, 130, 415–422.
- [27] Andreani, A.S., Kunarti, E.S., and Santosa, S.J., 2019, Synthesis of gold nanoparticles capped-benzoic acid derivative compounds (*o*-, *m*-, and *p*-hydroxybenzoic acid), *Indones. J. Chem.*, 19 (2), 376–385.
- [28] Ndikau, M., Noah, N.M., Andala, D.M., and Masika, E., 2017, Green synthesis and characterization of silver nanoparticles Using *Citrullus lanatus* fruit rind extract, *Int. J. Anal. Chem.*, 2017, 8108504.
- [29] Das, R., Sugimoto, H., Fujii, M., and Giri, P.K., 2020, Quantitative understanding of charge-transfer-mediated Fe^{3+} sensing and fast photoresponse by N-doped graphene quantum dots decorated on plasmonic Au nanoparticles, *ACS Appl. Mater. Interfaces*, 12 (4), 4755–4768.
- [30] Mohaghegh, N., Endo-Kimura, M., Wang, K., Wei, Z., Hassani Najafabadi, A., Zehtabi, F., Hosseinzadeh Kouchehbaghi, N., Sharma, S., Markowska-Szczupak, A., and Kowalska, E., 2023, Apatite-coated Ag/AgBr/ TiO_2 nanocomposites: Insights into the antimicrobial mechanism in the dark and under visible-light irradiation, *Appl. Surf. Sci.*, 617, 156574.
- [31] Wu, S.P., Chen, Y.P., and Sung, Y.M., 2011, Colorimetric detection of Fe^{3+} ions using pyrophosphate functionalized gold nanoparticles, *Analyst*, 136 (9), 1887–1891.
- [32] Buduru, P., and Reddy B.C., S.R., 2016, Oxamic acid and *p*-aminobenzoic acid functionalized gold nanoparticles as a probe for colorimetric detection of Fe^{3+} ion, *Sens. Actuators, B*, 237, 935–943.
- [33] Tripathy, S.K., Woo, J.Y., and Han, C.S., 2013, Colorimetric detection of Fe(III) ions using label-free gold nanoparticles and acidic thiourea mixture, *Sens. Actuators, B*, 181, 114–118.
- [34] Bindhu, M.R., and Umadevi, M., 2014, Green synthesized gold nanoparticles as a probe for the detection of Fe^{3+} ions in water, *J. Cluster Sci.*, 25 (4), 969–978.
- [35] González, A.G., Herrador, M.Á., and Asuero, A.G., 2010, Intra-laboratory assessment of method accuracy (trueness and precision) by using validation standards, *Talanta*, 82 (5), 1995–1998.
- [36] Hasanah, N., Manurung, R.V., Jenie, S.N.A., Indriyati, I., Prastya, M.E., and Andreani, A.S., 2023, The effect of size control of gold nanoparticles stabilized with α -cyclodextrin and β -cyclodextrin and their antibacterial activities, *Mater. Chem. Phys.*, 302, 127762.
- [37] Andreani, A.S., Kunarti, E.S., Hashimoto, T., Hayashita, T., and Santosa, S.J., 2021, Fast and selective colorimetric detection of Fe^{3+} based on gold nanoparticles capped with *ortho*-hydroxybenzoic acid, *J. Environ. Chem. Eng.*, 9 (5), 105962.

Spectrophotometric Determination of Amoxicillin Using New Organic Reagent via Different Analytical Methods

Helen Abd Alhassan Mahmood¹, Rulla Sabah^{2*}, and Nisreen Kais Abood²

¹Ministry of Sciences and Technology, Iraqi National Monitoring Authority, Baghdad 10064, Iraq

²Department of Chemistry, College of Science, Mustansiriyah University, Baghdad 10064, Iraq

* Corresponding author:

email:

rulla_sabah77@uomustansiriyah.edu.iq

Received: April 15, 2023

Accepted: May 17, 2023

DOI: 10.22146/ijc.83903

Abstract: New and simple spectrophotometric method was applied for amoxicillin determination by oxidative coupling with an organic reagent 1-(4-aminophenyl)-3-(5-(4-nitrophenyl)-furan-2-yl)-yl)-prop-2-en-1-one (H) to form an orange colored dye with λ_{max} of 490 nm. The molecular structure of the new compound H was characterized using spectral analysis including ¹H-NMR, FTIR, Mass spectroscopy, and UV-visible. The concentration range of oxidative coupling obeyed Beer's law was 2–50 $\mu\text{g/mL}$, the correlation coefficient was 0.9995, molar absorptivity was 0.63×10^4 L/mol cm, and the detection limit was 0.189 $\mu\text{g/mL}$. The concentration range of flow injection obeyed Beer's law was 1–150 $\mu\text{g/mL}$, the correlation coefficient was 0.9994, molar absorptivity was 0.295×10^4 L/mol cm, and the detection limit was 0.407 $\mu\text{g/mL}$. The proposed method was successfully applied in pharmaceutical formulation for amoxicillin determination. The results showed that amoxicillin could be reacted with a new compound H in the alkaline medium in the presence of oxidative agent NaIO_4 and automated by flow injection analysis. The proposed methods have the advantage of simple, fast, very sensitive, good precision and accuracy. The suggested technique was effectively used to estimate amoxicillin in both its pure form and pharmaceutical formulations.

Keywords: amoxicillin; chalcone; spectrophotometric; flow injection; oxidative coupling

■ INTRODUCTION

Amoxicillin (6-[(R)-(-)-2-amino-2-(p-hydroxyl phenyl)acetamido]-3,3-dimethyl-7-oxo-4-thia-1-azabicyclo[3.2.1]heptane-2-carboxylic acid trihydrate, AMX, (Fig. 1), is one of the mostly given semisynthetic penicillins for acute bacterial sinusitis and community-acquired pneumonia [1-2]. Several methods for AMX determination in pharmaceutical formulations and biological fluids have been reported including HPLC [3-5], chemiluminescence [6-8], spectrofluorimetric [9], and flow-injection analysis [10-14].

Chalcone has a unique structure that consists of two aromatic rings connected by a three-carbon unsaturated carbonyl system with a wide range of functional groups [15-17]. Chalcone and its derivatives have shown a wide spectrum of biological activities [18] such as anti-fungal, anti-microbial, anti-inflammatory, anti-malarial,

antiviral, anti-tumor, antioxidant, anti-leishmanial, and anti-cancer [19-20]. These activities were originated from the presence of a reactive keto-ethylenic moiety ($-\text{CO}-\text{CH}=\text{CH}-$) in their structure. The objective of this study is an alternative method that is more effective and inexpensive because it utilizes agriculture used or by-products such as grain, soybean husk, straw, cottonseed, bark, used newspaper, and others. Paper, such as newspaper, is a material that contains cellulose (50.1%), hemicellulose, and lignin (18.1%); thus, it can be used as

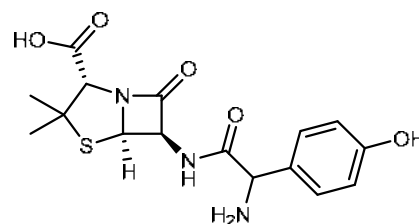


Fig 1. Structure of amoxicillin

an adsorbent [1]. In this work, a simple spectrophotometric method was established for AMX determination by oxidative coupling with a new chalcone reagent.

■ EXPERIMENTAL SECTION

Materials

The chemicals and solvents were obtained from Sigma Aldrich and BDH companies and were used without further purification to create the compounds in this study. 4-amino acetophenone, absolute ethanol, hydrochloric acid, 5-(4-nitrophenyl)furan-2-carbaldehyde and ethanol were obtained from Sigma-Aldrich company. Sodium hydroxide, sulfuric acid, sodium periodate, and nitric acid were obtained from BDH company. AMX was obtained by SDI, a general corporation for the production of pharmaceuticals and medical supplies, in Samara, Iraq.

Instrumentation

Using an open capillary tube in a Gallen-Kamp MFB-600 melting point apparatus, the melting point of produced chalcone was measured. A Shimadzu FTIR-8400S was used to register infrared spectra in the region of 4000–600 cm^{-1} . A mass spectroscopic was captured with Shimadzu QP 2010 Plus. With tetramethylsilane as an internal standard, the model ultra-shield $^1\text{H-NMR}$ spectra (DMSO- d_6 solvent) were registered at 300 MHz. The absorbance measurements were done in a spectrophotometric single-beam UV-visible 295 (Lasany-India) with 1.0 cm and 0.5 cm quartz cells. For the flow injection analysis (FIA), the configuration with the three channels (Fig. 2) was used. The peristaltic pump and reaction coil were both powered by a poly(vinyl chloride) tube (0.8 mm internal diameter) peristaltic pump (ALITEA, C4, produced in Sweden).

Procedure

The general procedure of preparation of compound H

Compound H was prepared using the method given in reference [20] with some changes. A 4-aminoacetophenone (0.005 mol, 0.67 g) was dissolved and stirred in a mixture of 30 mL of absolute ethanol and 4 mL of 10% NaOH solution at room temperature. Then,

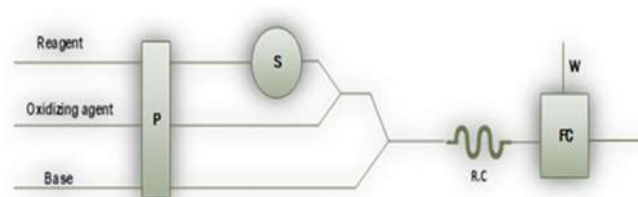


Fig 2. FIA manifolds, peristaltic pump (P), sample injection (S), reaction coil (R.C), flow cell (FC), detector (D), waste (W)

5-(4-nitrophenyl)furan-2-carbaldehyde (0.005 mol, 1.08 g) was added and stirred for 48 h. After the disappearance of the initial materials, as monitored by TLC, hydrochloric acid was added drop-wise with stirring to the reaction mixture until the formation of a precipitate which was collected after filtration. The product was washed with cold distilled water, dried, and purified by ethanol to afford the orange crystals.

Analytical methods

Preparation of stock solution and reagents solution.

To prepare an AMX stock solution (1000 mg/mL), 0.1 g of AMX was dissolved in 100 mL of distilled water. By combining 0.5 mL of sulfuric acid and 0.1 g of the organic reagent in distilled water and stirring, a stock solution of H 1000 g/mL was obtained. NaOH 2 M was obtained by dissolving 8 g of NaOH in 100 mL of distilled water. A 2.13 g of NaIO_4 and 1 mL of HNO_3 were dissolved, stirred, and added to 100 mL of distilled water to create 0.1 M NaIO_4 .

The general procedure of oxidative coupling reaction 1000 $\mu\text{g/mL}$.

The oxidative coupling reaction was prepared for AMX in 20 mL volumetric flask by the addition of 2 mL AMX (1000 $\mu\text{g/mL}$), 2 mL 1000 $\mu\text{g/mL}$ from organic reagent H with 1 mL of NaIO_4 0.1 M in present of NaOH 1 M that produced orange colored dye at λ_{max} 490 nm. The blank solution was prepared in the same way without the addition of AMX.

The procedure of flow injection

AMX was injected into a carrier stream made of three channels that were mixed together. The first channel carried 0.2 M organic reagent H, and the second channel carried 0.1 M NaIO_4 in a T-shape. The reaction is carried out by thoroughly mixing the ingredients in a 50 cm reaction coil, allowing the mixture to flow

through an injector, and then reacting the end product with a stream of 1 M NaOH. The absorbance of the resulting orange dye was then measured at 490 nm.

The Procedure for AMX in capsules

The AMX capsules 500 mg pharmaceutical, equivalent to 100 mg of pure AMX, were transferred into 100 mL volumetric flask to prepare 1000 $\mu\text{g/mL}$ and completed to 100 mL distilled water. Afterward, the solution was filtered to remove any interference. The diluted solution was prepared from the pharmaceutical and then used in the measurement of oxidative coupling and FIA.

RESULTS AND DISCUSSION

Compound H was prepared by the reaction of equivalents moles of 4-aminoacetophenone with 5-(4-nitrophenyl)furan-2-carbaldehyde in an appropriate solvent through the Claisen-Schmidt condensation using NaOH as a catalyst. Compound H showed a band at 3483 and 3388 cm^{-1} related to NH_2 , bands at 3230 and 3089 cm^{-1} regions due to $\text{CH}=\text{CH}$ and aromatic C-H bonds, respectively. The C=O absorption band appeared at 1639 cm^{-1} , while the C=C stretching frequency of compound H appeared at 1585 cm^{-1} . Bands at 1502 and

1332 cm^{-1} were related to the NO_2 absorption. The $^1\text{H-NMR}$ of compound H revealed a singlet band at 5.4 ppm due to NH_2 , the doublet appears at 7.03 ppm related to two Ar-H, while the multiple signals at 8.05–8.73 ppm due to other aromatic hydrogens and two hydrogen of the $\text{CH}=\text{CH}$ of chalcone.

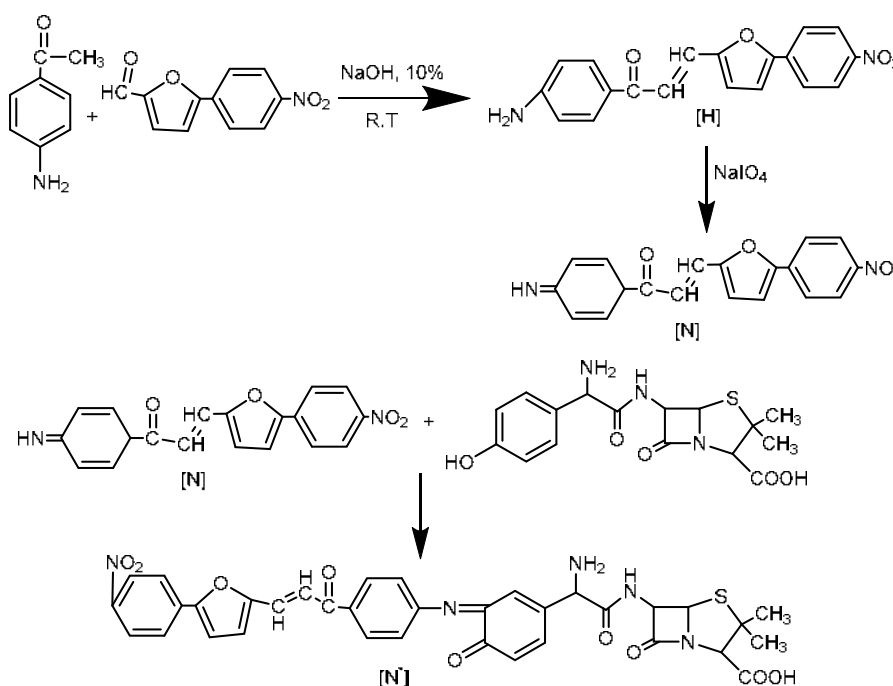
Scheme 1 shows the proposed reaction pathway between the prepared reagent and drug to produce the colored dye derivative. From the mole ratio method shown, the ratio between the drugs and reagents was 1:1, and the proposed formula for the resulting dye produced are therefore as follows [21-22] shown in Scheme 1.

Spectrophotometric Study

Oxidative coupling reaction preliminary investigation showed that the reaction of AMX with organic reagent H in the presences oxidizing of agent and in alkaline media was used to produce the orange-colored dye that has λ_{max} 490 nm, where the absorption spectra of the orange dye were measured against blank.

Effect of Experimental Conditions of Oxidative Coupling

The factors that effect on the stability and sensitivity of the colored product from the oxidative coupling of



Scheme 1. Synthesis of dye derivative

AMX with the organic reagent and oxidative reagent NaIO_4 present in an alkaline medium were studied. Different parameters that affected the colored intensity of the oxidative dye were studied, such as the addition of order and medium. The optimal amount of alkaline was 1.5 mL, as shown in Fig. 3(a), when several volumes of NaOH (0.25–2.50 mL) were investigated. Different volumes (0.5–3.0 mL) of 0.2 M organic reagent H were used; the results are shown in Fig. 3(b). The optimal volume of a reagent to produce the most intensely colored product was 2 mL. The amount of oxidizing agent 0.1 M NaIO_4 was studied by adding various amounts (0.25–2.50 mL) of an oxidizing agent into a volumetric flask of 20 mL. The greatest absorbance was achieved when 1 mL was employed, and the findings are shown in Fig. 3(c). Effects of temperature, reagent concentration, oxidizing agent quantity, NaOH concentration, and period of oxidation. It depended on experiments that affected the nature of the medium for the oxidative coupling reaction; diverse medium (alkaline, acidity, and neutral) was tested,

and the sequence addition (R+D+O+B) for AMX offered the larger intensity of colored. To increase the effectiveness of the oxidative coupling process, as shown in Fig. 3(d), oxidation reactions at different temperatures (0, 25, and 50 °C) were employed to explore the effects of temperature while maintaining the same circumstances. The time required to reach the output has been found to be stable, and it is composition is complete using optimal conditions of interaction. Under these conditions, the product is formed and stabilized after a period of 10 min, the absorption remains stable for not less than 2 h. The result was 0.852 for AMX.

Stoichiometric Ratio Determination

The stoichiometry of the oxidative reaction between AMX and chromogenic reagent H was investigated using the mole ratio method. Fig. 4 shows that the orange dye is formed in the ratio 1:1 chromogenic reagent H:AMX.

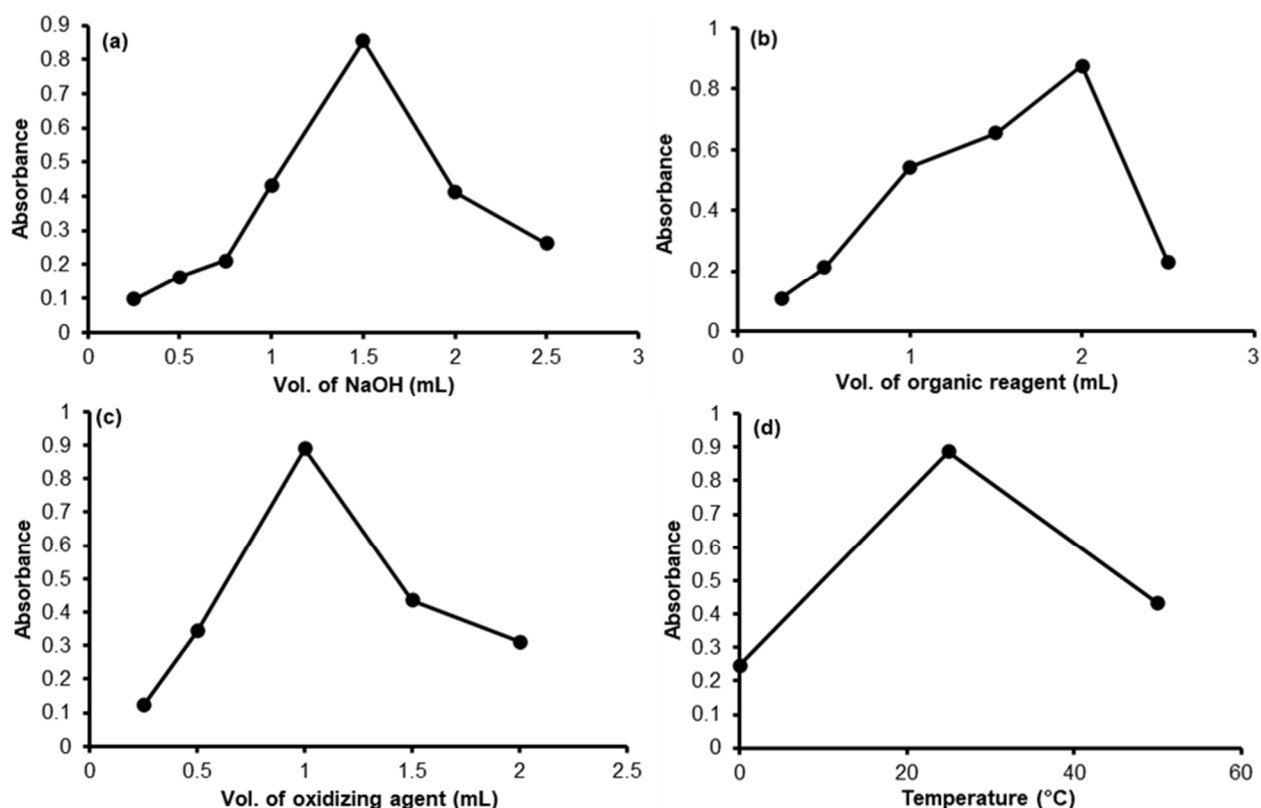


Fig 3. Effect of experimental conditions of oxidative coupling (a) Base, (b) reagent, (c) NaIO_4 , and (d) temperature

Study the Optimum Reaction Conditions for AMX Determination Using Flow Injection

The concentration of the reagent, the concentration of the oxidizing agent, and the concentration of NaOH were all studied as the chemical parameters' to get ideal conditions for this method. The highest absorbance intensity colored was into 0.2 M when several concentrations (0.025–0.300 M) organic reagent H for the AMX were examined; the findings are shown in Fig. 5(a). The best oxidizing agent concentrate, as shown in Fig. 5(b), was NaIO₄ 0.1 M at various concentrations (1×10^{-3} – 3×10^{-1} M). NaOH is used as the best alkaline in the flow injection for the AMX to accumulate into. When several NaOH concentrates (0.2–2 M) were examined, the greatest absorbance was at 0.8 M, as shown in Fig. 5(c).

Different physical parameters, such as reaction coil, were also investigated. The reaction coil's length ranged from 25 to 230 cm, and the best reaction coil was 50 cm because it gave the highest absorbance and was most sensitive to low dispersion. The results are shown in Fig.

6(a). The largest absorption occurred when the total flow rate was 2 mL/min because it took a long time for the reaction to complete and result in significant absorption, as shown in Fig. 6(b). Various injection sample volumes between (50–200 μ L) were investigated. A volume of 100 μ L was chosen as the optimal volume to yield the greatest absorbance and was used in all future trials. The findings are shown in Fig. 6(c).

The calibration graph for the AMX was established by plotting various concentrates of (2–50) and (1–150) μ g/mL, respectively. From the calibration graph,

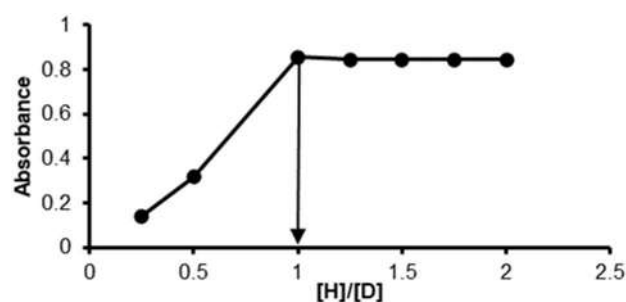


Fig 4. Mole ratio for oxidative AMOX coupled with chromogenic reagent H

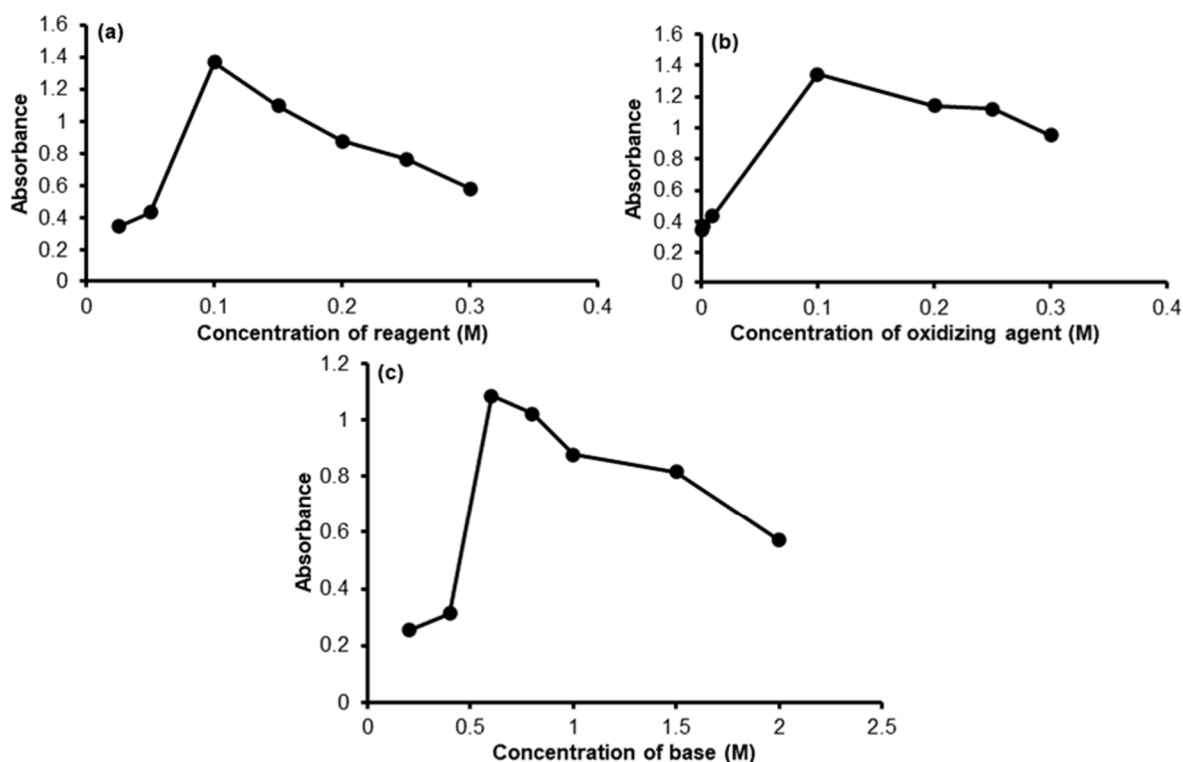


Fig 5. Effect of experimental conditions of flow injection chemical parameters, (a) Concentration of reagent, (b) concentration of oxidative agent, (c) concentration of NaOH

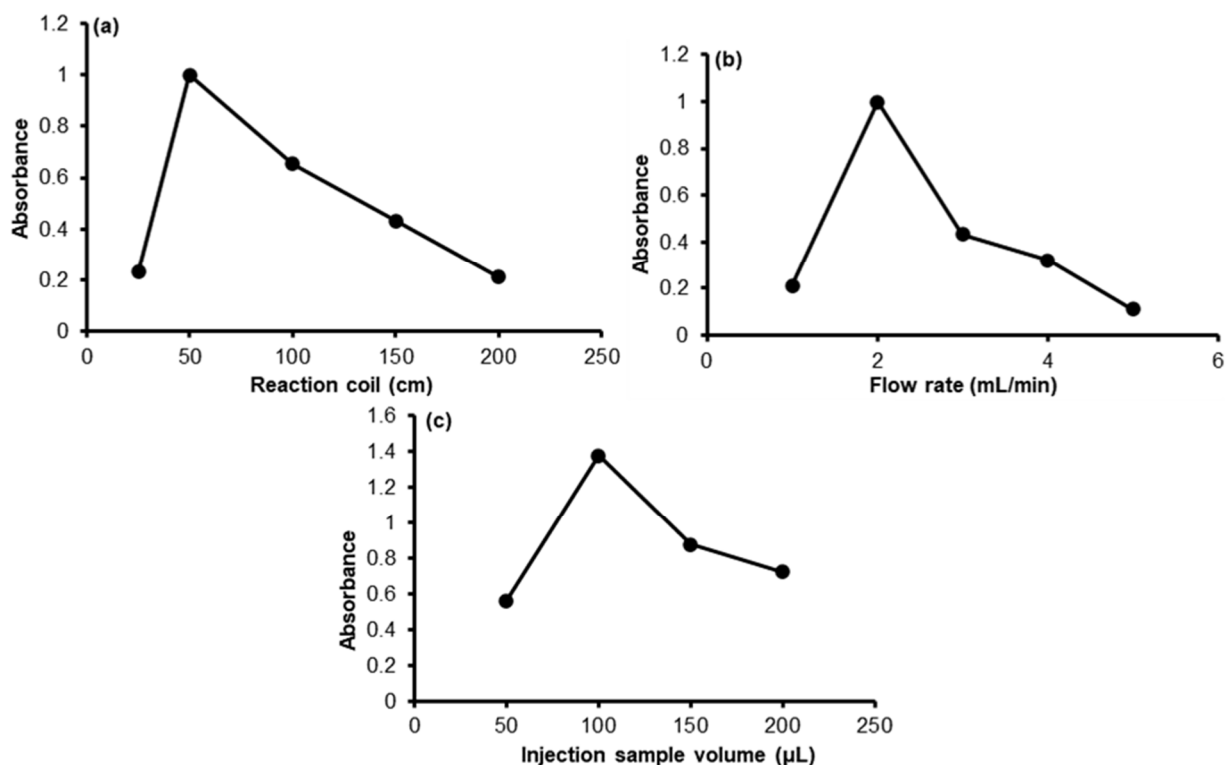


Fig 6. Effect of experimental conditions of flow injection physical parameters, (a) reaction coil, (b) flow rate, and (c) injection sample volume

the linear regression equation, correlation of coefficient (r), slope (a), and intercept (b), and optimal experimental conditions of oxidative coupling and flow injection were obtained. Fig. 7(a, b), and Table 1 display analytical results for the regression equation of the suggested oxidative coupling and FIA methods.

Studies on accuracy and precision were conducted

for the suggested methods of flow injection and oxidative coupling under ideal conditions and utilizing a range of concentrations, measuring absorbance at least five times for each concentration. As stated in Tables 2 and 3, relative error (%RE), recovery (%R), and relative standard deviation (%RSD) were used to calculate precision and accuracy.

Table 1. Characteristic parameter for the proposed oxidative coupling and flow injection regression equation

Parameters	Oxidative coupling	Flow injection
λ_{\max} (nm)	490	490
Color	Orange	Orange
Regression equation	$Y=0.0174x-0.0053$	$Y=0.0086x+0.1618$
Linearity range ($\mu\text{g/mL}$)	2–50	1–150
Correlation Coefficient (r)	0.9995	0.9995
ϵ (L/mol.cm)	0.630×10^4	0.295×10^4
Sandal' sensitivity ($\mu\text{g/cm}^2$)	0.0580	0.1200
Slope (b)	0.0174	0.0081
Intercept (a)	-0.0082	-0.0066
Limit of detection ($\mu\text{g/mL}$)	0.1890	0.4070
Limit quantification ($\mu\text{g/mL}$)	0.5710	1.2300

LOD = $3.3 \times \text{SDB}/S$, SDB = the standard deviation of intercepts of regression lines [22-23]

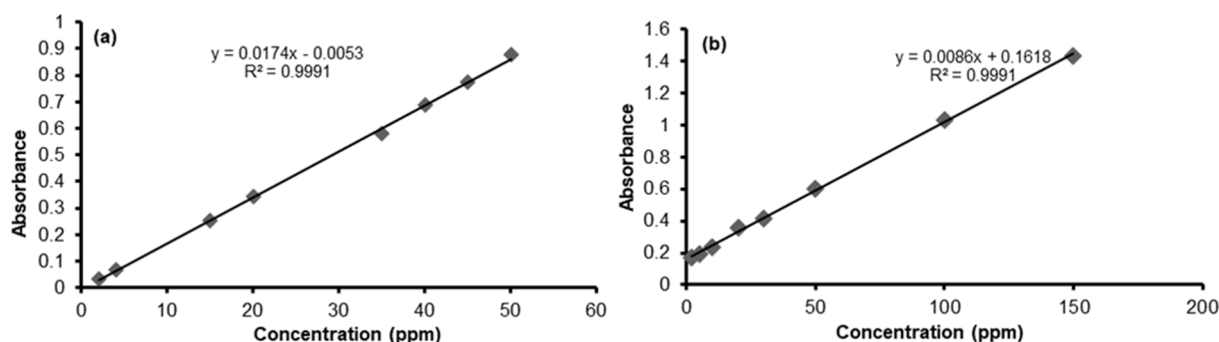


Fig 7. Calibration curve of AMX: (a) Oxidative coupling and (b) flow injection

Table 2. The precision and accuracy of suggested techniques for estimating pure samples

Drug	Amount of drugs ($\mu\text{g}/\text{mL}$)		%RE	%R	Average %R	%RSD (n=5)
	Taken	Found				
Oxidative method						
AMX	10	9.97	-0.30	99.70	99.94	0.13
	20	19.99	-0.05	99.95		0.42
	30	30.05	0.16	100.16		0.22
Flow injection method						
AMX	10	9.89	-1.10	98.90	99.72	0.26
	30	29.94	-0.40	99.60		0.59
	50	50.33	0.66	100.66		0.43

Table 3. The proposed method's accuracy and precision for identifying commercial medications

Type of drugs	Amount of drugs (mg)		%RE	%R	Average %R	%RSD (n=5)
	Taken	Found				
Oxidative method						
Amoxicillin trihydrate 500 mg Capsules (Global, UAE)	10	10.04	0.40	100.40	100.26	0.31
	20	19.97	-0.15	99.85		0.43
	30	29.95	-0.16	99.83		0.51
Amoxicillin 500 mg Capsules (Ajanta, India)	10	9.98	-0.20	99.80	99.97	0.76
	20	19.98	-0.10	99.90		0.21
	30	30.07	0.23	100.23		0.32
Flow injection method						
Amoxicillin trihydrate 500 mg Capsules (Global, UAE)	10	9.98	-0.20	99.80	99.96	0.65
	30	29.99	-0.03	99.98		0.22
	50	50.05	0.10	100.10		0.12
Amoxicillin 500 mg Capsules (Ajanta, India)	10	10.01	0.10	100.10	99.95	0.44
	50	49.97	-0.16	99.83		0.54
	30	29.95	-0.06	99.94		0.65

Average of five repeats, %E = relative error (Found-taken/taken \times 100), %R, and %RSD%

■ CONCLUSION

In this paper, amoxicillin reacts with a new chromogenic reagent, (*E*)-1-(4-aminophenyl)-3-(5-(4-nitrophenyl)furan-2-yl)prop-2-en-1-one (compound H), in the alkaline medium in the presence of oxidative agent NaIO_4 and automate by flow injection analysis. The ideal chemical parameters, such as the reagent concentration, oxidizing agent concentration, and sodium hydroxide concentration, were studied. These methods have the advantage of being simple, rapid, very sensitive, and having good precision and accuracy.

■ ACKNOWLEDGMENTS

The authors are grateful for the spectral analysis services and analytical experiences provided by Mustansiriyah University's Faculty of Science, Chemistry's supplier laboratory.

■ REFERENCES

- [1] Brunton, L.L., Hilal-Dandan, R., and Knollmann, B.C., 2018, *As Bases Farmacológicas da Terapêutica de Goodman e Gilman*, Artmed Editora, Brazil.
- [2] Al-Uzri, W.A., 2019, Determination of phenylephrine hydrochloride in pharmaceutical preparations using spectrophotometric method, *Asian J. Pharm. Clin. Res.*, 12 (5), 339–343.
- [3] Almalki, A.H., Hussein, E.A., Naguib, I.A., Abdelaleem, E.A., Zaazaa, H.E., and Abdallah, F.F., 2021, Development and validation of ecofriendly HPLC-MS method for quantitative assay of amoxicillin, dicloxacillin, and their official impurity in pure and dosage forms, *J. Anal. Methods Chem.*, 2021, 5570938.
- [4] Becze, A., Resz, M.A., Ilea, A., and Cadar, O., 2022, A validated HPLC multichannel DAD method for the simultaneous determination of amoxicillin and doxycycline in pharmaceutical formulations and wastewater samples, *Appl. Sci.*, 12 (19), 9789.
- [5] Gebretsadik, H., Kahsay, G., Eticha, T., and Gebretsadikan, T., 2023, A validated new RP-HPLC method for simultaneous determination of amoxicillin, ampicillin and cloxacillin in pharmaceutical formulations, *Acta Chromatogr.*, 35 (2), 193–203.
- [6] Pauter, K., Szultka-Młyńska, M., and Buszewski, B., 2020, Determination and identification of antibiotic drugs and bacterial strains in biological samples, *Molecules*, 25 (11), 2556.
- [7] Ahmed, A.M.K., and Shakkor, S.J., 2019, Determination of Amoxicillin in pharmaceutical preparations by spectrophotometric and flow Injection-activated chemiluminescence methods, *Tikrit J. Pharm. Sci.*, 14 (1), 63–79.
- [8] Salehian, S., Sohrabi, M.R., and Davallo, M., 2021, Rapid and simple spectrophotometric method using feedforward backpropagation and radial basis function neural networks for the simultaneous determination of amoxicillin and clavulanic acid in commercial tablet and human blood serum, *Optik*, 247, 167908.
- [9] Iaa Riezk, A., Wilson, R.C., Rawson, T.M., Vasikasini, V., Paul Arkel, P., Ferris, T.J., Haigh, L.D., Cass, A.E.G., and Holmes, A.H., 2023, A rapid, simple, high-performance liquid chromatography method for the clinical measurement of beta-lactam antibiotics in serum and interstitial fluid, *Anal. Methods*, 15 (6), 829–836.
- [10] Abood, N.K., and Hassana, M.J.M., 2021, Spectrophotometric determination of sulfadoxine drug use cloud point and flow injection methods in pharmaceutical formulations, *Egypt. J. Chem.*, 64 (6), 2913–2924.
- [11] Deng, Z.H., Li, N., Jiang, H.L., Lin, J.M., and Zhao, R.S., 2019, Pretreatment techniques and analytical methods for phenolic endocrine disrupting chemicals in food and environmental samples, *TrAC, Trends Anal. Chem.*, 119, 115592.
- [12] Halko, R., Hagarová, I., and Andruch, V., 2023, Innovative approaches in cloud-point extraction, *J. Chromatogr. A*, 1701, 464053.
- [13] Fathi, S.A., Othman, N.S., and AL-Tae, A.T., 2023, Indirect spectrophotometric method for determination of methyl dopa in pure and pharmaceutical formulation, *Biomed. Chem. Sci.*, 2 (2), 149–154.
- [14] Asan, A., and Seddiq, N., 2022, A simple spectrophotometric determination of amoxicillin in

- drug samples, *J. Turk. Chem. Soc., Sect. A*, 9 (2), 423–432.
- [15] Elkanzi, N.A.A., Hrichi, H., Alolayan, R.A., Derafa, W., Zahou, F.M., and Bakr, R.B., 2022, Synthesis of chalcones derivatives and their biological activities: A review, *ACS Omega*, 7 (32), 27769–27786.
- [16] Larin, A., Ovchinnikov, I., Fershtat, L., and Makhova, N., 2018, 3,3'-(Diazene-1,2-diyl)bis[4-(nitroamino)-1,2,5-oxadiazole 2-oxide], *Molbank*, 2018 (3), M1003.
- [17] Xu, M., Wu, P., Shen, F., Ji, J., and Rakesh, K.P., 2019, Chalcone derivatives and their antibacterial activities: Current development, *Bioorg. Chem.*, 91, 103133.
- [18] Sinha, S., Batovska, D.I., Medhi, B., Radotra, B.D., Bhalla, A., Markova, N., and Sehgal, R., 2019, *In vitro* anti-malarial efficacy of chalcones: Cytotoxicity profile, mechanism of action and their effect on erythrocytes, *Malar. J.*, 18 (1), 421.
- [19] Wangngae, S., Chansaenpak, K., Nootem, J., Ngivprom, U., Aryamueang, S., Lai, R.Y., and Kamkaew, A., 2021, Photophysical study and biological applications of synthetic chalcone-based fluorescent dyes, *Molecules*, 26 (10), 2979.
- [20] Abid, S., Abdula, A.M., Al Marjani, M., and Abdulhameed, Q., 2019, Synthesis, antimicrobial, antioxidant and docking study of some novel 3,5-disubstituted-4,5-dihydro-1*H*-pyrazoles incorporating imine moiety, *Egypt. J. Chem.*, 62 (4), 739–749.
- [21] Hashim, H.J., Abood, N.K., and Nief, O.A., 2021, Spectroscopic estimation of cefepime by using batch, cloud point extraction and flow injection analysis methods, *Egypt. J. Chem.*, 64 (12), 6891–6900.
- [22] Abdelazim, A.H., Abourehab, M.A., Abd Elhalim, L.M., Almrasy, A.A., and Ramzy, S., 2023, Green adherent spectrophotometric determination of molnupiravir based on computational calculations; application to a recently FDA-approved pharmaceutical dosage form, *Spectrochim. Acta, Part A*, 285, 121911.
- [23] Imam, M.S., Abdelazim, A.H., Batubara, A.S., Gamal, M., Almrasy, A.A., Ramzy, S., Khojah, H., and Hasanin, T.H.A., 2023, Simultaneous green TLC determination of nirmatrelvir and ritonavir in the pharmaceutical dosage form and spiked human plasma, *Sci. Rep.*, 13 (1), 6165.

Preparation and Performance of ZnO and ZnO/MnO₂ Nanostructures as Anode Electrodes in DSSCs

Suaad Abd Mahdi Abd Noor^{1*} and Amer Muosa Juda Al-Shamari²

¹Pharmacology College, University of Kufa, Najaf 54001, Iraq

²Department of Chemistry, College of Science, University of Kufa, Najaf 54001, Iraq

* **Corresponding author:**

tel: +964-7831130620

email: Suaad.toobi@uokufa.edu.iq

Received: April 25, 2023

Accepted: May 23, 2023

DOI: 10.22146/ijc.84037

Abstract: Nanoparticles and nanocomposites prepared by the hydrothermal method (ZnO, ZnO/MnO₂) were used to build dye-sensitized solar cells (DSSCs), which were used as photoelectrodes using two natural dyes as the absorbent media: red (*Hibiscus sabdariffa*) and green (*Apium graveolens*). The results showed the efficiency of the green dye in DSSCs is superior to the red dye in terms of conversion efficiency (η). The purpose of the study is to improve the performance of dye solar cells. The properties of nanomaterials were studied by X-ray diffraction (XRD), scanning electron microscopy (FE-SEM), and transmission electron microscopy (TEM) for the analysis of ZnO NPs and ZnO/MnO₂, whereas the sizes of the prepared materials are within the size of 1–100 nm. The solar cell parameters were obtained from simple (I-V) measurements for nanomaterials prepared using two-dye DSSCs where I_{sc} represents the short circuit current through the solar cell when the voltage across the solar cell is zero, and V_{oc} represents the open circuit voltage across the solar cell and is the maximum voltage available from the solar cell. The photoelectrochemical properties of the two dye DSSCs in this study were calculated at 22.53 mW/cm² of the light intensity.

Keywords: semiconductors; nano chemical synthesis; photoelectrodes; establishment of DSSCs; conversion efficiency

■ INTRODUCTION

Concerns about greenhouse gas emissions and climate change have increased along with the corresponding energy demands as the world's population keeps growing [1-2]. Dye-sensitized solar cells (DSSCs) [3], organic solar cells (OSCs) [4], and perovskite solar cells (PSCs) [5-6] are examples of third-generation photovoltaic technologies that have been developed using inexpensive, simple, plentiful materials, and scalable fabrication techniques. Nonetheless, they are perfect for portable electronics [7] since they can be produced as small, light, and flexible solar modules [8-9]. Furthermore, they are potential for ambient energy harvesting for the wireless sensors used in internet of things (IoT) devices due to their excellent efficiency in low light, which beats other existing technologies under typical indoor conditions. [7,10-12]. In this article, new

materials that can be used to create high-performance DSSC-based photovoltaic devices have recently made strides [13-22]. Together with the increased possibilities for their potential incorporation in portable electronics, wireless sensor networks, and IoT devices [12], innovative DSSC device designs that have emerged in recent years using alternate redox shuttles and catalyst materials are discussed. The development in the related materials is also compiled in this study, showing how each functional component of a DSSC has been enhanced using new materials and production techniques. Also, a method for creating a novel cell design is given, which might be accomplished soon with the use of scalable fabrication techniques. Hydrothermal was used to create nanomaterials in this study because of the ease and speed of the method as well as the formation of high-purity nanomaterials in a short time.

■ EXPERIMENTAL SECTION

Materials

Chemicals used in the preparation of zinc oxide nanoparticles included $\text{Zn}(\text{NO}_3)_2 \cdot 6\text{H}_2\text{O}$ purchased from Thomas baker (India) with a purity of 98%, sodium hydroxide (NaOH) from Fluka with a purity of 97%, and ethanol ($\text{C}_2\text{H}_5\text{OH}$) Riedel-De-Haen AG, (Germany), 100% pure.

The ZnO/MnO_2 nanocomposite was prepared using manganese chloride tetrahydrate ($\text{MnCl}_2 \cdot 4\text{H}_2\text{O}$) from Thomas baker (India) with a purity of 98%, and the zinc chloride (ZnCl_2) from Thomas baker (India) with a purity of 99%. In addition, urea ($\text{CH}_4\text{N}_2\text{O}$) from Thomas baker (India) with a purity of 98%, and ethylene glycol ($\text{C}_2\text{H}_6\text{O}_2$) Merck, (Germany) with a purity of 99.9% were used as well. The materials used in the preparation and application of solar cells included iodine (I_2) from Merck, (Germany) with a purity of 97%, potassium iodide (KI) from Thomas baker (India) with a purity of 97%, and acetic acid (CDH-INDIA) with a purity of 97%.

Instrumentation

A device autoclave (China), centrifuge Hettich EBA20 (Made in Germany), and field emission scanning electron microscopy (FESEM) TESCAN MIRA3 Hv 300 Zeiss (Made in Germany) were used in this study. A magnetic-stirrer hot plate VS-130-SH(vision)/scientific co, LTD (Korea), programmable Keithley electrometer (2400)Tektronix Company, and pH-Meter HI 96107 Water-Tester Reverse Osmosis/Hanna-Instrumentals (China) were used in this work. A sensitive balance electronic balance type ABS 120-4 Kern & Sohn GmbH, transmission electron microscopy (TEM): Zeiss EM 10 C, 100 kV (Germany), and the electrical furnace (CARBOLITE) homemade were used in this study. A UV-vis spectrophotometer single beam EMCLAB-11-U.V-1100.Vis 200–1100 nm sinco (Made in Germany), UV-vis spectrophotometer double beam SCINCO Mega-2100 (Korea), volt-meter DT-9205A CE Auto Power, and X-ray diffraction (XRD) 2700 AB Haoyuan Co. (China) were used in this work.

Procedure

Synthesis ZnO of nanoparticles using the hydrothermal method

ZnO nanoparticles are synthesized using hydrothermal technology. The materials used are $\text{Zn}(\text{NO}_3)_2 \cdot 6\text{H}_2\text{O}$ and NaOH pellets. Throughout the experiment, all ingredients needed to make the ZnO nanoparticles were diluted in deionized water (DIW). Zinc nitrate solutions at a concentration of 0.5 M were prepared with continuous stirring for 30 min using a mild magnetic stirrer to completely dissolve $\text{Zn}(\text{NO}_3)_2 \cdot 6\text{H}_2\text{O}$ in 30 mL of DIW. While this was happening, 30 mL of DIW was used to prepare a 5 M NaOH solution by agitating it for the same amount of time that the $\text{Zn}(\text{NO}_3)_2$ granules were dispersed. The NaOH solution is gradually added to the $\text{Zn}(\text{NO}_3)_2$ solution with continuous stirring until the pH of the reactants reaches 12. This solution mixture is placed in a Teflon-lined autoclave made of stainless steel with a capacity of 70 mL and heated to 100 °C for 2 h in the electric oven. Then, we take out the autoclave and let it cool down gradually to room temperature. After washing the precipitate repeatedly with deionized water and ethanol, it was dried and collected [23-28].

Preparation of ZnO/MnO_2 nanocomposites by the hydrothermal method

A hydrothermal technique was used to produce the ZnO/MnO_2 nanocomposite. The materials, 2.968 g of $\text{MnCl}_2 \cdot 4\text{H}_2\text{O}$, 6.133 g of ZnCl_2 , and 2.342 g of $\text{CH}_4\text{N}_2\text{O}$, were mixed and dissolved in 150 mL of $\text{C}_2\text{H}_6\text{O}_2$ under constant stirring for 30 min at 350 rpm under ambient conditions. Then the solution is transferred to an autoclave made of stainless steel and Teflon. The autoclave is closed and left in the oven for 24 h at a temperature of 200 °C. Then, the autoclave is taken out from the oven and left to cool at room temperature. Afterwards, the solution and the precipitate are separated by a centrifuge. Then, DIW mixed with ethanol is used to wash the sample several times until a precipitate is produced. The resulting material is then dried at 100 °C, crushed, and subjected to calcination at

600 °C for 6 h. After drying and cooling, the ZnO/MnO₂ nanocomposites appeared as a dark brownish-colored powder [29].

■ RESULTS AND DISCUSSION

Characterization of Prepared Compounds

XRD analysis

The density and full breadth at half the maximum size and position were found through analysis of the XRD results. Peaks at 2θ , 31.67°, 34.34°, 36.20°, 47.46°, 56.54°, 62.83°, and 67.91°, respectively, were observed in nine diffractions and corresponded to crystal levels of (100), (002), (101), (102), (110), (103), and (112). Broad neutrality and a sharper peak without any peak twisting were observed at (101) peaks. The analysis was that these many peaks showed crystals with irregular orientation. ZnO nanoparticles with an average crystal volume of D

were created using the Debye-Scherer formula [30]. Hexagonal nanostructures are observed in ZnO. The XRD results obtained for the ZnO nanoparticles are consistent with previous literary studies (Fig. 1) because of their strong and narrow diffraction peaks, particularly in (100), (002), and (003). The XRD data breakdown demonstrates that the ZnO nanoparticles sample has a high degree of crystalline quality (101). Fig. 2 illustrates how XRD was used to describe the crystalline nature and crystal phases of the ZnO/MnO₂. The diffraction peaks show that there are polycrystalline MnO₂ and ZnO crystal planes present. According to sources, the composite consists of a cubic type MnO₂ and a hexagonal phase of wurtzite type ZnO (JCPDS card number: 65-3411) and (JCPDS card number: 39-0375) [31] Using Scherrer's formula, the average crystal size ranges between 15.47 and 66.62 nm.

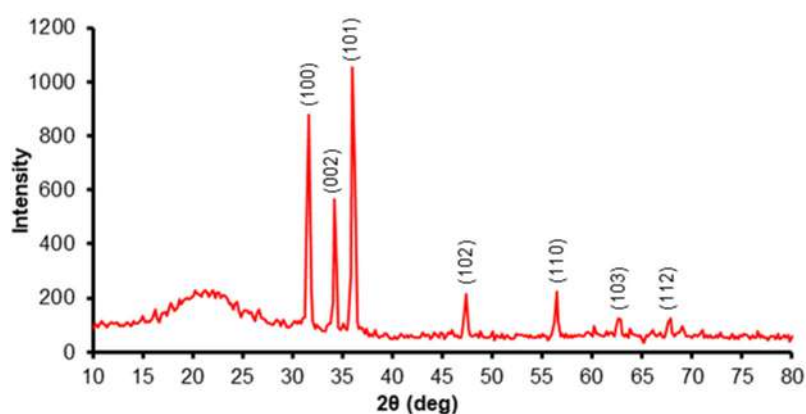


Fig 1. X-ray diffraction pattern of ZnO nanostructures

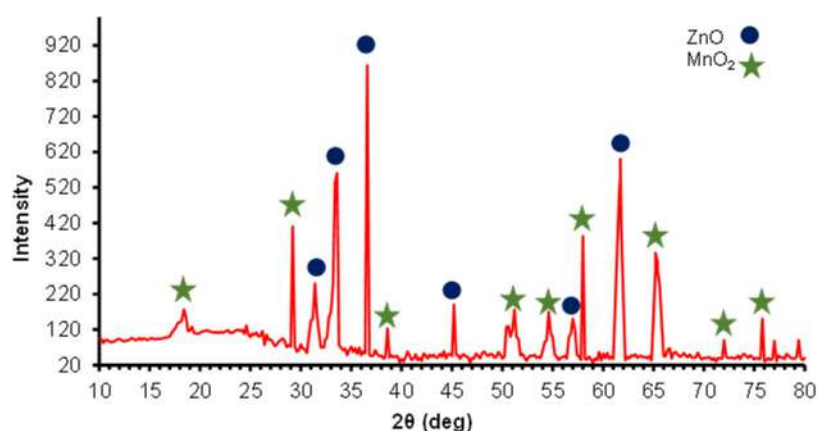


Fig 2. X-ray diffraction pattern of ZnO/MnO₂ nanocomposite

FE-SEM analysis

Fig. 3 displays FE-SEM images of ZnO nanostructures and ZnO/MnO₂ nanocomposites created. The typical diameter is 23.63 nm, more proof that ZnO is formed as a tangle of nanoparticles may be found in Fig. 3. The microstructural and textural properties of the prepared samples were decided by consulting the FESEM micrographs recorded at various scales. Fig. 4 shows the FESEM images of ZnO/MnO₂ at different magnification values, which demonstrated that the nanocomposite particles are composed of highly fibrous, gritty, and porous microstructures of 13–65 nm diameters with

vastly bumpy and uneven surfaces. Due to this, the surface area of the prepared is enhanced which has facilitated the adsorption and catalytic performance greatly.

TEM analysis

Analysis of TEM was employed to evaluate the created nanoparticles and nanocomposite materials. Fig. 5 illustrates the spherical shape of ZnO nanoparticles with sizes between 17.99 and 77.40 nm. The nanoparticles of the ZnO/MnO₂ nanocomposite are shown in Fig. (6) in terms of their shapes and sizes, and they range in size from 62.48–68.99 nm.

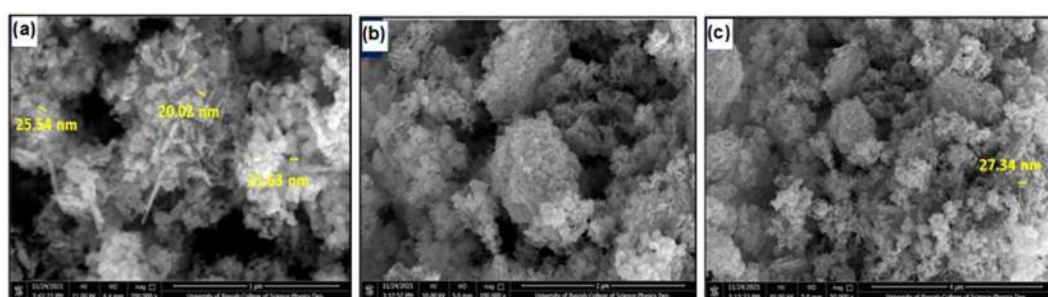


Fig 3. FE-SEM images of ZnO nanoparticles with a magnification of (a) 1 μm, (b) 2 μm, and (c) 4 μm

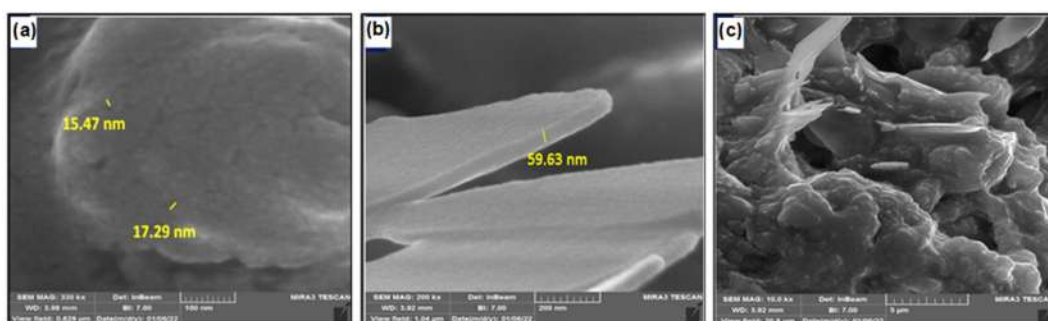


Fig 4. FE-SEM images of ZnO/MnO₂ nanocomposite with a magnification of (a) 100 nm, (b) 200 nm, and (c) 5 μm

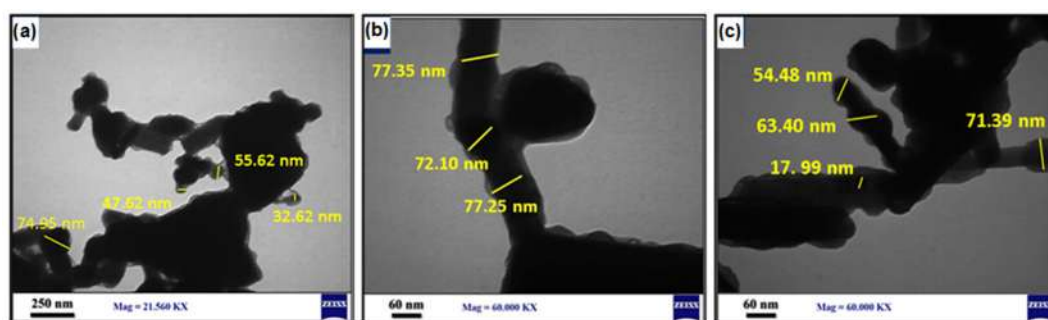


Fig 5. TEM images of ZnO nanoparticle with a magnification of (a) 250 nm, (b) 60 nm, and (c) 60 nm and an image of the oxide nanoparticles from another direction

Fabrication of Dye-Sensitized Solar Cells

In order to prepare DSSCs, ZnO nanoparticles and ZnO/MnO₂ nanocomposite were synthesized in the study and employed as a photoelectrode with two natural dyes as absorbent media: red dye from *Hibiscus sabdarriffa* and green dye from *Apium graveolens*. The I-V and characteristics of DSSCs made from nanosurfaces and natural dyes are shown in Fig. 7 and 8. As demonstrated in Table 1, the results indicated that the green dye improves the DSSCs conversion efficiency (η) over the red dye. There are various causes, one of which is the energy gap, which is different for the red and green dyes and is

larger for the green dye. As a result, more ray wavelengths travel through the cells and are absorbed by the dye [32]. Second, since each of them has a unique surface area, there are differences between the surface areas of various nanomaterials. The effectiveness of the constructed DSSC rises as the green dye's adsorption on nanoscale surfaces increases. Moreover, due to the increased concentration of natural dye impurities, the current yield of DSSCs made with the natural red dye is lower than that of DSSCs rises as the green dye's adsorption on nanoscale surfaces increases. Moreover, due to the increased concentration of natural dye impurities, the

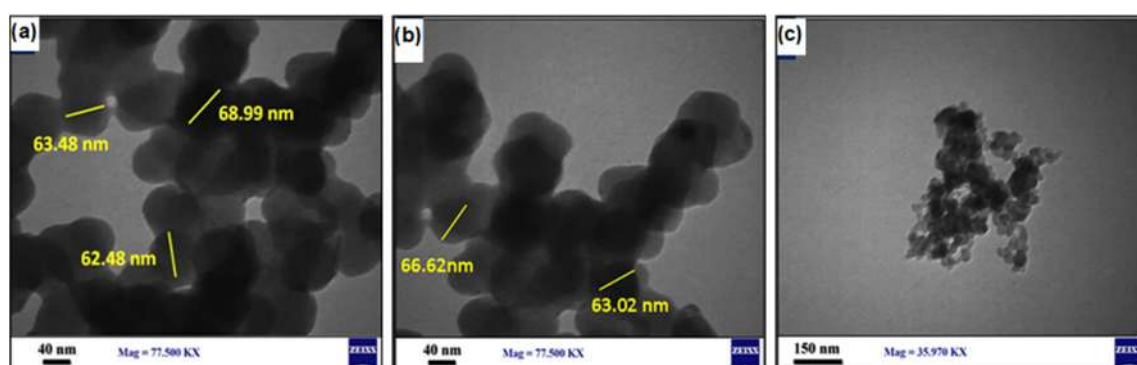


Fig 6. TEM images of ZnO/MnO₂ nanocomposite with a magnification (a) 40 nm, (b) 40 nm and an image of the oxide nanoparticles from another direction, and (c) 150 nm

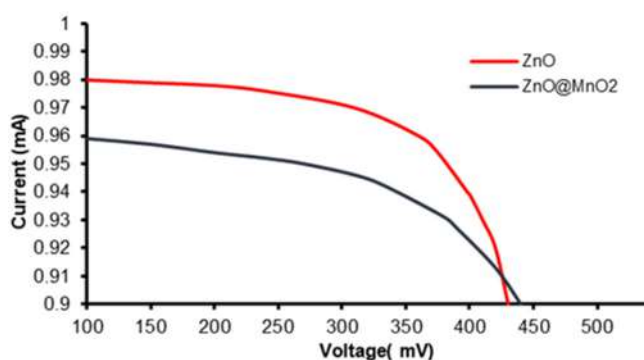


Fig 7. I-V characteristics of prepared DSSCs nanoparticles and nanocomposite prepared with red dye

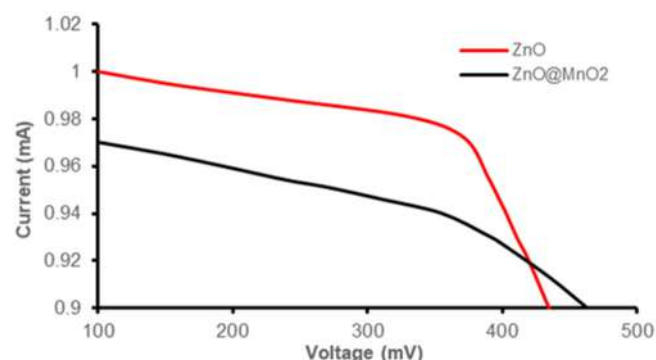


Fig 8. I-V characteristics of prepared DSSCs nanoparticles and nanocomposite prepared with green dye

Table 1. Photoelectrochemical characteristics of DSSCs ($A = 5.4 \text{ cm}^2$ red dye and 4.5 cm^2 green dye) at 22.53 mW/cm^2 of light intensity

Catalyst/dye	I_{SC} (mA)	V_{oc} (V)	I_{max} (mA)	V_{max} (V)	P_{max}	FF	η %	
ZnO	Red dye	0.980	430	0.974	368	358.43	0.8506	0.6640
	Green dye	1.000	435	0.980	380	372.40	0.8561	0.8276
ZnO/MnO ₂	Red dye	0.959	440	0.946	360	340.56	0.8071	0.6310
	Green dye	0.970	463	0.938	365	342.37	0.7623	0.7610

current yield of DSSCs made with the natural red dye is lower than that of DSSCs made with the green dye [33]. Also, the low intensity of 22.53 mW/cm^2 of the light source used is another factor contributing to the low value found for the manufactured DSSCs and the use of carbon as the cathode electrode on the FTO solar cell's rear surface. Moreover, a conduction electrolyte composed of an I_2/iodide solution is created. DSSCs produced using Keithley 2400 were used to measure the photovoltaic performance (Fig. 9). Most solar cell parameters can be obtained from simple I-V measurements. Table 1 shows the IV measurement of solar cells under forward prejudice and brightness. The short circuit current (I_{sc}) is the current through the solar cell when the voltage across the solar cell is zero. The open circuit voltage (V_{oc}) is the voltage across the solar cell when the current through the solar cell is zero and it is the maximum voltage available from the solar cell [34]. The maximum power point (P_{max}) is the state under which the solar cell generates its maximum power. The current and voltage in this condition are defined as I_{max} and V_{max} , respectively. The fill factor (FF) and the conversion efficiency (η) are metrics used to characterize the performance of the solar cell [35]. The fill factor is defined as the ratio of P_{max} divided by the product of V_{oc} and I_{sc} . The conversion efficiency is defined as the ratio of P_{max} to the product of the input light irradiance (E) and the solar cell surface area (A_c) (see Eq. (1-4)) [36].

$$FF = \frac{P_{max}}{V_{oc} \times J_{sc}} \quad (1)$$

$$\eta = \frac{V_{oc} \times J_{sc} \times FF}{E} \quad (2)$$

$$FF = \frac{V_{max} \times J_{max}}{V_{oc} \times J_{sc}} \quad (3)$$

$$\% \eta = \frac{V_{oc} \times J_{sc} \times FF}{P_{in}} \quad (4)$$

Preparation of the Anode Electrodes

As mentioned earlier, the hydrothermal process is used to prepare the nanomaterials. A small amount of prepared nanomaterials is added and mixed with acetic acid and DIW (paste form) and spread on FTO glass plates as an anode electrode, one of the types of solar cells, leaving the cell edges not coated with the nanomaterial.



Fig 9. The measurement setup of the solar cells under the light effect using the Keithley device

Then, the solar cell is placed in an oven at a temperature of $40\text{--}50 \text{ }^\circ\text{C}$ to dry sufficiently. The anode electrode prepared from the nanosurface and the FTO glass was immersed in the red dye solution (the first dye) in the vessel to allow it to adhere to the surface of the nanomaterial for 24 h in a dark place. Then, the solar cells were removed from the dye solution the next day and also dried in a dark place to obtain the anode electrode. The prepared binary nanocomposite (ZnO/MnO_2) goes through the same steps to form the anode electrode in this way with the two dyes.

In order to prepare the cathode electrode, carbon (craft) is applied to the solar cell's surface, leaving the edges unaffected. The cathode pole was therefore furnished.

CONCLUSION

ZnO nanoparticles and ZnO/MnO_2 nanocomposites were developed using a single-step hydrothermal process. ZnO nanoparticles and ZnO/MnO_2 nanocomposites have been used as electrodynamic catalysts, and the effectiveness of nanomaterials (semiconductors) in the formation of DSSCs has been investigated. The use of solar cells in daily life applications was also performed because of their wide characteristics in terms of surface area and smallness, size and the power it provides. The study also shows the possibility of producing nanomaterials in several ways, including the simple chemical method. To know the effectiveness of the green dye on DSSCs compared to the red dye in terms of transduction efficiency (η). The effect of prepared ZnO nanoparticles and ZnO/MnO_2 nanocomposites on the conversion efficiency (η) with the red (*Hibiscus sabdariffa*) and

green (*Apium Gravalens*) dyes was studied. One of the benefits of using different characterizations is to know the nature of the surfaces of nanomaterials and their effectiveness as photoelectrodes, in addition to their crystal structures and different shapes. We also conclude the possibility of developing solar cells using various nanomaterials to improve their work and electrical properties and use them in the future to provide energy and electricity at the lowest cost. The functionality improvement in solar cells is also affected by the size of the nanocrystals during the solid-to-solid phase transition. Therefore, phase control is a critical step.

■ ACKNOWLEDGMENTS

I would like to thank the Ministry of Higher Education and Scientific Research/Presidency of the University of the Cove and the Faculty of Science, Department of Chemistry, and the Faculty of Pharmacy for providing laboratories and equipment for the completion of research.

■ AUTHOR CONTRIBUTIONS

The authors made equal contributions to conceptualization, design, data acquisition, data analysis and interpretation based on current and past scientific facts and studies, participated in the drafting of articles or critical review of important intellectual content, agreed to submit them to the current magazine; gave its final approval for the publication of the version, and agreed to be responsible for all aspects of the work. Dr. Amer Muosa Juda Al-Shamari researcher had the idea of researching, proposing the method of work and checking scientific information after the research had been completed. Researcher Suaad Abd Al-Mahdi conducted the proposed methods of research and collected the results, as well as provided financial contribution to the completion of the research.

■ REFERENCES

- [1] Wu, Y., Li, C., Tian, Z., and Sun, J., 2020, Solar-driven integrated energy systems: State of the art and challenges, *J. Power Sources*, 478, 228762.
- [2] Yan, N., Zhao, C., You, S., Zhang, Y., and Li, W., 2020, Recent progress of thin-film photovoltaics for indoor application, *Chin. Chem. Lett.*, 31 (3), 643–653.
- [3] Metwally, R.A., El Nady, J., Ebrahim, S., El Sikaily, A., El-Sersy, N.A., Sabry, S.A., and Ghozlan, H.A., 2023, Biosynthesis, characterization and optimization of TiO₂ nanoparticles by novel marine halophilic *Halomonas* sp. RAM2: Application of natural dye-sensitized solar cells, *Microb. Cell Fact.*, 22 (1), 78.
- [4] Liu, S., Yuan, J., Deng, W., Luo, M., Xie, Y., Liang, Q., Zou, Y., He, Z., Wu, H., and Cao, Y., 2020, High-efficiency organic solar cells with low non-radiative recombination loss and low energetic disorder, *Nat. Photonics*, 14 (5), 300–305.
- [5] Wang, S.Y., Chen, C.P., Chung, C.L., Hsu, C.W., Hsu, H.L., Wu, T.H., Zhuang, J.Y., Chang, C.J., Chen, H.M., and Chang, Y.J., 2019, Defect passivation by amide-based hole-transporting interfacial layer enhanced perovskite grain growth for efficient *p-i-n* perovskite solar cells, *ACS Appl. Mater. Interfaces*, 11 (43), 40050–40061.
- [6] Omer, M.I., Ye, T., Li, X., Ma, S., Wu, D., Wei, L., Tang, X., Ramakrishna, S., Zhu, Q., Xiong, S., Xu, J., Vijila, C., and Wang, X., 2023, Two quasi-interfacial *p-n* junctions observed by a dual-irradiation system in perovskite solar cells, *npj Flexible Electron.*, 7 (1), 23.
- [7] Liao, Y., Tian, N., Wang, J., Yao, D., Zheng, G., Zhou, B., Yang, Y., and Long, F., 2022, Performance enhancement of evaporated CsPbI₂Br perovskite solar cells with a CuSCN hole transport layer via a cesium bromide buffer layer, *ACS Appl. Energy Mater.*, 5 (8), 9542–9548.
- [8] Mishu, M.K., Rokonzaman, M., Pasupuleti, J., Shakeri, M., Rahman, K.S., Hamid, F.A., Tiong, S.K., and Amin, N., 2020, Prospective efficient ambient energy harvesting sources for IoT-equipped sensor applications, *Electronics*, 9 (9), 1345.
- [9] Bardwell, M., Wong, J., Zhang, S., and Musilek, P., 2018, Design considerations for IoT-based PV charge controllers, *2018 IEEE World Congress on Services (SERVICES)*, San Francisco, CA, USA, 2-7 July 2018, 59–60.

- [10] Michaels, H., Rinderle, M., Freitag, R., Benesperi, I., Edvinsson, T., Socher, R., Gagliardi, A., and Freitag, M., 2020, Dye-sensitized solar cells under ambient light powering machine learning: Towards autonomous smart sensors for the internet of things, *Chem. Sci.*, 11 (11), 2895–2906.
- [11] Dhingra, S., Madda, R.B., Patan, R., Jiao, P., Barri, K., and Alavi, A.H., 2020, Internet of things-based fog and cloud computing technology for smart traffic monitoring, *Internet Things*, 14, 100175.
- [12] Lee, H.K.H., Barbé, J., Meroni, S.M.P., Du, T., Lin, C.T., Pockett, A., Troughton, J., Jain, S.M., De Rossi, F., Baker, J., Carnie, M.J., McLachlan, M.A., Watson, T.M., Durrant, J.R., and Tsoi, W.C., 2019, Outstanding indoor performance of perovskite photovoltaic cells – Effect of device architectures and interlayers, *Sol. RRL*, 3 (1), 1800207.
- [13] Prajapat, K., Dhonde, M., Sahu, K., Bhojane, P., Murty, V.V.S., and Shirage, P.M., 2023, The evolution of organic materials for efficient dye-sensitized solar cells, *J. Photochem. Photobiol., C*, 55, 100586.
- [14] Meador, W.E., Liyanage, N.P., Watson, J., Groenhout, K., and Delcamp, J.H., 2023, Panchromatic NIR-absorbing sensitizers with a thienopyrazine auxiliary acceptor for dye-sensitized solar cells, *ACS Appl. Energy Mater.*, 6 (10), 5416–5428.
- [15] Perrella, F., Li, X., Petrone, A., and Rega, N., 2023, Nature of the ultrafast interligands electron transfers in dye-sensitized solar cells, *JACS Au*, 3 (1), 70–79.
- [16] Kumar, D., Parmar, K.P.S., and Kuchhal, P., 2020, Optimizing photovoltaic efficiency of a dye-sensitized solar cell (DSSC) by a combined (modelling-simulation and experimental) study, *Int. J. Renewable Energy Res.*, 10 (1), 165–174.
- [17] Supriyanto, E., Kartikasari, H.A., Alviati, N., and Wiranto, G., 2019, Simulation of dye-sensitized solar cells (DSSC) performance for various local natural dye photosensitizers, *IOP Conf. Ser.: Mater. Sci. Eng.*, 515, 012048.
- [18] Bashir, M.B.A., Rajpar, A.H., Salih, E.Y., and Ahmed, E.M., 2023, Preparation and photovoltaic evaluation of CuO@Zn(Al)O-mixed metal oxides for dye-sensitized solar cell, *Nanomaterials*, 13 (5), 802.
- [19] Alizadeh, A., Roudgar-Amoli, M., Bonyad-Shekalgourabi S.M., Shariatinia, Z., Mahmoudi, M., and Saadat, F., 2022, Dye-sensitized solar cells go beyond using perovskite and spinel inorganic materials: A review, *Renewable Sustainable Energy Rev.*, 157, 112047.
- [20] Lu, J., Liu, S., and Wang, M., 2018, Push-pull zinc porphyrins as light-harvesters for efficient dye-sensitized solar cells, *Front. Chem.*, 6, 00541.
- [21] Kakiage, K., Aoyama, Y., Yano, T., Oya, K., Fujisawa, J., and Hanaya, M., 2015, Highly-efficient dye-sensitized solar cells with collaborative sensitization by silyl-anchor and carboxy-anchor dyes, *Chem. Commun.*, 51 (88), 15894–15897.
- [22] Cao, Y., Liu, Y., Zakeeruddin, S.M., Hagfeldt, A., and Grätzel, M., 2018, Direct contact of selective charge extraction layers enables high-efficiency molecular photovoltaics, *Joule*, 2, 1108–1117.
- [23] Abu Nayem, S.M., Shah, S.S., Chaity, S.B., Biswas, B.K., Nahar, B., Aziz, M.A., and Hossain, M.Z., 2022, Jute stick extract assisted hydrothermal synthesis of zinc oxide nanoflakes and their enhanced photocatalytic and antibacterial efficacy, *Arabian J. Chem.*, 15 (11), 104265.
- [24] Zhou, Y., Xu, L., Wu, Z., Li, P., and He, J., 2017, Optical and photocatalytic properties of nanocrystalline ZnO powders synthesized by a low-temperature hydrothermal method, *Optik*, 130, 673–680.
- [25] Raji, R., and Gopchandran, K.G., 2017, ZnO nanostructures with tunable visible luminescence: Effects of kinetics of chemical reduction and annealing, *J. Sci.: Adv. Mater. Devices*, 2 (1), 51–58.
- [26] Selim, H., Nada, A.A., El-Sayed, M., Hegazey, R.M., Souaya, E.R., and Kotkata, M.F., 2018, The effect of ZnO and its nanocomposite on the performance of dye sensitized solar cell, *Nano Sci. Nano Technol.*, 12 (1), 122.
- [27] Shanavas Khan, J., Asha Radhakrishnan, A., and Beena, B., 2018, Polyaniline/zinc oxide nanocomposite as a remarkable antimicrobial agent in contrast with PANI and ZnO, *Indian J. Adv. Chem. Sci.*, 6 (2), 71–76.

- [28] Quadri, T.W., Olasunkanmi, L.O., Fayemi, O.E., Solomon, M.M., and Ebenso, E.E., 2017, Zinc oxide nanocomposites of selected polymers: Synthesis, characterization, and corrosion inhibition studies on mild steel in HCl solution, *ACS Omega*, 2 (11), 8421–8437.
- [29] Anantha, M.S., Kiran Kumar, S.R., Anarghya, D., Venkatesh, K., Santosh, M.S., Yogesh Kumar, K., and Muralidhara, H.B., 2021, ZnO@MnO₂ nanocomposite modified carbon paste electrode for electrochemical detection of dopamine, *Sens. Int.*, 2, 100087.
- [30] Bulcha, B., Leta Tesfaye, J., Anatol, D., Shanmugam, R., Dwarampudi, L.P., Nagaprasad, N., Bhargavi, V.L.N., and Krishnaraj, R., 2021, Synthesis of zinc oxide nanoparticles by hydrothermal methods and spectroscopic investigation of ultraviolet radiation protective properties, *J. Nanomater.*, 2021, 8617290.
- [31] Acharyya, S., Dey, S., Nag, S., and Guha, P.K., 2018, ZnO cladded MnO₂ based resistive sensor device for Formaldehyde sensing, *2018 IEEE SENSORS*, New Delhi, India, 28-31 October 2018, 1–4.
- [32] Lokman, M.Q., Shafie, S., Shaban, S., Ahmad, F., Jaafar, H., Mohd Rosnan, R., Yahaya, H., and Abdullah, S.S., 2019, Enhancing photocurrent performance based on photoanode thickness and surface plasmon resonance using Ag-TiO₂ nanocomposites in dye-sensitized solar cells, *Materials*, 12 (13), 2111.
- [33] Schöttner, L., Nefedov, A., Yang, C., Heissler, S., Wang, Y., and Wöll, C., 2019, Structural evolution of α -Fe₂O₃ (0001) surfaces under reduction conditions monitored by infrared spectroscopy preview on related iron oxide, *Front. Chem.*, 7, 00451.
- [34] Fang, Y., Ma, P., Cheng, H., Tan, G., Wu, J., Zheng, J., Zhou, X., Fang, S., Dai, Y., and Lin, Y., 2019, Synthesis of low-viscosity ionic liquids for application in dye-sensitized solar cells, *Chem. - Asian J.*, 14 (23), 4201–4206.
- [35] Rangel, D., Gallegos, J.C., Vargas, S., García, F., and Rodríguez, R., 2019, Optimized dye-sensitized solar cells: A comparative study with different dyes, mordants and construction parameters, *Results Phys.*, 12, 2026–2037.
- [36] Abdul-Sajad Al-Hachamy, F.A., 2020, Preparation of High Activity Binary and Ternary MgO Nanocomposites Catalysts and Their Environmental Application, *Dissertation*, College of Science, University of Kufa.

Supplementary Data

This supplementary data is a part of a paper entitled “Synthesis and Characterization of Oligomer Bis(*trans*-2,3-dibromo-4-hydroxy-2-butenyl)terephthalate as a Green Corrosion Inhibitor on Mild Steel in 1 M H₃PO₄ Solution”.

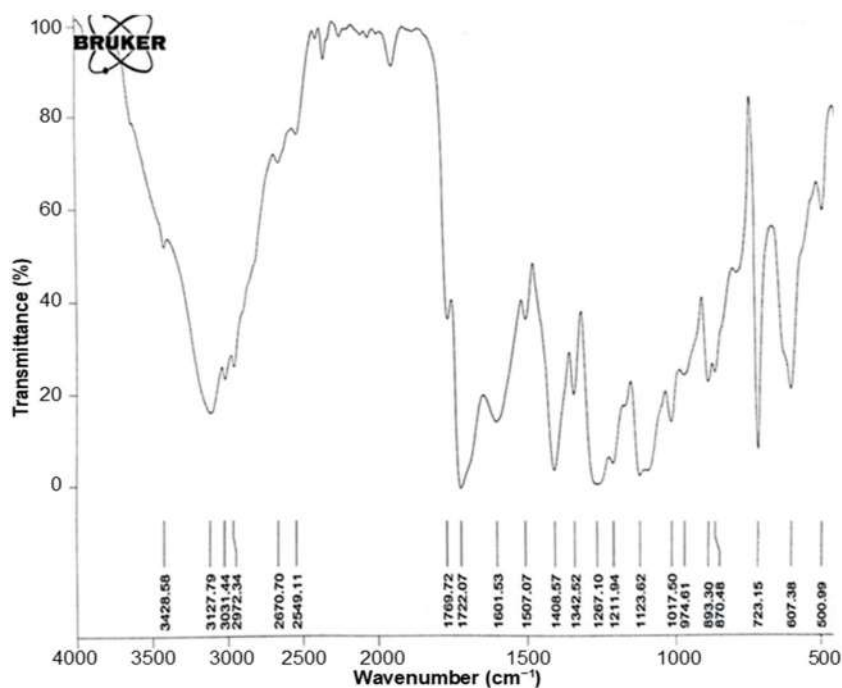


Fig S1. FTIR spectrum of BDBHBT

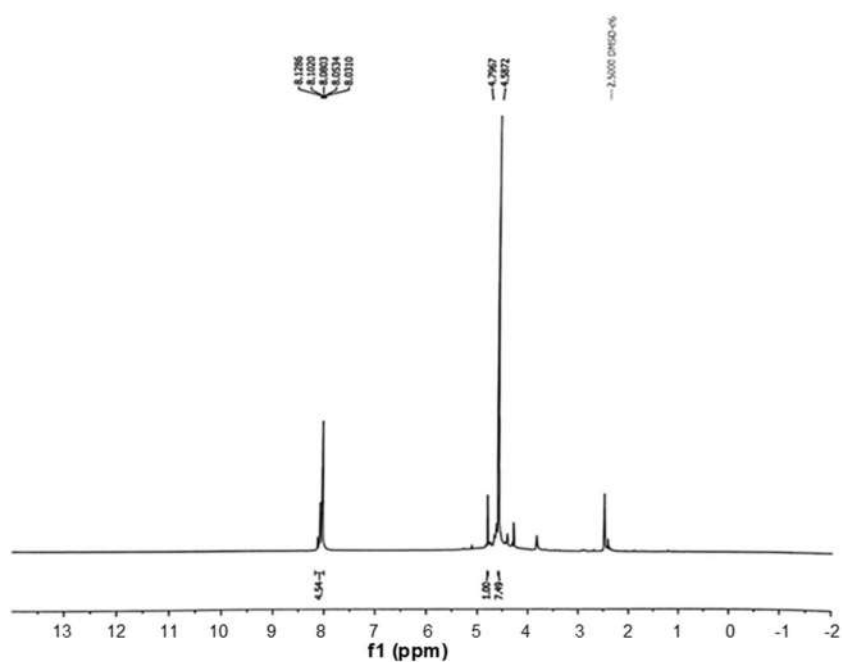


Fig S2. ¹H-NMR spectrum of BDBHBT

Synthesis and Characterization of Oligomer Bis(*trans*-2,3-dibromo-4-hydroxy-2-butenyl)terephthalate as a Green Corrosion Inhibitor on Mild Steel in 1 M H₃PO₄ Solution

Rasha Jasim Tuama*

Department of Chemistry, College of Science, University of Thi-Qar, Thi-Qar 64001, Iraq

* **Corresponding author:**

email: Rashajasim@utq.edu.iq

Received: April 26, 2023

Accepted: June 13, 2023

DOI: 10.22146/ijc.84060

Abstract: Poly(ethylene terephthalate) (PET) waste was depolymerized by *trans*-2,3-dibromo-2-butene-1,4-diol in the presence of manganese acetate as a catalyst using microwave irradiation as opposed to the conventional heating process in order to reduce the time required for PET depolymerization. The depolymerization product bis(*trans*-2,3-dibromo-4-hydroxy-2-butenyl)terephthalate (BDBHBT) was isolated, characterized, and evaluated as a green inhibitor for mild corrosion steel in corrosive 1 M H₃PO₄ medium. This product was characterized using FTIR and ¹H-NMR. The effects of immersion time, inhibitor concentration, and reaction temperature were studied. The chemical technique utilized in this study was weight loss, while the electrochemical technique employed an open circuit potential. With 0.6 g/L of BDBHBT inhibitor, the highest corrosion inhibition efficiency of 83.3% was observed. The kinetic and thermodynamic functions were calculated, and the results indicated that the investigated inhibitor was physically adsorbed on the surface and confirmed to the Langmuir adsorption isotherm. This study aims to lessen pollution of the environment by transforming PET waste to a beneficial oligomer BDBHBT and estimating the inhibitory effect of this product on the corrosion of mild steel in 1 M H₃PO₄.

Keywords: poly(ethylene terephthalate) waste; green corrosion inhibitor; phosphoric acid; weight loss; open circuit potential

■ INTRODUCTION

Poly(ethylene terephthalate) (PET) is an important polymer in the world of plastics and packaging due to its most significant applications [1-2]. Due to its non-biodegradability in the environment, it is widely used in thermoplastics, which generate tons of waste that would destabilize the ecosystem equilibrium; therefore, it is an excellent material for recycling [3-4]. Recycling PET is one of the most successful and widespread examples of polymer recycling, which has become the most important process from an ecological standpoint and provided a business opportunity due to the widespread use of PET bottles, fibers, and packaging [5-6]. PET waste can be recycled through various processes, including chemical and physical recycling. Chemical recycling can be defined as the reaction of PET with different chemicals to produce chemical industry-relevant products [7]. Various chemical

recycling methods for PET, including glycolysis, methanolysis, hydrolysis, ammonolysis, aminolysis, and hydrogenation, have been used to investigate the chain scission-induced degradation of PET's main chain [8-9]. Nathaniel Wyeth patented the PET container in 1973, and it became widely used in the 1980s to make throwaway soft drink bottles. In 1987, over 700 million pounds of PET were utilized to make them [10].

Besides, corrosion is the deterioration of metals and alloys in corrosive environments. Constantly occurring in nature, the corrosion reaction process of metals is one of the primary concerns of the gas and oil industry. Globally, the annual economic loss caused by corrosion is enormous; thus, controlling and reducing the cost of this economic issue costs billions of dollars [11-12]. Corrosion protection of metal constructions is therefore considered a very important subject. Acidic solutions are

utilized extensively to clean, descale, pick, and acidify oil wells. Inhibitors of corrosion are necessary to prevent corrosion of metal alloys in these acid solutions [13].

Phosphoric acid has numerous industrial uses and it is compatible with a great deal of chemical and petroleum apparatus [14-15]. The majority of this apparatus is composed of mild steel that is susceptible to corrosion when exposed to acid. For this reason, corrosion inhibitors are used to shield mild steel from different forms and corrosive conditions, and the presence of these inhibitors decreases the corrosion rate of steel, thereby increasing its lifetime [16-17]. The majority of efficient acid inhibitors are organic compounds with oxygen, nitrogen, and/or sulfur, and these compounds bind on the surface of the steel to inhibit corrosion [18-19].

This is one of a series of works aimed at mitigating environmental contamination by transforming waste PET into beneficial materials and evaluating the inhibitory effect of these useful products on the corrosion of certain metals and alloys in various aqueous media. In this study, *trans*-2,3-dibromo-2-butene-1,4-diol was used to convert PET waste into the oligomer bis(*trans*-2,3-dibromo-4-hydroxy-2-butenyl)terephthalate (BDBHBT). The product (oligomer) was investigated as a green inhibitor for the corrosion of mild steel in 1 M H₃PO₄.

■ EXPERIMENTAL SECTION

Materials

After removing covers and labels, used PET bottles were collected, washed, and dried before being reused. These bottles have been split into tiny chips (6 × 6 mm²). The materials *trans*-2,3-dibromo-2-butene-1,4-diol and manganese acetate were purchased from Sigma Aldrich Chemical Company in England. The corrosive solution (1 M H₃PO₄) was made by diluting H₃PO₄ of analytical grade with double-distilled water. Specimens of mild steel were used in all experiments; these specimens contained metals listed in Table 1.

Instrumentation

Using Fourier transform infrared spectral data recorded over the 400–4000 cm⁻¹ wavenumber range, a Bruker FTIR-spectrometer was utilized to determine the chemical's structure. The prepared substance was thawed by DMSO-*d*₆ and investigated with a ¹H-NMR spectrometer model Bruker spectrophotometer (500 MHz) as an additional spectroscopic method for determining the chemical structure.

Procedure

Microwave depolymerization of PET: The reaction of PET with *trans*-2,3-dibromo-2-butene-1,4-diol

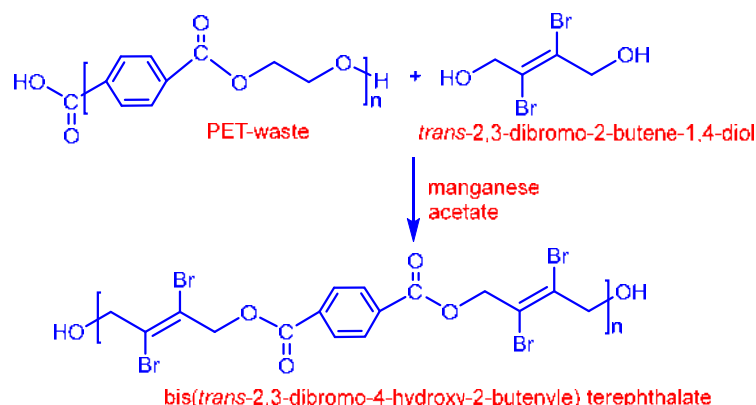
PET waste (1 g) was depolymerized with *trans*-2,3-dibromo-2-butene-1,4-diol (7.37 g) using 0.5% manganese acetate (0.005 g). PET was depolymerized using an electromagnetic source for microwave generation oven (LG, 2.45 GHz, maximal power: 900 W). The mixture was introduced into a reaction vial with a loose stopper, which was then placed in a microwave reactor. The reaction was permitted to continue with 450 W for a prolonged duration of time (30 min). This mixture was permitted to cool at room temperature. At the end of the reaction, an excess amount of distilled water was added to the mixture while vigorously stirring. The mixture was then separated. The collected filtrate was stored in a refrigerator for 24 h. Black crystalline powder was obtained in the filtrate, indicating that an oligomer BDBHBT had precipitated from the product, and it was separated and desiccated [20-21], yielding 4 g. The mechanism was illustrated in Scheme 1.

Weight loss measurements

Mild steel coupons of 4 × 8 × 0.1 cm dimensions were used as test specimens. Emery paper was used manually to clean them, degreased with acetone, rinsed with distillate water, and dried. The described treatment was performed promptly prior to each measurement.

Table 1. Contents of mild steel specimens

Element	C	Mn	P	Mo	Al	Sn	V	Nb	Ni	Cu	Fe
Weight (%)	0.170	0.057	0.011	0.022	0.011	0.005	0.004	0.007	0.027	0.043	Balance



Scheme 1. Preparation of bis(*trans*-2,3-dibromo-4-hydroxy-2-butenyl)terephthalate (BDBHBT)

Weight loss studies were conducted on specimens of mild steel submerged in 1 M H_3PO_4 medium in various concentrations of inhibitor (0, 0.1, 0.2, 0.4, and 0.6 g/L) at different temperatures (303, 323, and 333 K) for different immersion time (2, 4, and 8 h). The corrosion rate and efficiency of the inhibitor were determined based on weight loss for every coupon of every test configuration in every group. Corrosion rate (CR) is calculated from the change in weight of specimens in mils per year (mpy) using the relationship [22-23], Eq. (1):

$$\text{Corrosion rate (mpy)} = \frac{534 \cdot W}{A \cdot d \cdot t} \quad (1)$$

W is weight loss due to corrosion (mg), d is specimen's density (mg/cm^3), A is exposed surface area (in^2), and t is time of the immersion (h).

Regarding inhibitor efficiency (%IE) and surface coverage (θ), Eq. (2) and (3) are utilized [24-25]:

$$\%IE = \frac{W_0 - W}{W_0} \times 100 \quad (2)$$

$$\theta = \frac{W_0 - W}{W_0} \quad (3)$$

where W_0 , W indicate loss of weight the metal without and with inhibitor, respectively.

Adsorption mechanism for inhibitor on metal sample

In order to understand the relationship between an inhibitor (adsorbate) and an adsorbent surface, adsorption isotherms were utilized. Using the Langmuir, Freundlich, and Temkin adsorption isotherms, the mechanism of adsorption for inhibitor molecules on mild steel was predicted. Optimal adsorption isotherm was determined by using the equations of linear for their

models, plotting their individual graphs with the appropriate parameters, and comparing the R^2 values calculated from the line of best-fit plots for the three isotherms.

Open circuit potential measurements

The potential of a mild steel electrode was measured against a saturated calomel electrode (SCE) in a 1 M H_3PO_4 solution as a function of time of immersion without and with various concentrations of BDBHBT derived from PET waste until open circuit potential was reached. The open circuit potential test lasts a total of 30 min, allowing the electrochemical test system to reach equilibrium.

RESULTS AND DISCUSSION

Characterization for BDBHBT Inhibitor

From FTIR spectra, the structure of the obtained compound, BDBHBT was confirmed. The presence of a strong band at 3428 cm^{-1} in the spectra of BDBHBT in Fig. S1 indicates that the product terminates with hydroxyl groups. An absorption band at 3031 cm^{-1} corresponds to aromatic $=\text{C}-\text{H}$ stretching, whereas the peaks at 893 and 723 cm^{-1} correspond to aromatic and olefinic $=\text{C}-\text{H}$ out-of-plane bending, respectively. The other peak at 2972 cm^{-1} is determined to be stretching of vibration aliphatic $\text{C}-\text{H}$. The presence of peaks at 1722 and 1267 cm^{-1} are ascribed to stretching vibration of $\text{C}=\text{O}$ ester and stretching vibration of $\text{C}-\text{O}$ ester, while the peaks at 1507 and 1408 cm^{-1} indicate stretching of $\text{C}=\text{C}$, and the peak at 607 cm^{-1} correspond to $\text{C}-\text{Br}$ bending. Fig. S2 shows the $^1\text{H-NMR}$ of BDBHBT, the

peaks at 8.03, 8.05, 8.08, 8.10, and 8.13 ppm are imputed to protons of the aromatic ring, while the peak at 4.85 ppm is singlet attributed to the terminal O-H group. At the same time, 4.59 and 3.85 ppm are attributed to H-atoms of methylene groups nearer to carbonyl ester and O-H group, respectively. Whereas a peak at 2.50 ppm is assigned to the solvent DMSO- d_6 .

Weight Loss Measurements

Effect of immersion time and inhibitor concentration on the corrosion process

Table 2 shows the effect of increasing the immersion duration in 1 M H_3PO_4 containing the BDBHBT green inhibitor on the weight loss rate (W) and rate of corrosion (CR) of mild steel at various concentrations and temperatures. In general, as immersion time increased at a particular temperature, the weight loss of steel increased, and consequently, the corrosion rate decreased. As shown in Fig. 1-3, the relationship between weight loss and time in uninhibited and inhibited 1.0 M H_3PO_4 is linear. This demonstrates that during corrosion, there are no insoluble surface films. In this instance, an inhibitor is initially adsorbed on the surface of a metal,

and then it inhibits corrosion either by blocking the reaction sites (anodic and cathodic) or by changing the mechanism of anodic and cathodic partial processes [26-27]. In addition, at temperatures 303, 323, and 333 K, an increase in BDBHBT inhibitor concentration led to a decrease in the weight loss and corrosion rate. Thus, a BDBHBT inhibitor concentration of 0.6 g/L resulted in

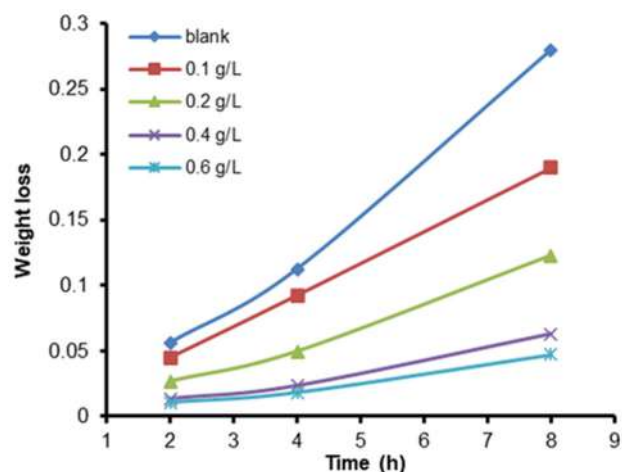


Fig 1. Curves of weight loss-time of mild steel in 1 M H_3PO_4 without and with various concentrations of PET waste-derived BDBHBT inhibitor in 303 K

Table 2. Weight loss and corrosion rate of steel in 1.0 M H_3PO_4 in the presence and absence of various concentrations of BDBHBT in various temperatures

Conc. g/L	T (K)	Time (h)					
		2		4		8	
		W (g)	CR (mpy)	W (g)	CR (mpy)	W (g)	CR (mpy)
blank	303	0.0562	401.6000	0.1125	330.0900	0.2799	333.2300
0.1		0.0449	320.3400	0.0924	254.0800	0.1898	224.3000
0.2		0.0269	195.9800	0.0498	151.0900	0.1231	144.8000
0.4		0.0134	97.1080	0.0234	69.4360	0.0632	62.0430
0.6		0.0109	89.0050	0.0185	66.0950	0.0475	55.0090
blank	323	0.0633	452.0600	0.1345	365.1100	0.3861	459.7600
0.1		0.0450	393.0000	0.0970	309.0000	0.2776	304.8000
0.2		0.0335	243.7900	0.0621	178.0000	0.1914	177.6000
0.4		0.0183	132.7100	0.0389	95.0090	0.0989	93.4000
0.6		0.0112	128.2300	0.0256	91.1900	0.0849	89.9000
blank	333	0.0694	495.0000	0.1566	462.1100	0.4335	531.9000
0.1		0.0552	465.6000	0.1339	406.8700	0.3147	395.8000
0.2		0.0395	287.2000	0.0745	230.4500	0.2167	227.2000
0.4		0.0201	182.0900	0.0413	150.2200	0.1611	148.6000
0.6		0.0172	197.8200	0.0368	167.0500	0.1287	163.0000

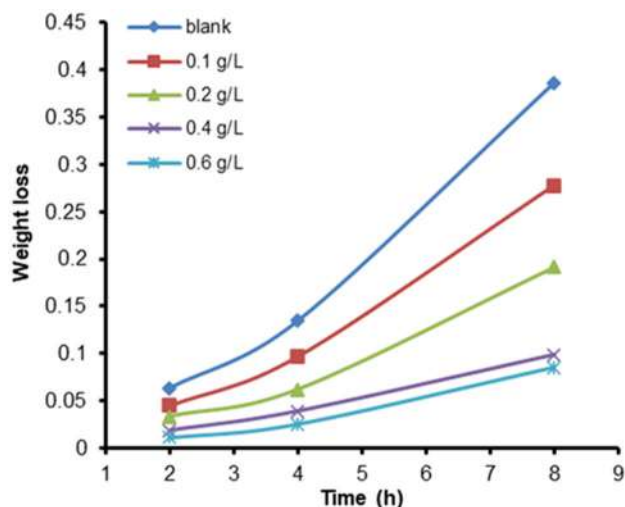


Fig 2. Curves of weight loss-time of mild steel in 1 M H_3PO_4 without and with various concentrations of PET waste-derived BDBHBT inhibitor in 323 K

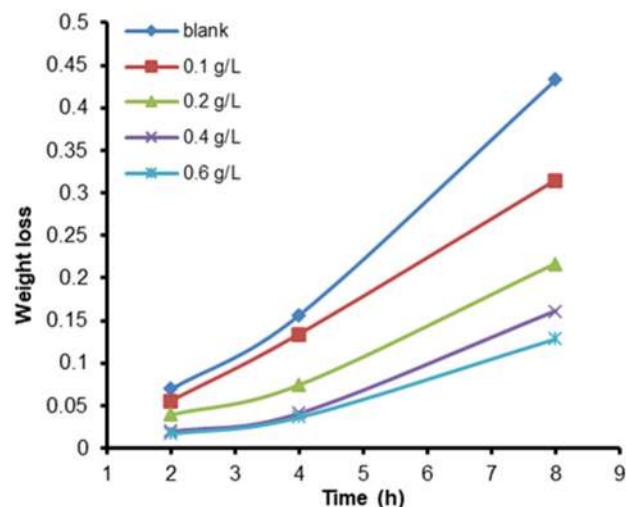


Fig 3. Curves of weight loss-time of mild steel in 1 M H_3PO_4 without and with various concentrations of PET waste-derived BDBHBT inhibitor in 333 K

Table 3. Effect of temperature on the rate of corrosion and effectiveness of preventing corrosion for mild steel in 1 M H_3PO_4 with various concentrations of BDBHBT inhibitor produced from PET waste for 8 h

Conc. (g/L)	T (K)	CR (mpy)	%IE	θ
blank		333.2300	-	-
0.1		224.3000	32.20	0.3220
0.2	303	144.8000	56.02	0.5602
0.4		62.0430	77.42	0.7742
0.6		55.0090	83.30	0.8330
blank		459.7600	0.00	0.0000
0.1		304.8000	28.10	0.2810
0.2	323	177.6000	50.42	0.5042
0.4		93.4000	74.38	0.7438
0.6		89.9000	78.01	0.7801
blank		531.9000	0.00	0.0000
0.1		395.8000	27.40	0.2740
0.2	333	227.2000	50.00	0.5000
0.4		148.6000	62.83	0.6283
0.6		163.0000	70.31	0.7031

the least amount of weight loss at each temperature considered. As the weight loss decreased as the concentration of the inhibitor increased, this indicated that the inhibitor was effective at inhibiting corrosion reactions.

Effect temperature on inhibition efficiency

Table 3 shows the results of CR and %IE of the inhibitor BDBHBT on mild-steel specimens when these

specimens were exposed to an acidic solution of 1 M H_3PO_4 for 8 h at various concentrations of inhibitor BDBHBT and temperatures. It is clear that as the temperature went up, the values of inhibition efficiency went down. That is, when the temperature went up, the rate of corrosion went up, which made the inhibitors less effective and sped up the corrosion process. This was because the molecules of the reactants had more kinetic

energy at higher temperatures, which made them move and crash into each other more quickly. This increased the rate of oxidation, or corrosion [28]. Fig. 4 shows how temperature affects the effectiveness of an inhibitor BDBHBT in the presence of different concentrations of the inhibitor. Fig. 5 shows how temperature affects the rate of corrosion in steel without and with different concentrations of the inhibitor.

Kinetic Study of the Corrosion of Steel in 1 M H₃PO₄

Thermodynamic parameters are essential for comprehending the inhibitive mechanism, activation energy (E_a^*) and thermodynamic functions of activations like activation enthalpy (ΔH_a^*) and activation entropy (ΔS_a^*) are studied. Thus, activation energy is calculated according to Arrhenius, Eq. (4):

$$CR = A \exp \frac{-E_a^*}{RT} \quad (4)$$

A represents the pre-exponential factor. Arrhenius plots for the corrosion of mild steel in 1 M H₃PO₄ (Fig. 6), slopes of these linear plots allow us to calculate E_a^* values, which are stated in Table 4. The results showed that the E_a^* value of the inhibited solutions was greater than that of the blank solution; this indicates that the corrosion process became more difficult in the presence of BDBHBT by increasing the energy barrier for the corrosion process [29-30]. Thermodynamic functions of

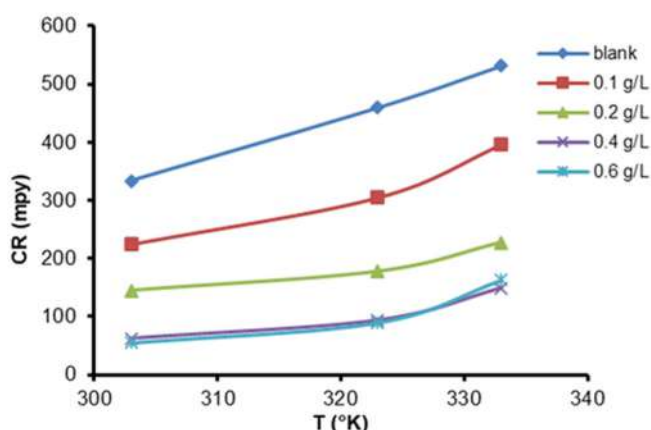


Fig 5. Relation between rate of corrosion and temperature for steel in 1 M H₃PO₄ with various concentrations of BDBHBT obtained from PET during 8 h

activation, such as ΔH_a^* and ΔS_a^* , can be determined using Eq. (5) of the transition state:

$$CR = \left(\frac{RT}{Nh} \right) \exp \left(\frac{\Delta S_a^*}{R} \right) \exp \left(\frac{-\Delta H_a^*}{RT} \right) \quad (5)$$

The plot of $\log (CR/T)$ versus $1/T$ of mild steel in 1 M H₃PO₄ solution with various concentrations of BDBHBT yields straight lines, as depicted in Fig. 7. The positive indications ΔH_a^* indicate the endothermic character and mean that mild steel corrosion is difficult in the presence of a BDBHBT inhibitor [31-32]. Whereas

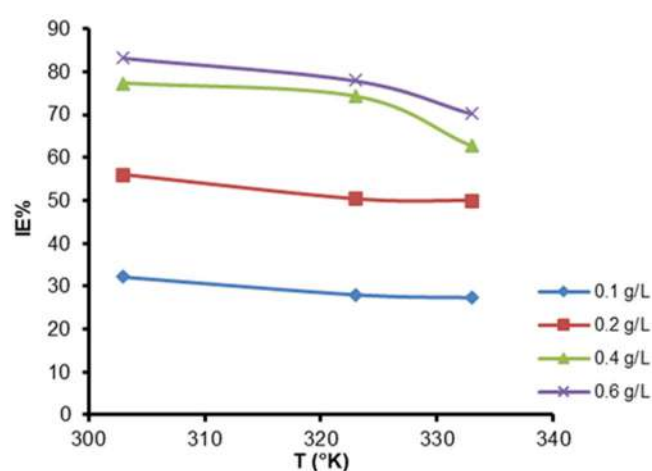


Fig 4. Relationship between percentage inhibition efficiency and temperature for steel in 1 M H₃PO₄ with various concentrations of BDBHBT obtained from PET during 8 h

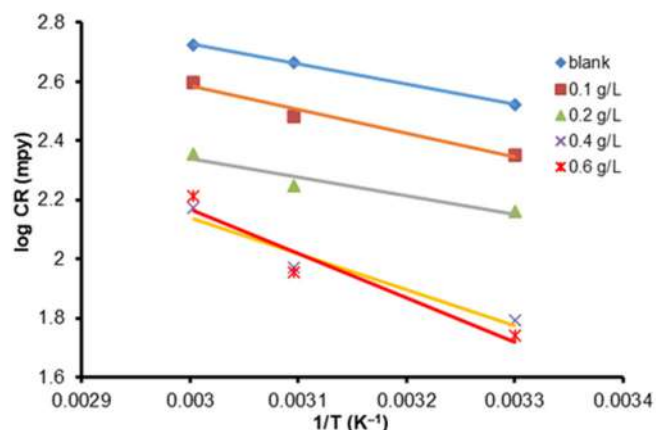


Fig 6. Arrhenius plots for mild steel after 8 h in corrosive solution in the absence and presence different concentrations of BDBHBT

Table 4. Parameters of thermodynamic activation of adsorption of steel in 1 M H₃PO₄ without and with different concentrations of BDBHBT inhibitor

Conc. (g/L)	E _a [*] (kJ/mol)	ΔH _a [*] (kJ/mol)	ΔS _a [*] (kJ/mol K)
Blank	13.08	10.45	-0.16
0.1	15.33	12.69	-0.16
0.2	11.90	9.26	-0.17
0.4	23.15	20.52	-0.14
0.6	28.68	26.04	-0.13

ΔS_a^{*} value is higher and negative, this indicates that the activated complex favors an association step over a dissociation step, resulting in a reduction of the disorder [33-34].

Results of Adsorption Isotherm of Corrosion Process

A mechanism for corrosion inhibition in the phosphoric acid solution can be explained by using an adsorption isotherm. The adsorption process findings demonstrated that the plot of the Langmuir isotherm model was the best appropriate isotherm for describing the adsorbed BDBHBT on a mild steel surface and gave R² values closer to 1, as shown in Fig. 8. The linear equation of this model is, Eq. (6) [35]:

$$\frac{C}{\theta} = \frac{1}{K_{ads}} + C \tag{6}$$

where C is the amount of inhibitor and K_{ads} is the adsorption equilibrium constant, and θ is the amount of

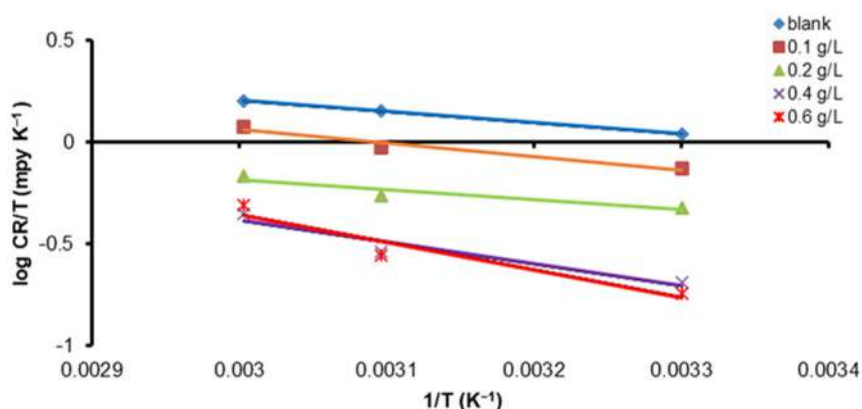


Fig 7. Transition state for mild steel after 8 h in corrosive solution in the absence and presence of different concentrations of BDBHBT

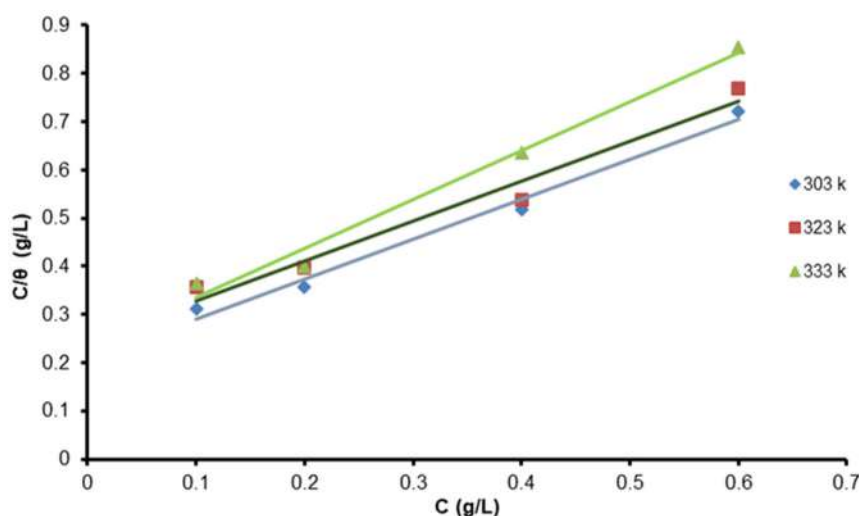


Fig 8. Langmuir isotherm of BDBHBT on steel in 1 M H₃PO₄ in various temperatures

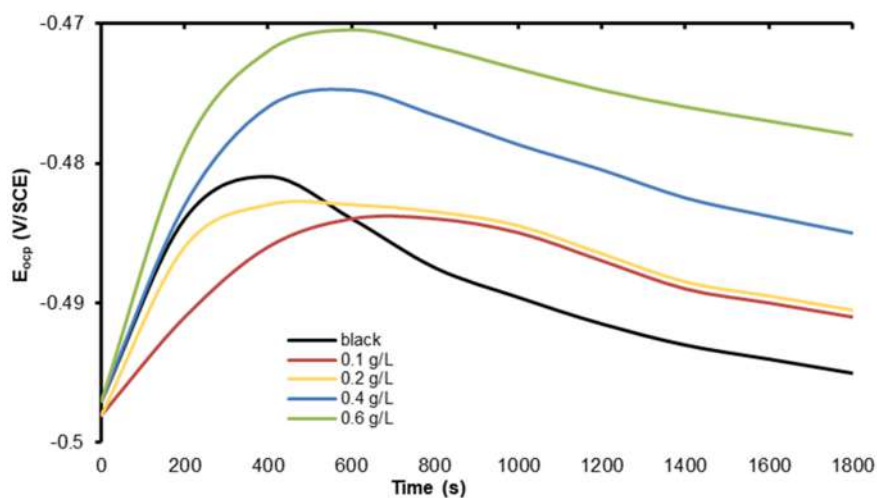


Fig 9. Open circuit potential of mild steel in 1 M H_3PO_4 without inhibitor and with different concentrations of BDBHBT

Table 5. Values of ΔG°_{ads} and K_{ads} registered in various temperatures using the Langmuir isotherm model

T (K)	K_{ads} (L/g)	ΔG°_{ads} (kJ/mol)
303	4.808	-21.357
323	4.072	-22.321
333	4.299	-23.163

surface coverage for various concentrations of inhibitor in acidic conditions. Table 5 illustrates values of the Gibbs free energy ΔG°_{ads} for the adsorption of BDBHBT inhibitor on steel surface in 1 M H_3PO_4 in various temperatures. The data of ΔG°_{ads} in Table 5 are negative, which shows that the adsorption of BDBHBT on mild steel in 1 M H_3PO_4 happens spontaneously and that the data are also approximately -20 kJ/mol, which shows that the process is physical [36-37].

Open Circuit Potential Measurements

Corrosion potential can be used to characterize the tendency of metals to corrode in a particular acidic environment. As depicted in Fig. 9, open circuit potential curves of mild steel in 1 M H_3PO_4 in the absence of inhibitor and the presence of various concentrations of BDBHBT inhibitor were plotted to provide a better understanding of this phenomenon. It is evident that the mild steel electrode's potential when submerged in 1 M H_3PO_4 solution (blank curve) first increased and then

tended gently; the constant state of each sample persists until the conclusion of the test. This shows the initial dissolution of the air-formed oxide film on the surface of mild steel [38]. The addition of BDBHBT inhibitor molecules in concentrations 0.1 and 0.2 g/L to the aggressive medium exhibited no difference in open circuit potential, whereas the corrosion potential of mild steel in concentrations 0.4 and 0.6 g/L moved to a more favorable state.

CONCLUSION

PET waste could be depolymerized by microwave irradiation with *trans*-2,3-dibromo-2-butene-1,4-diol with the presence of manganese acetate (0.5%, w/w). When compared to the traditional thermal glycolytic process, which needs at least 8 to 9 h, the use of a microwave could significantly shorten the reaction time needed for recycling (30 min). The weight loss measurements showed that oligomer BDBHBT obtained from PET waste was an excellent green inhibitor of corrosion of mild steel in H_3PO_4 solution. The corrosion inhibition efficiencies of BDBHBT rise with the rising of inhibitor concentration and with decreasing of temperatures. Adsorption of inhibitor BDBHBT on steel is slowed down corrosion and obeys Langmuir isotherm. Negative free energy ($-\Delta G^{\circ}_{ads}$) values imply spontaneous and strong adsorption of inhibitor BDBHBT on the mild steel surface.

■ ACKNOWLEDGMENTS

I would like to express my deep gratitude to the technical staff at the Department of Chemistry for providing the necessary technical assistance and support in the experiment.

■ REFERENCES

- [1] Singh, N., Hui, D., Singh, R., Ahuga, I.P.S., Feo L., and Fraternali, F., 2017, Recycling of plastic solid waste: A state of art review and future applications, *Composites, Part B*, 115, 409–422.
- [2] Siročić, A.P., Fijačko, A., and Hrnjak-Murčić, Z., 2013, Chemical recycling of postconsumer poly(ethylene-terephthalate) bottles - Depolymerization study, *Chem. Biochem. Eng. Q.*, 27 (1), 65–71.
- [3] Khoonkari, M., Haghghi, A.H., Sefidbakht, Y., Shekoohi, K., and Ghaderian, A., 2015, Chemical recycling of PET wastes with different catalysts, *Int. J. Polym. Sci.*, 2015, 124524.
- [4] Helms, B.A., and Russell, T.P., 2016, Reaction: Polymer chemistries enabling cradle-to-cradle life cycles for plastics, *Chem*, 1 (6), 816–818.
- [5] Archana, A., Moses, V., Sagar, S., Shivraj, V., and Chetan, S., 2015, A review on processing of waste PET (polyethylene terephthalate) plastics, *Int. J. Polym. Sci. Eng.*, 1 (2), 1–13.
- [6] Jamdar, V., Kathalewar, M., Dubey, K.A., and Sabnis, A., 2017, Recycling of PET wastes using electron beam radiations and preparation of polyurethane coatings using recycled material, *Prog. Org. Coat.*, 107, 54–63.
- [7] Aguado, A., Martínez, L., Becerra, L., Arieta-araunabeña, M., Arnaiz, S., Asueta, A., and Robertson, I., 2014, Chemical depolymerisation of PET complex waste: Hydrolysis vs. glycolysis, *J. Mater. Cycles Waste Manage.*, 16 (2), 201–210.
- [8] Ghaderian, A., Haghghi, A.H., Taromi, F.A., Abdeen, Z., Boroomand, A., and Taheri, S.M.R., 2015, Characterization of rigid polyurethane foam prepared from recycling of PET waste, *Period. Polytech., Chem. Eng.*, 59 (4), 296–305.
- [9] Fukushima, K., Lecuyer, J.M., Wei, D.S., Horn, H.W., Jones, G.O., Al-Megren, H.A., Alabdulrahman, A.M., Alsewailem, F.D., McNeil, M.A., Rice, J.E., and Hedrick, J.L., 2013, Advanced chemical recycling of poly(ethylene terephthalate) through organocatalytic aminolysis, *Polym. Chem.*, 4 (5), 1610–1616.
- [10] Al-Sabagh, A.M., Yehia, F.Z., Eissa, A.M.M.F., Moustafa, M.E., Eshaq, G., Rabie, A.R.M. and ElMetwally, A.E., 2014, Glycolysis of poly(ethylene terephthalate) catalyzed by the Lewis base ionic liquid [Bmim][OAc], *Ind. Eng. Chem. Res.*, 53 (48), 18443–18451.
- [11] Ugi, B.U., Obeten, M.E, Bassey, V.M., Hitler, L., Adalikwu, S.A., Omaliko, C.E., Nandi, D.O., and Uwah, I.E., 2022, Adsorption and inhibition analysis of aconitine and tubocurarine alkaloids as eco-friendly inhibitors of pitting corrosion in ASTM - A47 low carbon steel in HCl acid environment, *Indones. J. Chem.*, 22 (1), 1–16.
- [12] Salleh, N.I.H., and Abdullah, A., 2019, Corrosion inhibition of carbon steel using palm oil leaves extract, *Indones. J. Chem.*, 19 (3), 747–752.
- [13] Baari, M.J., Bundjali, B., and Wahyuningrum, D., 2021, Performance of N,O-carboxymethyl chitosan as corrosion and scale inhibitors in CO₂ saturated brine solution, *Indones. J. Chem.*, 21 (4), 954–967.
- [14] Khadom, A.A., and Farhan, S.N., 2018, Corrosion inhibition of steel in phosphoric acid, *Corros. Rev.*, 36 (3), 267–280.
- [15] Arab, S.T., and Al-Turkustani, A., 2006, Corrosion inhibition of steel in phosphoric acid by phenacyldimethyl sulfonium bromide and some of its *p*-substituted derivatives, *Port. Electrochim. Acta*, 24, 53–69.
- [16] Abdel Hameed, R.S., 2017, Solvent free glycolysis of plastic waste as green corrosion inhibitor for carbon steel in sulfuric acid, *J. New Mater. Electrochem. Syst.*, 20 (3), 141–149.
- [17] Alvarez-Pampliega, A., Hauffman, T., Petrova, M., Breugelmans, T., Muselle, T., Van den Bergh, K., De Strycker, J., Terryn, H., and Hubin, A., 2014, Corrosion study on Al-rich metal-coated steel by

- odd random phase multisine electrochemical impedance spectroscopy, *Electrochim. Acta*, 124, 165–175.
- [18] Abdallah, M., Al-Tass, H.M., AL Jahdaly, B.A., and Fouda, A.S., 2016, Inhibition properties and adsorption behavior of 5-arylazothiazole derivatives on 1018 carbon steel in 0.5M H₂SO₄ solution, *J. Mol. Liq.*, 216, 590–597.
- [19] Hamani, H., Douadi, T., Al-Noaimi, M., Issaadi, S., Daoud, D., and Chafaa, S., 2014, Electrochemical and quantum chemical studies of some azomethine compounds as corrosion inhibitors for mild steel in 1M hydrochloric acid, *Corros. Sci.*, 88, 234–245.
- [20] Al-Sabagh, A.M., Yehia, F.Z., Eshaq, G., Rabie, A.M., and ElMetwally, A.E., 2016, Greener routes for recycling of polyethylene terephthalate, *Egypt. J. Pet.*, 25 (1), 53–64.
- [21] Chaudhary, S., Surekha, P., Kumar, D., Rajagopal, C., and Roy, P.K., 2013, Microwave assisted glycolysis of poly(ethylene terephthalate) for preparation of polyester polyols, *J. Appl. Polym. Sci.*, 129 (5), 2779–2788.
- [22] Perez, N., 2016, *Electrochemistry and Corrosion Science*, 2nd Ed., Springer, Cham, Switzerland.
- [23] Machuca, L.L., Lepkova, K., and Petroski, A., 2017, Corrosion of carbon steel in the presence of oilfield deposit and thiosulphate-reducing bacteria in CO₂ environment, *Corros. Sci.*, 129, 16–25.
- [24] Chidiebere, M.A., Oguzie, E.E., Liu, L., Li, Y., and Wang, F., 2015, Adsorption and corrosion inhibiting effect of riboflavin on Q235 mild steel corrosion in acidic environments, *Mater. Chem. Phys.*, 156, 95–104.
- [25] Yohai, L., Vázquez, M., and Valcarce, M.B., 2013, Phosphate ions as corrosion inhibitors for reinforcement steel in chloride-rich environments, *Electrochim. Acta*, 102, 88–96.
- [26] Abdel Hameed, R.S., Al Elaimi, M., Qureshi, M.T., Farghaly, O.A., and Abd el-kader, M.F.H., 2021, Green synthesis for nonionic surfactants from poly(ethelene terephthalate) plastic waste, *Egypt. J. Chem.*, 64 (2), 773–780.
- [27] Yan, Y., Lin, X., Zhang, L., Zhou, H., Wu, L., and Cai, L., 2017, Electrochemical and quantum-chemical study on newly synthesized triazoles as corrosion inhibitors of mild steel in 1 M HCl, *Res. Chem. Intermed.*, 43 (5), 3145–3154.
- [28] Loto, R.T., and Olowoyo, O., 2018, Corrosion inhibition properties of the combined admixture of essential oil extracts on mild steel in the presence of SO₄²⁻ anions, *S. Afr. J. Chem. Eng.*, 26, 35–41.
- [29] Biswas, A., Pal, S., and Udayabhanu, G., 2015, Experimental and theoretical studies of xanthan gum and its graft co-polymer as corrosion inhibitor for mild steel in 15% HCl, *Appl. Surf. Sci.*, 353, 173–183.
- [30] Atta, A.M., El-Mahdy, G.A., Al-Lohedan, H.A., and Ezzat, A.O., 2014, Synthesis and application of hybrid polymer composites based on silver nanoparticles as corrosion protection for line pipe steel, *Molecules*, 19 (5), 6246–6262.
- [31] Tao, Z., He, W., Wang, S., Zhang, S., and Zhou, G., 2012, A study of differential polarization curves and thermodynamic properties for mild steel in acidic solution with nitrophenyltriazole derivative, *Corros. Sci.*, 60, 205–213.
- [32] Abdallah, M., Fawzy, A., and Alfakeer, M., 2020, Inhibition potentials and adsorption performance of two sulfonylurea antibiotic expired drugs on the corrosion of mild steel in 0.5 M H₂SO₄, *Int. J. Electrochem. Sci.*, 15, 10289–10303.
- [33] Mourya, P., Singh, P., Tewari, A.K., Rastogi, R.B., and Singh, M.M., 2015, Relationship between structure and inhibition behaviour of quinolinium salts for mild steel corrosion: Experimental and theoretical approach, *Corros. Sci.*, 95, 71–87.
- [34] Khaled, K.F., and Amin, M.A., 2008, Computational and electrochemical investigation for corrosion inhibition of nickel in molar nitric acid by piperidines, *J. Appl. Electrochem.*, 38 (11), 1609–1621.
- [35] Singh, A., Ansari, K.R., Haque, J., Dohare, P., Lgaz, H., Salghi, R., and Quraishi, M.A., 2018, Effect of electron donating functional groups on corrosion inhibition of mild steel in hydrochloric acid: Experimental and quantum chemical study, *J. Taiwan Inst. Chem. Eng.*, 82, 233–351.

- [36] Khaled, K.F., 2009, Experimental and atomistic simulation studies of corrosion inhibition of copper by a new benzotriazole derivative in acid medium, *Electrochim. Acta*, 54 (18), 4345–4352.
- [37] Zaafarany, I.A., and Ghulman, H.A., 2013, Ethoxylated fatty amines as corrosion inhibitors for carbon steel in hydrochloric acid solutions, *Int. J. Corros. Scale Inhib.*, 2 (2), 82–91.
- [38] Abdel Hameed, R.S., 2018, Cationic surfactant - Zn^{+2} system as mixed corrosion inhibitors for carbon steel in sodium chloride corrosive medium, *Port. Electrochim. Acta*, 36 (4), 271–283.

Synthesis, Characterization and Biological Activity of New Oleander Complexes against Bacteria Found in Polluted Water

Zainab Sabeer Abdulsada^{1*}, Sahar Sabeeh Hassan², and Sanaa Hitur Awad²

¹Ministry of Environment, Baghdad 10062, Iraq

²Department of Chemistry, College of Science for Women, University of Baghdad, Baghdad 10071, Iraq

* Corresponding author:

email:

zainab.sabeer1105a@cs.w.uobaghdad.edu.iq

Received: May 10, 2023

Accepted: August 11, 2023

DOI: 10.22146/ijc.84332

Abstract: Natural polymers are often non-toxic, biodegradable, biocompatible, and safe. A novel ligand was synthesized as a natural polymer using chitosan and oleander plant extract [(2R,3S,4R,5S)-5-(acetoxymino)-4-hydroxy-3,6-dimethoxytetrahydro-2H-pyran-2-yl) methyl (16R)-3-(((2S,4S,5R)-4-methoxy-2,5-dimethyltetrahydro-2H-pyran-2-yl)oxy)-10,13,16-trimethyl-17-(5-oxo-2,5-dihydrofuran-3-yl) hexadecahydro-14H-cyclopenta [a] phenanthren-14-yl) phthalate] (Chitosan-Ph-Oleander). This ligand and its complexes with several metals (Cr^{+3} , Mn^{+2} , Fe^{+3} , Ni^{+2} , Cu^{+2} , Zn^{+2}) were characterized using FTIR, UV-visible and 1H -NMR spectroscopy, as well as by molar conductivity, magnetic moment, and TGA analysis. The biological activity for the prepared polymer and its complexes was studied to inhibit the effectiveness of some bacteria found in polluted water taken from hospitals wastewater. The effectiveness of inhibition was tested on *Fusarium oxysporum* fungus, which causes wilting, rotting and seedling death diseases in various types of plants. The elemental and spectral investigation results showed that all prepared compounds had octahedral geometry. Compared to the free ligand, all metal complexes showed discernible antibacterial activity. The zinc(II) complex, in comparison to other metal complexes, showed higher antibacterial activity against Faecal streptococci bacteria (G^+) and *Pseudomonas aeruginosa* bacteria (G^-). In addition, the inhibition rate of the effectiveness of the *F. oxysporum* fungus reached ~50%.

Keywords: chitosan; contaminated water; inhibiting effectiveness; natural polymer

■ INTRODUCTION

Biological contaminants including several micro-organisms can interfere the other life forms. The most common transmission mode of these organisms is the fecal-oral pathway, where the major biological contaminants include pathogenic bacteria, coliforms, and *Fecal streptococci* [1-3].

Chitosan is produced by living organisms like fungi and crustaceans (whose shells serve as biomass) [4]. Chitosan is a non-toxic, biocompatible, and biodegradable polymer with antibacterial properties. Chitosan is the second most abundant non-synthetic biopolymer. Most chitosan studies have been used to remediate wastewater [5]. On the other hand, chitosan has been extensively used in synthesis research studies as a

functional polymer or a supporting matrix [6]. Amino and hydroxyl groups found in chitosan can interact with the functional groups of the template molecule. However, chitosan's fundamental weaknesses (poor mechanical strength) must be remedied to improve its chemical and physical properties [4]. Recently, chitosan has been used in various studies as an unconventional adsorbent to remove metallic pollutants with high metal adsorption affinities [7-8], as well as for the development of novel materials for wastewater treatment [9].

Apocynaceae is a family of evergreen, lovely flowering shrubs that includes *Nerium oleander*, known as karabi. *N. oleander*'s blooms have four lobes and they are funnel-shaped. They bloom in clusters in terminal branches and are either white or pink. The bark extract

of *N. oleander* has been found to contain a variety of plant secondary metabolites, including steroids, terpenoids, flavonoids, cardenolides, cardiac glycosides, and long-chain esters. Massive biological effects have been noted, including cardiac tonic, diuretic, cytotoxic, antibacterial, anti-platelet aggregation, anti-inflammatory, hepatoprotective, anticancer, anti-hyperlipidemic, anti-ulcer, and anti-depressant action in the central nervous system [10]. Plant extracts are rich in phytochemicals, which operate as reducing and stabilizing agents and demonstrate antibacterial activity against some bacterial and fungal strains. Plant components, including roots, leaves, stems, seeds, and fruits, have also been employed for nanoparticle manufacturing [11]. The plant extracts were economically and environmentally sustainable, opening up new opportunities for water treatment, biosensors, and nanotechnology [12]. The present work described the synthesis of some transition metal complexes using chitosan and oleander plant extract as ligands and then studied the ligand's antibacterial activity and its metal complexes against two types of bacteria found in polluted water.

■ EXPERIMENTAL SECTION

Materials

The oleander leaves were obtained from the University of Baghdad gardens in Al-Jadriya and sent to Ibnu Sina Company in the Ministry of Industry and Minerals to obtain the oleander extract. Chitosan (90%, Glentham, United Kingdom), acetic anhydride (99% B.D.H), phthalic anhydride (99% B.D.H), ethanol (99% B.D.H), and metal salts of ($\text{CrCl}_3 \cdot \text{H}_2\text{O}$, $\text{MnCl}_2 \cdot 4\text{H}_2\text{O}$, FeCl_3 , $\text{NiCl}_2 \cdot 6\text{H}_2\text{O}$, $\text{CuCl}_2 \cdot 2\text{H}_2\text{O}$, and ZnCl_2 , B.D.H) were used in this study.

Instrumentation

GMMallen Kampm measured the melting points of the synthesized compounds. MF-370 devised electro-thermal was measured at the University of Baghdad, College of Sciences for Women. SHIMADZU FTIR 8400S Fourier transform within the wavenumber region between 4000 and 400 cm^{-1} using KBr disc and 4000 and 200 cm^{-1} using CsI disc was used to test Fourier transform

infrared (FTIR) spectra. The UV-visible spectra at 200 – 1100 nm were measured using a SHIMADZU 1800 double-beam UV-vis spectrophotometer at the University of Baghdad. $^1\text{H-NMR}$ tested using a Bruker Ultra Shield 500 MHz in Tehran University (Iran). Thermal analyses (TGA) of samples were performed under nitrogen atmospheres at a heating range of (0 – $800 \text{ }^\circ\text{C}$) and a heating rate of $20 \text{ }^\circ\text{C}/\text{min}$ using STA500-Germany in Tehran University (Iran). Molar conductivity measurements ($\mu\text{s}/\text{cm}$) out using LASSCO Digital Conductivity Meter for metal complexes (10^{-3} M) in ethanol at room temperature ($25 \text{ }^\circ\text{C}$). Magnetic moments (eff. B.M) were measured according to Faraday's method using Bruker magnet B.M-6 for the prepared complexes in the solid state at room temperature ($25 \text{ }^\circ\text{C}$).

Procedure

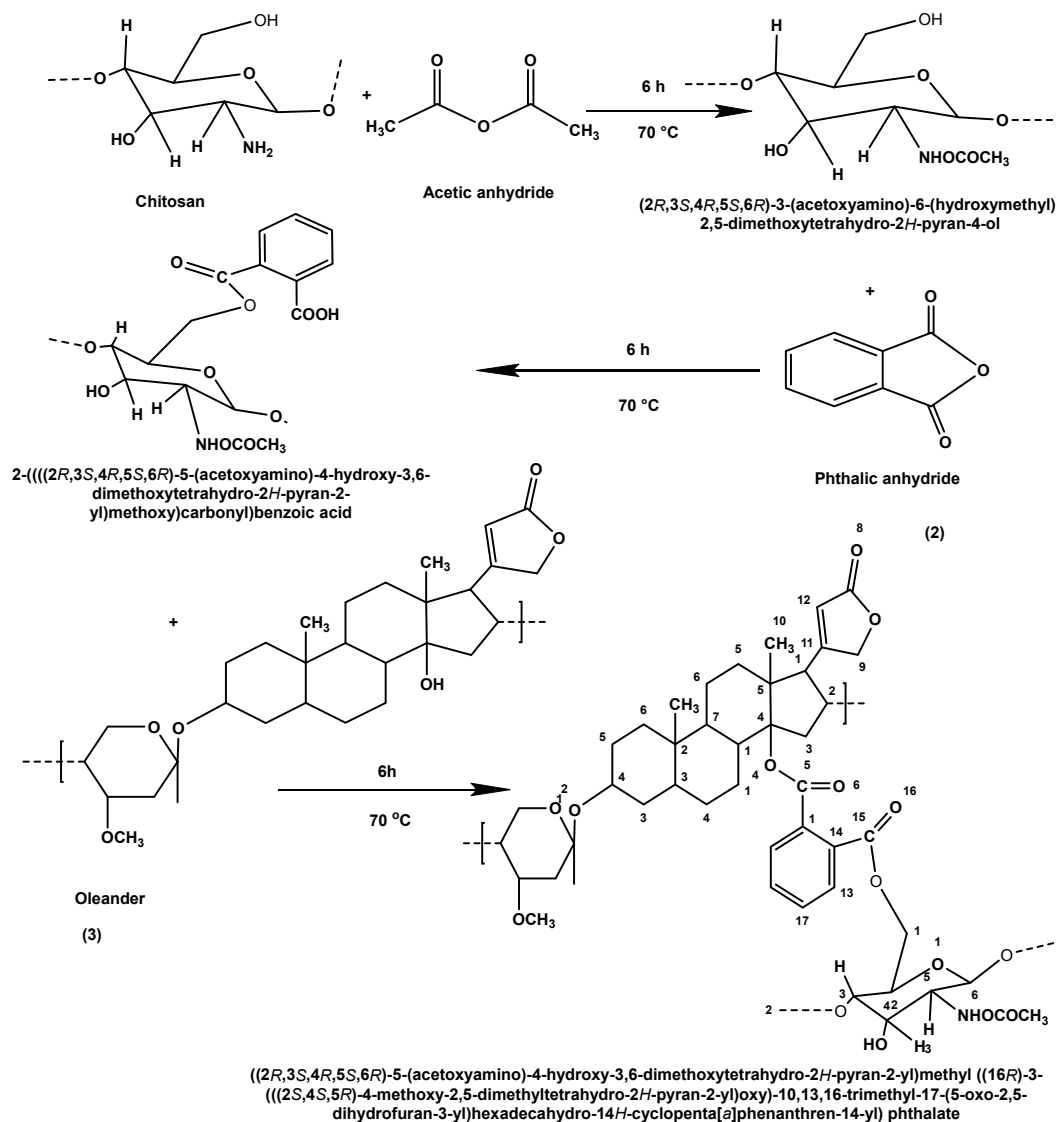
Synthesis of [(2R,3S,4R,5S)-5-(acetoxymino)-4-hydroxy-3,6-dimethoxytetrahydro-2H-pyran-2-yl)methyl (16R)-3-(((2S,4S,5R)-4-methoxy-2,5-dimethyltetrahydro-2H-pyran-2-yl)oxy-10,13,16-trimethyl-17-(5-oxo-2,5-dihydrofuran-3-yl)hexadecahydro-14H-cyclopenta[a] phenanthren-14-yl)phthalate]. (Chitosan-Ph-Oleander) ligand

To prepare Chitosan-Ph-Oleander, 2 g (0.0135 mol) of chitosan (off-white color) powder was dissolved in 30 mL of glacial acetic acid ($5\% \text{ v/v}$) with continuous stirring at room temperature. A solution of 1 M NaOH was added to reach pH 4. In a water bath, 2 mL of acetic anhydride was added and refluxed with continuous stirring at 60 – $75 \text{ }^\circ\text{C}$ for 6 h [13].

The second was the reaction of the mixture with 0.827 g of phthalic anhydride dissolved in 10 mL of DMF, for 6 h at $70 \text{ }^\circ\text{C}$. In the last step, the product was reacted with 0.7315 g of oleander extract dissolved in ethanol for 6 h at $70 \text{ }^\circ\text{C}$. The product was dried at room temperature ($25 \text{ }^\circ\text{C}$) for a whole night before being washed with diethyl ether (Scheme 1).

Synthesis of Chitosan-Ph-Oleander complexes

The Chitosan-Ph-Oleander complexes were prepared at a ratio of $1:1$ from the ligand to the element, whereby 0.1732 g (0.001 mol) of the ligand was dissolved



Scheme 1. Preparation of ligand (Chitosan-Ph-Oleander)

in 5 mL of distilled water and 20 mL of absolute ethanol with continuous stirring. Then, the mixture was added by the corresponding weight of 0.001 mol for element salt that dissolved in 10 mL of absolute ethanol with heating at 45 °C for 3 h.

Inhibition activity of ligands and complexes test

In this work, and for studying the biological effectiveness of the compounds that were prepared on each (*F. streptococci* and *P. aeruginosa*) in contaminated water. These compounds were applied using different concentrations (250, 500, and 1000 µg/mL) on each of the bacteria above [12]. The number of bacteria in contaminated water before and after applying these

compounds was calculated using the aerobic bacteria total count (ABTC) method.

RESULTS AND DISCUSSION

FTIR Spectra of L and Its Complexes

Specific vibrations of chemical bonds or functional groups within molecules appear as FTIR spectra peaks (Fig. 1). KBr in the 4000–400 cm^{-1} and CsI in the 4000–250 cm^{-1} range were used to determine the experimental and theoretical structure of the Chitosan-Ph-Oleander ligand and its complexes. The two absorption peaks at 2819 and 2929 cm^{-1} were due to the asymmetric stretching of chitosan by $-\text{CH}_3$ and $-\text{CH}_2$, respectively.

Due to -NH symmetry and O-H stretching, the signal at 3433–3176 cm^{-1} in ligand spectra was identified [4].

New bands at 1691–1716 cm^{-1} may be attributed to $\nu(\text{COO})$ stretching vibrations [14], whereas bands in the area 3433–3454 cm^{-1} may be assigned to $\nu(\text{OH})$ modes. For Chitosan-Ph-Oleander ligand, the bands at 1413 and 1614–1634 cm^{-1} can be attributed to C–N and C=O amide, respectively [15]. The $\nu(\text{C-N})$ and $\nu(\text{C=O})$ frequencies often rise during complexation. The coordination of the metal ion to the nitrogen of the amide group and the carbonyl oxygen of the carboxylate group could account for these frequency shifts relative to the bands of the ligand. Bands that emerge at 414–487 and 520–597 cm^{-1} were attributed to $\nu(\text{M-N})$ and $\nu(\text{M-O})$, respectively [16]. The Chitosan-Ph-Oleander ligand

appears to behave as a neutral tetradentate ligand, with metal(II) ions bonding through four oxygen atoms, two for the ester carbonyl groups, one for the amide group and one for pyran ring of chitosan (see Table 1, Fig. 1 and 2).

The UV-vis Electronic Spectra of L and Its Complexes

Intense absorption at 277 nm (36101 cm^{-1}) in the UV-vis spectrum of L was ascribed to the $n \rightarrow \pi^*$ transition, while intense absorption at 206 nm (48543 cm^{-1}) was ascribed to the $\pi \rightarrow \pi^*$ transition [17] and three bands appeared for complexes Fig. 3. Table 2 described the physical properties of the ligand and its complexes. Meanwhile, in Table 3, information can be

Table 1. FTIR spectra of the Chitosan-Ph-Oleander and its complexes

Compound	$\nu(\text{OH})$	$\nu(\text{COO})$ ester	$\nu(\text{CO-NH})$ amide	$\nu(\text{CH}_2\text{-CH})$	$\nu(\text{M-O})$	$\nu(\text{M-Cl})$
L	3433	1691	1639	2929 2962	-	
CrL	3444	1704	1614	2929 2860	557	314
MnL	3444	1714	1614	2923 2854	582	324
FeL	3444	1697	1614	2927 2819	580	327
NiL	3454	1716	1614	2925 2856	597	316
CuL	3446	1716	1622	2925 2856	514	316
ZnL	3450	1693	1614	2927 2856	551	312

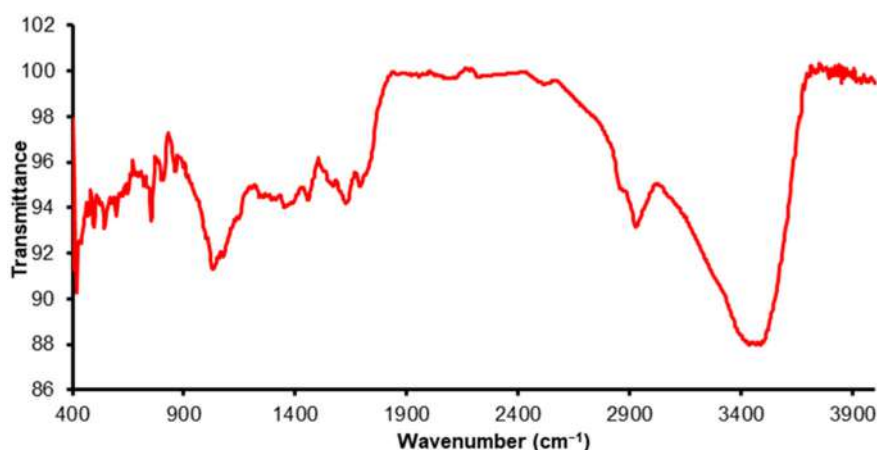


Fig 1. The FTIR spectrum for ligand

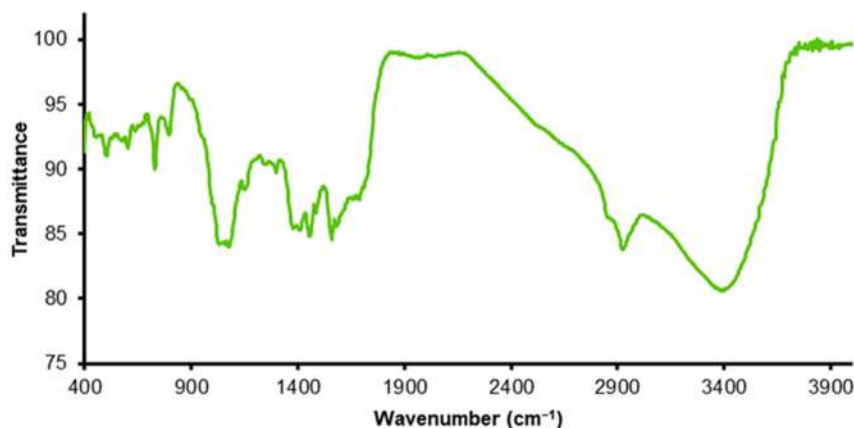


Fig 2. The FTIR spectrum for CuL complex

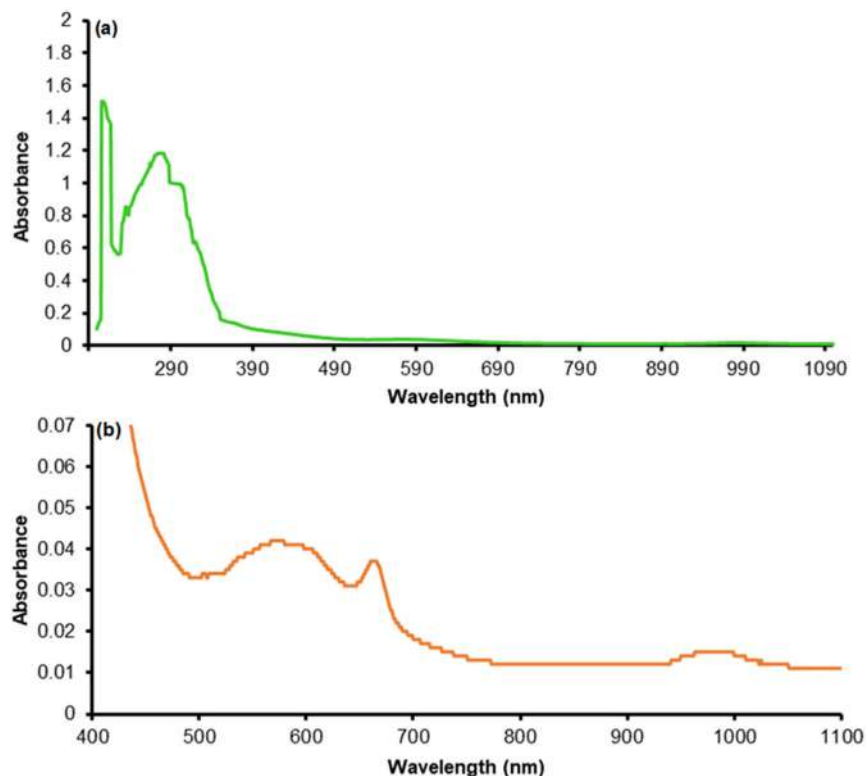


Fig 3. Electronic spectrum of (a) L and (b) CrL complex

Table 2. Physical properties of the ligand and its complexes

Compounds	m.p. (°C)	Color
L	180–182	Greenish brown
FeL	218–220	Yellowish brown
CuL	195–197	Green
MnL	200–202	Light brown
CrL	260–262	Olive
NiL	190–192	Yellowish green
ZnL	210–212	Greenish brown

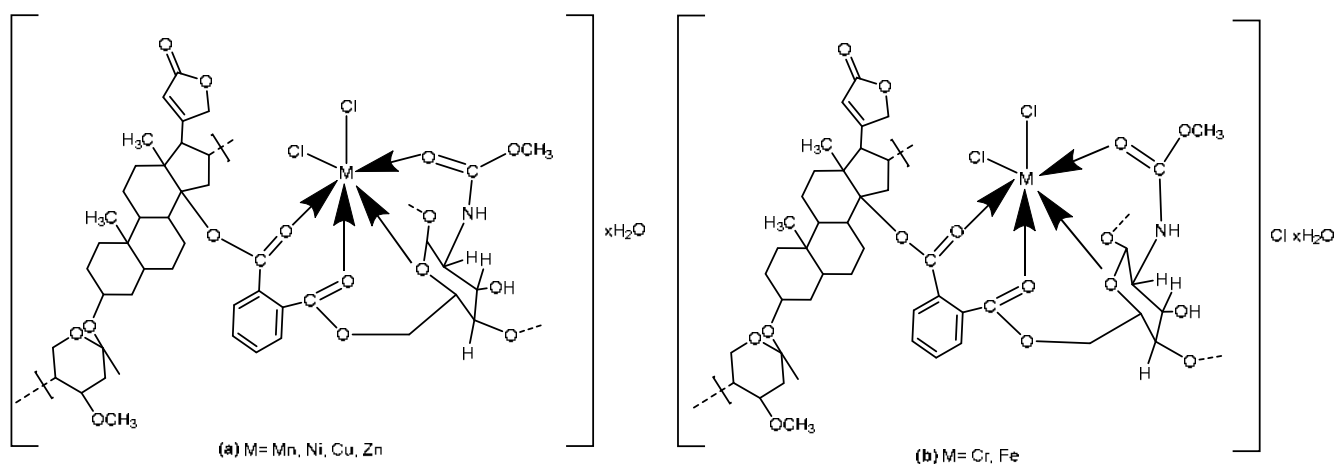
found on the spectra, magnetic moments, and molar conductivity of all metal complexes of the ligand in ethanol.

Three bands, corresponding to ${}^6A_{1g} \rightarrow {}^4T_{1g(G)}$, ${}^6A_{1g} \rightarrow {}^4T_{2g(G)}$, and ${}^6A_{1g} \rightarrow {}^4A_{2g} + E_{g(G)}$ were seen for the Mn(II) complex at 664, 606, and 503 nm with 15060, 16501, and 19880 cm^{-1} respectively.

The spectrum of Cr(III) complex olive showed three absorption bands at 978, 664, and 574 nm 10224,

Table 3. The UV-vis electronic spectra, molar conductivity, spectral parameters, and μ_{eff} of L and its complexes

Comp.	Wavelength (nm)	Wavenumber (cm ⁻¹)	Assignments	Molar cond.	μ_{eff} (B.M)	Structure
L	277	36101	$n \rightarrow \pi^*$	-	-	-
	206	48543	$\pi \rightarrow \pi^*$			
Cr-L	978	10224	${}^4A_{2g} \rightarrow {}^4T_{2g}$	24.5	3.7	Octahedral
	664	15060	${}^4A_{2g} \rightarrow {}^4T_{1g}$			
	575	17391	${}^4A_{2g} \rightarrow {}^4T_{1g}$			
Mn-L	664	15060	${}^6A_{1g} \rightarrow {}^4T_{1g(G)}$	10.2	5.2	Octahedral
	606	16501	${}^6A_{1g} \rightarrow {}^4T_{2g(G)}$			
	503	19880	${}^6A_{1g} \rightarrow {}^4A_{2g} + {}^4E_{g(G)}$			
Fe-L	966	10351	${}^6A_{1g} \rightarrow {}^4T_{1g}$	27.5	5.6	Octahedral
	664	15060	${}^6A_{1g} \rightarrow {}^4T_{2g}$			
	366	27322	${}^6A_{1g} \rightarrow {}^4A_{1g} + {}^4E_g$			
Ni-L	890	11235	${}^3A_{2g} \rightarrow {}^3T_{2g}$	7.3	2.3	Octahedral
	662	15105	${}^3A_{2g} \rightarrow {}^3T_{1g(F)}$			
	450	22222	${}^3A_{2g} \rightarrow {}^3T_{1g(P)}$			
Cu-L	652	15337	${}^2E_g \rightarrow {}^2T_{2g}$	4.8	1.2	Octahedral
	394	25380	C.T			
	284	35211	Intra ligand			
Zn-L	343	29154	C.T	9.8	Diamagnetic	Octahedral
	218	45871	Intra ligand			

**Scheme 2.** The geometrical structure of (a) $[MLCl_2] \cdot xH_2O$ and (b) $[MLCl_2]Cl \cdot xH_2O$

15060 and 17391 cm^{-1} assigned to ${}^4A_{2g} \rightarrow {}^4T_{2g}$, ${}^4A_{2g(F)} \rightarrow {}^4T_{1g}$ and ${}^4A_{2g(F)} \rightarrow {}^4A_{2g}$ transitions, suggesting an octahedral geometry. The spectrum of Fe(III) complex showed three bands at 966, 664, and 366 nm, with 10351, 15060, and 27322 cm^{-1} assigned to ${}^6A_{1g} \rightarrow {}^4T_{1g}$, ${}^6A_{1g} \rightarrow {}^4T_{2g}$, and ${}^6A_{1g} \rightarrow {}^4A_{1g} + {}^4E_g$, respectively, suggesting an octahedral geometry; the magnetic moment value is 5.6 BM (Scheme 2(b)). Ni(II) complex spectrum showed three bands at 890, 662, and 450 nm with 11235, 15105, and 22222 cm^{-1}

assigned to ${}^3A_{2g} \rightarrow E_g$, ${}^3A_{2g} \rightarrow {}^3T_{2g}$, ${}^3A_{2g} \rightarrow {}^3T_{1g(F)}$, and ${}^3A_{2g} \rightarrow {}^3T_{1g(P)}$ transition, respectively. The magnetic moment value was 2.3 BM, suggesting an octahedral geometry (Scheme 2(a)). Cu(II) complex spectrum showed one band at 652 and 394 nm with 15337 and 15380 cm^{-1} , assigned to ${}^2E_g \rightarrow {}^2T_{2g}$ and C.T transition, respectively. The magnetic moment value was 1.2 BM suggesting an octahedral geometry [18] (Scheme 2(a)). The magnetic moment value was diamagnetic for Zn(II)

complex, which was attributed to metal-to-ligand charge transfer, but the spectra show no d-d electronic transitions in the visible region. The absorption bands were located at 343 and 218 nm with 29154 and 45871 cm^{-1} assigned to C.T transition and intra ligand, respectively [19] (Scheme 2(a)).

¹H-NMR Spectrum

One of the most essential tools for studying substances and their structures is ¹H-NMR [20]. The ¹H-

NMR technique was used to characterize the synthetic polymer and its complexes. Fig. 4 and Table 4 showed that the methylene protons (H, cyclohexyl CH₂) corresponded to a signal at 1.12–1.43 ppm, and a signal at 1.80–2.99 ppm corresponded to methylene and methyl protons [21]. Proton of NH amide was observed at 6.87–7.85 ppm [22]. Amide-containing compounds are among the best examples for clearing the solvent influence on the N–H hydrogen NMR chemical shifts [23]. The protons of the aromatic ring are represented by

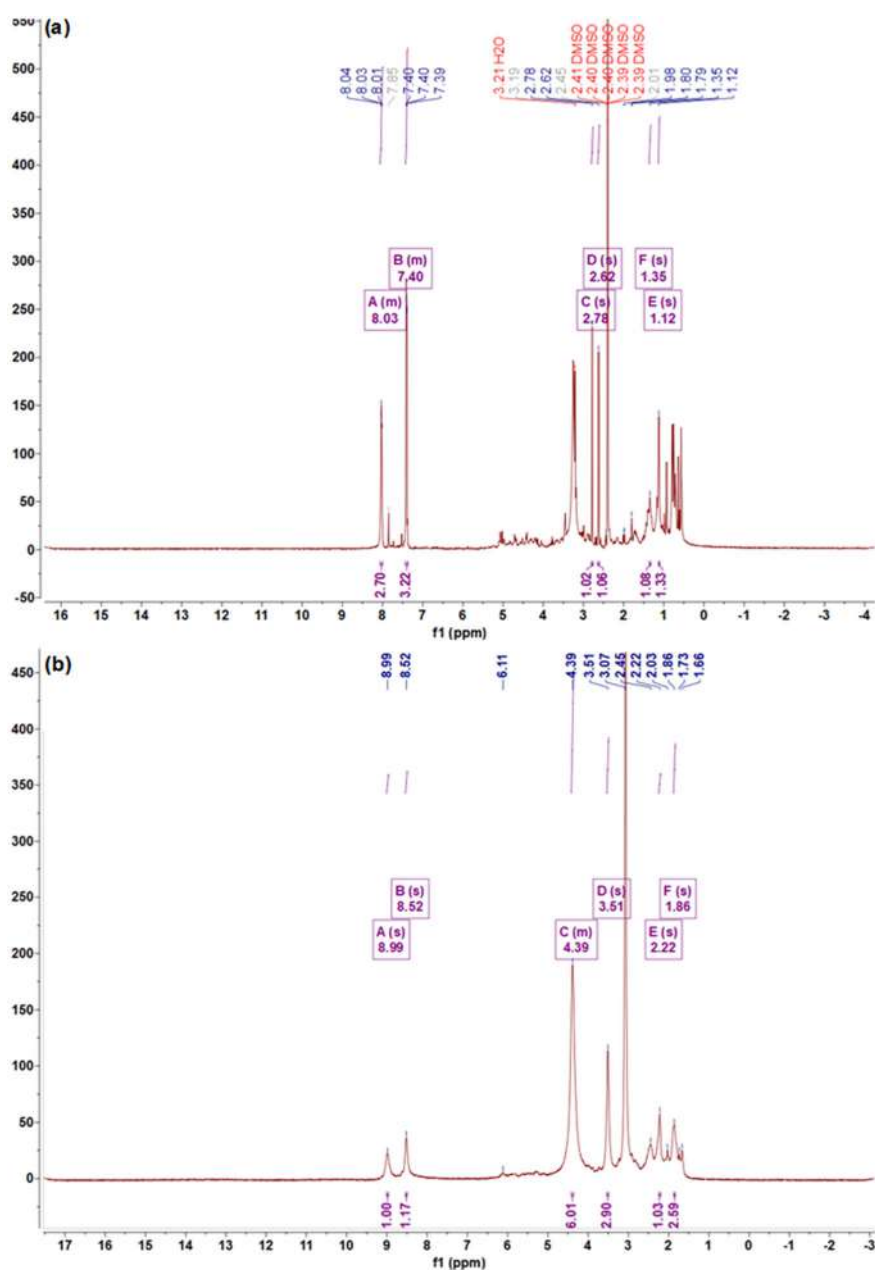


Fig 4. ¹H-NMR spectrum of (a) L and (b) FeL

Table 4. ^1H -NMR spectral data of L and FeL complex

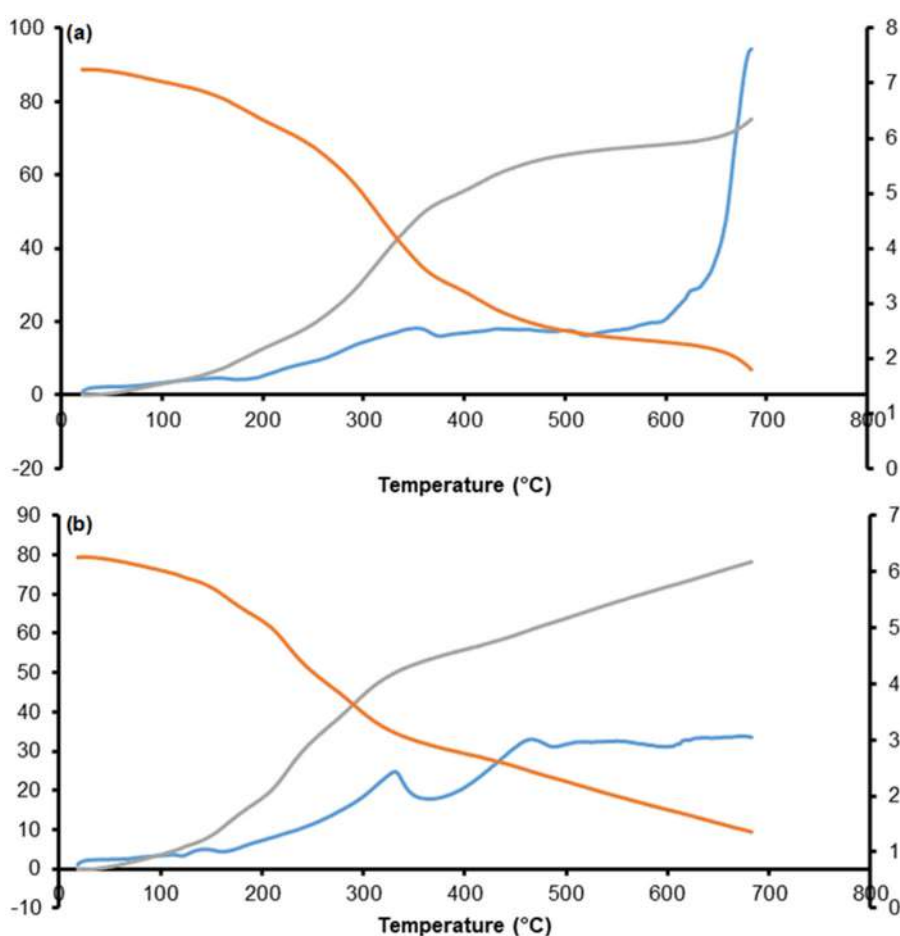
Chemical shifts (ppm)	Assignments in DMSO
1.12–1.43	Methylene of cyclohexyl protons
1.80–2.99	Methylene and methyl protons
6.87–7.85	Amide proton
8.01–10.09	Hydroxyl group proton
7.38–8.04	Ar-H proton

a multiplet at 7.38 to 8.04 ppm. The spectrum of the CuL and FeL complexes reveal this change to be accurate at the amide group, which gave a signal at 3.25 and 4.17 ppm for these complexes, respectively. Also, it showed a signal for the hydroxyl group at 8.01–10.09 ppm, whereas the methylene proton was represented by 4.40 ppm. CH-aliphatic protons were referred to as a quintet at 4.71 ppm [24].

TGA

TGA was frequently used to understand the effects of temperature and time on the weight of polymeric

materials. Polymeric materials can undergo weight changes due to decomposition and oxidation reactions and physical processes, including sublimation, evaporation, and desorption [25]. TGA curves of L and two complexes were illustrated in Fig. 5 and Table 5. The result of ligand presents three stages of weight loss (degradation patterns). Dehydration was the cause of the initial degradation, which begins at 20 °C and lasts until temperatures beyond 150 °C and manifests as a 6.3–8.5% weight loss. The existence of hydrogen bonds between functional groups in both polymer and chitosan and water molecules was the cause of the extended weight loss of water beyond 100 °C. The decomposition of chitosan main chains was responsible for the second weight loss, which starts at about 200 °C and results in a weight loss of roughly 50%. The natural polymer chain remnants go through a third step of decomposition that ranges from 40%. At roughly 800 °C, the ligand and their complexes lose ~85% of their total weight. About 15% of



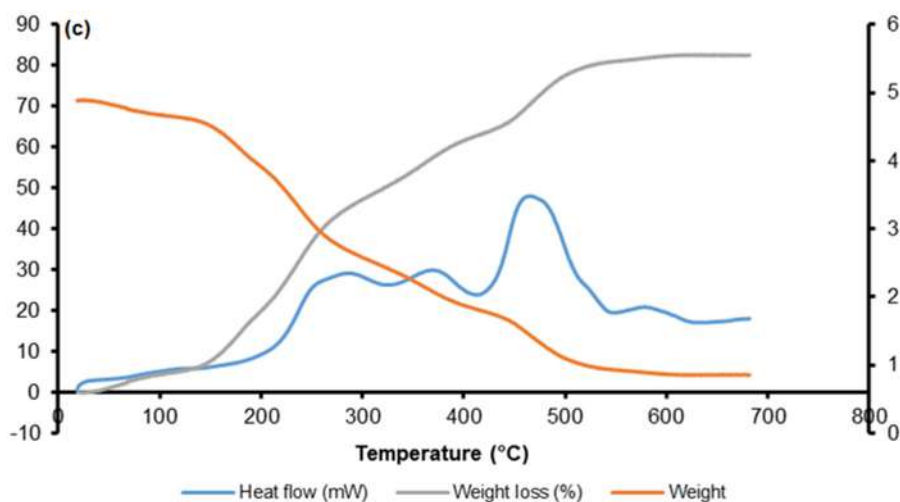


Fig 5. TGA analysis for (a) L, (b) CuL, and (c) FeL

Table 5. Thermal analyses data for L (Chitosan-Ph-Oleander), CuL, and FeL complexes

Compound	Dissociation stages	Temp. range (°C)	Weight loss (%)	Stable phase
L	Stage I	20–150	6.3	Dehydration
	Stage II	200–375	46.2	Chitosan main chains
	Stage III	375–800	38.9	Natural polymer chain residues
[CuLCl ₂] \cdot xH ₂ O	Stage I	20–150	8.5	Dehydration
	Stage II	150–340	42.5	Chitosan main chains
	Stage III	340–800	42.5	Natural polymer chain residues
[FeLCl ₃] \cdot xH ₂ O	Stage I	20–175	7.5	Dehydration
	Stage II	175–375	50.9	Chitosan main chains
	Stage III	375–800	34.2	Natural polymer chain residues

the compounds were still left over, and this residue was essentially the result of inorganic complexes, including C, N, and O. The literature suggested similar multi-degradation behavior for chitosan [26-28].

Studying of Biological Activity against Bacteria Types Found in Polluted Water

Antibacterial activity

Since human-specific enteric pathogens are more likely to be present in water polluted with human feces than animal feces, this is usually thought to pose a larger risk to human health [29-30]. Fecal waste contamination makes water unsuitable for drinking and contact recreation. Warm-blooded animals' intestines contain naturally occurring bacteria that have been used to detect fecal contamination. At different times, total coliforms, fecal coliforms, and *F. streptococci* have all been utilized as indications of pollution. The Gram-negative, obligatory

aerobic, rod-shaped bacteria *P. aeruginosa* is a member of the Pseudomonadaceae family. Although *P. aeruginosa* can develop in several environments, it prefers moist surroundings [31], even though many studies have focused on the characterization of clinical isolates from patients with *P. aeruginosa* infections. Few researchers examined the destiny and incidence of fluoroquinolone-resistant *P. aeruginosa* in clinical wastewater and in the downstream wastewater path [32].

Results of the antibacterial action of ligand and its metal complexes were described, and photographs of growth inhibition zones were illustrated in Fig. 6. Chitosan-Ph-Oleander ligand and its complexes CrL, MnL, FeL, NiL, CuL, and ZnL showed good antibacterial activity at 1000 mg/mL against both bacteria. These findings suggested that, compared to some complexes, the synthesized L showed outstanding activity against the two bacteria under study. Certainly, the mechanism

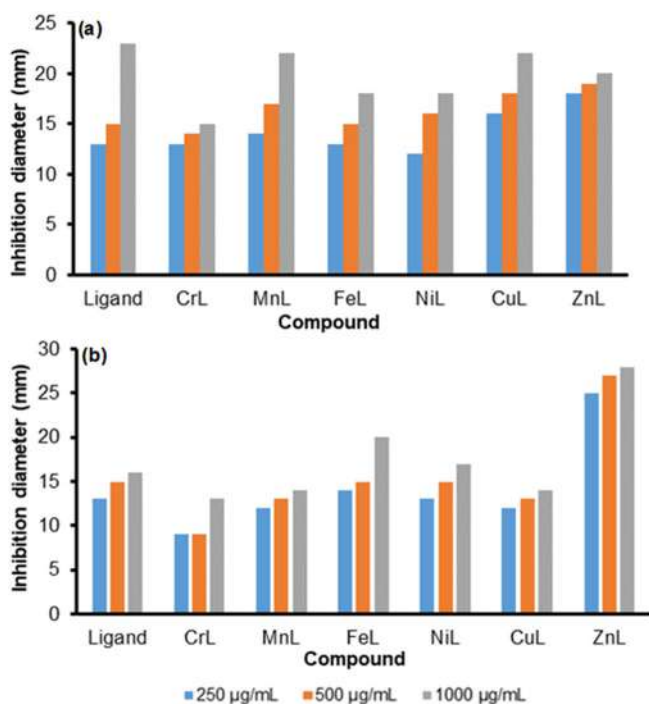


Fig 6. Antimicrobial activity of L and its complexes at 250, 500, and 1000 µg/mL for (a) *Fecal streptococci* and (b) *Pseudomonas aeruginosa*

of chitosan's antibacterial activity was still little understood [33], and three inhibitory mechanisms have thus been suggested. The positive charge amine groups (NH_3^+) of chitosan and the negative charges on the bacterial cell wall were attracted to one another electrostatically in the first mechanism, which prompts the leakage of intracellular components [34].

The second mechanism concerned chitosan's chelating capability toward metal ions such as Ca^{2+} , Mg^{2+} , and Zn^{2+} [35]. In addition to their function in the metabolic pathways, such as spore formation in Gram-positive bacteria, these metal ions were essential for bacterial growth. The third mechanism involves the entry of low-molecular-weight chitosan into the nuclei of microorganisms, which can subsequently interact with DNA, inhibit mRNA expression, and stop protein synthesis, leading to the death of bacterial cells [36].

Among the synthesized series of metal complexes, the MnL and CuL complexes were active against *F. streptococci* bacteria, while ZnL exhibited excellent activity against the two types of bacteria compared to another complex.

Similar observations have been reported by other researchers [37]; for instance, it is well known that both chitosan and Zn have the properties of disinfection and bactericide. After chitosan binds to Zn(II) ions through nitrogen, oxygen, or a combination of them, the bindings are likely to leave some potential donor atoms free, and these free donor atoms enhance biological activity. Thus, it stands a good chance that chitosan–Zn complexes exhibit an enhanced antimicrobial activity, which will be very favorable to chitosan–Zn complexes' applications in the medical and food industries. They investigated the antimicrobial activities of chitosan–Zn complexes and preliminarily explored structure-activity correlation. Five chitosan–Zn complexes with different Zn content were prepared, and their compositions and structures were analyzed through several physical methods. The complexes' antimicrobial activities against four Gram-positive bacteria, five Gram-negative bacteria, and two fungi were studied systematically [38]. Additionally, the ligand and some of its complexes were used in this study to treat dirty water taken from hospital effluent, and they showed high efficacy in removing any number of bacteria found there (Table 6).

Application of the Prepared Ligand and Its Complexes as an Inhibitor for *Fusarium oxysporum* Fungus

Fusarium wilt is the most dangerous and widespread disease in the world, caused by *F. oxysporum*, the main cause of wilting, rotting, and seedling death for more than 100 species of economically important plants. It is one of the fungi isolated from economic crops or soil [39–40]. Several species of *Fusarium* incite the disease, but the most devastating fungus is *F. oxysporum* [41–42].

The inhibition efficacy of the prepared ligand and its complexes at 250 µg/mL against *F. oxysporum* fungus was studied. Compared to the control, these compounds showed excellent efficacy in inhibiting the growth and activity of this fungus (Table 7). Both Tweedy's chelation theory and the overtone concept can be used to explain the better activities demonstrated by ligands and the inclusion of new complexes [43]. The oxygen that limits the ligand's ability to produce enzymes makes the donor

Table 6. The efficacy of Chitosan-Ph-Oleander Ligand and some of its complexes in removing several bacteria from wastewater

Test	Sample start	L	MnL	NiL
M.P.N of Total <i>coli</i> form/100mL	>16000	0	0	0
M.P.N of <i>Fecal coli</i> form/100mL	>16000	0	0	0
M.P.N of <i>E. coli</i> form/100mL	790	0	0	0
M.P.N of <i>F. streptococcus</i> form/100mL	230	0	0	0

Table 7. The antifungal activities of studied compounds (n = 2)

Comp.	Average colony diameter at 250 (µg/mL)	The inhibition percentage (%)
Ligand	4.05	46.60
CrL	3.90	46.60
MnL	3.75	50.00
FeL	3.90	48.00
NiL	3.75	50.00
CuL	3.85	48.60
ZnL	3.75	50.00
Control	7.50	

system more sensitive to metal ions deactivating it during chelation.

Numerous agents could be responsible for the differences in the synergistic effect between the type of metal ion and the associated ligand. The final geometric structure of these complexes, the oxidation state, the species of atoms connected with metal ions, the chelating affinity of the organic molecules utilized as ligands, the coordination number, and the arrangement of the ligand around the central ions are crucial [44]. The chelation mechanism partially shares the positive charge of the metal ion and overlaps the donor group of the ligand orbital, which decreases the polarity of the metal atom and increases the complexes' entry through the lipid layer of the cell membrane. Furthermore, metal complexes impede the cell's ability to respire, obstruct the production of proteins, and stop the organism from growing [45].

■ CONCLUSION

The results showed that the Chitosan-Ph-Oleander ligand and its six metal complexes were synthesized and characterized using various techniques. FTIR, UV-vis and NMR spectroscopy, as well as magnetic moment and conductivity, ensured the formation of compounds. The results explain and ensure metal complexes' geometry and

find helpful energy parameters. Furthermore, metal complexes showed an excellent inhibition of two types of bacteria that have all been used as pollution indicators at different times. Results of antibacterial activities revealed that some of these compounds can be used in wastewater treatment or antibiotic development. ZnL, MnL, FeL, and CuL complexes were the most active against these two types of bacteria. In addition, the inhibition rate of the effectiveness of the *F. oxysporum* fungus reached ~50%. Therefore, these results proved the success of the prepared compounds in treating water contaminated with bacteria. Further efforts should be made to explore the possible mechanistic pathways of their activity in wastewater treatment and *in vitro*.

■ ACKNOWLEDGMENTS

The authors acknowledge the staff of the Central Environmental Laboratory in the Ministry of Environment for their assistance.

■ AUTHOR CONTRIBUTIONS

This work has been done by collaboration between all authors. The above part was completed, the vehicles were prepared, the necessary tests were conducted to estimate them, samples were collected, and practical

applications were carried out, in addition to writing the work by Zainab Sabeer Abdulsada, while the work was reviewed and the results checked by Sahar Sabeeh Hassan and Sanaa Hitur Awad.

■ REFERENCES

- [1] Aliko, V., Multisanti, C.R., Turani, B., and Faggio, C., 2022, Get rid of marine pollution: Bioremediation an innovative, attractive, and successful cleaning strategy, *Sustainability*, 14 (18), 11784.
- [2] Jawad, W.A., Balakit, A.A.A., and Al-Jibouri, M.N.A., 2021, Synthesis, characterization and antibacterial activity study of cobalt(II), nickel(II), copper(II), palladium(II), cadmium(II) and platinum(IV) complexes with 4-amino-5-(3,4,5-trimethoxyphenyl)-4H-1,2,4-triazole-3-thione, *Indones. J. Chem.*, 21 (6), 1514–1525.
- [3] Fakhriza, M.A., Rusdiarso, B., Sunarintyas, S., and Nuryono, N., 2023, The addition of copper nanoparticles to mineral trioxide aggregate for improving the physical and antibacterial properties, *Indones. J. Chem.*, 23 (3), 692–701.
- [4] Rahimi, M., Bahar, S., and Amininasab, S.M., 2022, Preparation of molecular imprinted polymer based on chitosan as the selective sorbent for solid-phase microextraction of phenobarbital, *J. Anal. Methods Chem.*, 2022, 9027920.
- [5] Mahmoud, R.K., Mohamed, F., Gaber, E., and Abdel-Gawad, O.F., 2022, Insights into the synergistic removal of copper(II), cadmium(II), and chromium(III) ions using modified chitosan based on Schiff bases-g-poly(acrylonitrile), *ACS Omega*, 7 (46), 42012–42026.
- [6] Rabie, S.T., Mohamed, Y.M.A., Abdel-Monem, R.A., and El Nazer, H.A., 2022, Facile synthesis of chitosan-g-PVP/f-MWCNTs for application in Cu(II) ions removal and for bacterial growth inhibition in aqueous solutions, *Sci. Rep.*, 12 (1), 17354.
- [7] El-saied, H.A., and Motawea, E.A., 2020, Optimization and adsorption behavior of nanostructured NiFe₂O₄/Poly AMPS grafted biopolymer, *J. Polym. Environ.*, 28 (9), 2335–2351.
- [8] Adel, N., Hassan, S.S., and Awad, S.H., 2021, Green preparation of new nanoparticles composite from chitosan and zeolite to remove excess concentrations of iron and copper from waste water, *J. Green Eng.*, 11 (2), 1195–1212.
- [9] El Nazer, H.A., and Mohamed, Y.M.A., 2021, “Chalcogenide-Based Nanomaterials as Photocatalysts for Water Splitting and Hydrogen Production” in *Chalcogenide-based Nanomaterials as Photocatalysts*, Eds. Khan, M.M., Elsevier, Amsterdam, Netherlands, 73–183.
- [10] Ramadan, R.H., Abdel-Meguid, A., and Emara, M., 2020, Effects of synthesized silver and chitosan nanoparticles using *Nerium oleander* and *Aloe vera* on antioxidant enzymes in *Musca domestica*, *Catrina: Int. J. Environ. Sci.*, 21 (1), 9–14.
- [11] Suresh, J., Pradheesh, G., Alexramani, V., Sundrarajan, M., and Hong, S.I., 2018, Green synthesis and characterization of zinc oxide nanoparticle using insulin plant (*Costus pictus* D. Don) and investigation of its antimicrobial as well as anticancer activities, *Adv. Nat. Sci: Nanosci. Nanotechnol.*, 9 (1), 8–16.
- [12] Ashwini, J., Aswathy, T.R., Rahul, A.B., Thara, G.M., and Nair, A.S., 2021, Synthesis and characterization of zinc oxide nanoparticles using *Accia caesia* bark extract and its photocatalytic and antimicrobial activities, *Catalysts*, 11 (2), 1507.
- [13] Acemi, A., 2020, Polymerization degree of chitosan affects structural and compositional changes in the cell walls, membrane lipids, and proteins in the leaves of *Ipomoea purpurea*: An FTIR spectroscopy study, *Int. J. Biol. Macromol.*, 16, 715–722.
- [14] Ramalingan, A., Kuppusamy, M., Sambandam, S., Medimagh, M., Oyenyin, O.E., Shanmugasundaram, A., Issaoui, N., and Ojo, N.D., 2022, Synthesis, spectroscopic, topological, Hirschfeld surface analysis, and anti-covid-19 molecular docking investigation of isopropyl 1-benzoyl-4-(benzoyloxy)-2,6-diphenyl-1,2,5,6-tetrahydropyridine-3-carboxylate, *Heliyon*, 8 (10), 10831.

- [15] Pihtili, G., Hekim, S., and Pekdemir, M.E., 2022, Molecular structure, vibrational, spectral investigation and quantum chemical DFT calculations of poly(*N*-isopropyl acrylamide-co-nbutyl methacrylate), *Polym. Korea*, 46 (5), 559–565.
- [16] Alem, M.B., Damena, T., Desalegn, T., Koobotse, M., Eswaramoorthy, R., Ngwira, K.J., Ombito, J.O., Zachariah, M., and Demissie, T.B., 2022, Cytotoxic mixed-ligand complexes of Cu(II): A combined experimental and computational study, *Front. Chem.*, 10, 1028957.
- [17] Al-Bahadili, Z.R., AL-Hamdani, A.A.S., Rashid, F.A., Al-Zubaidi, L.A., and Ibrahim, S.M., 2022, An evaluation of the activity of prepared zinc nanoparticles with extracted alfalfa plant in the treatment of heavy metals, *Baghdad Sci. J.*, 19 (6), 1399–1409.
- [18] Hassan, S.S., Hassan, N.M., Baqer, S.R., and Saleh, A.M., 2021, Biological evaluation and theoretical study of bi-dentate ligand for amoxicillin derivative with some metal ions, *Baghdad Sci. J.*, 18 (4), 1269–1278.
- [19] Ali, H.R., and Hassan, S.S., 2022, Preparation and study of the physical properties of some complexes with Schiff base ligand for cefdinir derivative, *Iraqi J. Mark, Res. Consum. Prot.*, 14 (2), 110–120.
- [20] Baidurah, S., 2022, Methods of analyses for biodegradable polymers: A review, *Polymers*, 14 (22), 4928.
- [21] Basri, R., Khalid, M., Shafiq, Z., Tahir, M.S., Khan, M.U., Tahir, M.N., Naseer, M.M., and Braga, A.A.C., 2020, Exploration of chromone-based thiosemicarbazone derivatives: SC-XRD/DFT, spectral (IR, UV-vis) characterization, and quantum chemical analysis, *ACS Omega*, 5 (46), 30176–30188.
- [22] Fayyadh, B.M., Abd, N.A.B., and Sarhan, B.M., 2022, Synthesis and characterization of new Mn(II), Co(II), Cd(II) and Hg(II) complexes with ligand [*N*-(pyrimidin-2-ylcarbamoithiyl)benzamide] and their antibacterial study, *IOP Conf. Ser.: Earth Environ. Sci.*, 1029 (1), 012030.
- [23] Da Silva, H.C., and De Almeida, W.B., 2020, Theoretical calculations of ¹H NMR chemical shifts for nitrogenated compounds in chloroform solution, *Chem. Phys.*, 528, 110479.
- [24] Sharef, H.Y., and Fakhre, N.A., 2022, Rapid adsorption of some heavy metals using extracted chitosan anchored with new aldehyde to form a Schiff base, *PLoS One*, 17 (9), e0274123.
- [25] Dilkes-Hoffman, L.S., Lant, P.A., Laycock, B., and Pratt, S., 2019, The rate of biodegradation of PHA bioplastics in the marine environment: A meta-study, *Mar. Pollut. Bull.*, 142, 15–24.
- [26] Elhefian, E.A., Nasef, M.M., and Yahaya, A.H., 2012, Preparation and characterization of chitosan/agar blended films: Part 2., Thermal, mechanical, and surface properties, *E-J. Chem.*, 9, 285318.
- [27] Barleany, D.R., Jayanudin, J., Utama, A.S., Riyupi, U., Alwan, H., Lestari, R.S.D., Pitaloka, A.B., Yulvianti, M., and Erizal, E., 2023, Synthesis and characterization of chitosan/polyvinyl alcohol crosslinked poly(*N*-isopropylacrylamide) smart hydrogels via γ -radiation, *Mater. Today: Proc.*, 87 (2), 1–7.
- [28] Wang, S., and Xing, Q., 2022, Preparation and *in vitro* biocompatibility of PBAT and chitosan composites for novel biodegradable cardiac occluders, *e-Polym.*, 22 (1), 705–718.
- [29] Zhang, Q., Gallard, J., Wu, B., Harwood, V.J., Sadowsky, M.J., Hamilton, K.A., and Ahmed, W., 2019, Synergy between quantitative microbial source tracking (qMST) and quantitative microbial risk assessment (QMRA): A review and prospectus, *Environ. Int.*, 130, 104703.
- [30] Abdul Hassan, M.M., Hassan, S.S., and Hassan, A.K., 2022, Green and chemical synthesis of bimetallic nanoparticles (Fe/Ni) supported by zeolite 5A as a heterogeneous Fenton-like catalyst and study of kinetic and thermodynamic reaction for decolorization of reactive red 120 dye from aqueous pollution, *Eurasian Chem. Commun.*, 4, 1062–1086.
- [31] Spencer, R.C., 1996, Predominant pathogens found in the European prevalence of infection in intensive care study, *Eur. J. Clin. Microbiol. Infect. Dis.*, 15 (4), 281–285.

- [32] Schwartz, T., Volkmann, H., Kirchen, S., Kohnen, W., Schön-Hölz, K., Jansen, B., and Obst, U., 2006, Real-time PCR detection of *Pseudomonas aeruginosa* in clinical and municipal wastewater and genotyping of the ciprofloxacin-resistant isolates, *FEMS Microbiol. Ecol.*, 57 (1), 157–167.
- [33] Omer, A.M., Eltaweil, A., El-Fakharany, E.M., Abd El-Monaem, E.M., Ismail, M.M.F., Mohy-Eldin, M.S., and Ayoup, M.S., 2023, Novel cytocompatible chitosan Schiff base derivative as a potent antibacterial, antidiabetic, and anticancer agent, *Arabian J. Sci. Eng.*, 48 (6), 7587–7601.
- [34] Li, J., and Zhuang, S., 2020, Antibacterial activity of chitosan and its derivatives and their interaction mechanism with bacteria: Current state and perspectives, *Eur. Polym. J.*, 138, 109984.
- [35] Malekshah, R.E., Shakeri, F., Aallaei, M., Hemati, M., and Khaleghian, A., 2021, Biological evaluation, proposed molecular mechanism through docking and molecular dynamic simulation of derivatives of chitosan, *Int. J. Biol. Macromol.*, 166, 948–966.
- [36] Helander, I.M., Nurmiäho-Lassila, E.L., Ahvenainen, R., Rhoades, J., and Roller, S., 2001, Chitosan disrupts the barrier properties of the outer membrane of Gram-negative bacteria, *Int. J. Food Microbiol.*, 71 (2-3), 235–244.
- [37] Joshi, N.R., Mule, S.G., Gore, V.A., Suryawanshi, R.D., Pawar, G.T., Bembalkar, S.R., and Pawar, R.P., 2022, Synthesis and biological study of novel Schiff base (1-(3-(4-fluorophenyl)-1-isopropyl-1H-indol-2-yl)methylene)hydrazine ligand and metal complexes, *J. Explor. Res. Pharmacol.*, 7 (4), 202–207.
- [38] Wang, X., Du, Y., and Liu, H., 2004, Preparation, characterization and antimicrobial activity of chitosan-Zn complexes, *Carbohydr. Polym.*, 56 (1), 21–26.
- [39] Kavi Sidharthan, V., Aggarwal, R., Surenthiran, N., Pothiraj, G., Kowsalya, P., and Shanmugam, V., 2018, Selection and characterization of the virulent *Fusarium oxysporum* f. sp. *lycopersici* isolate inciting vascular wilt of tomato, *Int. J. Curr. Microbiol. Appl. Sci.*, 7 (2), 1749–1756.
- [40] Al-aamel, A.N.A., Al-maliky, B.S.A., 2023, Control pepper fusarium wilting by biocontrol agent *Trichoderma harzianum* and chelated iron Fe-EDDHA, *Baghdad Sci. J.*, In Press.
- [41] Rafique, K., Rauf, C.A., Naz, F., and Shabbir, G., 2015, DNA sequence analysis, morphology and pathogenicity of *Fusarium oxysporum* f. sp. *lentis* isolates inciting lentil wilt in Pakistan, *Int. J. Biosci.*, 7 (6), 74–91.
- [42] Dongzhen, F., Xilin, L., Xiaorong, C., Wenwu, Y., Yunlu, H., Yi, C., Jia, C., Zhimin, L., Litao, G., Tuhong, W., Xu, J., and Chunsheng, G., 2020, *Fusarium* species and *Fusarium oxysporum* species complex genotypes associated with yam wilt in South-Central China, *Front. Microbiol.*, 11, 01964.
- [43] Oyeyinka, S.A., Adepegba, A.A., Oyetunde, T.T., Oyeyinka, A.T., Olaniran, A.F., Iranloye, Y.M., Olagunju, O.F., Manley, M., Kayitesi, E. and Njobeh, P.B., 2021, Chemical, antioxidant and sensory properties of pasta from fractionated whole wheat and Bambara groundnut flour, *LWT*, 138, 110618.
- [44] Qasem, H.A., Aouad, M.R., Al-Abdulkarim, H.A., Al-Farraj, E.S., Attar, R.M., El-Metwaly, N.M., and Abu-Dief, A.M., 2022, Tailoring of some novel bis-hydrazone metal chelates, spectral based characterization and DFT calculations for pharmaceutical applications and *in-silico* treatments for verification, *J. Mol. Struct.*, 1264, 133263.
- [45] Pasdar, H., Hedayati Saghavaz, B., Foroughifar, N., and Davallo, M., 2017, Synthesis, characterization and antibacterial activity of novel 1,3-diethyl-1,3-bis(4-nitrophenyl)urea and its metal(II) complexes, *Molecules*, 22 (12), 2125.

Synthesis, Optimization and Antibacterial Performance of Colloidal Silver Nanoparticles in Chitosan

Endang Susilowati*, Lina Mahardiani, Sri Retno Dwi Ariani, and Ilham Maulana Sulaeman

Department of Chemistry Education, Faculty of Teacher Training and Education, Universitas Sebelas Maret, Jl. Ir. Sutami 36A, Surakarta 57126, Indonesia

* **Corresponding author:**

email: endang_s70@staff.uns.ac.id

Received: May 26, 2023

Accepted: July 13, 2023

DOI: 10.22146/ijc.84822

Abstract: Colloidal silver nanoparticles were successfully synthesized via the chemical reduction method. The synthesis used AgNO_3 as the precursor, chitosan as the reducing and stabilizing agents, and NaOH as the accelerator. The synthesis parameters were optimized. The samples were tested with a UV-vis spectrophotometer to observe their localized surface plasmon resonance (LSPR) phenomenon, a transmission electron microscope (TEM), and a particle size analyzer (PSA) to investigate their particle shape and size distribution. Further, silver nanoparticles were tested for their storage stability and antibacterial performance. The UV-vis spectroscopy data exhibited that the silver nanoparticles have been successfully synthesized, validating via the emergence of the LSPR absorption band at 402–418 nm. At 50 °C, the optimum synthesis was achieved for 100 min of reaction time by adding 0.033 M NaOH and AgNO_3 4.00% (w/w, AgNO_3 /chitosan). TEM results showed spherical silver nanoparticles of 1–8 nm, while the PSA results exhibited particles sizes of about 12–59 nm. The colloidal silver nanoparticles were stable in storage for 8 weeks and had good antibacterial performance against *E. coli*, *S. aureus*, extended-spectrum beta-lactamases (ESBL), and methicillin-resistant *S. aureus* (MRSA). Therefore, colloidal silver nanoparticles have the potential as a material for medical applications.

Keywords: antibacterial performance; colloidal silver nanoparticles; chitosan; synthesis optimization

■ INTRODUCTION

The health sector is crucial in human life, so things related to medicine are constantly being developed. Studies regarding new antibacterial materials are fascinating because of the growing demand for medical applications. One of the developed materials for the fabrication of antibacterial agents is chitosan. Chitosan is a natural polymer derived from chitin isolated from fishery garbage, such as shrimp and crab shells. Chitin is a natural biopolymer found abundant after cellulose [1]. The result of the deacetylation of chitin is called chitosan, which has many benefits because of its properties, namely non-toxic compound possessing excellent biodegradability, antibacterial and antifungal characteristics, and biocompatibility [2].

Chitosan has antibacterial performance as a result of the existence of positively charged clusters $[-\text{NH}_3^+]$ which will interact with the negative charges on the bacterial cell membrane and change the cell permeability properties [2]. However, the antibacterial performance of chitosan is still relatively low and depends on the pH [3]. The pH has been considered as the most significant factor that influences the antimicrobial activity of chitosan. It impacts the solubility and the electrical charge of chitosan molecules. So, this is a limitation of chitosan as an antibacterial. The antibacterial performance of chitosan can be advanced by adding other antibacterial materials. Silver nanoparticles include metal nanoparticles often studied and act as antibacterial material [4]. Completed with their antimicrobials [5], anti-inflammatory [6], and drug

delivery systems [7], silver nanoparticles are commonly applied to the medical world. The incorporation of silver nanoparticles into chitosan can produce a colloidal silver nanoparticle system.

Silver nanoparticles can be synthesized with numerous methods. Still, chemical reduction is the most commonly employed method because it is easy, simple, and effective that could yield satisfactory results [8]. Besides, the method is relatively affordable and can be performed on large-scale production. In general, metal nanoparticle synthesis with this method requires a reductant to reduce metal ions and a stabilizer to stabilize the nanoparticles [9]. Reducing agents widely used are sodium borohydride, sodium citrate, ascorbate, and Tollens reagent. One of these is sodium borohydride (NaBH_4), which is the most commonly used reducing agent in synthesizing silver nanoparticles. This is because NaBH_4 is a potent reducing agent that can reduce the temperature and reduction time of silver metal ions. However, the usage of this chemical in the synthesis can lead to health and environmental problems [10].

Considering this matter, it is necessary to develop a green synthesis to produce silver nanoparticles. Several scientists have established the usage of environmentally friendly weak reducing agents such as liginosulphonate acid [10], banana peel extract [11], *n*-hexane extract of *Malachra capitata* (L.) leaf [12], glucose [13], and chitosan [14]. Chitosan is a biopolymer that can reduce metal ions, enabling the synthesis of nanoparticles of controlled shape, size, and stability [14].

Chitosan is an attractive reducing agent to be studied because it can act as a stabilizer simultaneously. Referring to previous research, chitosan could reduce silver ions, but it required a high temperature (95 °C) and a relatively long reaction time (12 h) [15]. Meanwhile, other studies succeeded in synthesizing silver nanoparticles with glucose as a reducing agent, gelatin as a stabilizer, and NaOH as an accelerator which only required 60 °C temperature and 15 min reaction time [16]. Reducing silver ions with a weak reducing agent such as glucose is effective when conducted under alkaline conditions [13]. This study provides a solution to synthesize silver nanoparticles using chitosan as a

reducing agent and NaOH as an accelerator to reduce the temperature and the formation time of silver nanoparticles. Synthesis optimization of silver nanoparticles in chitosan needs to be done to find the synthesis conditions with the best and most efficient results. Furthermore, this result will be important to be applied for producing antibacterial materials for medical applications, especially for wound dressing.

Various stabilizing agents, such as gelatin [16] and polyvinyl alcohol [17] at different concentrations, affect the size and shape of the resulting silver nanoparticles. Chitosan is one of the stabilizing agents to be examined because of its ability as a stabilizer and antibacterial properties. Studies on silver nanoparticle synthesis using chitosan as the stabilizing agent have been conducted previously [18-19]. Stabilizing agents are essential to control the formation of well-dispersed nanoparticles with uniform particle sizes. Silver nanoparticles yield a colloidal system when dispersed in a chitosan solution.

Here, colloidal silver nanoparticles were synthesized with AgNO_3 as the precursor, chitosan as the reducing and stabilizing agent, and NaOH as the accelerator. The synthesis parameters were optimized to determine the best conditions by varying reaction temperature and time, NaOH concentration, and AgNO_3 concentration. Besides, the antibacterial performance of colloidal silver nanoparticles was tested against standard bacteria (*E. coli* and *S. aureus*) and multiresistant bacteria (ESBL and MRSA).

■ EXPERIMENTAL SECTION

Materials

The starting materials were chitosan made from crab shells (Biotech Surindo Indonesia), glacial acetic acid (CH_3COOH), silver nitrate (AgNO_3), and sodium hydroxide (NaOH) (Merck); and distilled water from Integrated Laboratory of Universitas Sebelas Maret, Indonesia.

Instrumentation

To characterize the formation of silver nanoparticles, the UV-vis Shimadzu UV-1800 spectrophotometer was used. The shape and size

distribution of the particles were characterized using the JIOL JEM-1400 series transmission electron microscope (TEM) instrument with a voltage of 80 KeV. The particle size distribution was also tested using the Malvern Zetasizer particle size analyzer (PSA).

Procedure

First, chitosan was diluted in 0.5% (v/v) CH₃COOH solution, producing a 0.5% (w/v) chitosan solution. Then, 12.5 mL of 0.5% chitosan solution was added into 0.8 mL of AgNO₃ solution (0.01 g/mL) while stirred for 5 min. Next, it was added with 1.25 mL of NaOH (2 M) solution while stirring for 5 min, forming a gel in the solution with the color changing to brown. The solution was then treated with temperature variations at room temperature (26 °C), 30, 40, 50, and 60 °C for 90 min. Afterward, 47.5 mL of 0.5% chitosan was added to each solution and stirred until completely dissolved. The resulting colloid was put into bottles and stored at room temperature.

The same process was performed to optimize the synthesis of silver nanoparticles with the independent and dependent variables, as shown in Table 1. The silver nanoparticle samples with various concentrations of AgNO₃ were then tested for stability in storage for 8 weeks based on the LSPR phenomenon characterized via a UV-vis spectrophotometer.

This procedure of analysis was completed to ensure the successful synthesis of the silver nanoparticles through the LSPR phenomenon. The first step was diluting the samples into distilled water as much as 10

times. The solution was then tested with a UV-vis Shimadzu UV-1800 spectrophotometer to measure the absorbance and maximum wavelength in the wavelength range (λ) of 600–300 nm.

Analysis using TEM and PSA was performed to examine the particle shape and size distribution. In this step, the samples were thinned and then placed in a copper grid. Then, the samples were observed using the TEM instrument with a voltage of 80 KeV. The particle shape and size distribution were determined manually. The samples were also analyzed with the Malvern Zetasizer PSA to investigate the particle size distribution. Before testing, the colloid samples were diluted and filtered.

The antibacterial performance of colloidal silver nanoparticles with various AgNO₃ concentrations was tested against *S. aureus* ATCC 25922, *E. coli* ATCC 25923, MRSA, and ESBL with the well-diffusion method in duplicate [20]. Tests were carried out using Mueller Hinton Agar (MHA) as a material medium. The MHA solid media smeared with bacteria was perforated with a diameter of 7 mm and then filled with 50 μL of colloidal silver nanoparticles samples. It was then followed by incubation at 37 °C for 24 h. The clear zone which is the diameter of the inhibition zone is measured using a digital caliper.

RESULTS AND DISCUSSION

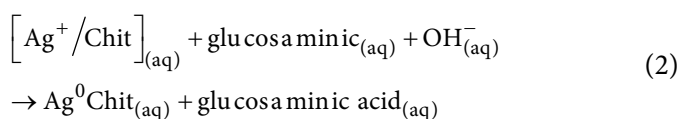
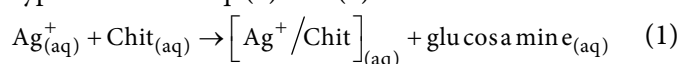
Here, colloidal silver nanoparticles have been successfully synthesized by the chemical reduction

Table 1. Synthesis condition for the optimization process

No	Independent variables	Dependent variables
1	Temperature = 26, 30, 40, 50, and 60 °C	Time = 90 min [NaOH] = 0.042 M [AgNO ₃] = 2.66%
2	Time = 20, 40, 60, 80, 100, and 120 min	Temperature = 50 °C [NaOH] = 0.042 M [AgNO ₃] = 2.66%
3	[NaOH] = 0, 0.008, 0.017, 0.025, 0.033, 0.042, 0.050, 0.058, and 0.067 M	Temperature = 50 °C Time = 100 min [AgNO ₃] = 2.66%
4	[AgNO ₃] = 0.66, 1.33, 2.00, 2.66, 3.33 and 4.00%	Temperature = 50 °C Time = 100 min [NaOH] = 0.033 M

procedure. This research applied green synthesis because the chemicals used are non-toxic, environmentally friendly solvents and renewable materials. The synthesis employed AgNO_3 as the silver precursor, chitosan as the reducing and stabilizing agents, and NaOH as the accelerator. The prior study performed chitosan as the reducing agent to synthesize gold nanoparticles under alkaline environments through hydrolysis and degradation to yield glucosamine [21]. Thus, associated with this study, glucosamine will reduce metal ions to yield silver zero valences and glucosaminic acid. It is similar to reducing glucose under alkaline conditions [13-16].

In this study, the colloid color changed from transparent to yellow to brown, denoting the success of the silver nanoparticle formation [16]. This color appeared as a result of the LSPR phenomenon. Metallic surfaces possess free electrons in the conduction band (CB) and a positively charged nucleus [8]. LSPR is the electron excitation group in the CB nearby the surface of the nanoparticles. Metal nanoparticles exhibit a particular absorption spectrum on the surface so that the LSPR phenomenon can be detected by UV-vis spectrophotometer [18]. The LSPR band of silver nanoparticles produces a typical absorption band spectrum in the 400–450 nm wavelength range [22]. Here, the mechanism for the silver nanoparticles formation is hypothesized as Eq. (1) and (2).



When AgNO_3 is added to the chitosan solution, Ag^+ ions will be chelated in the chitosan structure by forming coordinate bonds with amino groups ($-\text{NH}_2$) and hydroxyl ($-\text{OH}$) written as $[\text{Ag}^+/\text{Chit}]$. In the next step, by adding the NaOH accelerator containing OH^- ions, the glucosamine group from chitosan can perform as a reducing agent, which converts Ag^+ ions into metal Ag and glucosaminic acid as a result of the oxidation of glucosamine. Ag crystal growth will be limited by chitosan polymer so that Ag with nano size (< 100 nm) can be obtained.

Synthesis Optimization of Silver Nanoparticles

The effects of heating temperatures on the LSPR band were observed. The temperature variations were 26, 30, 40, 50, and 60 °C with 90 min reaction time, 0.042 M NaOH , and AgNO_3 2.66% (w/w; $\text{AgNO}_3/\text{chitosan}$). Fig. 1(a) shows that the resulting colloid is darker with higher heating temperatures. Temperature is an important aspect significantly affecting the synthesis results of colloidal silver nanoparticles. The typical LSPR band for silver nanoparticles is about 407–418 nm. The heating temperature is directly proportional to the absorbance produced. The higher temperature leads to greater absorbance, denoting an enhancement in the concentration of silver nanoparticles [5]. The absorbance band due to LSPR silver nanoparticles experience a blue shift from 418 to 407 nm as the increasing temperature from 30 to 60 °C, revealing that the sizes of silver nanoparticles decrease with the higher heating temperature. It is considered because of the rapid reaction rate at high temperatures. At high temperatures, the kinetic energy is enhanced, so silver ions are reduced more rapidly, thereby reducing the possibility of particle size growth. Consequently, at higher heating temperatures, smaller particles with uniform distribution are produced [5]. In this variation, the temperature of 50 °C was chosen for optimization of other parameters because it had a high absorbance, which was slightly different from the temperature of 60 °C and was more efficient from the aspect of energy use.

Furthermore, the influence of reaction time on the LSPR band was also investigated. Fig. 1(b) presents the UV-vis absorption spectra and colloid color for each sample. In general, the absorbance improves with increasing heating time. It shows that the longer heating time causes a greater amount of silver nanoparticles to be produced. However, the samples have almost the same absorbance values at 100 and 120 min. It means that, at a certain time, the silver nanoparticles produced will be constant, where the formation of silver nanoparticles will no longer occur because the silver nitrate has been completely reduced [5]. The typical LSPR band for silver nanoparticles was about 410–414 nm.

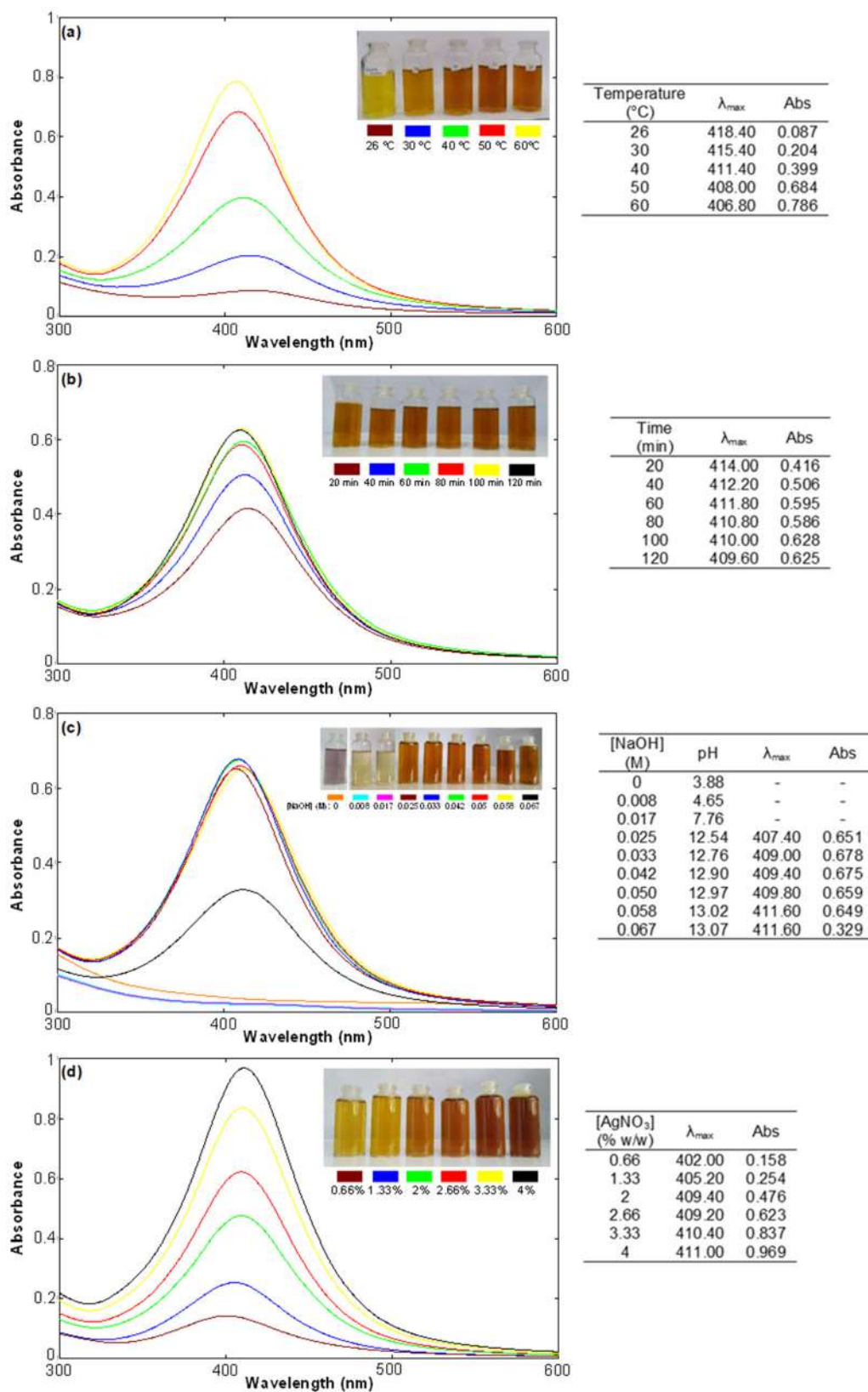


Fig 1. UV-vis spectrum of colloidal silver nanoparticles with variations: (a) temperature, (b) reaction time, (c) NaOH concentration, and (d) AgNO₃ concentrations

The absorbance band due to LSPR silver nanoparticles experience a blue shift (20–120 min), exhibiting that the sizes of the silver nanoparticles decline with the longer heating time. The optimal reaction time needed for forming silver nanoparticles was 100 min since, after that, no addition of silver nanoparticles was observed.

In this study, NaOH acts as an accelerator, added to provide time efficiency and effectiveness in preparing silver nanoparticles. Fig. 1(c) shows that the resulting colloid's color tended to be darker with a higher NaOH concentration. However, at NaOH concentrations of 0.025–0.067 M, the colloid did not exhibit a significant color gradation. It implies that the silver nitrate in the colloid has been completely reduced [5]. In comparison, at the concentration of 0, 0.008, and 0.017 M, the colloid did not experience a color change to brown, which might be because the colloid does not contain silver nanoparticles. Based on Fig. 1(c), the LSPR band could not be identified without NaOH addition. Besides, it also could not be identified with the addition of a small amount of NaOH at the concentrations of 0.008 and 0.017 M. The absorbance values at the NaOH concentration of 0.025–0.058 M differed slightly. The absorbance enhanced from 0.025 to 0.033 M concentrations, indicating that the higher NaOH concentration resulted in a more significant number of silver nanoparticles. However, the introduction of NaOH further declined the absorbance (concentrations of 0.042–0.067 M) and significantly decreased at 0.067 M.

It is considered due to the construction of a denser gel at a higher NaOH concentration which inhibits the reduction of silver ions to silver nanoparticles [13]. At the NaOH concentrations of 0, 0.008, and 0.017 M, the colloidal silver nanoparticles had a pH value of less than 8 and did not exhibit an absorbance band. In contrast, at concentrations of 0.025–0.067 M, they had a pH value above 12, which emerged absorbance band. These follow the results of previous research, where a pH of about 9–13 is the most ideal for synthesizing silver nanoparticles [5]. The typical LSPR band for silver nanoparticles was at 407–412 nm wavelength. The absorbance band due to LSPR silver nanoparticles experienced a red shift at the NaOH concentrations of 0.042–0.067 M, demonstrating

an enlargement in the size of silver nanoparticles as the higher NaOH concentration. The optimal NaOH concentration needed to form silver nanoparticles was 0.033 M since, after that, no addition of the silver nanoparticles number was observed.

Next, the influence of AgNO₃ concentration on the LSPR band was observed. Fig. 1(d) shows that the higher AgNO₃ concentration led to a darker color of the colloid produced. The higher AgNO₃ concentration from samples 0.66–4.00% was proportional to the increase in the absorbance value. The typical LSPR band for silver nanoparticles is at 402–411 nm wavelength. The emergence of the LSPR absorption band at around 400 nm demonstrates that the particles are spherical [8]. The absorbance band due to LSPR silver nanoparticles experienced a redshift (0.66–4.00%), revealing that the sizes of silver nanoparticles enlarge as the higher AgNO₃ concentration. Colloidal silver nanoparticles with a further variation of AgNO₃ concentration were then tested for their stability and antibacterial performance.

Based on the results of the optimization parameters of temperature (Fig. 1(a)), time (Fig. 1(b)), and NaOH concentration (Fig. 1(c)), the optimal conditions for synthesizing silver nanoparticles were at 50 °C for 100 min with 0.033 M NaOH. These results are more efficient than similar research reported by Kalaivani et al. [23], where silver nanoparticles were synthesized at 90 °C for 10 h.

The higher AgNO₃ concentration induced a higher absorbance, indicating a higher concentration of silver nanoparticles formed. Fig. 2 shows that the relationship between the AgNO₃ concentration was linearly proportional to the absorbance with a coefficient of determination of $R^2 = 0.992$. It strengthens the argument that the higher AgNO₃ concentration used induces, the greater concentration of silver nanoparticles yielded.

Stability of Colloidal Silver Nanoparticles

Colloidal silver nanoparticles are called stable if the concentration, size, and shape of the particles do not change. The concentration of silver nanoparticles correlates with the absorbance intensity in the UV-vis spectra. Therefore, the stability of silver nanoparticles can

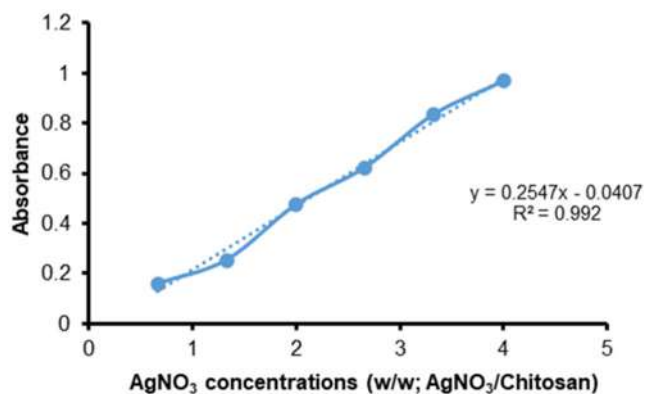


Fig 2. Relationship between concentration precursor of AgNO_3 and absorbance

be investigated based on their absorbance and maximum wavelength. The stability of colloidal silver nanoparticles was carried out by measuring the absorbance and maximum wavelength at various AgNO_3 concentrations every week for 8 weeks. Colloidal silver nanoparticles were stored at room temperature. Before measurement, the samples were diluted 10 times into distilled water. The change in the LSPR band of the UV-vis spectrum is presented in Fig. 3(a) and 3(b). Absorbance for AgNO_3 concentration of 0.66–4% (w/w; AgNO_3 /chitosan) tended to decrease at week 1 of storage compared to weeks 2–8. This indicates that, in the first week, there may be more silver nanoparticle aggregation than in weeks 2–8. At lower concentrations, silver nanoparticles tended to be more stable than at high concentrations (Fig. 3(a)).

The results of the UV-vis absorption spectra also showed maximum wavelength data for each sample. The samples experienced a shift in the maximum wavelength to the right and the left, but only slightly. Seen from the

maximum wavelength, it tended to be a red shift in all samples, indicating a larger particle size during storage (Fig. 3(b)). This is in line with the decreasing absorption band, demonstrating that silver nanoparticles tend to experience aggregation during storage. These results differ from previous studies, where silver nanoparticles were still stable after week 8 of storage using glucose as a reducing agent and chitosan as a stabilizer [13].

TEM Analysis

TEM analysis was employed to observe the shape and size distribution of silver nanoparticles in the colloidal system. The samples observed were AgNO_3 with concentrations of 2.66 and 4.00% (w/w; AgNO_3 /chitosan), respectively. These two samples represented the observed particle size distribution of silver at low and high concentrations using TEM. The emergence of the LSPR absorption band at about 400 nm denotes the spherical-shaped particles that follow the resulting TEM images in the previous report [8]. Based on Fig. 4(a) and 4(b), the use of AgNO_3 as silver nanoparticle precursor with a concentration of 4.00% produced more silver nanoparticles than AgNO_3 at 2.66%. The TEM image of Sample A4 exhibits flakes on the sample. It may be due to the colloid preparation that is too thick.

The higher AgNO_3 concentration induces a higher concentration of silver nanoparticles [14]. In the same area, there were 65 particles at the AgNO_3 concentration of 2.66% and 95 particles at the AgNO_3 of 4.00%, calculated with the ImageJ application. It is in line with the rise in absorbance from 0.623 to 0.969 (Fig. 1(d)). Fig. 5(a) and 5(b) show that, at the AgNO_3 concentration

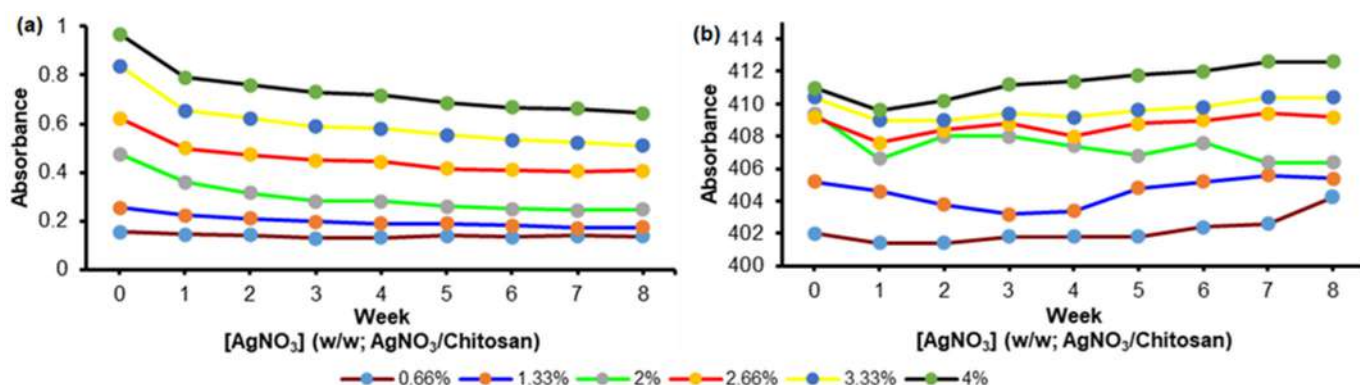


Fig 3. Stability of colloidal silver nanoparticles changes in (a) absorbance and (b) maximum wavelength

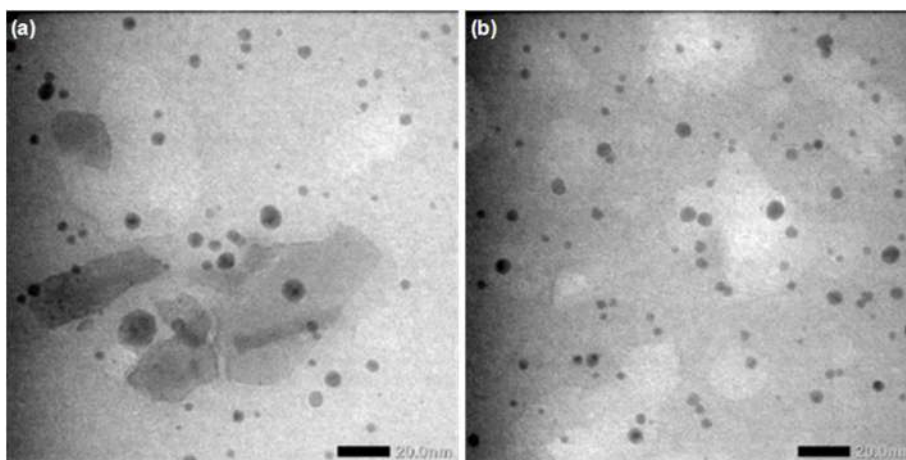


Fig 4. TEM images of colloidal silver nanoparticles (a) 2.66% and (b) 4.00% (w/w; AgNO₃/chitosan)

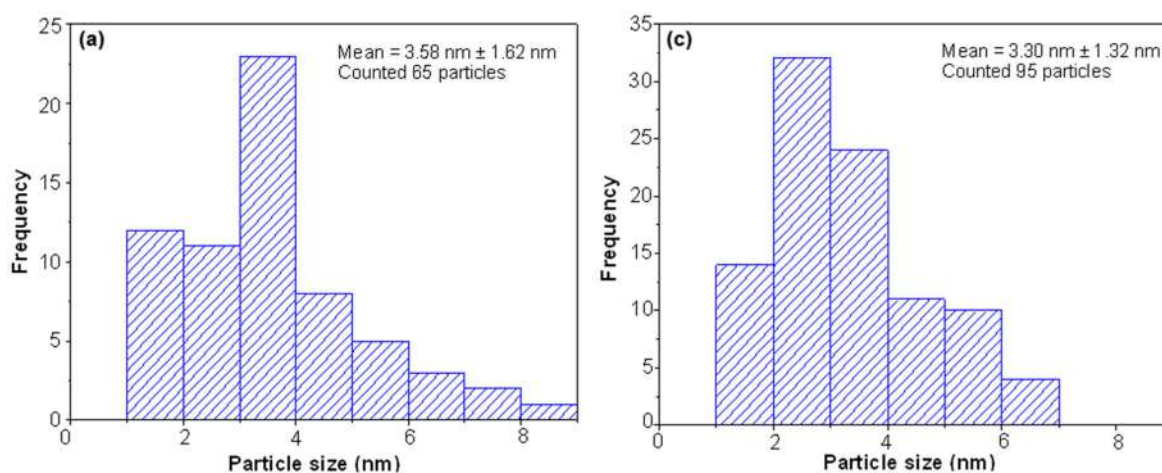


Fig 5. Size distribution of colloidal silver nanoparticles (a) 2.66% and (b) 4.00% (w/w; AgNO₃/chitosan)

of 2.66%, the average particle diameter was 3.58 nm with a range of 1–8 nm. In contrast, at the AgNO₃ concentration of 4.0, the average particle diameter was 3.30 nm, with a 1–7 nm range. Thus, the particle size at the AgNO₃ concentration of 2.66% was slightly larger than at 4.00%. It does not align with the LSPR absorption band, which reveals a redshift from 409.20 to 411.00 nm. In this study, the slight difference in maximum wavelength does not significantly affect the particle size. According to the distribution frequency, silver nanoparticles were conquered by particles with 2–4 nm size. On the other, the results of other researchers who have synthesized silver nanoparticles using *Malachra capitata* (L.) leaf showed that the particle size ranged from 30 to 35 nm with an average diameter of 35 nm. The size distribution curve revealed that the particles ranged from 5–70 nm, and the mean particle

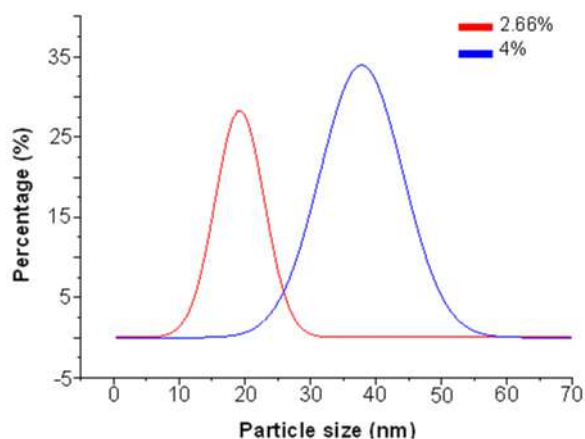
diameter was about 5 nm [12]. It shows that previous research obtained a larger particle size than this research.

PSA Analysis

PSA was completed to observe the size and distribution of silver nanoparticles. The samples analyzed were AgNO₃ with 2.66 and 4.00% concentrations (w/w; AgNO₃/chitosan), respectively. Here, the distribution number was exploited to estimate the relative number of distribution percentages of each size (Fig. 6). Table 2 shows data on the polydispersity index (PDI), mean size, and standard deviation of samples with AgNO₃ concentrations of 2.66 and 4.00%. The particle sizes resulting from TEM were smaller than those from PSA. The particle sizes from TEM were 1–8 nm, while those from PSA were 12–38 nm (2.66%) and

Table 2. PSA characterization result

AgNO ₃ (as precursor)	PDI	Average size (nm)	Standard deviation (nm)
2.66%	0.341	19.80	4.569
4%	0.482	38.22	6.776

**Fig 6.** Particle size distribution of silver nanoparticles by frequency (%)

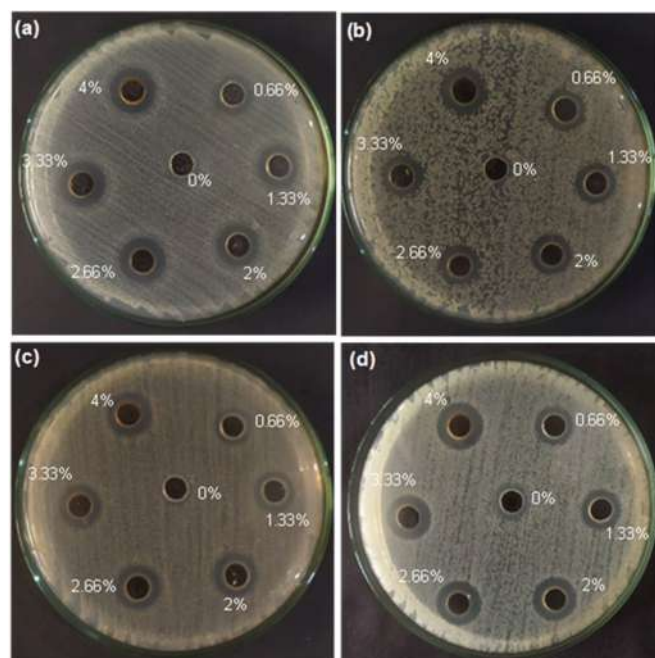
28–59 nm (4.00%). Measurement with PSA used a water dispersion medium so that the chance of small particles sticking together is enormous during the measurement. Thus, the particle size obtained is larger due to agglomeration. In addition, the particle size of the PSA characterization is a hydrodynamic diameter measure, where the particle size includes the Ag particles and the stabilizer agent surrounding the particles [24].

The polydispersity index (PDI) reveals the level of confidence in the size of the dispersed particles in colloidal silver nanoparticles. The PDI value closer to zero indicates a uniform particle. If the PDI value is greater than 0.7, it reveals high heterogeneity and is probably unsuitable for analysis by the dynamic light scattering (DLS) method [25]. The use of AgNO₃ with concentrations of 2.66 and 4.00% as a precursor for silver nanoparticles had a PDI value of less than 0.5, indicating a relatively good level of particle uniformity. The PDI value is associated with the standard deviation value and the particle size distribution curve presented in Fig. 6. The smaller PDI value means a lower standard deviation, representing high accuracy. At the AgNO₃ concentration of 2.66%, the standard deviation value was 4.569 nm, lower than that of a 4.00% concentration with a value of 6.776 nm. In addition, the

smaller PDI value means a narrower particle size distribution. The AgNO₃ concentration of 2.66% exhibited a narrower distribution curve than 4.00%, where the particle sizes were about 12–38 nm (2.66%) and 28–59 nm (4.00%). These results denote that the concentration of AgNO₃ as the silver nanoparticles precursor has an effect on particle size. At a high AgNO₃ concentration, a larger size of silver is produced.

Antibacterial Performance of Colloidal Silver Nanoparticles

The antibacterial performance of colloidal silver nanoparticles with diverse concentrations of AgNO₃ precursors represents the number of silver nanoparticles in colloids. The colloids tested were all samples with concentrations of 0.66–4.00% (w/w; AgNO₃/chitosan) and a chitosan solution without AgNO₃ for comparison. The ability of colloidal silver nanoparticles to inhibit the growth of bacteria was tested by the well-diffusion method. The bacteria included gram-positive bacteria (*S. aureus* and MRSA) and gram-negative bacteria (*E. coli* and ESBL). The results are presented in Fig. 7.

**Fig 7.** Inhibition area of colloidal silver nanoparticles with various AgNO₃ concentrations (w/w; AgNO₃/chitosan) against (a) *S. aureus*, (b) *E. coli*, (c) MRSA, and (d) ESBL

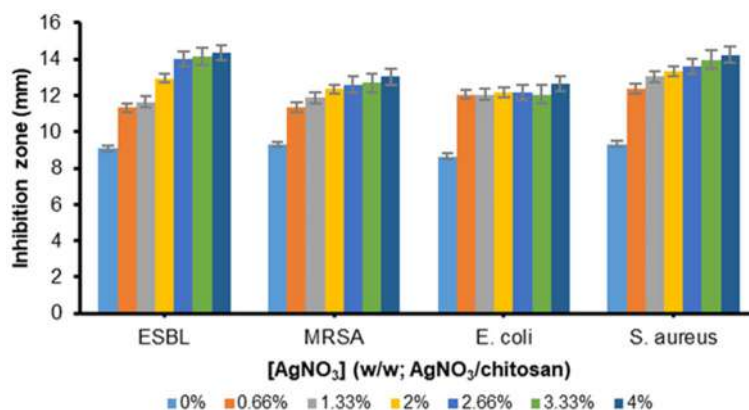


Fig 8. Antibacterial performance of colloidal silver nanoparticles

The antibacterial performance was examined based on the diameter of the inhibition area indicated by the appearance of a clear area around the hole comprising colloidal silver nanoparticles. The wide clear area suggests that the samples have high antibacterial performance and *vice versa*.

Two sources inhibiting bacterial growth are chitosan and silver nanoparticles. Chitosan solution (0% AgNO₃) had lower antibacterial performance than all colloidal silver nanoparticles with AgNO₃ concentrations of 0.66–4.00% as precursor silver nanoparticles. Previous researchers proposed several mechanisms for the inhibition of bacterial growth by chitosan; however, one mechanism is most believed. The mechanism is an interaction between the positive charges of chitosan (NH₃⁺) with the negative charges of the outer membrane of the microbial cell. It changes the structure and permeability of the cell membrane, contaminating proteins and other intracellular components. It thereby challenges the biochemical and physiological competence of the bacteria, causing the loss of replicative ability, and, eventually, the bacteria die [2].

Several factors influencing the antibacterial performance of silver nanoparticles are particle size, surface area, morphology, and distribution degree [26]. There are three most common mechanisms for silver nanoparticles in inhibiting bacterial growth: (1) Ag⁺ ions absorption followed by the interference of ATP construction and DNA replication, (2) silver nanoparticles and Ag⁺ ions making reactive oxygen species (ROS), and (3) silver nanoparticles directly devastating cell membranes [27].

Colloidal silver nanoparticles are a sol-colloid type system, so all three mechanisms can occur. When silver penetrates bacterial cells, some particles can release silver ions and silver nanoparticles at the same time, form ROS and then prevent ATP production and DNA replication. When the colloid diffuses in the bacterial medium, the silver nanoparticles insert the bacterial cell and impact the permeability and function of the membrane [18].

Chitosan solution without silver nanoparticles possessed the smallest diameter of the inhibition area compared to others (0.66–4.00% AgNO₃ concentrations). Thus, it is proven that the addition of silver nanoparticles could increase antibacterial performance. Colloidal silver nanoparticles had good antibacterial performance against all bacteria tested, both non-multiresistant bacteria (*S. aureus* and *E. coli*) and multiresistant bacteria (MRSA and ESBL). Based on Fig. 8, in general, the increase in AgNO₃ concentration was in line with the enlargement in the diameter of the inhibition area in the four bacteria. This means that colloidal silver nanoparticles with higher concentrations have higher antibacterial activity.

CONCLUSION

Colloidal silver nanoparticles were successfully formed by chemical reduction. Chitosan acted as the reducing and stabilizing agents, and NaOH was the accelerator. The silver nanoparticles formed were confirmed with the emergence of the LSPR absorption band at 402.0–418.4 nm. At 50 °C and 4.00% (w/w)

AgNO₃ concentration, the synthesis of colloidal silver nanoparticles was optimal at 100 min of reaction time with a concentration of 0.033 M NaOH. Based on the LSPR phenomenon identified by the UV-vis spectrophotometer, colloidal silver nanoparticles were stable in storage for 8 weeks at room temperature. The nanoparticles were spherical with 1–8 nm size based on the TEM analysis, while from the PSA analysis, the particle size was 12–59 nm. The higher silver nanoparticle concentration in colloidal resulted in higher antibacterial performance against *S. aureus*, *E. coli*, MRSA, and ESBL.

■ ACKNOWLEDGMENTS

The acknowledgment is delivered for the Directorate of Research, Technology and Community Service, Directorate General of Higher Education, Research and Technology of Indonesia, which funded this research through the *Penelitian Unggulan Perguruan Tinggi* (PDUPT) grant 2022 in Universitas Sebelas Maret with contract number 1035.1/UN27.22/PT.01.03/2022.

■ AUTHOR CONTRIBUTIONS

Endang Susilowati conducted the conceptualization, project leader, project administration, supervision, writing the original and revision of the manuscript. Lina Mahardiani contributed on translation, editing, and revision of the manuscript. Sri Retno Dwi Ariani was responsible for analysis data and editing the original manuscript. Ilham Maulana Sulaeman conducted the experiments and analysis data.

■ REFERENCES

- [1] Iber, B.T., Kasan, A., Torsabo, D., and Omuwa, J.W., 2022, A review of various sources of chitin and chitosan in nature, *J. Renewable Mater.*, 10 (4), 1097–1123.
- [2] Badawy, M.E.I., and Rabea, E.I.A., 2011, A biopolymer chitosan and its derivatives as promising antimicrobial agents against plant pathogens and their applications in crop protection, *Int. J. Carbohydr. Chem.*, 2011, 460381.
- [3] Ardean, C., Davidescu, C.M., Nemeş, N.S., Negrea, A., Ciopec, M., Duteanu, N., Negrea, P., Duda-Seiman, D., and Musta, V., 2021, Factors influencing the antibacterial activity of chitosan and chitosan modified by functionalization, *Int. J. Mol. Sci.*, 22 (14), 7449.
- [4] Valverde-Alva, M.A., García-Fernández, T., Villagrán-Muniz, M., Sánchez-Aké, C., Castañeda-Guzmán, R., Esparza-Alegria, E., Sánchez-Valdés, C.F., Llamazares, J.L.S., and Herrera, C.E.M., 2015, Synthesis of silver nanoparticles by laser ablation in ethanol: A pulsed photoacoustic study, *Appl. Surf. Sci.*, 355, 341–349.
- [5] Verma, A., and Mehata, M.S., 2015, Controllable synthesis of silver nanoparticles using neem leaves and their antimicrobial activity, *J. Radiat. Res. Appl. Sci.*, 9 (1), 109–115.
- [6] David, L., Moldovan, B., Vulcu, A., Olenic, L., Perde-Schrepler, M., Fischer-Fodor, E., Florea, A., Crisan, M., Chiorean, I., Clichici, S., and Filip, G.A., 2014, Green synthesis, characterization and anti-inflammatory activity of silver nanoparticles using European black elderberry fruits extract, *Colloids Surf., B*, 122, 767–777.
- [7] Gholamali, I., Asnaashariisfahani, M., and Alipour, E., 2020, Silver nanoparticles incorporated in pH-sensitive nanocomposite hydrogels based on carboxymethyl chitosan-poly (vinyl alcohol) for use in a drug silver system, *Regener. Eng. Transl. Med.*, 6 (2), 138–153.
- [8] Guzmán, M.G., Dille, J., and Godet, S., 2009, Synthesis of silver nanoparticles by chemical reduction method and their antibacterial activity, *Int. J. Chem. Biomol. Eng.*, 2 (3), 104–111.
- [9] Iravani, S., Korbekandi, H., Mirmohammadi, S.V., and Zolfaghari, B., 2014, Synthesis of silver nanoparticles: Chemical, physical and biological methods, *Res. Pharm. Sci.*, 9 (6), 385–406.
- [10] Reddy, G., and Thakur, A., 2017, Biogenic synthesis of silver nanoparticles using plant waste material, *Rasayan J. Chem.*, 10 (3), 695–699.
- [11] Ibrahim, H.M.M., 2015, Green synthesis and characterization of silver nanoparticles using banana peel extract and their antimicrobial activity against representative microorganisms, *J. Radiat. Res. Appl. Sci.*, 8 (3), 265–275.

- [12] Srirangam, G.M., and Rao, K.P., 2017, Synthesis and characterization of silver nanoparticles from the leaf extract of *Malachra capitata* (L.), *Rasayan J. Chem.*, 10 (1), 46–53.
- [13] Susilowati, E., Triyono, T., Santosa, S.J., and Kartini, I., 2015, Synthesis of silver-chitosan nanocomposites colloidal by glucose as reducing agent, *Indones. J. Chem.*, 15 (1), 29–35.
- [14] Susilowati, E., Masykuri, M., Ulfa, M., and Puspitasari, D., 2020, Preparation of silver-chitosan nanocomposites colloidal and film as antibacterial material, *JKPK*, 5 (3), 300–310.
- [15] Wei, D., Sun, W., Qian, W., Ye, Y., and Ma, X., 2009, The synthesis of chitosan-based silver nanoparticles and their antibacterial activity, *Carbohydr. Res.*, 344 (17), 2375–2382.
- [16] Darroudi, M., Ahmad, M., Abdullah, A.H., and Ibrahim, N.A., and Shameli, K., 2010, Effect of accelerator in green synthesis of silver nanoparticles, *Int. J. Mol. Sci.*, 11 (10), 3898–3905.
- [17] Ardani, H.K., Imawan, C., Handayani, W., Djuhana, D., Harmoko, A., and Fauzia, V., 2017, Enhancement of the stability of silver nanoparticles synthesized using aqueous extract of *Diospyros discolor* Willd. leaves using polyvinyl alcohol, *IOP Conf. Ser.: Mater. Sci. Eng.*, 188, 012056.
- [18] Susilowati, E., Maryani, M., and Ashadi, A., 2019, Green synthesis of silver-chitosan nanocomposite and their application as antibacterial material, *J. Phys.: Conf. Ser.*, 1153, 012135.
- [19] Susilowati, E., Ariani, S.R.D., Mahardiani, L., and Izzati, L., 2021, Synthesis and characterization chitosan film with silver nanoparticles addition as a multiresistant antibacterial material, *JKPK*, 6 (3), 371–383.
- [20] Jahangirian, H., Haron, M.J., Ismail, M.H.S., Rafiee-Moghaddam, R., Afsah-Hejri, L., Abdollahi, Y., and Vafaei, N., 2013, Well diffusion method for evaluation of antibacterial activity, *Dig. J. Nanomater. Biostruct.*, 8 (3), 1263–1270.
- [21] Pestov, A., Nazirov, A., Modin, E., Mironenko, A., and Bratskaya, S., 2015, Mechanism of Au(III) reduction by chitosan: Comprehensive study with ^{13}C and ^1H NMR analysis of chitosan degradation products, *Carbohydr. Polym.*, 117, 70–77.
- [22] Patra, J.K., and Baek, K.H., 2014, Green nanobiotechnology: Factors affecting synthesis and characterization techniques, *J. Nanomater.*, 2014, 417305.
- [23] Kalaivani, R., Maruthupandy, M., Muneeswaran, T., Hameedha Beevi, A., Anand, M., Ramakritinan, C.M., and Kumaraguru, A.K., 2018, Synthesis of chitosan mediated silver nanoparticles (AgNPs) for potential antimicrobial applications, *Front. Lab. Med.*, 2 (1), 30–35.
- [24] Maguire, C.M., Rösslein, M., Wick, P., and Prina-Mello, A., 2018, Characterisation of particles in solution – A perspective on light scattering and comparative technologies, *Sci. Technol. Adv. Mater.*, 19 (1), 732–745.
- [25] Danaei, M., Dehghankhold, M., Ataei, S., Davarani, F.H., Javanmard, R., Dokhani, A., Khorasani, S., and Mozafari, M.R., 2018, Impact of particle size and polydispersity index on the clinical applications of lipidic nanocarrier systems, *Pharmaceutics*, 10 (2), 57.
- [26] Regiel, A., Irusta, S., Kyzioł, A., Arruebo, M., and Santamaria, J., 2013, Preparation and characterization of chitosan-silver nanocomposite films and their antibacterial activity against *Staphylococcus aureus*, *Nanotechnology*, 24, 015101.
- [27] Marambio-Jones, C., and Hoek, E.M.V., 2010, A review of the antibacterial effects of silver nanomaterials and potential implications for human health and the environment, *J. Nanopart. Res.*, 12 (5), 1531–1551.

Synthesis, Characterization and Breast Anti-cancer Activity of Iron(II), Cobalt(II), Nickel(II), and Copper(II) Complexes with a Hexadentate Schiff Base Ligand Derived from 2,5-Dihydroxy-1,4-benzoquinone with 5-Amino-2-methylphenol

Riyam Baqer Ibrahim and Suad Taha Saad*

Department of Chemistry, College of Science for Women, University of Babylon, Hilla 51002, Iraq

* **Corresponding author:**

email: wsci.suaad.taha@uobabylon.edu.iq

Received: June 12, 2023

Accepted: July 5, 2023

DOI: 10.22146/ijc.85611

Abstract: The complexes of Fe(II), Co(II), Ni(II), and Cu(II) Schiff base ligand derived from 2,5-dihydroxy-1,4-benzoquinone and 5-amino-2-methylphenol were synthesized. The ligand was synthesized by the reaction between the mentioned ketone and amine in 1:2 molar ratio, respectively. The four metal complexes were synthesized by refluxing the ligand with the related metal(II) chloride salts. The synthesized compounds were characterized using FTIR spectroscopy, UV-visible, ¹H-NMR, conductivity, atomic absorption, magnetic susceptibility, and thermogravimetric analysis. According to the results, the chelation between metals and ligand occurs with the imine groups and the deprotonated hydroxyl groups of 2,5-dihydroxy-1,4-benzoquinone and 5-amino-2-methylphenol in the ligand. The conductivity test of the four complexes shows the non-electrolytic nature of them. The magnetic susceptibility values of Fe(II), Co(II), Ni(II), and Cu(II) complexes are 4.20, 4.11, 2.97, and 2.34 B.M, respectively. The thermogravimetric and atomic absorption analyses suggest the general chemical formula for the complexes is [M₂(L)(H₂O)₆]. In addition, the ligand and one of its metal complexes (Co(II) complex) were examined against breast cancer cells, and they gave the IC₅₀ of 101.24 and 129.2 µg/mL, respectively. This result suggests that Co(II) complex is a better anti-cancer agent in comparison with the ligand.

Keywords: metal complexes; Schiff base; 2,5-dihydroxy-1,4-benzoquinone; 5-amino-2-methylphenol

■ INTRODUCTION

The German scientist Hugo Schiff gave the term "Schiff base" to a compound with the functional group –HC=N– where the nitrogen atom is attached to the organic structure instead of the hydrogen [1-2]. This group can be obtained by the reaction between amine with carbonyl compounds [3-4]. By this reaction, the carbonyl group in the ketone or the aldehyde is replaced by the imine group [5]. Many studies have revealed the considerable chemical and biological importance of the electron lone pair of nitrogen's imine group [6]. This group can be considered crucial for Schiff base exploitation in biology and various branches of chemistry and reactions [7-9]. For example, in the coordination chemistry, Schiff bases have the ability to act as ligands and chelate with

metals through the nitrogen in the imine group and an adjacent donor atom such as nitrogen, sulfur, and oxygen [10-13]. Schiff bases are the most common and favorable ligands thanks to stabilizing metal ions in various oxidation states [14]. This stability is due to the presence of the basic donor nitrogen atom of the azomethine group. Furthermore, Schiff bases are designed and synthesized widely because of the attachment with metal ions in different manners, their stability, and their biological effects [15-16].

In this work, a Schiff base ligand was derived from 2,5-dihydroxy-1,4-benzoquinone and 5-amino-2-methylphenol. Various Fe(II), Co(II), Ni(II), and Cu(II) complexes with this Schiff base ligand were synthesized, characterized, and tested against breast cancer-affected cells.

■ EXPERIMENTAL SECTION

Materials

2,5-Dihydroxy-1,4-benzoquinone and 5-amino-2-methylphenol were purchased from Macklin biochemical. Metal(II) chlorides were supplied from Merck and C.D.H. ethanol, while hydrochloric acid was supplied from Thomas Baker for chemicals. All the chemicals were used with no further purification.

Instrumentation

The infrared spectra were recorded by Fourier transform infrared spectrophotometer (FTIR 8400S, Shimadzu). The UV-visible spectrum was measured by using a UV-visible spectrophotometer (Peak Instruments C-7200) from Shimadzu. Bruker spectrometer instruments operating at 400 MHz were used to measure ¹H-NMR spectra. The metal content in all complexes was measured using Nova 350 spectrophotometer. The compound's decomposition was measured using the differential thermal gravimeter (DTG-160-FC-60A). Complexes conductivity was recorded by WTW SERIES, cond 722. The Sherwood Scientific auto balance magnetic susceptibility balance was used to measure magnetic susceptibility. Melting points were measured by melting point/SMP30 Stuart device.

Procedure

Synthesis of Schiff base ligand (L)

The 2,5-dihydroxy-1,4-benzoquinone (1 g, 7.138 mmol) was mixed with 5-amino-2-methylphenol (1.758 g, 14.276 mmol) in ethanol (25 mL) as a reaction solvent. Hydrochloric acid (3 drops) was added and the mixture was refluxed for 6 h. The brown precipitate of the Schiff base ligand was filtrated, washed with water and ethanol, and then recrystallized from ethanol.

Synthesis of Fe(II), Co(II), Ni(II) and Cu(II) complexes

The four metal complexes were synthesized by dissolving the prepared ligand (0.5 g, 0.95 mmol) in ethanol (20 mL). This solution was mixed with the corresponding hydrated metal(II) chloride salts in 1:2 ligand:metal ratio. The reaction mixture was left to reflux for 12 h. Brown complexes precipitates were filtered and washed with water and ethanol.

Anti-cancer study

The human breast cancer cell line (MCF-7) and the non-malignant breast epithelial cells (MCF10A) were supplied by the National Cell Bank of Iran (Pasteur Institute, Iran). The growth of these cells was carried out in Roswell Park Memorial Institute medium and Dulbecco's Modified Eagle Medium/Nutrient Mixture F-12 with 10% of fetal bovine serum and 100 U/mL penicillin and 100 µg/mL streptomycin. Cells were kept at 37 °C with humid air (5% CO₂) and treated with trypsin/EDTA and phosphate buffer saline solution. The growth process was 3D colonies and a monolayer cell culture.

The cell viability was detected by [3-(4,5-dimethylthiazol-2-yl)-2,5-diphenyltetrazolium bromide. The cells were cultured and digested with trypsin adjusted to a density of 1.4×10^4 cells/well and seeded to 96-well plates filled with 200 µL fresh medium per well for 24 h. Then, these cells were treated with the ligand and Co(II) complex in five concentrations (300–18 µg/mL). After 24 h the supernatant was separated and 200 µL/well of [3-(4,5-dimethylthiazol-2-yl)-2,5-diphenyltetrazolium bromide solution and 0.5 mg/mL of phosphate buffer saline were added. The incubation for the plate was carried out at 37 °C for an extra 4 h. The 3-(4,5-dimethylthiazol-2-yl)-2,5-diphenyltetrazolium bromide solution was then removed and added with DMSO (100 µL per well). The crystals were dissolved after the incubation of cells in a shaker at 37 °C. Cell viability was quantified by measuring absorbance at 570 nm.

■ RESULTS AND DISCUSSION

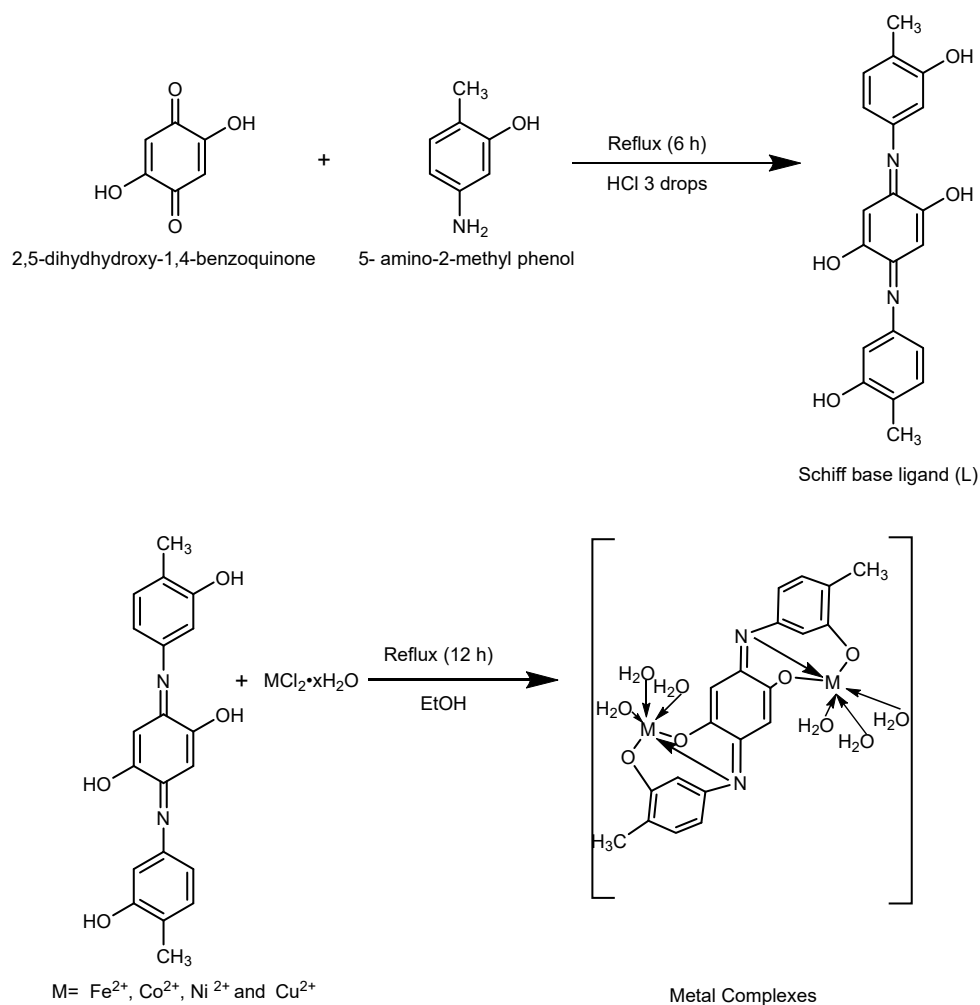
Ligand and Metal Complexes Synthesis

The typical procedure for making the Schiff base ligand involves the condensation of the ketone (2,5-dihydroxy-1,4-benzoquinone) and the amine (5-amino-2-methylphenol) in a 1:2 molar ratio, respectively. In this reaction, the two carbonyl groups in the 2,5-dihydroxy-1,4-benzoquinone structure will be replaced by the new imine groups. HCl was used as a catalyst to fasten the reaction time and ensure the complete conversion of the carbonyl groups to imine groups. The

created brown ligand was then used to form complexes with Fe(II), Co(II), Ni(II), and Cu(II) in also 1:2 (L:M) molar ratio. The use of this molar ratio ensures the coordination of two similar metal ions with the separated three coordination sites. Scheme 1 shows steps to ligand synthesis and its metal complexes, while Table 1 shows some properties of them.

¹H-NMR of the Ligand

¹H-NMR spectroscopy was used to determine the presence of protons in the Schiff base ligand using DMSO-*d*₆ as a solvent which can be detected at 2.50 ppm as a single signal. The main signals for the protons of L have been detected. Each -CH₃ and -OH proton signals emerged at about 1.0 and 9.5 ppm, respectively. Several



Scheme 1. Schiff base ligand synthesis with its Fe(II), Co(II), Ni(II), and Cu(II) complexes

Table 1. Some properties of the ligand and the metal complexes

Complexes and ligand	Color	Melting point (°C)	Molecular weight (g/mol)	Yield (%)	Metal content (%)	
					Theoretical value	Experimental value
Ligand	Brown	205–207	350.00	78	-	-
[Fe ₂ L(H ₂ O) ₆]	Brown	344	567.03	77	6.08	6.50
[Co ₂ L(H ₂ O) ₆]	Brown	284–286	572.20	52	6.30	6.80
[Ni ₂ L(H ₂ O) ₆]	Brown	233–235	571.72	75	6.30	7.20
[Cu ₂ L(H ₂ O) ₆]	Brown	293–295	585.44	44	6.60	7.30

signals between 6 and 9 ppm are related to the aromatic protons [17-20].

FTIR Spectra

The FTIR spectra (Fig. 1) of the ligand and the metal complexes show the characteristic bands that related to the significant groups in ligand structure and how they changed upon the complex formation. For example, the formation of the imine group was seen as a new band at 1570 cm^{-1} in the free ligand. The formation of this group was also supported by the absence of both bands of the amino group in 5-amino-2-methylphenol and the carbonyl group in 2,5-dihydroxy-1,4-benzoquinone which appeared at 3385 , 3319 , and 1647 cm^{-1} , respectively.

The $\nu(\text{O-H})$ stretching frequency was seen around 3387 and 3323 cm^{-1} as single bands in the free ligand spectra also. When the metal complexes formed, the characteristic bands were changed and shifted which confirmed the complexes' formation. The imine group frequency is shifted to higher frequencies of 1627 , 1600 , 1602 , and 1600 cm^{-1} in $[\text{Fe}_2\text{L}(\text{H}_2\text{O})_6]$, $[\text{Co}_2\text{L}(\text{H}_2\text{O})_6]$, $[\text{Ni}_2\text{L}(\text{H}_2\text{O})_6]$ and $[\text{Cu}_2\text{L}(\text{H}_2\text{O})_6]$, respectively. This shift confirms the metal coordination with the ligand imine groups. This linkage was also confirmed by the new bands in the range $559\text{--}599\text{ cm}^{-1}$ which refers to M-N bond in these metal complexes.

The hydroxyl groups at the phenyl ring in the ligand structure are deprotonated and coordinated with the metal ions through the free oxygen atoms. This was confirmed by the absence of hydroxyl group bands at 3387 and 3323 cm^{-1} . The FTIR spectra of the complexes also show broad bands in the region $3600\text{--}3200\text{ cm}^{-1}$, which refers to water molecules. The coordination with deprotonated hydroxyl groups and water molecules was confirmed by the appearance of new bands related to $\nu(\text{M-O})$ bonds in the range $518\text{--}545\text{ cm}^{-1}$ in the metal complexes. Table 2 gives a summary of the FTIR characteristic bands of all compounds.

Conductance Measurements and Magnetic Susceptibility

As a solvent, ethanol was used to test the conductivity of the produced complexes at a concentration of $1 \times 10^{-3}\text{ M}$. According to the results, all complexes are classified as non-electrolytes, as shown in Table 3 [21].

On the other hand, the magnetic susceptibility measurements were carried out at 298 K . It is obvious from the magnetic susceptibility values in Table 3. The Fe(II) complex is in a high spin electronic configuration and its μ_{eff} value (4.2 B.M) agrees with the presence of four unpaired electrons in d -orbitals and this also confirms

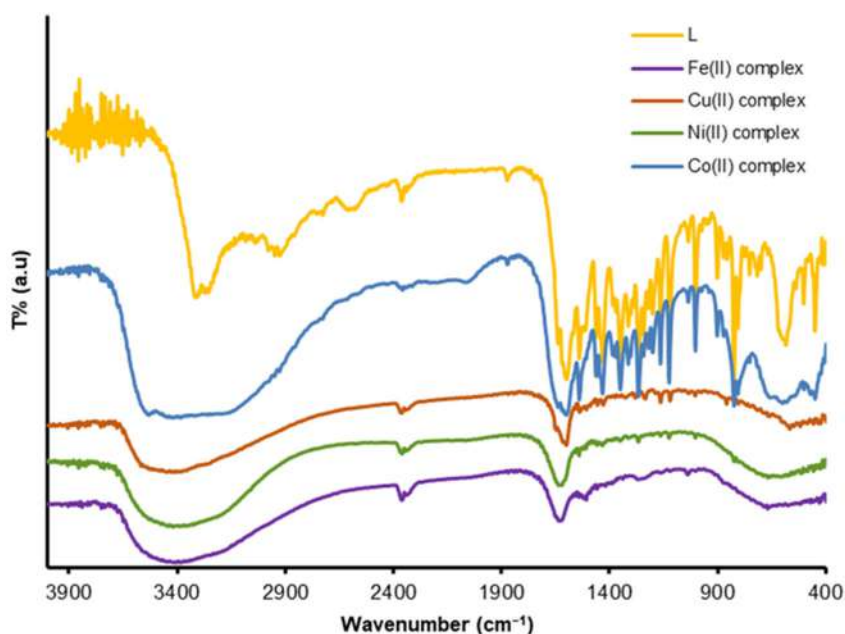


Fig 1. FT-IR spectra of L and the metal complexes

Table 2. A summary of the characteristic bands in the FTIR spectrum in cm^{-1} of L and metal complexes

Compound	$\nu(\text{H}_2\text{O})$	$\nu(\text{OH})$	$\nu(\text{C}=\text{N})$	$\nu(\text{M}-\text{N})$	$\nu(\text{M}-\text{O})$
Ligand	-	3387–3323	1570	-	-
$[\text{Fe}_2\text{L}(\text{H}_2\text{O})_6]$	3600–3200	-	1627	597	518
$[\text{Co}_2\text{L}(\text{H}_2\text{O})_6]$	3600–3200	-	1600	599	545
$[\text{Ni}_2\text{L}(\text{H}_2\text{O})_6]$	3600–3200	-	1602	559	522
$[\text{Cu}_2\text{L}(\text{H}_2\text{O})_6]$	3600–3200	-	1600	567	518

Table 3. The value of molar conductivity of metal complexes at 10^{-3} M concentration in ethanol

Compound	Molar conductivity ($\text{Ohm}^{-1} \text{cm}^2 \text{mol}^{-1}$)	μ_{eff} (B.M)	Suggested complex shape
$[\text{Fe}_2\text{L}(\text{H}_2\text{O})_6]$	7.70	4.20	Octahedral
$[\text{Co}_2\text{L}(\text{H}_2\text{O})_6]$	7.80	4.11	Octahedral
$[\text{Ni}_2\text{L}(\text{H}_2\text{O})_6]$	8.90	2.97	Octahedral
$[\text{Cu}_2\text{L}(\text{H}_2\text{O})_6]$	8.16	2.34	Octahedral

the octahedral shape of Fe(II) complex [22].

Co(II) complex is also paramagnetic with a magnetic susceptibility value of 4.11 B.M. Therefore, Co(II) is present with a high spin d^7 electronic configuration and this agrees with the three unpaired electrons in the d -orbitals of Co(II) and the octahedral shape [23-24].

Ni(II) complex has a μ_{eff} value (2.97 B.M), which shows that it has a paramagnetic property due to the two unpaired electrons in d -orbitals and its shape is also octahedral [25-26]. For the Cu(II) complex its μ_{eff} is 2.34 B.M also suggests the paramagnetic characteristics of this ion and agrees with the octahedral structure of the Cu(II) complex and the presence of one electron [8].

Electronic Spectra

The UV-vis spectra (Fig. 2) of the ligand and the metal complexes were recorded in ethanol in the range 200–1000 nm. Table 4. shows the UV-Vis. peaks and the related transitions. The ligand spectra show three peaks at 344, 421, and 594 nm, which are related to $\pi \rightarrow \pi^*$ and $n \rightarrow \pi^*$, respectively. These peaks were shifted when the metal complexes are formed, which suggests the M-L coordination and the MLCT [27]. In Fe(II) complex, peaks appear at 365, 438, and 573 nm. In $[\text{Co}_2\text{L}(\text{H}_2\text{O})_6]$, peaks are shifted to 369, 411, and 578 nm. For $[\text{Ni}_2\text{L}(\text{H}_2\text{O})_6]$, they are also shifted to 367, 436, and 562 nm. While a broad peak at 389 nm is assigned to two

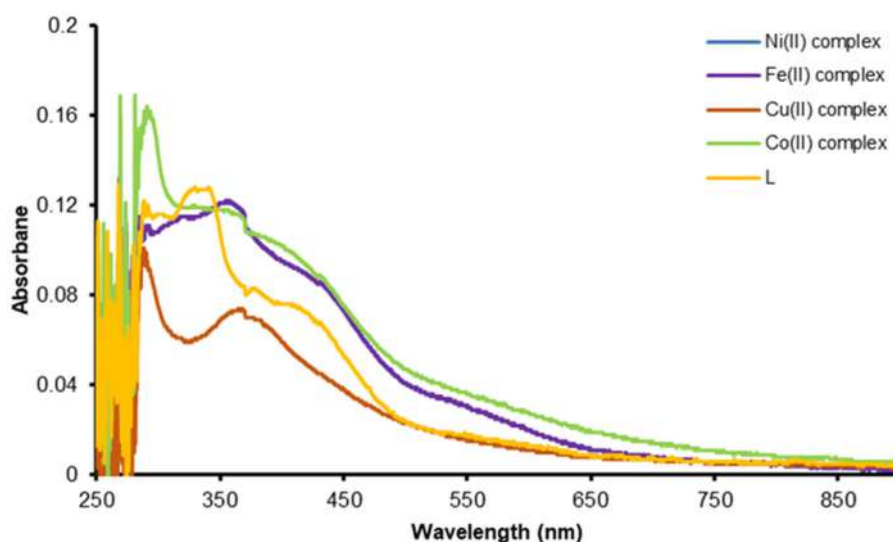
**Fig 2.** UV-vis spectra of L and the metal complexes

Table 4. Transition types in the UV-Vis spectra with their λ_{\max} for the ligand and the metal complexes

Compound	λ_{\max} (nm)	Type of transition
Ligand	344, 421, 594	$\pi \rightarrow \pi^*$, $n \rightarrow \pi^*$
[Fe ₂ L(H ₂ O) ₆]	365, 438, 573	MLCT
[Co ₂ L(H ₂ O) ₆]	369, 411, 578	MLCT
[Ni ₂ L(H ₂ O) ₆]	367, 436, 562	MLCT
[Cu ₂ L(H ₂ O) ₆]	290, 389	intraligand transition ${}^2B_{1g} \rightarrow {}^2E_g$ ${}^2B_{1g} \rightarrow {}^2A_{1g}$

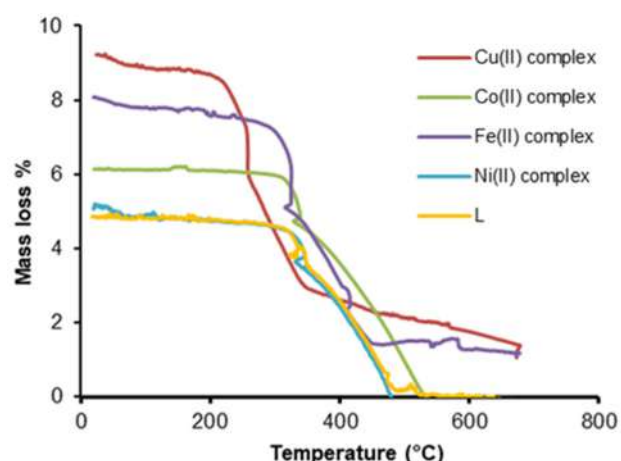
transitions ${}^2B_{1g} \rightarrow {}^2E_g$ and ${}^2B_{1g} \rightarrow {}^2A_{1g}$, respectively, in [Cu₂L(H₂O)₆], and that at 290 nm related to intraligand transition.

Thermal Analysis

Fig. 3 shows the thermal analysis curves for the ligand and the four metal complexes. This analysis was carried out under air with a temperature range 0–800 °C. Table 5 gives a summary of the decomposition temperature range and the mass loss and the proposed formed fragments from all the studied compounds. The ligand decomposed in two steps in the temperature range 27.77–429.57 °C. The first step starts at 27.77–331.88 °C includes the loss of the –OH and –CH₃ groups. At the same time, the second step shows the loss of C=N, –OH, –CH₃, and –C₅H₆ at 331.88–429.57 °C.

Fe(II) complex decomposition curve shows three steps of decomposition. The first one shows the loss of 2H₂O in 6.86% loss percentage in the temperature range

34.94–258.46 °C. The second step includes the loss of 4H₂O, 4O and 2CH₃ in the temperature range 258.46–330.07 °C. While the third step shows the loss of 2C₅H₆ and C=N in the temperature range 330.07–420.20 °C. The decomposition of the cobalt complex shows two steps of decomposition in the temperature range 40.68–572.17 °C. The first step shows the loss of 3H₂O, 4O and CH₃ in the temperature range 40.68–383.31 °C with a mass loss of 25.5%, while the second shows the loss of C=N, 3H₂O, 12H, 2C₆H₅ at 383.31–487.57 °C with a loss of 46.6%. The decomposition of [Ni₂L(H₂O)₆] complex also goes in two steps. The first one shows the loss of 3H₂O in the range 37.18–278.34 °C with a loss of 10.2%, while the second shows the loss of 3H₂O, 4OH, 2CH₃, 2(C=N), 6H and C₆H₅ at 278.34–412.07 °C with a loss of 44.0%.

**Fig 3.** TGA curve of Schiff base ligand and the complexes**Table 5.** Thermal analysis results for the ligand, [Fe₂L(H₂O)₆], [Co₂L(H₂O)₆], [Ni₂L(H₂O)₆], and [Cu₂L(H₂O)₆]

Compound	Steps of degradation	Decomposition temperature (°C)	Mass loss (%)	Type of lost species
Ligand	1	27.33-331.88	13.8%	CH ₃ , 2OH
	2	331.88-429.57	47.3%	C=N, OH, CH ₃ , C ₅ H ₆
[Fe ₂ L(H ₂ O) ₆]	1	34.94-258.48	6.86%	2H ₂ O
	2	258.48-330.07	31.3%	4H ₂ O, 4O, 2CH ₃
	3	330.07-420.20	35.0 %	2C ₅ H ₆ , C=N
[Co ₂ L(H ₂ O) ₆]	1	40.68-383.31	25.5%	3H ₂ O, 4O, CH ₃
	2	383.31-487.57	46.6%	C=N, 3H ₂ O, 12H, 2C ₆ H ₅
[Ni ₂ L(H ₂ O) ₆]	1	37.18-278.34	10.2%	3H ₂ O
	2	278.34-412.07	44.0%	3H ₂ O, 4OH, 2CH ₃ , 2C=N, 6H, C ₆ H ₅
[Cu ₂ L(H ₂ O) ₆]	1	43.49-237.65	13.3%	3H ₂ O
	2	237.65-261.27	19.5%	3H ₂ O, 2O, 2CH ₃
	3	261.27-332.47	27.5%	C ₅ H ₆ , C=N, 2O, 6H

Copper complex decomposition in the temperature range 43.49–332.47 °C in three steps. The beginning starts at 43.49–237.65 °C with the loss of 3H₂O and O in 13.3% loss percentage. The second occurs in the range 237.65–261.27 °C with the loss of 3H₂O, 2O, and 2CH₃ in 19.5% loss percentage, while the third occurs in the range 261.27–332.47 °C with the loss of C₆H₅, C=N, O₂, and 6H in 27.5% loss percentage.

Anti-cancer Activity

The anti-cancer activity of the ligand and its Co(II) complex was tested against MCF-7 and MCF10A with the concentration range 18.75–300 µg/mL. The results are shown in Table 6. and Fig. 4 and 5. According to the results [Co₂L(H₂O)₆] shows a high anti-cancer effect in comparison with the ligand with IC₅₀ values of 101.24 and 129.2 µg/mL, respectively. This shows the increase of

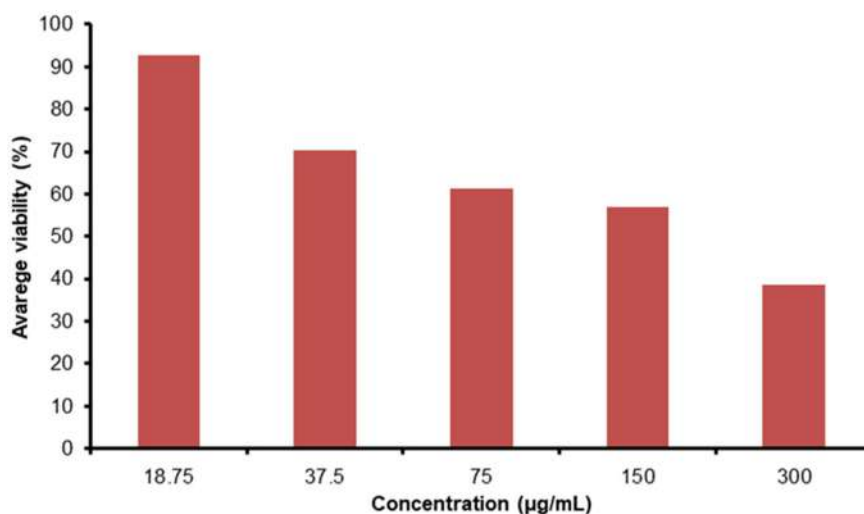


Fig 4. IC₅₀ for the ligand against a human breast cancer cell line

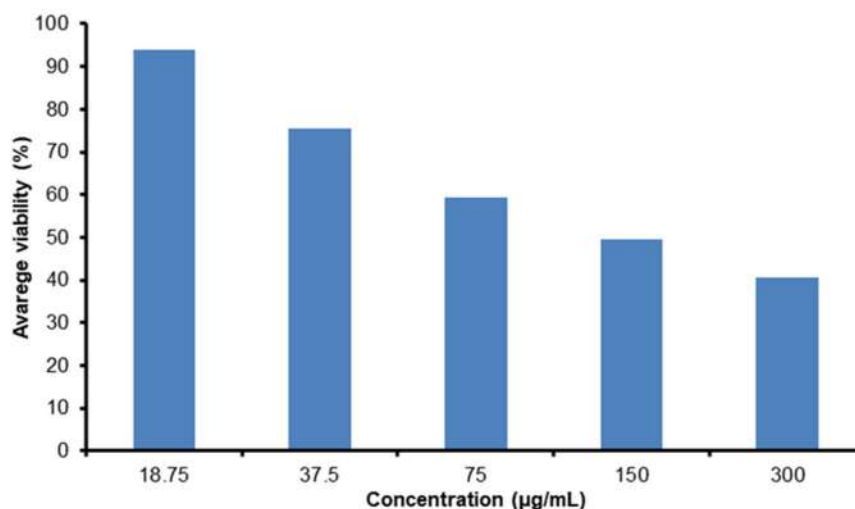


Fig 5. IC₅₀ for [Co₂L(H₂O)₆] against a human breast cancer cell

Table 6. The effect of complexes and ligand to healthy cell and infected cells

Compound	IC ₅₀ (µg/mL) healthy cell	IC ₅₀ (µg/mL) infected cell
Ligand	166.25	129.20
[Co ₂ L(H ₂ O) ₆]	153.39	101.24

the anti-cancer activity when the metal coordinates with the ligand. This activity can be attributed to the chelation theory. According to this theory, when the metal chelates with the ligand, its polarity will decrease due to the share of its positive charge with the electron-rich ligand. As a result, the lipophilicity of the metal and the resulting complex will increase and that leads to better penetration of the cell membrane, which consists of lipids [28-29].

■ CONCLUSION

The condensation reaction between 2,5-dihydroxy-1,4-benzoquinone and 5-amino-2-methylphenol in a 1:2 molar ratio produced a Schiff base ligand. By the ligand imine and phenol groups, it acts as a hexadentate ligand and coordinates with Fe(II), Co(II), Ni(II), and Cu(II). This coordination takes place with 1:2 molar ratio of ligand:metal. The produced compounds were characterized by FTIR, UV-vis, thermal analysis, conductivity, magnetic susceptibility, and atomic absorption. At the same time, the ligand was identified by ¹H-NMR and FTIR. All the complexes are non-electrolytes and the octahedral structure was suggested for them by the obtained results. The ligand and Co(II) complex were tested against breast cancer cells and the latest complex shows better anti-cancer activity with IC₅₀ values of 101.24 and 129.20 µg/mL for the ligand. This result encourages the test of the other prepared metal complexes against the same type of cancer cells or other types.

■ ACKNOWLEDGMENTS

The authors would like to thank the Department of Chemistry of the University of Babylon for providing all the support and facilities to complete this work.

■ REFERENCES

- [1] Catalano, A., Sinicropi, M.S., Iacopetta, D., Ceramella, J., Mariconda, A., Rosano, C., Scali, E., Saturnino, C., and Longo, P., 2021, A review on the advancements in the field of metal complexes with Schiff bases as antiproliferative agents, *Appl. Sci.*, 11 (13), 6027.
- [2] Otani, N., Fayeulle, A., Nakane, D., Léonard E., and Akitsu T., 2022, Synthesis, identification and antibacterial activities of amino acid Schiff base Cu(II) complexes with chlorinated aromatic moieties, *Appl. Microbiol.*, 2 (2), 438–448.
- [3] Mahmoud, W., Refaat, A.M., and Mohamed, G.G., 2020, Nano Schiff base and its metal complexes: Synthesis, characterization tools, biological applications and molecular docking studies, *Egypt. J. Chem.*, 63 (6), 2157–2176.
- [4] Rashad, A.A., Ibrahim, F.M., Ahmed, A., Salman, E.A., and Akram, E., 2020, Synthesis and photophysical study of divalent complexes of chelating Schiff base, *Baghdad J. Biochem. Appl. Biol. Sci.*, 1 (01), 5–17.
- [5] Adeleke, A.A., Zamisa, S.J., Islam, M.S., Olofinisan, K., Salau, V.F., Mocktar, C., and Omondi, B., 2021, Quinoline functionalized Schiff base silver(I) complexes: Interactions with biomolecules and *in vitro* cytotoxicity, antioxidant and antimicrobial activities, *Molecules*, 26 (5), 1205.
- [6] More, M.S., Joshi, P.G., Mishra, Y.K., and Khanna, P.K., 2019, Metal complexes driven from Schiff bases and semicarbazones for biomedical and allied applications: A review, *Mater. Today Chem.*, 14, 100195.
- [7] Sumrra, S.H., Anees, M., Asif, A., Zafar, M.N., Mahmood, K., Nazar, M.F., Khalid, M., Nadeem, M.A., and Khan, M.U., 2020, Synthesis, structural, spectral and biological evaluation of metals endowed 1,2,4-triazole, *Bull. Chem. Soc. Ethiop.*, 34 (2), 335–351.
- [8] Sunjuk, M., Al-Najjar, L., Shtaiwi, M., El-Eswed, B., Al-Noaimi, M., Al-Essa, L., and Sweidan, K., 2022, Transition metal complexes of Schiff base ligands prepared from reaction of aminobenzothiazole with benzaldehydes, *Inorganics*, 10 (4), 43.
- [9] İdil, Ö., Şahal, H., Canpolat, E., and Özkan, M., 2023, Synthesis, characterization, antimicrobial and time killing activities of new sulfa-derived Schiff bases coordinated with Cu(II), *Indones. J. Chem.*, 23 (3), 831–842.
- [10] Abd-Elzaher, M.M., Labib, A.A., Mousa, H.A., Moustafa, S.A., Ali, M.M., and El-Rashedy, A.A., 2016, Synthesis, anti-cancer activity and molecular docking study of Schiff base complexes containing

- thiazole moiety, *Beni-Suef Univ. J. Basic Appl. Sci.*, 5 (1), 85–96.
- [11] Abdelnabi, S., Bkhakh, C.K., and Kadhum, M.Y., 2017, Synthesis, spectroscopic characterization and biological study of some new Schiff bases based on 2-hydroxybenzadehyde, *J. Adv. Chem.*, 13 (2), 5995–6005.
- [12] Lupaşcu, G., Pahonţu, E., Shova, S., Bărbuceanu, S.F., Badea, M., Paraschivescu, C., Neamţu, J., Dinu, M., Ancuceanu, R.V., Drăgănescu D., and Dinu-Pîrvu, E.C., 2021, Co(II), Cu(II), Mn(II), Ni(II), Pd(II), and Pt(II) complexes of bidentate Schiff base ligand: Synthesis, crystal structure, and acute toxicity evaluation, *Appl. Organomet. Chem.*, 35 (4), e6149.
- [13] Raczuk, E., Dmochowska, B., Samaszko-Fiertek, J., and Madaj, J., 2022, Different Schiff bases—structure, importance and classification, *Molecules*, 27 (3), 787.
- [14] Sarker, D., Hossen, F.M., Zahan, M.K., Haque, M.M., Zamir, R., and Asraf, M.A., 2020, Synthesis, characterization, thermal analysis and antibacterial activity of Cu(II) and Ni(II) complexes with thiosemicarbazone derived from thiophene-2-aldehyde, *J. Mater. Sci. Res. Rev.*, 5 (2), 15–25.
- [15] Xu, P.Y., Wang, Y.T., Yu, Z.M., Li, Y.H., and Wang, S., 2021, New mononuclear Mn(III) complexes with hydroxyl-substituted hexadentate Schiff base ligands, *Magnetochemistry*, 7 (1), 12.
- [16] Abdalrazaq, E., Jbarah, A.A.Q., Al-Noor, T.H., Shinain, G.T., and Jawad, M.M., 2022, Synthesis, DFT calculations, DNA interaction, and antimicrobial studies of some mixed ligand complexes of oxalic acid and Schiff base trimethoprim with various metal ions, *Indones. J. Chem.*, 22 (5), 1348–1364.
- [17] Hayder Muneam, A.M., and Al-Amery, M.H.A., 2019, *In vitro* antioxidant activity of new Schiff base ligand and its metal ion complexes, *J. Pharm. Sci. Res.*, 11 (5), 2051–2061.
- [18] Kudelko, A., Olesiejuk, M., Luczynski, M., Swiatkowski, M., Sieranski, T., and Kruszynski, R., 2020, 1,3,4-Thiadiazole-containing azo dyes: Synthesis, spectroscopic properties and molecular structure, *Molecules*, 25 (12), 2822.
- [19] Aldelfy, Z., Al-Shamkani, Z., and Al-assadi, M., 2019, 2-Hydroxybenzylidene-4-(4-substituted phenyl)-2-amino thiazole and their Pt(II) complexes: Synthesis, characterization and biological study, *Egypt. J. Chem.*, 62 (10) 1851–1867.
- [20] Özdemir, Ö., 2020, Bis-azo-linkage Schiff bases—Part(II): Synthesis, characterization, photoluminescence and DPPH radical scavenging properties of their novel luminescent mononuclear Zn(II) complexes, *J. Photochem. Photobiol., A*, 392, 112356.
- [21] Hameed, G.F., Wadday, F.Y., Farhan, M.A., and Hussain, S.A., 2021, Synthesis, spectroscopic characterization and bactericidal valuation of some metal(II) complexes with new tridentate heterocyclic azo ligand type (NNO) donor, *Egypt. J. Chem.*, 64 (3), 1333–1345.
- [22] Ali, F.J., AL-Ameri, L.A.M., and Ali, A.M., 2021, Synthesis and identification and biological studies of new azo dyes derived from imidazole and their chelate complexes, *Indian J. Forensic Med. Toxicol.*, 15 (2), 1253–1260.
- [23] Ahmed, A.H., and Moustafa, M.G., 2020, Spectroscopic, morphology and electrical conductivity studies on Co(II), Ni(II), Cu(II) and Mn(II)-oxaloyldihydrazone complexes, *J. Saudi Chem. Soc.*, 24 (5), 381–392.
- [24] Jailani, A., 2020, Synthesis, characterisation and biological evaluation of tyramine derived Schiff base ligand and its transition metal(II) complexes, *Karbala Int. J. Mod. Sci.* 6, 225–234.
- [25] Özkınalı, S., Yavuz, S., Tosun, T., Ali Köse, D., Gür, M., and Kocaokutgen, H., 2020, Synthesis, spectroscopic and thermal analysis and investigation of dyeing properties of *o*-hydroxy Schiff bases and their metal complexes, *ChemistrySelect*, 5 (40), 12624–12634.
- [26] Uddin, M.N., Chowdhury, D.A., Rony, M.M., and Halim, M.E., 2014, Metal complexes of Schiff bases

- derived from 2-thiophenecarboxaldehyde and mono/diamine as the antibacterial agents, *Mod. Chem.*, 2 (2), 6–14.
- [27] Ali, A.A.M., and Alabidi, H.M., 2019, Synthesis and spectroscopic study of some transition metal complexes with 2-(4-iodo phenyl azo)-4,5-diphenyl imidazol, *J. Phys.: Conf. Ser.*, 1294 (5), 052021.
- [28] Fekri, R., Salehi, M., Asadi, A., and Kubicki, M., 2019, Synthesis, characterization, anti-cancer and antibacterial evaluation of Schiff base ligands derived from hydrazone and their transition metal complexes, *Inorg. Chim. Acta*, 484, 245–254.
- [29] Deghadi, R.G., Mahmoud, W.H., and Mohamed, G.G., 2020, Metal complexes of tetradentate azo-dye ligand derived from 4,4-oxydianiline: Preparation, structural investigation, biological evaluation and MOE studies, *Appl. Organomet. Chem.*, 34 (10), e5883.

Exploring the Predictive Value of Inflammatory Biomarkers in COVID-19 Patients: A Prospective Cohort Study in Malang, Indonesia

Agustin Iskandar^{1,2,3,4}, Hambiah Hari Oki^{2,4}, Catur Suci Sutrisnani^{2,4}, Novi Khila Firani^{2,4}, Nur Samsu^{4,5}, Agustina Tri Endharti^{3*}, and Edi Widjajanto^{2,4}

¹Doctoral Program in Medical Science, Faculty of Medicine, Universitas Brawijaya, Jl. Veteran, Malang 65145, Indonesia

²Department of Clinical Pathology, Faculty of Medicine, Universitas Brawijaya, Jl. Veteran, Malang 65145, Indonesia

³Department of Parasitology, Faculty of Medicine, Universitas Brawijaya, Jl. Veteran, Malang 65145, Indonesia

⁴Saiful Anwar General Hospital, Jl. Jaksa Agung Suprpto No. 2, Malang 65112, Indonesia

⁵Department of Internal Medicine, Faculty of Medicine, Universitas Brawijaya, Jl. Veteran, Malang 65145, Indonesia

* **Corresponding author:**

email: tinapermana.fk@ub.ac.id

Received: June 15, 2023

Accepted: July 12, 2023

DOI: 10.22146/ijc.85738

Abstract: The objective of this study was to assess the predictive value of inflammatory biomarkers in COVID-19 patients, namely the CRP/albumin ratio (CAR), interleukin 6 (IL-6), IL-6/lymphocyte ratio (IL-6/LY), and neutrophil/lymphocyte ratio (NLR). A prospective cohort study was conducted between January to June 2021 at Dr. Saiful Anwar General Hospital, Malang, East Java, Indonesia. CRP and albumin levels were measured using COBAS C6000. IL-6 was measured using the enzymatic chemiluminescence immunoassay (ECLIA) method and NLR was calculated based on flow cytometry evaluation of neutrophil and lymphocyte. Patient outcomes were obtained from medical records. Out of the 102 COVID-19 patients, 60 were non-survivors. The findings revealed that the area under the receiver (AUC) for CAR, IL-6, IL-6/LY, and NLR were 0.71, 0.77, 0.75, and 0.65, respectively. Kaplan-Meier curve analysis demonstrated significant differences between the groups stratified by these cut-off values. Notably, CAR and IL-6 exhibited the most accurate predictive values for mortality in COVID-19 patients. These findings suggest that CAR and IL-6 may serve as valuable biomarkers for predicting mortality in COVID-19 patients. Importantly, CAR offers an advantage over IL-6 as it is relatively more affordable, making it a viable option even if COVID-19 becomes endemic.

Keywords: CAR; IL-6; IL-6/LY; mortality; COVID-19

■ INTRODUCTION

The global healthcare system has faced unprecedented challenges over the past three years due to the COVID-19 pandemic caused by SARS-CoV-2 infection. The management of critically ill patients in intensive care settings poses significant difficulties in developing predictive models due to the unpredictable nature of COVID-19 outcomes, especially in developing countries such as Indonesia.

In Indonesia, the mortality rate among COVID-19 patients, especially those in critical condition, remains relatively high. According to the Indonesian Ministry of

Health, the country's COVID-19 patient mortality rate stands at 3.9%. According to this, Indonesia has the eighth-highest number of COVID-19 cases in Asia. Although severe COVID-19 cases have a higher death rate, there are currently no commonly used prognostic tools for estimating in-hospital mortality [1-2].

The inflammatory process is essential to the development of COVID-19. Cytokine storms or hyperinflammatory situations can be brought on by the immune system's activation of cytokines and chemokines, which can result in life-threatening organ malfunction and severe lung damage. Individual

differences in the degree of the inflammatory response lead to some patients' reactions being more pronounced than those of other patients. This emphasizes the value of individualized treatment plans that take into account each patient's particular immune response and inflammatory profile. Furthermore, gaining a deeper understanding of the inflammatory mechanisms involved in COVID-19 can facilitate the development of novel therapies that specifically target these processes. This holds the potential for more effective treatments and improved outcomes for patients [3-4].

One of the pro-inflammatory cytokines that exhibit an increase in COVID-19 patients is IL-6. Previous research has demonstrated a significant disparity in IL-6 levels between patients receiving intensive care treatment and those receiving standard care [3]. This elevation of IL-6 stimulates the production of acute-phase reactants, including CRP, by hepatocytes. CRP, as an acute phase reactant, plays a crucial role in the complement system and phagocytosis during the body's immune response to pathogenic infections. Numerous studies have indicated elevated CRP levels in patients with severe pneumonia, showing a correlation with the extent of inflammation. Conversely, inflammatory conditions lead to a reduction in albumin levels, which correlates with the deterioration of symptoms in COVID-19 patients [5]. The adaptive immune response also contributes to the SARS-CoV-2 infection. Severe cases of COVID-19 commonly exhibit a decline in lymphocyte count, particularly in the CD8+ subset [6-7]. Additionally, an upsurge in neutrophil count in COVID-19 patients is often associated with bacterial or fungal infections, frequently observed in these patients [8-10]. The utilization of inflammatory marker parameters, such as CAR, IL-6, IL-6/LY, and NLR, is expected to assist in the management of COVID-19 patients, given the pivotal role of the inflammatory process in their disease progression.

■ EXPERIMENTAL SECTION

Materials

In this study, various materials were utilized for different purposes. Samples from the naso- and oropharynx were collected to confirm the diagnosis of

COVID-19 in patients. Serum from peripheral blood was used to measure CRP, albumin, and IL-6 levels. Additionally, plasma EDTA samples were obtained to measure the counts of neutrophils and lymphocytes.

Instrumentation

Several instrumental methods were employed for different measurements. The Sysmex XN-1000 series was utilized to measure neutrophil and lymphocyte counts. The COBAS Chemistry system was used to measure CRP and albumin levels. Additionally, the Elecsys series, specifically the ECLIA, was employed to measure IL-6 levels. Furthermore, medical records were also utilized in the study to determine the outcomes of the patients.

Procedure

The procedures can be divided into several steps. Firstly, the study obtained approval (Approval No. 400/011/K.3/302/2021) from the Saiful Anwar General Hospital's ethics committee, ensuring ethical conduct. All participants in the study provided informed consent and met the requirements of the Declaration of Helsinki. The minimum age requirement for participants was 20 years. It took place from January to June 2021. Patients with a history of cancer, liver illness, hemostatic dysfunction, autoimmune diseases, or heart failure were excluded.

The diagnosis of COVID-19 was confirmed using the RT-PCR method. Following the patients' discharge from the hospital, their medical records were examined to determine their outcomes. On the first day of admission, peripheral blood samples were collected to measure CAR, IL-6, IL-6/LY, and NLR. Data analysis was performed using IBM SPSS Statistics 26. Initially, independent t-tests and chi-square tests were conducted to examine the characteristics of the study subjects. Receiver operating characteristic (ROC) analysis was then carried out to determine the area under the curve (AUC) and the cut-off for each variable. Additionally, a survival analysis utilizing Kaplan-Meier curves and Hazard Ratio (HR) was employed to create a predictive model for COVID-19 patients.

■ RESULTS AND DISCUSSION

Since COVID-19 was deemed a global public health emergency three years ago, it has posed ongoing difficulties for patient care. Numerous reasons, including the introduction of novel viral variations that contribute to recurrent waves of infection, can be blamed for these ongoing medical issues. In addition, the clinical course of the illness is highly unpredictable and challenging to predict, particularly in critically ill individuals. Hyperinflammation is the fundamental pathogenic process causing SARS-CoV-2 infection to progress to severe symptoms, such as acute respiratory distress syndrome, multiple organ failure, and lethal consequences [11]. A total of 102 COVID-19 patients were included in this study, with 39 subjects (38.23%) were female and 63 subjects (61.76%) were male. The mean age of the patients was 57.51 ± 14.05 years. Data collection was completed at the end of the study period.

Based on Table 1, the p-value for CAR, IL-6, IL-6/LY, and NLR, which were examined in this study, was found to be < 0.05 , indicating a significant difference in the median value between the survivor and non-survivor groups. However, no statistically significant differences were found in the parameters of sex, age, albumin, and lymphocyte count.

The development of a panel of standard laboratory tests is essential for patient risk assessment, optimum

clinical care, and the effective use of medical resources. In this study, we sought to determine the prognostic value of inflammatory biomarkers in predicting COVID-19 patients' in-hospital mortality. Inflammatory markers such as CAR, IL-6, the IL-6/LY ratio, and NLR have the potential to be used as predictors of in-hospital mortality for COVID-19 patients, according to our data. These results offer the foundation for the creation of a prognostic scoring system that can efficiently stratify the risk of COVID-19 patients who are critically ill.

Our study indicated that there was a substantial increase in CRP, CAR, IL-6, IL-6/LY, WBC, neutrophils, and NLR in the non-survivor group compared to the survivor group. This study was aligned with other studies that have also demonstrated higher levels of CRP, CAR, and IL-6 in severe COVID-19 cases and an association between increased CRP levels and disease severity or poor outcomes [10-11]. In addition, IL-6 was found to be a strong independent predictor of mortality in a retrospective examination of severely ill COVID-19 patients who were admitted to the intensive care unit (ICU). Similar to this, cohort research focusing on sick patients with SARS-CoV-2 infection showed that elevated baseline levels of both IL-6 and CRP were significantly related to illness progression and increased death within a 60-day window [9]. Therefore, it has been demonstrated that excessive CRP levels can predict the

Table 1. Demographic data of the subject

Variables	Survivors (n = 42)	Non-Survivors (n = 60)	p.s
Sex			
Male	24 (58.06%)	39 (65.00%)	
Female	18 (41.93%)	21(35.00%)	0.643 ^a
Age(year)*	54.29 ± 15.07	59.50 ± 13.15	0.105 ^b -
CRP (mg/dL) [#]	3.94 (2.19–7.45)	12.06 (7.94–18.41)	0.000 ^c -
Albumin (g/dL)*	3.50 ± 0.50	3.29 ± 0.54	0.078 ^b -
CAR [#]	1.50 (0.68–3.68)	4.29 (2.23–6.71)	0.001 ^c -
IL-6 (pg/mL) [#]	24.08 (14.25–80.12)	111.55 (52.03–269.23)	0.000 ^c -
Lymphocyte count (cells/mm ³) [#]	1210 (770–1680)	1040 (702.50–1382.50)	0.319 ^c -
IL-6/LY [#]	26.26 (9.59–71.6)	106.57 (41.85–292.11)	0.000 ^c -
Leukocyte count (cells/mm ³) [#]	8880 (6660–12250)	11640 (8025–18045)	0.021 ^c -
Neutrophil count (cell/mm ³) [#]	6360 (4190–10000)	9820 (5872.50–16165)	0.011 ^c -
NLR [#]	5.59 (3.02–9.94)	8.59 (4.81–16.76)	0.000 ^c -

*mean (\pm SD); [#]median (Q1-Q3)

severity and mortality of COVID-19, but low albumin levels are linked to higher mortality. It is possible to state that albumin levels in COVID-19 patients are predominantly affected by this fact, which is directly associated with the hyperinflammatory states that are frequently discovered in severe cases. Therefore, a CRP-to-albumin ratio might offer greater performance.

The optimal cut-off for each parameter (Table 2) was determined using ROC analysis (AUROC), with COVID-19 patient mortality being used as the comparison, where 0 represents survivors, and 1 represents non-survivors. Fig. 1 shows the area under the receiver operating characteristic curve (AUROC) for each variable. It is evident that IL-6 has the highest AUROC value in predicting mortality in COVID-19 patients, with a value of 0.77. Following IL-6, IL-6/LY, CAR, and NLR had AUROC values of 0.75, 0.71, and 0.65, respectively.

Fig. 2 shows the survival curves, indicating that individuals with elevated levels or ratios of the studied parameters exhibit lower survival rates compared to those with lower levels or ratios. After performing the logistic regression test, HR values of 7.706, 14.131, 0.807, and 1.926 were obtained for CAR, IL-6, IL-6/LY, and NLR, respectively.

In this study, ROC curve analysis showed IL-6 has the highest AUROC value in predicting death in COVID-19 patients, with a value of 0.77. Following IL-6, IL-6/LY, CAR, and NLR had AUROC values of 0.75, 0.71, and 0.65, respectively. These findings are comparable with those of a prior study, which also established the predictive usefulness of these inflammatory markers in COVID-19 patients. IL-6 shows a strong correlation and the greatest performance in predicting the severity and death of COVID-19 patients [12]. The study conducted by Zhou et al. [13] indicated that people who were seriously ill with COVID-19 had increased levels of IL-6. This conclusion

was similarly observed in a study by El-Shabrawy et al. [14], albeit with a different cut-off value of 32.3 pg/mL. Similarly, a different study with a lower cut-off value of 26.09 pg/mL revealed equivalent sensitivity. According to these findings, our study also found that people with severe and very severe COVID-19 cases had considerably higher IL-6 levels than those with mild to moderate instances [13-14].

In COVID-19 patients with severe disease, elevated IL-6 levels are frequently seen. This is related to a hyperinflammatory condition brought on by excessive synthesis of pro-inflammatory cytokines, such as IL-6. The IL-6 level in our investigation had a cut-off value of 47.5 pg/mL, showing potential as a predictor of mortality with a sensitivity of 80%, a PPV of 83.3%, and an AUROC value of 77.3% (95% CI: 66–88.6%; $p = 0.000$). A study by El-Shabrawy et al. [14] revealed a cut-off value of 32.3 pg/mL, and our results were in agreement with that study's findings. A level of IL-6 greater than 25 pg/mL is regarded as a risk factor for fatal illness. IL-6 levels could therefore be a potential indicator of serious

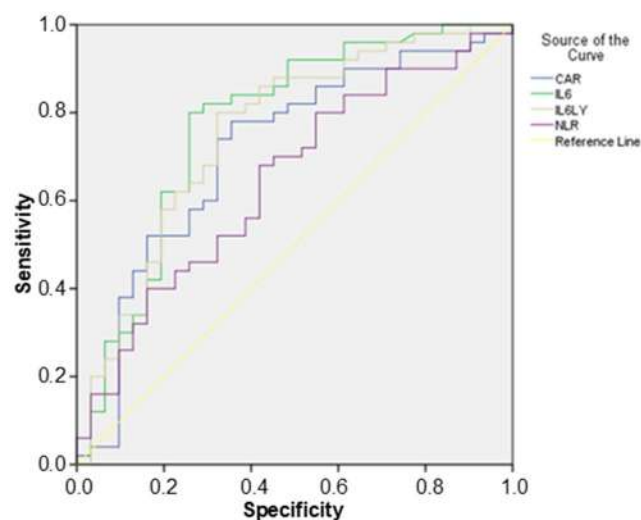


Fig 1. ROC Curve of CAR, IL-6, IL-6/LY, and NLR

Table 2. CAR, IL-6, IL-6/LY, NLR cut-off values and performance in determining mortality

Variables	Cut off	units	Sensitivity (%)	Specificity (%)	PPV (%)	NPV (%)	Accuracy (%)
CAR	2.70	ratio	74	67.7	78.7	61.8	71.6
IL-6	47.50	pg/mL	80	74.2	83.3	69.7	77.8
IL-6/LY	39.30	ratio	80	67.7	80.0	67.7	75.3
NLR	5.59	ratio	68	58.1	72.3	52.9	64.2

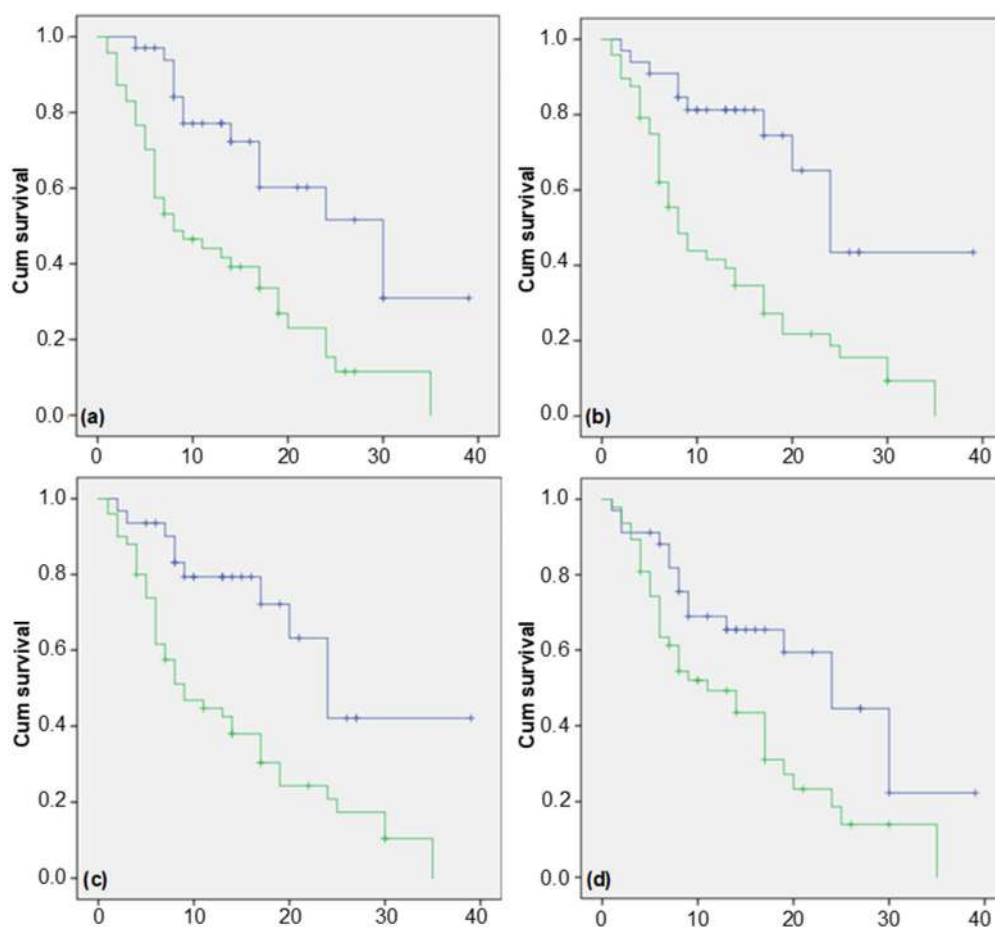


Fig 2. CAR, IL-6, IL-6/LY, and Kaplan-Meier curves NLR's blue line designates the group above the cut-off, and its green line designates the group below the cut-off

illness and mortality. Sabaka et al. [15] also included IL-6 value > 24 pg/mL to screen COVID-19 individuals at risk of worsening, particularly those requiring supplemental oxygen due to hypoxemia [14-15].

The predictive value of IL-6/LY in COVID-19 mortality is consistent with that of IL-6. IL-6/LY is a new marker used to predict worsening symptoms and mortality in COVID-19 patients [16]. The hyperinflammatory process associated with severe COVID-19 symptoms leads to an increase in inflammatory markers, including IL-6, and a decrease in lymphocyte count, particularly the T lymphocyte subset. The combination of these markers has been reported to have better clinical value in describing hyperinflammatory condition and immune system dysfunction [16-17]. In this study, the optimal cut-off value for IL-6/LY was 39.3, with an AUROC of 75.5%

(95% CI: 64.3–86.8%; $p = 0.000$) and a sensitivity and PPV of 80%. This value is higher than that reported in several other studies, possibly due to differences in the population of research subjects. For instance, a study limited to patients with severe COVID-19 treated in the ICU reported a cut-off value of 2.5 for IL-6/LY, whereas another study with a more heterogeneous population from asymptomatic to severe symptoms found a higher cut-off value of 19 [18-19].

This study indicated that NLR has the lowest predictive value for mortality compared to other markers. NLR has been frequently utilized to screen for systemic inflammatory illnesses such as ischemic heart disease and acute pancreatitis, and it has also been extensively investigated in COVID-19 as a predictor of severity and death [20]. High NLR values have been associated with greater severity of the disease. In this

study, the NLR cut-off value was determined to be 5.59, with an AUROC value of 64.6% (95% CI: 52.3–76.9%; $p = 0.028$) and a positive predictive value of 72.3%. A study by Bellan et al. [21], which discovered an NLR cut-off value of 4.68 as a predictor of death in COVID-19 patients [21], reported a similar value. Increased neutrophil counts or decreased lymphocyte counts can also contribute to increased NLR [22]. Neutrophils play several roles in the infection process, including the formation of NETs, which are known to be associated with hyperinflammatory conditions that can lead to a cytokine storm. However, an increase in neutrophils can also be caused by a bacterial infection. In contrast, the depletion of CD8+ T cells, which are frequently present in severe cases of COVID-19, is the key factor contributing to the decrease in the number of lymphocytes in COVID-19 [21-22]. The fact that data were only gathered once during the patient's initial hospital admission is one of the study's shortcomings. This restriction may have an impact on how well the mortality predictors function, particularly for the IL-6/LY and NLR parameters. Serial studies of these variables may offer a more thorough understanding of their functions in predicting patient outcomes because it is known that the levels of these inflammatory biomarkers fluctuate throughout the progression of COVID-19 disease.

The research findings have several implications for developing countries. First, CAR and IL-6 may be useful biomarkers for predicting mortality in COVID-19 patients in developing countries. This is important because developing countries often have limited access to sophisticated medical equipment and expertise. CAR and IL-6 are relatively simple and inexpensive biomarkers that can be measured using widely available assays.

CAR may be a more cost-effective option for predicting mortality in COVID-19 patients in these settings. Second, the findings suggest that CAR and IL-6 may be useful for identifying patients who are at high risk of mortality from COVID-19. This information could then be used to prioritize these patients for early treatment or admission to the ICU. This could help to improve their chances of survival.

■ CONCLUSION

Our study demonstrated that inflammatory biomarkers, such as CAR, IL-6, the IL-6/LY ratio, and NLR, were predictive of in-hospital mortality in COVID-19 patients. Following IL-6/LY, CAR, and NLR as the best predictors of mortality, IL-6 had the highest AUROC value. These findings imply that routine monitoring of these inflammatory biomarkers may help to better classify COVID-19 patients' risks, particularly for those with severe disease. CAR, which performs as well as IL-6, is relatively simple, inexpensive, and easy to measure. Therefore, it has the potential to serve as a promising biomarker for patient stratification, not only in COVID-19 but also in other hyperinflammatory diseases.

■ ACKNOWLEDGMENTS

The author would like to extend sincere thanks to the Dean of the Faculty of Medicine, Universitas Brawijaya, for partially providing funding through the Applied Research Grant with contract number of 2664/25/UN10.F08/PN/2022.

■ AUTHOR CONTRIBUTIONS

Agustin Iskandar contributed to the conceptualization of the study, methodology design, visualization of data, and writing of the original draft. Hambiah Hari Oki was involved in data collection, analysis of the data, and contributed to the review and editing of the manuscript. Catur Suci Sutrisnani played a role in methodology development, database management, and contributed to the review and editing of the manuscript. Novi Khila Firani contributed to the review and editing of the manuscript. Nur Samsu was responsible for data visualization, validation of results, and contributed to the review and editing of the manuscript. Agustina Tri E provided supervision throughout the study and contributed to the review and editing of the manuscript. Edi Widjajanto contributed to result validation, provided supervision, and contributed to the review and editing of the manuscript. All authors have made significant contributions to the article, have

reviewed and edited the manuscript, and have approved the final version for submission.

■ REFERENCES

- [1] WHO, 2021, *COVID-19 Weekly Epidemiological Update*, <https://covid19.who.int/>, accessed on March 20, 2023.
- [2] Indonesian Ministry of Health, 2023, *COVID-19 Distribution Map*, <https://covid19.go.id/peta-sebaran>, accessed on February 5, 2023.
- [3] Zeng, F., Huang, Y., Guo, Y., Yin, M., Chen, X., Xiao, L., and Deng, G., 2020, Association of inflammatory markers with the severity of COVID-19: A meta-analysis, *Int. J. Infect. Dis.*, 96, 467–474.
- [4] Mazzoni, A., Salvati, L., Maggi, L., Capone, M., Vanni, A., Spinicci, M., Mencarini, J., Caporale, R., Peruzzi, B., Antonelli, A., Trotta, M., Zammarchi, L., Ciani, L., Gori, L., Lazzeri, C., Matucci, A., Vultaggio, A., Rossi, O., Almerigogna, F., Parronchi, P., Fontanari, P., Lavorini, F., Peris, A., Rossolini, G.M., Bartoloni, A., Romagnani, S., Liotta, F., Annunziato, F., and Cosmi, L., 2020, Impaired immune cell cytotoxicity in severe COVID-19 is IL-6 dependent, *J. Clin. Invest.*, 130 (9), 4694–4703.
- [5] Wang, L., 2020, C-reactive protein levels in the early stage of COVID-19, *Med. Mal. Infect.*, 50 (4), 332–334.
- [6] Huang, W., Li, C., Wang, Z., Wang, H., Zhou, N., Jiang, J., Ni, L., Zhang, X.A., and Wang, D.W., 2020, Decreased serum albumin level indicates poor prognosis of COVID-19 patients: Hepatic injury analysis from 2,623 hospitalized cases, *Sci. China Life Sci.*, 63 (11), 1678–1687.
- [7] Soy, M., Keser, G., Atagündüz, P., Tabak, F., Atagündüz, I., and Kayhan, S., 2020, Cytokine storm in COVID-19: Pathogenesis and overview of anti-inflammatory agents used in treatment, *Clin. Rheumatol.*, 39 (7), 2085–2094.
- [8] Yuki, K., Fujiogi, M., and Koutsogiannaki, S., 2020, COVID-19 pathophysiology: A review, *Clin. Immunol.*, 215, 108427.
- [9] Borges, L., Pithon-Curi, T.C., Curi, R., and Hatanaka, E., 2020, COVID-19 and neutrophils: The relationship between hyperinflammation and neutrophil extracellular traps, *Mediators Inflammation*, 2020, 8829674.
- [10] Didangelos, A., 2020, COVID-19 hyperinflammation: What about neutrophils?, *mSphere*, 5 (3), e00367-20.
- [11] Rabaan, A.A., Al-Ahmed, S.H., Garout, M.A., Al-Qaaneh, A.M., Sule, A.A., Tirupathi, R., Mutair, A.A., Alhumaid, S., Hasan, A., Dhawan, M., Tiwari, R., Sharun, K., Mohapatra, R.K., Mitra, S., Emran, T.B., Bilal, M., Singh, R., Alyami, S., Moni, M.A., and Dhama, K., 2021, Diverse immunological factors influencing pathogenesis in patients with COVID-19: A review on viral dissemination, immunotherapeutic options to counter cytokine storm and inflammatory responses, *Pathogens*, 10 (5), 565.
- [12] Pál, K., Molnar, A.A., Huțanu, A., Szederjesi, J., Branea, I., Timár, Á., and Dobreanu, M., 2022, Inflammatory biomarkers associated with in-hospital mortality in critical COVID-19 patients, *Int. J. Mol. Sci.*, 23 (18), 10423.
- [13] Zhou, J., He, W., Liang, J., Wang, L., Yu, X., Bao, M., and Liu, H., 2021, Association of interleukin-6 levels with morbidity and mortality in patients with coronavirus disease 2019 (COVID-19), *Jpn. J. Infect. Dis.*, 74 (4), 293–298.
- [14] El-Shabrawy, M., Alsadik, M.E., El-Shafei, M., Abdelmoaty, A.A., Alazzouni, A.S., Esawy, M.M., and Shabana, M.A., 2021, Interleukin-6 and C-reactive protein/albumin ratio as predictors of COVID-19 severity and mortality, *Egypt. J. Bronchol.*, 15 (1), 5.
- [15] Sabaka, P., Koščálová, A., Straka, I., Hodosy, J., Lipták, R., Kmotorková, B., Kachlíková, M., and Kušnířová, A., 2021, Role of interleukin 6 as a predictive factor for a severe course of Covid-19: Retrospective data analysis of patients from a long-term care facility during Covid-19 outbreak, *BMC Infect. Dis.*, 21 (1), 308.
- [16] Liu, B., Li, M., Zhou, Z., Guan, X., and Xiang, Y., 2020, Can we use interleukin-6 (IL-6) blockade for coronavirus disease 2019 (COVID-19)-induced

- cytokine release syndrome (CRS)?, *J Autoimmun.*, 111, 102452.
- [17] Liu, X., Wang, H., Shi, S., and Xiao, J., 2022, Association between IL-6 and severe disease and mortality in COVID-19 disease: A systematic review and meta-analysis, *Postgrad. Med. J.*, 98 (1165), 871–879.
- [18] Masotti, L., Grifoni, E., Pelagalli, G., Cioni, E., Mattaliano, C., Cioffi, E., Mattaliano, C., Cioffi, E., Maggi, F., Pinto, G., Madonna, E.M., Micheletti, I., Gelli, A.M.G., Ciambotti, B., Mannucci, A., Bello, R., Cei, F., Dolenti, S., Tarquini, R., Montenora, I., Spina, R., and Vanni, S., 2022, Prognostic role of Interleukin-6/lymphocytes ratio in SARS-CoV2 related pneumonia, *Int. Immunopharmacol.*, 103, 108435.
- [19] Rotundo, S., Borelli, M., Scaglione, V., Lionello, R., Biamonte, F., Olivadese, V., Quirino, A., Morrone, H.L., Matera, G., Costanzo, F.S., Russo, A., Trecarichi, E.M., Torti, C., and IDTM UMG COVID-19 Group, 2023, Interleukin-6/lymphocyte as a proposed predictive index for COVID-19 patients treated with monoclonal antibodies, *Clin. Exp. Med.*, 1–7.
- [20] Palladino, M., 2021, Complete blood count alterations in COVID-19 patients: A narrative review, *Biochem. Med.*, 31 (3), 030501.
- [21] Bellan, M., Azzolina, D., Hayden, E., Gaidano, G., Pirisi, M., Acquaviva, A., Aimaretti, G., Aluffi Valletti, P., Angilletta, R., Arioli, R., Avanzi, G.C., Avino, G., Balbo, P.E., Baldon, G., Baorda, F., Barbero, E., Baricich, A., Barini, M., Barone-Adesi, F., Battistini, S., Beltrame, M., Bertoli, M., Bertolin, S., Bertolotti, M., Betti, M., Bobbio, F., Boffano, P., Bogliione, L., Borrè, S., Brucoli, M., Calzaducca, E., Cammarata, E., Cantaluppi, V., Cantello, R., Capponi, A., Carriero, A., Casciaro, G.F., Castello, L.M., Ceruti, F., Chichino, G., Chirico, E., Cisari, C., Cittone, M.G., Colombo, C., Comi, C., Croce, E., Daffara, T., Danna, P., Della Corte, F., De Vecchi, S., Dianzani, U., Di Benedetto, D., Esposto, E., Faggiano, F., Falaschi, Z., Ferrante, D., Ferrero, A., Gagliardi, I., Galbiati, A., Gallo, S., Garavelli, P.L., Gardino, C.A., Garzaro, M., Gastaldello, M.L., Gavelli, F., Gennari, A., Giacomini, G.M., Giacone, I., Gai Via, V., Giolitti, F., Gironi, L.C., Gramaglia, C., Grisafi, L., Inserra, I., Invernizzi, M., Krenghli, M., Labella, E., Landi, I.C., Landi, R., Leone, I., Lio, V., Lorenzini, L., Maconi, A., Malerba, M., Manfredi, G.F., Martelli, M., Marzari, L., Marzullo, P., Mennuni, M., Montabone, C., Morosini, U., Mussa, M., Nerici, I., Nuzzo, A., Olivieri, C., Padelli, S.A., Panella, M., Parisini, A., Paschè, A., Patrucco, F., Patti, G., Pau, A., Pedrinelli, A.R., Percivale, I., Ragazzoni, L., Re, R., Rigamonti, C., Rizzi, E., Rognoni, A., Roveta, A., Salamina, L., Santagostino, M., Saraceno, M., Savoia, P., Sciarra, M., Schimmenti, A., Scotti, L., Spinoni, E., Smirne, C., Tarantino, V., Tillio, P.A., Tonello, S., Vaschetto, R., Vassia, V., Zagaria, D., Zavattaro, E., Zeppegno, P., Zottarelli, F., and Sainaghi, P.P., 2021, Simple parameters from complete blood count predict in-hospital mortality in COVID-19, *Dis. Markers*, 2021, 8863053.
- [22] Tadesse, Z., Bekele Bayissa, A., Diriba, T., Chernet, N., Tsegaye, S., and Tsega, M., 2022, Neutrophil-to-lymphocyte ratio and cut-off values as predictor of severity and mortality in COVID-19 patients in millennium COVID-19 care center, Addis Ababa, Ethiopia, *Int. J. Gen. Med.*, 15, 6739–6755.

PLA/LLDPE/Organo-Precipitated Calcium Carbonate Composites Containing LLDPE-g-OA Compatibilizers: Mechanical, Physical, Thermal, and Morphology

Ahmad Hafizullah Ritonga^{1*}, Barita Aritonang¹, Gusliani Eka Putri², Khairiah Khairiah³, Enzo Wiranta Battra Siahaan⁴, and Debi Meilani¹

¹Institut Kesehatan Medistra Lubuk Pakam, Jl. Sudirman No. 38, Deli Serdang 20512, Indonesia

²Department of Medical Laboratory Technology, Sekolah Tinggi Ilmu Kesehatan Syedza Sainika, Jl. Prof. Dr. Hamka No. 228, Padang 25132, Indonesia

³Universitas Muslim Nusantara Al Washliyah, Jl. Garu IIA No. 93, Medan 20147, Indonesia

⁴Department of Mechanical Engineering, Universitas Darma Agung, Jl. Dr. Td. Pardede No. 21, Medan 20153, Indonesia

* **Corresponding author:**

email: ahmad.hafizullah.r@gmail.com

Received: July 16, 2023

Accepted: August 24, 2023

DOI: 10.22146/ijc.86983

Abstract: A plastic composite consisting of polylactic acid (PLA), linear low-density polyethylene (LLDPE), oleic acid-grafted linear low-density polyethylene (LLDPE-g-OA) compatibilizer, and organo-precipitated calcium carbonate (O-PCC) have been successfully made in the molten state. This study aims to characterize the mechanical, physical, thermal, and morphological characteristics of the PLA/LLDPE/O-PCC plastic composite in the presence of an LLDPE-g-OA compatibilizer. The plastic composite was prepared by blending PLA, LLDPE, LLDPE-g-OA, and O-PCC using an internal mixer with a heating of 160 °C and a rotation of 100 rpm. LLDPE and LLDPE-g-OA are put together into the inner mixer chamber until melted, followed by PLA and O-PCC. The most optimum plastic composite composition is PLA/LLDPE/LLDPE-g-g-OA/O-PCC (67.5:22.5:5:5). The mechanical properties showed an increase in tensile strength of 9.78 MPa. The physical properties showed that the minimum water absorption was 0.74%, the biodegradation in humus soil showed a degradation rate of 0.09% per day, and the thermal properties showed better stability with a melting point of 146.5 °C. The FTIR spectrum is similar to the polymer blend without O-PCC. The morphology indicates that the composite is compatible and homogeneous. This semi-biodegradable plastic composite has significant implications for reducing the accumulation of plastic waste in the environment.

Keywords: PLA; LLDPE; O-PCC; LLDPE-g-OA; composite

■ INTRODUCTION

Over the past decade, the demand for plastic has increased significantly, which has been widely applied to households, industry, electronics, food packaging, and various other sectors. Plastics that are quite popular for use by the public as food packaging are synthetic plastics such as Linear Low-Density Polyethylene (LLDPE). LLDPE is synthetic plastic obtained from non-renewable materials and difficult to degrade in the soil, which causes severe problems for the environment, such as the accumulation of plastic waste [1-3]. In addition, LLDPE

has poor compatibility with other materials with different polarities. Efforts made to reduce the impact of using LLDPE on the environment are utilizing natural materials to produce biodegradable plastics or combining thermoplastic polymer materials with biopolymers [4-5].

Biodegradable plastic such as polylactic acid (PLA) is an alternative to eco-friendly packaging because PLA is easily degraded naturally into CO₂ and water by microorganisms. PLA is a type of biopolymer made from renewable resources via a starch fermentation process

using lactic acid bacteria and chemical polymerization. PLA also has good biocompatibility with thermoplastic materials and can be fabricated. However, PLA also has weaknesses due to its brittle structure and high gas permeability [6-8]. The development of PLA is currently being carried out to produce better properties and compatibility by blending it with other materials.

Several studies on PLA/LLDPE blends have been performed, such as Engku Zawawi et al. [9] have blended PLA with LLDPE, showing that the two polymers are immiscible blends. Singh et al. [10] have prepared PLA/LLDPE blends with polyethylene-g-glycidyl methacrylate (PE-g-GMA) compatibilizers, in which LLDPE with a larger fraction has more prominent hardening characteristics. Bhasney et al. [11] have studied the influence of micro-cellulose fibers (MCC) of 5% on PLA/LLDPE blends, which resulted in relatively high crystallinity and decreased tensile strength values. The PLA/LLDPE blends are expected to produce semi-biodegradable plastic blends with good tensile mechanical properties, with most of the components of the plastic blends being degradable. However, the PLA/LLDPE blends will result in poor compatibility because the two have different polarities, which can be overcome by adding compatibilizers, such as LLDPE-g-oleic acid (LLDPE-g-OA). This LLDPE-g-OA compatibilizer was obtained from grafting OA monomer onto LLDPE in the presence of a BPO initiator via the molten state or solvent system. This compatibilizer is effectively used in LLDPE/Cyclic Natural Rubber (CNR) blends. LLDPE-g-OA is also believed to be effective in reducing the surface tension of the PLA/LLDPE blends, where the functional group of the OA monomer is compatible with the hydrophilic group of PLA from its carbonyl group. In contrast, the polymer part remains compatible with the LLDPE matrix of the C-H group, and it has also been applied to LLDPE/CNR blends [12]. Adding additives to polymer blends is required as fillers and co-compatibilizers, such as precipitated calcium carbonate (PCC). PCC is a natural material processing product that contains calcite with an amorphous crystal structure and low hardness. PCC has been widely used as a filler material in polymer composites. Modifying organic PCC

with oleic acid to form organo-PCC (O-PCC) effectively reduces the surface tension and increases the fit in the polymer matrix [13-17].

This study used O-PCC as filler in the PLA/LLDPE blends containing LLDPE-g-OA to improve the mechanical, physical, thermal, and morphological properties. The novelty of this research is a semi-biodegradable PLA/LLDPE composite containing hydrophobic modified PCC with oleic acid as filler and LLDPE-g-OA graft copolymer as compatibilizers. This study aims to prepare a semi-biodegradable PLA/LLDPE/O-PCC plastic composite in the presence of LLDPE-g-OA compatibilizer via the blending method using an internal mixer in the molten state and characterize its mechanical, physical, thermal, and morphological.

■ EXPERIMENTAL SECTION

Materials

The materials used in this study were polylactic acid (3052D) with a melt flow rate (MFR) of 14 g/10 min (210 °C/2.16 kg) and a density of 1.24 g/cm³ purchased from NatureWorks LLC, Minnesota, US. Linear low-density polyethylene (Asrene UF-1810MH) with MFR of 1.0 g/10 min (190 °C/2.16 kg) and density of 0.918 g/cm³ was purchased from Chandra Asri Petrochemical Company, Jakarta, Indonesia. Oleic acid with a density of 0.895 g/mL was obtained from HK Chemical Company, Bekasi, Indonesia. Precipitated calcium carbonate (Schaefer Precarb 100) with a density of 0.0027 g/cm³ was supplied by Schaefer Kalk, Kuala Lumpur, Malaysia. Benzoyl peroxide initiator, acetone, ethanol, methanol, and xylene were all chemical reagents obtained from Merck, Darmstadt, Germany.

Instrumentation

The PCC and O-PCC nanofillers were characterized using an XRF (PANalytical Epsilon-3). Tensile strength testing was determined using an Ultimate Testing Machine (GoTech AI-7000) at 10 mm/min speed with test specimens referring to ASTM D638-14 (type I). Thermal stability was characterized using TGA/DTA (Hitachi STA-7300) with a heating rate

of 10 °C/min. Functional groups were analyzed using an FTIR spectrometer (Agilent Cary 630) at wave numbers 650–4000 cm⁻¹. Morphology was characterized using a Scanning Electron Microscope (ZEISS EVO@MA10).

Procedure

Surface modification of precipitated calcium carbonate with oleic acid

The oleic acid (OA) of 9 mL was put into the beaker glass containing 300 mL of o-xylene, stirred, and PCC nanoparticles of 6 g were added while still stirring and heating at 50 °C for 2 h. The blends were separated by centrifugation at 15000 rpm for 15 min, washed with toluene four times repetitions to remove unreacted OA, and dried at room temperature for 24 h. The O-PCC sample was weighed and characterized using XRF [17-18].

Grafting of an oleic acid monomer onto LLDPE

LLDPE of 30 g was put into the internal mixer at a heating of 160 °C and a speed of 100 rpm for 5 min. Next, 5.0 mL of OA and 1.5 g of BPO initiator were added, and the blending process was allowed for 15 min. The sample was removed from the internal mixer, left for 15 min, and cut into small pieces. The LLDPE/OA sample was put into a bottom flask containing 200 mL xylene, refluxed at 180 °C, and stirred at 60 rpm until a solution formed. The solution was added with 80 mL of acetone to separate the unreacted OA and the OA homopolymer. The formed LLDPE-g-OA precipitate was filtered, washed with 150 mL of methanol (2 times repetitions), dried in an oven at 85 °C for 6 h, cooled, removed, and stored in a desiccator for 24 h. The LLDPE-g-OA sample was weighed and analyzed using FTIR [12,19-20].

Synthesize of PLA/LLDPE/Organo-PCC composites containing LLDPE-g-OA

The LLDPE and LLDPE-OA were slowly put into the internal mixer at a heating 160 °C with a speed of 100 rpm for 5 min. Next, PLA was added into the LLDPE/LLDPE-g-OA blends for 5 min. After that, O-PCC was added to the PLA/LLDPE/LLDPE-g-OA (PLC) blend according to the variation in Table 1. The blending process was left for 10 min. The polymer composite was removed from the internal mixer, left for 10 min, and cut into small pieces [17,21]. The obtained PLA/LLDPE/LLDPE-g-OA/O-PCC (PLCO) composite was weighed and characterized.

Water absorption test of polymer composites

This water absorption test was conducted on polymer blends and composites. The test sample was prepared in a size of 20 mm² with a thickness of 3 mm. The sample is cleaned, weighed, and called dry mass (Md). After that, the sample is soaked in water for 24 h, removed, cleaned, and weighed, called the wet mass (Mw). Next, the percentage of water absorption is calculated [22].

Biodegradable test of polymer composites

Samples were prepared in a size of 20 mm² with a thickness of 3 mm. The tested sample is cleaned, weighed, and called the initial mass (Mi). Next, the samples were planted using humus soil as deep as 10 cm from the soil surface and monitored regularly for 15, 30, 45, and 60 d. After that, the sample is cleaned, washed, dried, and weighed to a constant weight called the final mass (Mf). The results obtained measured the value of

Table 1. Composition of PLA/LLDPE/ LLDPE-g-OA/O-PCC composites

Sample code	PLA (wt.%)	LLDPE (wt.%)	LLDPE-g-OA (wt.%)	O-PCC (wt.%)
PLCO-0	70.0	25.0	5.0	-
PLCO-1	69.5	24.5	5.0	1.0
PLCO-2	69.0	24.0	5.0	2.0
PLCO-3	68.5	23.5	5.0	3.0
PLCO-4	68.0	23.0	5.0	4.0
PLCO-5	67.5	22.5	5.0	5.0
PLCO-6	67.0	22.0	5.0	6.0
PLCO-7	66.5	21.5	5.0	7.0
PLCO-8	66.0	21.0	5.0	8.0

weight loss percentage. This biodegradation test was conducted in a room with a humidity of 45–65% RH [22].

RESULTS AND DISCUSSION

X-ray Fluorescence

PCC and O-PCC fillers were characterized by XRF (Table 2). In the PCC sample, the concentration of elemental Ca was 98.1%, and CaO was 97.8%. It is suitable in prior work [23-24]. Meanwhile, in the O-PCC, the concentration of elemental Ca is 98.0%, and CaO is 97.5%. These results indicate that after PCC was modified with OA, the concentration of elemental Ca was decreased by 0.1% and CaO by 0.3%.

Mechanical Properties

The polymer composite's mechanical properties were analyzed via a tensile strength test on all variations of the polymer composite samples. The test results obtained tensile strength values, elongation at break, and Young's modulus, as shown in Fig. 1. The PLCO-1 to PLCO-8 samples showed increased tensile strength, elongation at break, and Young's modulus compared to the PLCO-0 sample (absence of O-PCC filler). The surface interaction between the polymers and the O-PCC has caused the polymer blends to be adsorbed on the O-PCC surface, which causes an increase in mechanical properties. The even dispersion of the O-PCC in polymer blends occurred because it has the same polarity, which affects the increase in tensile strength, elongation at break, and Young's modulus [25-26]. The increasing number of O-PCC filler components added to polymer composites impacts the mechanical properties of polymer composites. However, a certain amount can weaken the chemical bonds in polymer composites, causing a decrease in their mechanical properties because the elasticity of the polymer

blends is getting smaller. The optimal value for adding O-PCC to polymer composites is 5% by weight. The O-PCC filler evenly distributed in the polymer composite can also act as a co-compatibilizer because the mechanical properties of tensile strength, elongation at break, and Young's modulus increase significantly [17-18,27]. The increased elongation at break value after reaching the yield point indicates that the polymer composite is a hard and tough material [12]. Likewise, Young's modulus value increases with increasing tensile strength and elongation at break, indicating a strong bond between PLA and LLDPE in the presence of LLDPE-g-AO compatibilizer and O-PCC filler. The addition of the O-PCC concentration of above 5% will cause the elongation at break distance to decrease and reduce the bond strength, which means the optimum composition for variations of PLA/LLDPE/LLDPE-g-g-OA/O-PCC (67.5:22.5:5:5).

Physical Properties

The physical properties of polymer composites were determined by testing their water absorption. The water

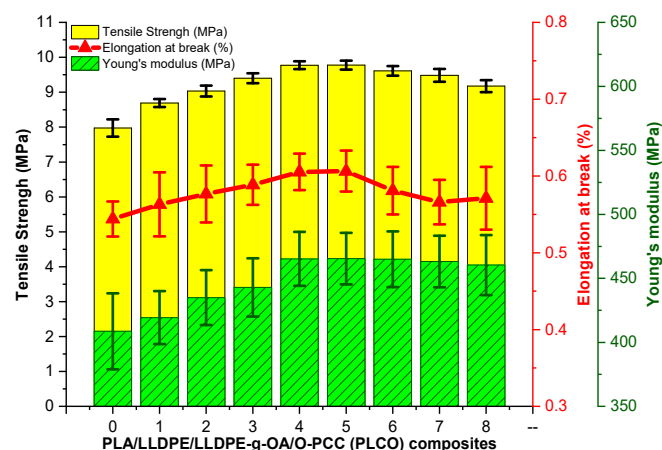


Fig 1. Tensile strength, elongation at break, and Young's modulus of polymer composites

Table 2. X-ray fluorescence of PCC and O-PCC

PCC				O-PCC			
Element	Conc (%)	Oxides	Conc (%)	Element	Conc (%)	Oxides	Conc (%)
Al	0.2	Al ₂ O ₃	0.4	Al	0.3	Al ₂ O ₃	0.4
P	0.4	P ₂ O ₅	0.8	P	0.5	P ₂ O ₅	1.1
Ca	98.1	CaO	97.8	Ca	98.0	CaO	97.5
Zn	0.5	ZnO	0.4	Zn	0.4	ZnO	0.3
Ag	0.7	Ag ₂ O	0.6	Ag	0.7	Ag ₂ O	0.6

absorption test aims to determine the ability limit of the polymer composite to absorb water up to a maximum limit for 24 h. The water absorption test result is presented in Fig. 2. The existence of O-PCC as fillers in the polymer composite dramatically influences the water absorption percentage. The more filler in the polymer composite, the higher the water absorption percentage was, indicating an interfacial bond between the polymer blends and the filler, which has been modified with oleic acid. This polymer composite has water-resistant physical properties, characterized by a decrease in the water absorption percentage as the number of fillers increases, the best variation being the PLCO-5 sample. However, when O-PCC is added again into the polymer composite, it causes an increase in the water absorption percentage. This condition can be caused by the uneven dispersion of the filler in the polymer composite or agglomeration [22,25]. In polymer composites with O-PCC concentrations above 5%, there is an increase in water absorption because O-PCC only acts as a filler and is no longer a co-compatible in the PLA and LLDPE mixture so that water is more easily absorbed in the polymer composite, besides the uneven dispersion of the O-PCC also can cause that.

Biodegradation

The biodegradation test of polymer composites was carried out in humus soil with a depth of 10 cm from the surface of the tested soil for 15, 30, 45, and 60 d. The biodegradation test results for this polymer composite are presented in Fig. 3. PLA, which is biodegradable and more dominant in these polymer composites, dramatically influences the degraded polymer material. The biodegradation test results indicated that O-PCC in polymer composites would increase the degradation percentage of the sample. The higher the degradation percentage, the more O-PCC fraction was added into the polymer composite. It is suitable with prior studies [11,28], where the presence of inorganic materials as fillers in polymer composites positively affects the degradation percentage. The PLCO-5 sample showed a significant increase in degradation percentage compared to samples PLCO-4, which means that the optimum value

for adding O-PCC is 5 wt.%. Whether the fraction of filler in the polymer composite is increased will certainly impact the decrease in its mechanical and physical properties [18]. In PLCO-5, the degradation percentage was 2.12% in 30 d, 3.24% in 45 d, and 5.54% in 60 d, with an average degradation rate of 0.092% per day for 60 d. The PLCO-6, PLCO-7, and PLCO-8, respectively, showed a non-significant increase in mass degradation rate per day of 0.093, 0.094, and 0.094%, and this means that the degradation process continues even though the duration of biodegradation time increases.

Thermal Analysis

Thermal analysis was performed to investigate the stability, degradation, and thermal properties using

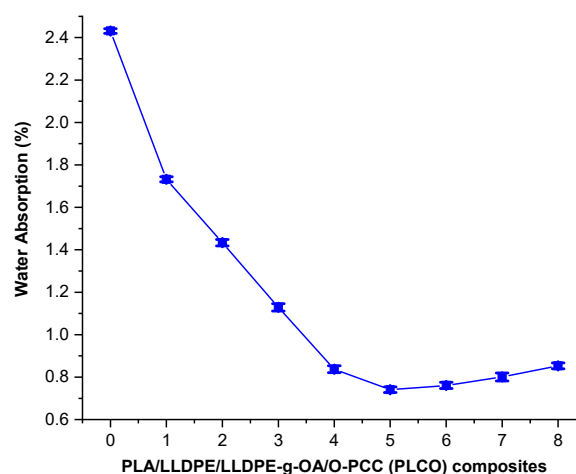


Fig 2. Water absorption of PLCO composites

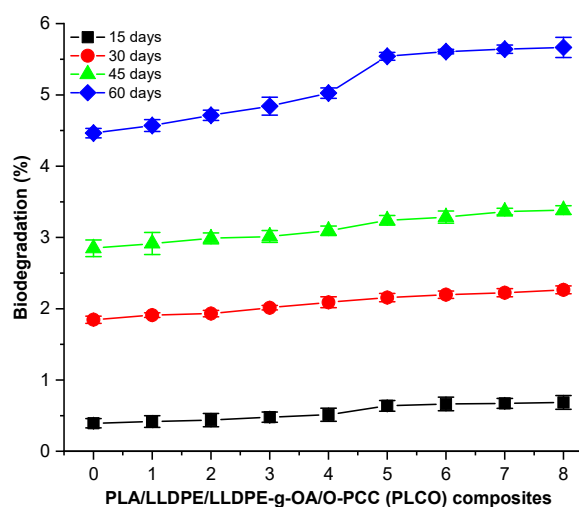


Fig 3. Biodegradation of PLCO composites

TGA-DTA on PLA/LLDPE (PL) blend (70:30), PLA/LLDPE/LLDPE-g-OA (PLC) blend (70:25:5), and PLA/LLDPE/LLDPE-g-OA/O-PCC (PLCO) composite (67.5:22.5:5:5). In the TGA and DTG curves (Fig. 4(a) and Fig. 4(b)), the mass degradation percentage of 1, 5, and 10%, and the maximum expressed as a function of temperature at $T_{1\%}$, $T_{5\%}$, $T_{10\%}$, and T_{max} . The existence of compatibilizers and fillers has increased the mass degradation temperature of the PLC blend and PLCO composite compared to the PL blend presented at $T_{1\%}$, $T_{5\%}$, and $T_{10\%}$. The O-PCC in the PLCO composite has significantly increased thermal stability. Meanwhile, the maximum mass degradation temperature (T_{max}) occurs twice in the PLC blend and PLCO composite, which means that the existence of PLA in the compatible blend or composite is degraded faster than LLDPE. The melting point and decomposition temperatures are expressed as T_m and T_d in the DTA curve (Fig. 4(c)) and Table 3. The PL blend shows T_m at 106.3 and 141.3 °C, while the PLC

blend and the PLCO composite have just one T_m . According to prior research, if the polymer blend has two T_m , it indicates that the polymer blend is incompatible. It demonstrates that the presence of compatibilizers and fillers has produced a compatible polymer blend or composite [21,29]. The PLC blend and PLCO composite are compatible but have two T_d , meaning the PLA has decomposed earlier than LLDPE. The presence of O-PCC filler can cause the T_d in PLCO to increase compared to PLC, which means that O-PCC also acts as a co-compatibilizer in the PLA/LLDPE blend.

FTIR Analysis

FTIR spectra of LLDPE-g-OA, LLDPE, PLA/LLDPE (PL) blend, PLA/LLDPE/LLDPE-g-OA (PLC) blend, PLA/LLDPE/LLDPE-g-OA/O-PCC (PLCO) composite, PLA, and O-PCC presented in Fig. 5. All samples analyzed resulted in a band at 2914.7–2847.6 cm^{-1} , indicating

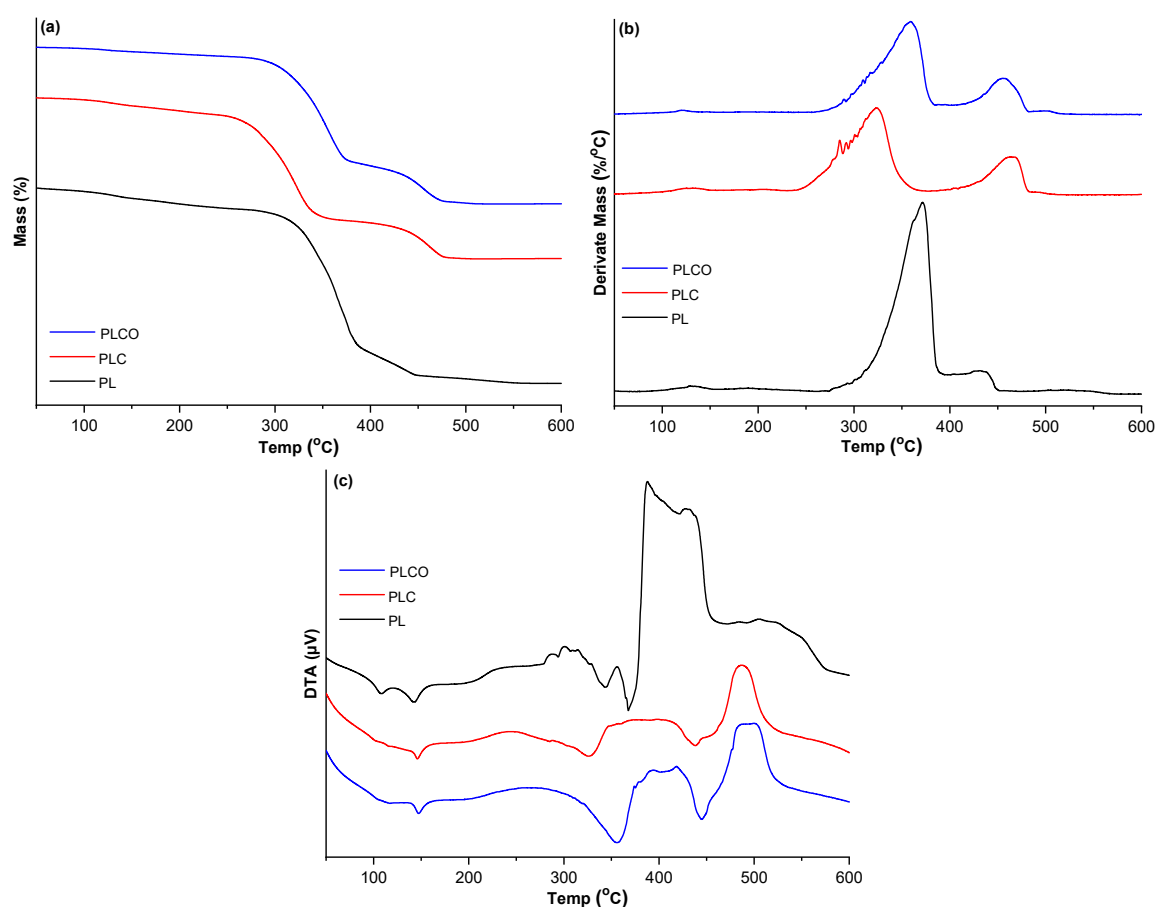


Fig 4. (a) TGA, (b) DTG, (c) DTA curves of PL, PLC, and PLCO

Table 3. Thermal analysis of PL, PLC, and PLCO

Sample	T _{1%} (°C)	T _{5%} (°C)	T _{10%} (°C)	T _{max} (°C)	T _m (°C)	T _d (°C)
PL	47.3	132.5	216.3	371.9	-	106.3
PLC	79.8	148.2	233.0	323.1	454.0	146.4
PLCO	92.9	209.5	294.8	359.2	462.7	146.5

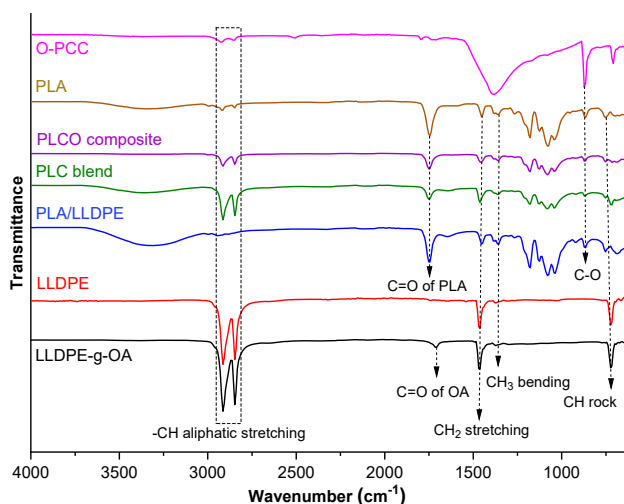


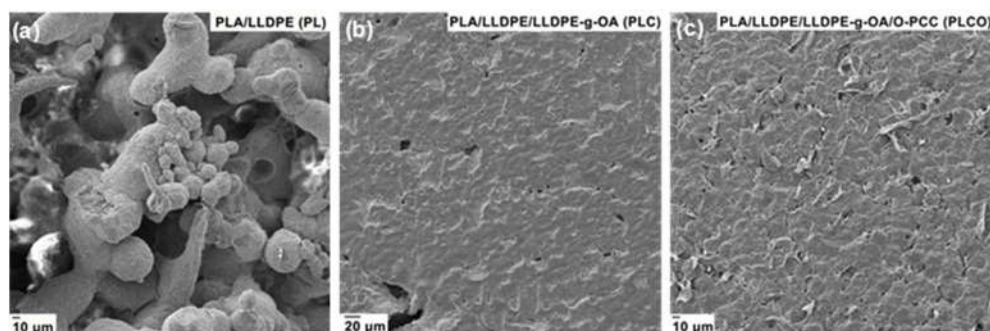
Fig 5. FTIR spectra of LLDPE-g-OA, LLDPE, PLA/LLDPE, PLA/LLDPE/LLDPE-g-OA (PLC) blend, PLA/LLDPE/LLDPE-g-OA/O-PCC (PLCO) composite, PLA, and O-PCC

saturated aliphatic hydrocarbon compounds. The PLA/LLDPE blend resulted in a small band in that area, which means that there is no bond between the two materials because what is visible is only the absorption band of PLA. The band at 1751.8 cm^{-1} indicates the presence of a carbonyl group from PLA, while the small band at 1707.1 cm^{-1} is a carbonyl group from oleic acid grafted onto LLDPE. The bands at 1461.1 and 1371.6 cm^{-1} indicate the presence of CH_2 and CH_3 vibrations. The band at 864.7 cm^{-1} shows the C–O vibration of PLA and

O-PCC. A band at 752.9 cm^{-1} in the fingerprint area indicates a C–H rock vibration. The PLC blend and the PLCO composite had almost identical spectra, indicating that the two samples had chemical bonds between PLA and LLDPE in the presence of LLDPE-g-OA compatibilizers. The filler in the polymer composite has also resulted in a difference in the intensity of each absorption band from the two samples [18,25].

Morphological Analysis

Morphological analysis of the PL blend, PLC blend, and PLCO composite (Fig. 6) was performed to observe the surface structure of the samples. The PL blend surface morphology (Fig. 6(a) and Fig. 6(d)) shows a surface structure of an incompatible blend, where the blending of PLA and LLDPE is not homogeneous and appears to form aggregations. This is due to the difference in polarity between the two polymeric materials. The surface morphology of the PLC blend (Fig. 6(b) and Fig. 6(c)) shows a surface structure of a compatible blend, where the blending of PLA and LLDPE is homogeneous, where PLA and LLDPE appear to merge to form a compatible blend after adding the LLDPE-g-OA compatibilizer. The PLC blend surface structure also appears smooth with tiny pores. The surface morphology of the PLCO composite (Fig. 6(c) and Fig. 6(f)) also shows a surface structure of a compatible O-PCC filler, which is evenly dispersed even though there



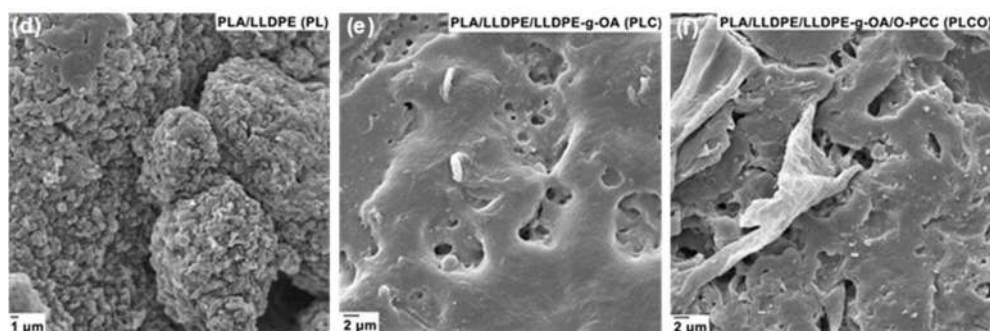


Fig 6. SEM micrographs of (a) PL, (b) PLC, (c) PLCO at 1000 \times magnification, and (d) PL, (e) PLC, (f) PLCO at 5000 \times magnification

are tiny pores formed in the composite. The presence of O-PCC in the composite functions as a filler and compatibilizer, making the composite more compatible with its constituent materials [17-18,30].

■ CONCLUSION

The semi-biodegradable PLA/LLDPE/O-PCC plastic composite in the presence of LLDPE-g-OA compatibilizer can be produced in a molten state at 160 °C using an internal mixer with the most optimum variation is PLA/LLDPE/LLDPE-g-g-OA/O-PCC (67.5:22.5:5:5). The mechanical properties of PLCO composites resulted in the most optimum tensile strength of 9.78 MPa, elongation at break of 0.61%, and Young's modulus of 465.48 MPa. The physical properties of PLCO composites resulted in a minimum water absorption of 0.74%. The biodegradation of PLCO composites in humus soil was 0.64% in 15 d, 2.12% in 30 d, 3.24% in 45 d, and 5.54% in 60 d, with a degradation rate of 0.09%/d, which is not significantly different from the variations above it. The thermal properties of PLCO composites resulted in better thermal stability than the PL and PLC blends, with a melting point temperature of 146.5 °C and a decomposition temperature of 444.1 °C. The FTIR spectrum of PLCO composites showed spectrum similarity with the PLC blend and had CaCO₃ characteristics at 864.7 and 1701.1 cm⁻¹, indicating the presence of O-PCC in the PLCO composite. The morphology of PLCO composites has resulted in a compatible, homogeneous surface structure with evenly dispersed O-PCC.

■ ACKNOWLEDGMENTS

The author would like to thank the DRPM of the Ministry of Education, Culture, Research and Technology of the Republic of Indonesia for funding this fundamental research in 2023 with the main research contract number 177/E5/PG.02.00.PL/2023, the first derivative research contract number: 047/LL1/AL.04.03/2023, and the second derivative research contract number: 01.AK/LPPM/INKES-MLP/VI/2023.

■ AUTHOR CONTRIBUTIONS

Ahmad Hafizullah Ritonga, Barita Aritonang, and Debi Meilani conducted the experiment. Ahmad Hafizullah Ritonga, Gusliani Eka Putri, and Khairiah conducted the calculations and analysis. Ahmad Hafizullah Ritonga wrote the manuscript. Ahmad Hafizullah Ritonga, Gusliani Eka Putri, and Enzo Wiranta Battra Siahaan revised the manuscript. All authors agreed to the final version of this manuscript.

■ REFERENCES

- [1] Zhao, X., Wang, Y., Chen, X., Yu, X., Li, W., Zhang, S., Meng, X., Zhao, Z.M., Dong, T., Anderson, A., Aiyedun, A., Li, Y., Webb, E., Wu, Z., Kunc, V., Ragauskas, A., Ozcan, S., and Zhu, H., 2023, Sustainable bioplastics derived from renewable natural resources for food packaging, *Matter*, 6 (1), 97–127.
- [2] Ahamed, A., Veksha, A., Giannis, A., and Lisak, G., 2021, Flexible packaging plastic waste – environmental implications, management

- solutions, and the way forward, *Curr. Opin. Chem. Eng.*, 32, 100684.
- [3] Kan, M., and Miller, S.A., 2022, Environmental impacts of plastic packaging of food products, *Resour. Conserv. Recycl.*, 180, 106156.
- [4] Alshabanat, M., 2019, Morphological, thermal, and biodegradation properties of LLDPE/treated date palm waste composite buried in a soil environment, *J. Saudi Chem. Soc.*, 23 (3), 355–364.
- [5] Jaiswal, P.B., Pushkar, B.K., Maikap, K., and Mahanwar, P.A., 2022, Abiotic aging assisted bio-oxidation and degradation of LLDPE/LDPE packaging polyethylene film by stimulated enrichment culture, *Polym. Degrad. Stab.*, 206, 110156.
- [6] Qin, Q., Yang, Y., Yang, C., Zhang, L., Yin, H., Yu, F., and Ma, J., 2022, Degradation and adsorption behavior of biodegradable plastic PLA under conventional weathering conditions, *Sci. Total Environ.*, 842, 156775.
- [7] Kalita, N.K., Sarmah, A., Bhasney, S.M., Kalamdhad, A., and Katiyar, V., 2021, Demonstrating an ideal compostable plastic using biodegradability kinetics of poly(lactic acid) (PLA) based green biocomposite films under aerobic composting conditions, *Environ. Challenges*, 3, 100030.
- [8] Andrade, M.S., Ishikawa, O.H., Costa, R.S., Seixas, M.V.S., Rodrigues, R.C.L.B., and Moura, E.A.B., 2022, development of sustainable food packaging material based on biodegradable polymer reinforced with cellulose nanocrystals, *Food Packag. Shelf Life*, 31, 100807.
- [9] Engku Zawawi, E.Z., Kamarun, D., Mohd Dahan, R., and Adzhar, N.H.M., 2018, Mechanical, morphological and thermal properties of linear low density polyethylene/poly(lactic acid) blends, *AIP Conf. Proc.*, 1985 (1), 30012.
- [10] Singh, S., Ghosh, A.K., Maiti, S.N., Gupta, R.K., and Bhattacharya, S., 2021, Rheological aspects and film processability of poly(lactic acid)/linear low-density polyethylene blends, *Polym. Eng. Sci.*, 61 (1), 85–94.
- [11] Bhasney, S.M., Bhagabati, P., Kumar, A., and Katiyar, V., 2019, Morphology and crystalline characteristics of polylactic acid [PLA]/linear low density polyethylene [LLDPE]/microcrystalline cellulose [MCC] fiber composite, *Compos. Sci. Technol.*, 171, 54–61.
- [12] Ritonga, A.H., Jamarun, N., Arief, S., Aziz, H., Tanjung, D.A., and Isfa, B., 2023, The effect of oleic acid-grafted linear low-density polyethylene as compatibilizer on the properties of linear low-density polyethylene/cyclic natural rubber blends, *Int. J. Technol.*, 14 (1), 162–172.
- [13] Petchwattana, N., Naknaen, P., and Narupai, B., 2020, Combination effects of reinforcing filler and impact modifier on the crystallization and toughening performances of poly (lactic acid), *eXPRESS Polym. Lett.*, 14 (9), 848–859
- [14] Piekarska, K., Piorkowska, E., and Bojda, J., 2017, The influence of matrix crystallinity, filler grain size and modification on properties of PLA/calcium carbonate composites, *Polym. Test.*, 62, 203–209.
- [15] Kudryavtseva, V.L., Zhao, L., Tverdokhlebov, S.I., and Sukhorukov, G.B., 2017, Fabrication of PLA/CaCO₃ hybrid micro-particles as carriers for water-soluble bioactive molecules, *Colloids Surf., B*, 157, 481–489.
- [16] Islam, M.S., Islam, M.M., and Islam, K.N., 2020, "The effect of CaCO₃ nanoparticles and chitosan on the properties of PLA based biomaterials for biomedical applications" in *Encyclopedia of Renewable and Sustainable Materials*, Eds. Hashmi, S., and Choudhury, I.A., Elsevier, Oxford, 736–745.
- [17] Ritonga, A.H., Jamarun, N., Arief, S., Aziz, H., Tanjung, D.A., Isfa, B., Sisca, V., and Faisal, H., 2022, Organic modification of precipitated calcium carbonate nanoparticles as filler in LLDPE/CNR blends with the presence of coupling agents: Impact strength, thermal, and morphology, *J. Mater. Res. Technol.*, 17, 2326–2332.
- [18] Zapata, P.A., Palza, H., Díaz, B., Armijo, A., Sepúlveda, F., Ortiz, J.A., Ramírez, M.P., and Oyarzún, C., 2019, Effect of CaCO₃ nanoparticles on the mechanical and photo-degradation properties of LDPE, *Molecules*, 24 (1), 126.
- [19] Aritonang, B., Tamrin, T., Wirjosentono, B., and Eddiyanto, E., 2020, Effect of Graft

- copolymerization of oleic acid on to cyclic natural rubber in polyamide, *Case Stud. Therm. Eng.*, 21, 100690.
- [20] Rahayu, I., Zainuddin, A., and Hendrana, S., 2020, Improved maleic anhydride grafting to linear low density polyethylene by microencapsulation method, *Indones. J. Chem.*, 20 (5), 1110–1118.
- [21] dos Anjos, E.G.R., Backes, E.H., Marini, J., Pessan, L.A., Montagna, L.S., and Passador, F.R., 2019, Effect of LLDPE-g-MA on the rheological, thermal, mechanical properties and morphological characteristic of PA6/LLDPE blends, *J. Polym. Res.*, 26 (6), 134.
- [22] Tanjung, D.A., Jamarun, N., Arief, S., Aziz, H., Ritonga, A.H., and Isfa, B., 2022, Influence of LLDPE-g-MA on mechanical properties, degradation performance and water absorption of thermoplastic sago starch blends, *Indones. J. Chem.*, 22 (1), 171–178.
- [23] Sisca, V., Tanjung, D.A., Syukri, S., Zilfa, Z., and Jamarun, N., 2021, Catalytic activity of precipitated calcium carbonate for biodiesel production, *Rasayan J. Chem.*, 14 (3), 1587–1593.
- [24] Azis, Y., Jamarun, N., Alfarisi, C.D., Mutamima, A., and Sisca, V., 2022, Precipitated calcium carbonate (PCC) from coral reef as raw material for synthesis of hydroxyapatite nanoparticles, *Rasayan J. Chem.*, 15 (1), 96–101.
- [25] Ritonga, A.H., Jamarun, N., Arief, S., Aziz, H., Tanjung, D.A., and Isfa, B., 2022, Improvement of mechanical, thermal, and morphological properties of organo-precipitated calcium carbonate filled LLDPE/cyclic natural rubber composites, *Indones. J. Chem.*, 22 (1), 233–241.
- [26] Avolio, R., Gentile, G., Avella, M., Carfagna, C., and Errico, M.E., 2013, Polymer–filler interactions in PET/CaCO₃ nanocomposites: Chain ordering at the interface and physical properties, *Eur. Polym. J.*, 49 (2), 419–427.
- [27] Hafidzah, F., Bijarimi, M., Alhadadi, W., Salleh, S., Norazmi, M., and Normaya, E., 2021, Statistical study on the interaction factors of polypropylene-graft-maleic anhydride (PP-g-MA) with graphene nanoplatelet (GNP) at various poly(lactic acid)/polypropylene (PLA/PP) blends ratio, *Indones. J. Chem.*, 21 (1), 234–242.
- [28] Amato, P., Muscetta, M., Venezia, V., Cocca, M., Gentile, G., Castaldo, R., Marotta, R., and Vitiello, G., 2023, Eco-sustainable design of humic acids-doped ZnO nanoparticles for UVA/light photocatalytic degradation of LLDPE and PLA plastics, *J. Environ. Chem. Eng.*, 11 (1), 109003.
- [29] Doufnoune, R., Haddaoui, N., and Riahi, F., 2008, The effects of coupling agents on the mechanical, rheological and thermal properties of calcium carbonate-filled LDPE compatibilized with maleic anhydride-g-LDPE (Part II), *Int. J. Polym. Mater. Polym. Biomater.*, 57 (7), 690–708.
- [30] Song, L., Yang, B., Du, X., Ren, J., Wang, W., Zhang, Q., Chi, W., Cong, F., and Shi, Y., 2023, Functionalized poly(ethylene-octene)/linear low-density polyethylene prepared by melt free-radical grafting reaction and its potential in toughening poly(butylene terephthalate) resins, *Ind. Eng. Chem. Res.*, 62 (19), 7464–7480.

Phenolic Compounds from Moroccan *Retama monosperma* L. Boiss, *Berberis vulgaris* L. and *Ricinus communis* L.: Characterization, Antioxidant Activity and Performance Criteria of the Validated Method Using UHPLC/DAD/ESI-MS

Meriem Outaki^{1*}, Manal Zefzoufi², Amal Sammama³, Khadija El Gadali⁴, Rabiaa Fdil², and Layla El Gaini^{3,5}

¹Laboratory of Applied Chemistry and Environment, Faculty of Sciences and Technologies, University Hassan I, PC. 577, Settat, Morocco

²Laboratory of Bioorganic Chemistry, Department of Chemistry, Faculty of Sciences, University Chouaib Doukkali, PC. 20, El Jadida, Morocco

³Center of Analysis and Characterization, University Cadi Ayyad, PC. 511, Marrakech, Morocco

⁴Laboratory of Sustainable Development and Health Research, Faculty of Sciences and Technologies, University Cadi Ayyad, PC. 549, Marrakech, Morocco

⁵Laboratory of Applied Chemistry and Biomass, Department of Chemistry, Faculty of Sciences Semlalia, University Cadi Ayyad, PC. 2390, Marrakech, Morocco

* **Corresponding author:**

email: meriem.outaki@gmail.com

Received: July 22, 2023

Accepted: September 12, 2023

DOI: 10.22146/ijc.87157

Abstract: Components of medicinal plants have many pharmacological activities, including antioxidant activity, playing an important role in limiting oxidative stress that can cause several damages. This paper characterizes polyphenols of *Retama monosperma* L., *Berberis vulgaris* L. and *Ricinus communis* L. plant extracts and evaluates their antioxidant activity by DPPH, conjugated diene and TBARS assay. To ensure the quality of analytical results, this paper presents performance criteria of the validated method using UHPLC/DAD/ESI-MS. Regarding method validation, the results confirm different used tests and evaluate detection and quantification limits. Concerning the characterization and study of antioxidant activity, realized testing showed that *R. monosperma* is rich in isoflavone, flavone and flavonol. For *R. communis*, we notice the presence of rutin as a major compound. Meanwhile, *B. vulgaris* contains significant amounts of gallic acid and p-coumaric acid. These plant extracts have high antioxidant activity due to the presence of phenolic compounds.

Keywords: polyphenol; antioxidant activity; method validation; UHPLC/DAD/ESI-MS

■ INTRODUCTION

Since ancient times, many plants have attracted interest as sources of natural products [1]. Various plants have been used not only as a food source but also as medicine. The benefits of these practices are known to be supported by many scientific studies [2-4]. It is known that the vast majority of active ingredients in medicines are obtained from plants. Phytotherapy is once again in the spotlight because of the possible adverse effects of synthetic drugs and the multiple benefits obtained from

plant-based medicines [2]. Medicinal plants produce several secondary metabolites like phenols, flavonoids, quinones, and tannins with numerous promising pharmacological activities, such as antioxidant [5-9], anti-inflammatory [10], anti-allergic [11], anticancer, antitumor [12-14], and anti-atherosclerosis [15]. They also provide cardiovascular protection [16]. More specifically, polyphenolic compounds are the most studied plant secondary metabolites due to their abundance and possible positive effects on human health [17]. They have received considerable attention in recent years

because they are considered high-added-value molecules due to their antioxidant and antimicrobial effects [18-19]. Their potential use in the formulation of cosmetics, and as an alternative to chemical food additives, has drawn the attention of a number of researchers. Some of these compounds have also been explored in the packaging and textile industries [20].

In this paper, we will be focusing on antioxidant activity, which acts against oxidative stress. In the human body, environmental radiation splits water to form hydroxyl radicals, and normal metabolism produces oxygen radicals [21]. Oxidative stress is an imbalance between reactive oxygen species formation and antioxidant defense mechanisms. If cellular antioxidants do not eliminate free radicals, the latter can react with different macromolecules [22-23]. At their high concentrations, free radicals attack and damage proteins, lipids, and nucleic acids, thereby causing many health problems. Over time, free radicals can cause a negative chain reaction in the human body, which can block the action of key enzymes, destroy the cell membrane, prevent normal cell division, avoid cellular processes necessary for proper body functioning, and block energy production [24]. Also, these free radicals cause DNA damage and lipid peroxidation, leading to cancerous cells [21]. The human body possesses a natural defense system against these free radicals [21-22]. Once the excessive generation of free radicals attacks the internal antioxidant defense system, external antioxidants are needed to prevent oxidative damage [25]. Antioxidants are considered molecules that prevent the formation of free radicals and seek to neutralize or repair the damage they cause [24].

The biological activities of many phytochemicals are attributed to their antioxidant properties [21]. Experimental and epidemiological evidence shows that dietary antioxidants, such as flavonoids and other phenolic compounds, are also important components of the body's defense [21]. Several studies support a direct link between the antioxidant properties of extracts and the medicinal benefits of plants and their potential use as an alternative to chemical preservatives [26]. Phenolic antioxidants have been reported to inhibit DNA fragmentation. Studies on animal and cell cultures

confirm the anti-cancer effects of antioxidants; epidemiological studies show that high consumption of antioxidant-rich foods is inversely related to cancer risk [27]. Evidence from various *in vitro* studies supports a potential protective role for dietary polyphenols in the prevention of cardiovascular disease, neurodegenerative disease, cancer, diabetes, inflammation-related, and infectious diseases [28]. In addition to their importance in the diet, antioxidants can also contribute to the stability and taste of food products. From a plant specialist's point of view, their role in the plant as a defense against biotic and abiotic stresses must also be taken into account [21]. All these benefits justify the considerable interest in researching safe natural antioxidants which are in high demand by the pharmaceutical industry and as food preservatives [29].

Therefore, it is important to study the phenolic composition of various plant extracts and assess their antioxidant activity in order to provide scientific results that would greatly support different sectors such as pharmaceuticals, cosmetics, and food industry. This revelation would be an excellent addition to the scientific literature.

It is within this context that this paper falls. It presents the chemical composition of extracts of three medicinal and aromatic plants: *Retama monosperma*, *Ricinus communis*, and *Berberis vulgaris* followed by an evaluation of the antioxidant activity of their phenolic compounds. For nutritional purposes, many scientific studies have been conducted on the chemical composition of these plant extracts grown in various parts of the world and which are of great interest [30-34]. However, this paper is the first to characterize different extracts of these plants growing in Morocco. Therefore, a lot of effort has been engaged in developing different techniques and methods for the identification of phenolic compounds from natural resources. In most cases, these compounds are analyzed by high-performance liquid chromatography-mass spectrometry (HPLC-MS) and HPLC-diode-array detector (HPLC-DAD). As an important step to ensure the quality of analytical results and to provide researchers with performance criteria, the authors followed a process for

validation of the method chosen for the characterization and quantification of polyphenols before use. The validation process was focused on six polyphenols known as antioxidant standards, such as gallic acid, vanillic acid, *p*-coumaric acid, rutin, quercetin, and genistein [35-40].

This paper details the tests that were carried out, such as specificity, linearity, repeatability, intermediate precision, detection limit, quantification limit, and recovery. It also details the statistical methods used because they are often perceived as a constraint since they are generally poorly used by analysts. The objective of publishing this paper, with supplementary material, is also to provide people wishing to perform a method validation with a document that describes in detail the followed approach, avoiding them to search several references to first understand the experimental plan to be implemented and several others to subsequently find the statistical methods to apply.

■ EXPERIMENTAL SECTION

Materials

Chemical materials

The materials used in this study were methanol (HPLC grade $\geq 99.9\%$ from Honeywell Riedel-de Haen, Germany) used as solvent B and 0.1% formic acid (98% for LC-MS, Merck Germany) aqueous solution (ultra-pure water from Pure Lab) used as solvent A. The gallic acid was purchased from Merck (Germany), and the other phenolic compounds (vanillic acid, *p*-coumaric acid, rutin, quercetin, and genistein) were purchased from Sigma-Aldrich (USA). The 2,2-diphenyl-2'-picrylhydrazyl (DPPH), linoleic acid, ethylenediaminetetraacetic acid (EDTA), thiobarbituric acid, and trichloroacetic acid (Sigma-Aldrich, USA) were used as an antioxidant reagent and the butylated hydroxytoluene (BHT, Merck Germany) as antioxidant standard.

Plant materials

R. monosperma flowers and seeds were collected in February and April 2017, respectively, from Al-Haouzia forest in the region of El Jadida-Morocco. *R. communis* leaves were collected in February 2018 in the region of El Jadida-Morocco. These plant materials were identified by Dr. Fennane from the Scientific Institute of Rabat,

Morocco. A voucher specimen (77816 RAB) was deposited in the Herbarium of the Institute. For the *B. vulgaris*, root was collected in March 2019 in the region of Marrakech-Morocco. This plant material was identified by Dr. Ouhamou from the Faculty of Sciences, Cadi Ayyad University, Marrakech, Morocco.

Instrumentation

The instrumentations used in this study were chromatographic separation performed on Dionex Ultimate 3000 UHPLC-DAD system (CA, USA), equipped with a quaternary pump (HPG-3400RS), an autosampler (WPS-3000TSL), and a column oven (TCC-3000). A Vertex plus C18 reversed-phase column (250 \times 4.6 mm, Eurospher II 100-5) provided by Knauer was used for the proposed method. The mass spectrometer was a TSQ Endura (Thermo Fisher Scientific) triple quadrupole equipped with heated-electrospray ionization (H-ESI).

Procedure

Extraction

The flowers (600 g) and seeds (400 g) of *R. monosperma* were air-dried for two weeks. The extraction was performed three times by maceration (room temperature, 3 d) with 2 L of *n*-hexane to remove lipophilic compounds. After evaporation of *n*-hexane under vacuum, the resulting mark was extracted three times by maceration with 2 L of ethyl acetate (room temperature, 3 d) for flowers and 2 L of diethyl ether for seeds (room temperature, 3 d). The resulting extract was then evaporated using a rotary evaporator.

R. communis leaves (200 g) and *B. vulgaris* roots (300 g) were air-dried for two weeks. Each sample was extracted using Soxhlet and methanol as solvent. The extracts were evaporated under reduced pressure to give methanol crude extracts. This later was solubilized in water and extracted with ethyl acetate. The resulting extract was then evaporated using a rotary evaporator.

UHPLC-DAD-ESI/MS method

The separation gradient was created using solvent A (0.1% formic aqueous solution) and solvent B (methanol), as shown in Table 1. The mobile phase flow rate was 1 mL/min. The injection volume was 10 μ L, and

Table 1. UHPL-DAD separation gradient

Time (min)	% of solvent B	Time (min)	% of solvent B
0	5	18	54
3	25	22	54
6	25	26	95
9	37	29	95
13	37	29.15	5
		31	5

the wavelength was 280 nm. For the LC-MS experiment, negative mode was used. Sheath gas, ion sweep gas, and auxiliary gas were nitrogen (purity > 99.98%) at flow rates of 65, 0, and 40 arbitrary units (a.u.), respectively. The vaporizer temperature and ion transfer tube temperature were set at 350 °C. The electrospray voltage was set at -2.5 kV. Full scan MS acquisition mode (m/z 100–1000) in Q1 (mass resolution of 0.7 m/z full-width half maximum (FWHM)) with a scan time of 0.5 s was used [41].

Antioxidant activity

DPPH-radical scavenging activity. Free radical-scavenging activity of *R. monosperma*, *B. vulgaris*, and *R. communis* extracts was evaluated using a modified DPPH method. One milliliter of concentrations of samples (5–100 µg/mL) was added to 1 mL of DPPH solution (40 µg/mL), and the mixture was incubated for 30 min [42]. Afterward, the absorbance was measured at 517 nm in a UV spectrophotometer. BHT, rutin, gallic acid, and quercetin were used as a standard antioxidant. Scavenging activity was expressed as IC₅₀, an effective concentration in µg/mL of samples or standard that reduces the absorbance of DPPH by 50 % when compared with negative control. The experiment was carried out in triplicate.

Conjugate diene scavenging activity. Conjugate diene scavenging activity was determined by UV absorbance [43]. A linoleic acid emulsion was prepared in tampon phosphate at pH 7 (10 mM; 10 mL) mixed with the linoleic acid (5.96 µL) and tween 20 (0.1%; 10 mL). Linoleic acid emulsion (1 mL) was added to various concentrations of studies extracts (5–100 µg/mL) and 100 µL of CuSO₄ (1.6 g/L). After that, the mixture was incubated at 37 °C in the dark for 1 h. To stop the reaction, 10 µL of EDTA and 10 µL of BHT (1 mg/mL) were added to the mixture. Then, the absorbance was

measured at 234 nm. The conjugate diene scavenging activity was calculated using Eq. (1).

$$\text{Scavenging activity (\%)} = \frac{A_0 - A_1}{A_0} \times 100 \quad (1)$$

A₀ is the absorbance of the control (sample without extracts), and A₁ is the absorbance of the sample. The results were expressed as IC₅₀. The experiment was carried out in triplicate.

Thiobarbituric acid-reactive substances assay.

The thiobarbituric acid-reactive substances (TBARS) assay determined the inhibition of lipid peroxidation according to Ohkawa method [44] with some modifications [45]. A 1 mL of linoleic acid emulsion was added to various concentrations of extracts (5–100 µg/mL) and 100 µL of CuSO₄ (1.6 g/L), and then was left to incubate at 37 °C in the dark for 3 h. The reaction was stopped by putting the mixture of products and reagents in ice and adding 10 µL of EDTA (20 mM). Then, 1 mL of TBA (0.78%) and 1 mL of trichloroacetic acid (TCA 20%) were added to the mixture which was incubated at 95 °C in the dark for 45 min. The *n*-butanol (0.8 mL) was added to the mixture. The absorbance was measured at 532 nm in a UV spectrophotometer. The estimation of TBARS was calculated using Eq. (1). Scavenging activity was expressed as IC₅₀. The experiment was carried out in triplicate.

Method validation

As an important step to ensure the quality of analytical results and to provide researchers with performance criteria, the authors followed a process for validation of the method chosen for the characterization and quantification of polyphenols before use. The validation process was focused on six polyphenols known as antioxidant standards, such as gallic acid, vanillic acid, *p*-coumaric acid, rutin, quercetin, and genistein. Method validation was carried out using the five extracts that contain one or two compounds of interest (Table 2).

The experimental plan of method validation is presented in Table 3. It concerns several studies such as specificity, linearity, repeatability, intermediate precision, detection limit, and quantification limit. As an example, recovery was studied using *R. monosperma*

ethyl acetate extract from the flowers. The choice of the different concentration levels used was made to cover the concentration range of the majority of samples.

■ RESULTS AND DISCUSSION

Characterization of Phenolic Compounds by UHPLC/DAD/ESI-MS

A total of 14 phenolic compounds have been tentatively identified based on their wavelength of maximum UV absorption and mass spectrometry (MS) fragments in the negative mode corresponding to these peaks, alongside literature data on the chemical composition of *Retama*, *Berberis*, and *Ricinus* genus.

The chromatographic profile of *R. communis* methanol extract (RM) showed the presence of phenolic acid (peak 2), ellagitannins, members of the tannin family, are characterized as hydrolyzable conjugates containing

one or more hexahydroxydiphenoyl (HHDP) group(s) to esterify a sugar like gallic derivative (peaks 4–6), and flavonoid glycosides like rutin and quercetin (peaks 10 and 11) (Table 4, Fig. 1).

The UHPLC/DAD/ESI-MS results of *B. vulgaris* ethyl acetate showed the predominance of pyrogallol acid (peak 1) followed by vanillic acid and *p*-coumaric acid; however, in methanolic extracts in the same species, we notice the predominance of gallic acid (peak 3) followed by *p*-coumaric acid (Table 4, Fig. 1). Concerning *R. monosperma* extracts, the chromatographic profile of flower ethyl acetate extracts showed the predominance of genistein as isoflavone (peak 13) followed by apigenin (peak 14) as a flavone. For diethyl ether extracts of *R. monosperma* seeds, we can see the taxifolin flavanonols (peak 8) as a major compound, followed by genistein (peak 13) (Table 4, Fig. 1).

Table 2. Information about the matrixes used to validate the method

Matrix	Part of the plant	Nature of the extract	Identified compounds
<i>Retama monosperma</i> *	Flowers	Ethyl acetate	Genistein
<i>Berberis vulgaris</i>	Roots	Methanol	<i>p</i> -Coumaric acid
		Ethyl acetate	Vanillic acid
<i>Ricinus communis</i>	Leaves	Methanol	Gallic acid and rutin
		Ethyl acetate	Gallic acid

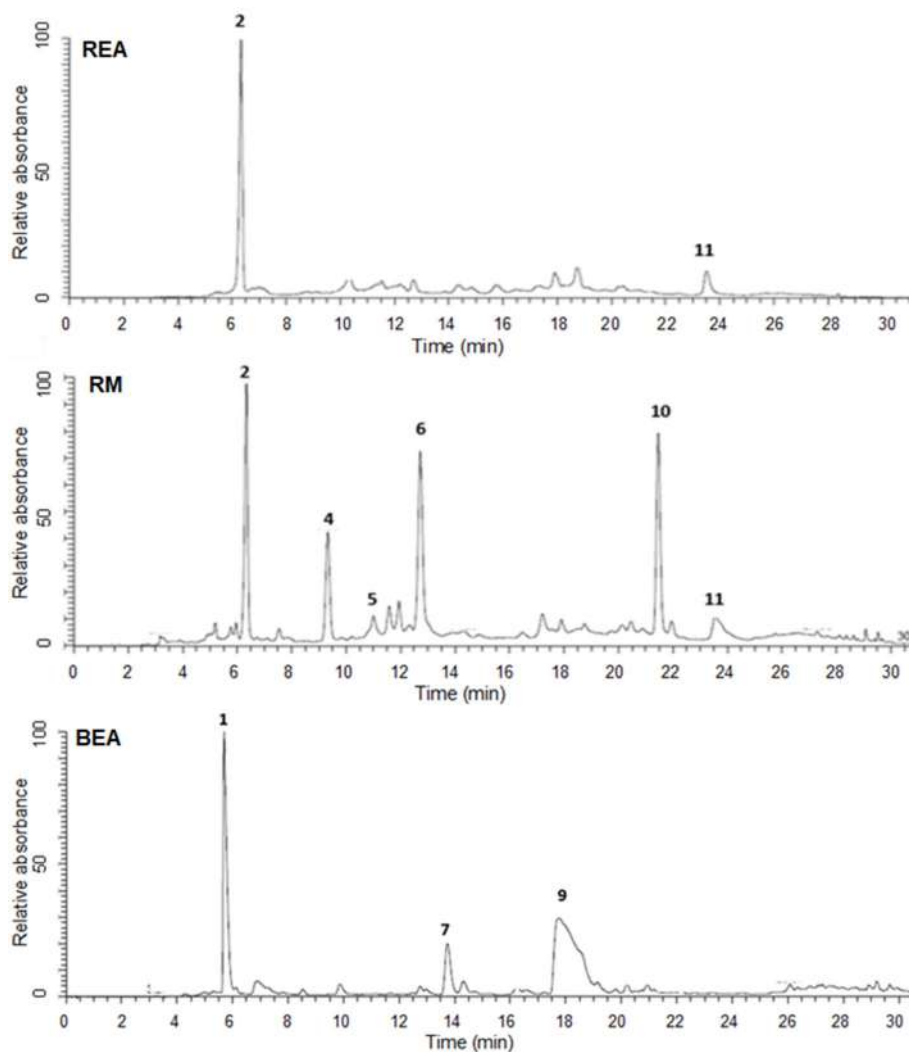
*In Morocco, Zefzoufi et al. [34] revealed that the diethyl ether extract of flowers and ethyl acetate extract of seeds of *R. monosperma* rich in flavonoid compounds such as genistein, quercetin, kaempferol. Other extracts of this plant are used in this paper

Table 3. Experimental plan of method validation

Parameter	Experience
Specificity	Method 1: Each extract sample (Table 2) was analyzed using UHPLC-DAD-ESI/MS [46]. Method 2: Some authors use the recovery [47-48] method to prove the specificity of the method. The experience carried out to perform the recovery test is detailed in the last row of the table.
Linearity	Three series of multi-standard solutions at 5 concentration levels were used (10, 50, 100, 150 and 200 mg/L). Three repetitions for each level of each series were performed by UHPLC-DAD [49].
Detection limit	Ten repetitions for the control sample (methanol) were performed by UHPLC-DAD [48].
Quantification limit	
Repeatability	Two concentration levels (50 and 200 mg/L) of multi-standard solution were prepared by the same operator and analyzed by UHPLC-DAD. Ten repetitions were performed for each level on the same day [48].
Precision	Every day for 3 d, a series of multi-standard solutions with 5 concentrations levels (10, 50, 100, 150 and 200 mg/L) was prepared by the same operator. Three repetitions for each level of each series were performed by UHPLC-DAD [49].
Intermediate precision	
Recovery	Six samples of the ethyl acetate extract of <i>Retama monosperma</i> flowers were used to perform the recovery test. The final concentrations of the standard (Genistein) added are as follows: 0, 10, 50, 100, 150, and 200 mg/L. Three repetitions were performed for each sample using UHPLC-DAD [50].

Table 4. Tentatively identification of phenolic compounds (with their percentage area) from three medicinal plants using UHPLC/DAD/ESI-MS

Peak number	Rt	(M-H) ⁻ m/z	MS fragments	UV _{max}	Identified compound	Molecular formula	Ref.	REA (%)	RM (%)	BEA (%)	BM (%)	RSDE (%)	RFEA (%)
1	5.9	125	-	270	Pyrogallol	C ₆ H ₆ O ₃	-	-	-	58.74	-	-	-
2	6.1	331	169	270, 310	Galloyl-glucoside	C ₁₃ H ₁₆ O ₁₀	[57]	70.82	20.15	-	-	-	-
3	6.5	169	125	272	Gallic acid	C ₇ H ₆ O ₅	[57]	-	-	-	38.07	-	-
4	9.3	483	313, 169	256, 310	Digalloyl-glucoside	C ₂₀ H ₂₀ O ₁₄	[57]	-	9.33	-	-	-	-
5	11.0	635	465, 283, 169	270, 310	Trigalloyl-glucoside	C ₂₇ H ₂₄ O ₁₈	[57]	-	2.33	-	-	-	-
6	12.7	633	463, 169	269, 310	Galloyl-HHDP-glucoside	C ₂₇ H ₂₂ O ₁₈	[57]	-	25.83	-	-	-	-
7	13.8	167	-	261, 295	Vanillic acid	C ₈ H ₈ O ₄	-	-	-	10.50	-	-	-
8	18.1	315	-	228, 290	Taxifolin	C ₁₅ H ₁₂ O ₇	[58]	-	-	-	-	71.32	-
9	18.6	163	-	310	<i>p</i> -Coumaric acid	C ₉ H ₈ O ₃	-	-	-	30.02	45.17	-	-
10	21.8	609	463, 301	257, 357	Rutin	C ₂₇ H ₃₀ O ₁₆	[59]	-	25.55	-	-	-	-
11	23.6	447	301	255, 356	Quercitrin	C ₂₁ H ₂₀ O ₁₁	[59]	10.20	3.10	-	-	-	-
12	26.7	301	-	355, 368	Quercetin	C ₁₅ H ₁₀ O ₇	[34]	-	-	-	-	20.05	-
13	27.1	269	-	261, 302 _{sh}	Genistein	C ₁₅ H ₁₀ O ₅	[34]	-	-	-	-	-	74.35
14	27.7	269	-	236, 336	Apigenin	C ₁₅ H ₁₀ O ₅	[51]	-	-	-	-	-	21.02



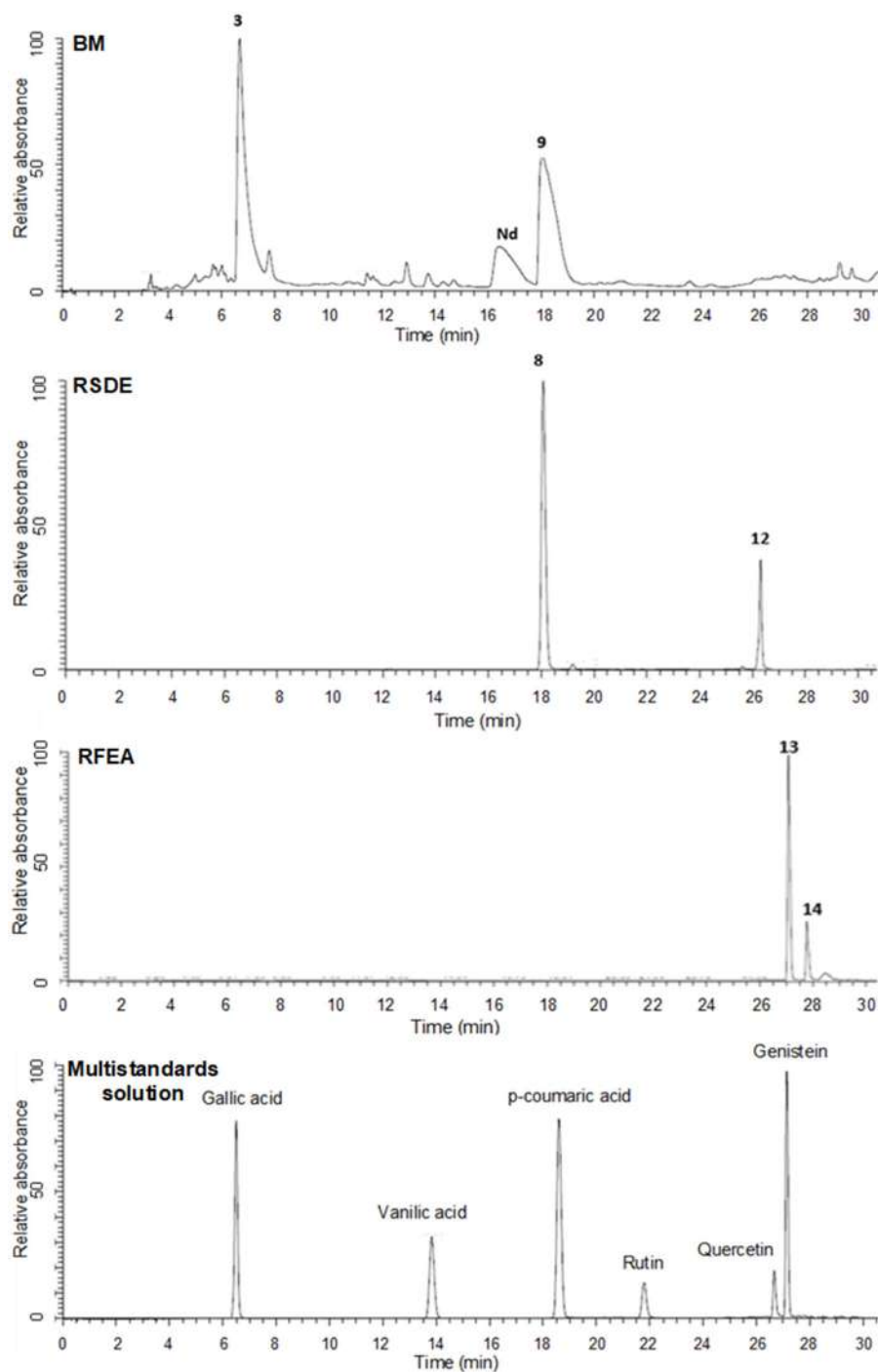


Fig 1. Chromatographic profile of *R. communis* methanolic extract (RM), *R. communis* ethyl acetate extract (REA), *B. vulgaris* methanolic extract (BM), *B. vulgaris* ethyl acetate extract (BEA), *R. monosperma* flowers ethyl acetate extract (RFEA), *R. monosperma* seeds diethyl acetate extract (RSDE) and multi-standards solution at 280 nm

In this study, we tentatively identified in three medicinal plants diverse phenolic compounds like phenolic acid (gallic acid, vanillic acid, *p*-coumaric acid), isoflavone (genistein), flavone (apigenin), flavanonols

(taxifolin), flavonol (quercetin), glycoside flavonol (rutin and quercitrin), and ellagitannins (galloyl-HHDP-glucoside).

For *Retama* genus, based on the literature, we found

our results closely similar to other papers. Researchers identified genistein, luteolin, apigenin, and rutin in aqueous extract of *R. monosperma* growing in Spain [51]. Recently, researchers reported the presence of taxifolin and quercetin in ethyl acetate seeds extract and genistein and apigenin in diethyl ether flower extract of Moroccan *R. monosperma* [34]. In our study, we identified genistein as a major compound, followed by apigenin in another extract (ethyl acetate extract) of *R. monosperma* flowers.

For *Ricinus* genus, we found dissimilarities in chemical composition between our results and the literature. For example, researchers reported five phenolic compounds isolated from *R. communis* growing in Vietnam such as gallic acid, vanillic acid, kaempferol-3-O- β -D-glucopyranoside, and kaempferol-3-O- β -D-xylopyranoside [52]. Another research determined the presence of gallic acid, genistic acid, vitexin, naringenin and rutin in leaves of *R. communis* from Tunisia [53]. In 2016, researchers reported the presence of some alkaloids in the same species as ricinine and bufotenine O-glucoside. To our knowledge, this paper is the first to identify digallyl-glucose, trigallyl-glucose, gallyl-HDDP-glucose, rutin, and quercitrin in *R. communis* native to Morocco.

For *Berberis*, many studies focused on the identification of *B. vulgaris* alkaloid compounds like berberine, which is known as an important major compound in this plant. In Morocco, researchers reported the presence of some alkaloids in *B. vulgaris* dichloromethane extract such as berberine, palmatine, and epi berberine [54]. To our knowledge, this paper is the first to identify pyrogallol and *p*-coumaric acid in *B. vulgaris* from Morocco. These observed differences in chemical profiles can be explained by the geographic origin of the species [55], the extraction method (maceration in our case), the extraction solvent [56], and the part of the plant used for the preparation of the extracts.

Antioxidant Activity

Natural antioxidants are currently the subject of numerous studies because they can reduce the harmful effects of free radicals in neurodegenerative diseases and cardiovascular, arthritis, cancer, and autoimmune diseases

in which oxidative stress is incriminated [60]. Numerous works carried out on the anti-free radical activity of plant extracts have shown that phenolic compounds and, more particularly, flavonoids are recognized as potentially antioxidant substances with the ability to trap free radical species and reactive forms of oxygen. The IC₅₀ value represents the concentration of extract that neutralizes or reduces 50% of free radicals. The lower the IC₅₀, the more the extract has a powerful antioxidant potential. Therefore, we evaluated the antioxidant activity of RFEA, RSDE, REA, RM, BEA and BM by three tests, conjugated diene scavenging activity, TBARS assay and DPPH (Table 5). We used rutin, gallic acid, quercetin, and BHT as standards.

DPPH Scavenging Activity

REA showed a higher antiradical activity (IC₅₀ = 12.5 μ g/mL) followed by RFEA, RM compared to standards BHT, quercetin and gallic acid, but still less than rutin standard. However, the antioxidant capacity of RSDE, BM and BEA were moderate compared to the other extracts and standards (Table 5).

Conjugated Diene Scavenging Activity

The conjugate diene scavenging activity of REA was more effective than BHT, quercetin and gallic acid, but it is similar to rutin. BEA showed moderate antioxidant activity followed by RM, BM, RFEA, and RSDE with IC₅₀ values of 59.02, 60.09, 72.47, and 98.08 μ g/mL, respectively (Table 5).

TBARS Assay

TBARS assay of RM was significantly greater, followed by BEA and BM but still less than four standards. However, the inhibition of lipid peroxidation of RFEA, RSDE and REA was lower than in other samples (Table 5). Based on the literature, several studies reported the antioxidant activity of these three plants' medicinal extracts. Concerning *R. communis*, researchers revealed that the antioxidant capacity of butanol extract of the aerial part of *R. communis* growing in Pakistan (IC₅₀ = 140 μ g/mL) is higher than that of ethyl acetate extract (IC₅₀ = 190 μ g/mL) [61]. In 2009, a paper described that leaves methanolic extract of *R. communis* has a strong antiradical activity with IC₅₀ of 4.6 μ g/mL

Table 5. Antioxidant activity of standards and samples in terms of IC₅₀ (µg/mL) values with $p < 0.05$

	DPPH	Conjugated diene	TBARS
	Standards		
BHT	28.41 ± 0.06	36.55 ± 0.28	40.06 ± 0.15
Gallic acid	30.55 ± 0.02	36.52 ± 0.12	40.08 ± 0.15
Quercetin	35.65 ± 0.25	30.05 ± 0.15	38.42 ± 0.05
Rutin	10.02 ± 0.05	26.02 ± 0.11	30.05 ± 0.05
	Samples		
RFEA	19.59 ± 0.11	72.47 ± 0.25	68.12 ± 0.12
RSDE	84.95 ± 0.16	98.08 ± 0.50	82.26 ± 0.12
REA	12.50 ± 0.11	29.59 ± 0.11	69.02 ± 0.11
RM	20.45 ± 0.11	59.02 ± 0.11	50.30 ± 0.11
BEA	38.05 ± 0.15	44.12 ± 0.02	52.89 ± 0.10
BM	55.32 ± 0.14	60.09 ± 0.22	55.90 ± 0.15

RFEA: *Retama* flowers ethyl acetate; RSDE: *Retama* seeds diethyl ether; REA: *Ricinus* ethyl acetate; RM: *Ricinus* methanol; BEA: *Berberis* ethyl acetate; BM: *Berberis* methanol

followed by ethyl acetate extract (IC₅₀ = 6.04 µg/mL) [62]. For *R. monosperma*, previous work reported that the antiradical activity of ethyl acetate extracts of seeds (IC₅₀ = 15.13 µg/mL) was significantly higher than quercetin (IC₅₀ = 19.43 µg/mL) and BHT standards (IC₅₀ = 30.21 µg/mL) [34]. Regarding *B. vulgaris*, recently, a paper reported higher antioxidant activity using a DPPH assay of ethanol and ethyl acetate extract of *B. vulgaris* roots with IC₅₀ of 69.65 and 77.75 µg/mL, respectively [63].

Performance Criteria of the Validated Characterization Method Using the UHPLC-DAD

Use of purity for the calculation of the real concentrations of the standards used

Preparation of the standard solutions required weighing a certain mass of the standards in powder form. Since the purity of standards is different from 100%, the calculation of the real concentrations is necessary. Table 6 shows the different concentrations used, taking their purity into consideration.

Specificity

The plant extracts and multi-standards solutions were analyzed by UHPLC/DA/DESI-MS, and each peak concerned was detected at 280 nm. Table 7 and Fig. 1 show the found results. As can be seen in Fig. 1, the chromatograms show that the separation of all six phenolic compounds was successfully achieved with good resolution. Additionally, no interfering peaks were observed.

Linearity

Linearity is the ability of a method to elicit test results that are proportional to analyte concentration within a given range. The range of the analytical method is the interval between the highest and lowest concentrations in which linearity has been confirmed. Many tests are used to validate method linearity. These tests are presented in Table 8.

The results showed that regression curves of each phenolic compound were found to be linear with R²

Table 6. Real concentrations (mg/mL) of the standards used

Standards	Gallic acid	Vanillic acid	<i>p</i> -Coumaric acid	Rutin	Quercetin	Genistein
Level 1	9.90	9.80	10.00	9.59	9.90	9.90
Level 2	49.49	48.98	49.98	47.94	49.49	49.49
Level 3	98.98	97.97	99.96	95.88	98.98	98.98
Level 4	148.47	146.95	149.94	143.82	148.47	148.47
Level 5	197.96	195.94	199.92	191.76	197.96	197.96

Table 7. Quantitative analysis of phenols in different plant extracts using UHPLC-DAD-ESI/MS at UV 280 nm

Rt	(M-H) ⁻ m/z	Molecular weight	UV _{max}	Identified compound	Molecular formula	REA mg/L	RM mg/L	BEA mg/L	BM mg/L	RSDE mg/L	RFEA mg/L
6.50	169	170	272	Gallic acid	C ₇ H ₆ O ₅				29.81		
13.81	167	168	261, 295	Vanillic acid	C ₈ H ₈ O ₄			56.61			
18.57	163	164	310	<i>p</i> -Coumaric acid	C ₉ H ₈ O ₃			10.36	11.84		
21.78	609	610	257, 357	Rutin	C ₂₇ H ₃₀ O ₁₆		12.35				
26.66	301	302	355, 368	Quercetin	C ₁₅ H ₁₀ O ₇					69.64	
27.13	269	270	261, 302 _{sh}	Genistein	C ₁₅ H ₁₀ O ₅						102.02

Table 8. Tests used to validate method linearity for the six compounds of interest

Standard	Gallic acid	Vanillic acid	<i>p</i> -Coumaric acid	Rutin	Quercetin	Genistein	Conclusion	
Slope a*	23967.90	15588.78	34637.73	6532.57	5797.53	24364.42	-	
Standard deviation of the slope S _a *	350.71	227.08	545.51	96.98	44.14	400.97	-	
Intercept b*	37743.55	24710.59	70174.89	9438.12	5939.70	51282.24	-	
Standard deviation of the intercept S _b *	42543.71	27265.38	66829.07	11396.44	5355.25	48640.90	-	
Coefficient of determination R ² *	0.9994	0.9994	0.9993	0.9993	0.9998	0.9992	-	
Cochran test	C _(0.95, 3, 14)	0.33	0.34	0.34	0.33	0.35	0.34	The homogeneity of variances is confirmed
Acceptance criteria	Between 0.55 and 0.60 according to the Cochran table							
t	There is a homogeneity of variances if C _{calculated} ≤ C _(1-α, s, nk-1)							
Test of intercept [64]	t _(0.975, 3)	0.89	0.91	1.05	0.83	1.11	1.05	The line passes through the origin
Acceptance criteria	The line passes through the origin if t _{calculated} ≤ t _(1-α/2, k-2) **							
Test of the nullity of the slope [65]	t _(0.975, 3)	68.34	68.65	63.50	67.36	131.32	60.76	
Acceptance criteria	The slope is null if t _{calculated} ≤ t _(1-α/2, k-2) **							
Test of significance of the slope [64]	F _(0.95, 1, 43)	26011.31	23034.82	23098.18	24269.19	17330.50	22560.96	The slope is different from zero, there is a linear relationship between x and y
Acceptance criteria	The slope is not significance if F _{calculated} ≤ F _(1-α, 1, Nk-2)							
Test of significance of the regression [64]	F _(0.95, 1, 3)	4670.40	4712.56	4031.72	4536.86	17246.08	3692.10	
Acceptance criteria	The slope is not different from zero if F _{calculated} ≤ F _(1-α, 1, k-2)							

•Notes: *Calculated using the LINEST function in Microsoft Excel; **One-tail student test; Equation of regression curve: $y = (a \times x) + b$ (y: area; x: concentration mg/L)/α: risk = 0.05/s: Number of series/n: number of repetitions per level in the series/k: number of concentration levels/N: number of repetitions per level all series combined. Details of the calculations performed are shown in the supplementary material

greater than 0.999. This value means that 99.9% of the variation in the concentration (within the range of the minimum and maximum concentrations taken into consideration) is expressed by the correlation.

Linearity validation was confirmed by: i) firstly, the Cochran test that confirmed the homogeneity of variances, ii) secondary, the intercept test according to which it can be concluded that the line passes through the origin, and iii) finally, by a number of t and F tests to which it can be concluded that the slope is different from 0 and there is a linear relationship between the concentration of the compound and the peak area.

Repeatability

The repeatability of the method was examined by analysis of two concentration levels by performing 10 repetitions. The results of this test are presented in Table 9.

Intermediate precision

The intermediate precision of the method was examined by analysis of 5 concentration levels three times for three days and calculation of the coefficient of variation and the intermediate precision. The found results are presented in Table 10.

Table 9. Repeatability study results for the six compounds of interest

Compound	Gallic acid		Vanillic acid		<i>p</i> -Coumaric acid		Rutin		Quercetin		Genistein	
Concentration (mg/L)	49.49	197.96	48.98	195.94	49.98	199.92	47.94	191.76	49.49	197.96	49.49	197.96
Average of 10 repetitions (mg/L)	50.42	196.51	50.40	195.32	51.32	198.62	48.98	190.45	48.53	190.24	51.09	197.05
Standard deviation of 10 repetitions (mg/L)	0.82	2.21	0.80	2.33	0.78	2.29	0.86	2.24	1.02	2.22	0.82	2.20
Coefficient of variation (CV)	1.63	1.12	1.60	1.19	1.52	1.16	1.75	1.18	2.09	1.16	1.61	1.12
Repeatability <i>r</i>	2.30	6.18	2.25	6.52	2.19	6.42	2.40	6.27	2.85	6.21	2.30	6.16
Acceptance criteria	If the calculated CV is less than 5%, the proposed method is repeatable.											
Conclusion	For the six phenolic compounds, the CV is less than 5%, which is acceptable. These results showed that the current method for quantification of the six phenolic compounds is repeatable.											
•Notes:	Coefficient of variation: $CV = \frac{STD}{\bar{x}} \times 100$						Repeatability <i>r</i> [67]: $r = 2.8 \times STD$					
	STD: Standard deviation of 10 repetitions; \bar{x} : Average of 10 repetitions											

Table 10. Intermediate precision study results for the six compounds of interest

Gallic acid	Concentration level (mg/L)	9.90	49.49	98.98	148.47	197.96
	Average of 9 repetitions (mg/L)	8.63	49.34	100.48	150.74	195.61
	Standard deviation of 9 repetitions (mg/L)	0.20	1.13	1.86	3.88	2.43
	Coefficient of variation (CV)	2.31	2.30	1.85	2.57	1.24
	Intermediate precision R	0.56	3.17	5.20	10.86	6.80
Vanillic acid	Concentration level (mg/L)	9.80	48.99	97.97	146.96	195.94
	Average of 9 repetitions (mg/L)	8.55	48.84	99.45	149.18	193.63
	Standard deviation of 9 repetitions (mg/L)	0.32	1.34	2.05	4.16	2.69
	Coefficient of variation (CV)	3.73	2.75	2.06	2.79	1.39
	Intermediate precision R	0.89	3.76	5.73	11.65	7.54
<i>p</i> -Coumaric acid	Concentration level (mg/L)	10.00	49.98	99.96	149.94	199.92
	Average of 9 repetitions (mg/L)	8.55	49.89	101.64	152.34	197.37
	Standard deviation of 9 repetitions (mg/L)	0.19	1.33	1.99	4.11	2.52
	Coefficient of variation (CV)	2.26	2.67	1.96	2.70	1.28
	Intermediate precision R	0.54	3.73	5.58	11.50	7.05
Rutin	Concentration level (mg/L)	9.59	47.94	95.88	143.82	191.76
	Average of 9 repetitions (mg/L)	8.42	47.66	97.40	146.05	189.46
	Standard deviation of 9 repetitions (mg/L)	0.27	1.13	1.80	4.02	2.40
	Coefficient of variation (CV)	3.16	2.37	1.85	2.75	1.27
	Intermediate precision R	0.75	3.16	5.05	11.25	6.72
Quercetin	Concentration level (mg/L)	9.90	49.49	98.98	148.47	197.96
	Average of 9 repetitions (mg/L)	9.24	49.35	99.90	149.56	196.75
	Standard deviation of 9 repetitions (mg/L)	0.25	1.20	2.92	4.40	5.41
	Coefficient of variation (CV)	2.72	2.44	2.93	2.94	2.75
	Intermediate precision R	0.70	3.37	8.19	12.33	15.14
Genistein	Concentration level (mg/L)	9.90	49.49	98.98	148.47	197.96
	Average of 9 repetitions (mg/L)	8.23	49.58	100.87	150.76	195.36

	Standard deviation of 9 repetitions (mg/L)	0.31	1.39	1.78	3.89	2.74
	Coefficient of variation (CV)	3.75	2.81	1.77	2.58	1.40
	Intermediate precision R	0.86	3.90	4.99	10.88	7.66
Acceptance criteria	If the calculated CV is less than or equal to 5 %, the intermediate precision of the proposed method is validated.					
Conclusion	It can be seen that all coefficients of variation are less than 5 %, which is acceptable. So, the intermediate precision of the method is validated.					
•Notes:	Coefficient of variation $CV = \frac{STD}{\bar{x}} \times 100$		Intermediate precision [67]: $R = 2.8 \times STD$			
	STD: Standard deviation of 9 repetitions; \bar{x} : Average of 9 repetitions					

Detection and Quantification Limits

The detection limit is the lowest concentration of the analyte that can be detected but not necessarily quantified. The quantification limit is the lowest concentration of the analyte that can be quantified at the experimental conditions. In the present paper, the limits were calculated using the graphic approach.

This approach can be applied to analytical methods that provide a graphic recording (e.g., chromatography) with background noise. This method requires the determination of [48]: i) h_{max} is the greatest difference in amplitude on the y-axis of the signal observed between two acquisition points, excluding drift, over a distance

equal to twenty times the width at mid-height of the peak corresponding to the analyte, centered on its (analyte) retention time. An explanatory diagram for the calculation of the h_{max} is presented at the level of the reference [66-68]; ii) Factor R is the quantity/signal response factor expressed in height. This factor corresponds to the slope of the regression curve, representing the concentration as a function of the peak height. It was calculated using the same data recorded to perform the intermediate precision test (5 concentration levels analyzed by performing 3 repetitions per day for 3 d). Data used for the calculation of the detection and quantification limits are presented in Table 11.

Table 11. Data used for the calculation of the detection and quantification limits

Standard	Gallic acid	Vanillic acid	p-Coumaric acid	Rutin	Quercetin	Genistein
Retention time (min)*	6.46	13.79	18.55	21.75	26.64	27.11
Width at half height (min)*	0.12	0.22	0.19	0.25	0.16	0.11
h_{max}^{**}	752.64	266.59	381.97	431.90	989.67	885.96
Factor R	3.18×10^{-04}	7.76×10^{-04}	3.35×10^{-04}	1.69×10^{-03}	1.29×10^{-03}	2.69×10^{-04}
Detection limit DL (mg/L)	0.72	0.62	0.38	2.11	3.84	0.71
Quantification limit QL (mg/L)	2.39	2.07	1.28	7.30	12.80	2.38

Notes: *Retention time and width at half height are average values calculated using data from the intermediate precision study (3 repetitions per day for 3 d) for the lowest concentration level; ** h_{max} : Average of h_{max} of each repetition of the control sample (10 repetitions in total); Detection and quantification limits were calculated using the following equations [48]: $DL = 3 \times h_{max} \times R$, $QL = 10 \times h_{max} \times R$

Table 12. Results of the recovery test

Concentration level	Added concentration (mg/L)	Concentration after addition (3 repetitions average) (mg/L)	Recovered concentration (level X - level 1) (mg/L)	Recovery (%)	Recovery average (%)	100.63
Level 1	0.00	100.90	-	-	Standard deviation (%)	1.70
Level 2	9.90	111.04	10.14	102.44	Coefficient of variation (CV)	1.68
Level 3	147.98	247.51	146.62	99.08	$t_{(0.975,2)}$	4.30
Level 4	197.96	299.60	198.70	100.38	Confidence interval \pm	4.21

Acceptance criteria	The CV must be less than 2 %, and the confidence interval must include the value 100 % [50]	
Conclusion	The coefficient of variation is less than 2%, and the recovery average interval of confidence (CI = 100.63% ± 4.21) includes 100%, so the method is accurate.	
•Notes:		
Coefficient of variation	Recovery	Confidence interval [64]
$CV = \frac{STD}{\bar{x}} \times 100$	$Recovery = \frac{RC}{AC} \times 100$	$\bar{x} - t(1 - \frac{\alpha}{2}, v)STD/\sqrt{n} < m < \bar{x} + t(1 - \frac{\alpha}{2}, v)STD/\sqrt{n}$
STD: Standard deviation	RC: Recovered concentration	m: Confidence interval average
\bar{x} : Recovery average	AC: Added concentration	$t_{(1-\alpha/2, k-1)}$: $t_{critical}$ value, it is read on one-tailed Student table (with, α : risk = 0.05); v: degree of liberty, $v = k - 1$; k: number of recovered concentration levels

Table 13. Results of the specificity study further to the regression curve representing recovered concentrations as a function of added concentrations – Genistein in the EAE of *Retama monosperma* flowers

Slope a^*	Standard deviation of the slope S_a^*	Intercept b^*	Standard deviation of the intercept S_b^*	$t_{calculated}$ for the test of the hypothesis of “the slope is equivalent to 1”***	$t_{calculated}$ for the test of the hypothesis of “the intercept b equivalent to 0”***	Critical value of Student test $t_{(0.01, 1)}$
1.00	0.01	-0.08	1.61	0.03	0.05	63.66
Acceptance criteria	The slope of the regression curve is equivalent to 1 if $t_{calculated}$ is less than $t_{(\alpha, k-2)}$ read on a two-tailed Student table (with k: number of concentration levels; α : risk = 0.01) [48]					
Conclusion	The intercept of the regression curve is equivalent to 0 if $t_{calculated}$ is less than $t_{(\alpha, k-2)}$ read on a two-tailed Student table (with, k: number of concentration levels; α : risk = 0.01) [48]					
	The slope of the regression curve is equivalent to 1					
	The intercept of the regression curve is equivalent to 0					

•Notes: $y = (a \times x) + b$ (y: recovered concentration (mg/L); x: added concentration (mg/L)); *Calculated using the LINEST function in Microsoft Excel; **Calculated with the following equation [48]: $t = \frac{|a-1|}{S_a}$; *** Calculated with the following equation [48]: $t = \frac{|b|}{S_b}$

Table 14. Results of the specificity study further the two calibration curves (without matrix and with matrix) – Genistein in the EAE of *Retama monosperma* flowers

Calibration curve without matrix		Calibration curve with matrix		$t_{calculated}^{**}$	Critical value of Student test $t_{(0.95, 5)}$
Slope a^*	Standard deviation of the slope S_a^*	Slope a'^*	Standard deviation of the slope $S_a'^*$		
24349.22	156.18	24364.42	400.98	0.04	2.02
Acceptance criteria	The two slopes are equal if $t_{calculated}$ is less than or equal to $t_{(1-\alpha/2, k + k' - 4)}$ read on one-tail Student table				
Conclusion	The two slopes are equal				

•Notes: *Calculated using the LINEST function in Microsoft Excel; Calibration curve without matrix $y = (a \times x) + b$ (y: peak area; x: concentration (mg/L)); Calibration curve with matrix $y = (a' \times x) + b'$ (y: peak area; x: added concentration (mg/L)); **Calculated with the following equation [66]: $t_{calculated} = \frac{|a-a'|}{\sqrt{S_a^2 + S_a'^2}}$; k is the number of the concentration levels used for the calibration curve without matrix; k' is the number of the concentration levels used for the calibration curve with matrix; α : risk = 0.1

Recovery

In this paper, we will deal with an example of the recovery test which concerns the matrix of *R. monosperma* flowers of the ethyl acetate extract. This test can be used to assess the accuracy of the method (Table

12) but also, by some authors [47], to confirm specificity (Table 13-14).

The concentration after addition was calculated using the calibration curve results for the linearity test. Further to the statistical tests carried out, of which the

results are presented in Tables 13 and 14, we can confirm that the method is specific.

■ CONCLUSION

Extracts characterization using UHPLC/DAD/ESI-MS showed i) the richness of *R. monosperma* of flavonol, isoflavone and flavone, ii) the presence of flavonol glycoside in *R. communis*, iii) the richness of *B. vulgaris* of galloyl-glucose and phenolic acids. These plant extracts have a high antioxidant capacity due to the presence of phenolic compounds. The higher capacity concerns *R. communis* methanolic extract with IC₅₀ of 12.5, 29.59, and 50.3 µg/mL for DPPH assay, conjugated diene, and TBARS assay, respectively. As an important step to ensure the quality of analytical results, this paper presented the performance criteria of the validated method using UHPLC/DAD/ESI-MS and focusing on six polyphenols known as antioxidant standards (gallic acid, vanillic acid, *p*-coumaric acid, rutin, quercetin, and genistein). The results of all released tests in the process of method validation are very satisfactory. In short, the polyphenol content of the plants studied in this article makes them an important subject for future research realized by industries, such as pharmaceuticals and cosmetics, seeking to exploit natural products such as plants to develop products with high antioxidant activity.

■ AUTHOR CONTRIBUTIONS

Meriem Outaki, Manal Zefzoufi and Amal Sammama contributed equally to this work. Meriem Outaki prepared the experimental plan for the "method validation" part. Manal Zefzoufi prepared the experimental plan for the "antioxidant activity" part. Meriem Outaki, Manal Zefzoufi, Amal Sammama and Khadija El Gadali carried out the experiments in the laboratory and performed the necessary calculations. All the authors wrote the paper (each a part) and revised it. All authors agreed to the final version of this manuscript.

■ REFERENCES

- [1] Nasim, N., Sandeep, I.S., and Mohanty, S., 2022, Plant-derived natural products for drug discovery: Current approaches and prospects, *Nucleus*, 65 (3), 399–411.
- [2] Dastan, S.D., 2023, Chemical and functional composition and biological activities of Anatolian *Hypericum scabrum* L. plant, *J. Mol. Struct.*, 1275, 134561.
- [3] Oglah, M.K., Mustafa, Y.F., Bashir, M.K., and Jasim, M.H., 2020, Curcumin and its derivatives: A review of their biological activities, *Syst. Rev. Pharm.*, 11 (3), 472–481.
- [4] Ismael, R.N., Mustafa, Y.F., and Al-Qazaz, H.K., 2022, Cancer-curative potential of novel coumarins from watermelon princess: A scenario of their isolation and activity, *Eurasian Chem. Commun.*, 4, 657–672.
- [5] Loukmas, S., Kerak, E., Outaki, M., Belaqziz, M., and Harrak, H., 2020, Assessment of minerals, bioactive compounds, and antioxidant activity of ten Moroccan pomegranate cultivars, *J. Food Qual.*, 2020, 8844538.
- [6] Loukmas, S., Outaki, M., Ettalibi, F., Kharbouch, H.A., Kerak, E., and Harrak, H., 2021, Physicochemical criteria, bioactive compounds, antioxidant activity and sensory attributes of ten Moroccan pomegranate cultivars, *Eur. J. Hortic. Sci.*, 86 (4), 339–353.
- [7] Rachmayanti, Y., Firmansyah, D., Umma, R.R., Hertanto, D.M., Sudiana, I.K., Santoso, D., Nandika, D., Karlinasari, L., Arinana, A., Batubara, I., and Witasari, L.D., 2022, Antioxidant activity of fungus comb extracts isolated from Indo-Malayan termite *Macrotermes gilvus* Hagen (Isoptera: Termitidae), *Indones. J. Chem.*, 22 (6), 1693–1704.
- [8] Efdi, M., Pratama, D., Itam, A., and Okselni, T., 2022, Antioxidant flavonoid glycoside from leaves of cacao mistletoe (*Scurrula ferruginea* (Jack) Danser), *Indones. J. Chem.*, 22 (4), 944–952.
- [9] Benmekhbi, L., Mosbah, S., Laamraoui, H., Hamlaoui, I., Bencheriet, S., and Ibrahim, D., 2022, Evaluation of phytochemical properties and biological activities of leaf extracts and oil of *Petroselinum sativum* collected from Algeria, *Indones. J. Chem.*, 22 (6), 1566–1573.
- [10] Chandrasekara, A., and Josheph Kumar, T., 2016, Roots and tuber crops as functional foods: A review

- on phytochemical constituents and their potential health benefits, *Int. J. Food Sci.*, 2016, 3631647.
- [11] Jo, B.G., Bong, S.K., Jegal, J., Kim, S.N., and Yang, M.H., 2020, Antiallergic effects of phenolic compounds isolated from *Stellera chamaejasme* on RBL-2H3 cells, *Nat. Prod. Commun.*, 15 (7), 1934578X20942352.
- [12] Mustafa, Y.F., 2023, Harmful free radicals in aging: A narrative review of their detrimental effects on health, *Ind. J. Clin. Biochem.*, s12291-023-01147-y.
- [13] Luo, K.W., Ko, C.H., Yue, G.G.L., Lee, J.K.M., Li, K.K., Lee, M., Li, G., Fung, K.P., Leung, P.C., and Lau, C.B.S., 2014, Green tea (*Camellia sinensis*) extract inhibits both the metastasis and osteolytic components of mammary cancer 4T1 lesions in mice, *J. Nutr. Biochem.*, 25 (4), 395–403.
- [14] Chandra, S., Gahlot, M., Choudhary, A.N., Palai, S., de Almeida, R.S., de Vasconcelos, J.E.L., dos Santos, F.A.V., de Farias, P.A.M., and Coutinho, H.D.M., 2023, Scientific evidences of anticancer potential of medicinal plants, *Food Chem. Adv.*, 2, 100239.
- [15] Lee, C.C., Dudonné, S., Dubé, P., Desjardins, Y., Kim, J.H., Kim, J.S., Kim, J.E., Park, J.H.Y., Lee, K.W., and Lee, C.Y., 2017, Comprehensive phenolic composition analysis and evaluation of Yak-Kong soybean (*Glycine max*) for the prevention of atherosclerosis, *Food Chem.*, 234, 486–493.
- [16] Khali, R.R., Mohammed, E.T., and Mustafa, Y.F., 2021, Various promising biological effects of cranberry extract: A review, *Clin. Schizophr. Relat. Psychoses*, 15, S6.
- [17] Mallmann, L.P., O. Rios, A., and Rodrigues, E., 2023, MS-FINDER and SIRIUS for phenolic compound identification from high-resolution mass spectrometry data, *Food Res. Int.*, 163, 112315.
- [18] Prasetyaningrum, A., Jos, B., Ratnawati, R., Rokhati, N., Riyanto, T., and Prinanda, G.R., 2022, Sequential microwave-ultrasound assisted extraction of flavonoid from *Moringa oleifera*: Product characteristic, antioxidant and antibacterial activity, *Indones. J. Chem.*, 22 (2), 303–316.
- [19] Rusli, R., Ningsih, B.A., Rahmadani, A., Febrina, L., Maulidya, V., and Fadraersada, J., 2019, Isolation and antioxidant and antibacterial activity of flavonoid from *Ficus variegata* Blume, *Indones. J. Chem.*, 19 (2), 538–543.
- [20] Dias, R., Oliveira, H., Fernandes, I., Simal-Gandara, J., and Perez-Gregorio, R., 2021, Recent advances in extracting phenolic compounds from food and their use in disease prevention and as cosmetics, *Crit. Rev. Food Sci. Nutr.*, 61 (7), 1130–1151.
- [21] Peterson, D.M., 2001, Oat antioxidants, *J. Cereal Sci.*, 33 (2), 115–129.
- [22] Boulanouar, B., Abdelaziz, G., Aazza, S., Gago, C., and Miguel, M.G., 2013, Antioxidant activities of eight Algerian plant extracts and two essential oils, *Ind. Crops Prod.*, 46, 85–96.
- [23] Abd El-Wahab, M., and El-Desouky, M.G., 2022, Study the effect of antioxidants on biological activity and on homopolypropylene; Mechanical and physical properties, *J. Indian Chem. Soc.*, 99 (12), 100764.
- [24] Sharifi-Rad, M., Anil Kumar, N.V., Zucca, P., Varoni, E.M., Dini, L., Panzarini, E., Rajkovic, J., Tsouh Fokou, P.V., Azzini, E., Peluso, I., Prakash Mishra, A., Nigam, M., El Rayess, Y., Beyrouthy, M.E., Polito, L., Iriti, M., Martins, N., Martorell, M., Docea, A.O., Setzer, W.N., Calina, D., Cho, W.C., and Sharifi-Rad, J., 2020, Lifestyle, oxidative stress, and antioxidants: Back and forth in the pathophysiology of chronic diseases, *Front. Physiol.*, 11, 00694.
- [25] Zhang, Y., Li, Y., Ren, X., Zhang, X., Wu, Z., and Liu, L., 2023, The positive correlation of antioxidant activity and prebiotic effect about oat phenolic compounds, *Food Chem.*, 402, 134231.
- [26] Jalloul, A.B., Garzoli, S., Chaar, H., el Jribi, C., and Abderrabba, M., 2023, Seasonal effect on bioactive compounds recovery using aqueous extraction, antioxidant activities, and volatile profiles of different parts of *Scabiosa maritima* L. (= *Scabiosa atropurpurea* subsp. *maritima* (L.) Arcang.), *S. Afr. J. Bot.*, 152, 63–79.
- [27] Yang, J., Qian, S., Na, X., and Zhao, A., 2023, Association between dietary and supplemental antioxidants intake and lung cancer risk: Evidence

- from a cancer screening trial, *Antioxidants*, 12 (2), 338.
- [28] Rudrapal, M., Khairnar, S.J., Khan, J., Dukhyil, A.B., Ansari, M.A., Alomary, M.N., Alshabrimi, F.M., Palai, S., Deb, P.K., and Devi, R., 2022, Dietary polyphenols and their role in oxidative stress-induced human diseases: insights into protective effects, antioxidant potentials and mechanism(s) of action, *Front. Pharmacol.*, 13, 806470.
- [29] Chaudhary, P., Janmeda, P., Docea, A.O., Yeskaliyeva, B., Abdull Razis, A.F., Modu, B., Calina, D., and Sharifi-Rad, J., 2023, Oxidative stress, free radicals and antioxidants: Potential crosstalk in the pathophysiology of human diseases, *Front. Chem.*, 11, 1158198.
- [30] Mariem, S., Hanen, F., Inès, J., Mejdj, S., and Riadh, K., 2014, Phenolic profile, biological activities and fraction analysis of the medicinal halophyte *Retama raetam*, *S. Afr. J. Bot.*, 94, 114–121.
- [31] Santos, P.M., Batista, D.L.J., Ribeiro, L.A.F., Boffo, E.F., de Cerqueira, M.D., Martins, D., de Castro, R.D., de Souza-Neta, L.C., Pinto, E., Zambotti-Villela, L., Colepicolo, P., Fernandez, L.G., Canuto, G.A.B., and Ribeiro, P.R., 2018, Identification of antioxidant and antimicrobial compounds from the oilseed crop *Ricinus communis* using a multiplatform metabolite profiling approach, *Ind. Crops Prod.*, 124, 834–844.
- [32] Eroğlu, A.Y., Çakır, Ö., Sağdıç, M., and Dertli, E., 2020, Bioactive characteristics of wild *Berberis vulgaris* and *Berberis crataegina* fruits, *J. Chem.*, 2020, 8908301.
- [33] Tuyen, P.N.K., Linh, T.T.T., Son, D.V., Thang, N.V., Son, D.V., Trang, N.T.Q., Chi, H.B.L., Ky, N.D.X., Phat, N.T., and Duong, H.T., 2020, Phenolic compounds from the leaves of *Ricinus communis* Linn, *VNUHCM Sci. Technol. Dev.*, 23 (3), 694–698.
- [34] Zefzoufi, M., Fdil, R., Bouamama, H., Gadhi, C., Katakura, Y., Mouzdahir, A., and Sraidi, K., 2021, Effect of extracts and isolated compounds derived from *Retama monosperma* (L.) Boiss. on anti-aging gene expression in human keratinocytes and antioxidant activity, *J. Ethnopharmacol.*, 280, 114451.
- [35] Kiliç, I., and Yeşiloğlu, Y., 2013, Spectroscopic studies on the antioxidant activity of *p*-coumaric acid, *Spectrochim. Acta, Part A*, 115, 719–724.
- [36] Mozaffari Godarzi, S., Valizade Gorji, A., Gholizadeh, B., Mard, S.A., and Mansouri, E., 2020, Antioxidant effect of *p*-coumaric acid on interleukin 1- β and tumor necrosis factor- α in rats with renal ischemic reperfusion, *Nefrología*, 40 (3), 311–319.
- [37] Salau, V.F., Erukainure, O.L., Ibeji, C.U., Olasehinde, T.A., Koobanally, N.A., and Islam, M.S., 2020, Vanillin and vanillic acid modulate antioxidant defense system via amelioration of metabolic complications linked to Fe²⁺-induced brain tissues damage, *Metab. Brain Dis.*, 35 (5), 727–738.
- [38] Enogieru, A.B., Haylett, W., Hiss, D.C., Bardien, S., and Ekpo, O.E., 2018, Rutin as a potent antioxidant: implications for neurodegenerative disorders, *Oxid. Med. Cell. Longevity*, 2018, 6241017.
- [39] Rahman Mazumder, M.A., and Hongsprabhas, P., 2016, Genistein as antioxidant and antibrowning agents in *in vivo* and *in vitro*: A review, *Biomed. Pharmacother.*, 82, 379–392.
- [40] Badhani, B., Sharma, N., and Kakkar, R., 2015, Gallic acid: A versatile antioxidant with promising therapeutic and industrial applications, *RSC Adv.*, 5 (35), 27540–27557.
- [41] Puigventós, L., Navarro, M., Alechaga, É., Núñez, O., Saurina, J., Hernández-Cassou, S., and Puignou, L., 2015, Determination of polyphenolic profiles by liquid chromatography-electrospray-tandem mass spectrometry for the authentication of fruit extracts, *Anal. Bioanal. Chem.*, 407 (2), 597–608.
- [42] Malki, F., Alouache, A., and Krimat, S., 2023, Effects of various parameters on the antioxidant activities of the synthesized heterocyclic pyrimidinium betaines, *Indones. J. Chem.*, 23 (1), 90–100.
- [43] Kleinveld, H.A., Hak-Lemmers, H.L., Stalenhoef, A.F., and Demacker, P.N., 1992, Improved measurement of low-density-lipoprotein susceptibility to copper-induced oxidation: Application of a short procedure for isolating low-density lipoprotein, *Clin. Chem.*, 38 (10), 2066–2072.

- [44] Ohkawa, H., Ohishi, N., and Yagi, K., 1979, Assay for lipid peroxides in animal tissues by thiobarbituric acid reaction, *Anal. Biochem.*, 95 (2), 351–358.
- [45] El Abbouyi, A., Khelifi, S., El Hachimi, Y., Khalil, A., Es-Safi, N., Belahyan, A., Tellal, R., and El Abbouyi, A., 2006, *In vitro* antioxidant properties of *Salvia verbenaca* L. hydromethanolic extract, *Indian J. Pharmacol.*, 38 (4), 276–280.
- [46] Abraham, J., 2009, “International Conference on Harmonisation of Technical Requirements for Registration of Pharmaceuticals for Human Use” in *Handbook of Transnational Economic Governance Regimes*, Eds. Brouder, A., and Tietje, C., Brill, Leiden, Netherland, 1041–1054.
- [47] Feinberg, M., 2001, *Validation Interne des Méthodes d’Analyse*, Techniques de l’Ingénieur, P224: 1–23.
- [48] OIV, 2005, Guide pratique pour la validation, le contrôle qualité, et l’estimation de l’incertitude d’une méthode d’analyse œnologique alternative, Recueil des Méthodes Internationales d’Analyses – OIV Guide de validation – Contrôle qualité, International Organization of Vine and Wine, Dijon, France, OIV-MA-AS1-12.
- [49] Mayor, M., and Bourrié, G., 2010, “Validation d’une méthode de chimie analytique - Application au dosage des anions fluorure, chlorure, nitrite, bromure, nitrate, phosphate et sulfate par chromatographie ionique” in *Validation des méthodes d’analyse quantitative par le profil d’exactitude*, Le Cahier des Techniques de l’Inra, 117–134.
- [50] Bouaissi, W., Abidi, M., and Ben Hamida, N., 2013, Optimisation et validation d’une méthode de dosage par HPLC/DAD d’un antihypertenseur le Zofenopril, *J. Soc. Chim. Tunis.*, 15, 39–50.
- [51] González-Mauraza, H., Martín-Cordero, C., Alarcón-de-la-Lastra, C., Rosillo, M.A., León-González, A.J., and Sánchez-Hidalgo, M., 2014, Anti-inflammatory effects of *Retama monosperma* in acute ulcerative colitis in rats, *J. Physiol. Biochem.*, 70 (1), 163–172.
- [52] Kim, D.O., and Lee, C.Y., 2004, Comprehensive study on vitamin C equivalent antioxidant capacity (VCEAC) of various polyphenolics in scavenging a free radical and its structural relationship, *Crit. Rev. Food Sci. Nutr.*, 44 (4), 253–273.
- [53] Wafa, G., Amadou, D., Larbi, K.M., and Héla, E.F.O., 2014, Larvicidal activity, phytochemical composition, and antioxidant properties of different parts of five populations of *Ricinus communis* L., *Ind. Crops Prod.*, 56, 43–51.
- [54] El khalki, L., Tilaoui, M., Jaafari, A., Ait Mouse, H., and Zyad, A., 2018, Studies on the dual cytotoxicity and antioxidant properties of *Berberis vulgaris* extracts and its main constituent berberine, *Adv. Pharmacol. Sci.*, 2018, 3018498.
- [55] Yang, L., Zhang, Z., Hu, X., You, L., Khan, R.A.A., and Yu, Y., 2022, Phenolic contents, organic acids, and the antioxidant and bio activity of wild medicinal *Berberis* plants- as sustainable sources of functional food, *Molecules*, 27 (8), 2497.
- [56] Jebir, R.M., and Mustafa, Y.F., 2022, Watermelon allsweet: A promising natural source of bioactive products, *J. Med. Chem. Sci.*, 5 (5), 652–666.
- [57] Yisimayili, Z., Abdulla, R., Tian, Q., Wang, Y., Chen, M., Sun, Z., Li, Z., Liu, F., Aisa, H.A., and Huang, C., 2019, A comprehensive study of pomegranate flowers polyphenols and metabolites in rat biological samples by high-performance liquid chromatography quadrupole time-of-flight mass spectrometry, *J. Chromatogr. A*, 1604, 460472.
- [58] Saada, M., Falleh, H., Catarino, M., Cardoso, S., and Ksouri, R., 2018, Plant growth modulates metabolites and biological activities in *Retama raetam* (Forssk.) Webb, *Molecules*, 23 (9), 2177.
- [59] Chouhan, H.S., Swarnakar, G., and Jogpal, B., 2021, Medicinal properties of *Ricinus communis*: A review, *Int. J. Pharm. Sci. Res.*, 12 (7), 3632–3642.
- [60] Żymanińczyk-Duda, E., Szmigiela-Merena, B., Brzezińska-Rodak, M., and Klimek-Ochab, M., 2018, Natural antioxidants—properties and possible applications, *J. Appl. Biotechnol. Bioeng.*, 5 (4), 251–258.
- [61] Iqbal, J., Zaib, S., Farooq, U., Khan, A., Bibi, I., and Suleman, S., 2012, Antioxidant, antimicrobial, and free radical scavenging potential of aerial parts of

- Periploca aphylla* and *Ricinus communis*, *ISRN Pharmacol.*, 2012, 563267.
- [62] Singh, P.P., Ambika, A., and Chauhan, S.M.S., 2009, Activity guided isolation of antioxidants from the leaves of *Ricinus communis* L., *Food Chem.*, 114 (3), 1069–1072.
- [63] Nuralin, L., and Gürü, M., 2022, *Berberis vulgaris* fruit: Determination of phenolic compounds in extracts obtained by supercritical CO₂ and Soxhlet methods using HPLC, *Food Anal. Methods*, 15 (4), 877–889.
- [64] Bouklouze, A., and Digua, K., 2006, Démarche statistique de la validation analytique dans le domaine pharmaceutique (Méthodologie et exemple pratique), *Les technologies de laboratoire*, 1 (1), 20–24.
- [65] Nascu, H., Jäntschi, L., Hodisan, T., Cimpoi, C., and Cimpan, G., 1999, Some applications of statistics in analytical chemistry, *Rev. Anal. Chem.*, 18 (6), 409–456.
- [66] Andrade, J.M., and Estévez-Pérez, M.G., 2014, Statistical comparison of the slopes of two regression lines: A tutorial, *Anal. Chim. Acta*, 838, 1–12.
- [67] OIV, 2005, *Practical guide for the validation, quality control, and uncertainty assessment of an alternative oenological analysis method*, Compendium of International Analysis of Methods - OIV Guide for the validation – quality Control, International Organization of Vine and Wine, Dijon, France, OIV-MA-AS1-12.
- [68] OIV, 2000, *Estimation de la limite de détection et de quantification d'une méthode d'analyse*, Recueil international des méthodes d'analyses – OIV Estimation de la limite de détection et de quantification, International Organization of Vine and Wine, Dijon, France, OIV-MA-AS1-10.

Phenolic Compounds from Moroccan *Retama monosperma* L. Boiss, *Berberis vulgaris* L. and *Ricinus communis* L.: Characterization, Antioxidant Activity and Performance Criteria of the Validated Method Using UHPLC/DAD/ESI-MS

Meriem Outaki^{1*}, Manal Zefzoufi², Amal Sammama³, Khadija El Gadali⁴, Rabiaa Fdil², and Layla El Gaini^{3,5}

¹Laboratory of Applied Chemistry and Environment, Faculty of Sciences and Technologies, University Hassan I, PC. 577, Settat, Morocco

²Laboratory of Bioorganic Chemistry, Department of Chemistry, Faculty of Sciences, University Chouaib Doukkali, PC. 20, El Jadida, Morocco

³Center of Analysis and Characterization, University Cadi Ayyad, PC. 511, Marrakech, Morocco

⁴Laboratory of Sustainable Development and Health Research, Faculty of Sciences and Technologies, University Cadi Ayyad, PC. 549, Marrakech, Morocco

⁵Laboratory of Applied Chemistry and Biomass, Department of Chemistry, Faculty of Sciences Semlalia, University Cadi Ayyad, PC. 2390, Marrakech, Morocco

* **Corresponding author:**

email: meriem.outaki@gmail.com

Received: July 22, 2023

Accepted: September 12, 2023

DOI: 10.22146/ijc.87157

Abstract: Components of medicinal plants have many pharmacological activities, including antioxidant activity, playing an important role in limiting oxidative stress that can cause several damages. This paper characterizes polyphenols of *Retama monosperma* L., *Berberis vulgaris* L. and *Ricinus communis* L. plant extracts and evaluates their antioxidant activity by DPPH, conjugated diene and TBARS assay. To ensure the quality of analytical results, this paper presents performance criteria of the validated method using UHPLC/DAD/ESI-MS. Regarding method validation, the results confirm different used tests and evaluate detection and quantification limits. Concerning the characterization and study of antioxidant activity, realized testing showed that *R. monosperma* is rich in isoflavone, flavone and flavonol. For *R. communis*, we notice the presence of rutin as a major compound. Meanwhile, *B. vulgaris* contains significant amounts of gallic acid and p-coumaric acid. These plant extracts have high antioxidant activity due to the presence of phenolic compounds.

Keywords: polyphenol; antioxidant activity; method validation; UHPLC/DAD/ESI-MS

■ INTRODUCTION

Since ancient times, many plants have attracted interest as sources of natural products [1]. Various plants have been used not only as a food source but also as medicine. The benefits of these practices are known to be supported by many scientific studies [2-4]. It is known that the vast majority of active ingredients in medicines are obtained from plants. Phytotherapy is once again in the spotlight because of the possible adverse effects of synthetic drugs and the multiple benefits obtained from

plant-based medicines [2]. Medicinal plants produce several secondary metabolites like phenols, flavonoids, quinones, and tannins with numerous promising pharmacological activities, such as antioxidant [5-9], anti-inflammatory [10], anti-allergic [11], anticancer, antitumor [12-14], and anti-atherosclerosis [15]. They also provide cardiovascular protection [16]. More specifically, polyphenolic compounds are the most studied plant secondary metabolites due to their abundance and possible positive effects on human health [17]. They have received considerable attention in recent years

because they are considered high-added-value molecules due to their antioxidant and antimicrobial effects [18-19]. Their potential use in the formulation of cosmetics, and as an alternative to chemical food additives, has drawn the attention of a number of researchers. Some of these compounds have also been explored in the packaging and textile industries [20].

In this paper, we will be focusing on antioxidant activity, which acts against oxidative stress. In the human body, environmental radiation splits water to form hydroxyl radicals, and normal metabolism produces oxygen radicals [21]. Oxidative stress is an imbalance between reactive oxygen species formation and antioxidant defense mechanisms. If cellular antioxidants do not eliminate free radicals, the latter can react with different macromolecules [22-23]. At their high concentrations, free radicals attack and damage proteins, lipids, and nucleic acids, thereby causing many health problems. Over time, free radicals can cause a negative chain reaction in the human body, which can block the action of key enzymes, destroy the cell membrane, prevent normal cell division, avoid cellular processes necessary for proper body functioning, and block energy production [24]. Also, these free radicals cause DNA damage and lipid peroxidation, leading to cancerous cells [21]. The human body possesses a natural defense system against these free radicals [21-22]. Once the excessive generation of free radicals attacks the internal antioxidant defense system, external antioxidants are needed to prevent oxidative damage [25]. Antioxidants are considered molecules that prevent the formation of free radicals and seek to neutralize or repair the damage they cause [24].

The biological activities of many phytochemicals are attributed to their antioxidant properties [21]. Experimental and epidemiological evidence shows that dietary antioxidants, such as flavonoids and other phenolic compounds, are also important components of the body's defense [21]. Several studies support a direct link between the antioxidant properties of extracts and the medicinal benefits of plants and their potential use as an alternative to chemical preservatives [26]. Phenolic antioxidants have been reported to inhibit DNA fragmentation. Studies on animal and cell cultures

confirm the anti-cancer effects of antioxidants; epidemiological studies show that high consumption of antioxidant-rich foods is inversely related to cancer risk [27]. Evidence from various *in vitro* studies supports a potential protective role for dietary polyphenols in the prevention of cardiovascular disease, neurodegenerative disease, cancer, diabetes, inflammation-related, and infectious diseases [28]. In addition to their importance in the diet, antioxidants can also contribute to the stability and taste of food products. From a plant specialist's point of view, their role in the plant as a defense against biotic and abiotic stresses must also be taken into account [21]. All these benefits justify the considerable interest in researching safe natural antioxidants which are in high demand by the pharmaceutical industry and as food preservatives [29].

Therefore, it is important to study the phenolic composition of various plant extracts and assess their antioxidant activity in order to provide scientific results that would greatly support different sectors such as pharmaceuticals, cosmetics, and food industry. This revelation would be an excellent addition to the scientific literature.

It is within this context that this paper falls. It presents the chemical composition of extracts of three medicinal and aromatic plants: *Retama monosperma*, *Ricinus communis*, and *Berberis vulgaris* followed by an evaluation of the antioxidant activity of their phenolic compounds. For nutritional purposes, many scientific studies have been conducted on the chemical composition of these plant extracts grown in various parts of the world and which are of great interest [30-34]. However, this paper is the first to characterize different extracts of these plants growing in Morocco. Therefore, a lot of effort has been engaged in developing different techniques and methods for the identification of phenolic compounds from natural resources. In most cases, these compounds are analyzed by high-performance liquid chromatography-mass spectrometry (HPLC-MS) and HPLC-diode-array detector (HPLC-DAD). As an important step to ensure the quality of analytical results and to provide researchers with performance criteria, the authors followed a process for

validation of the method chosen for the characterization and quantification of polyphenols before use. The validation process was focused on six polyphenols known as antioxidant standards, such as gallic acid, vanillic acid, *p*-coumaric acid, rutin, quercetin, and genistein [35-40].

This paper details the tests that were carried out, such as specificity, linearity, repeatability, intermediate precision, detection limit, quantification limit, and recovery. It also details the statistical methods used because they are often perceived as a constraint since they are generally poorly used by analysts. The objective of publishing this paper, with supplementary material, is also to provide people wishing to perform a method validation with a document that describes in detail the followed approach, avoiding them to search several references to first understand the experimental plan to be implemented and several others to subsequently find the statistical methods to apply.

■ EXPERIMENTAL SECTION

Materials

Chemical materials

The materials used in this study were methanol (HPLC grade $\geq 99.9\%$ from Honeywell Riedel-de Haen, Germany) used as solvent B and 0.1% formic acid (98% for LC-MS, Merck Germany) aqueous solution (ultra-pure water from Pure Lab) used as solvent A. The gallic acid was purchased from Merck (Germany), and the other phenolic compounds (vanillic acid, *p*-coumaric acid, rutin, quercetin, and genistein) were purchased from Sigma-Aldrich (USA). The 2,2-diphenyl-2'-picrylhydrazyl (DPPH), linoleic acid, ethylenediaminetetraacetic acid (EDTA), thiobarbituric acid, and trichloroacetic acid (Sigma-Aldrich, USA) were used as an antioxidant reagent and the butylated hydroxytoluene (BHT, Merck Germany) as antioxidant standard.

Plant materials

R. monosperma flowers and seeds were collected in February and April 2017, respectively, from Al-Haouzia forest in the region of El Jadida-Morocco. *R. communis* leaves were collected in February 2018 in the region of El Jadida-Morocco. These plant materials were identified by Dr. Fennane from the Scientific Institute of Rabat,

Morocco. A voucher specimen (77816 RAB) was deposited in the Herbarium of the Institute. For the *B. vulgaris*, root was collected in March 2019 in the region of Marrakech-Morocco. This plant material was identified by Dr. Ouhamou from the Faculty of Sciences, Cadi Ayyad University, Marrakech, Morocco.

Instrumentation

The instrumentations used in this study were chromatographic separation performed on Dionex Ultimate 3000 UHPLC-DAD system (CA, USA), equipped with a quaternary pump (HPG-3400RS), an autosampler (WPS-3000TSL), and a column oven (TCC-3000). A Vertex plus C18 reversed-phase column (250 \times 4.6 mm, Eurospher II 100-5) provided by Knauer was used for the proposed method. The mass spectrometer was a TSQ Endura (Thermo Fisher Scientific) triple quadrupole equipped with heated-electrospray ionization (H-ESI).

Procedure

Extraction

The flowers (600 g) and seeds (400 g) of *R. monosperma* were air-dried for two weeks. The extraction was performed three times by maceration (room temperature, 3 d) with 2 L of *n*-hexane to remove lipophilic compounds. After evaporation of *n*-hexane under vacuum, the resulting mark was extracted three times by maceration with 2 L of ethyl acetate (room temperature, 3 d) for flowers and 2 L of diethyl ether for seeds (room temperature, 3 d). The resulting extract was then evaporated using a rotary evaporator.

R. communis leaves (200 g) and *B. vulgaris* roots (300 g) were air-dried for two weeks. Each sample was extracted using Soxhlet and methanol as solvent. The extracts were evaporated under reduced pressure to give methanol crude extracts. This later was solubilized in water and extracted with ethyl acetate. The resulting extract was then evaporated using a rotary evaporator.

UHPLC-DAD-ESI/MS method

The separation gradient was created using solvent A (0.1% formic aqueous solution) and solvent B (methanol), as shown in Table 1. The mobile phase flow rate was 1 mL/min. The injection volume was 10 μ L, and

Table 1. UHPL-DAD separation gradient

Time (min)	% of solvent B	Time (min)	% of solvent B
0	5	18	54
3	25	22	54
6	25	26	95
9	37	29	95
13	37	29.15	5
		31	5

the wavelength was 280 nm. For the LC-MS experiment, negative mode was used. Sheath gas, ion sweep gas, and auxiliary gas were nitrogen (purity > 99.98%) at flow rates of 65, 0, and 40 arbitrary units (a.u.), respectively. The vaporizer temperature and ion transfer tube temperature were set at 350 °C. The electrospray voltage was set at -2.5 kV. Full scan MS acquisition mode (m/z 100–1000) in Q1 (mass resolution of 0.7 m/z full-width half maximum (FWHM)) with a scan time of 0.5 s was used [41].

Antioxidant activity

DPPH-radical scavenging activity. Free radical-scavenging activity of *R. monosperma*, *B. vulgaris*, and *R. communis* extracts was evaluated using a modified DPPH method. One milliliter of concentrations of samples (5–100 µg/mL) was added to 1 mL of DPPH solution (40 µg/mL), and the mixture was incubated for 30 min [42]. Afterward, the absorbance was measured at 517 nm in a UV spectrophotometer. BHT, rutin, gallic acid, and quercetin were used as a standard antioxidant. Scavenging activity was expressed as IC₅₀, an effective concentration in µg/mL of samples or standard that reduces the absorbance of DPPH by 50 % when compared with negative control. The experiment was carried out in triplicate.

Conjugate diene scavenging activity. Conjugate diene scavenging activity was determined by UV absorbance [43]. A linoleic acid emulsion was prepared in tampon phosphate at pH 7 (10 mM; 10 mL) mixed with the linoleic acid (5.96 µL) and tween 20 (0.1%; 10 mL). Linoleic acid emulsion (1 mL) was added to various concentrations of studies extracts (5–100 µg/mL) and 100 µL of CuSO₄ (1.6 g/L). After that, the mixture was incubated at 37 °C in the dark for 1 h. To stop the reaction, 10 µL of EDTA and 10 µL of BHT (1 mg/mL) were added to the mixture. Then, the absorbance was

measured at 234 nm. The conjugate diene scavenging activity was calculated using Eq. (1).

$$\text{Scavenging activity (\%)} = \frac{A_0 - A_1}{A_0} \times 100 \quad (1)$$

A₀ is the absorbance of the control (sample without extracts), and A₁ is the absorbance of the sample. The results were expressed as IC₅₀. The experiment was carried out in triplicate.

Thiobarbituric acid-reactive substances assay.

The thiobarbituric acid-reactive substances (TBARS) assay determined the inhibition of lipid peroxidation according to Ohkawa method [44] with some modifications [45]. A 1 mL of linoleic acid emulsion was added to various concentrations of extracts (5–100 µg/mL) and 100 µL of CuSO₄ (1.6 g/L), and then was left to incubate at 37 °C in the dark for 3 h. The reaction was stopped by putting the mixture of products and reagents in ice and adding 10 µL of EDTA (20 mM). Then, 1 mL of TBA (0.78%) and 1 mL of trichloroacetic acid (TCA 20%) were added to the mixture which was incubated at 95 °C in the dark for 45 min. The *n*-butanol (0.8 mL) was added to the mixture. The absorbance was measured at 532 nm in a UV spectrophotometer. The estimation of TBARS was calculated using Eq. (1). Scavenging activity was expressed as IC₅₀. The experiment was carried out in triplicate.

Method validation

As an important step to ensure the quality of analytical results and to provide researchers with performance criteria, the authors followed a process for validation of the method chosen for the characterization and quantification of polyphenols before use. The validation process was focused on six polyphenols known as antioxidant standards, such as gallic acid, vanillic acid, *p*-coumaric acid, rutin, quercetin, and genistein. Method validation was carried out using the five extracts that contain one or two compounds of interest (Table 2).

The experimental plan of method validation is presented in Table 3. It concerns several studies such as specificity, linearity, repeatability, intermediate precision, detection limit, and quantification limit. As an example, recovery was studied using *R. monosperma*

ethyl acetate extract from the flowers. The choice of the different concentration levels used was made to cover the concentration range of the majority of samples.

■ RESULTS AND DISCUSSION

Characterization of Phenolic Compounds by UHPLC/DAD/ESI-MS

A total of 14 phenolic compounds have been tentatively identified based on their wavelength of maximum UV absorption and mass spectrometry (MS) fragments in the negative mode corresponding to these peaks, alongside literature data on the chemical composition of *Retama*, *Berberis*, and *Ricinus* genus.

The chromatographic profile of *R. communis* methanol extract (RM) showed the presence of phenolic acid (peak 2), ellagitannins, members of the tannin family, are characterized as hydrolyzable conjugates containing

one or more hexahydroxydiphenoyl (HHDP) group(s) to esterify a sugar like galloyl derivative (peaks 4–6), and flavonoid glycosides like rutin and quercetin (peaks 10 and 11) (Table 4, Fig. 1).

The UHPLC/DAD/ESI-MS results of *B. vulgaris* ethyl acetate showed the predominance of pyrogallol acid (peak 1) followed by vanillic acid and *p*-coumaric acid; however, in methanolic extracts in the same species, we notice the predominance of gallic acid (peak 3) followed by *p*-coumaric acid (Table 4, Fig. 1). Concerning *R. monosperma* extracts, the chromatographic profile of flower ethyl acetate extracts showed the predominance of genistein as isoflavone (peak 13) followed by apigenin (peak 14) as a flavone. For diethyl ether extracts of *R. monosperma* seeds, we can see the taxifolin flavanonols (peak 8) as a major compound, followed by genistein (peak 13) (Table 4, Fig. 1).

Table 2. Information about the matrixes used to validate the method

Matrix	Part of the plant	Nature of the extract	Identified compounds
<i>Retama monosperma</i> *	Flowers	Ethyl acetate	Genistein
<i>Berberis vulgaris</i>	Roots	Methanol	<i>p</i> -Coumaric acid
		Ethyl acetate	Vanillic acid
<i>Ricinus communis</i>	Leaves	Methanol	Gallic acid and rutin
		Ethyl acetate	Gallic acid

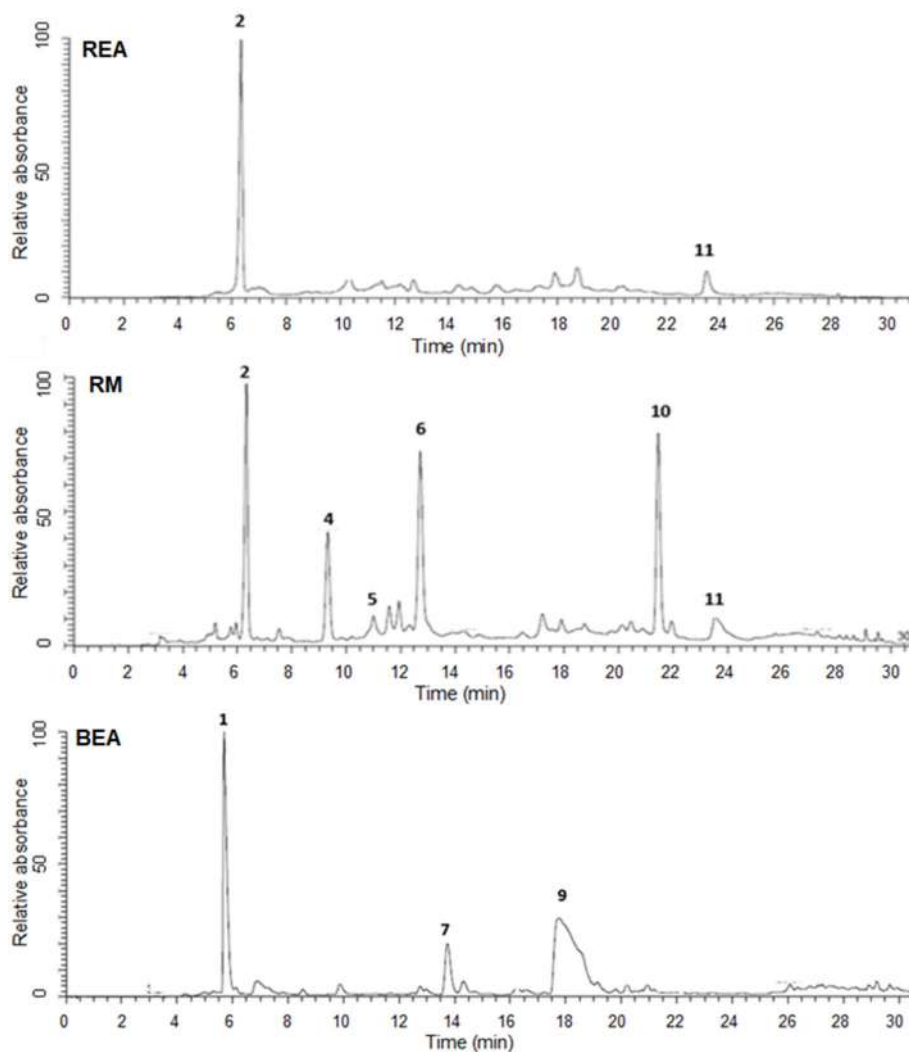
*In Morocco, Zefzoufi et al. [34] revealed that the diethyl ether extract of flowers and ethyl acetate extract of seeds of *R. monosperma* rich in flavonoid compounds such as genistein, quercetin, kaempferol. Other extracts of this plant are used in this paper

Table 3. Experimental plan of method validation

Parameter	Experience
Specificity	Method 1: Each extract sample (Table 2) was analyzed using UHPLC-DAD-ESI/MS [46]. Method 2: Some authors use the recovery [47-48] method to prove the specificity of the method. The experience carried out to perform the recovery test is detailed in the last row of the table.
Linearity	Three series of multi-standard solutions at 5 concentration levels were used (10, 50, 100, 150 and 200 mg/L). Three repetitions for each level of each series were performed by UHPLC-DAD [49].
Detection limit Quantification limit	Ten repetitions for the control sample (methanol) were performed by UHPLC-DAD [48].
Repeatability	Two concentration levels (50 and 200 mg/L) of multi-standard solution were prepared by the same operator and analyzed by UHPLC-DAD. Ten repetitions were performed for each level on the same day [48].
Precision Intermediate precision	Every day for 3 d, a series of multi-standard solutions with 5 concentrations levels (10, 50, 100, 150 and 200 mg/L) was prepared by the same operator. Three repetitions for each level of each series were performed by UHPLC-DAD [49].
Recovery	Six samples of the ethyl acetate extract of <i>Retama monosperma</i> flowers were used to perform the recovery test. The final concentrations of the standard (Genistein) added are as follows: 0, 10, 50, 100, 150, and 200 mg/L. Three repetitions were performed for each sample using UHPLC-DAD [50].

Table 4. Tentatively identification of phenolic compounds (with their percentage area) from three medicinal plants using UHPLC/DAD/ESI-MS

Peak number	Rt	(M-H) ⁻ m/z	MS fragments	UV _{max}	Identified compound	Molecular formula	Ref.	REA (%)	RM (%)	BEA (%)	BM (%)	RSDE (%)	RFEA (%)
1	5.9	125	-	270	Pyrogallol	C ₆ H ₆ O ₃	-	-	-	58.74	-	-	-
2	6.1	331	169	270, 310	Galloyl-glucoside	C ₁₃ H ₁₆ O ₁₀	[57]	70.82	20.15	-	-	-	-
3	6.5	169	125	272	Gallic acid	C ₇ H ₆ O ₅	[57]	-	-	-	38.07	-	-
4	9.3	483	313, 169	256, 310	Digalloyl-glucoside	C ₂₀ H ₂₀ O ₁₄	[57]	-	9.33	-	-	-	-
5	11.0	635	465, 283, 169	270, 310	Trigalloyl-glucoside	C ₂₇ H ₂₄ O ₁₈	[57]	-	2.33	-	-	-	-
6	12.7	633	463, 169	269, 310	Galloyl-HHDP-glucoside	C ₂₇ H ₂₂ O ₁₈	[57]	-	25.83	-	-	-	-
7	13.8	167	-	261, 295	Vanillic acid	C ₈ H ₈ O ₄	-	-	-	10.50	-	-	-
8	18.1	315	-	228, 290	Taxifolin	C ₁₅ H ₁₂ O ₇	[58]	-	-	-	-	71.32	-
9	18.6	163	-	310	<i>p</i> -Coumaric acid	C ₉ H ₈ O ₃	-	-	-	30.02	45.17	-	-
10	21.8	609	463, 301	257, 357	Rutin	C ₂₇ H ₃₀ O ₁₆	[59]	-	25.55	-	-	-	-
11	23.6	447	301	255, 356	Quercitrin	C ₂₁ H ₂₀ O ₁₁	[59]	10.20	3.10	-	-	-	-
12	26.7	301	-	355, 368	Quercetin	C ₁₅ H ₁₀ O ₇	[34]	-	-	-	-	20.05	-
13	27.1	269	-	261, 302 _{sh}	Genistein	C ₁₅ H ₁₀ O ₅	[34]	-	-	-	-	-	74.35
14	27.7	269	-	236, 336	Apigenin	C ₁₅ H ₁₀ O ₅	[51]	-	-	-	-	-	21.02



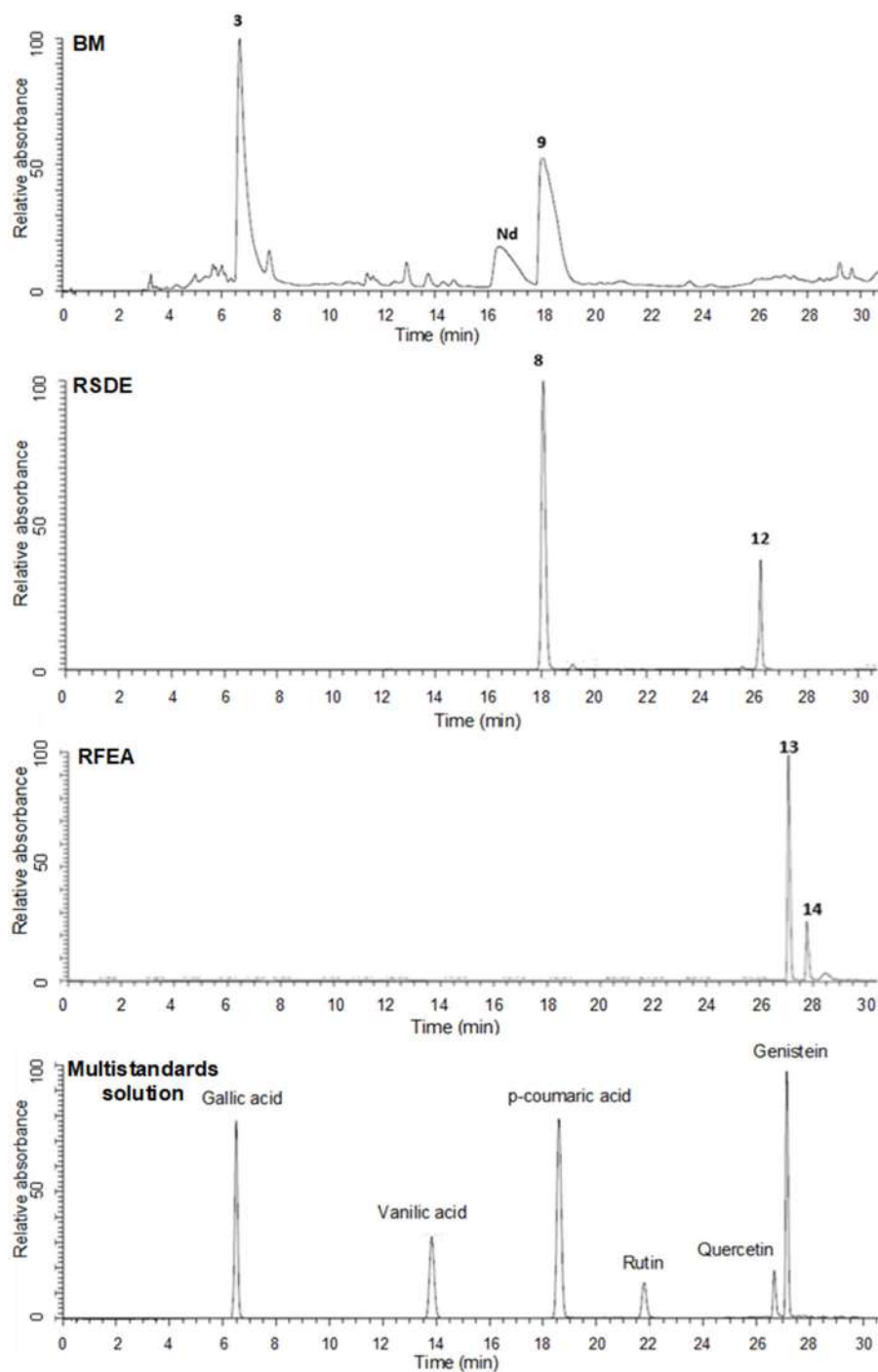


Fig 1. Chromatographic profile of *R. communis* methanolic extract (RM), *R. communis* ethyl acetate extract (REA), *B. vulgaris* methanolic extract (BM), *B. vulgaris* ethyl acetate extract (BEA), *R. monosperma* flowers ethyl acetate extract (RFEA), *R. monosperma* seeds diethyl acetate extract (RSDE) and multi-standards solution at 280 nm

In this study, we tentatively identified in three medicinal plants diverse phenolic compounds like phenolic acid (gallic acid, vanillic acid, *p*-coumaric acid), isoflavone (genistein), flavone (apigenin), flavanonols

(taxifolin), flavonol (quercetin), glycoside flavonol (rutin and quercitrin), and ellagitannins (galloyl-HHDP-glucoside).

For *Retama* genus, based on the literature, we found

our results closely similar to other papers. Researchers identified genistein, luteolin, apigenin, and rutin in aqueous extract of *R. monosperma* growing in Spain [51]. Recently, researchers reported the presence of taxifolin and quercetin in ethyl acetate seeds extract and genistein and apigenin in diethyl ether flower extract of Moroccan *R. monosperma* [34]. In our study, we identified genistein as a major compound, followed by apigenin in another extract (ethyl acetate extract) of *R. monosperma* flowers.

For *Ricinus* genus, we found dissimilarities in chemical composition between our results and the literature. For example, researchers reported five phenolic compounds isolated from *R. communis* growing in Vietnam such as gallic acid, vanillic acid, kaempferol-3-O- β -D-glucopyranoside, and kaempferol-3-O- β -D-xylopyranoside [52]. Another research determined the presence of gallic acid, genistic acid, vitexin, naringenin and rutin in leaves of *R. communis* from Tunisia [53]. In 2016, researchers reported the presence of some alkaloids in the same species as ricinine and bufotenine O-glucoside. To our knowledge, this paper is the first to identify digallyl-glucose, trigallyl-glucose, gallyl-HDDP-glucose, rutin, and quercitrin in *R. communis* native to Morocco.

For *Berberis*, many studies focused on the identification of *B. vulgaris* alkaloid compounds like berberine, which is known as an important major compound in this plant. In Morocco, researchers reported the presence of some alkaloids in *B. vulgaris* dichloromethane extract such as berberine, palmatine, and epi berberine [54]. To our knowledge, this paper is the first to identify pyrogallol and *p*-coumaric acid in *B. vulgaris* from Morocco. These observed differences in chemical profiles can be explained by the geographic origin of the species [55], the extraction method (maceration in our case), the extraction solvent [56], and the part of the plant used for the preparation of the extracts.

Antioxidant Activity

Natural antioxidants are currently the subject of numerous studies because they can reduce the harmful effects of free radicals in neurodegenerative diseases and cardiovascular, arthritis, cancer, and autoimmune diseases

in which oxidative stress is incriminated [60]. Numerous works carried out on the anti-free radical activity of plant extracts have shown that phenolic compounds and, more particularly, flavonoids are recognized as potentially antioxidant substances with the ability to trap free radical species and reactive forms of oxygen. The IC₅₀ value represents the concentration of extract that neutralizes or reduces 50% of free radicals. The lower the IC₅₀, the more the extract has a powerful antioxidant potential. Therefore, we evaluated the antioxidant activity of RFEA, RSDE, REA, RM, BEA and BM by three tests, conjugated diene scavenging activity, TBARS assay and DPPH (Table 5). We used rutin, gallic acid, quercetin, and BHT as standards.

DPPH Scavenging Activity

REA showed a higher antiradical activity (IC₅₀ = 12.5 μ g/mL) followed by RFEA, RM compared to standards BHT, quercetin and gallic acid, but still less than rutin standard. However, the antioxidant capacity of RSDE, BM and BEA were moderate compared to the other extracts and standards (Table 5).

Conjugated Diene Scavenging Activity

The conjugate diene scavenging activity of REA was more effective than BHT, quercetin and gallic acid, but it is similar to rutin. BEA showed moderate antioxidant activity followed by RM, BM, RFEA, and RSDE with IC₅₀ values of 59.02, 60.09, 72.47, and 98.08 μ g/mL, respectively (Table 5).

TBARS Assay

TBARS assay of RM was significantly greater, followed by BEA and BM but still less than four standards. However, the inhibition of lipid peroxidation of RFEA, RSDE and REA was lower than in other samples (Table 5). Based on the literature, several studies reported the antioxidant activity of these three plants' medicinal extracts. Concerning *R. communis*, researchers revealed that the antioxidant capacity of butanol extract of the aerial part of *R. communis* growing in Pakistan (IC₅₀ = 140 μ g/mL) is higher than that of ethyl acetate extract (IC₅₀ = 190 μ g/mL) [61]. In 2009, a paper described that leaves methanolic extract of *R. communis* has a strong antiradical activity with IC₅₀ of 4.6 μ g/mL

Table 5. Antioxidant activity of standards and samples in terms of IC₅₀ (µg/mL) values with $p < 0.05$

	DPPH	Conjugated diene	TBARS
Standards			
BHT	28.41 ± 0.06	36.55 ± 0.28	40.06 ± 0.15
Gallic acid	30.55 ± 0.02	36.52 ± 0.12	40.08 ± 0.15
Quercetin	35.65 ± 0.25	30.05 ± 0.15	38.42 ± 0.05
Rutin	10.02 ± 0.05	26.02 ± 0.11	30.05 ± 0.05
Samples			
RFEA	19.59 ± 0.11	72.47 ± 0.25	68.12 ± 0.12
RSDE	84.95 ± 0.16	98.08 ± 0.50	82.26 ± 0.12
REA	12.50 ± 0.11	29.59 ± 0.11	69.02 ± 0.11
RM	20.45 ± 0.11	59.02 ± 0.11	50.30 ± 0.11
BEA	38.05 ± 0.15	44.12 ± 0.02	52.89 ± 0.10
BM	55.32 ± 0.14	60.09 ± 0.22	55.90 ± 0.15

RFEA: *Retama* flowers ethyl acetate; RSDE: *Retama* seeds diethyl ether; REA: *Ricinus* ethyl acetate; RM: *Ricinus* methanol; BEA: *Berberis* ethyl acetate; BM: *Berberis* methanol

followed by ethyl acetate extract (IC₅₀ = 6.04 µg/mL) [62]. For *R. monosperma*, previous work reported that the antiradical activity of ethyl acetate extracts of seeds (IC₅₀ = 15.13 µg/mL) was significantly higher than quercetin (IC₅₀ = 19.43 µg/mL) and BHT standards (IC₅₀ = 30.21 µg/mL) [34]. Regarding *B. vulgaris*, recently, a paper reported higher antioxidant activity using a DPPH assay of ethanol and ethyl acetate extract of *B. vulgaris* roots with IC₅₀ of 69.65 and 77.75 µg/mL, respectively [63].

Performance Criteria of the Validated Characterization Method Using the UHPLC-DAD

Use of purity for the calculation of the real concentrations of the standards used

Preparation of the standard solutions required weighing a certain mass of the standards in powder form. Since the purity of standards is different from 100%, the calculation of the real concentrations is necessary. Table 6 shows the different concentrations used, taking their purity into consideration.

Specificity

The plant extracts and multi-standards solutions were analyzed by UHPLC/DA/DESI-MS, and each peak concerned was detected at 280 nm. Table 7 and Fig. 1 show the found results. As can be seen in Fig. 1, the chromatograms show that the separation of all six phenolic compounds was successfully achieved with good resolution. Additionally, no interfering peaks were observed.

Linearity

Linearity is the ability of a method to elicit test results that are proportional to analyte concentration within a given range. The range of the analytical method is the interval between the highest and lowest concentrations in which linearity has been confirmed. Many tests are used to validate method linearity. These tests are presented in Table 8.

The results showed that regression curves of each phenolic compound were found to be linear with R²

Table 6. Real concentrations (mg/mL) of the standards used

Standards	Gallic acid	Vanillic acid	<i>p</i> -Coumaric acid	Rutin	Quercetin	Genistein
Level 1	9.90	9.80	10.00	9.59	9.90	9.90
Level 2	49.49	48.98	49.98	47.94	49.49	49.49
Level 3	98.98	97.97	99.96	95.88	98.98	98.98
Level 4	148.47	146.95	149.94	143.82	148.47	148.47
Level 5	197.96	195.94	199.92	191.76	197.96	197.96

Table 7. Quantitative analysis of phenols in different plant extracts using UHPLC-DAD-ESI/MS at UV 280 nm

Rt	(M-H) ⁻ m/z	Molecular weight	UV _{max}	Identified compound	Molecular formula	REA mg/L	RM mg/L	BEA mg/L	BM mg/L	RSDE mg/L	RFEA mg/L
6.50	169	170	272	Gallic acid	C ₇ H ₆ O ₅				29.81		
13.81	167	168	261, 295	Vanillic acid	C ₈ H ₈ O ₄			56.61			
18.57	163	164	310	<i>p</i> -Coumaric acid	C ₉ H ₈ O ₃			10.36	11.84		
21.78	609	610	257, 357	Rutin	C ₂₇ H ₃₀ O ₁₆		12.35				
26.66	301	302	355, 368	Quercetin	C ₁₅ H ₁₀ O ₇					69.64	
27.13	269	270	261, 302 _{sh}	Genistein	C ₁₅ H ₁₀ O ₅						102.02

Table 8. Tests used to validate method linearity for the six compounds of interest

Standard	Gallic acid	Vanillic acid	<i>p</i> -Coumaric acid	Rutin	Quercetin	Genistein	Conclusion	
Slope a*	23967.90	15588.78	34637.73	6532.57	5797.53	24364.42	-	
Standard deviation of the slope S _a *	350.71	227.08	545.51	96.98	44.14	400.97	-	
Intercept b*	37743.55	24710.59	70174.89	9438.12	5939.70	51282.24	-	
Standard deviation of the intercept S _b *	42543.71	27265.38	66829.07	11396.44	5355.25	48640.90	-	
Coefficient of determination R ² *	0.9994	0.9994	0.9993	0.9993	0.9998	0.9992	-	
Cochran test	C	0.33	0.34	0.34	0.33	0.35	0.34	The homogeneity of variances is confirmed
Acceptance criteria	Between 0.55 and 0.60 according to the Cochran table							
t	There is a homogeneity of variances if C _{calculated} ≤ C _(1-α, s, nk-1)							
Test of intercept [64]	t	0.89	0.91	1.05	0.83	1.11	1.05	The line passes through the origin
Acceptance criteria	The line passes through the origin if t _{calculated} ≤ t _(1-α/2, k-2) **							
Test of the nullity of the slope [65]	t	68.34	68.65	63.50	67.36	131.32	60.76	
Acceptance criteria	The slope is null if t _{calculated} ≤ t _(1-α/2, k-2) **							
Test of significance of the slope [64]	F	26011.31	23034.82	23098.18	24269.19	17330.50	22560.96	The slope is different from zero, there is a linear relationship between x and y
Acceptance criteria	The slope is not significance if F _{calculated} ≤ F _(1-α, 1, Nk-2)							
Test of significance of the regression [64]	F	4670.40	4712.56	4031.72	4536.86	17246.08	3692.10	
Acceptance criteria	The slope is not different from zero if F _{calculated} ≤ F _(1-α, 1, k-2)							

•Notes: *Calculated using the LINEST function in Microsoft Excel; **One-tail student test; Equation of regression curve: $y = (a \times x) + b$ (y: area; x: concentration mg/L)/α: risk = 0.05/s: Number of series/n: number of repetitions per level in the series/k: number of concentration levels/N: number of repetitions per level all series combined. Details of the calculations performed are shown in the supplementary material

greater than 0.999. This value means that 99.9% of the variation in the concentration (within the range of the minimum and maximum concentrations taken into consideration) is expressed by the correlation.

Linearity validation was confirmed by: i) firstly, the Cochran test that confirmed the homogeneity of variances, ii) secondary, the intercept test according to which it can be concluded that the line passes through the origin, and iii) finally, by a number of t and F tests to which it can be concluded that the slope is different from 0 and there is a linear relationship between the concentration of the compound and the peak area.

Repeatability

The repeatability of the method was examined by analysis of two concentration levels by performing 10 repetitions. The results of this test are presented in Table 9.

Intermediate precision

The intermediate precision of the method was examined by analysis of 5 concentration levels three times for three days and calculation of the coefficient of variation and the intermediate precision. The found results are presented in Table 10.

Table 9. Repeatability study results for the six compounds of interest

Compound	Gallic acid		Vanillic acid		<i>p</i> -Coumaric acid		Rutin		Quercetin		Genistein	
Concentration (mg/L)	49.49	197.96	48.98	195.94	49.98	199.92	47.94	191.76	49.49	197.96	49.49	197.96
Average of 10 repetitions (mg/L)	50.42	196.51	50.40	195.32	51.32	198.62	48.98	190.45	48.53	190.24	51.09	197.05
Standard deviation of 10 repetitions (mg/L)	0.82	2.21	0.80	2.33	0.78	2.29	0.86	2.24	1.02	2.22	0.82	2.20
Coefficient of variation (CV)	1.63	1.12	1.60	1.19	1.52	1.16	1.75	1.18	2.09	1.16	1.61	1.12
Repeatability r	2.30	6.18	2.25	6.52	2.19	6.42	2.40	6.27	2.85	6.21	2.30	6.16
Acceptance criteria	If the calculated CV is less than 5%, the proposed method is repeatable.											
Conclusion	For the six phenolic compounds, the CV is less than 5%, which is acceptable. These results showed that the current method for quantification of the six phenolic compounds is repeatable.											
•Notes:	Coefficient of variation: $CV = \frac{STD}{\bar{x}} \times 100$						Repeatability r [67]: $r = 2.8 \times STD$					
	STD: Standard deviation of 10 repetitions; \bar{x} : Average of 10 repetitions											

Table 10. Intermediate precision study results for the six compounds of interest

Gallic acid	Concentration level (mg/L)	9.90	49.49	98.98	148.47	197.96
	Average of 9 repetitions (mg/L)	8.63	49.34	100.48	150.74	195.61
	Standard deviation of 9 repetitions (mg/L)	0.20	1.13	1.86	3.88	2.43
	Coefficient of variation (CV)	2.31	2.30	1.85	2.57	1.24
	Intermediate precision R	0.56	3.17	5.20	10.86	6.80
Vanillic acid	Concentration level (mg/L)	9.80	48.99	97.97	146.96	195.94
	Average of 9 repetitions (mg/L)	8.55	48.84	99.45	149.18	193.63
	Standard deviation of 9 repetitions (mg/L)	0.32	1.34	2.05	4.16	2.69
	Coefficient of variation (CV)	3.73	2.75	2.06	2.79	1.39
	Intermediate precision R	0.89	3.76	5.73	11.65	7.54
<i>p</i> -Coumaric acid	Concentration level (mg/L)	10.00	49.98	99.96	149.94	199.92
	Average of 9 repetitions (mg/L)	8.55	49.89	101.64	152.34	197.37
	Standard deviation of 9 repetitions (mg/L)	0.19	1.33	1.99	4.11	2.52
	Coefficient of variation (CV)	2.26	2.67	1.96	2.70	1.28
	Intermediate precision R	0.54	3.73	5.58	11.50	7.05
Rutin	Concentration level (mg/L)	9.59	47.94	95.88	143.82	191.76
	Average of 9 repetitions (mg/L)	8.42	47.66	97.40	146.05	189.46
	Standard deviation of 9 repetitions (mg/L)	0.27	1.13	1.80	4.02	2.40
	Coefficient of variation (CV)	3.16	2.37	1.85	2.75	1.27
	Intermediate precision R	0.75	3.16	5.05	11.25	6.72
Quercetin	Concentration level (mg/L)	9.90	49.49	98.98	148.47	197.96
	Average of 9 repetitions (mg/L)	9.24	49.35	99.90	149.56	196.75
	Standard deviation of 9 repetitions (mg/L)	0.25	1.20	2.92	4.40	5.41
	Coefficient of variation (CV)	2.72	2.44	2.93	2.94	2.75
	Intermediate precision R	0.70	3.37	8.19	12.33	15.14
Genistein	Concentration level (mg/L)	9.90	49.49	98.98	148.47	197.96
	Average of 9 repetitions (mg/L)	8.23	49.58	100.87	150.76	195.36

	Standard deviation of 9 repetitions (mg/L)	0.31	1.39	1.78	3.89	2.74
	Coefficient of variation (CV)	3.75	2.81	1.77	2.58	1.40
	Intermediate precision R	0.86	3.90	4.99	10.88	7.66
Acceptance criteria	If the calculated CV is less than or equal to 5 %, the intermediate precision of the proposed method is validated.					
Conclusion	It can be seen that all coefficients of variation are less than 5 %, which is acceptable. So, the intermediate precision of the method is validated.					
•Notes:	Coefficient of variation $CV = \frac{STD}{\bar{x}} \times 100$		Intermediate precision [67]: $R = 2.8 \times STD$			
	STD: Standard deviation of 9 repetitions; \bar{x} : Average of 9 repetitions					

Detection and Quantification Limits

The detection limit is the lowest concentration of the analyte that can be detected but not necessarily quantified. The quantification limit is the lowest concentration of the analyte that can be quantified at the experimental conditions. In the present paper, the limits were calculated using the graphic approach.

This approach can be applied to analytical methods that provide a graphic recording (e.g., chromatography) with background noise. This method requires the determination of [48]: i) h_{max} is the greatest difference in amplitude on the y-axis of the signal observed between two acquisition points, excluding drift, over a distance

equal to twenty times the width at mid-height of the peak corresponding to the analyte, centered on its (analyte) retention time. An explanatory diagram for the calculation of the h_{max} is presented at the level of the reference [66-68]; ii) Factor R is the quantity/signal response factor expressed in height. This factor corresponds to the slope of the regression curve, representing the concentration as a function of the peak height. It was calculated using the same data recorded to perform the intermediate precision test (5 concentration levels analyzed by performing 3 repetitions per day for 3 d). Data used for the calculation of the detection and quantification limits are presented in Table 11.

Table 11. Data used for the calculation of the detection and quantification limits

Standard	Gallic acid	Vanillic acid	p-Coumaric acid	Rutin	Quercetin	Genistein
Retention time (min)*	6.46	13.79	18.55	21.75	26.64	27.11
Width at half height (min)*	0.12	0.22	0.19	0.25	0.16	0.11
h_{max}^{**}	752.64	266.59	381.97	431.90	989.67	885.96
Factor R	3.18×10^{-04}	7.76×10^{-04}	3.35×10^{-04}	1.69×10^{-03}	1.29×10^{-03}	2.69×10^{-04}
Detection limit DL (mg/L)	0.72	0.62	0.38	2.11	3.84	0.71
Quantification limit QL (mg/L)	2.39	2.07	1.28	7.30	12.80	2.38

Notes: *Retention time and width at half height are average values calculated using data from the intermediate precision study (3 repetitions per day for 3 d) for the lowest concentration level; ** h_{max} : Average of h_{max} of each repetition of the control sample (10 repetitions in total); Detection and quantification limits were calculated using the following equations [48]: $DL = 3 \times h_{max} \times R$, $QL = 10 \times h_{max} \times R$

Table 12. Results of the recovery test

Concentration level	Added concentration (mg/L)	Concentration after addition (3 repetitions average) (mg/L)	Recovered concentration (level X - level 1) (mg/L)	Recovery (%)	Recovery average (%)	100.63
Level 1	0.00	100.90	-	-	Standard deviation (%)	1.70
Level 2	9.90	111.04	10.14	102.44	Coefficient of variation (CV)	1.68
Level 3	147.98	247.51	146.62	99.08	$t_{(0.975,2)}$	4.30
Level 4	197.96	299.60	198.70	100.38	Confidence interval \pm	4.21

Acceptance criteria	The CV must be less than 2 %, and the confidence interval must include the value 100 % [50]	
Conclusion	The coefficient of variation is less than 2%, and the recovery average interval of confidence (CI = 100.63% ± 4.21) includes 100%, so the method is accurate.	
•Notes:		
Coefficient of variation	Recovery	Confidence interval [64]
$CV = \frac{STD}{\bar{x}} \times 100$	$Recovery = \frac{RC}{AC} \times 100$	$\bar{x} - t(1 - \frac{\alpha}{2}, v)STD/\sqrt{n} < m < \bar{x} + t(1 - \frac{\alpha}{2}, v)STD/\sqrt{n}$
STD: Standard deviation	RC: Recovered concentration	m: Confidence interval average
\bar{x} : Recovery average	AC: Added concentration	$t_{(1-\alpha/2, k-1)}$: $t_{critical}$ value, it is read on one-tailed Student table (with, α : risk = 0.05); v: degree of liberty, $v = k - 1$; k: number of recovered concentration levels

Table 13. Results of the specificity study further to the regression curve representing recovered concentrations as a function of added concentrations – Genistein in the EAE of *Retama monosperma* flowers

Slope a^*	Standard deviation of the slope S_a^*	Intercept b^*	Standard deviation of the intercept S_b^*	$t_{calculated}$ for the test of the hypothesis of “the slope is equivalent to 1”***	$t_{calculated}$ for the test of the hypothesis of “the intercept b equivalent to 0”***	Critical value of Student test $t_{(0.01, 1)}$
1.00	0.01	-0.08	1.61	0.03	0.05	63.66
Acceptance criteria	The slope of the regression curve is equivalent to 1 if $t_{calculated}$ is less than $t_{(\alpha, k-2)}$ read on a two-tailed Student table (with k: number of concentration levels; α : risk = 0.01) [48]					
Conclusion	The intercept of the regression curve is equivalent to 0 if $t_{calculated}$ is less than $t_{(\alpha, k-2)}$ read on a two-tailed Student table (with, k: number of concentration levels; α : risk = 0.01) [48]					
	The slope of the regression curve is equivalent to 1					
	The intercept of the regression curve is equivalent to 0					

•Notes: $y = (a \times x) + b$ (y: recovered concentration (mg/L); x: added concentration (mg/L)); *Calculated using the LINEST function in Microsoft Excel; **Calculated with the following equation [48]: $t = \frac{|a-1|}{S_a}$; *** Calculated with the following equation [48]: $t = \frac{|b|}{S_b}$

Table 14. Results of the specificity study further the two calibration curves (without matrix and with matrix) – Genistein in the EAE of *Retama monosperma* flowers

Calibration curve without matrix		Calibration curve with matrix		$t_{calculated}^{**}$	Critical value of Student test $t_{(0.95, 5)}$
Slope a^*	Standard deviation of the slope S_a^*	Slope a'^*	Standard deviation of the slope $S_a'^*$		
24349.22	156.18	24364.42	400.98	0.04	2.02
Acceptance criteria	The two slopes are equal if $t_{calculated}$ is less than or equal to $t_{(1-\alpha/2, k + k' - 4)}$ read on one-tail Student table				
Conclusion	The two slopes are equal				

•Notes: *Calculated using the LINEST function in Microsoft Excel; Calibration curve without matrix $y = (a \times x) + b$ (y: peak area; x: concentration (mg/L)); Calibration curve with matrix $y = (a' \times x) + b'$ (y: peak area; x: added concentration (mg/L)); **Calculated with the following equation [66]: $t_{calculated} = \frac{|a-a'|}{\sqrt{S_a^2 + S_a'^2}}$; k is the number of the concentration levels used for the calibration curve without matrix; k' is the number of the concentration levels used for the calibration curve with matrix; α : risk = 0.1

Recovery

In this paper, we will deal with an example of the recovery test which concerns the matrix of *R. monosperma* flowers of the ethyl acetate extract. This test can be used to assess the accuracy of the method (Table

12) but also, by some authors [47], to confirm specificity (Table 13-14).

The concentration after addition was calculated using the calibration curve results for the linearity test. Further to the statistical tests carried out, of which the

results are presented in Tables 13 and 14, we can confirm that the method is specific.

■ CONCLUSION

Extracts characterization using UHPLC/DAD/ESI-MS showed i) the richness of *R. monosperma* of flavonol, isoflavone and flavone, ii) the presence of flavonol glycoside in *R. communis*, iii) the richness of *B. vulgaris* of galloyl-glucose and phenolic acids. These plant extracts have a high antioxidant capacity due to the presence of phenolic compounds. The higher capacity concerns *R. communis* methanolic extract with IC_{50} of 12.5, 29.59, and 50.3 $\mu\text{g/mL}$ for DPPH assay, conjugated diene, and TBARS assay, respectively. As an important step to ensure the quality of analytical results, this paper presented the performance criteria of the validated method using UHPLC/DAD/ESI-MS and focusing on six polyphenols known as antioxidant standards (gallic acid, vanillic acid, *p*-coumaric acid, rutin, quercetin, and genistein). The results of all released tests in the process of method validation are very satisfactory. In short, the polyphenol content of the plants studied in this article makes them an important subject for future research realized by industries, such as pharmaceuticals and cosmetics, seeking to exploit natural products such as plants to develop products with high antioxidant activity.

■ AUTHOR CONTRIBUTIONS

Meriem Outaki, Manal Zefzoufi and Amal Sammama contributed equally to this work. Meriem Outaki prepared the experimental plan for the "method validation" part. Manal Zefzoufi prepared the experimental plan for the "antioxidant activity" part. Meriem Outaki, Manal Zefzoufi, Amal Sammama and Khadija El Gadali carried out the experiments in the laboratory and performed the necessary calculations. All the authors wrote the paper (each a part) and revised it. All authors agreed to the final version of this manuscript.

■ REFERENCES

- [1] Nasim, N., Sandeep, I.S., and Mohanty, S., 2022, Plant-derived natural products for drug discovery: Current approaches and prospects, *Nucleus*, 65 (3), 399–411.
- [2] Dastan, S.D., 2023, Chemical and functional composition and biological activities of Anatolian *Hypericum scabrum* L. plant, *J. Mol. Struct.*, 1275, 134561.
- [3] Oglah, M.K., Mustafa, Y.F., Bashir, M.K., and Jasim, M.H., 2020, Curcumin and its derivatives: A review of their biological activities, *Syst. Rev. Pharm.*, 11 (3), 472–481.
- [4] Ismael, R.N., Mustafa, Y.F., and Al-Qazaz, H.K., 2022, Cancer-curative potential of novel coumarins from watermelon princess: A scenario of their isolation and activity, *Eurasian Chem. Commun.*, 4, 657–672.
- [5] Loukmas, S., Kerak, E., Outaki, M., Belaqziz, M., and Harrak, H., 2020, Assessment of minerals, bioactive compounds, and antioxidant activity of ten Moroccan pomegranate cultivars, *J. Food Qual.*, 2020, 8844538.
- [6] Loukmas, S., Outaki, M., Ettalibi, F., Kharbouch, H.A., Kerak, E., and Harrak, H., 2021, Physicochemical criteria, bioactive compounds, antioxidant activity and sensory attributes of ten Moroccan pomegranate cultivars, *Eur. J. Hortic. Sci.*, 86 (4), 339–353.
- [7] Rachmayanti, Y., Firmansyah, D., Umma, R.R., Hertanto, D.M., Sudiana, I.K., Santoso, D., Nandika, D., Karlinasari, L., Arinana, A., Batubara, I., and Witasari, L.D., 2022, Antioxidant activity of fungus comb extracts isolated from Indo-Malayan termite *Macrotermes gilvus* Hagen (Isoptera: Termitidae), *Indones. J. Chem.*, 22 (6), 1693–1704.
- [8] Efdi, M., Pratama, D., Itam, A., and Okselni, T., 2022, Antioxidant flavonoid glycoside from leaves of cacao mistletoe (*Scurrula ferruginea* (Jack) Danser), *Indones. J. Chem.*, 22 (4), 944–952.
- [9] Benmekhbi, L., Mosbah, S., Laamraoui, H., Hamlaoui, I., Bencheriet, S., and Ibrahim, D., 2022, Evaluation of phytochemical properties and biological activities of leaf extracts and oil of *Petroselinum sativum* collected from Algeria, *Indones. J. Chem.*, 22 (6), 1566–1573.
- [10] Chandrasekara, A., and Josheph Kumar, T., 2016, Roots and tuber crops as functional foods: A review

- on phytochemical constituents and their potential health benefits, *Int. J. Food Sci.*, 2016, 3631647.
- [11] Jo, B.G., Bong, S.K., Jegal, J., Kim, S.N., and Yang, M.H., 2020, Antiallergic effects of phenolic compounds isolated from *Stellera chamaejasme* on RBL-2H3 cells, *Nat. Prod. Commun.*, 15 (7), 1934578X20942352.
- [12] Mustafa, Y.F., 2023, Harmful free radicals in aging: A narrative review of their detrimental effects on health, *Ind. J. Clin. Biochem.*, s12291-023-01147-y.
- [13] Luo, K.W., Ko, C.H., Yue, G.G.L., Lee, J.K.M., Li, K.K., Lee, M., Li, G., Fung, K.P., Leung, P.C., and Lau, C.B.S., 2014, Green tea (*Camellia sinensis*) extract inhibits both the metastasis and osteolytic components of mammary cancer 4T1 lesions in mice, *J. Nutr. Biochem.*, 25 (4), 395–403.
- [14] Chandra, S., Gahlot, M., Choudhary, A.N., Palai, S., de Almeida, R.S., de Vasconcelos, J.E.L., dos Santos, F.A.V., de Farias, P.A.M., and Coutinho, H.D.M., 2023, Scientific evidences of anticancer potential of medicinal plants, *Food Chem. Adv.*, 2, 100239.
- [15] Lee, C.C., Dudonné, S., Dubé, P., Desjardins, Y., Kim, J.H., Kim, J.S., Kim, J.E., Park, J.H.Y., Lee, K.W., and Lee, C.Y., 2017, Comprehensive phenolic composition analysis and evaluation of Yak-Kong soybean (*Glycine max*) for the prevention of atherosclerosis, *Food Chem.*, 234, 486–493.
- [16] Khali, R.R., Mohammed, E.T., and Mustafa, Y.F., 2021, Various promising biological effects of cranberry extract: A review, *Clin. Schizophr. Relat. Psychoses*, 15, S6.
- [17] Mallmann, L.P., O. Rios, A., and Rodrigues, E., 2023, MS-FINDER and SIRIUS for phenolic compound identification from high-resolution mass spectrometry data, *Food Res. Int.*, 163, 112315.
- [18] Prasetyaningrum, A., Jos, B., Ratnawati, R., Rokhati, N., Riyanto, T., and Prinanda, G.R., 2022, Sequential microwave-ultrasound assisted extraction of flavonoid from *Moringa oleifera*: Product characteristic, antioxidant and antibacterial activity, *Indones. J. Chem.*, 22 (2), 303–316.
- [19] Rusli, R., Ningsih, B.A., Rahmadani, A., Febrina, L., Maulidya, V., and Fadraersada, J., 2019, Isolation and antioxidant and antibacterial activity of flavonoid from *Ficus variegata* Blume, *Indones. J. Chem.*, 19 (2), 538–543.
- [20] Dias, R., Oliveira, H., Fernandes, I., Simal-Gandara, J., and Perez-Gregorio, R., 2021, Recent advances in extracting phenolic compounds from food and their use in disease prevention and as cosmetics, *Crit. Rev. Food Sci. Nutr.*, 61 (7), 1130–1151.
- [21] Peterson, D.M., 2001, Oat antioxidants, *J. Cereal Sci.*, 33 (2), 115–129.
- [22] Boulanouar, B., Abdelaziz, G., Aazza, S., Gago, C., and Miguel, M.G., 2013, Antioxidant activities of eight Algerian plant extracts and two essential oils, *Ind. Crops Prod.*, 46, 85–96.
- [23] Abd El-Wahab, M., and El-Desouky, M.G., 2022, Study the effect of antioxidants on biological activity and on homopolypropylene; Mechanical and physical properties, *J. Indian Chem. Soc.*, 99 (12), 100764.
- [24] Sharifi-Rad, M., Anil Kumar, N.V., Zucca, P., Varoni, E.M., Dini, L., Panzarini, E., Rajkovic, J., Tsouh Fokou, P.V., Azzini, E., Peluso, I., Prakash Mishra, A., Nigam, M., El Rayess, Y., Beyrouthy, M.E., Polito, L., Iriti, M., Martins, N., Martorell, M., Docea, A.O., Setzer, W.N., Calina, D., Cho, W.C., and Sharifi-Rad, J., 2020, Lifestyle, oxidative stress, and antioxidants: Back and forth in the pathophysiology of chronic diseases, *Front. Physiol.*, 11, 00694.
- [25] Zhang, Y., Li, Y., Ren, X., Zhang, X., Wu, Z., and Liu, L., 2023, The positive correlation of antioxidant activity and prebiotic effect about oat phenolic compounds, *Food Chem.*, 402, 134231.
- [26] Jalloul, A.B., Garzoli, S., Chaar, H., el Jribi, C., and Abderrabba, M., 2023, Seasonal effect on bioactive compounds recovery using aqueous extraction, antioxidant activities, and volatile profiles of different parts of *Scabiosa maritima* L. (= *Scabiosa atropurpurea* subsp. maritima (L.) Arcang.), *S. Afr. J. Bot.*, 152, 63–79.
- [27] Yang, J., Qian, S., Na, X., and Zhao, A., 2023, Association between dietary and supplemental antioxidants intake and lung cancer risk: Evidence

- from a cancer screening trial, *Antioxidants*, 12 (2), 338.
- [28] Rudrapal, M., Khairnar, S.J., Khan, J., Dukhyil, A.B., Ansari, M.A., Alomary, M.N., Alshabrimi, F.M., Palai, S., Deb, P.K., and Devi, R., 2022, Dietary polyphenols and their role in oxidative stress-induced human diseases: insights into protective effects, antioxidant potentials and mechanism(s) of action, *Front. Pharmacol.*, 13, 806470.
- [29] Chaudhary, P., Janmeda, P., Docea, A.O., Yeskaliyeva, B., Abdull Razis, A.F., Modu, B., Calina, D., and Sharifi-Rad, J., 2023, Oxidative stress, free radicals and antioxidants: Potential crosstalk in the pathophysiology of human diseases, *Front. Chem.*, 11, 1158198.
- [30] Mariem, S., Hanen, F., Inès, J., Mejdj, S., and Riadh, K., 2014, Phenolic profile, biological activities and fraction analysis of the medicinal halophyte *Retama raetam*, *S. Afr. J. Bot.*, 94, 114–121.
- [31] Santos, P.M., Batista, D.L.J., Ribeiro, L.A.F., Boffo, E.F., de Cerqueira, M.D., Martins, D., de Castro, R.D., de Souza-Neta, L.C., Pinto, E., Zambotti-Villela, L., Colepicolo, P., Fernandez, L.G., Canuto, G.A.B., and Ribeiro, P.R., 2018, Identification of antioxidant and antimicrobial compounds from the oilseed crop *Ricinus communis* using a multiplatform metabolite profiling approach, *Ind. Crops Prod.*, 124, 834–844.
- [32] Eroğlu, A.Y., Çakır, Ö., Sağdıç, M., and Dertli, E., 2020, Bioactive characteristics of wild *Berberis vulgaris* and *Berberis crataegina* fruits, *J. Chem.*, 2020, 8908301.
- [33] Tuyen, P.N.K., Linh, T.T.T., Son, D.V., Thang, N.V., Son, D.V., Trang, N.T.Q., Chi, H.B.L., Ky, N.D.X., Phat, N.T., and Duong, H.T., 2020, Phenolic compounds from the leaves of *Ricinus communis* Linn, *VNUHCM Sci. Technol. Dev.*, 23 (3), 694–698.
- [34] Zefzoufi, M., Fdil, R., Bouamama, H., Gadhi, C., Katakura, Y., Mouzdahir, A., and Sraidi, K., 2021, Effect of extracts and isolated compounds derived from *Retama monosperma* (L.) Boiss. on anti-aging gene expression in human keratinocytes and antioxidant activity, *J. Ethnopharmacol.*, 280, 114451.
- [35] Kiliç, I., and Yeşiloğlu, Y., 2013, Spectroscopic studies on the antioxidant activity of *p*-coumaric acid, *Spectrochim. Acta, Part A*, 115, 719–724.
- [36] Mozaffari Godarzi, S., Valizade Gorji, A., Gholizadeh, B., Mard, S.A., and Mansouri, E., 2020, Antioxidant effect of *p*-coumaric acid on interleukin 1- β and tumor necrosis factor- α in rats with renal ischemic reperfusion, *Nefrología*, 40 (3), 311–319.
- [37] Salau, V.F., Erukainure, O.L., Ibeji, C.U., Olasehinde, T.A., Koobanally, N.A., and Islam, M.S., 2020, Vanillin and vanillic acid modulate antioxidant defense system via amelioration of metabolic complications linked to Fe²⁺-induced brain tissues damage, *Metab. Brain Dis.*, 35 (5), 727–738.
- [38] Enogieru, A.B., Haylett, W., Hiss, D.C., Bardien, S., and Ekpo, O.E., 2018, Rutin as a potent antioxidant: implications for neurodegenerative disorders, *Oxid. Med. Cell. Longevity*, 2018, 6241017.
- [39] Rahman Mazumder, M.A., and Hongsprabhas, P., 2016, Genistein as antioxidant and antibrowning agents in *in vivo* and *in vitro*: A review, *Biomed. Pharmacother.*, 82, 379–392.
- [40] Badhani, B., Sharma, N., and Kakkar, R., 2015, Gallic acid: A versatile antioxidant with promising therapeutic and industrial applications, *RSC Adv.*, 5 (35), 27540–27557.
- [41] Puigventós, L., Navarro, M., Alechaga, É., Núñez, O., Saurina, J., Hernández-Cassou, S., and Puignou, L., 2015, Determination of polyphenolic profiles by liquid chromatography-electrospray-tandem mass spectrometry for the authentication of fruit extracts, *Anal. Bioanal. Chem.*, 407 (2), 597–608.
- [42] Malki, F., Alouache, A., and Krimat, S., 2023, Effects of various parameters on the antioxidant activities of the synthesized heterocyclic pyrimidinium betaines, *Indones. J. Chem.*, 23 (1), 90–100.
- [43] Kleinveld, H.A., Hak-Lemmers, H.L., Stalenhoef, A.F., and Demacker, P.N., 1992, Improved measurement of low-density-lipoprotein susceptibility to copper-induced oxidation: Application of a short procedure for isolating low-density lipoprotein, *Clin. Chem.*, 38 (10), 2066–2072.

- [44] Ohkawa, H., Ohishi, N., and Yagi, K., 1979, Assay for lipid peroxides in animal tissues by thiobarbituric acid reaction, *Anal. Biochem.*, 95 (2), 351–358.
- [45] El Abbouyi, A., Khelifi, S., El Hachimi, Y., Khalil, A., Es-Safi, N., Belahyan, A., Tellal, R., and El Abbouyi, A., 2006, *In vitro* antioxidant properties of *Salvia verbenaca* L. hydromethanolic extract, *Indian J. Pharmacol.*, 38 (4), 276–280.
- [46] Abraham, J., 2009, “International Conference on Harmonisation of Technical Requirements for Registration of Pharmaceuticals for Human Use” in *Handbook of Transnational Economic Governance Regimes*, Eds. Brouder, A., and Tietje, C., Brill, Leiden, Netherland, 1041–1054.
- [47] Feinberg, M., 2001, *Validation Interne des Méthodes d'Analyse*, Techniques de l'Ingénieur, P224: 1–23.
- [48] OIV, 2005, Guide pratique pour la validation, le contrôle qualité, et l'estimation de l'incertitude d'une méthode d'analyse œnologique alternative, Recueil des Méthodes Internationales d'Analyses – OIV Guide de validation – Contrôle qualité, International Organization of Vine and Wine, Dijon, France, OIV-MA-AS1-12.
- [49] Mayor, M., and Bourrié, G., 2010, “Validation d'une méthode de chimie analytique - Application au dosage des anions fluorure, chlorure, nitrite, bromure, nitrate, phosphate et sulfate par chromatographie ionique” in *Validation des méthodes d'analyse quantitative par le profil d'exactitude*, Le Cahier des Techniques de l'Inra, 117–134.
- [50] Bouaissi, W., Abidi, M., and Ben Hamida, N., 2013, Optimisation et validation d'une méthode de dosage par HPLC/DAD d'un antihypertenseur le Zofenopril, *J. Soc. Chim. Tunis.*, 15, 39–50.
- [51] González-Mauraza, H., Martín-Cordero, C., Alarcón-de-la-Lastra, C., Rosillo, M.A., León-González, A.J., and Sánchez-Hidalgo, M., 2014, Anti-inflammatory effects of *Retama monosperma* in acute ulcerative colitis in rats, *J. Physiol. Biochem.*, 70 (1), 163–172.
- [52] Kim, D.O., and Lee, C.Y., 2004, Comprehensive study on vitamin C equivalent antioxidant capacity (VCEAC) of various polyphenolics in scavenging a free radical and its structural relationship, *Crit. Rev. Food Sci. Nutr.*, 44 (4), 253–273.
- [53] Wafa, G., Amadou, D., Larbi, K.M., and Héla, E.F.O., 2014, Larvicidal activity, phytochemical composition, and antioxidant properties of different parts of five populations of *Ricinus communis* L., *Ind. Crops Prod.*, 56, 43–51.
- [54] El khalki, L., Tilaoui, M., Jaafari, A., Ait Mouse, H., and Ziyad, A., 2018, Studies on the dual cytotoxicity and antioxidant properties of *Berberis vulgaris* extracts and its main constituent berberine, *Adv. Pharmacol. Sci.*, 2018, 3018498.
- [55] Yang, L., Zhang, Z., Hu, X., You, L., Khan, R.A.A., and Yu, Y., 2022, Phenolic contents, organic acids, and the antioxidant and bio activity of wild medicinal *Berberis* plants- as sustainable sources of functional food, *Molecules*, 27 (8), 2497.
- [56] Jebir, R.M., and Mustafa, Y.F., 2022, Watermelon allsweet: A promising natural source of bioactive products, *J. Med. Chem. Sci.*, 5 (5), 652–666.
- [57] Yisimayili, Z., Abdulla, R., Tian, Q., Wang, Y., Chen, M., Sun, Z., Li, Z., Liu, F., Aisa, H.A., and Huang, C., 2019, A comprehensive study of pomegranate flowers polyphenols and metabolites in rat biological samples by high-performance liquid chromatography quadrupole time-of-flight mass spectrometry, *J. Chromatogr. A*, 1604, 460472.
- [58] Saada, M., Falleh, H., Catarino, M., Cardoso, S., and Ksouri, R., 2018, Plant growth modulates metabolites and biological activities in *Retama raetam* (Forssk.) Webb, *Molecules*, 23 (9), 2177.
- [59] Chouhan, H.S., Swarnakar, G., and Jogpal, B., 2021, Medicinal properties of *Ricinus communis*: A review, *Int. J. Pharm. Sci. Res.*, 12 (7), 3632–3642.
- [60] Żymanińczyk-Duda, E., Szmigiela-Merena, B., Brzezińska-Rodak, M., and Klimek-Ochab, M., 2018, Natural antioxidants—properties and possible applications, *J. Appl. Biotechnol. Bioeng.*, 5 (4), 251–258.
- [61] Iqbal, J., Zaib, S., Farooq, U., Khan, A., Bibi, I., and Suleman, S., 2012, Antioxidant, antimicrobial, and free radical scavenging potential of aerial parts of

- Periploca aphylla* and *Ricinus communis*, *ISRN Pharmacol.*, 2012, 563267.
- [62] Singh, P.P., Ambika, A., and Chauhan, S.M.S., 2009, Activity guided isolation of antioxidants from the leaves of *Ricinus communis* L., *Food Chem.*, 114 (3), 1069–1072.
- [63] Nuralin, L., and Gürü, M., 2022, *Berberis vulgaris* fruit: Determination of phenolic compounds in extracts obtained by supercritical CO₂ and Soxhlet methods using HPLC, *Food Anal. Methods*, 15 (4), 877–889.
- [64] Bouklouze, A., and Digua, K., 2006, Démarche statistique de la validation analytique dans le domaine pharmaceutique (Méthodologie et exemple pratique), *Les technologies de laboratoire*, 1 (1), 20–24.
- [65] Nascu, H., Jäntschi, L., Hodisan, T., Cimpoi, C., and Cimpan, G., 1999, Some applications of statistics in analytical chemistry, *Rev. Anal. Chem.*, 18 (6), 409–456.
- [66] Andrade, J.M., and Estévez-Pérez, M.G., 2014, Statistical comparison of the slopes of two regression lines: A tutorial, *Anal. Chim. Acta*, 838, 1–12.
- [67] OIV, 2005, *Practical guide for the validation, quality control, and uncertainty assessment of an alternative oenological analysis method*, Compendium of International Analysis of Methods - OIV Guide for the validation – quality Control, International Organization of Vine and Wine, Dijon, France, OIV-MA-AS1-12.
- [68] OIV, 2000, *Estimation de la limite de détection et de quantification d'une méthode d'analyse*, Recueil international des méthodes d'analyses – OIV Estimation de la limite de détection et de quantification, International Organization of Vine and Wine, Dijon, France, OIV-MA-AS1-10.

Supplementary Data

This supplementary data is a part of a paper entitled "Synthesis, Thermal, DFT Calculations, HOMO-LUMO, MEP, and Molecular Docking Analysis of New Derivatives of Imidazolin-4-Ones".

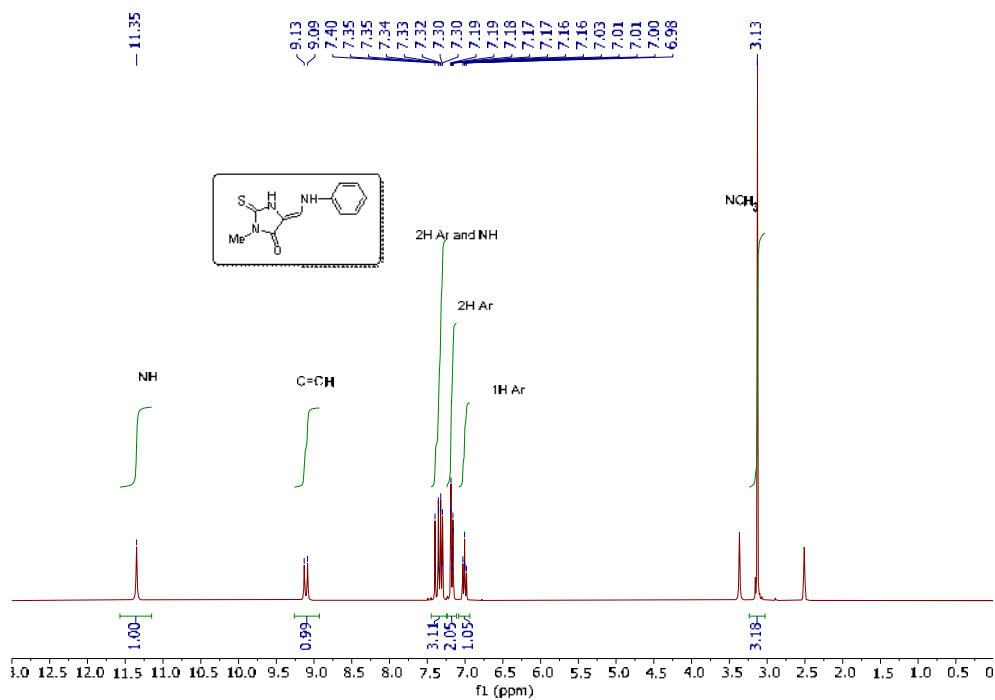


Fig S1. ¹H-NMR spectrum of 3-methyl-5-phenylaminomethylene-2-thioxoimidazolidin-4-one

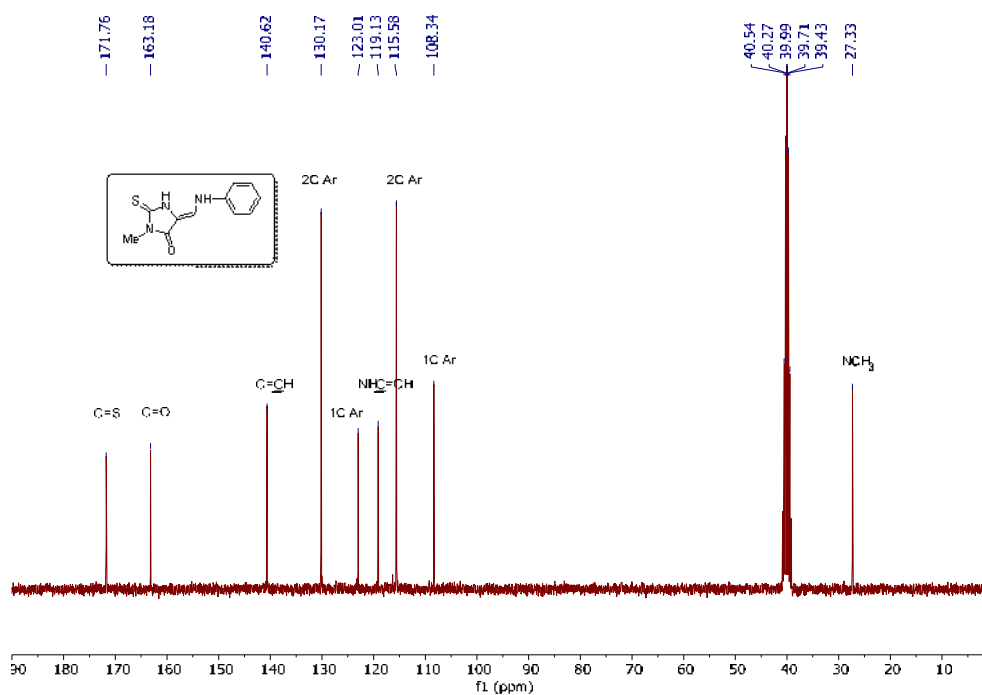
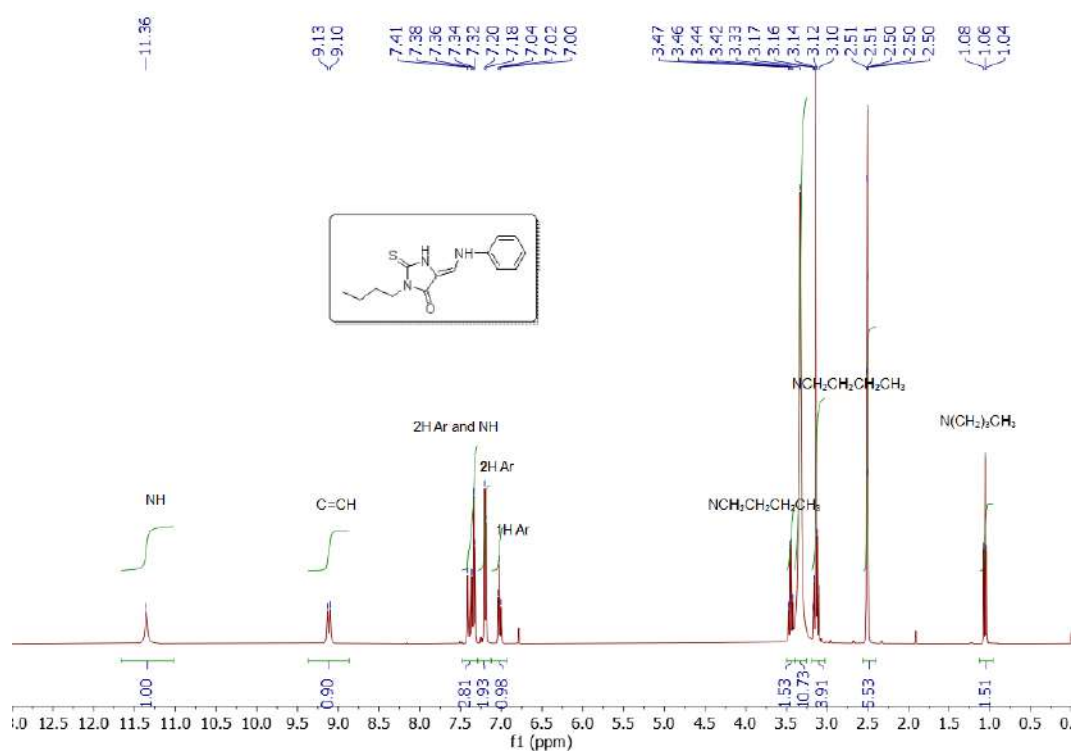
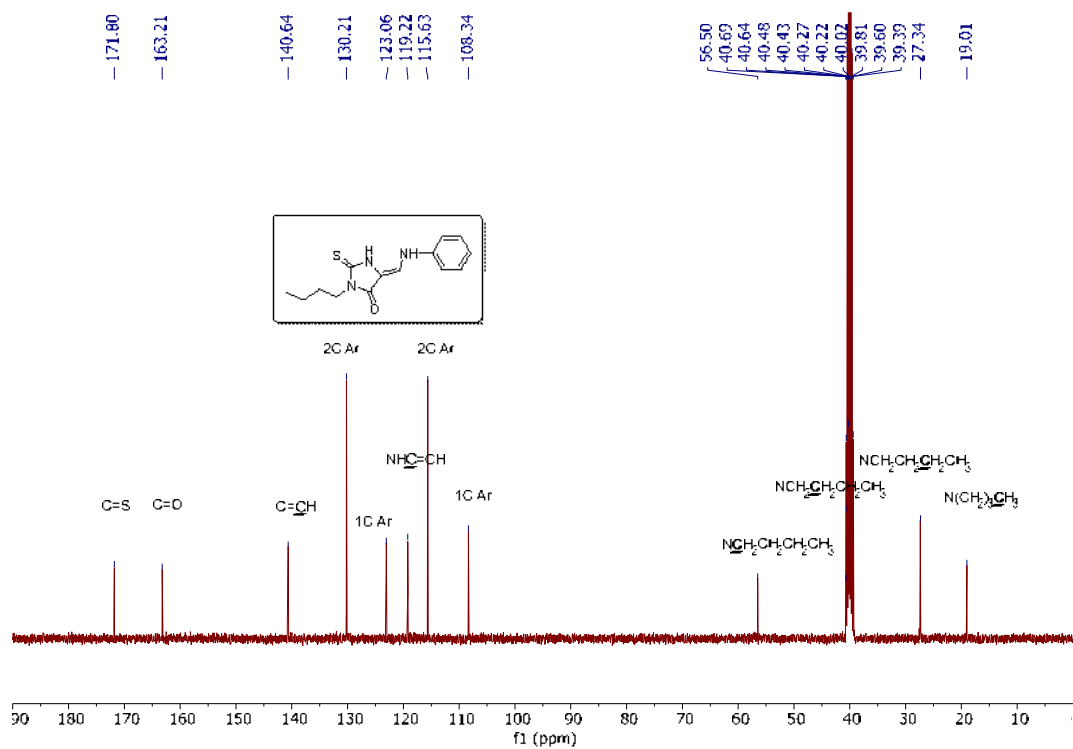


Fig S2. ¹³C-NMR spectrum of 3-methyl-5-phenylaminomethylene-2-thioxoimidazolidin-4-one

Fig. S3. ¹H-NMR spectrum of 3-butyl-5-phenylaminomethylene-2-thioxoimidazolidin-4-oneFig S4. ¹³C-NMR spectrum of 3-butyl-5-phenylaminomethylene-2-thioxoimidazolidin-4-one

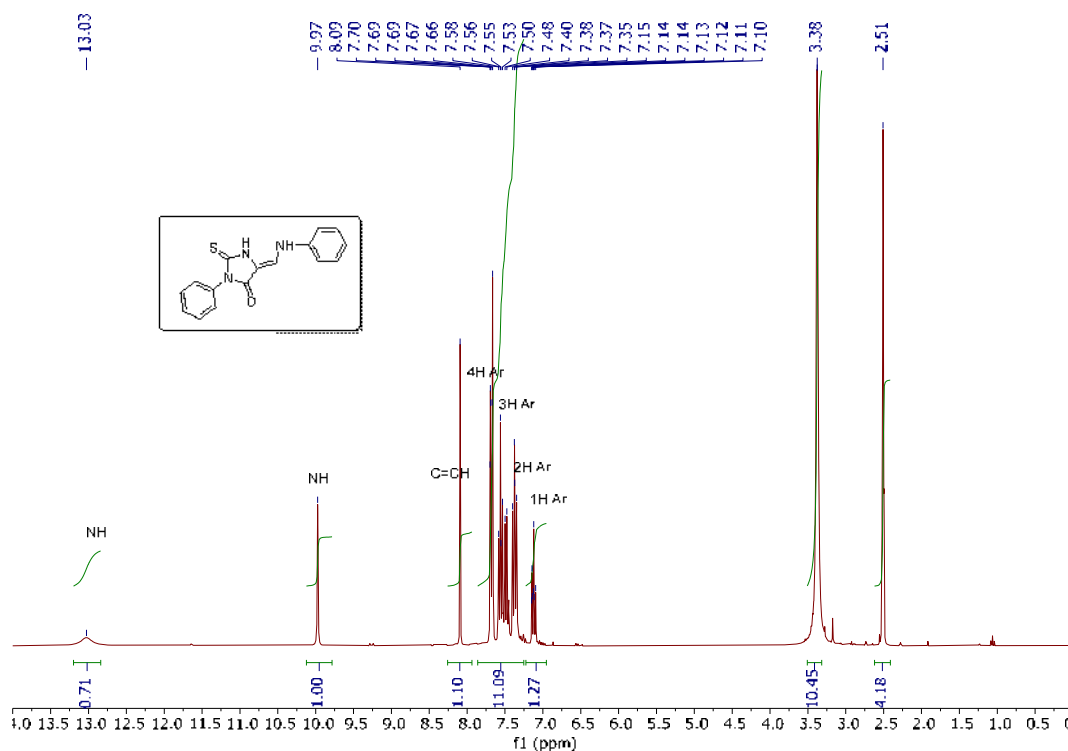


Fig S5. ¹H-NMR spectrum of 3-phenyl-5-phenylaminomethylene-2-thioxoimidazolidin-4-one

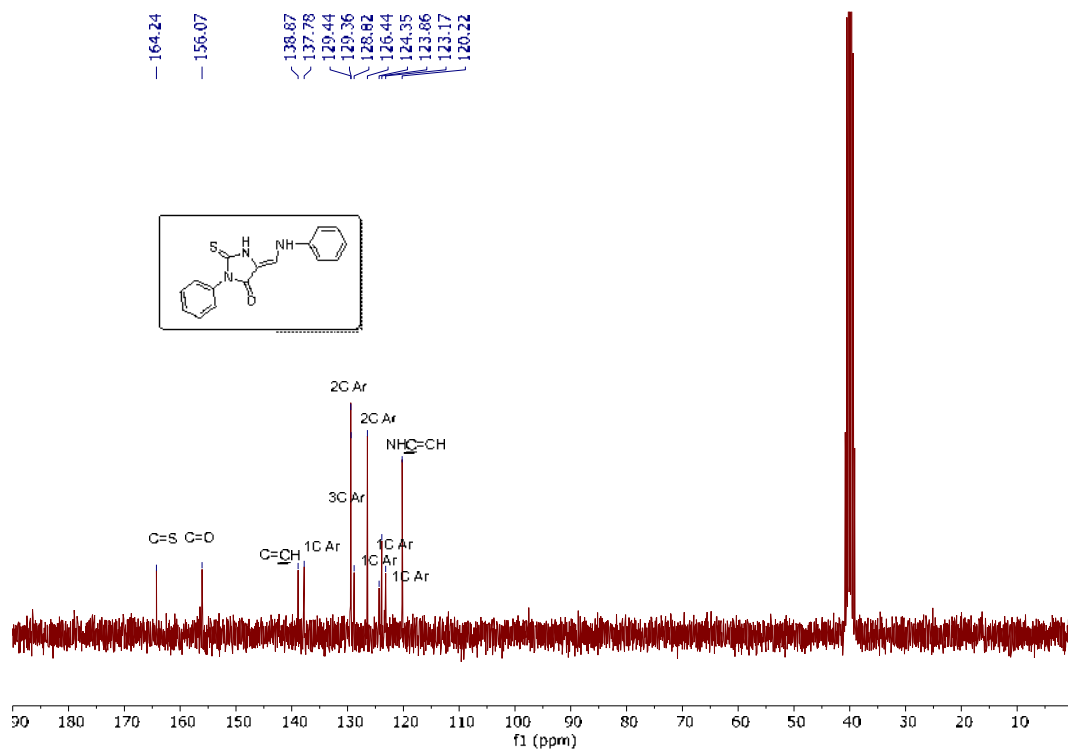


Fig S6. ¹³C-NMR spectrum of 3-phenyl-5-phenylaminomethylene-2-thioxoimidazolidin-4-one

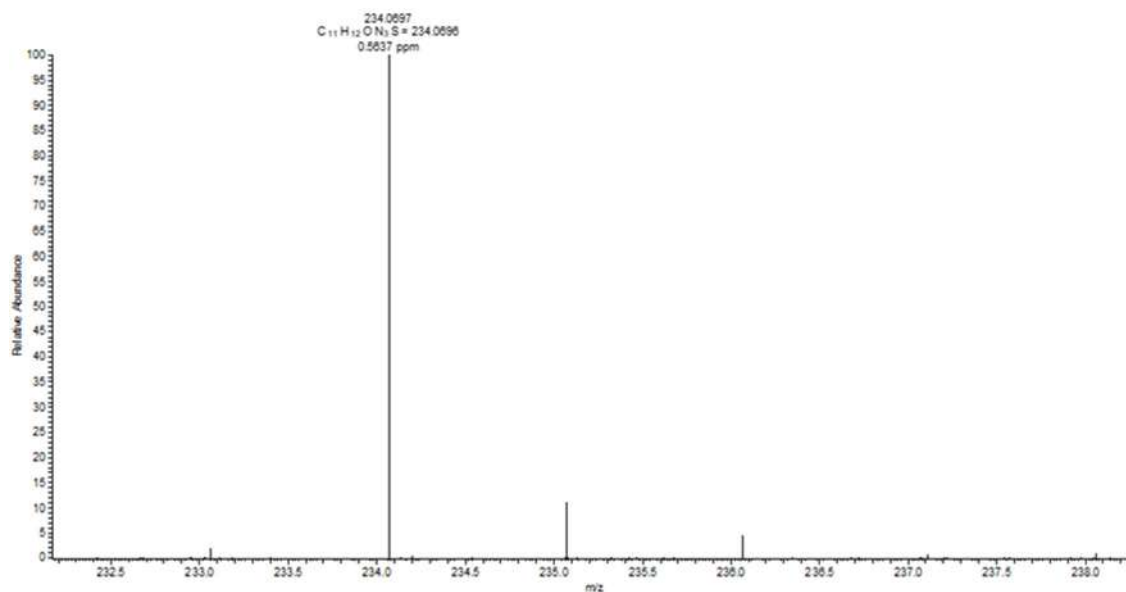


Fig S7. MS spectrum of 3-methyl-5-phenylaminomethylene-2-thioxoimidazolidin-4-one

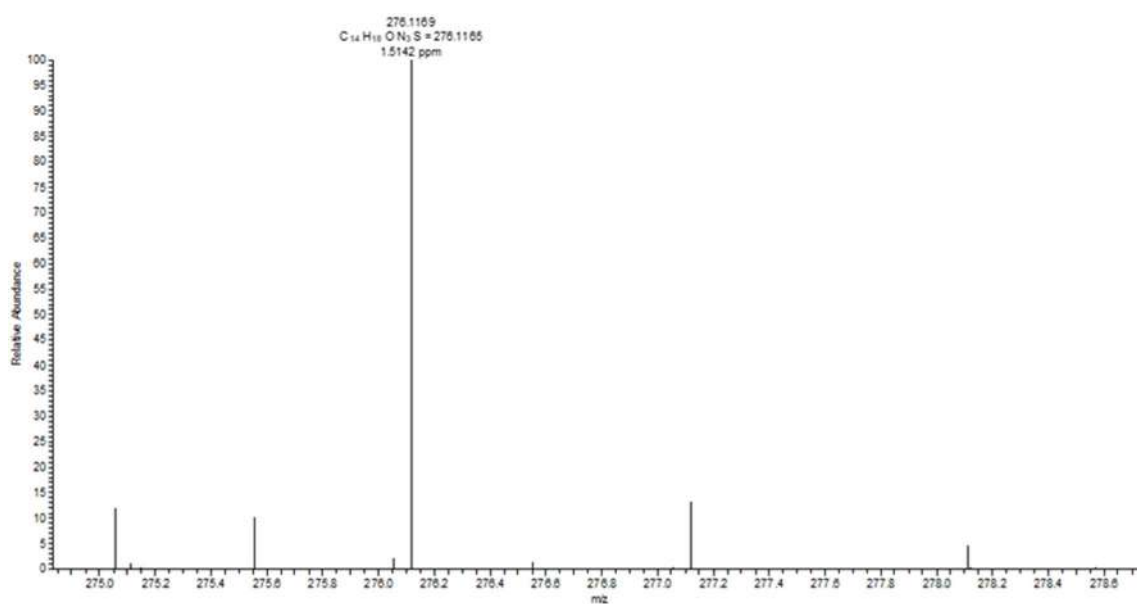


Fig S8. MS spectrum of 3-butyl-5-phenylaminomethylene-2-thioxoimidazolidin-4-one

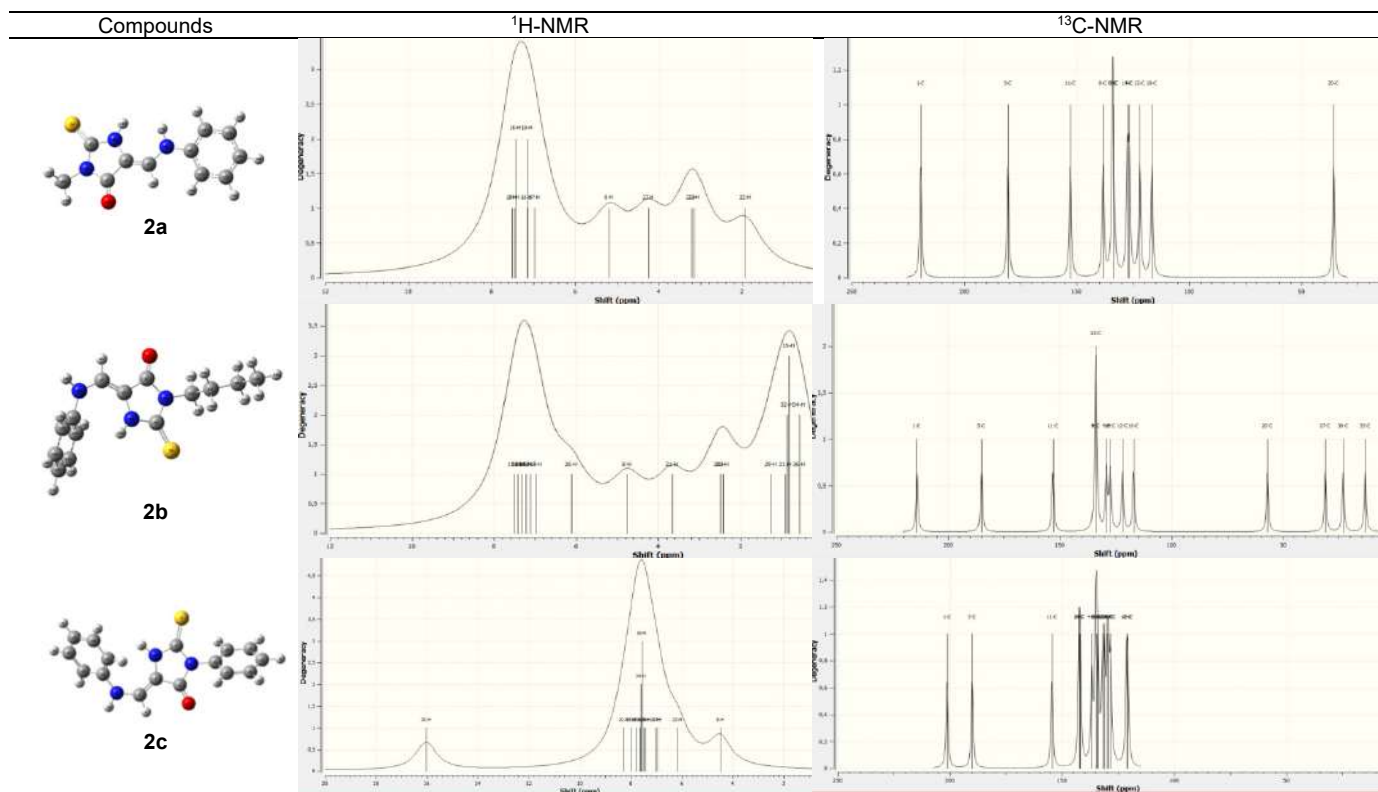


Fig S9. Theoretical NMR spectra of compounds 2a-c

Synthesis, Thermal, DFT Calculations, HOMO-LUMO, MEP, and Molecular Docking Analysis of New Derivatives of Imidazolin-4-Ones

Khedidja Merdja^{1,2}, Choukry Kamel Bendeddouche¹, Mokhtaria Drissi², Farah Chafika Kaouche², Nassima Medjahed^{3,4}, José Manuel Padrón⁵, Mansour Debdab^{2*}, Mustapha Rahmouni², and El Habib Belarbi²

¹Laboratory of Applied Organic Synthesis, Faculty of Exact and Applied Sciences, University Oran1 Ahmed Ben Bella, El M'Naouer, Oran 31000, Algeria

²Laboratory of Synthesis and Catalysis (LSCT), Faculty of Materials Sciences, University Ibn Khaldoun-Tiaret, Tiaret 14000, Algeria

³Laboratoire de Catalyse et Synthèse en Chimie Organique, Faculté des Sciences, Université de Tlemcen, Tlemcen 13000, Algeria

⁴Faculté des Sciences et de la Technologie, Université d'Ain Témouchent, Ain Témouchent 46000, Algeria

⁵BioLab, Instituto Universitario de Bio-Organica "Antonio González", Universidad de La Laguna, La Laguna 38200, Spain

* **Corresponding author:**

email: mansour.debdab@univ-tiaret.dz

Received: July 29, 2023

Accepted: September 20, 2023

DOI: 10.22146/ijc.87476

Abstract: This work focuses on synthesizing new imidazolin-4-one derivatives (**2a-c**), akin to leucettamine B analogs, via microwave-assisted transamination reactions. This reaction was carried out between 3-alkyl-5-dimethylamino-2-thioxo-imidazolidin-4-one (**1a-c**) and aniline. The structural integrity of the synthesized compounds was confirmed using NMR and MS spectroscopy, and their configurations were validated through DFT calculations. Analyses encompassed molecular electrostatic potential, frontier molecular orbitals, HOMO-LUMO energies, energy band gap, and global chemical reactivity descriptors, providing comprehensive insights into their characteristics. The investigation extended to the biological domain, employing substance activity spectra prediction (PASS) and molecular docking with Autodock Vina4 program. Notably, this holistic assessment aimed to gauge the potential regulatory effect of the compounds on cholesterol. This integrated approach contributes to compound design understanding and potential applications, spanning drug design and broader biomedical contexts.

Keywords: DFT calculations; imidazolin-4-ones derivatives; HOMO-LUMO energies; microwave irradiation; molecular docking

■ INTRODUCTION

Marine natural products have evolved considerably and have become very interesting sources of inspiration for new drug discovery [1]. Most of the compounds have spurred improvements in organic chemistry, especially in synthesis methodologies, thereby paving the way to synthesize analogs with improved pharmacological or pharmaceutical properties [2-5]. From this point of view, marine sponges provide without a doubt a vast store of unique and physiologically active natural compounds that need to be studied.

The study of 2-thiohydantoin derivatives as well as 2-aminoimidazolin-4-one has attracted the interest of many researchers both in synthesis and in the study of their properties [6-7], particularly as a material first for the preparation of synthetic intermediates with a wide range of applications in several fields as therapeutic agents [8-9] antifungals, herbicides [10-11], antitumors [12], and other biological activities [13]. As a consequence, the development of solvent-free organic synthesis using microwaves has gained much interest [14-15].

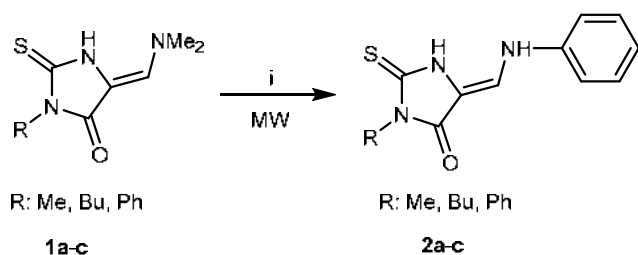
The purpose of this study is to synthesize new molecule derivatives of 2-thiohydantoin using aniline as the aromatic amine in the transamination step, and then we conducted *in silico* investigations using DFT calculations, activity prediction, and molecular docking. Chérouvrier et al. [16] used this strategy to obtain analogues of leucettamine B. However, aniline was not used in this reaction.

As far as we know, the transamination of 5-dimethylaminomethylene-3-alkyl-2-thioxoimidazolidin-4-ones (**1a-c**) using aniline under microwave irradiation (M.W.I.) has not been described previously. In this framework, we report our first results concerning this strategy for the synthesis of new derivatives of imidazolidin-4-ones according to Scheme 1.

It is widely established that in organic frameworks with large delocalized π -systems, π -electrons are more polarizable due to their further enhancement by the donor and acceptor substituents incorporation at the extremities of the conjugated system [17]. The magnitude of the charge transfer is largely determined by these groups at the opposite ends.

The compounds **1a-c** and **2a-c** were calculated using the density functional theory (DFT) method with B3LYP/6-311G(d,p) basis set. The molecular electrostatic potential (MEP) shape is a plot of electrostatic potential mapped onto the constant electron density surfaces, which provides information about charge density distributions, nucleophilic, and electrophilic reaction sites for hydrogen bonding interactions in a molecule.

The MEP map and the energies (HOMO and LUMO) of the compound were determined using DFT/B3LYP method with 6-311G(d,p) basis set in Gaussian 09 software



Scheme 1. Reagents and conditions: (i) Ph-NH₂ (4 eq), MW, for **2a**: R = Me, 70 °C, 5 min; for **2b**: R = Bu, 70 °C, 5 min for **2c**: R = Ph, 70 °C, 10 min

program. In addition, the prediction of activity spectra for substances (PASS) and molecular docking methods were employed to conduct a comprehensive investigation, yielding essential information for determining the biological activity of the investigated compounds.

■ EXPERIMENTAL SECTION

Materials

The reagents used in this study without any further purification are *N,N*-dimethylformamide dimethyl acetal 94% (DMF-DMA) and aniline ($\geq 99\%$).

Instrumentation

A Bruker Ascend TM 300 was used to record the ¹H-NMR and ¹³C-NMR spectra at 300 and 75 MHz, respectively. Shifts (δ) are presented in ppm relative to the residual proton signal of DMSO-*d*₆ at 2.50 ppm (m). A Q-exactive mass spectrometer and electrospray ionization (ESI) were used to record mass spectra. Sample injection (MeOH as solvent) was carried out using UHPLC without a column (50 L and 3 min acquisition at 0.200 mL/min). The acquisition was carried out with a full scan at 60,000 resolutions. The capillary temperature was 350 °C and the source voltage was 3.5 kV. Spectra were recorded in positive mode and calibrated using the Pierce™ LTQ Velos ESI Positive Ion Calibration Solution (Thermo Fisher Scientific). A Kofler melting point apparatus was used to determine the melting points (m.p.) of all products with a temperature reading scale graduated from 50 °C to 260 °C.

Procedure

Synthesis and characterization of 5-dimethylaminomethylene-3-alkyl-2-thioxoimidazolidin-4-ones (**1a-c**)

5-Dimethylaminomethylene-3-alkyl-2-thioxoimidazolidin-4-ones (**1a-c**) were synthesized following procedures described in the literature [16,18]. Briefly, a mixture of 3-alkyl-2-thioxo-imidazolidin-4-one and DMF-DMA (1.2 eq) was reacted in a microwave for 30 min at 70–80 °C. After cooling at room temperature, the crude products were washed with

ethanol. The aminomethylenation products (**1a-c**) were obtained as a solid in yields ranging from 74 to 77%.

General method for the synthesis of 3-alkyl-5-phenylaminomethylene-2-thioxoimidazolidin-4-ones (**2a-c**)

A mixture of 5-dimethylaminomethylene-3-alkyl-2-thioxoimidazolidin-4-one (**1a-c**) and aniline (4 eq) was reacted in a microwave at 70 °C for 5 to 10 min (Scheme 2). When the reaction was completed, the crude reaction mixture was allowed to cool down at room temperature, and then ethanol was added until the compounds had completely precipitated. The expected compounds were obtained after filtration on sintered glass.

RESULTS AND DISCUSSION

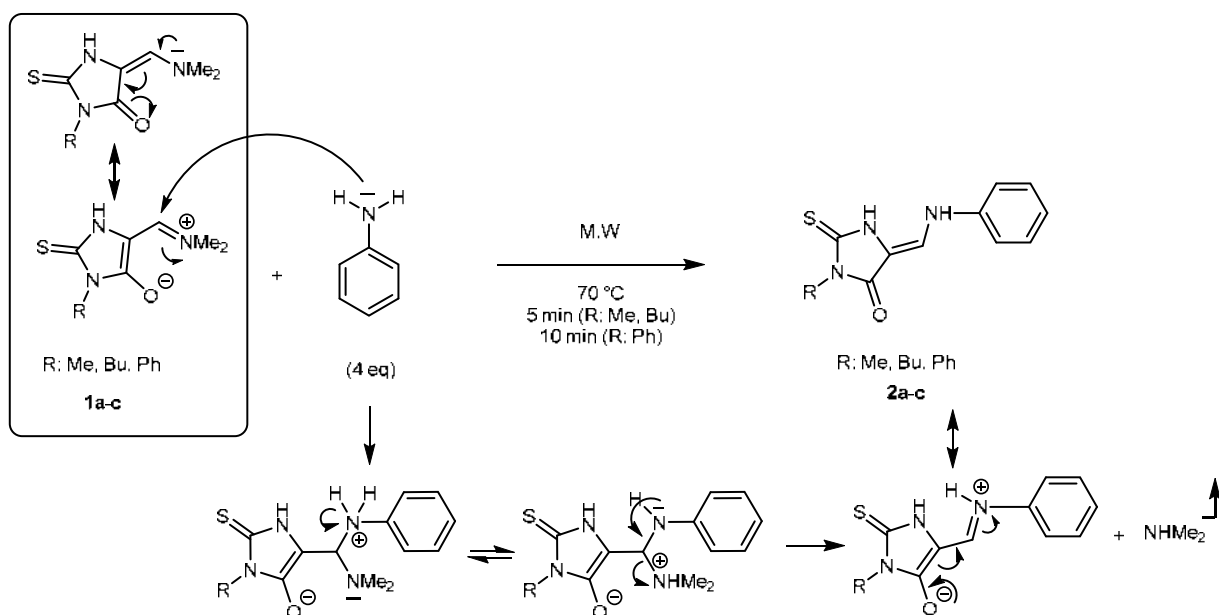
The new imidazolin-4-ones **2a-c** were obtained by a simple transamination reaction between 3-alkyl-5-dimethylamino-2-thioxo-imidazolidin-4-ones **1a-c** and aniline using the eco-friendly solventless methodology under microwave irradiation. The expected compounds were obtained in good yields ranging from 70 to 84% after filtration and by adding the ethanol. ¹H-NMR, ¹³C-NMR, and mass spectrometry were used to confirm the obtained product structures. The ¹H-NMR shows that the reaction is stereospecific. In fact, only one stereoisomer is observed in ¹H-NMR of the reaction product. The exocyclic double

bond proton C=CH has a chemical shift of about 9 ppm. The coupling constant ³J = 13.2 Hz [19] for compounds **2a** and **2b** that exists between the exocyclic vinyl proton C–H and the amino proton N–H lead to the suggestion of the trans relation between these two hydrogens about the C–N bond which acquires partial double character due to conjugation. However, this vinylic C–H appears as a singlet in the case of **2c** caused by the fast exchange of the proton of the amine group. The appearance of the signals of phenyl and N–H groups at respectively 7.00 and 7.40 ppm (**2b**) affirm the transamination reaction. This result is confirmed by ¹³C-NMR, which shows the signals of *sp*² carbons of the phenyl group varying from 108 to 138 ppm. Moreover, the comparison between experimental and theoretical ¹H- and ¹³C-NMR spectra obtained by Gaussian 09 confirms the obtaining of imidazolin-4-ones derivatives (**2a-c**) (Fig. S9).

NMR and MS Spectroscopies Results

3-Methyl-5-phenylaminomethylene-2-thioxoimidazolidin-4-one (**2a**)

Yield: 70%; yellow powder; m.p. > 260 °C. ¹H-NMR (300 MHz, DMSO-*d*₆): δ 3.13 (s, 3H, NCH₃), 7.00 (t, *J* = 7.3 Hz, 1H, Ar), 7.16–7.19 (m, 2H, Ar), 7.30–7.40 (m, 3H, Ar, NH), 9.09–9.13 (d, *J* = 13.2 Hz, 1H, C=CH), 11.35 (br s, 1H, NH) (Fig. S1). ¹³C-NMR (75 MHz, DMSO-*d*₆):



Scheme 2. Synthesis of 3-alkyl-5-phenylaminomethylene-2-thioxoimidazolidin-4-ones (**2a-c**) with mechanism

δ 27.33 (NCH₃), 108.34 (C-Ar), 115.58 (2 C-Ar), 119.13 (NHC=CH), 123.01 (C-Ar), 130.17 (2 C-Ar); 140.62 (C=CH), 163.18 (C=O), 171.76 (C=S) (Fig. S2). HRMS, m/z : 234.0697 found (calculated for C₁₁H₁₂N₃OS, [M + H]⁺ requires: 234.0696) (Fig. S7).

3-Butyl-5-phenylaminomethylene-2-thioxoimidazolidin-4-one (2b)

Yield: 82%; light brown powder; m.p. = 224–226 °C. ¹H-NMR (300 MHz, DMSO-*d*₆): δ 1.06 (t, J = 7.0 Hz, 3H, NCH₂CH₂CH₂CH₃), 3.10–3.17 (m, 4H, NCH₂CH₂CH₂CH₃), 3.42–3.47 (q, J = 7.0 Hz, 2H, NCH₂CH₂CH₂CH₃), 7.02 (t, J = 7.3 Hz, 1H, Ar), 7.19 (d, J = 8.0 Hz, 2H, Ar), 7.32–7.41 (m, 3H, Ar, NH), 9.10–9.13 (d, J = 13.1 Hz, 1H, C=CH), 11.36 (br s, 1H, NH) (Fig. S3). ¹³C-NMR (75 MHz, DMSO-*d*₆): δ 19.01 (NCH₂CH₂CH₂CH₃), 27.34 (NCH₂CH₂CH₂CH₃), 39.60 (NCH₂CH₂CH₂CH₃), 56.50 (NCH₂CH₂CH₂CH₃), 108.34 (C-Ar), 115.63 (2 C-Ar), 119.22 (NHC=CH), 123.06 (C-Ar), 130.21 (2 C-Ar), 140.64 (C=CH), 163.21 (C=O), 171.80 (C=S). (Fig. S4). HRMS, m/z : 276.1169 found (calculated for C₁₄H₁₈N₃OS, [M + H]⁺ requires: 276.1165) (Fig. S8).

3-Phenyl-5-phenylaminomethylene-2-thioxoimidazolidin-4-one (2c)

Yield: 84%; dark brown powder; m.p. > 260 °C. ¹H-NMR (300 MHz, DMSO-*d*₆): δ 7.12 (t, J = 7.4 Hz, 1H, Ar), 7.35–7.40 (m, 2H, Ar), 7.48–7.58 (m, 3H, Ar), 7.66–7.70 (m, 4H, Ar), 8.09 (s, 1H, C=CH), 9.97 (s, 1H, NH), 13.03 (br s, 1H, NH) (Fig. S5). ¹³C-NMR (75 MHz, DMSO-*d*₆): δ 120.22 (NHC=CH), 123.17 (C-Ar), 123.86 (C-Ar), 124.35 (C-Ar), 126.44 (2 C-Ar), 128.82 (C-Ar), 129.36 (2 C-Ar), 129.44 (3 C-Ar), 137.78 (C-Ar), 138.87 (C=CH), 156.07 (C=O), 164.24 (C=S) (Fig. S6).

Computational Results and Discussion

The Gaussian 09 set of quantum chemistry codes were used to perform the ground state calculations [20]. Gauss View 5 software was used to visualize the output files [21]. The structural properties of compounds **1a-c** and **2a-c** were determined by applying Becke's three-parameter hybrid functional (B3) for the exchange part and the Lee-Yang-Parr (LYP) correlation function [22] with 6-31G(d,p) level in order to obtain the optimized geometrical parameters of the compound. The MEP and

HOMO–LUMO energies were calculated at the same level. Additionally, the global reactivity descriptors and the dipole moment are also calculated to understand the reactive nature of the compound. For a more in-depth study to provide additional information as a basis for determining the biological activity of the studied compounds, we used PASS and the molecular docking method using Autodock Vina4 [23].

We harnessed Autodock Vina4 for conducting molecular docking and leveraged the Pass Online tool to predict the biological activity of the identified compounds namely, **lig1 (2a)**, **lig2 (2b)**, and **lig3 (2c)**. Our discerned results substantiate the potential of these compounds to function as enhancers of HMGCS2 expression. Employing molecular docking, we delved into the preferred orientations and binding mechanisms of these molecules within HMGCS2's active site. This comprehensive exploration facilitates insights into intricate molecular interactions, encompassing hydrogen bonding, hydrophobic interactions, and electrostatic forces. These interactions collectively underscore the fundamental stabilizing factors governing the system's integrity.

Frontier molecular orbital's (FMOs) studies: Global reactivity descriptors

The charge transfer placed within the molecule was explained by analyzing the HOMO and LUMO. Both orbitals named as FMOs. The FMOs energies (E_{HOMO} , E_{LUMO}) were employed to determine the global chemical reactivity descriptors of the molecule such as the ionization potential electron affinity, the electronegativity, the global hardness, the global softness, the chemical potential, and the electrophilicity index [24–25]. Two important molecular properties, electronegativity and hardness, are useful for interpreting and understanding the stability and reactivity of molecular systems [26].

The HOMO-LUMO energy gap explains the concluding charge transfer interaction within the molecule and is useful in determining molecular electrical transport properties. A molecule with a small frontier orbital gap (HOMO-LUMO energy gap) has high chemical reactivity and low kinetic stability [27–29]

because it is energetically favorable to add an electron to the high-lying LUMO in order to remove electrons from the low-lying HOMO. Therefore, HOMO-LUMO energies are used to determine different chemical properties such as the global reactivity descriptors (ΔE), ionization potential ($IP = -E_{HOMO}$), electron affinity ($EA = -E_{LUMO}$), global chemical hardness ($\eta = (IP - EA)/2$), global chemical softness ($s = 1/2\eta$), electronegativity ($\chi = (IP + EA)/2$), chemical potential ($\mu = -(IP + EA)/2$) and electrophilicity index ($\omega = \mu^2/2\eta$).

The HOMO-LUMO gap energy and the dipole moment listed in Table 1 of the title compound were computed with DFT/B3LYP/6-311G(d,p) method. The calculated values of the global reactivity descriptors are also listed in Table 1. The FMO's atomic orbital compositions can be seen in Fig. 1 and 2.

In the group of **2a-c**, the best electron donor is compound **2b**, which has the highest HOMO energy ($E_{HOMO} = -5.385$ eV) and the lowest ionization value ($IP = 5.385$ eV), while the best electron acceptor is compound **2c**, which has the lowest LUMO energy ($E_{LUMO} = -1.673$ eV), the highest electron affinity ($EA = 1.673$ eV), and the highest ionization value ($IP = 0.5413$ eV) (Table 2). Furthermore, compound **2c** showed the smallest orbital energy gap ($\Delta E = 3.74$ eV) among the investigated products as the consequence of the highest chemical reactivity, least kinetically stable "soft molecule", and the most polarizable form (Fig. 2). The reactivity of these compounds is the greatest based on energy gap (ΔE) parameters, which support that compound **2a** is the most stable as compared to others as follow the order **2a** > **2b** > **2c** (Fig. 2). It is important

Table 1. Some quantum chemical molecular descriptors computed of the **1a-c** compounds using DFT/B3LYP/6-311G(d,p)

Compounds	Compound 1a	Compound 1b	Compound 1c
E_{HOMO} (eV)	-5.277	-5.252	-5.279
E_{LUMO} (eV)	-1.281	-1.265	-1.321
$ E_{HOMO} - E_{LUMO} $ (eV)	3.996	3.987	3.957
Dipole moment μ (Debye)	6.784	6.584	6.741
IP (eV)	5.277	5.252	5.279
EA (eV)	1.281	1.265	1.321
η (eV)	1.998	1.993	1.979
S (eV^{-1})	0.250	0.251	0.253
χ (eV)	3.279	3.258	3.300
μ (eV)	-3.279	-3.258	-3.300
ω (eV)	2.690	2.662	2.753

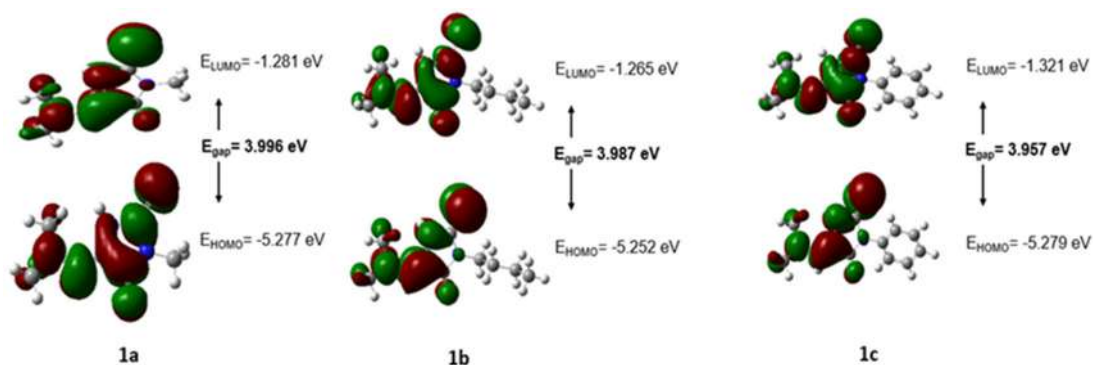
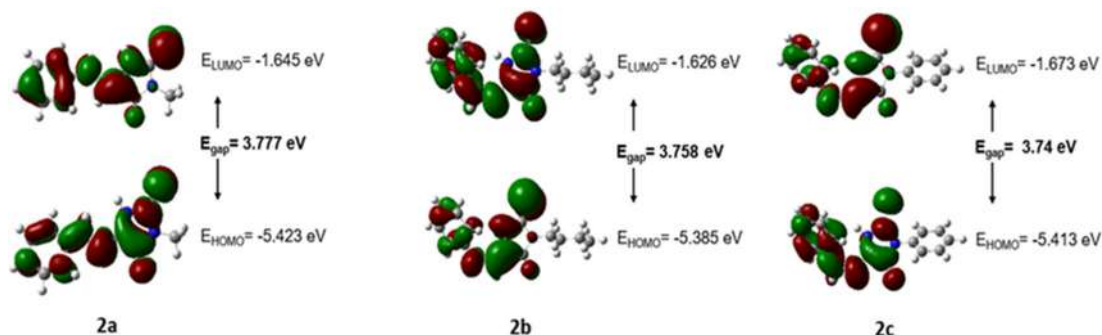


Fig 1. The molecular orbitals and energies for the HOMO and LUMO with the numbering of atoms for the 5-dimethylaminomethylene-3-alkyl-2-thioxoimidazolidin-4-ones (**1a-c**)

Table 2. Some computed quantum chemical molecular descriptors of the **2a-c** compounds using DFT/B3LYP/6-311G(d,p)

Compounds	Compound 2a	Compound 2b	Compound 2c
E_{HOMO} eV	-5.423	-5.385	-5.413
E_{LUMO} eV	-1.645	-1.626	-1.673
$ E_{\text{HOMO}} - E_{\text{LUMO}} $ (eV)	3.777	3.758	3.740
Dipole moment μ (Debye)	5.783	5.577	5.668
IP (eV)	5.423	5.385	5.413
EA (eV)	1.645	1.626	1.673
η (eV)	1.889	1.879	1.870
S (eV^{-1})	0.265	0.266	0.267
χ (eV)	3.534	3.505	3.543
μ (eV)	-3.534	-3.505	-3.543
ω (eV)	3.305	3.268	3.356

**Fig 2.** The molecular orbitals and energies for the HOMO and LUMO with the numbering of atoms for the titles compounds 3-alkyl-5-phenylaminomethylene-2-thioxoimidazolidin-4-one (**2a-c**)

to measure other important parameters such as η , S , and μ to measure the stability of the compound.

Mulliken population analysis

Quantifying the electronic structure changes caused by atomic displacements can be done by using atomic charge calculations, which can be used to explain changes in molecular properties. The Mulliken [30] population analysis is the most widely known of all models for predicting individual atomic charges, and it is highly computationally popular due to its simplicity. It was observed that Mulliken charges are highly dependent on basis sets and unpredictable, with significant fluctuations in partial charges [31].

The atomic charge values calculated by Mulliken analysis for **1a-c** and **2a-c** at the BPV86 functional with the 6-311G(d,p) basis set are summarized in Table 3 and

4. According to Mulliken results, all of the hydrogen atoms are positively charged. In these molecules, the H_1 and H_3 atoms have high positive Mulliken charges of 0.273 and 0.279 e, respectively. These charges are important compared to the other hydrogen atoms due to the electronegative character of the N_2 and N_3 atoms. The large positive charge values of hydrogen atoms indicate the presence of intra and inter-molecular hydrogen bonding in the crystal packing. On the other hand, the sulfur, oxygen, and nitrogen atoms have the most negative charges in the four title molecules. The carbon atoms bound to the sulfur, oxygen, and nitrogen atoms have positive charges due to their electron-withdrawing nature. The calculated Mulliken charges are in complete agreement with the molecular electrostatic potential results using the BPV86/6-311G(d,p) level of theory.

Table 3. Atomic charges distribution for 5-dimethylaminomethylene-3-alkyl-2-thioxoimidazolidin-4-ones (**1a-c**) calculated by Mulliken method using the BPV86/6-311G(d,p) level in the gas phase

Compound 1a		Compound 1b		Compound 1c	
1C	0.553	1C	0.555	1C	0.556
2C	0.214	2C	0.272	2C	0.275
3C	0.360	3C	0.360	3C	0.362
4N	-0.498	4N	-0.499	4N	-0.509
5S	-0.288	5S	-0.270	5S	-0.271
6N	-0.631	6N	-0.624	6N	-0.626
7C	0.121	7C	0.077	7C	0.077
8H	0.140	8H	0.145	8H	0.145
9N	-0.422	9N	-0.606	9N	-0.607
10C	-0.176	10C	-0.176	10C	-0.176
10HA	0.126	10HA	0.126	10HA	0.126
10HB	0.125	10HB	0.125	10HB	0.125
10HC	0.136	10HC	0.136	10HC	0.136
11C	-0.190	11C	0.289	11C	-0.190
11HA	0.138	11HA	0.138	11HA	0.138
11HB	0.127	11HB	0.127	11HB	0.127
11HC	0.130	11HC	0.130	11HC	0.130
12H	0.273	12H	0.273	12H	0.273
13O	-0.527	13O	-0.527	13O	-0.527
14C	-0.176	14C	-0.050	14C	0.264
14HA	0.144	14HA	0.113	15C	-0.081
14HB	0.145	14HB	0.134	15HA	0.104
14HC	0.146	15C	-0.176	16C	-0.104
		15HA	0.118	16HA	0.081
		15HB	0.108	17C	-0.074
		16C	-0.178	17HA	0.085
		16HA	0.100	18C	-0.103
		16HB	0.096	18HA	0.090
		17C	-0.319	19C	-0.064
		17HA	0.107	19HA	0.110
		17HB	0.104		
		17HB	0.100		

Molecular electrostatic potential

Generally, the electrophilic and nucleophilic sites of a molecule can be located by studying electrostatic potential (ESP) [32]. It is a valuable and useful tool for molecular modeling studies. Predicting the interaction between different geometries can be done easily using the MEP contour map [33]. The total charge distribution of a molecule can be used to define the MEP at a given point

Table 4. Atomic charges distribution for and3-alkyl-5-phenylaminomethylene-2-thioxoimidazolidin-4-ones (**2a-c**) calculated by Mulliken method using the BPV86/6-311G(d,p) level in the gas phase

Compound 2a		Compound 2b		Compound 2c	
1C	0.555	1C	0.556	1C	0.553
2C	0.272	2C	0.275	2C	0.273
3C	0.360	3C	0.362	3C	0.359
4N	-0.499	4N	-0.509	4N	-0.613
5S	-0.270	5S	-0.271	5S	-0.255
6N	-0.624	6N	-0.626	6N	-0.523
7C	0.077	7C	0.077	7C	0.078
8H	0.145	8H	0.145	8H	0.146
9N	-0.606	9N	-0.607	9N	-0.606
11C	0.289	11C	0.289	11C	0.289
24C	-0.176	24C	-0.050	15O	-0.508
24HA	0.146	24HA	0.139	10H	0.276
24HB	0.147	24HB	0.130	12C	-0.139
24HC	0.148	15O	-0.525	13C	-0.113
14H	0.286	10H	0.276	14C	-0.091
15O	-0.519	12C	-0.139	15H	0.119
10H	0.270	13C	-0.113	16C	-0.088
12C	-0.139	14C	-0.091	17H	0.089
13C	-0.113	15H	0.119	18C	-0.083
14C	-0.091	16C	-0.088	19H	0.105
15H	0.119	17H	0.089	20H	0.098
16C	-0.088	18C	-0.083	21H	0.096
17H	0.089	19H	0.105	24C	0.261
18C	-0.083	20H	0.098	25C	-0.052
19H	0.105	21H	0.096	26C	-0.061
20H	0.098	27C	-0.175	27C	-0.103
21H	0.096	28H	0.108	28H	0.110
		29H	0.118	29C	-0.103
		30C	-0.179	30H	0.103
		31H	0.100	31C	-0.073
		32H	0.096	32H	0.091
		33C	-0.319	33H	0.090
		34H	0.101	34H	0.087
		35H	0.104		

around it and it is connected to dipole moments. By analyzing the electron density, it can be used to determine electrophilic reactivity, nucleophilic reactivity, and hydrogen-bonding interactions [34-35]. The electrostatic potential, $V(\vec{r})$ at any point \vec{r} is given by Eq. (1) [35]:

$$V(\vec{r}) = \sum_A \frac{Z_A}{|\vec{R}_A - \vec{r}|} - \int \frac{\rho(\vec{r}') d\vec{r}'}{|\vec{r}' - \vec{r}|} \quad (1)$$

where $\rho(\vec{r})$ is the electronic density function molecule, Z_A is the charge on the nucleus A located at \vec{R}_A , and r' is the dummy integration variable. In order to predict the molecular reactive sites, the electrostatic potential surface maps have been plotted for the title compounds with B3LYP/6-311G(d,p) level shown in Fig. 3.

According to this MEP map, there are two possibilities for the electrophilic attack on the oxygen atoms (red), while the nucleophilic attack sites are located over the hydrogen atoms (yellow). These sites give information about the intermolecular interactions of our compounds. As a result, the compounds can have non-covalent interactions.

Molecular docking

Molecular docking serves as a crucial tool for investigating the optimal interaction between ligands and proteins. In our study, we employed the Pass Online tool [36] to identify promising biological activities associated with the ligands under examination, aiding us in selecting the most relevant protein targets (Table 5). Notably, HMGCS2 holds a pivotal role within the mevalonate pathway, a significant process for cholesterol synthesis. The potential to modulate HMGCS2 expression offers an innovative avenue for managing elevated cholesterol levels in cases of hypercholesterolemia. Interestingly, the ligands **2a**, **2b**, and **2c**, as indicated by Pass Online, exhibit the capacity to enhance this particular enzyme Protein PDB file was

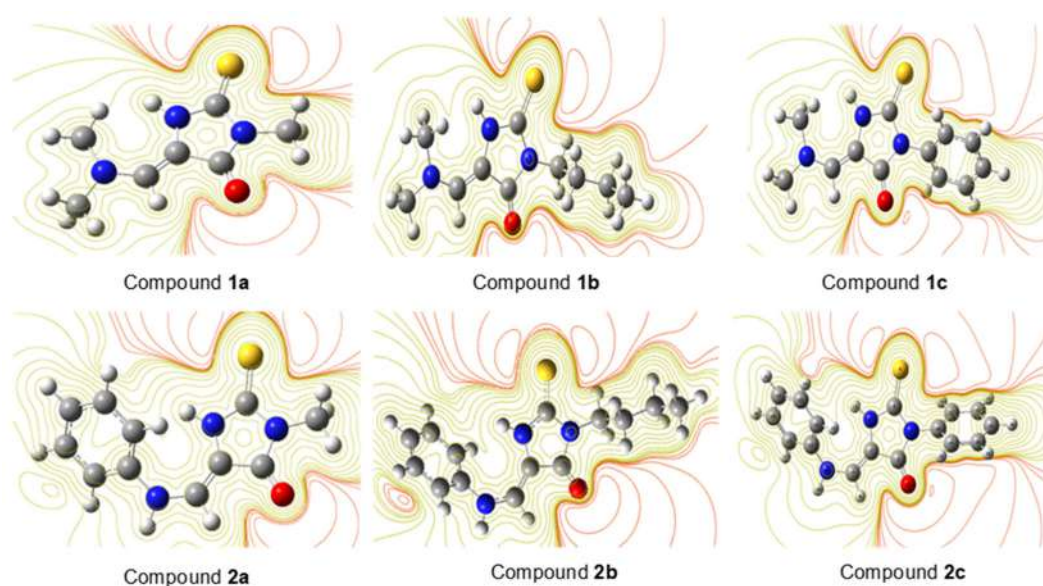


Fig 3. Molecular electrostatic potential maps calculated at B3LYP/6-311G (d,p) level

Table 5. Biological activity of ligands **2a-c** predicted by Pass Online

Compound 2a			Compound 2b			Compound 2c		
Biological activity	PA	PI	Biological activity	PA	PI	Biological Activity	PA	PI
HMGCS2 expression enhancer	0.858	0.004	HMGCS2 expression enhancer	0.793	0.005	HMGCS2 expression enhancer	0.869	0.003
Chloride peroxidase inhibitor	0.712	0.009	Chloride peroxidase inhibitor	0.526	0.044	Chloride peroxidase inhibitor	0.740	0.007
N-methylhydantoinase (ATP-hydrolyzing) inhibitor	0.613	0.010	Antineurotic	0.563	0.085	Mcl-1 antagonist	0.672	0.005
Nicotinic $\alpha 2\beta 2$ receptor antagonist	0.642	0.039	Glutaminy-peptide cyclotransferase inhibitor	0.472	0.005	Antineoplastic (breast cancer)	0.554	0.014

downloaded from the RSCB protein database using the URL (<https://www.rcsb.org/>). The binding energy for ligands **2a-c** are listed in Table 6.

The **lig2** (**2b**) shows better binding energy to HMGCS protein, suggesting that phenyl substituent is better than methyl and butyl substituents in **lig1** (**2a**) and **lig2** (**2b**). Visualization is done on Discovery Studio [19] of **lig1** (**2a**), **lig2** (**2b**), and **lig3** (**2c**) and they are depicted in Fig. 4, 5 and 6, respectively. Despite the fact that the docking was carried out with the same active site, each ligand has interactions with different residues. In **lig1** (**2a**), Asn164 residue formed two conventional hydrogen bonds with nitrogen atoms labeled 4 and 15, exhibiting distances of 2.60 and 2.45 Å, respectively. Additionally, the phenyl substituent displayed two π -alkyl interactions with Ala165 and Lys243 residues, at distances of 4.84 and 4.14 Å, respectively. Furthermore, a carbon-hydrogen bond

Table 6. HMGCS expression enhancer predicted Pa and Pi by molecular docking

Ligand	Binding energy (kcal/mol)
lig1 (2a)	-6.5
lig2 (2b)	-6.2
lig3 (2c)	-7.1

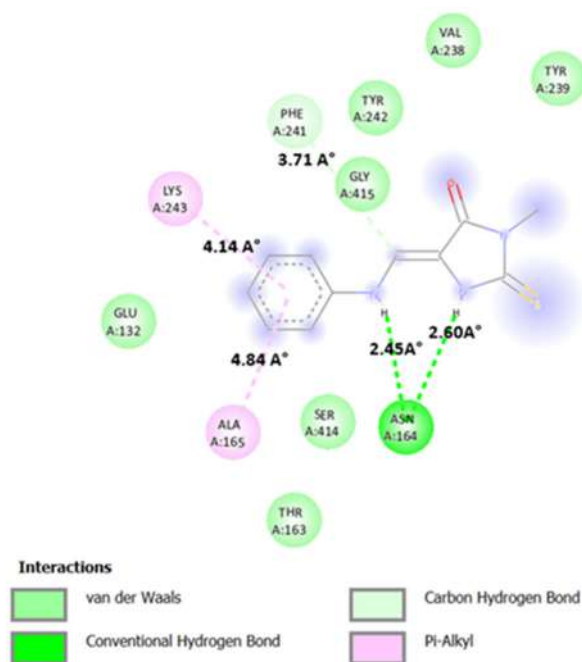


Fig 4. Molecular docking results of **lig1**-HMGCS2 complex

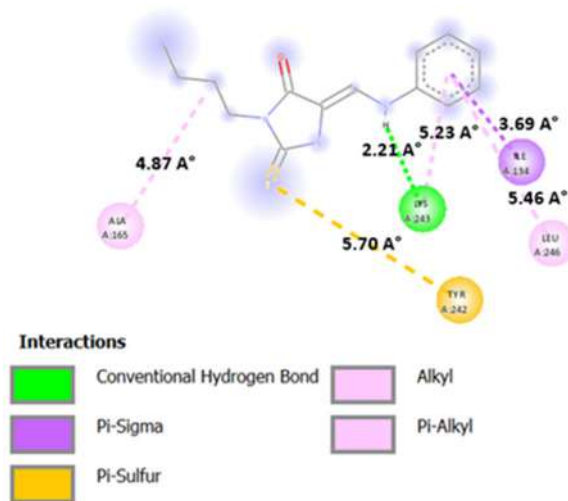


Fig 5. Molecular docking results of **lig2**-HMGCS2 complex

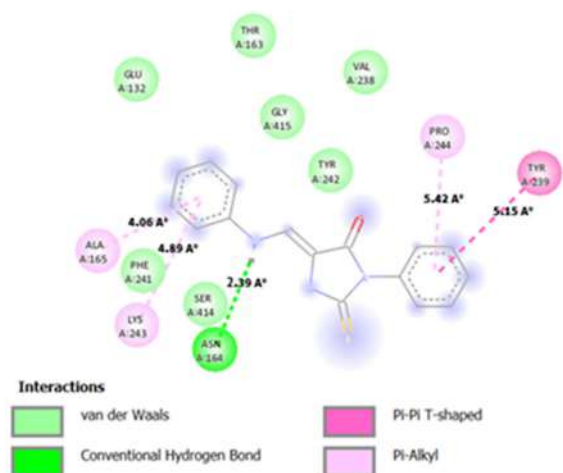


Fig 6. Molecular docking results of **lig3**-HMGCS2 complex

was observed between the carbon atom labeled 13 and Phe241 residue, with a favorable distance of 3.71 Å (Fig. 4).

In the case of **lig2** (**2b**), an alkyl interaction was established between the carbon atom labeled 27 and Ala165 residue, displaying a distance of 4.87 Å. Moreover, a pi-sulfur interaction occurred between Tyr242 and a sulfur atom labeled 7, with a distance of 5.70 Å. Lys243 residue exhibited both a conventional hydrogen bond and a π -alkyl interaction with the nitrogen atom and the phenyl group, respectively, at distances of 2.21 and 5.23 Å. Additionally, π -sigma and π -alkyl interactions were formed between the phenyl

group and residues of Ile134 and Leu246, featuring distances of 3.69 and 5.46 Å, respectively (Fig. 5).

For **lig3** (**2c**), the phenyl substituent engaged in both π -alkyl and π - π interactions with Pro244 and Tyr239, separated by distances of 5.42 and 5.15 Å, respectively. Furthermore, a conventional hydrogen bond formed between Asn164 and the nitrogen atom, with a distance of 2.39 Å. Two additional π -alkyl interactions were identified, involving the second phenyl group in the molecular structure and residues Lys243 and Ala165, with distances of 4.89 and 4.06 Å, respectively (Fig. 6).

■ CONCLUSION

In conclusion, the successful synthesis of 3-alkyl-5-phenylaminomethylene-2-thioxoimidazolidin-4-ones (**2a-c**) using microwave technology has been achieved with good yields. Structural confirmation was established through comprehensive NMR and MS spectroscopic analyses. Theoretical analysis of the electrostatic potential distribution within the compounds revealed distinct regions of electropositive and electronegative potential, aiding in the identification of donor and acceptor groups as well as charge transfer patterns and intramolecular contacts. Among the evaluated ligands, **lig2** exhibited the most favorable binding energy, indicating robust potential for meaningful interactions with the target protein. The **lig2** formed pivotal π -alkyl and π - π interactions with Pro244 and Tyr239, in conjunction with a conventional hydrogen bond involving Asn164. These interactions, coupled with the favorable binding energy, underscore the high affinity and strong molecular recognition between **lig2** and the binding site. While **lig1** displayed conventional hydrogen bonds with Asn164, along with π -alkyl interactions with Ala165 and Lys243, **lig3** demonstrated alkyl interaction with Ala165, pi-sulfur interaction with Tyr242, and both conventional hydrogen bond and π -alkyl interaction with Lys243. However, **lig2**'s superior binding energy positions it as a more promising candidate for forming a stable complex with the target protein. This highlights the potential of **lig2** as a lead compound or viable drug candidate in the realm of drug discovery and development. Continued exploration and optimization of **lig2** could further capitalize on its

favorable binding attributes, potentially paving the way for enhanced therapeutic efficacy.

■ ACKNOWLEDGMENTS

This work was carried out in the Synthesis and Catalysis Laboratory (LSCT) as part of PRFU projects (code: B00L01UN140120220002) funded by the Ministry of Higher Education and Scientific Research of Algeria. We thank Prof. Óscar López (University of Seville) for his support and assistance in conducting the MS analysis and Mr. Mokhtari Zohir Abdelhak (University Ibn Khaldoun-Tiaret) for his contribution in theoretical NMR calculation.

■ AUTHOR CONTRIBUTIONS

Khedidja Merdja and Mansour Debdab wrote the paper and conducted the experiment, Mokhtaria Drissi and Farah Kaouche conducted the DFT calculations, Mustapha Rahmouni El Habib Belarbi revised the manuscript, Choukry Kamel Bendeddouche conducted the NMR experiment, Nassima Medjahed, and José Manuel Padrón conducted the MS experiment. All authors agreed to the final version of this manuscript.

■ REFERENCES

- [1] Banerjee, P., Mandhare, A., and Bagalkote, V., 2022, Marine natural products as source of new drugs: An updated patent review (July 2018-July 2021), *Expert Opin. Ther. Pat.*, 32 (3), 317–363.
- [2] Debdab, M., Carreaux, F., Renault, S., Soundararajan, M., Fedorov, O., Filippakopoulos, P., Lozach, O., Babault, L., Tahtouh, T., Baratte, B., Ogawa, Y., Hagiwara, M., Eisenreich, A., Rauch, U., Knapp, S., Meijer, L., and Bazureau, J.P., 2011, Leucettines, a class of potent inhibitors of cdc2-like kinases and dual specificity, tyrosine phosphorylation regulated kinases derived from the marine sponge leucettamine B: Modulation of alternative pre-RNA splicing, *J. Med. Chem.*, 54 (12), 4172–4186.
- [3] Najmi, A., Javed, S.A., Al Bratty, M., and Alhazmi, H.A., 2022, Modern approaches in the discovery and development of plant-based natural products and their analogues as potential therapeutic agents,

- Molecules*, 27 (2), 349.
- [4] Sengupta, S., Pabbaraja, S., and Mehta, G. 2023., C–H modification of natural products: A minimalist enabling tactic for drug discovery, API processing and bioconjugation, *Chem. Commun.*, 59 (62), 9445–9456.
- [5] Nicolaou, K.C., and Rigol, S., 2020, Perspectives from nearly five decades of total synthesis of natural products and their analogues for biology and medicine, *Nat. Prod. Rep.*, 37 (11), 1404–1435.
- [6] Debdab, M., Renault, S., Lozach, O., Meijer, L., Paquin, L., Carreaux, F., and Bazureau, J.P., 2010, Synthesis and preliminary biological evaluation of new derivatives of the marine alkaloid leucettamine B as kinase inhibitors, *Eur. J. Med. Chem.*, 45 (2), 805–810.
- [7] Keel, K.L., and Tepe, J.J., 2020, The preparation of (4*H*)-imidazol-4-ones and their application in the total synthesis of natural products, *Org. Chem. Front.*, 7 (20), 3284–3311.
- [8] Cho, S., Kim, S.H., and Shin, D., 2019, Recent applications of hydantoin and thiohydantoin in medicinal chemistry, *Eur. J. Med. Chem.*, 164, 517–545.
- [9] de Carvalho, P.G.C., Ribeiro, J.M., Garbin, R.P.B., Nakazato, G., Yamada Ogatta, S.F., de Fátima, Â., de Lima Ferreira Bispo, M., and Macedo, F., 2020, Synthesis and antimicrobial activity of thiohydantoin derivatives obtained from L-amino acids, *Lett. Drug Des. Discovery*, 17 (1), 94–102.
- [10] Li, Y., Zhang, T., Ma, H., Xu, L., Zhang, Q., He, L., Jiang, J., Zhang, Z., Zhao, Z., Wang, M., and Wang, M., 2023, Design, synthesis, and antifungal/antioomycete activity of thiohydantoin analogues containing spirocyclic butenolide, *J. Agric. Food Chem.*, 71 (16), 6249–6267.
- [11] Elhady, H.A., Mohammed, S.M., Al-Shareef, H.F., and El-Mekawy, R.E., 2019, Synthesis, reactions, and applications of 2-thiohydantoin derivatives, *Acta Pol. Pharm.*, 76 (6), 971–986.
- [12] Hsu, M.H., Hsieh, C.Y., Kapoor, M., Chang, J.H., Chu, H.L., Cheng, T.M., Hsu, K.C., Lin, T.E., Tsai, F.Y., and Horng, J.C., 2020, Leucettamine B analogs and their carborane derivative as potential anti-cancer agents: Design, synthesis, and biological evaluation, *Bioorg. Chem.*, 98, 103729.
- [13] Khodair, A.I., El-Barbary, A.A., Imam, D.R., Kheder, N.A., Elmalki, F., and Ben Hadda, T., 2021, Synthesis, antiviral, DFT and molecular docking studies of some novel 1,2,4-triazine nucleosides as potential bioactive compounds, *Carbohydr. Res.*, 500, 108246.
- [14] Bendeddouche, C.K., Adjdir, M., and Benhaoua, H., 2016, Stereoselective cyclopropanation under solvent free conditions: Catalyzed by a green and efficient recyclable Cu-exchanged bentonite, *Lett. Org. Chem.*, 13 (3), 217–223.
- [15] Bendeddouche, S., Bendeddouche, C.K., and Benhaoua, H., 2021, A Convenient stereoselective method for synthesis of β -lactams under microwave irradiation with [BmIm] OH as a reusable ionic liquid, *Lett. Org. Chem.*, 18 (12), 929–935.
- [16] Chérouvrier, J.R., Carreaux, F., and Bazureau, J.P., 2002, A practical and eco-friendly synthesis of stereo controlled alkylaminomethylidene derivatives of 2-thiohydantoin by dimethylamine substitution, *Tetrahedron Lett.*, 43 (48), 8745–8749.
- [17] Kourat, O., Djafri, A., Benhalima, N., Megrouss, Y., Belkafouf, N.E.H., Rahmani, R., Daran, J.C., Djafri, A., and Chouaih, A., 2020, Synthesis, crystal structure, Hirshfeld surface analysis, spectral characterization, reduced density gradient and nonlinear optical investigation on (*E*)-*N'*-(4-nitrobenzylidene)-2-(quinolin-8-yloxy) acetohydrazide monohydrate: A combined experimental and DFT approach, *J. Mol. Struct.*, 1222, 128952.
- [18] Metwally, M.A., and Abdel-Latif, E., 2012, Thiohydantoin: Synthetic strategies and chemical reactions, *J. Sulfur Chem.*, 33 (2), 229–257.
- [19] Osyandin, V.A., Korzhenko, K.S., Rashchepkina, D.A., Osipov, D.V., and Klimochkin, Y.N., 2021, Nucleophilic vinylic substitution in perfluoroacylchromenes. Diastereoselective synthesis of push–pull enamino ketones, *Russ. J. Org. Chem.*, 57 (7), 1053–1062.
- [20] Frisch, M.J., Trucks, G.W., Schlegel, H.B., Scuseria, G.E., Robb, M.A., Cheeseman, J.R., Scalmani, G.,

- Barone, V., Mennucci, B., Petersson, G.A., Nakatsuji, H., Caricato, M., Li, X., Hratchian, H.P., Izmaylov, A.F., Bloino, J., Zheng, G., Sonnenberg, J.L., Hada, M., Ehara, M., Toyota, K., Fukuda, R., Hasegawa, J., Ishida, M., Nakajima, T., Honda, Y., Kitao, O., Nakai, H., Vreven, T., Montgomery, Jr., J.A., Peralta, J.E., Ogliaro, F., Bearpark, M., Heyd, J.J., Brothers, E., Kudin, K.N., Staroverov, V.N., Kobayashi, R., Normand, J., Raghavachari, K., Rendell, A., Burant, J.C., Iyengar, S.S., Tomasi, J., Cossi, M., Rega, N., Millam, J.M., Klene, M., Knox, J.E., Cross, J.B., Bakken, V., Adamo, C., Jaramillo, J., Gomperts, R., Stratmann, R.E., Yazyev, O., Austin, A.J., Cammi, R., Pomelli, C., Ochterski, J.W., Martin, R.L., Morokuma, K., Zakrzewski, V.G., Voth, G.A., Salvador, P., Dannenberg, J.J., Dapprich, S., Daniels, A.D., Farkas, O., Foresman, J.B., Ortiz, J.V., Cioslowski, J., and Fox, D.J., 2009, *Gaussian 09, Revision A.02*, Gaussian, Inc., Wallingford CT.
- [21] Dennington, R., Keith, T.A., and Millam, J.M., 2009, *GaussView*, Version 5, Semichem Inc., Shawnee Mission, KS.
- [22] Raczyńska, E.D., Gal, J.F., Maria, P.C., Sakhawat, G.S., Fahim, M.Q., and Saeidian, H., 2022, Nitriles with high gas-phase basicity—Part II Transmission of the push-pull effect through methylenecyclopropene and cyclopropenimine scaffolds intercalated between different electron donor(s) and the cyano *N*-protonation site, *Molecules*, 27 (14), 4370.
- [23] Eberhardt, J., Santos-Martins, D., Tillack, A Forli, S., 2021, AutoDock Vina 1.2.0: New docking methods, expanded force field, and python bindings, *J. Chem. Inf. Model.*, 61 (8), 3891–3898.
- [24] Boukabcha, N., Direm, A., Drissi, M., Megrouss, Y., Khelloul, N., Dege, N., Tuna, M., and Chouaih, A., 2021, Synthesis, structural determination, Hirshfeld surface analysis, 3D energy frameworks, electronic and (static, dynamic) NLO properties of *o*-Nitroacetanilide (*o*-NAA): A combined experimental and quantum chemical study, *Inorg. Chem. Commun.*, 133, 108884.
- [25] Mollaamin, F., and Monajjemi, M., 2023, Molecular modelling framework of metal-organic clusters for conserving surfaces: Langmuir sorption through the TD-DFT/ONIOM approach, *Mol. Simul.*, 49 (4), 365–376.
- [26] Suresh, C.H., Remya, G.S., and Anjalikrishna, P.K., 2022, Molecular electrostatic potential analysis: A powerful tool to interpret and predict chemical reactivity, *WIREs Comput. Mol. Sci.*, 12 (5), e1601.
- [27] Nehra, N., Tittal, R.K., and Ghule, V.D., 2021, 1,2,3-Triazoles of 8-hydroxyquinoline and HBT: Synthesis and studies (DNA binding, antimicrobial, molecular docking, ADME, and DFT), *ACS Omega*, 6 (41), 27089–27100.
- [28] Singh, J.S., Khan, M.S., and Uddin, S., 2023, A DFT study of vibrational spectra of 5-chlorouracil with molecular structure, HOMO–LUMO, MEPs/ESPs and thermodynamic properties, *Polym. Bull.*, 80 (3), 3055–3083.
- [29] Li, D.D., and Greenfield, M.L., 2014, Chemical compositions of improved model asphalt systems for molecular simulations, *Fuel*, 115, 347–356.
- [30] Mulliken, R.S., 1962, Criteria for the construction of good self-consistent-field molecular orbital wave functions, and the significance of ICAO-MO population analysis, *J. Chem. Phys.*, 36 (12), 3428–3439.
- [31] Rigby, J., and Izgorodina, E.I., 2013, Assessment of atomic partial charge schemes for polarisation and charge transfer effects in ionic liquids, *Phys. Chem. Chem. Phys.*, 15 (5), 1632–1646.
- [32] Drissi, M., Benhalima, N., Megrouss, Y., Rachida, R., Chouaih, A., and Hamzaoui, F., 2015, Theoretical and experimental electrostatic potential around the *m*-nitrophenol molecule, *Molecules*, 20 (3), 4042–4054.
- [33] Abraham, C.S., Prasana, J.C., Muthu, S., Rizwana B, F., and Raja, M., 2018, Quantum computational studies, spectroscopic (FT-IR, FT-Raman and UV–Vis) profiling, natural hybrid orbital and molecular docking analysis on 2,4 Dibromoaniline, *J. Mol. Struct.*, 1160, 393–405.
- [34] Guediri, A., Bouguettoucha, A., Chebli, D., Chafai, N., and Amrane, A., 2020, Molecular dynamic simulation and DFT computational studies on the

- adsorption performances of methylene blue in aqueous solutions by orange peel-modified phosphoric acid, *J. Mol. Struct.*, 1202, 127290.
- [35] Politzer, P., and Murray, J.S., 2021, Electrostatic potentials at the nuclei of atoms and molecules, *Theor. Chem. Acc.*, 140 (1), 7.
- [36] Filimonov, D.A., Lagunin, A.A., Glorizova, T.A., Rudik, A.V., Druzhilovskii, D.S., Pogodin, P.V., and Poroikov, V.V., 2014, Prediction of the biological activity spectra of organic compounds using the PASS online web resource, *Chem. Heterocycl. Compd.*, 50 (3), 444–457.